Study and optimization of cooling conditions of titanium alloy parts manufactured by superplastic forming process

Maxime Rollin

▶ **To cite this version:**

Maxime Rollin. Study and optimization of cooling conditions of titanium alloy parts manufactured by superplastic forming process. Materials. Ecole des Mines d'Albi-Carmaux, 2021. English. NNT : 2021EMAC0003 . tel-04213361

HAL Id: tel-04213361
https://theses.hal.science/tel-04213361

Submitted on 21 Sep 2023

HAL is a multi-disciplinary open access archive for the deposit and dissemination of scientific research documents, whether they are published or not. The documents may come from teaching and research institutions in France or abroad, or from public or private research centers.

L'archive ouverte pluridisciplinaire **HAL**, est destinée au dépôt et à la diffusion de documents scientifiques de niveau recherche, publiés ou non, émanant des établissements d'enseignement et de recherche français ou étrangers, des laboratoires publics ou privés.

Université Fédérale

Toulouse Midi-Pyrénées

THÈSE

en vue de l'obtention du

DOCTORAT DE L'UNIVERSITÉ DE TOULOUSE

délivré par

IMT – École Nationale Supérieure des Mines d'Albi-Carmaux

---

présentée et soutenue par

Maxime ROLLIN

le 04 Fevrier 2021

Study and Optimization of Cooling Conditions of Titanium Alloy Parts Manufactured by Superplastic Forming Process

---

École doctorale et discipline ou spécialité :
MEGEP : Génie mécanique, mécanique des matériaux

Unité de recherche :
Institut Clément Ader, UMR CNRS 5312, IMT Mines Albi

Directeurs de thèse :
Luc Penazzi, Maitre-Assistant, IMT Mines Albi, *(Directeur)*
Vincent Velay, Maitre-Assistant, IMT Mines Albi, *(Co-directeur)*

Autres membres du jury :
Sandrine Thuillier, Professeur, Univ. Bretagne Sud, Lorient, *(Présidente)*
Jean-Michel Bergheau, Professeur, ENISE, Saint-Etienne, *(Rapporteur)*
Donato Sorgente, Ass. Prof., Univ. degli Studi della Basilicata, Potenza, Italie, *(Rapporteur)*
Michel Bellet, Professeur, Mines ParisTech, Sophia-Antipolis, *(Examinateur)*
Frédéric Deschaux-Beaume, Professeur, Univ. de Montpellier, *(Examinateur)*
Thomas Pottier, Maitre-Assistant, IMT Mines Albi, *(Encadrant)*
Thierry Sentenac, Professeur, IMT Mines Albi, *(Invité)*
Alain Dupuy, Ingénieur, Airbus, Toulouse, *(Invité)*
Sylvie Gallet, Ingénieure, Airbus, Toulouse, *(Invitée)*

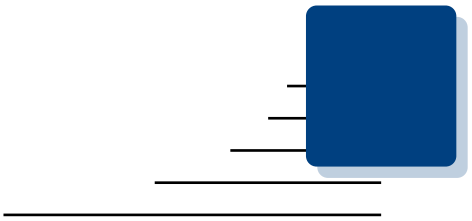

Remerciements

Nous sommes aujourd'hui le dimanche 20 Juin 2021, en plein Euro 2020, 7 années après avoir commencé à travailler sur une thèse censée se terminer en 2018, Einstein avait raison, le temps se dilate.

Je me souviens avoir échangé avec mes directeurs de thèses au démarrage « officiel » de ma thèse (en mai 2018). Nous évoquions le fait qu'il arrive parfois que le temps nécessaire pour finaliser une thèse dépasse les trois années imparties. J'avais dit à l'époque « Je ne ferai pas un jour de plus !! »... Oups Effectivement, j'avais commencé à travailler sur le sujet de la thèse depuis le mois d'avril 2014 en tant qu'intérimaire à AIRBUS. Les lenteurs administratives pour l'obtention de la convention CIFRE m'ont conduit à travailler en tant qu'ingénieur recherche à l'Institut Clément Ader (ICA) pour «combler les trous» avant le démarrage officiel de la thèse. J'avais donc déjà travaillé plus d'un an avant même de commencer. Voilà pourquoi il était hors de question de rallonger encore plus la durée de cette thèse.

Je tiens à remercier Thierry Cutard, jadis directeur du Laboratoire de l'ICA-Albi, pour m'avoir accueilli au sein du laboratoire, mais également pour m'avoir permis une continuité d'activité. Je remercie également l'ensemble des membres du jury présents pour ma soutenance ce 4 février 2021. Premièrement, merci d'avoir pris le temps nécessaire et non négligeable pour lire ce « pavé », mais également pour les discussions qui en ont découlées. Merci à Sandrine Thuillier, Professeur à l'Université Bretagne Sud de Lorient pour avoir accepté de présider le jury de cette thèse. Merci à Jean-Michel Bergheau professeur à l'ENISE et Donato Sorgente assistant professeur à l'Université degli Studi della Basilicata à Potenza (Italie) pour avoir rapporté ce travail. Pour finir, je remercie Frédéric Deschaux-Beaume Professeur à l'Université de Montpellier, et Michel Bellet, professeur à l'école des Mines ParisTech à Sophia-Antipolis pour avoir examiné ce travail.

Je souhaite également remercier Alain Dupuy, Sylvie Gallet, et César Garnier, tous trois travaillant aux méthodes de l'usine d'AIRBUS Saint Eloi au moment des faits, pour avoir participé à ma soutenance et pour leur accompagnement sur ces longues années. Je souhaite particulièrement remercier Alain pour son soutien professionnel et humain. Concernant AIRBUS, je suis bien entendu reconnaissant d'avoir pu réaliser ma thèse dans cette entreprise, tant sur le plan scientifique et industriel que pour la formation qu'une thèse CIFRE peut apporter pour la suite. Je tiens aussi à remercier toutes les personnes de Saint Eloi qui ont pu de près ou de loin contribuer à ce travail.

Je remercie chaleureusement l'ensemble de mes encadrants pour m'avoir accompagné depuis 2014. Merci, Luc Penazzi, mon directeur de thèse, pour avoir pleinement joué ton rôle du premier jusqu'au dernier jour. Par ton recul scientifique, ton abnégation, ta rigueur, et tout l'investissement que tu as mis dans ton suivi (même avant 6 h du matin, parfois le weekend, les jours fériés...), tu m'as permis d'arriver à ce résultat. Merci à Vincent Velay, mon co-directeur. Tu as été parfait dans ton rôle. Lors de ma première visite, Serge m'avait dit : « Tu es avec Dédé tronche plate ? Tu as de la chance mon petit ». Je n'avais pas tout compris, mais je pense qu'il avait raison. Merci également à Thierry Sentenac et Thomas Pottier, mes deux derniers encadrants dans cette équipe de quatre. Vous avez été présents entre autres sur la partie thermique, qui n'était pas forcément ce que je préférais au premier abord. Cependant, vos critiques, justes et pertinentes, m'ont poussé à aller plus loin sur cette problématique complexe des échanges thermiques.

Au-delà des membres qui ont encadré cette thèse, je souhaite remercier tout un écosystème de personnes de l'ICA qui m'a apporté son aide. Je pense à Thomas Papaix pour les essais mécaniques, tout comme Aurélien Mazzoni pour les essais mécaniques et thermiques. Je remercie également Rémi Gilblas qui m'a été d'un grand support pour la mise en place et l'exploitation des mesures sans contact pour les essais de refroidissement. Merci à Jean-Michel Mouys et Fabrice Rossi pour leur support en électronique et sur la mise en place des essais. Merci à Serge Tovar pour son expertise en analyse métallurgique, mais également pour tous nos fous rires. Merci également à Medhi Salem, toujours disponible pour discuter des questions du moment où pour venir accompagner un échange philosophique en salle MEB. Pour finir, j'ai n'ai pas été un membre « permanent» des doctorants du laboratoire car partagé entre Toulouse où je vivais et travaillais en partie sur le site d'AIRBUS Saint-Eloi et Albi. Je n'ai donc pas participé à autant de choses qu'il aurait été possible. Cependant, j'ai vraiment apprécié cette ambiance quasi familiale au sein du laboratoire. Merci à tous les doctorants avec qui j'ai partagé ces moments, ils se reconnaîtront !

Concernant ma famille, ma belle-famille, et l'ensemble de mes proches, je ne vous remercierai pas pour la technique. Presque aucun d'entre vous n'était capable de dire sur quoi je travaillais. La seule chose qui vous intéressait c'était « quand est-ce-que tu la termines ta thèse qu'on boive un coup». Je vous remercie plutôt pour le soutien dont vous avez-fait preuve lorsque nous avons dû faire face à certains « tracas » de la vie. Pour le reste, c'est personnel, donc pas de commentaire.

Je souhaite dédier cette thèse à tous mes proches et particulièrement à mon grand-père parti il y a peu.

Résume détaillé en français

Cette thèse de doctorat a été réalisée au sein de l'institut Clément Ader (UMR CNRS 5312) d'Albi pour la division des avions commerciaux d'AIRBUS avec le site.

Contexte, problématiques et objectifs

Le procédé de formage superplastique (SPF) consiste en une opération de formage à haute température de tôles minces de métal par gonflage. Les alliages dits superplastiques utilisés pour ce procédé permettent un allongement très important dans des conditions de mise en forme particulières: température élevée et faibles vitesses de déformation. Dans ces conditions, le matériau présente une sensibilité à la vitesse de déformation (SRS) très élevée qui limite les phénomènes localisés de strictions et plus globalement l'amincissement local des pièces formées. Ce procédé permet de former des géométries complexes en une seule étape avec un rapport buy-to-fly intéressant. Chez AIRBUS, le procédé SPF est utilisé pour former les pièces complexes de carénage du mât réacteur et les cloisons de renfort d'entrées d'air des nacelles en alliages de titane Ti-6Al-4V (Ti-64) et Ti-6Al-2Sn-4Zr-2Mo (Ti-6242).

La plupart des pièces sont produites sur des presses équipées de robots de chargement et de déchargement automatiques telles que représenté dans la Figure 1a. Ces robots possèdent des bras qui attrapent le cadre de manutention sur lequel la pièce est fixée avant l'enfournement. La Figure 1b montre une tôle fixée sur un cadre avant l'enfournement avec un zoom sur une des fixations par un système de goupille. Avant de démouler la pièce, elle est refroidie grâce à un système de soufflage d'air associé au robot de manutention qui permet de rigidifier la pièce et de faciliter l'opération de démoulage tel que présenté dans la Figure 1a. En effet, les alliages Ti-64 et Ti-6242 présentent des propriétés mécaniques très basses à la température de mise en forme qui implique que les pièces soient refroidies pour être manipulées. Ensuite, la pièce est refroidie à l'extérieur de la presse jusqu'à la température ambiante.

Cependant, les pièces finales obtenues après détourage laser peuvent parfois présenter des distorsions. Ceci est une conséquence des opérations de refroidissement et de défournement de la pièce après mise en forme qui produisent des déformations plastiques et une accumulation de contraintes résiduelles libérées lors de l'étape de détourage. Ces distorsions présentent un problème majeur en raison de la difficulté et du temps nécessaire pour les faire corriger par les chaudronniers.

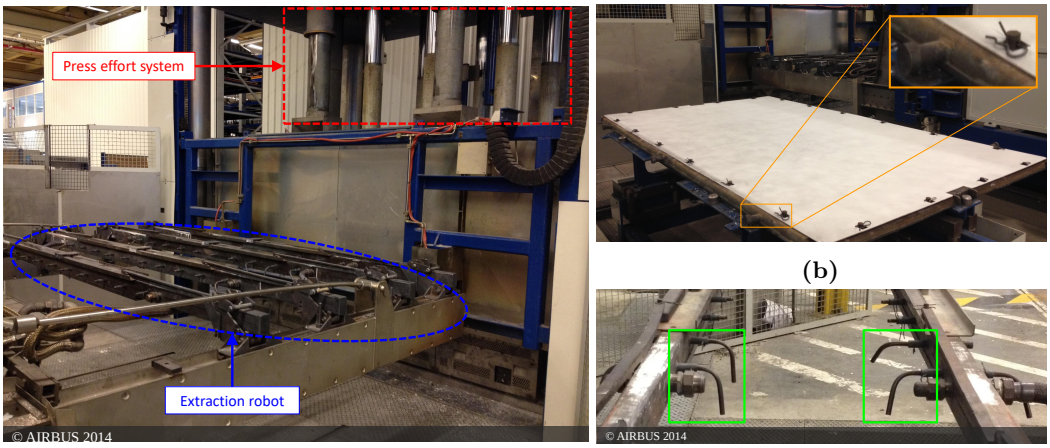

Figure 1 – Environnement presse: (a) presse fermée et robot d'extraction, (b) tôle préparée au Nitrure de Bore fixée sur un cadre de chargement, (c) zoom sur des buses de soufflage

L'objectif de cette thèse est d'optimiser les opérations de refroidissement et de défournement des pièces après l'opération de formage afin de minimiser les étapes de chaudronnerie nécessaires pour reprendre les distorsions géométriques. L'utilisation de la méthode par éléments finis (MEF) avec le logiciel ABAQUS® a été choisie pour reproduire les sollicitations thermomécaniques subies par les pièces lors des étapes de refroidissement et de défournement. Un enjeu de la thèse est de savoir modéliser les conditions limites (CL) thermiques et mécaniques complexes, hétérogènes et variables au cours des différentes phases du défournement combinées à l'évolution du comportement thermomécanique du matériau. Un tel modèle nous permettrait d'obtenir les déformations plastiques et les contraintes résiduelles accumulées tout au long du processus de fabrication pour une stratégie de refroidissement donnée, pour ensuite être capable de l'optimiser.

Dans la thèse, l'étude s'est concentrée sur la fabrication d'une portion de la cloison avant de l'entrée d'air des nacelles de l'avion A350-900 en alliage de titane Ti-64. Deux premières étapes de caractérisation ont été réalisées, une sur le comportement du matériau de l'alliage Ti-64 et une seconde sur les CL thermiques rencontrés par la pièce au cours de son défournement. Ces deux étapes visaient à définir les équations et paramètres des lois à implémenter dans une simulation du procédé par MEF. La dernière étape de la thèse a consisté à construire un modèle numérique sur le logiciel ABAQUS® capable de reproduire les distorsions de façon à pouvoir les minimiser.

Modélisation du comportement matériau

L'étude du comportement du matériau avait pour objectif de construire une loi rhéologique capable de reproduire le bon état de déformation et de contrainte en fonction de paramètres macroscopiques tels que la température, la vitesse de déformation, la déformation, etc. Le procédé de formage et de défournement des pièces implique une très grande plage de température (20-870 °C), des vitesses de refroidissement élevées et hétérogènes (0-20 $°C.s^{-1}$) et des grandes déformations (jusqu'à 50 %). Cela implique un large spectre de mécanismes de déformation dans diverses conditions de microstructure qui ont rendu très complexes les investigations expérimentales.

État de l'art

Un état de l'art concernant les comportements matériaux a été réalisé pour l'ensemble des conditions opératoires mises en jeux lors du procédé. La littérature a mentionné l'importance de la microstructure (initiale et son évolution), des chargements thermiques (températures et vitesses de refroidissement) sur les mécaniques de déformation actifs et les lois de comportements associées. Un couplage probable et non-trivial existe entre les conditions de formage, les conditions de refroidissement et les propriétés mécaniques instantanées des tôles. Pour ces raisons, mais également du fait d'un nombre élevé de paramètres et conditions de sollicitations thermo-mécaniques, des essais préliminaires ont été réalisés.

Essais Préliminaires

Plusieurs sessions d'essais préliminaires ont été réalisées pour comprendre l'influence des différents paramètres du procédé afin de discriminer les paramètres de premier ordre dans la modélisation du comportement du matériau. Une première session d'essais a visé à tester l'influence du formage superplastique sur la microstructure du matériau au travers du temps de maintien à la température de formage. Ces essais (présentés dans l'annexe A.2.1) ont confirmé la forte influence du temps de maintien sur la croissance de la taille des grains.

Suite à cela, l'influence de l'augmentation de cette taille de grain sur les propriétés mécaniques a été analysée pour un temps de maintien court (5 min) et un temps de maintien de 100 min correspondant à une opération de formage classique (chauffage et formage). Différents chargements mécaniques ont été testés à l'issue de ces deux temps de maintien à une température de 650 °C (intermédiaire dans la gamme de température). Pour atteindre la température d'essais de 650 °C, deux vitesses de refroidissement (5 °C/s et 15 °C/s) ont été testées de façon à également évaluer son effet. Les résultats de contraintes d'écoulement en fonction de la vitesse de déformation pour les différents essais de tractions-fluage (présentés dans la Figure 2) ont mis en évidence l'influence significative de la croissance de grain générée par le maintien à la température de formage sur les propriétés mécaniques. Au contraire, l'influence de la vitesse de refroidissement s'est avérée négligeable dans les conditions testées.

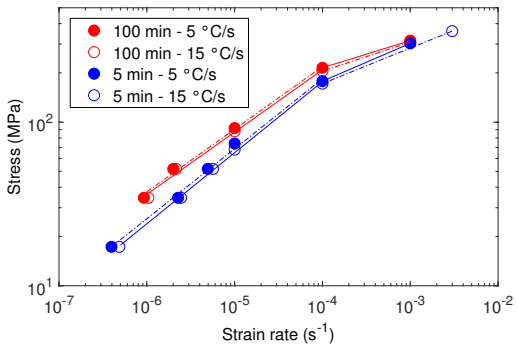

Figure 2 – Courbes log-log de la contrainte d'écoulement en fonction de la vitesse de déformation à 650 °C- influence de la vitesse de refroidissement et du temps de maintien à la température SPF

A l'issue de ces essais, une dernière session d'essais mécaniques a été réalisée sur la base des essais à 650 °C pour deux autres températures de façon à valider les phénomènes observés sur toute la plage de température. L'absence d'effets significatifs de la vitesse de refroidissement a également été observée pour les températures de 350 °C et 750 °C.

A l'issue de ces essais préliminaires, une procédure de traitement thermique (TTh) préalable aux essais de caractérisation a été définie. Elle a consisté en un maintien thermique de

100 minutes équivalent à la phase de chauffe et formage. Ensuite un seul et unique TTh composé d'une première vitesse lente (correspondant à la phase d'ouverture de la presse) suivie d'une vitesse plus rapide (correspondant à la phase de soufflage d'air) appliquée jusqu'à la température d'essai. De cette façon, l'effet du formage sur la croissance de grain est reproduit, et un TTh de refroidissement « moyen » est appliqué de façon à se rapprocher le plus possible du procédé bien que les vitesses de refroidissement n'aient pas démontré d'effet significatif sur le comportement mécanique.

Éssais de caractérisation

La procédure de caractérisation était composée de deux essais de traction complexes basés sur des étapes de traction-relaxation successives. Ces procédures ont été conçues pour être capables de reproduire les différents comportements rencontrés au cours du processus qui peuvent finalement affecter les distorsions telles que l'élasticité, la plasticité, la viscosité, la sensibilité à la vitesse de déformation, les comportements de durcissement et d'adoucissement des contraintes par restauration. La première procédure consistait en un essai de traction par saut de vitesse de déformation suivi d'une phase de relaxation. Le second consistait en deux essais de traction-relaxation consécutifs avec la première charge légèrement au-dessus de la limite d'élasticité estimée afin d'évaluer la limite d'élasticité vraie. L'ensemble des courbes d'essais de ces deux procédures est présenté dans la Figure 3.

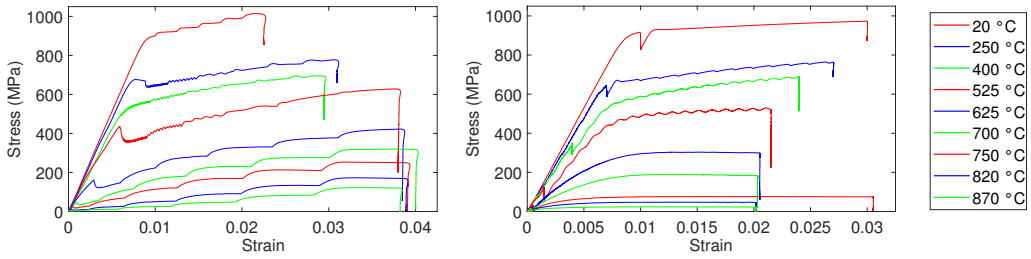

Figure 3 – Courbes contrainte-déformations: procédures d'essais (a) 1 and (b) 2

Les résultats de ces essais ont mis en évidence des comportements bien décrits dans la littérature pour certains, et plus singuliers pour d'autres. Une décroissance du module d'Young a bien été observée avec l'augmentation de la température avec une certaine variabilité pour les mesures effectuées aux différentes phases de charge-décharge des deux essais. Ensuite, une partie d'un essai de traction à très faible niveau de contrainte-déformation suivi d'une relaxation a permis d'évaluer précisément la limite d'élasticité réelle du matériau. Il est mis en évidence une forte décroissance de celle-ci avec la température jusqu'à atteindre une limite nulle pour les températures supérieures à 700 °C. Concernant la sensibilité aux vitesses de déformations, une augmentation globale a été observée avec la température pour conduire à une très forte sensibilité pour les températures supérieures à 700 °C pour lesquelles le matériau atteint un comportement parfaitement viscoplastique. Cependant, une forte non-linéarité de comportement est observée avec un minimum local de SRS pour des températures intermédiaires (aux alentours de 400 °C). Le comportement en écrouissage a quant à lui montré deux formes d'augmentation de la contrainte avec la déformation plastique. Pour les températures basses (inférieures à 500 °C) l'écrouissage est plutôt linéaire tandis que pour les températures « hautes » il est complètement de type Voce (exponentiel). Pour finir, les différentes portions de courbes de relaxations montrent clairement une augmentation de la vitesse de relaxation avec la température, et notamment une restauration quasi-total pour les températures supérieures à 700 °C.

Les résultats des deux types d'essais mis au point sur la gamme entière de température ont démontré des changements importants de comportement au cours du refroidissement. Ces changements n'interviennent pas tous aux mêmes températures. Une première transition de comportement affectant la limite d'élasticité, la SRS et la restauration interviennent autour de 700 °C. Une seconde transition affectant l'écrouissage et la SRS avec notamment une inversion du comportement de SRS se produit pour des températures intermédiaires (autour de 400 °C) pour ensuite reprendre pour les températures proches de la température ambiante.

Identification de la loi de comportement

Un modèle élasto-viscoplastique basé sur une loi sinus hyperbolique a été choisi pour reproduire la forte sensibilité aux vitesses de déformations tel que défini dans l'équation ci-dessous:

$$\dot{\bar{\varepsilon}}_p = \dot{\varepsilon}_0 \sinh\left(\beta\langle\sigma_v\rangle\right)^n \tag{1}$$

Un modèle phénoménologique de limite d'élasticité basé sur une évolution d'écrouissage-adoucissement isotrope a été utilisé pour reproduire les évolutions de comportements observées lors des phases de tractions et relaxations aux différentes températures présenté dans les équations ci-dessous:

$$\sigma_v = \overline{\sigma} - \sigma_y = \overline{\sigma} - (k + R) \tag{2}$$

$$\dot{R} = \left\{ \begin{array}{cc} b\left(R - Q\right)\dot{\bar{\varepsilon}}_p - \gamma R^c & \text{si } \overline{\sigma} > k \\ 0 & \text{si } \overline{\sigma} \leq k \end{array} \right\} \tag{3}$$

Les sept paramètres (trois pour la fonction de plasticité et quatre pour la limite d'élasticité) de ce modèle ont été identifiés température par température dans un premier temps. De cette façon, une esquisse d'évolution de ces paramètres avec la température a pu être générée. Ensuite, des fonctions d'interpolation ont été construites pour chacun des sept paramètres de façon à reproduire les transitions de comportements observées expérimentalement et également identifiables au travers de l'évolution des paramètres obtenus pour chaque température. Pour finir, les paramètres des fonctions d'interpolation ont été identifiés de façon globale en utilisant l'ensemble des courbes pour chaque température.

La méthode d'identification des paramètres pour chacune des étapes était basée sur un calcul explicite de l'évolution de la contrainte en fonction du temps, et une réduction de l'écart avec les courbes expérimentales. Des fonctions coûts spécifiques basées sur un calcul de l'écart quadratique ont été enrichies de façon à bien identifier l'effet des comportements thermo-mécaniques intervenant à différents moments de nos courbes d'essais. Plusieurs étapes ont été réalisées pour permettre l'identification des paramètres des fonctions d'interpolations. Des fonctions d'optimisations basées sur des algorithmes génétiques et des fonctions propres à Matlab de minimisation contraintes et non-contraintes (« fmincon » et « fminsearch ») ont été utilisées successivement pour obtenir un jeu de vingt-six paramètres pour les fonctions d'interpolation des paramètres de la loi viscoplastique. La Figure 4 représente ces fonctions d'interpolation sur la gamme de température du procédé. De plus, deux jeux de quatre paramètres permettent de modéliser l'évolution continue sur la gamme de températures du module d'Young et de la limite d'élasticité vraie.

Le modèle identifié reproduit assez bien le comportement du matériau non seulement au travers des courbes d'essais isothermes, mais aussi de manière anisotherme. En effet, des essais de traction simple et traction-relaxation anisothermes ont été réalisés à des températures critiques où le comportement et le modèle sont respectivement très variables et non linéaires. Le modèle, qui a été identifié en intégrant ces courbes d'essais, à plutôt bien répondu pour ces phases de sollicitations anisothermes telles qu'observées dans la Figure 5 pour les essais de traction à vitesse de déformation constante et pour différentes vitesses de refroidissement. Néanmoins une légère sous-estimation des contraintes a été observée, notamment pour les

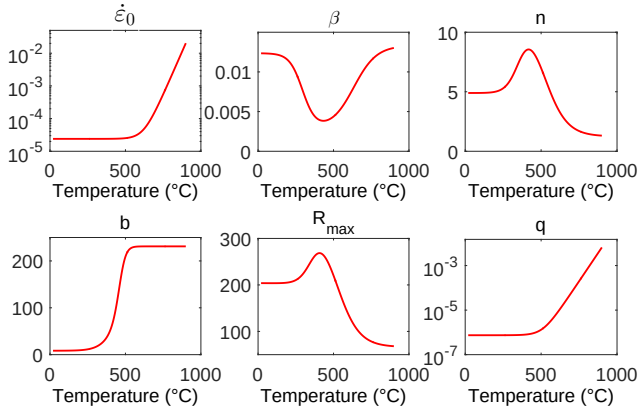

Figure 4 – Evolution des fonctions d'interpolation des paramètres du modèle

vitesses de refroidissement rapides depuis la température de formage. Ces écarts ont été attribués aux retards de transformation de phase $\beta \rightarrow \alpha$ qui interviennent lors des essais anisothermes à fortes vitesses de refroidissement.

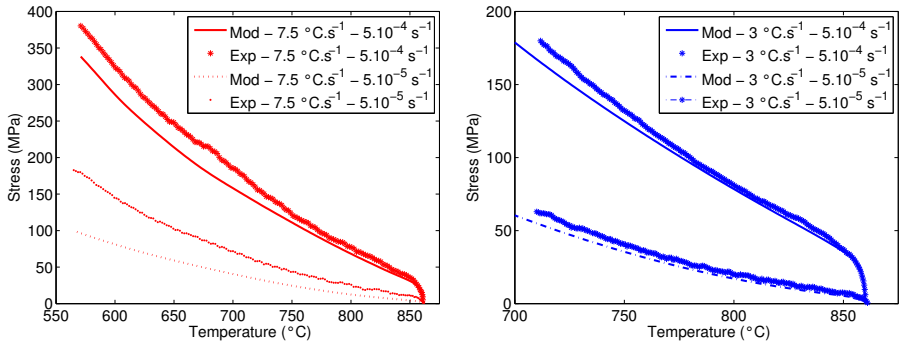

(a) **(b)**

Figure 5 – Essais anisothermes - comparaison des courbes expérimentales et du modèle: (a) 7.5 °C.s^{-1} and (b) 3 °C.s^{-1}

Modélisation des transferts thermiques

L'évolution de la température de la pièce est un aspect crucial dans la simulation du procédé. En effet, elle contrôle l'évolution du comportement du matériau, les contraintes thermiques produites par la dilatation du matériau et in-fine l'évolution des conditions de contact de la pièce avec le moule. Lors de l'opération de défournement, il existe une combinaison complexe de transferts thermiques (TT) qui contrôlent l'évolution de la température: les transferts radiatifs, la convection naturelle, la convection forcée et la conduction thermique aux interfaces de contact. Chaque mode de TT intervient à une phase spécifique du défournement comme illustré dans la Figure 6 qui décrit l'ensemble des différentes phases du procédé et les TT opérants. Cependant ils sont concomitants, ce qui rend leur caractérisation complexe.

État de l'art

Dans un premier temps, un état de l'art a été réalisé pour chacun des modes de TT de façon à établir les équations et paramètres permettant de les modéliser pour les différentes

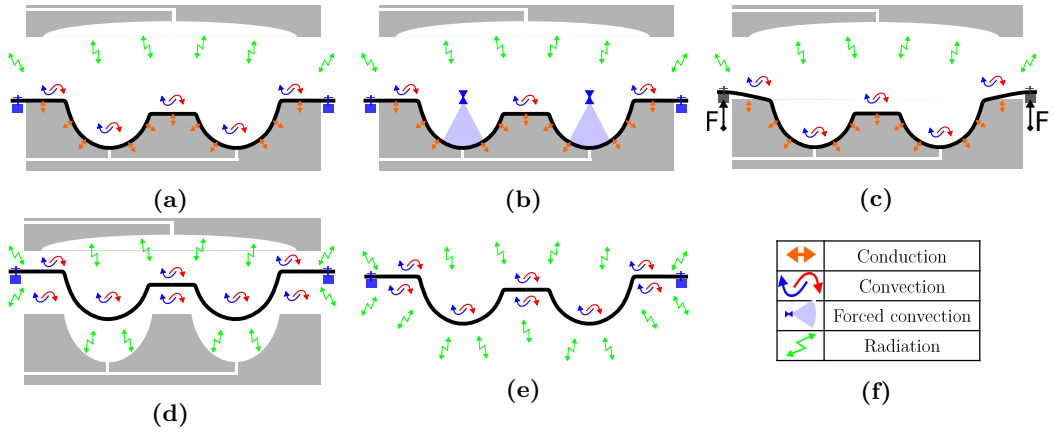

Figure 6 – Illustration des phases d'échanges thermiques: (a) Ouverture de la presse, (b) Soufflage, (c) Extraction, (d) Transfert, (e) Refroidissement extérieur et (f) légende

conditions opératoires du procédé. Trois paramètres ont une influence majeure: l'émissivité pour le rayonnement, le coefficient d'échange (ou de convection) pour la convection (naturelle et forcée) et le coefficient de conductance pour la conduction. Différentes lois associées à l'évolution de ces trois paramètres en fonction des paramètres du procédé (température, géométries, états de surface, oxydation etc.) ont été présentées. Aussi, différentes méthodes d'implémentation des conditions limites (CL) pour chaque mode de TT ont été discutées sur la base de travaux bibliographiques, mais également en lien avec le logiciel de modélisation ABAQUS® qui a été utilisé dans la thèse.

Conception des essais

La deuxième étape du travail a consisté à concevoir une procédure expérimentale afin de caractériser ou valider les différents paramètres des modèles de CL thermique à mettre en œuvre dans la simulation. Il a été choisi d'utiliser un outillage SPF industriel de petite échelle pour réaliser des essais de refroidissement plutôt que de réaliser des essais de laboratoire plus conventionnels pour chacun des modes de TT.

En effet, chacun des modes de TT nécessite un nombre important de paramètres à tester pour des conditions opératoires très larges. De plus, les conditions industrielles telles que l'état de surface des tôles (recouvertes de lubrifiant au nitrure de bore) déformées, les pressions de contact, les épaisseurs d'oxydes, etc., sont tellement variables et hétérogènes qu'il est difficile d'établir une plage de variation des paramètres à tester. De ce fait, Il aurait été très compliqué dans le cadre de la thèse de réaliser des essais de caractérisation pour chacun des modes de TT indépendamment.

C'est pourquoi il a été choisi de reproduire les conditions exactes de mise en forme pour se rapprocher au plus près des conditions industrielles. Pour se faire, un outillage de petite taille (450x500x110 mm) a été adapté et utilisé (Figure 7a) pour former plusieurs tôles sur une presse de 250 tonnes dans l'usine d'AIRBUS Saint-Eloi. L'ensemble de l'outillage et les tôles formées ont été utilisés pour reproduire les conditions de refroidissement dans un four de laboratoire équipé de différents moyens de mesure (Figure 7b). Diverses configurations expérimentales ont été définies de façon à isoler au maximum les modes de TT les uns des autres et faciliter leur caractérisation.

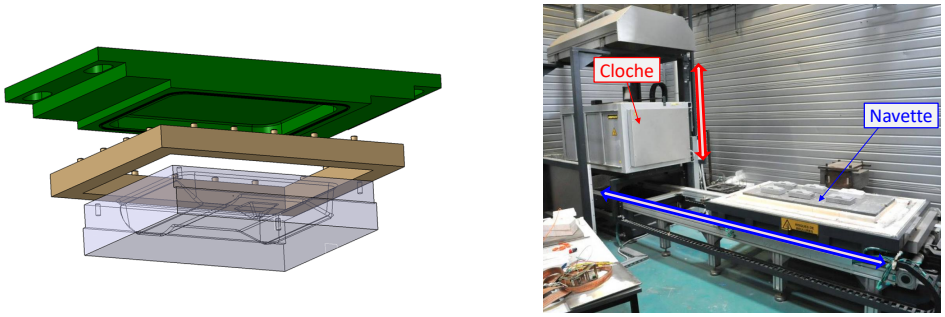

(a) (b)

Figure 7 – Essais de refroidissement: (a) CAO de l'outillage et (b) Four navette de l'ICA

Mesures expérimentales

Les différents essais ont consisté à chauffer les pièces dans un four équipé d'une cloche et d'une navette permettant de déplacer les pièces de façon automatisée vers une zone de mesure dans un environnement d'échange contrôlé tel que représenté dans la Figure 7b. La procédure d'essais a consisté à chauffer et maintenir les pièces aux températures de formage, puis déplacer la navette pour réaliser un refroidissement dans différentes conditions. Trois moyens différents de mesures ont été mis en place : des thermocouples, un pyro-réflectomètre et une caméra thermique. Le premier moyen permet une mesure de température vraie à des points d'intérêts, alors que les deux derniers permettent une mesure sans contact. Le pyro-réflectomètre a l'avantage de restituer une température vraie et une émissivité en un point alors que la caméra donne une mesure de champs de la température de luminances.

Un premier essai a consisté à valider la méthode expérimentale du point de vue du système four-navette et thermocouples, mais également pour la mesure sans contact. Aussi, il a permis de valider le bon repositionnement des tôles dans l'outillage. En effet, leur refroidissement post-formage aurait pu déformer les pièces et rendre difficile leur retour dans les conditions de contact post-formage.

Suite à cette validation, plusieurs essais mettant en jeu différentes configurations de pièces (moule, cadre et tôle) et de refroidissement ont été réalisés. Trois configurations ont été testées : le moule seul (Figure 8a), le cadre (surélevé) et la tôle (Figure 8b), et l'ensemble moule, cadre et tôle (Figure 8c). Les deux premières configurations ont permis de retirer voir limiter les échanges par conduction thermique avec la tôle (ou la surface de l'outillage), et donc de favoriser les échanges convecto-radiatif pour deux configurations de convection nettement différentes. La dernière configuration a été utilisée pour réaliser un refroidissement forcé avec une buse (de type industrielle) et deux refroidissements libres avec et sans couche de nitrure de bore sur la surface supérieure. Les conditions d'échanges radiatifs et convectifs pour la configuration moule cadre et tôle, étant proche de la configuration moule seul, ont permis de caractériser la convection forcée et la conduction.

Identification des modèles de conditions limites

Une méthode d'analyse inverse a été utilisée pour ajuster les paramètres des modèles des différentes CL. Des jumeaux numériques ont été construits sur la base des trois configurations testées. Les modèles de CL utilisés ont été tirés de la littérature, à l'exception du coefficient de convection naturelle.

Des simulations de dynamique des fluides (CFD) ont été réalisées avec ABAQUS® pour les configurations moule seul ou accompané du cadre et de la tôle. Des fonctions simples (constantes, linéaires ou bilinéaires) ont été utilisées pour modéliser l'évolution spatiale et

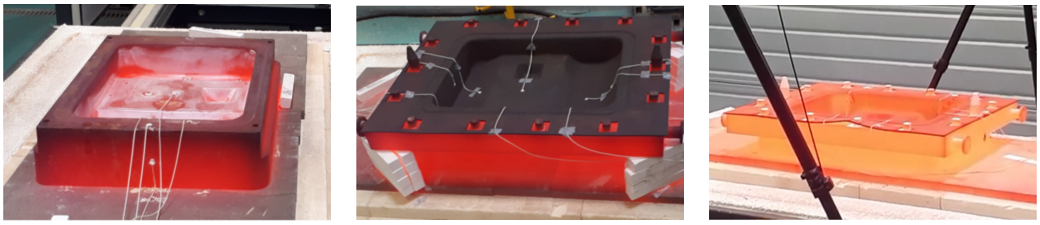

(a) (b) (c)

Figure 8 – Essais de refroidissement: configurations (a) moule seul (b) tôle et cadre et (c) moule cadre et tôle

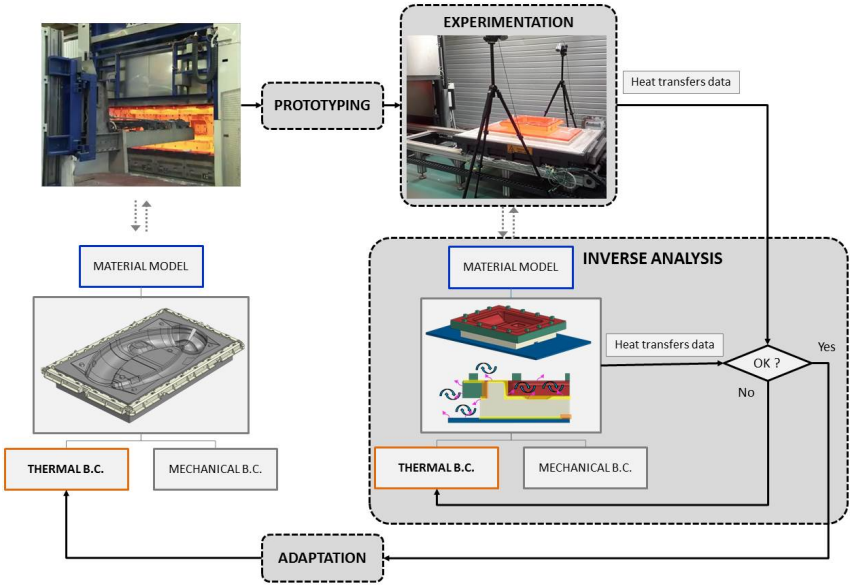

Figure 9 – Essais de refroidissement: méthode d'identification des conditions limites

temporelle des coefficients de convection sur la base des résultats des simulations CFD. Les modèles de CFD utilisés sont basés sur une résolution transitoire en fluide incompressible mettant en jeu un modèle de turbulence de type Reynolds Averaged Navier-Stokes (RANS) k-ω. La Figure 10a montre les résultats types obtenus pour une température d'outillage fixée dans en environnement à température ambiante. La distribution du coefficient de convection (Figure 10b) est extraite pour les surfaces considérées. Cette approche a tout d'abord été validée sur un cas simple de plaque horizontale et confrontée à des résultats de la littérature.

Les deux premières configurations d'essais ont été utilisées pour recaler les modèles de rayonnement et de convection, notamment pour valider les émissivités de l'outillage et de la tôle (également mesurées à froid par spectrométrie), mais également la méthode basée sur la CFD. La configuration moule, cadre et tôle avec le système de soufflage a été utilisée pour recaler les modèles de convection forcée et de conductance. Pour chacune des analyses inverses, une méthode itérative visant à tester dans un premier temps la justesse des modèles de CL issus de la littérature ou des caractérisations préliminaires, pour ensuite identifier les meilleurs paramètres par des analyses de sensibilité.

Les résultats de ces identifications ont permis de reproduire avec justesse l'évolution des courbes expérimentales de températures. Dans le cas des échanges radiatifs, il a été démontré que l'émissivité tend à augmenter au cours du refroidissement jusqu'à atteindre un palier tel qu'observé à partir des mesures. Concernant les modèles de convection issus des simulations

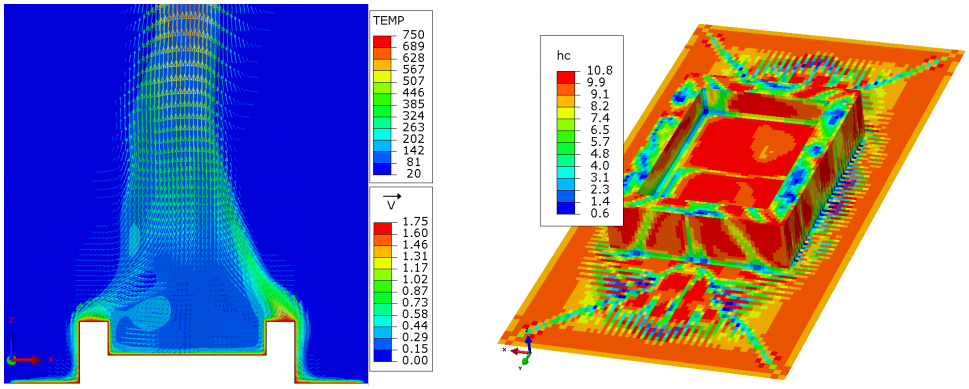

(a) **(b)**

Figure 10 – Analyse CFD: (a) superposition des contours de température et des vecteurs vitesses, (b) coefficients de convection calculés dans des conditions de régime permanent à 750 °C

CFD, ils ont démontré de bons résultats bien que difficile à recaler car définis par surface de façon non constante. Pour la convection forcée et la conduction, des modèles issus de la littérature ont été caractérisés. Cependant, l'essai utilisé a montré ses limites bien que les résultats obtenus en terme de température soient satisfaisant. En effet, les conditions de contact initiales de notre essai n'étaient pas maitrisées du fait des essais successifs et des potentielles déformations de notre tôle. De ce fait, les échanges par conduction et indirectement le refroidissement généré par convection forcée ont été caractérisés en prenant en compte l'inconnue des conditions initiales de contact. Aussi, le modèle de conductance s'est avéré quasiment insensible aux pressions de contact ce qui n'est pas conforme avec la littérature. Ceci est une fois de plus la conséquence des conditions initiales non parfaites entre la tôle et le moule, mais également du fait des faibles pressions de contact mises en jeu pour cet essai.

Pour finir, la configuration moule, cadre et tôle soumise à un refroidissement libre a servi à valider les CL caractérisées pour tous les modes dans une configuration non isolée. Les résultats de température pour nos modèles CL sont en accord avec les courbes expérimentales, notamment dans le cas où la surface supérieure de la tôle n'était pas recouverte de peinture lubrifiante. En effet, chacun des essais utilisés pour l'identification ne comportait pas de couche de nitrure de bord pour s'affranchir de ses effets sur l'émissivité.

Simulation numérique du procédé

La mise en œuvre d'un modèle capable d'optimiser les opérations de post-formage pour minimiser les distorsions finales implique de prendre en compte tous les paramètres susceptibles d'affecter les distorsions. Cela a conduit à introduire la phase de formage et l'opération finale de détourage dans le cadre de l'analyse EF avec ABAQUS® . En effet, le processus de formage produit une distribution d'épaisseur hétérogène et l'opération de détourage libère les contraintes résiduelles de sorte que les deux sont nécessaires pour obtenir les déformations finales d'une pièce en fin de procédé de fabrication. Ces deux opérations n'ont pas été détaillées dans la thèse bien qu'inclues dans le modèle et nécessaires pour reproduire correctement l'effet des conditions thermo-mécaniques subies lors du défournement.

Description du modèle éléments finis

L'ensemble de la simulation est constitué d'une première étape de refroidissement naturel à l'intérieur de la presse, puis d'une phase de refroidissement par soufflage suivie d'étapes

successives d'extraction jusqu'au démoulage et enfin d'un dernier refroidissement à l'extérieur de la presse (illustré dans la Figure 6).

Un couplage fort en température et déplacement a été utilisé pour tenir compte de l'évolution des TT avec les déformations de la pièce, notamment l'influence de la variation des conditions de contact (pression et écart) sur les échanges par conduction. Il a été choisi de modéliser la pièce formée, le moule et le cadre d'extraction. L'ensemble des outillages et l'environnement de la presse sont pris en compte au travers de CL thermiques et mécaniques. Une CL mécanique de symétrie est utilisée de façon à minimiser les temps de calcul. Les trois pièces sont considérées comme des solides déformables modélisés par des éléments coques. L'ensemble des hypothèses mentionnées sont illustrées dans la Figure 11 qui montre la différence entre les géométries réelles et celles modélisées dans la simulation où la pièce est partiellement représentée. Un schéma de résolution implicite du problème a été choisi avec prise en compte du comportement elasto-viscoplastique au travers d'une routine *CREEP.

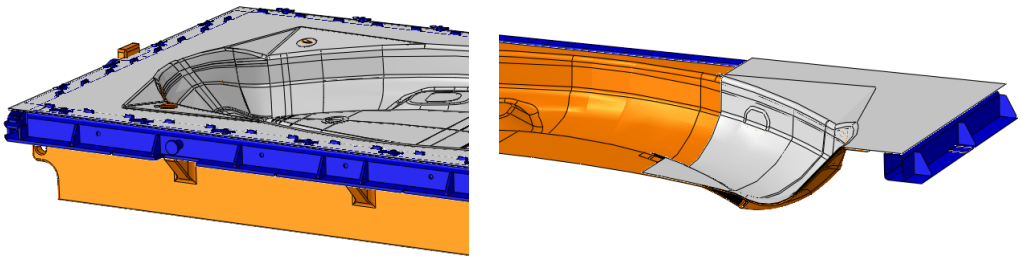

(a) **(b)**

Figure 11 – CAO de l'ensemble moule cadre et tôle: (a) CAO 3D des pièces et (b) version surfaciues simplifiées

L'évolution des conditions de refroidissement et d'extraction de la pièce sont prises en compte au travers de conditions limites mécaniques, thermiques et d'interfaces. Les différents TT, caractérisés à l'échelle de l'outillage d'essais, ont été adaptés à l'environnement industriel. Concernant les échanges par convection naturelle, des hypothèses issues des littératures nous ont permis de définir un coefficient de convection homogène lors de la phase dans la presse. Une fois démoulée et sortie de la presse, un modèle a été caractérisé à partir de simulations CFD telles que réalisées pour l'outillage d'essais. Pour la convection forcée, le modèle caractérisé dans le cas d'une surface perpendiculaire au jet a été étendu aux surfaces complexes en prenant en compte l'évolution de la distance d'impact. Concernant la conduction, un modèle basé sur celui identifié grâce aux essais a été implémenté. Cependant une valeur non nulle de la composante de sensibilité à la pression a été intégrée de façon à ne pas mettre de côté les échanges thermiques intervenant pour des pressions de contact nettement supérieures à celles générées lors de nos essais.

Pour finir, une méthode de calcul des échanges radiatifs a été développée sur la base de celle proposée par ABAQUS® non disponible pour les simulations couplées en température-déplacement. En effet, la méthode de calcul du flux de chaleur radiatif intégrant la somme des contributions de chaque élément rapportée aux facteurs de vue est disponible uniquement pour les analyses purement thermiques. La méthode développée dans cette thèse est basée sur un calcul thermique a-priori qui permet d'obtenir une approximation de l'évolution de la température des pièces (sans prise en compte de l'effet des déformations sur la conduction). De cette évolution sont définies des surfaces pour lesquelles la température est homogène au cours du refroidissement. Suite à cela, des matrices de facteurs de vues associées à chacune de ces surfaces aux températures homogènes sont extraites de façon à pouvoir reconstruire la somme des contributions par surfaces au cours de la simulation couplée du refroidissement. Cette méthode a été comparée à la méthode classique proposée par ABAQUS® (*Cavity

radiation) et a donné d'excellents résultats. L'affectation des flux de chaleurs s'est faite sur la base d'une géométrie complète en intégrant la non-symétrie du problème, notamment causée par le rayonnement au travers de la porte de la presse.

Résultats de la simulation du procédé

La stratégie industrielle de refroidissement et d'extraction a été testée dans le modèle EF. Celle-ci est composée d'une activation/désactivation de certaines buses du robot souffleur de façon à localiser le refroidissement forcé sur des zones spécifiques telles que présentées dans la Figure 12a. Concernant l'extraction, le robot applique une consigne de déplacement jusqu'au défournement ou lorsqu'une limite d'effort est atteinte. Dans ce dernier cas, une phase de soufflage supplémentaire est réalisée jusqu'à une prochaine étape d'extraction. Dans le cas contraire, la pièce est défournée et transférée à l'extérieur de la presse puis refroidie jusqu'à la température ambiante. La Figure 12b montre la courbe d'effort type obtenue pour un défournement sur le moyen industriel où l'on peut observer les phases d'extraction successives et l'atteinte d'un effort critique.

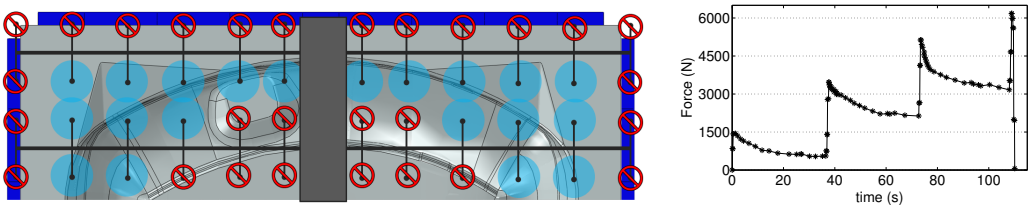

(a) **(b)**

Figure 12 – (a) Strategie de soufflage, (b) courbe d'effort d'extraction

La simulation de la stratégie industrielle a montré de nombreux résultats intéressants. La simulation donne un aperçu global de l'évolution de la température et les contraintes thermiques qui en découlent sur la pièce mais aussi sur l'outillage. La Figure 13 donne l'évolution des champs de température sur la pièce à différents moments de la simulation et l'évolution locale en quatre points au cours du temps. On peut observer de forts gradients thermiques et une variation des vitesses de refroidissement au cours du défournement.

Un aspect important concerne la phase de soufflage. On a pu voir qu'elle produit la majeure partie des déformations plastiques, ce qui démontre l'importance de la stratégie de soufflage. Ensuite, un autre aspect important concerne l'effet de l'asymétrie des TT au travers de la porte ouverte, en particulier le TT radiatif. En effet, le refroidissement du cadre est fortement influencé par le rayonnement thermique avec l'environnement. Les gradients de température à l'intérieur du cadre d'extraction produisent des contraintes et déformations très importantes qui peuvent être préjudiciables pour lui-même et la pièce formée.

Le modèle est tout à fait satisfaisant par rapport aux objectifs de la thèse. Les distorsions obtenues en fin de processus après détourage sont en accord avec la forme typique des distorsions obtenues dans l'usine, mais elles sont néanmoins plus faibles. La Figure 14 illustre ces déformations comparées à la forme théorique des pièces.

Cependant, deux détails ont remis en cause la validité du modèle: l'absence de déformation plastique lors de l'effort impulsion et l'absence de conditions de contact collant observées à partir des comparaisons de courbes d'effort d'extraction. Ces aspects mettent en évidence un problème concernant le traitement numérique du contact. En effet, des phénomènes de frottement se produisent pendant le processus d'extraction. Ils sont clairement visibles par les ouvriers de l'atelier mais aussi au travers des courbes d'effort d'extraction du robot. Une comparaison entre courbes industrielles et elles issues de la simulation est donnée dans la Figure 15. Elle montre clairement cette lacune dans le modèle. C'est pourquoi une

analyse de sensibilité sur deux paramètres numériques (associés au contact) a été menée pour comprendre l'origine du problème.

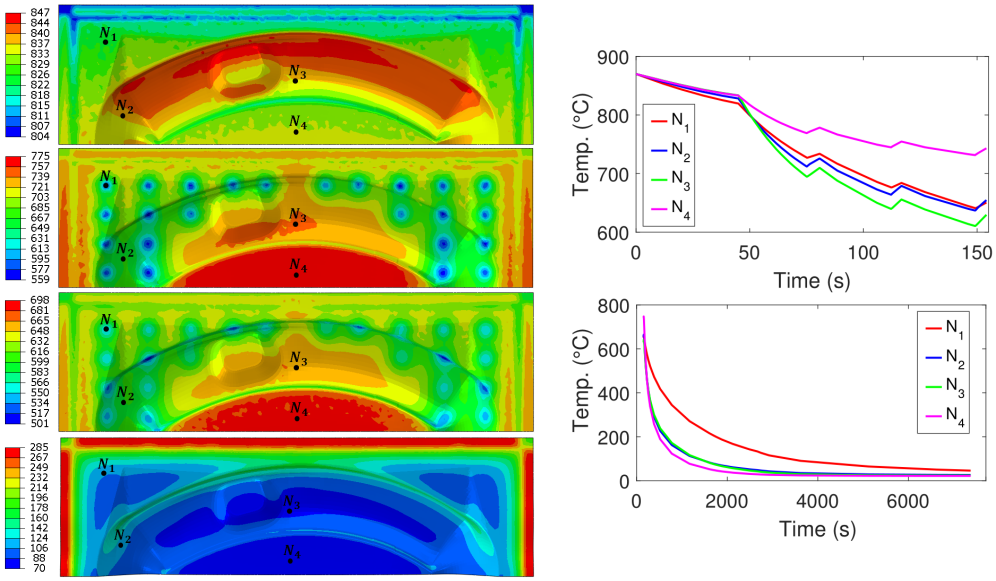

Figure 13 – (a) champs de température de la pièce (de haut en bas) avant le soufflage, après la 1ère et la 4ème phase de soufflage et après 1000s de refroidissement à l'extérieur de la presse, (b) Courbes de température-temps aux noeuds représenté sur la pièce

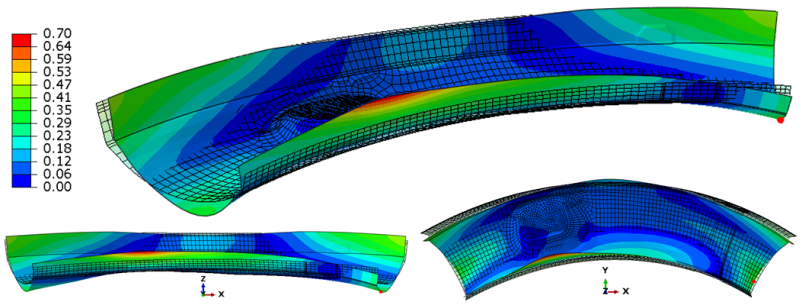

Figure 14 – Superposition de la pièce déformée (facteur d'échelle x100) avec la pièce théorique - norme des vecteurs déplacement (mm)

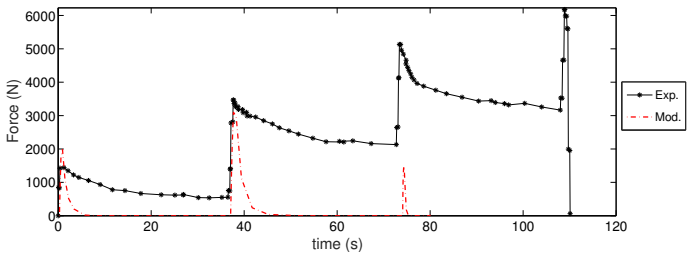

Figure 15 – Comparaison des forces d'extraction expérimentale et numérique

Analyse de sensibilité

Une analyse de sensibilité menée sur une version simplifiée du modèle industriel a été réalisée sur plusieurs paramètres affectant le contact. Une simplification des géométries et de la procédure d'extraction a été faite. Le premier paramètre qui a été analysé est le facteur d'amortissement du contact (FAC). Ce facteur est un coefficient appliqué à la valeur du paramètre d'amortissement calculé automatiquement par ABAQUS® . Il a pour but de favoriser la stabilité numérique relative aux problématiques de rupture/mise en contact. Cet outil numérique introduit une force visqueuse proportionnelle à la vitesse de déplacement des nœuds à distance de contact. Pour notre modèle, il aurait été idéal de ne pas avoir recours à cet outil, cependant les simulations ne convergent pas sans celui-ci. Le second paramètre est le coefficient de frottement utilisé dans la loi de Coulomb qui n'a pas fait l'objet d'une caractérisation expérimentale.

Pour effectuer cette analyse, deux critères ont été surveillés, l'effort d'extraction et les distorsions générées après détourage. Ces deux paramètres sont des moyens concrets pour mesurer l'efficacité d'une stratégie de refroidissement et de démoulage. Il a été mis en évidence que l'outil d'amortissement de contact a une influence critique sur la solution. L'effort d'extraction et les distorsions finales sont impactés par le FAC. La Figure 16 montre clairement l'influence du FAC sur l'intensité et la forme de la courbe d'effort.

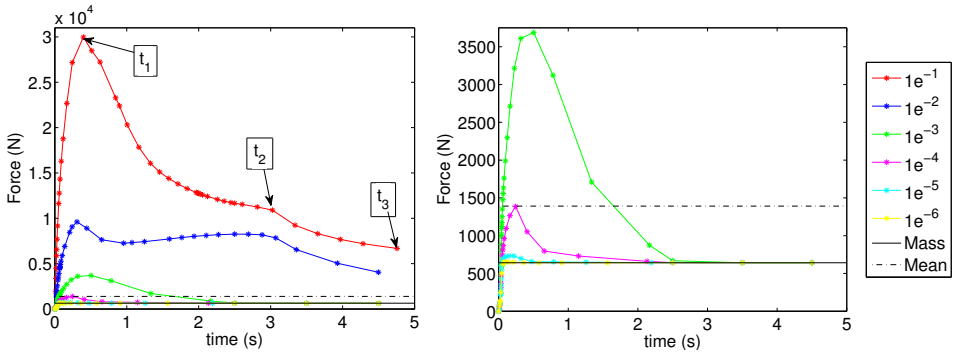

(a) **(b)**

Figure 16 – Evolution de l'effort d'extraction en fonction du FAC: (a) échelle globale, (b) zoom

Il a été démontré que l'outil d'amortissement de contact produit des contraintes négatives normales à la surface de contact qui n'ont aucun sens physique. La Figure 17 met en évidence ce phénomène pour différentes valeurs de FAC au moment du pic d'effort d'extraction.

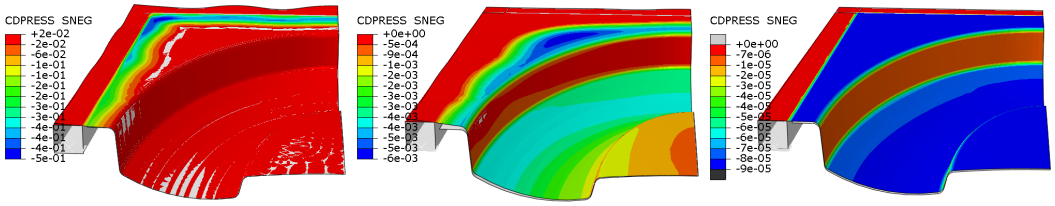

(a) FAC=1e^{-1} **(b)** FAC=1e^{-3} **(c)** FAC=1e^{-5}

Figure 17 – Champs de contrainte normale d'amortissement du contact au moment du pic d'effort pour trois valeurs de FAC

Le problème du FAC, outre l'effort d'extraction surestimé, est qu'il influence l'effet d'une stratégie de refroidissement sur les déformations de la pièce. En effet, le chemin de contraintes

généré par l'amortissement de contact suit les zones de rupture du contact. Plusieurs solutions ont été testées pour corriger ce problème. Une solution testée consiste à affecter divers valeurs de FAC en fonction des zones susceptibles de générer du frottement. En sélectionnant a priori les surfaces susceptibles de frotter, cela influence inévitablement les pressions de contact et l'effort nécessaire pour les vaincre. Une autre solution testée consiste à réduire au minimum le FAC pour éviter toute force artificielle. Dans ce cas, le modèle ne génère aucun frottement.

De plus, l'analyse de sensibilité du frottement a démontré que l'effort d'extraction n'était quasiment pas impacté par celui-ci, même pour des valeurs de frottement surévaluée. Cela peut venir d'une hypothèse erronée des conditions initiales de contact, ou du modèle de frottement de contact qui n'est pas adapté aux conditions de contact, notamment associé à des phénomènes d'adhérences ou de collage local par diffusion sous la pression de formage.

Optimisation du refroidissement

Une optimisation de la stratégie de refroidissement par soufflage a été réalisée sur une géométrie industrielle simplifiée pour deux conditions de fixation de la tôle sur le cadre et deux valeurs de FAC. Quatre zones différentes (représentées Figure 18) et trois temps de soufflages (15, 30 et 45 secondes) ont été testés. La courbe d'effort d'extraction, et la moyenne des distorsions ont été analysées pour évaluer la meilleure solution.

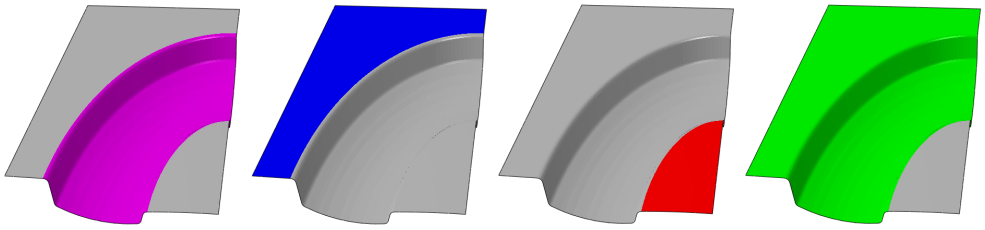

(a) "Part" **(b)** "Ext" **(c)** "Dome" **(d)** "optim"

Figure 18 – Representation des zones de soufflage testées

L'analyse des stratégies de soufflage a été réalisée pour deux types de conditions limites modélisant les fixations de la tôle sur le cadre au ours du défournement: une CL entièrement bridée (fixe) comme utilisé pour l'étude de sensibilité, et une CL permettant les mouvements dans le plan de contact uniquement. L'objectif de l'utilisation des deux conditions de fixation est d'évaluer la sensibilité du modèle à ce paramètre sachant que le procédé industriel se situe entre les deux CL. En effet, la fixation industrielle ne permet pas de déplacements perpendiculairement au plan de contact alors qu'un léger déplacement est autorisé dans le plan de contact. L'étude de sensibilité a montré les limites du modèle quant à la prise en compte des forces de frottement lors de l'opération d'enlèvement des pièces. Par conséquent, chaque cas testé a été calculé pour deux FAC homogènes (1e-3 et 1e-6) afin d'évaluer si le FAC influence la stratégie de soufflage.

La principale conclusion est que l'emplacement du soufflage a un effet insignifiant sur l'effort d'extraction par rapport à la fixation mécanique entre la pièce formée et le cadre d'extraction (indépendamment du FAC). Ceci est une bonne indication pour l'amélioration des systèmes de fixation des pièces. De plus, les résultats ont confirmé l'effet néfaste de l'outil d'amortissement par contact. En effet, il a produit soit des contraintes de contact non physiques pour une valeur de FAC élevée comme dans l'étude de sensibilité, soit aucune contrainte de contact pour un FAC faible. Le dernier cas a confirmé les interrogations sur la validité de l'implémentation du contact faite dans le modèle face aux efforts de retenus de la pièce observés expérimentalement lors du défournement. La Figure 19 compare l'effet des stratégies de refroidissement sur les distorsions (rapport de la moyenne des distorsions avec

le cas le plus défavorable – soufflage extérieur pendant 15 secondes) dans le cas où le FAC est très faible (FAC=1e-6).

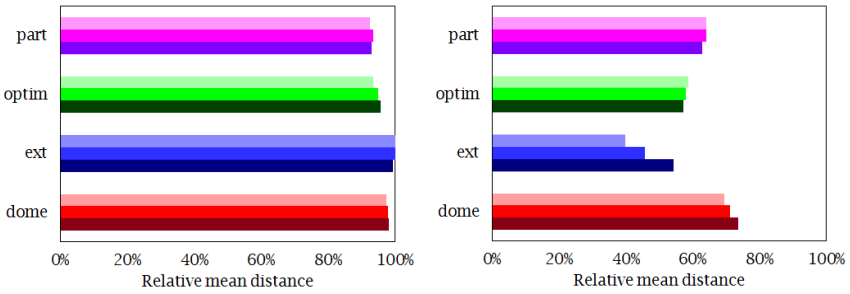

Figure 19 – Diagramme en barres de la distance moyenne à la surface théorique: influence des conditions de fixation de la tôle (a) encastrée et (b) libre dans le plan pour une valeur du FAC=1e-6

Conclusion

Les modèles de comportement du matériau et de TT obtenus à partir de la caractérisation ont été inclus dans un modèle numérique de la simulation du procédé construit sur ABAQUS® . La simulation de la stratégie industrielle actuelle a donné des résultats intéressants et importants sur l'impact du chargement thermomécanique subi pendant les étapes de refroidissement et de défournement du procédé. Cependant, l'ensemble des phénomènes physiques produit lors de la phase de démoulage et conduisant aux distorsions n'est pas totalement pris en compte. En effet, l'effort d'extraction nécessaire pour démouler la pièce n'est que la conséquence d'un artéfact numérique utilisé pour la résolution du contact.

Dans l'état actuel, le modèle permet de bien modéliser l'impact des contraintes thermiques au cours du refroidissement associé à l'évolution du comportement du matériau avec la température. Les distorsions obtenues sont comparables à celles générées pour des conditions parfaites de contact que l'on observe pour les premières pièces formées en début de campagne lorsque les conditions de lubrification n'ont pas été impactées par les formages successifs. Cependant lorsque ces conditions se dégradent, le modèle ne reproduit pas correctement l'impact des conditions de refroidissement sur le démoulage et le chargement mécanique qui en découle.

Néanmoins, une étude de l'impact de la stratégie de refroidissement a été réalisée pour différentes conditions de bridage de la pièce formée. Deux stratégies de soufflage spécifiques ont mis en évidence des distorsions plus faibles que d'autres. Ces stratégies semblaient en accord avec les tendances industrielles. Cependant, une amélioration à différents niveaux du modèle est nécessaire pour être pleinement confiant dans les résultats qui souffrent actuellement d'incertitudes. Par conséquent, plusieurs perspectives de travaux complémentaires sont proposées pour approfondir le travail de ce doctorat.

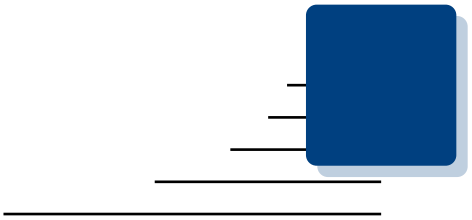

Contents

List of Figures

List of Tables

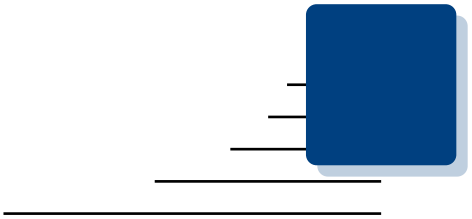

List of Abbreviations

AR aspect ratio(s)

BC boundary condition(s)
BCC body centered cubic
BL boundary layer
BN boron nitride

C&U cooling and unloading
CDf contact damping factor
CFD computational fluid dynamics
CRSS critical resolved shear stress

DGG dynamic grain growth
DMM deformation mechanism map
DRX dynamic recrystallization

FB-NAI forward bulkhead of the nacelle air inlets
FCC forced convetion coefficient
FE finite element
FEA finite element analysis
FEM finite element method

GBS grain boundary sliding

HT heat transfer(s)
HTC heat transfer coefficient(s)

IDD immobile dislocation density

KM Kocks-Mecking

NCC natural convection coefficient
NH Norton Hoff
NIR near infra-red
NSE Navier-Stokes equations

RANS Reynolds-averaged Naviers-Stokes

SEM Scanning Electron Microscope
SGG static grain growth
SPF superplastic forming
SRS strain rate sensitivity

TCR thermal contact resistance
THC thermocouple(s)
Ti-64 Ti-6AL-4V
TP1 testing procedure 1
TP2 testing procedure 2
TT threeshold transition

VF view factors

wBN without boron nitride
WRM weak radiation method

Chapter

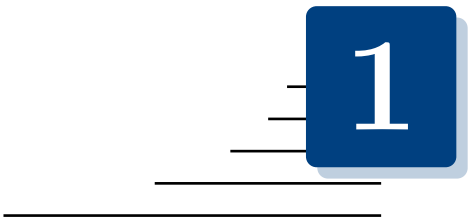

Introduction

1.1 Context

1.1.1 AIRBUS company

AIRBUS is an international reference in the aerospace sector. AIRBUS designs, manufactures and delivers industry-leading commercial aircraft, helicopters, military transports, satellites and launch vehicles. It also provides data services, navigation, secure communications, urban mobility and other solutions for customers on a global scale. The aircraft branch is the international leader of the passengers planes with several families: A220, A320, A330, A350 and A380.

The study of the the present work concerns the superplastic forming (SPF) process used in the Saint-Eloi plant in Toulouse which mainly deals with the propulsion sector of the planes. This plant provides all the pylons of the AIRBUS fleet. The forward bulkhead of the nacelle air inlets (FB-NAI) of reactors and complex shaped fairing parts of the pylon are manufactured in the plant. Both types of parts are highlighted in red and green in the Figure 1.1 which represents a A380-plus aircraft.

During the year 2018, AIRBUS approximately manufactured a total of 50 single aisles (the A320 aircraft family) and 10 long ranges (A330, A350 and A380 families) monthly. Each plane is composed by two to four pylons for the A380, each composed by different parts manufactured with the SPF process such as portions of forward bulkhead of the nacelle air inlets and after pylon fairing (APF) elements. It leads to a total of around 7500-8000 parts a year manufactured by AIRBUS and its subcontractors.

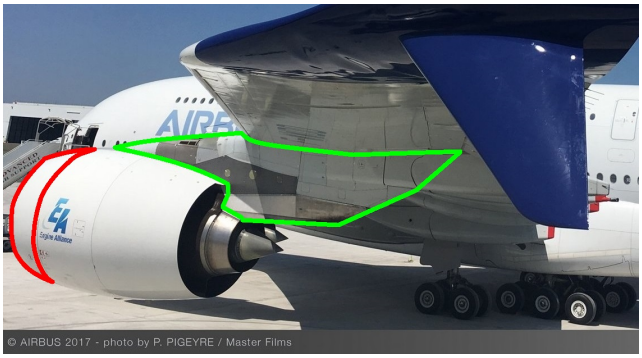

Figure 1.1 – Parts manufactured with SPF process: shaped fairing parts of the pylon (green) and forward bulkhead of the nacelle air inlet (red)

1.1.2 SPF Process

AIRBUS Company produces some parts of its planes with SPF process. SPF is a high temperature blow forming process of sheet metal which was invented and has largely been developed since the sixties [41]. It enables to manufacture complex parts in a single operation. The finished product has excellent precision and a fine surface finish. The specificity of SPF is to form thin sheet metal with large deformation and limited thinning. The process is relatively expensive because of the long forming time (around 1-2 hours a forming cycle) and the high temperatures required for superplasticity that imply to design high temperature tooling so that to resist the hard thermomechanical loading. However, it proposes a very good compromise between material properties, design to cost and yield rate. That is why the SPF process is used to form parts for aerospace industry [41, 42] as shown in the Figure 1.2, and also for specific parts in the automobile industry [43, 44, 45] and for dental surgery parts [46].

Figure 1.2 – Example of aeronautical parts manufactured with the SPF process [42]

The SPF process is composed by a first heating phase during what a sheet metal blank is heated up to a target temperature, afterward it is formed at a constant temperature. Then, the part is removed from the mold and finally cools down to the ambient temperature. During the forming operation, a pressure P is imposed in a chamber on a surface of the sheet to form on the opposite matrix of the mold as described in Figure 1.3. The press has to impose an effort T in opposition to the effort generated by the forming pressure on the superior matrix. The maximum T value defines the capacity of the press and depends on the size and the thickness of parts.

The process requires particular alloys which allow superplastic deformation. These materials are principally metals like titanium, aluminum, nickel superalloys and magnesium alloys, but there are also ceramics [1]. The superplastic alloys promote very high elongation and high strain rate sensitivity (SRS). These properties are due to particular deformation mechanisms

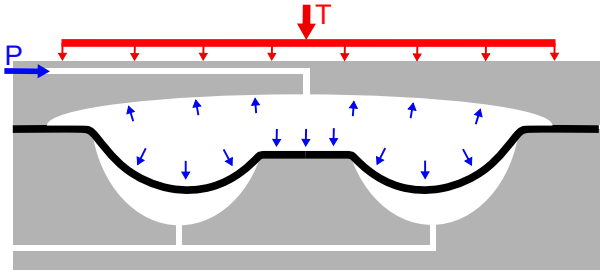

Figure 1.3 – Schematic of superplastic forming operation

that work for specific microstructure and thermomechanical solicitations. The high SRS is the key of SPF process because it enables to limit thinning of the sheet metal by opposing to strain localization.
The Figure 1.4 represents the trends of classical material and a superplastic material. The superplastic domain corresponds to the region II where the slope is high. The dashed lines represents the slopes of these curves also called the SRS exponent m. The superplastic domain is restricted to a specific range of strain rate. Consequently, it is important to control the pressure during forming in order to promote the deformation in region II. In these conditions, the thinning is limited and the thickness distribution is improved as the stiffness of part.

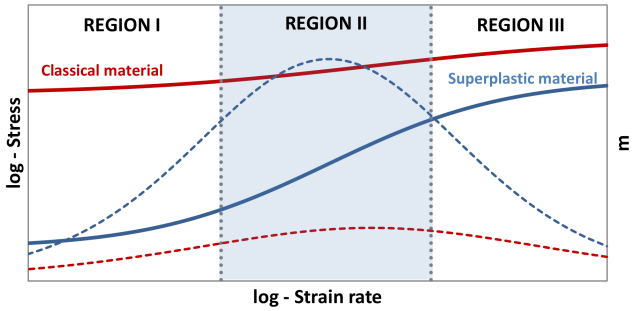

Figure 1.4 – Logarithmic stress-strain rate (solid lines) and SRS exponent-strain rate (dashed lines) of classical metals (in red) and superplastic materials (in blue) from [1]

One challenge of the past and future decades has been and will be to improve forming sequences which are rather long due to low superplastic strain rates. On the one hand, a large work has been made on material properties to increase the acceptable strain rate range and reduce the forming temperatures [47, 48, 49, 50, 51]. On the other hand, a large work has been made to implement finite element (FE) models to optimize pressure cycles [52, 53, 54, 55, 56, 57, 58, 59]. Indeed, the problematic of the process resides in the pressure cycle that need to be controlled so that to produce strain rate in the superplastic range to prevent from necking but also to promote the highest SRS that limit the thinning of parts. A new method has been proposed in the frame of this PhD thesis to use statistics to estimate the strain rate distribution and override the numerical singularities inherent to FE modeling and finally reduce the forming cycles [60].

1.1.3 SPF in AIRBUS

1.1.3.1 Forming step

In AIRBUS, the SPF process is used to form large parts (from 1x1 to 1.75x2.75 m^2 sheet metal blanks) in Ti-6Al-4V (Ti-64) and Ti-6Al-2Sn-4Zr-2Mo (Ti-6242) titanium alloys. Most

of the parts are produced on presses equipped with automatic loading and unloading machines. The Figure 1.5 shows several pictures of the press environment. The Figure 1.5a shows loading phase where the robot arms catch the handling frame on which the part is fixed. Then, the robot rotates and loads the blank on the forming mold. At the end of forming stage, the part is automatically removed from the mold inside the press thanks to a handling robot as shown in the Figure 1.5b. Before to pull on the frame, the part is cooled down thanks to localized air blowing in order to stiffen the part and ease the removing operation from the mold. Then the part is cooled down outside the press to the ambient temperature.

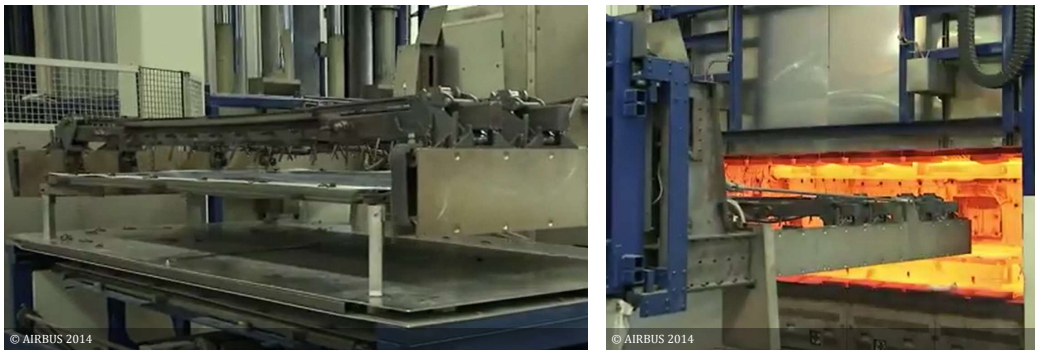

(a) **(b)**

Figure 1.5 – Pictures of the press environment (a) loading step (b) unloading step

The Figure 1.6a shows several nozzles used for blowing operation. They are activated or deactivated according to the area to target. The Figure 1.6b shows a blank fixed on its frame. A focus is made on one pin fixation and a handle of the frame. The sheel metal is prepared with Boron Nitride (BN) lubricant which gives a white color finish to the blank.

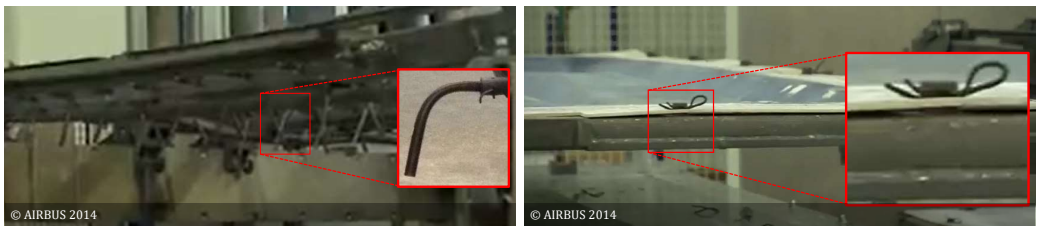

(a) **(b)**

Figure 1.6 – Pictures of (a) blowing nozzles and (b) boron nitride prepared blank fixed on a handling frame

A classical SPF production batch consists in successive forming between sixteen to more than fifty parts. The Figure 1.7 represents the averaged temperature of dies during a batch. There is a first heating phase and a final cooling of the massive refractory metallic dies. In between, the temperature variations corresponds to different configuration of the press during forming and part removing operations. When a part is transferring to the ambient cooling zone, the press' door is closed to minimize the heat loos. The dies inside furnace are heated back while a new blank is being loaded.

More generally, the heat loss is an important issue to focus on to limit the pre-heating time from which pressure cycle can be started such as shown in the Figure 1.7. Indeed, the temperature of SPF for Ti-64 alloy is considered at 870°C ± 20°C such that SPF cycle is started from 850°C. Thus, the cooling operation before unloading is crucial to ease part removing without producing irreversible deformation while limiting heat dissipation.

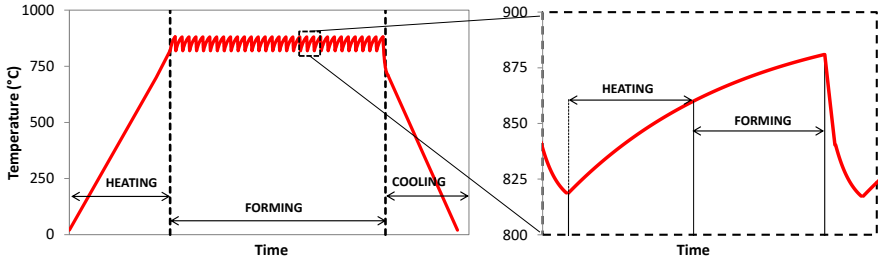

Figure 1.7 – Illustration of the temperature cycle at the scale of a batch and a forming cycle

The Figure 1.8 schematically represents the different step during part cooling and removal operations. Each step follows different heat transfer (HT) modes illustrated by symbols defined in the Figure 1.8f:

1. Press' door opening (Figure 1.8a): it consists of the time necessary to open the press' front door and to introduce the automatic cooling and extraction system. During this step the HT are free convection and radiation inside the press and through the open door.
2. Air Blowing (Figure 1.8b): forced cooling is induced by air jet nozzles located in specific areas. The air is blown until the part to be rigid enough to be extracted.
3. Extraction (Figure 1.8c): a vertical displacement of the handling robot's arms is induced until the target force is reached.
4. Transfer (Figure 1.8d): when the part is removed from the mold, it is transfered outside the furnace. The environment temperatures at stake in thermal radiation HT vary during this step.
5. Ambient cooling (Figure 1.8e): the part cooled down at the exterior of the press at ambient temperature. It is placed at elevated position from the floor to avoid confined space HT.

Sometimes the part cannot be removed with the first force pulse. In this case the blowing and extraction steps are repeated until unloading while the target of force pulse is incrementally increased as a function of the part.

1.1.3.2 Additional manufacturing steps

The automation of the part removal operation has been implemented to make the process reproducible and also to increase the rate of this operation. It may lead to part deformations and geometrical distortions on final parts after trimming. Therefore, the manufacturing process is composed by several extra operations to take back the geometric defects:

❒ The calibration forming

it consists of forming a part a second time directly after a previous extraction sequence. This enables to limit the deformations that happened during first operation. This operation is rare.

❒ The pre-trimming operation

A pre-trimming is sometimes necessary when the part is too much deformed for trimming operation. The part is generally trimmed with a few percentage more to let a maximum stress relived. The Figure 1.9 schematically represents this problem. Obviously this implies a second trimming operation after sheet metal working. The pre-trimming is more frequent especially for FBNAI parts.

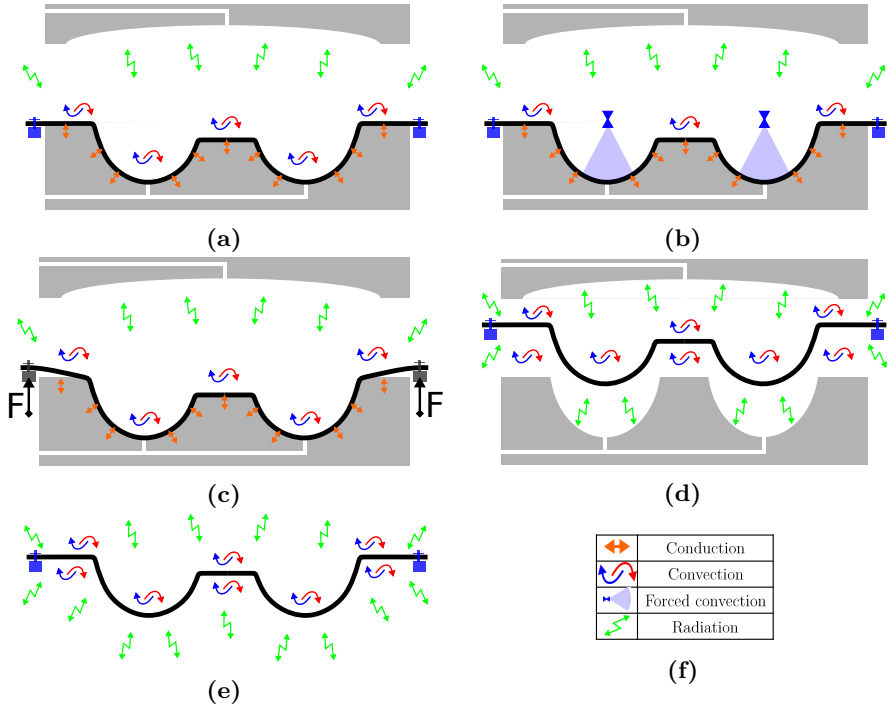

Figure 1.8 – Schematic of heat transfer phases: (a) press opening, (b) blowing, (c) extraction, (d) transfer, (e) outside cooling and (f) legend of heat transfer modes

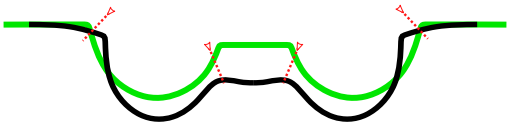

Figure 1.9 – Schematic of deformations during trimming operation

❒ Sheet metal working

Sheet metal working consists in making the part fitting into the shape tolerances. There are different operations from hammer, to complex dedicated tooling. Sheet metal working is always made for every part. This operation can take between 15 min to 10 hours for complex distortions.

❒ Additional heat treatments

This treatment is sometimes required due to hard deformations imposed during sheet metal working that can induce detrimental microstructural changes or simply to recover elongation for further metal working. These modifications can be dangerous from material specification point of view.

The global manufacturing process is shown in the Figure 1.10. The additional operation box corresponds to surface finishing operations like sand blasting and hand sanding, etc.

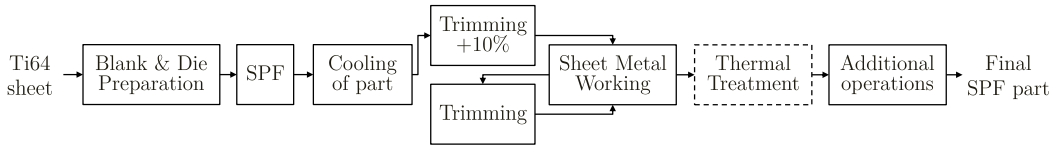

Figure 1.10 – Flowchart of the whole manufacturing process of SPF

1.2 Problematics

The multiple additional manufacturing operations are a consequence of part distortions and residual stresses relieve after forming. Indeed, the behavior of the material quickly changes during cooling and extraction steps due to high cooling rates. In addition, the thermal stresses and those imposed by the extraction system generate complex loading because of the complex shapes, the heterogeneity of thickness and the material behavior.

Several hypothesis can be taken as the root causes of the part deformations: the thermo-mechanical loading undergone during part removal, the dies deformation, and also the BN degradation along batches.

❒ Thermomechanical loading

The mechanical loading is a combination of thermal stresses due to the temperature gradient generated during cooling, the contact stresses between mold and part and unloading forces imposed through the frame. These stresses cause deformations due to a low strength of the material at high temperature.

The Figure 1.11 represents principal cases of part "sticking" where the red lines correspond to high friction zones. The Figure 1.11a highlights the expansion issues that can promote part clamping on mold geometry. The Figure 1.11b illustrates how the cooling sequence may be detrimental if it is not adapted to the geometry . It can finally lead to deformations under the extraction tooling effort.

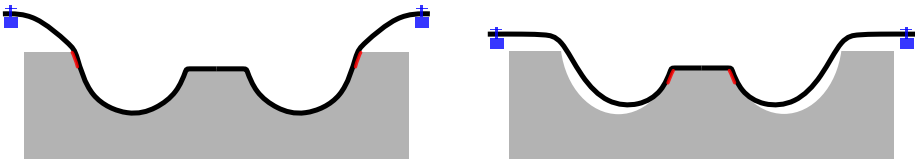

Figure 1.11 – Schematic of deformations under extraction effort: (a) lack of rigidity for efforts transmission, (b) male/female clamping of the part

The Figure 1.12 represents the deformations undergone by a part in the conditions inside the press (Figure 1.12a) and outside the press (Figure 1.12b). Moreover, it is enhanced by the large part dimensions formed at AIRBUS (up to 2000*3000 mm*mm).

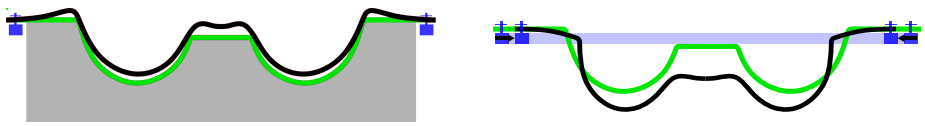

(a) (b)

Figure 1.12 – Schematic of deformations under thermal stresses: (a) inside mold, (b) outside press

❒ Dies deformations

The dies can deform through thermal stresses, mechanical loading during forming or a combination of both. The deformations can lead to wrong surface geometry and finally wrong part geometry. The dies follow important thermal stresses during the initial heating and final cooling phases of a batch. They are produced by the heating power that is transmitted though platen or radiant panels that induce radiative heating on their exterior surfaces. Moreover, the successive temperature variations during loading and unloading phases contribute to dies deformations through cyclic plasticity.

The closing force (represented in the Figure 1.3) is transmitted to the sealing zone to ensure airtightness during forming. It may be very high to compensate the tool deformations and avoid possible leaks. The contact stresses generated by pressure onto the forming die are induced at each forming cycle and finally enhance surface degradations and appearance of cracks [61, 62].

❒ BN degradation

During a batch, the blanks and the forming die are coated with BN lubricant that limits friction and reduces the thinning of the sheet metal. However, the forming die is only coated once before the initial heating. The repeated contact loading onto forming surface promotes BN coating degradations. Finally, the friction conditions become harder and thickness distribution so as part removing conditions can deteriorate.

1.3 Industrial objectives

The objective of the study is to minimize the distortion of the parts after forming. Indeed, the distortions appears after the forming and cooling phases, but also after trimming operation because of the residual stress relief. By reducing the post forming distortions it would suppress or at least reduce the operations after SPF, especially sheet metal working which is expensive and recurrent for every part. Then the possibility to suppress pre-trimming operation is a subsidiary objective but nevertheless important because it would suppress two operations.

The FE modeling of the process has been chosen to reproduce the post SPF process in order to optimize the part removal strategy. The scope of this optimization is focused on the automatic part removal procedure. The levers of this problem are the blowing strategy (the positioning of nozzles, the sequencing of the step, the gas pressure, etc.), the extraction procedure (the pulse sequencing, the force of the extraction pulse, the frame properties, fasteners configuration, etc.). No modifications of the mold geometry are considered.

It has been chosen to model each step of the process: SPF, unloading and trimming of the part. Therefore, it is possible to properly reproduce the effect of a process configuration and to measure concretely the associated final geometry of a part. Indeed the SPF promotes a specific thickness distribution, and possibly heterogeneous material properties which contributes to

the stiffness of the part during cooling and unloading. The trimming operation is the step which reveals the final geometry thanks to the residual stress relief.

The deliverable of this PhD is a thermomechanical FE model of the cooling and part removal operations after forming of SPF parts. In addition, an optimized part removal sequence has been proposed according to different possible recommendations:

- The sequencing of air jet blowing, the positioning on part.
- An extraction procedure for the automatic machine. ie. the sequencing of extraction pulses type.
- The design of the extraction frame, the type and the position of fastening.
- Recommendations on the cooling conditions outside the press.

This study has been performed on a specific part: a portion (among four) of the FB-NAI of the A350-900. The FB-NAI is a structural and functional part that is placed behind the nose lip of the air inlet as represented in the Figures 1.13c and 1.13b. The Figure 1.13a shows drawing views of the portion studied in the PhD. It has a hole, contrary to the other portions, that is used for the anti-ice system. This part is a typical geometry shared by every AIRBUS programs that has particular sheet metal working operations. The material used is a Ti-64 grade 5 largely used for SPF applications.

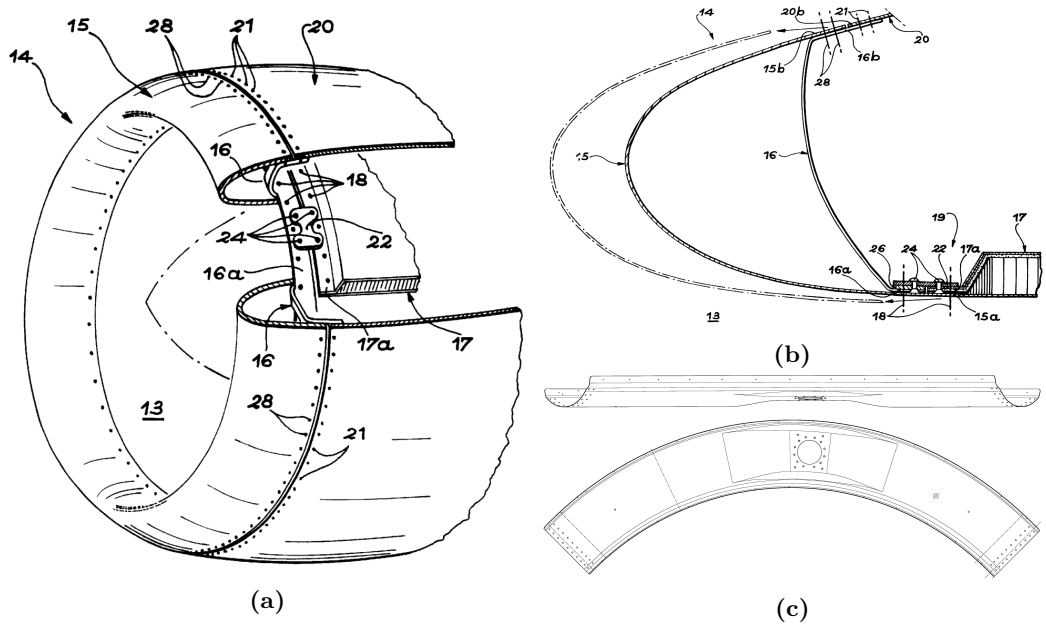

Figure 1.13 – Air intake (inlet) structure for aircraft engine: (a) a perspective and (b) sectional views [2], (c) drawing views of the NAI portion of forward bulkhead of the nacelle air inlet of the A350-900

1.4 State of the art

The effect of thermomechanical conditions followed by parts after SPF process and the impact of cooling after high temperature manufacturing processes are important issues. Indeed, in some cases, the temperature gradients generated during cooling are significant and may produce plastic deformation, residual stresses, heterogeneous material behaviors and some

other important aspects that can affect final geometry and mechanical properties of final parts. This question has not been approached for the SPF process in the litterature. However, it has been made for several manufacturing processes that share specific problematics with the SPF process. A brief review of FEA performed on some of these high temperature processes is provided hereafter. They are clustered into several categories.

❒ Quenching-Solidification analysis

High temperature manufacturing processes like casting or continuous-casting ([36, 63]), extrusion ([64]), hot rolling [65, 66, 67] and others are always followed by a cooling phase. This step can have an important role for revealing mechanical properties like with quenching of carbon steel alloys for instance. However, it may produce a high residual stress amount especially with massive parts. A common issue of theses different fields of investigations is the impact of cooling on phase transformations induced plastic strain. The material models are most of the time purely plastic with no possible stress relaxation phenomena that is an important issue in our case. The HT are mostly defined for steady state, constant and homogeneous conditions. Thomas et al [36] include a viscoplastic behavior and a pressure and gap dependent thermal contact resistance (TCR) model in their simulation of hot tearing process.

❒ Welding analysis

The FEM analysis of welding processes can share similarities with SPF Processes. Indeed, the high cooling rates produce heterogeneous cooling conditions and thermal stresses that are similar to SPF cooling operations at AIRBUS. It exists numerous studies on the FEM analysis of welding processes such as TIG process [68], laser welding, etc. Laser welding has been properly addressed by Robert et al [69, 70, 16] with multiphase thermo-elasto-viscoplastic material model. An important work has been made on Friction Stir Welding process, and the impact of process parameters on residual stresses accumulation [71, 72, 73]. In these studies, the material behaviors are modeled with high strain rate application laws like Johnson Cook based models.

❒ Hot stamping analysis

The hot stamping and SPF are both high temperature sheet metal forming processes which are fairly similar regarding the cooling and unloading phases. Indeed, the HT modes are equivalent even if the forming temperature are higher for SPF. The impact of cooling on the heterogeneity of the tool temperature for thermal conduction issues has been addressed thanks to multi physics (fluid and solid mechanics) analysis by several authors [74, 75]. Pressure dependent TCR are introduced to take account of the thermomechanical coupling that affects part deformations [75, 76]. In such application, the temperatures at which unmolding operation is performed are lower. Therefore, simple elasto-plastic models are generally used which might not be adapted for highly viscous behaviour of superplastic materials.

The cooling and unloading processes gather the whole problematics that are generally addressed in the previous mentioned studies independently. Indeed, in the case of thin sheet metal, the cooling and unloading steps at such high temperature generate fast cooling that produces important and heterogeneous variation of the material behavior, mechanical and thermal stresses. All these aspects and their relations to the plastic deformations and final residual stresses need to be investigated.

1.5 Scientific objectives

The scientific objectives are directly related to the industrial ones and the barriers that exist to answer to. The state of the art on high temperature process modeling showed that some specific topics of the SPF process have already been addressed. However there is a lack regarding the application of this work at the SPF process conditions like, temperature, HT modes etc. The modeling of the process brings some difficulties that are divided in three principle axes:

- ❒ Material behavior modeling

The challenge of the thesis on the material aspect is to be able to reproduce and characterize the conditions of thermomechanical loading during the process while accounting the material history. Indeed, the influence of the SPF deformation on the material properties during cooling has to be determined. Moreover, the heterogeneity of the cooling rate distribution combined with the mechanical stresses make the loading paths very complex to reproduce. Therefore, a first objective has been to determine the process parameters that influence the material behavior before (during forming) and during cooling. Then, it has been necessary to define and perform a test procedure capable of reproducing the conditions of the process. Finally, a model has been characterized using the experimental results.

- ❒ Heat transfer modeling

The first work consists in evaluating the HT in the specific conditions of the AIRBUS process. The combination of the three modes (convection, radiation and conduction) that significantly evolve over the process makes difficult the characterization and the modeling through "simplified" boundary conditions (BC).
A first objective has been to develop a methodology to measure the most faithfully the exchanges at stake during the cooling phase. The second objective has been to implement in the model, numerical BC characterized from the experimental data and able to numerically reproduce the process cooling conditions.

- ❒ Modeling of the process

One difficulty to model such a complex process is to take relevant assumptions that simplify the problem. Indeed, there are multi-physics coupling in this process that could require associated simulation. For instance, there are complex fluid to structure HT that could be modeled with computation fluid dynamic (CFD) simulations. Then, there are large deformations that can influence material properties and that can be modeled with complex microstructure based material models. In addition, the part deformations influence the HT in conduction especially. The question of the coupling between temperature and displacement has to be discussed.
The aim of this thesis upon simulation purpose has been to develop a global model of the different phases from forming to trimming. The model should be able to reproduce faithfully the impact of the thermomechanical conditions of the process on the state of stress and geometry of the parts at the end. Then, another objective has been to implement a methodology to optimize the cooling and part removal sequence with complex, various and of different order parameters.

1.6 Content of the thesis

The complexity of the problem and the industrial-based objectives have encouraged to finally adapt the experimental work to limit its quantity but also ensure industrial relevance of the developed models. The work has been divided into three principal axes that are presented

into three chapters. A significant part of the work considered useful and scientifically relevant but not essential for the understanding is placed in several appendices to ease the global reading of the thesis.

Chapter 2: Material modeling:

A bibliographic review on behavior, characterization and modeling of the Ti-64 alloy has been made first. The literature has highlighted that a large number of microstructure and process parameters influence the material behavior. Preliminary testing sessions were performed in order to develop a judicious material testing procedure and also to discriminate some of the numerous influencing parameters. The results of this work is detailed in the Appendices A.1 and A.2. A thermomechanical procedure composed by two specific tensile-relaxation tests for a set of ten temperatures has been proposed to characterize Ti-64 behavior in the process conditions. A thermo-elasto-viscoplastic model based on a hyperbolic sine formulation coupled with hardening-softening variables has been characterized from experimental data. The Appendix A.3 describes the optimization methodology implemented to fit the 26 parameters of the viscoplastic function. Complex functions were developed to reproduce the transition of behaviors (hardening, viscosity, etc.) with temperature variations from forming to ambient. The model has been validated on anisothermal tensile tests.

Chapter 3 - Heat transfers modeling:

A bibliographic review on thermal radiation, convection (natural and forced), and conduction HT has been performed. Various models associated to specific process conditions and there dependencies to the process parameters are depicted for each mode of HT.
The numerous configurations of heat transfers followed during the process made difficult to reproduce dedicated laboratory experiments to characterize the models of thermal boundary condition (BC) for each conditions. Therefore, it has been chosen to use a small scale SPF tooling to form parts in industrial conditions. Then, several cooling procedures on instrumented parts were performed in laboratory conditions to get data for the HT characterization. A set of cooling experiments has been carefully designed in order to isolate the HT modes to ease characterization.
A first development experiment was used to implement and validate several instrumentation means during cooling procedure on the laboratory furnace (Appendix B.1). Then five different cooling procedures were performed and used for characterization. In addition, laboratory experiments have been performed to obtain emissivities of materials in various surface conditions.
Four inverse analyses were used to fit each thermal boundary conditions associated to radiation, convection and conduction HT. Concerning convection, CFD analyses were used to evaluate the distribution of the convection coefficient over the parts surfaces. Indeed, the convection HT are fairly complex in the process conditions contrary to the homogeneous coefficients that are used in the literature. The Appendix C presents bibliographic review on high temperature natural convection, a model and its validation regarding literature results (horizontal plates natural convection problem).

Chapter 4 - Modeling of the process:

The modeling procedure of the full manufacturing process (forming, in-press cooling, part removing, out-press cooling and trimming) is presented. The physical equations involved in the coupled thermomecanical problem, the associated domains considered in the model are presented. The simplifications, the hypothesis and the thermal BC adapted from the prototype based to industrial conditions are detailed.
Once the model is completely presented, the results of the currently used industrial cooling and part removal sequence are presented. The temperature, and mechanical quantities affecting the final distortions are analyzed from the press opening to the post trimming state.

The results of the simulation give an overview of the global temperature evolution and the consequence in terms of thermal stresses induced on the part but also on the tooling.
Then a sensitivity analysis (with a simplified geometry) of the model to the friction coefficient and the numerical damping (necessary for convergence) is performed. Both parameters are supposed to contribute to the friction It is demonstrated that the contact damping tool provided by ABAQUS® modifies the solution. The pulling effort for extraction is artificially increased, and the contact stress are modified such that a negative normal stress may be imposed oppositely to the contact opening. The contact control modifies the model response to the thermo-mechanical loading.
An optimization of the cooling sequence is proposed regarding the pulling effort and the final distortions after trimming for the simplified geometry. Two contact damping parameters are considered to evaluate the impact on the optimization results. The results reveal that the cooling strategy has a small impact even for both contact damping cases. Two part-frame fastening conditions (plane free or clamped) are tested and shows that it is of first order compared to cooling strategy.
Finally the model is applied on the industrial geometry. The strategy used in AIRBUS plant and a global blowing of the part are compared. The impact of contact damping is also analyzed for the industrial geometry.

Chapter 5 - Conclusions and prospective:

A general conclusion is made to evaluate how the present work have helped to answer the different objectives. A base of prospective work is proposed to improve the proposed FE model and the process.

Chapter

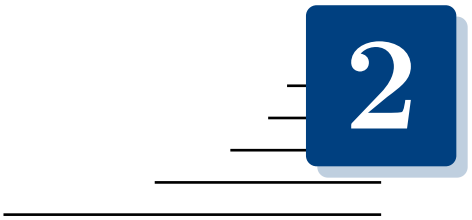

Material modeling

2.1 Introduction

2.1.1 Context

A material model has to be input in the FE model of the process. This law has to reproduce the thermo-mechanical properties and behaviors of the Ti-64 alloy from the end of SPF process until the laser trimming operation. The developed model must be able to reproduce

the distortions obtained at the end of the process. This implies that the plastic deformations and the residual stresses accumulated during part removal sequence must be reproduced by the model. Indeed, the trimming operation may produce elastic deformations because of residual stresses relieve. Thus, a particular attention need to be paid on the flow stress relation that determines the inelastic deformations and the evolution of elastic domain through thermomechanical loadings that generate the residual stresses.

The Figure 2.1 represents how the evolution of the material happens and is observed in this study. The scope of this study focuses on the cooling and part removal operations that happen post SPF process. However, Each step is likely to have an impact on the microstructure that influences the thermomechanical properties and the behavior. Indeed, the SPF process may have an impact on microstructure so as to the high cooling rate during the cooling operation. These properties of microstructure are at the origin of macroscopic material behaviors like the elasticity, hardening properties etc.

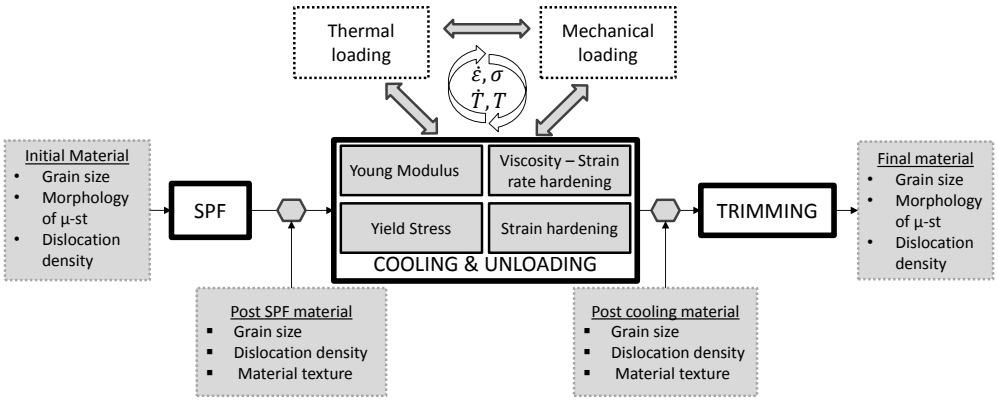

Figure 2.1 – Schematic of material behavior and microstructural evolution during the manufacturing process

2.1.2 Problematics and objectives

The problematic of material modeling of such a complex process lies in the choice of an adequate model and the associated testing characterization. This imply to know the material behaviors and the associated macroscopic and microstructural parameters that influence them.

Indeed, the inelastic deformation that leads to distortions and residual stresses is a consequence of the deformation mechanisms acting at the microstrucutral scale. These mechanisms are sensitive to the temperature and strain rate and may evolve as the microstructure is changing under high cooling rate, large deformation range and so on.

There is a large quantity of parameter that may influence the material behavior of the Ti64 alloy, and the first objective was to identify them. The second objective was to implement a material testing procedure to test the effect of the identified parameters on the mechanical properties. The last objective was to select and characterize an appropriate model to be implemented in the FE model.

2.2 Bibliographic review

2.2.1 Material behavior

From modeling point of view, the study of metallic materials behavior can be divided into three main topics:

- **Elasticity** refers to the reversible deformation of materials. It involves electromagnetic forces related to atomic interactions. The elastic behavior of metals can be considered to be visco-independent.
- **Plasticity** refers to time independent inelastic deformations. It is usually associated to low temperature deformation mechanisms because of the absence of atomic diffusion processes which are rate dependent.
- **Viscoplasticity** is related to rate dependent inelastic deformations. It groups many different and complex deformation mechanisms that are influenced by temperature, stress, and microstructure morphology.

During material processing, each of these three generic behaviors acts together and are influenced by each others and also by loading conditions. In the next paragraphs, a bibliographic review is made to attempt to understand the deformation mechanisms at stake during the process, how they are influenced by process conditions and which kind of model can be employed for FEM analysis.

2.2.2 Deformation mechanisms

As explained above, the different deformation mechanisms can act at the same time, yet, they have preferential range of temperature and loading conditions. Ashby and Frost [3] have widely studied the deformation mechanisms of metals. They evaluated the operating zones of deformation mechanisms (where a mechanism dominates the others) for various metals so that to draw deformation mechanism map (DMM). The Figure 2.2a shows a stress-temperature DMM and the Figure 2.2b a strain rate-stress DMM of pure titanium with a 100 μm grain size.

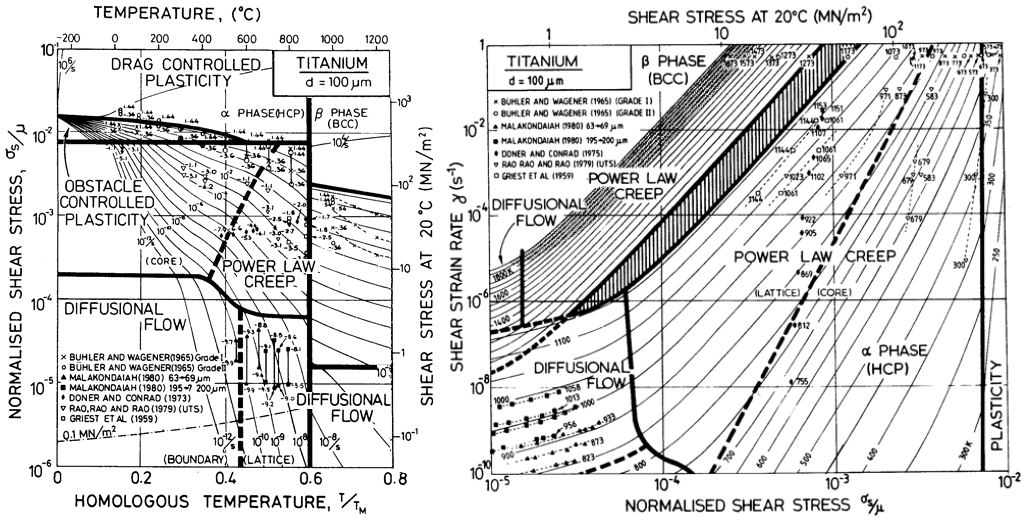

(a) **(b)**

Figure 2.2 – Deformation mechanisms maps for commercially pure titanium with a grain size of 0.1 mm (a) stress-temperature and (b) strain rate-stress [3]

The different mechanisms are considered dominant and separated by boundaries by using the governing stress-strain rate equations. Indeed, each mechanism is governed by a stress-strain rate equation that is used to discriminate the operating range of the mechanism. For the Figure 2.2a, the lines define the iso-strain rate curves associated to a couple of temperature

and stress while for the Figure 2.2b, they correspond to iso-temperature associated to a couple of stress and strain rate.

Actually, the deformation mechanisms do not independently act until stress and temperature transition. However, this kind of map enables to evaluate the type of equations that govern the material behavior in specific process conditions. Each mechanism is approached hereafter. In the next paragraph related to the deformation mechanisms, some non cited information were taken from thoroughgoing books of Lütjering and Williams [4] on titanium, and Ashby and Frost on deformation mechanisms of metals [3].

2.2.2.1 Crystal plasticity

The crystal plasticity in titanium alloys refers to plastic deformation by dislocation motion within slip planes or by twinning. Twinning in Ti-6Al-4V is most of the time mentioned in literature in the cases of very high strain rates [77, 78], or cryogenic temperatures [79, 80], and more generally when critical resolved shear stress (CRSS) is high. In our process it is not the case. Thus, twinning was not considered in this thesis.

The slip planes in a crystal are the closed packed planes which have the highest atom density, and so the minimum inter-atomic slip distance. The titanium is a dual phase material with α and β phases. α phase is a hexagonal close packed structure which is present in pure titanium at temperatures below 882 °C [4]. Above this temperature α phase transforms into β phase, a body centered cubic (BCC) structure. In Ti-6Al-4V alloy, the presence of aluminum and vanadium, respectively α and β stabilizers, modifies the equilibrium phase content at ambient temperature and its evolution up to β-transus (around 980 °C).

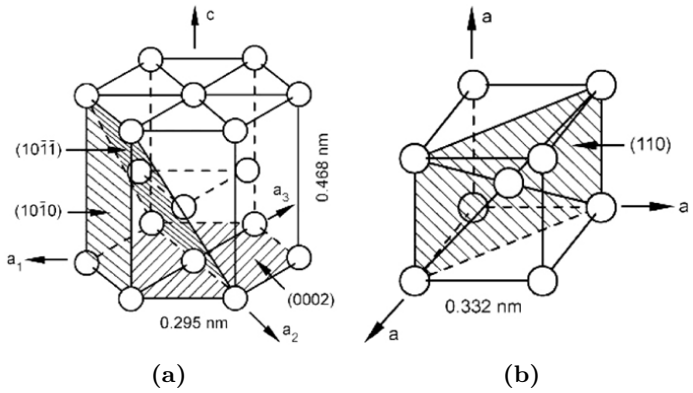

Figure 2.3 – Critallographic representation of slip system in (a) α HCP structure and (b) β BCC structure [4]

Each phase has its own slip systems. There are four different families of slip systems in the primary α phase: 3 basal, 3 prismatic, 6 first order and 12 second order pyramidal slip systems illustrated in the Figure 2.3a. The dominant slip systems of the primary α phase are the basal and prismatic slips due to their relatively low CRSS [81]. Concerning β phase, BCC structure has not true closed packed planes that is why it requires heat to activate slip systems. However it has a family of 6 planes having close packed directions with two slip directions, which together form 12 different slip systems. Therefore the β phase is found to be more ductile compared to the α phase. Moreover, the BCC mentioned slip planes are not fully closed packed, which bring higher diffusion rate inside β grains [12].

The evolution of plastic deformation mechanisms with temperature is related to many complex parameters. There is firstly, the complexity of the different slip systems of both α and β phases that exist inside Ti-6Al-4V alloy and the evolution of associated CRSS with

temperature and phase content evolution [4]. Moreover, there are different morphologies of grains with different types of interfaces on which dislocation can be blocked. Also, the appearance of thermal activation makes atomic diffusion disturbing dislocation glide on dominant slip systems.

Therefore, in the frame of the study, the deformation mechanisms were not be studied in details, but simply on mechanical properties and modeling point of view.

2.2.2.2 Low temperature plasticity

At low temperature, plasticity is induced by dislocation glide. It is the most classical way for dislocation to move following slip systems. Dislocation glide is limited by lattice resistance and also by the presence of obstacles to slip: impurities, solute, other dislocations or precipitates. The Figure 2.4a and 2.4b illustrates how the dislocations glide in both lattice resistance or obstacle limiting glide conditions.

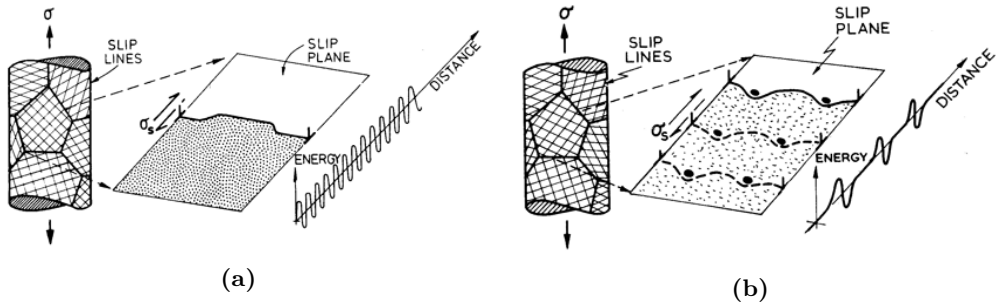

Figure 2.4 – Schematic representation of (a) lattice resistance dominated plasticity (b) obstacle controlled plasticity [3]

The rate equation that governs glide mechanisms can be obtained from Orowan relation [82] defined by the Equation (2.1) where the shear strain rate $\dot{\gamma}$ is proportional to the average velocity of dislocation $\overline{\nu}$ and the density of mobile dislocation ρ_m multiplied by the magnitude of burger's vector b. Kocks et al. [83, 84] used an Arrhenius equation to relate the shear strain rate to the applied shear stress defined by the Equation (2.2) where $\dot{\gamma}_0$, ΔF, τ_0, p, q are relatively a constant associated to steady state dislocation density for specific shear stress τ_s, the free energy also called activation energy, the athermal stress referring to yield stress and material exponents. This equation is generalized for every types of dislocation motion limiting effects. ΔF, p and q are dependent of the type of obstacles. The Figure 2.5a gives the parameters tendencies for the different obstacles conditions.

$$\dot{\gamma} = \rho_m b \overline{\nu} \tag{2.1}$$

$$\dot{\gamma} = \dot{\gamma}_0 \; exp\left[-\frac{\Delta F}{kT}\left(1 - \frac{\tau_s}{\tau_0}\right)^p\right]^q \tag{2.2}$$

- Lattice resistance
  At the scale of one slip system, Pieirls-Nabarro stress [85] relates the stress necessary to move dislocation as a function of crystal parameters (see Equation (2.3) where μ is the shear modulus, ν the Poisson's ratio, ζ the width of dislocation and b the burger's vector).
  The stress necessary to promote glide in Ti-6Al-4V corresponds to CRSS of the different slip systems. The Figure 2.5b shows the evolution of CRSS for the three principal slip systems of α phase.

- Obstacle resistance
  When glide is obstacle limited, the material exponents p=q=1 [83] and the equation can be simplified.

$$\sigma_{PN} = \frac{2\mu}{1-\nu} exp\left(\frac{-2\pi\zeta}{b}\right) \tag{2.3}$$

Obstacle strength	ΔF	$\hat{\tau}$	*Example*
Strong	$2\ \mu b^3$	$> \frac{\mu b}{\ell}$	Dispersions; large or strong precipitates (spacing ℓ)
Medium	$0{\cdot}2$–$1{\cdot}0\ \mu b^3$	$\approx \frac{\mu b}{\ell}$	Forest dislocations, radiation damage; small or weak precipitates (spacing ℓ)
Weak	$<0{\cdot}2\ \mu b^3$	$\ll \frac{\mu b}{\ell}$	Lattice resistance; solution hardening (solute spacing ℓ)

(a)

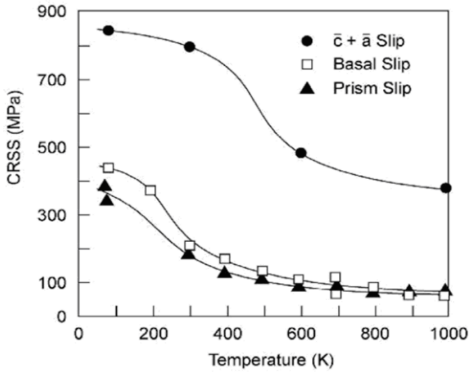

(b)

Figure 2.5 – (a) Characteristics of obstacles [3], (b) CRSS evolution with temperature for the three principal slide systems in α HCP crystalographic structure [4]

Ashby and Frost proposed an equation for any gliding conditions where the flow stress is proportional to $\mu b/l$, where l is the obstacle spacing and b the Burger's vector [3]. The Equation (2.4) defines dislocation glide relation where k is Boltzmarm's constant, T the absolute temperature, a the activation area, and σ_0 is a cut-off stress, sometimes called the "athermal part of flow stress". The pre-exponential term $\dot{\varepsilon}_0$, is the strain-rate when $\sigma = \mu b/l$.

$$\dot{\varepsilon}_{gl} = \begin{cases} \dot{\varepsilon}_0 exp\left(-\frac{\mu b/l - \sigma}{kT} ba\right) & \frac{\sigma}{\mu} > \frac{\sigma_0}{\mu} \\ 0 & \frac{\sigma}{\mu} < \frac{\sigma_0}{\mu} \end{cases} \tag{2.4}$$

2.2.2.3 Dislocation creep

Dislocation creep mechanisms include several deformation mechanisms that are characteristics of power law creep area of DMM. The rate equation in this domain can be presented in the power law form as presented in the Equation (2.5) [86, 87] where D_v is the bulk-volume diffusion coefficient, n is the stress exponent and A is a dimensionless constant.

$$\dot{\varepsilon} = A\frac{D_v \mu b}{kT}\left(\frac{\sigma}{\mu}\right)^n \tag{2.5}$$

At moderate stress, dislocation density inside the crystal generates high amount of free energy and thermal activation enables dislocation to climb between parallel slip planes to overcome obstacles and glide up to the next obstacle. This mechanism is helped by vacancy diffusion processes. It is an intra-granular dislocation process. n exponent parameter can vary around 4-6 [86]. The vacancy diffusion process passes from lattice to core diffusion as a function of temperature [88], which makes varying the diffusion coefficient.
Another dislocation creep mechanism that can operate in metals is Harper–Dorn creep [89]. It is a low stress level mechanism which operates in low dislocation density level by climb. It is characterized by a linear dependence to the stress (n=1). It also operates in Ti-6Al-4V at

low stress regime [90, 91]. Harper–Dorn creep is sometimes assimilated to diffusion creep mechanisms because of its dependency to stress which is equivalent to diffusion process.
At sufficiently high stresses, it is observed that the power law breaks down so that the strain rate sensitivity decreases. This phenomena is due to a transition from climb-controlled to glide-controlled dislocation creep. The stress exponent rises to 10-20 according to material and temperatures.
In Ti-6Al-4V, dislocation creep is controlled by climb [91] at moderate stress ($3< n <6$), and glide assisted climb for higher stress values in power law breakdown (not considered because high stress level).

2.2.2.4 Diffusion creep

Diffusion creep is a process that requires low stresses to work. It refers to stress directed flow of vacancies that accommodates deformation [92]. The diffusion processes can operate at grain boundaries known as Coble diffusion creep [93] or bulk diffusion known as Nabarro-Hearing creep [92]. Coble creep works at lower temperature whereas Nabarro-Hearing creep requires superior thermal activation for vacancies to move inside grain.

The Equation (2.6) defines the strain rate-stress relation for both Coble and Nabarro-Hearing diffusion mechanisms [3] where Ω is the atomic volume, d the grain size, D_v the bulk self-diffusion coefficient, D_{gb} the grain boundary diffusion coefficient and δ the effective cross section of a boundary for diffusional transport.

$$\dot{\varepsilon}_{diff} = \frac{42\Omega\sigma}{kTd^2} D_v \left(1 + \frac{\pi\delta}{d}\frac{D_{gb}}{D_v}\right) \tag{2.6}$$

2.2.2.5 Others mechanisms

2.2.2.5.1 Grain boundary sliding (GBS)

GBS is another high temperature deformation mechanism that involves complex phenomena. Basically, GBS refers to the lateral motion of grains at their interface. Sliding is enabled thanks to the motion of dislocations along boundaries. However, the dislocation pills-up ends to generate stress concentrations at triple junction and grain boundary ledge so that to slip inside the adjacent grain until obstacles [94].
When the microstructure presents specific properties (equiaxed grains, grain size inferior to critical value - $d < \lambda$) and the loading conditions are diffusion creep mechanisms favorable, the GBS mechanism leads to superplasticity [94, 7]. Indeed, when GBS is accommodated by diffusion creep mechanisms, the microstructure is not affected by the deformation, and the condition for GBS are still favorable. On the contrary, when the conditions are not favorable ($d > \lambda$) dislocations tend to regroup in subgrains inside initial grain [95]. Moreover when too high stresses do not enable accumulated dislocation at a triple junction to slip, cavitation can nucleate and finally promote fracture.
The Equation (2.7) defines the rate equation [96] for GBS deformation mechanisms where D is the diffusion coefficient, p is the grain size exponent. In superplastic conditions ($d < \lambda$), p=n=2 and D corresponds to the grain boundary diffusion coefficient whereas in creep conditions ($d > \lambda$), p=1, n=3 and D corresponds to the self diffusion coefficient [94].

$$\dot{\varepsilon} = \frac{AD\mu b}{kT}\left(\frac{b}{d}\right)^p \left(\frac{\sigma}{\mu}\right)^n \tag{2.7}$$

One big advantage of superplasticity is that the strain rate sensitivity exponent m ($= 1/n$) is high and has the effect to limit strain localization during forming processes. Ti-6Al-4V presents very interesting superplastic properties and has been largely study in the literature

[97, 7, 98]. The superplastic material usually presents high values of m (between 0.3 and 0.85). Ti-6Al-4V fairly exhibits high value around m=0.85 at specific temperature of 927 °C [99].

2.2.2.5.2 Dynamic recristalization/recovery

The dynamic recrystallization (DRX) and recovery are not deformation mechanisms, but consequences of dislocation motion inside material during deformation. During DRX, the nucleation and growth of new grains occur during deformation. This phenomenon is due to the re-arrangement of dislocations inside grains up to nucleation of new grains inside. Dynamic recovery can act as a complementary process of DRX. Indeed, dynamic recovery consists in the annihilation, the re-covering of motion of dislocations during deformation and in some specific conditions it promotes re-arranging of dislocation to group them and create bigger grains. Both dynamic processes consequently and periodically act as a function of processing conditions (Temperature and strain rate) [100].
DRX is a process that occurs at high temperature ($T>0.5T_m$) where β phase has high content. Indeed, β is the phase that generates recrystallized refine grains [101]. In Ti-6Al-4V, DRX is mainly used to create grain refinement to obtain ultrafine grains microstructures [100].
In our process conditions, the temperature and principally the strain rate conditions are too low to generate DRX or recovery processes as steady state mechanisms. Therefore, theses mechanisms are not considered.

2.2.2.6 Synthesis

The plastic deformation mechanisms are guided by the motion of dislocations, themselves guided by the slip planes of the phases met by the dislocations. At low temperature, dislocations move by glide in the α phase principally. The gliding can be controlled by obstacles or lattice resistance.
When the temperature increases, the vacancy diffusion is activated and the dislocation glide and climb processes are activated. At moderate and high temperature, dislocation creep is controlled by climb and obeys to power law creep mode. However, at low stress, Harper-Dorn creep mechanisms can operate with a linear dependence to stress while at high stress power law creep breaks down because of transition of glide plus climb process to viscous glide only. Finally, at high temperature and low stresses, two diffusion processes as Coble and Nabarro-hearing creep can operate respectively at grain boundaries (lower temperature) and through the grains (higher temperature). Both mechanisms generate a deformation with a linear dependence to stress but with two different diffusion energy levels. Moreover, grain boundary sliding operates at high temperature and low or moderate stress simultaneously to diffusion creep. Stress strain rate relation during GBS can be defined with power law. The Figure 2.6 is a deformation map that summarizes the deformation mechanisms and defines the associated relations of steady state strain rate with stress.

2.2.3 Material behavior

In the previous section, it has been discussed that the material behavior is governed by the motion of dislocations inside latices, grains, grain boundaries, at phase interfaces and so one. The Figure 2.7 illustrates the interconnection of the different scales until macroscopic description. In this section, the macroscopic (related to microscopic phenomena) material behavior of titanium alloys and especially Ti-6Al-4V are detailed.

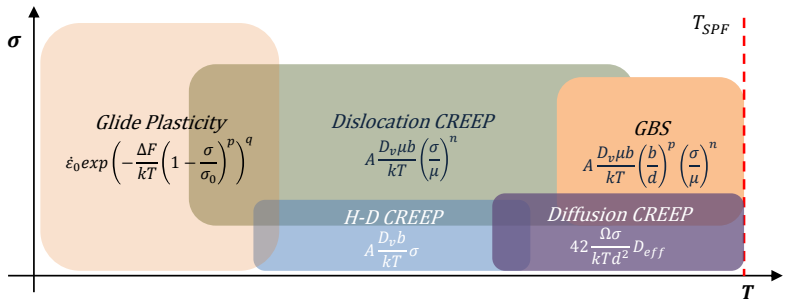

Figure 2.6 – Schematic deformation mechanisms map for Ti-6Al-4V in the post SPF process conditions

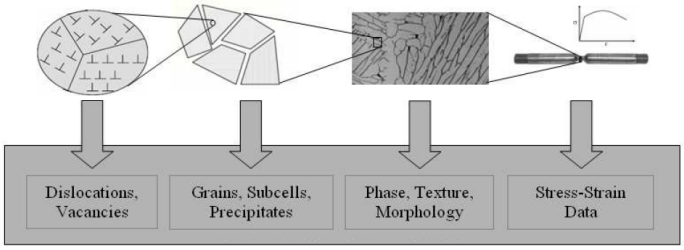

Figure 2.7 – Illustration of the different scales to describe material behavior from dislocation to macroscopic behavior [5]

2.2.3.1 Strain rate sensitivity

One important behavior of titanium alloys is the SRS. This phenomenon is a consequence of dislocation and diffusion creep mechanisms that are stress dependent. The SRS is often described thanks to the SRS exponent m defined from the Equation (2.8) and (2.9). The Equation (2.8) is the Norton Hoff (NH) power law [102] used to model creep viscoplastic behavior.

$$\sigma = K\dot{\varepsilon}^m \tag{2.8}$$

$$m = \frac{\partial ln(\sigma)}{\partial ln(\dot{\varepsilon})} \tag{2.9}$$

SRS has been largely studied from decades to evaluate the elongation capacity of metals. Indeed, Woodford [6] related the strain rate sensitivity as a measure of ductility (seen in the Figure 2.8). This phenomena is directly related to the fact that high SRS exponent prevents material from strain localization and tends to propagate strain during tensile tests particularly.

As for deformation mechanisms, for which the stress exponent varies with temperature and dominant mechanisms, the SRS evolves with thermomechanical loading conditions. The Figure 2.9a represents the stress strain-rate data obtained from load-relaxation tests at various temperature, and in the Figure 2.9b is plotted the contour map of iso-values of m from the data of the Figure 2.9a [7].

The sensitivity of m on temperature and strain rate for Ti-6Al-4V alloy is most of the case investigated in the frame of high temperature creep and superplasticity [103, 104, 7]. However, some works were performed at low temperatures [91, 8]. The Figure 2.10 reports the SRS exponent computed from strain rate jump tests at various temperatures from 20 °C to 700 °C. This graph highlights an interesting phenomenon around 400 °C where the SRS is null. Vigié et al. depicted three different zones of temperature separated by dotted lines.

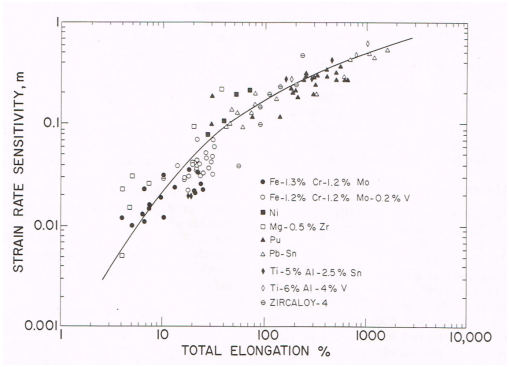

Figure 2.8 – Correlation between strain rate sensitivity and total elongation for a variety of materials [6]

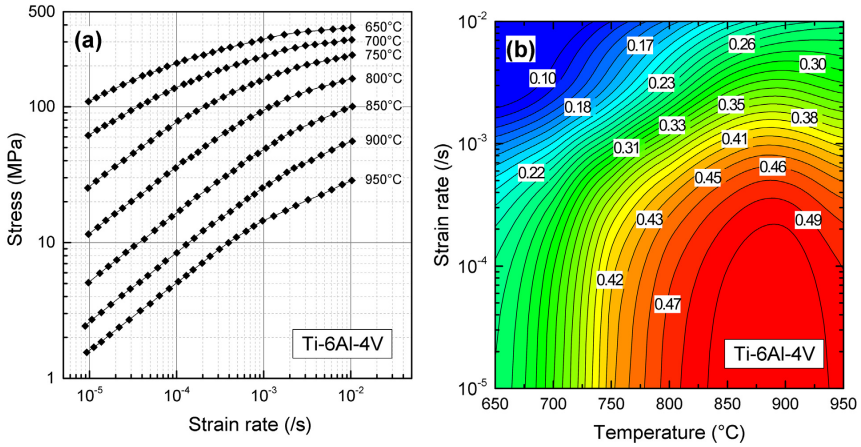

Figure 2.9 – (a) stress dependence on strain rate of Ti-6Al-4V at temperatures between 650 °C and 950 °C obtained by stress relaxation techniques. (b) contour map of the SRS exponent m as a function of temperature and strain rate derived from (a). [7]

According to Conrad [105], this phenomenon is related to a strong increase of the activation volume of basal slip system around these temperatures for pure titanium (where activation volume is inversely proportional to SRS).

2.2.3.2 Strain hardening

As explained above, the dislocation density evolves as a function of dislocation motion inside the material. When a dislocations struggles to move inside lattice, it is blocked and another dislocation is emitted from dislocation sources. The increase of dislocation density can increase critical resolved shear stress because the dislocations can become themselves obstacles. Strain hardening phenomena traduces the increase of the shear stress necessary to promote plastic deformation. This phenomenon is more effective when diffusion processes are inactive because diffusion helps dislocation to overcome obstacles by climb. Therefore, strain hardening is more active at low than high temperatures.

The last decades, lot of studies on strain hardening processes in titanium alloys have been made for rapid forming or forging conditions at high temperature [106, 107, 108]. At high strain rate and high temperature, the competition between hardening and softening mechanisms can lead to small hardening level due to low stresses required for diffusion processes.

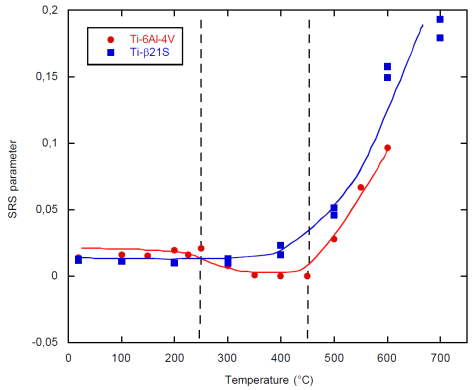

Figure 2.10 – Evolution of the strain rate sensitivity parameter versus temperature of the Ti-6Al-4V and the Ti-β21S alloys computed by strain rate jump tests [8]

The Figure 2.11 shows some tensile test curves performed at 0.01 s^{-1} for various temperatures on Ti-6Al-4V samples [9]. The work hardening rate is computed by deriving the stress-strain curves. The experimental data highlight a decrease of hardening rate more rapidly with the increase of temperature. The flow stress seems to reach an asymptote for 700 °C. At temperature below 700 °C, hardening rate seems to stay positive all along tensile test. During first part of the test, between 0 and 0.05 plastic strain, the high decrease of hardening rate can be partly a consequence of hardening but also to the viscosity of the material.

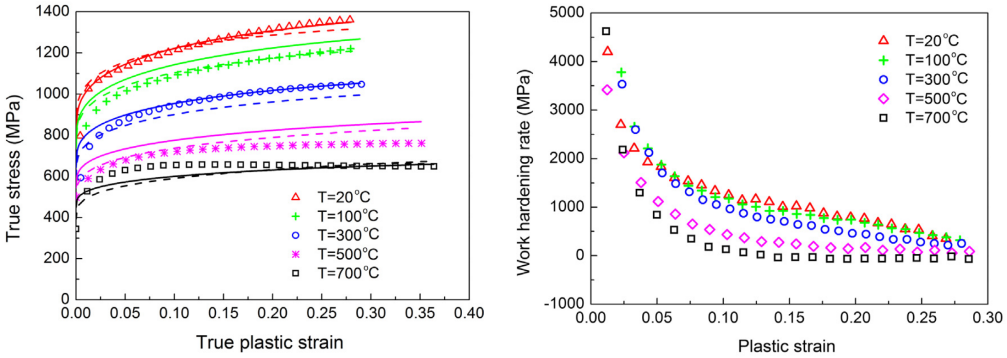

Figure 2.11 – (a) comparison of experimental (symbols), Johnson Cook (JC) model (dash lines) and JC-modified models (solid lines) prediction of the flow stresses for 0.01 s^{-1}, (b) Work hardening rate of the Ti–6Al–4V [9]

Kocks and Mecking [83, 84] develop work hardening theory on dislocation density. Indeed, they differentiate the effect of mobile and immobile dislocations. The mobile dislocations impact the viscoplastic behavior into a "thermal stress" affected by short range obstacles. Immobile dislocations influence the hardening behavior through an "athermal" part of the stress which refers to long range obstacles. The Equation (2.10) defines the athermal stress σ_μ where m, α, μ, b and ρ_i are respectively the Taylor orientation factor, a proportionality factor, the shear modulus, the magnitude of burger's vector and the immobile dislocations density (IDD).

$$\sigma_\mu = m\alpha\mu b\sqrt{\rho_i} \tag{2.10}$$

According to Kocks-Mecking theory [84, 109], the immobile dislocations variations can be divided into hardening (positive contribution $\dot{\rho}_i^{(+)}$) and restoration (negative contribution $\dot{\rho}_i^{(-)}$) processes as defined in the Equation (2.11). They defined the variation of dislocation density with strain presented in the Equation (2.12) where k_1 represents the hardening process due to dislocation immobilization after having traveled a mean free path. k_2 is associated to thermally activated dynamic recovery.

$$\dot{\rho}_i = \dot{\rho}_i^{(+)} - \dot{\rho}_i^{(-)} \tag{2.11}$$

$$\frac{\partial \rho_i}{\partial \varepsilon} = k_1 \sqrt{\rho_i} - k_2 \rho_i \tag{2.12}$$

Assuming that dislocation hardening process is promoted by dislocation blocking during gliding, it is possible to express the positive hardening contribution thanks to Orowan equation [82] (Equation (2.1)) using the mean free path $\frac{1}{\Lambda}$ [5]. $\frac{1}{\Lambda}$, defined by the Equation (2.14), represents the average of characteristic path distance traveled by a dislocation, where d is the mean grain size, s is the mean subgrain size and "others" means any other obstacles.

$$\dot{\rho}_i^{(+)} = \frac{m}{b} \frac{1}{\Lambda} \dot{\bar{\varepsilon}}_p \tag{2.13}$$

$$\frac{1}{\Lambda} = \left(\frac{1}{d} + \frac{1}{s} + others \right) \tag{2.14}$$

Another hardening mechanism, which is related to dislocation motion and main free path concerns grain size hardening. Hall-Petch relation [110] defines the dependence of athermal stress to the grain size. The Equation (2.15) defines this relation where the first term can be associated to athermal part of the stress related to IDD (Equation (2.10)), and the second term corresponds to Hall-petch effect where k_d is a material parameter.

$$\sigma_\mu = \sigma_0(\mu, \rho_i) + \frac{k_d}{\sqrt{d}} \tag{2.15}$$

In many studies on viscoplastic behavior of titanium alloys, kinematic hardening is investigated. Kinematic hardening refers to the non-symmetrical evolution of elastic domain and hardening characteristics as a function of stress state. The Bauschinger effect is a famous example that implies an increase in tensile yield strength which occurs at the expense of compressive yield strength. However, this kind of investigations requires to perform cyclic mechanical testing, which has no real interest in the frame of our study and has not been considered.

2.2.3.3 Recovery

The Recovery phenomena refers to the annihilation of immobile dislocations either by annihilation or by recovering mobility. The effect of recovery processes is to soften yield strength of material. Recovery can process by glide or climb. Each of these mechanisms respectively requires more thermal activation to operate such as for mobile dislocations. The Equation (2.16) defines the total contribution of recovery mechanisms on IDD rate $\dot{\rho}_i^{(-)}$ as the sum of the climb $\dot{\rho}_i^{(cl)}$ and glide $\dot{\rho}_i^{(gl)}$ contributions.

$$\dot{\rho}_i^{(-)} = \dot{\rho}_i^{(cl)} + \dot{\rho}_i^{(gl)} \tag{2.16}$$

IDD variation under glide is defined by the Equation (2.17) where Ω is the glide probability of the remobilization factor [111]. Ω is strain independent and for $T<0.5T_m$, Ω tends to zero. Babu [5] defined the IDD variation under climb given in the Equation (2.18) where D_l,

c_v, c_v^{eq} and ρ_{eq} are respectively the self diffusion coefficient, the vacancy concentration, the equilibrium vacancy concentration and the equilibrium dislocation density.

$$\dot{\rho}_i^{(gl)} = \Omega \rho_i \dot{\bar{\varepsilon}}_p \tag{2.17}$$

$$\dot{\rho}_i^{(cl)} = 2D_l \frac{c_v}{c_v^{eq}} \frac{Gb^3}{kT} \left(\rho_i^2 - \rho_{eq}^2\right) \tag{2.18}$$

A distinction is made between dynamic recovery usually associated to DRX process, and static or time recovery associated to thermal effect and/or quasi-static deformation. However, the operating mechanisms are the same ones [112].

2.2.4 Microstructure evolutions

One important issue of phase transformations in the context of our process, is to understand how β phase transforms from the SPF temperature (below β transus), with post SPF miscrostructure, under heterogeneous cooling rate conditions. The second important issue results from the first one and brings the next question: are the potential heterogeneous transformations responsible to an heterogeneous material behavior ? In other words, is it necessary to consider the phase transformations inside the material model ?
These two aspects are detailed in the next section from bibliographic point of view. Some additional topics regarding microstructure evolutions are also addressed.

2.2.4.1 Impact of SPF on the microstructure

SPF is processed at constant temperature so that α and β phases content does not evolve. The main evolutions concern the morphology of microstructure such as grain size and cavity issues.

- Grain size

Ghosh and Hamilton [97] worked on the impact of grain size evolution under superplastic tensile test conditions on Ti-6Al-4V at 927 °C at various strain rates. The Figure 2.12a compares grain growth under different strain rate from zero to 5.10^{-3} s^{-1}. This highlighted that it exists a static grain growth (SGG) and dynamic grain growth (DGG). The Figure 2.12b highlights that this grain size evolution has an impact on the strain rate sensitivity during forming. The grain growth kinetics and models have been largely investigated these past decades [113, 97, 114, 115, 116, 11, 18] Globally, grain growth is due to the grain boundary mobility activated by diffusion and promoted by excess of vacancy concentration generated by GBS. The grain growth sensitivity to strain rate is related to the acceleration of vacancy concentration when increasing GBS [117]. Usually grain growth models are split into SGG $\dot{d}_{static}$ and DGG $\dot{d}_{dynamic}$ as respectively defined by the Equation (2.19) and the Equation (2.20). The dependency of these parameters can be modeled by Arrhenius form with a very good approximation [18].

$$\dot{d}_{static} = \alpha_1 d^{-\gamma_1} \tag{2.19}$$

$$\dot{d}_{dynamic} = \alpha_2 \dot{\varepsilon}^{\delta_2} d^{-\gamma_2} \tag{2.20}$$

Finally, anisotropic grain growth can promote texture during superplastic forming [118]. Indeed this phenomenon is related to the absence of intragranular dislocation creep during GBS [119], which generally happens in Al-Mg alloys.

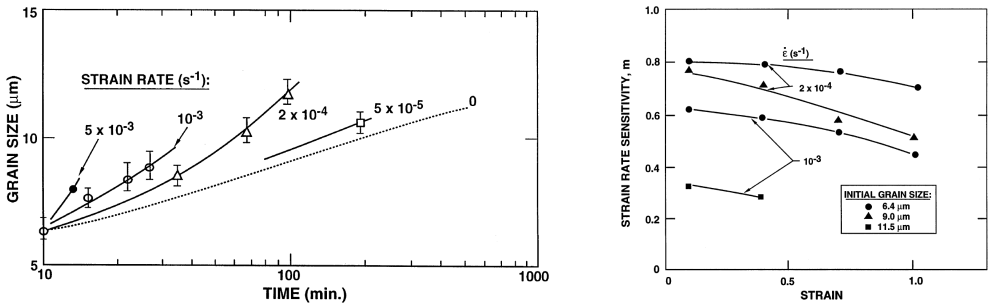

(a) **(b)**

Figure 2.12 – Effect of deformation on the behavior of Ti–6Al–4V samples at 927 °C: (a) comparison of dynamic and static grain growth kinetics for samples with an initial grain size of 6.4 mm, (b) variation of the SRS exponent m with the strain showing the effect of dynamic grain growth on m for samples with initial grain sizes of 6.4, 9 or 11.5 mm [10]

- Cavity

As defined in the paragraph describing GBS deformation mechanism, cavity nucleation is a mechanism that operates when grain boundary sliding is not accommodated by diffusion creep mechanisms [120, 121, 122]. The mechanisms are slightly different between single or dual phase superplastic materials. For dual phase such as Ti-6Al-4V, cavities nucleate at triple junctions, but it is rather negligible between 850 °C and 950 °C in superplastic deformation conditions [123, 11]. The Figure 2.13 shows different micrographs of tensile

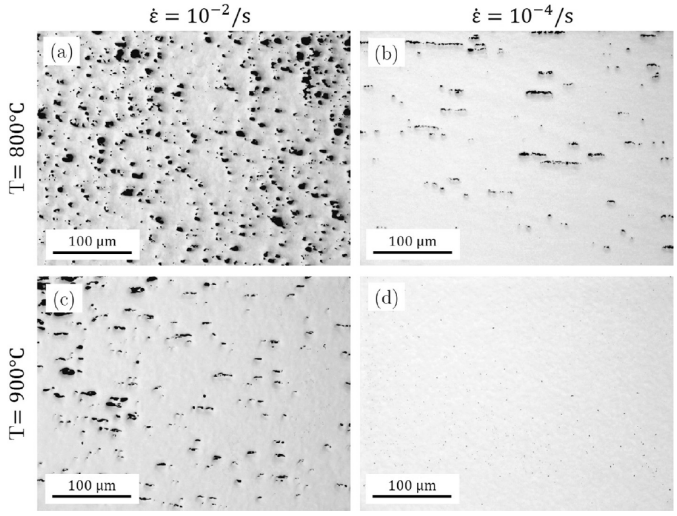

Figure 2.13 – Micrographs reveling voids generated in Ti–6Al–4V after tensile deformation for (a) ε=0.5, (b) ε=1.45, (c) ε=1, (d) ε=1.25 [11]

tests performed at 800 °C and 900 °C, at 10^{-2} and 10^{-4} s^{-1} for large strains. In AIRBUS, the maximum plastic strain goes around 0.5 in general and for some specific part can reach 0.8. The temperature of the process (T_{SPF}=870 °C) is closer to 900 °C, with strain rates fairly closed to 10^{-4} s^{-1} ($\dot{\varepsilon}_{SPF}$ <3.10^{-4} s^{-1}), and the maximum strain can be locally 1.5 to 2 times lower than (b) and (d) micrographs of the Figure 2.13. Therefore, and also because cavities are not observed on post SPF micrographs of specimen cut on industrial parts, the cavity nucleation processes are not considered in the thesis.

2.2.4.2 Phase transformations during cooling

According to Ti-6Al-4V equilibrium phase diagram presented in the Figure 2.14a, β phase is supposed to transform into α phase during cooling in order to respect the phase content equilibrium. The $\beta \rightarrow \alpha$ transformation from above β transus (T_β) is more usually studied than below. Indeed, when the cooling starts from T> T_β, α phase nucleates and growth from boundaries or bulk as platelet colonies which forms so called Widmanstätten secondary alpha α_s phase as represented in the Figure 2.14b. The Figure 2.14c shows the influence of cooling rate on lamellae formation. Lamellae thickness are thinner as the cooling rate increases.

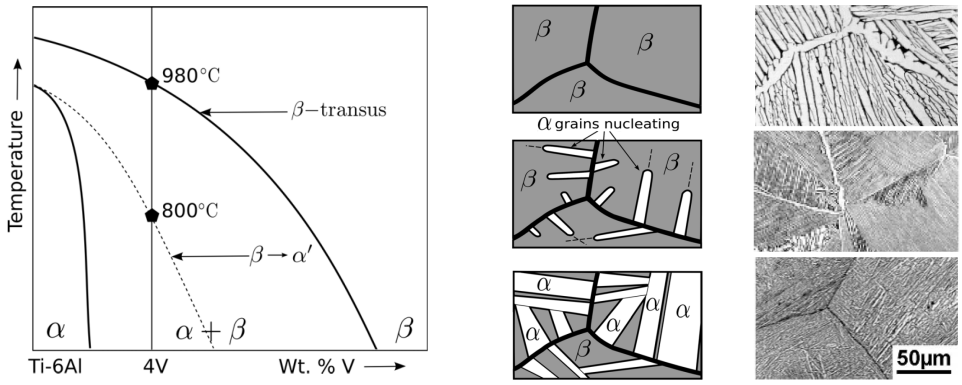

Figure 2.14 – (a) phase diagram of Ti-6Al-4V [5], (b) formation of Widmanstätten structure [5], (c) effect of cooling rate from the β phase field on lamellar microsturctures, Ti-6242, from up to down: 1 °C/min, 100 °C/min, 8000 °C/min [12]

However, when cooling starts from T< T_β, the α phase can transform from grain boundaries as described before, but also from prior alpha phase α_p growth. The Figure 2.15 represents the three different types of secondary β transformed structures as a function of cooling rate [13]. These micrographs were cooled by different means (oiled quenched, air and furnace cooled) from 930 °C. The oiled quenched micrograph presents martensitic phase $\alpha^{'}$ that transforms for high cooling rate (superior to 410 °C/s) by a non-diffusional transformation [124]. The air cooled micrograph presents α_s with a needle type morphology. Indeed, this structure is formed for rapid cooling that promotes large nucleation of α phase within grains with multiple random nucleation directions. The furnace cooled micrographs of the Figure 2.15 presents a mix transformations structure with Widmanstätten structure and α_p phase transformation (grain growth of α_p grains).

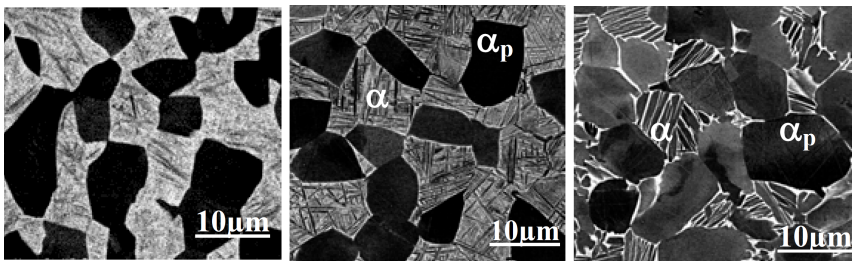

Figure 2.15 – Micrographs of samples heat treated at 930 °C and from left to right water quenched, cooled in the air and cooled in furnace Figure [13]

Semiatin et al. [14] performed battery of cooling heat treatments on Ti-6Al-4V after previous soaking at 955 °C for 20 min. The obtained microstructures are analogous to Homporová et al. [13] for some cooling rates. Nevertheless, they performed low cooling (11 °C/min) from 955 °C to 870 °C close to the temperature of SPF process at AIRBUS. The Figure 2.16 shows micrographs of quenched microstructures at near equilibrium phase content at 955 °C, 870 °C and at ambient temperature. The potential β phase to transform at 870 °C reduced more than a half. It exists several functions to model the phase content evolution

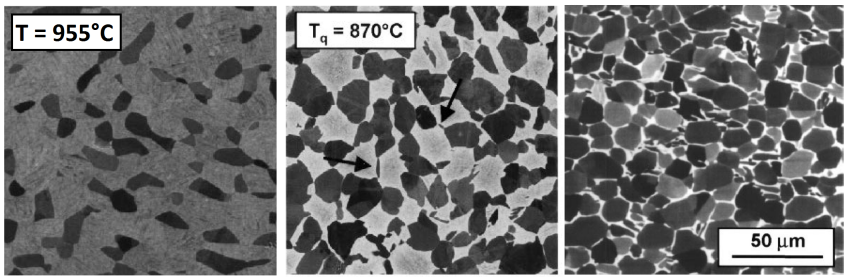

Figure 2.16 – Microstructures developed in Ti-6Al-4V samples during induction heat treatment comprising soaking at 955 °C for 20 min, cooling at a rate of 11 °C/min and water quenching at the temperatures (Tq) indicated. [14]

in Ti-6Al-4V. Castro [125] used an exponential model defined by the Equation (2.21). This formula gives the following results: $f_\beta(955)$=82.3 %, $f_\beta(870)$=43.8 % and $f_\beta(20)$=7.5 %. Thus, in our process, the β phase to transform is around 36 % (more than a half compared to 955 °C).

$$f_\beta = 0.075 + (1 - 0.075) exp\left(-0.0085\,(980 - T)\right) \tag{2.21}$$

2.2.4.3 Influence of heat treatment

According to Semiatin et al. [14], the final properties of a part heat treated in $\alpha + \beta$ domain depends on the volume fraction and size of α_p grains and the characteristics of α_s platelet. During cooling, the presence of Widmanstätten microstructure that catches α phase content, finally decreases the effective size of α_p grains that influences the low temperature behavior. Concerning creep behavior, it is influenced by β grains which is the ductile phase. The increase of α phase interfaces in the Widmanstätten morphology limits the creep properties of the material.
Julien et al. [15] studied the effect of several cooling rate from the soak temperature of 950 °C on the tensile properties of Ti-64. The Figure 2.17 shows the impacts of the tested cooling rates on load-relaxation tests at 20 °C and 700 °C. The difference are not negligible especially for the data at 5 °C/min. They relate the changes of behavior to the impact of cooling rate on lamellae thicknesses for Widmanstatten microstructure.

The influence of microstructure evolution on material behavior has been widely studied in welding industry or recent 3D printing technologies such as Selective layer melting of high deposition rate processes. Indeed, with these technologies, the material can exceed the melting point and follow complex thermal loading that generates residual stresses in the manufactured workpieces. Longuet et al. [16] used a multiphase model to take account of the impact of phase transformation under laser melting conditions. tT cooling rates of the process. Each phase evolution were defined as a function of cooling [69] and the properties of each phase were established by mechanical testing as defined in the Figure 2.18. With this technique, and by using dynamic phase transformations models, the influence of phase transformations on mechanical properties are considered.

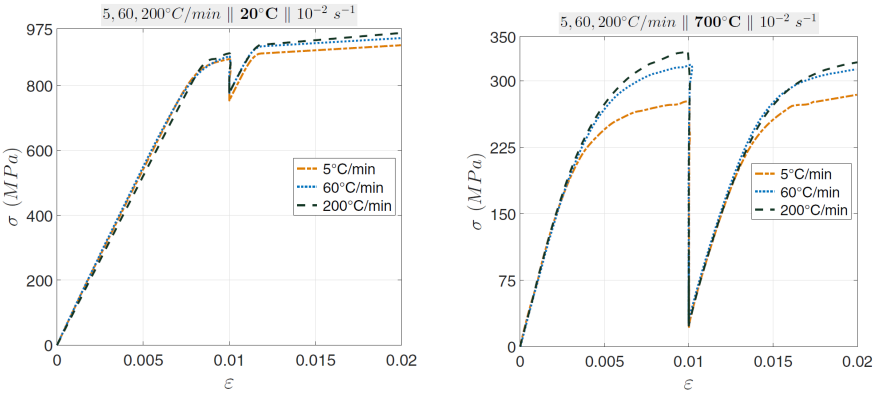

(a) **(b)**

Figure 2.17 – Stress-strain response for different cooling rates at (a) 20 °C and (b) 700 ° [15]

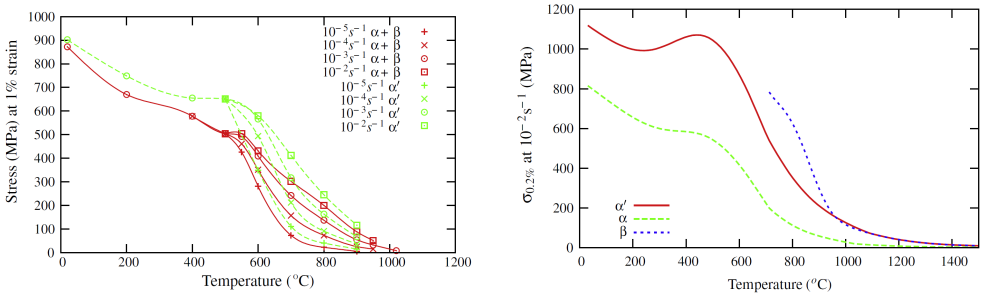

(a) **(b)**

Figure 2.18 – (a) Experimental flow stress at 1% strain with respect to temperature for different strain rates (b) Computed stress at 0.2% strain and a strain rate of 10^{-2} s^{-1} for each phase [16]

2.2.5 Material modeling

In a first time, some laws and models related to specific behaviors described above (Viscoplasticity/SRS, hardening, softening/recovery) are presented. Then a review of constitutive modeling equations is presented.

2.2.5.1 Behavior modeling

- Strain rate sensitivity

The SRS is usually modeled by the inverse NH law where the stress exponent n defined in the creep strain rate laws is the inverse of SRS exponent m. It was seen that the stress exponent and even the strain rate-stress relation change with temperature and stress level. Sellars and Tegart [126] defined a general relation that fits the whole range of stress level (Equation (2.22)).

$$\dot{\varepsilon} = \begin{cases} A^{''} exp(\beta\sigma) & low\ \sigma \\ A^{'}\sigma^{n} & high\ \sigma \\ A\left[sinh(\beta\sigma)\right]^{n} & \forall\ \sigma \end{cases} \tag{2.22}$$

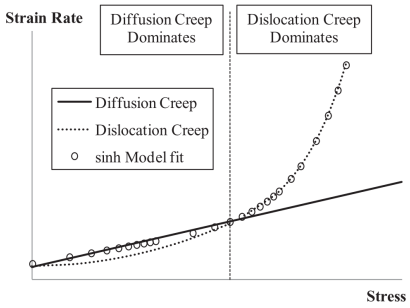

Figure 2.19 – Typical stress-strain-rate behaviour of the mechanisms of deformation for P91 steel and a hyperbolic sine fit to the dominant creep process [17]

The hyperbolic sine form has the advantage to promote natural variable sensitivity of SRS exponent to strain rate [127, 128] contrary to Norton Hoff power law. The Figure 2.19 illustrates the effect of hyperbolic sine law in accordance with deformation mechanisms transition between dislocation and diffusion creep. The Equation (2.23) gives the computation of m from the Equation (2.22). The last raw which corresponds to the hyperbolic sine formulation, clearly shows a strain rate dependence. Another possibility to introduce SRS, is to associate a variable definition of m into NH power law. Sung et al. [129] used such method with a temperature and strain rate sensitive m exponent defined in the Equation (2.24).

$$m = \frac{\partial ln(\sigma)}{\partial ln(\dot{\varepsilon})} = \begin{cases} 1/(\beta\sigma) & low\ \sigma \\ 1/n & high\ \sigma \\ \frac{1}{\beta n}\frac{1}{\sigma}\frac{(\dot{\varepsilon}/A)^{1/n}}{\sqrt{1+(\dot{\varepsilon}/A)^{2/n}}} & \forall\ \sigma \end{cases} \tag{2.23}$$

$$m = m_1 + m_2(T - T_0) + m_3 ln(\frac{\dot{\varepsilon}}{\dot{\varepsilon}_0}) \tag{2.24}$$

- Hardening & Softening

There are various possibilities to model hardening and softening effects at different scales. Indeed, at dislocations scale, combining the Equation (2.15) and (2.10), it is possible to model both the effects of the evolution of immobile dislocation density and also the effect of grain size evolution through grain boundary migration (Equation (2.25)). In this equation the evolution of internal variables ρ_i and d can be described by the Equations (2.16), (2.17), (2.18), (2.19) and (2.20).

$$\sigma_\mu = m\alpha\mu b\sqrt{\rho_i} + \frac{K_d}{\sqrt{d}} \tag{2.25}$$

Another possibility is to use experimental or phenomenological laws. There is a large quantity of exiting laws. The hardening models are based on two different kind of mathematical formulations. There are multiplicative and additive formulations such as respectively defined in the Equations (2.26) and (2.27) where σ_0, R, σ_v are the yield stress, the hardening value and the viscous stress, and g and h are the strain and strain rate hardening functions where α_i and β_i are internal variables. The base of isotropic hardening models is build either on power laws (type Hollomon [130]), or exponential saturated (type Voce [131]) types or combination of both with or without threshold. The formulation can contain recovery terms (static or dynamic). The Table 2.1 shows some advanced hardening models.

$$\sigma = \sigma_0(T) + R(\bar{\varepsilon}, T, \alpha_i) + \sigma_v(\dot{\bar{\varepsilon}}, T, \beta_i) \tag{2.26}$$

$$\sigma = g(\bar{\varepsilon}, T, \alpha_i) * h(\dot{\bar{\varepsilon}}, T, \beta_i) \tag{2.27}$$

The Swift model (1) is a classical model used for cold metal forming. The Hansel-Spittel model (2) is used for bulk forming and forging operations at any range of temperature (thanks to temperature dependence of n_i parameters and additional temperature sensitivity terms). It is used in the FEM software Forge ®. The complete formulation has a viscous multiplicative term. The Voce model (3) is largely used for high temperature saturated hardening behavior. This formulation takes account strain hardening and dynamic recovery (by glide/climb). Chaboche (Equation (4)) proposed an evolution of Voce model with a static recovery effect and a saturation recovery term Q_r. At high temperature, Q_r can be null. Finally, the Equation (5) provides a mixed model with both Voce and Swift formulations weighted by a rule of mixture.

Each of these models may reproduce the Ti-6Al-4V hardening behavior at specific range of temperature. At low temperature, the behavior tends to be linear while at high temperature it is saturated. The inclusion of the static recovery term is very important due to the highly viscous nature (high strain rate sensitivity) of superplastic materials [132].

	Equation	Parameters	Ref
	Unsaturated models		
(1)	$\sigma_y = K(\varepsilon + \varepsilon_0)^n$	K, ε_0, n	Swift [133]
(2)	$\sigma_y = A\varepsilon^{n_1}(1+\varepsilon)^{n_2}e^{n_3/\varepsilon}e^{n_4\varepsilon}$	A, n_1, n_2, n_3, n_4	Hensel-Spittel [134]
	Saturated models		
(3)	$\sigma_y = \sigma_0 + Q(1-e^{-b\varepsilon})$	Q, b, σ_0	Voce [131]
(4)	$\sigma_y = \sigma_0 + \int \dot{R}dt$ $\dot{R} = b(Q-R)\dot{\varepsilon}$ $-\gamma\|Q_r - R\|^{m-1}(Q_r - R)$	σ_0, b, Q, b, γ, c	Chaboche [135]
	Mixed		
(5)	$\sigma_y = \sigma_0 + \int \dot{R}dt$ $\dot{R} = \alpha\dot{R}_{voce} + (1-\alpha)\dot{R}_{swift}$	σ_0, α, P_{voce}, P_{swift}	Pipard et al.[136]

Table 2.1 – Phenomenological hardening models

2.2.5.2 Global models

Many material models are only valid on specific range associated to forming or operating process conditions. In the frame of the FEM of the process, it is necessary to be able to model the behavior on the whole range of temperature and strain rate. The temperature goes from T_{spf}=870 °C until the room temperature. It globally decreases along cooling operation, but it can rise locally due to heat transfers with the hot tools. A large amount of work has been done on these problematics, and some advanced models are presented below.

2.2.5.2.1 Empirical/Phenomenological models

One usual and fairly simple phenomenological model is the Johnson-Cook model [137] (Equation (2.28)). This model is largely used in machining modeling [138, 139, 140, 141], and globally high strain rate applications [142]. However, it is also used for forming application and even high temperature forming [143, 144].

$$\sigma = \left(A + B\varepsilon_p^n\right)\left(1 + Cln\frac{\dot{\varepsilon_p}}{\dot{\varepsilon}_p^0}\right)\left(1 - \left(\frac{T - T_0}{T_m - T_0}\right)^m\right) \tag{2.28}$$

Chaboche [145] made a large review of viscoplasticity functions used in unified viscoplastic theories. Two models are largely used for high temperature creep and superplasticity models (ie. capable to model high temperature and low stress level).

The first one is the unified viscoplastic Chaboche model [135] built on the Norton Hoff power law. The Equation (2.29b) shows the set of equations of the isotropic hardening with time recovery. Some additional terms can be added to study the influence of microstructure parameters. Lin et al. [146] showed the influence of such a model for superplastic forming conditions with and without influence of microstructure evolutions (Equation (2.30)) where d and μ are the grain size and the grain size exponent.

$$\dot{\varepsilon}^{in} = \left(\frac{\langle \overline{\sigma} - \sigma_0 - R \rangle}{K} \right)^n \tag{2.29a}$$

$$\dot{R} = b(Q - R)\dot{\varepsilon} - \gamma \|Q_r - R\|^{m-1}(Q_r - R) \tag{2.29b}$$

$$\dot{\varepsilon}^{in} = \left(\frac{\langle \overline{\sigma} - \sigma_0 - R \rangle}{K} \right)^n d^{-\mu} \tag{2.30}$$

The second one is a hyperbolic sine based formulation as proposed by Sellars and Tegart [126]. Some authors worked on the definition of viscoplastic functions on the basis of Sellars and Tegart's one [147, 148, 149] with hardening-softening effects. Anand's formulation is defined in the Equation (2.31a), where A and B are material parameters, Q is the activation energy, m is the strain rate sensitivity, R_G is the gas constant, T is the absolute temperature and s is an inelastic strain dependent internal variable. Its evolution is defined by the Equation (2.31b) and (2.31c) where s^* represents a saturation value of s. $\hat{s}$ is a material parameter. The parameter h_0 is hardening/softening coefficient and n is a rate sensitivity parameter for the saturation value of s. Finally, there was nine temperature-independent parameters to be identified which are Q, A, n, m, a, h_0, $\hat{s}$, B and s_0 the initial value of the deformation resistance.

$$\dot{\varepsilon}^{in} = Aexp\left(\frac{-Q}{R_G T} \right) sinh(B\frac{\sigma}{s})^{1/m} \tag{2.31a}$$

$$\dot{s} = h_0 \left(1 - \frac{s}{s^*} \right)^{a-1} \left(1 - \frac{s}{s^*} \right) \tag{2.31b}$$

$$s^* = \hat{s} \left(\frac{\dot{\varepsilon}^{in}}{A} exp\left(\frac{-Q}{R_G T} \right) \right)^n \tag{2.31c}$$

Msolli et al. [150] made a comparison between both types of models, and the results were better for Chaboche model. One reason of these differences comes from the temperature dependence of the material parameters that are fixed with an Arrhenius-based variation in Anand's formulation while they are free from any mathematical formulation in Chaboche one. Moreover, this type of evolution (Arrhenius type) is a good choice for single deformation mechanism in steady strain rate conditions.

2.2.5.2.2 Physically/microstructure-based models

Kocks and Mecking have largely contributed to the development of Kocks-Mecking (KM) model based on theory of the kinetics of slip [83, 112, 84]. The KM model is built on a thermodynamic analysis of dislocation slips in the crystal. They introduced hardening and recovery mechanisms through immobile dislocation density and friction stress (thermally activated) through mobile dislocation (governed by glide or climb). The basis of KM model have been largely used to develop large temperature range model [151, 78, 152, 153, 154]. These extensions of KM model can be divided into phenomenological hardening definition

(with exponential or hyperbolic tangent formulation for example [151, 78]), microstructure based hardening definition [153] with multi-phase components and phenomenological hardening-recovery laws based on dislocation density, and finally dislocation density based multi-phase model [154, 155].

The basis of the multiphase KM-based model is presented in the Table 2.2 with the equations of the columns Stress where M is the Taylor factor converting shear stress to normal stress ($M \approx 3$), f_β is the fraction of β phase. n_1 and n_2 are strengthening coefficients (greater than 1) that enable a better fit than those obtained by a classical rule of mixture. τ_i^* and τ_μ are the thermal and athermal parts of stress of each phase. However, athermal stress exists only for α phase, present at higher temperature for which only thermally activated stress is considered.
As explained above, it is possible to build different hardening-softening functions that influence ρ, d variation in τ_μ expression. The equations of column "Dislocation density" define one possible evolution of ρ [154] where α_1, α_2 and Q_{dm} are material constants.
The equations of the column "Grain size" define the grain size evolution [154] where $\dot{d}_{static}$, $\dot{d}_{dynamic}$ and $\dot{d}_{dis}$ represents respectively the SGG, the DGG and the grain size evolution due to DRX and recovery phenomena.

Stress	Dislocation density	Grain size
$\sigma = M\tau$		
$\tau = n_1 (1 - f_\beta) \tau_\alpha + n_2 f_\beta \tau_\beta$	$\dot{\rho} = \dot{\rho}_{stor} - \dot{\rho}_{annih}$	$\dot{d} = \dot{d}_{sta} + \dot{d}_{dyn} + \dot{d}_{dis}$
$\tau_\alpha = \tau_\alpha^* + \tau_{\alpha\mu}$, $\tau_\beta = \tau_\beta^*$	$\dot{\rho}_{annihil} = \alpha_2 e^{-\frac{Q_{dm}}{RT}} \rho$	$\dot{d}_{static} = \beta_0 d^{-\gamma_0} T^{-1} e^{-\frac{Q_{pd}}{RT}}$
$\tau_\mu = a\mu(T) b\sqrt{\rho} + Kd^{-1/2}$	$\dot{\rho}_{storage} = \alpha_1 \sqrt{\rho} \lvert\dot{\varepsilon}\rvert$	$\dot{d}_{dynamic} = \beta_1 \lvert\dot{\varepsilon}\rvert d^{-\gamma_1}$
$\tau^* = \tau^0 \left[1 - \left(\frac{RT}{\Delta G} \ln \frac{\dot{\gamma}_0}{\dot{\gamma}}\right)^{\frac{1}{q}}\right]^{\frac{1}{p}}$		$\dot{d}_{dis} = \beta_2 \dot{\rho}^{-\gamma_3} d^{-\gamma_2}$

Table 2.2 – Equations of the multi-phase KM-based model

2.2.5.2.3 Dynamic multi-phase models

The use of such models may be required when the phase transformations vary as a function of the heterogeneous cooling rate met during the process. It is particularly the case for welding [156, 70, 16] and 3D printing processes [16] (trouver une ref 3D printing) where heat transfers generate various microstructure morphologies in the heat affected zones.

The mechanical equations of their models are globally the sames than for classical models. However, there is a fine description of the evolution of the phases content as a function of time and temperature. There is one main method that describe this evolution in multi-phase metals, the Johnson-Mel-Avrami. It is based on empirical equations that relate the kinetics of a phase content variation as a function of its difference with the equilibrium content (usually obtained from phase diagrams or CALPHAD methods) and thermodynamic parameters. The main advantage of theses methods is that any kind of thermal history followed by a material during a process, such as complex cyclic temperature history, can be modeled.

2.2.6 Material testing characterization

A material testing procedure needs to be developed to be able to characterize a model. Indeed, it is important that the mechanical tests involve each specific behavior that the mathematical formulation proposes. Inversely, the material model may not allow to reproduce particular behavior observed during tests.

The elasto-viscoplastic models described above have been mainly characterized with three different testing procedures (excluding cyclic procedure for kinematic hardening-based model):

- Single-rate tensile/compression tests [152, 153, 154, 155]: these tests are the simplest procedure to characterize material behavior. However it requires lot of tests to cover large strain rate and temperature ranges.
- Load-relaxation tests [157, 158, 155, 17]: it has the advantage to mix hardening evolution in a first part, then viscous relaxation (SRS behavior on various strain rates) and finally softening by recovery mechanisms.
- Jump (strain rate) tensile tests [151, 159, 129, 150, 8]: this kind of test enables to get flow-stress to strain rate data (for SRS behavior) more easily exploitable than relaxation tests.

2.3 Strategy of material characterization

2.3.1 Material testing context

The bibliographic review has shown that for the thermomechanical process conditions, there can be many interactions between the microstructure and the mechanical behavior. The effect of SPF also need to be included in the scope of material characterization. Indeed, it is important to understand how the process generates microstructure changes and finally material behavior evolution.

The Figure 2.20 shows how the grain size is strain rate sensitive during SPF at 870 °C [18]. During SPF, the strain rate is supposed to be controlled by the pressure, but the distribution is dependent on the workpiece geometry anyhow. Therefore, it is important to evaluate the possible range of these microstructure evolutions under SPF process loading conditions. Then, the Figure 2.20 shows some microstructures from post cooling conditions obtained from samples cut on formed parts. They highlight the heterogeneous microstructure which can be due to different thermomechanical loading, but also different initial state at the end of forming. Therefore, not only the impact of SPF process on material properties needs to be investigated, but also the effect of thermomechanical loading of the post forming steps on these hypothetical heterogeneous microstructures and mechanical properties.

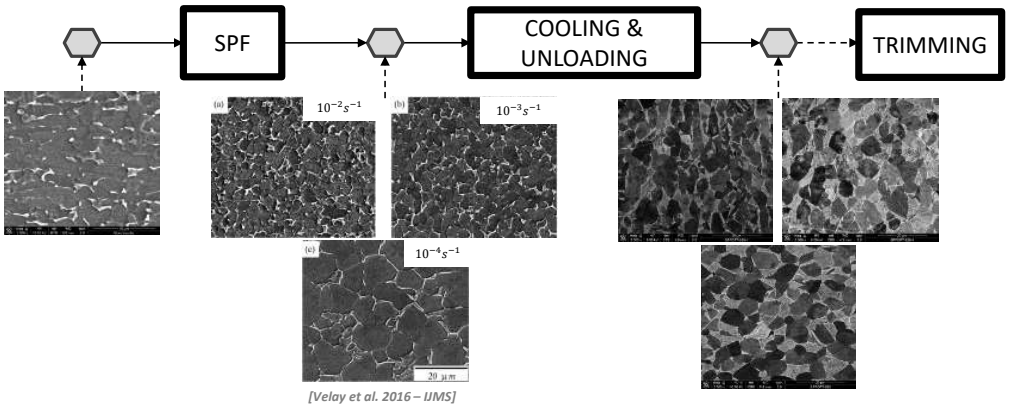

Figure 2.20 – Schematic of microstructure evolution of the material at process intermediate steps - intermediate mirographies after SPF taken from Velay et al. [18]

Moreover, beyond the possible effects of SPF on material properties, a procedure needs to be precisely defined to prepare the material from initial sheet metal state. The Figure

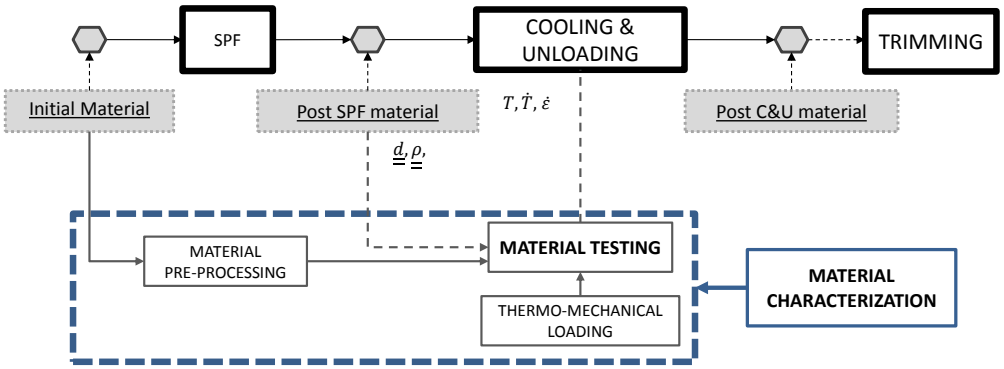

Figure 2.21 – Schematic of the material characterization procedure

2.21 schematically represents how material characterization is built to reproduce the process conditions. Two different stages of material characterization were performed.

Considering the complexity of the problem in the frame of a PhD, it would have not been possible to include every possible parameter and their interactions into a design of experiment for material characterization. Therefore, it was chosen to perform a first battery of tests in order to discriminate the influence and the dependency of the material behavior on some parameters. These tests enabled to build a simplified design of experiment (DOE), that enables to characterize the material behavior.

2.3.2 Testing machine

The whole material characterization was performed on a hydraulic MTS 100 kN tensile test machine. It is equipped with an induction heating system composed by a powering system, an Eurotherm enslavement system and an induction coil for heat treating.

The induction heating technology is very efficient for rapid heating and cooling heat treatment. One condition is that the heated material has to be ferromagnetic so that electric current can be induced in the material and heated by Joule effect. As Ti-6Al-4V is weakly ferromagnetic, a specific induction coil was designed for flat specimens. A cooling system was developed to enable rapid and homogeneous cooling rate and to reproduce process conditions. The MTS machine is equipped with a force and a displacement sensors. A MTS 632.53F-14 high temperature axial extensometer provides a measurement of local deformation by contact between two alumina ceramic rods. The measurement range is limited to 20% in tensile test with an initial gauge length of 12 mm.

The Figure 2.22a represents the whole testing assembly without extensometer. The Figure 2.22b shows the machine with the coil A, heating a localized useful portion of the specimen. The cooling system B is equipped with four sprinklers that blow air around the specimen leading to an homogeneous cooling of the specimen. The extensometer C is visible in the Figure 2.22b.

The design of the coil and the cooling system are presented in the Appendix A.1. They ensure an homogeneous temperature in the useful portion of the specimen in steady state as well for transient behavior. The results of these investigations are presented in Appendix A.1.3.

The testing machine was chosen for its capability to produce rapid cooling, thanks to the induction heating and the developed cooling system. However, the machine had several drawbacks:

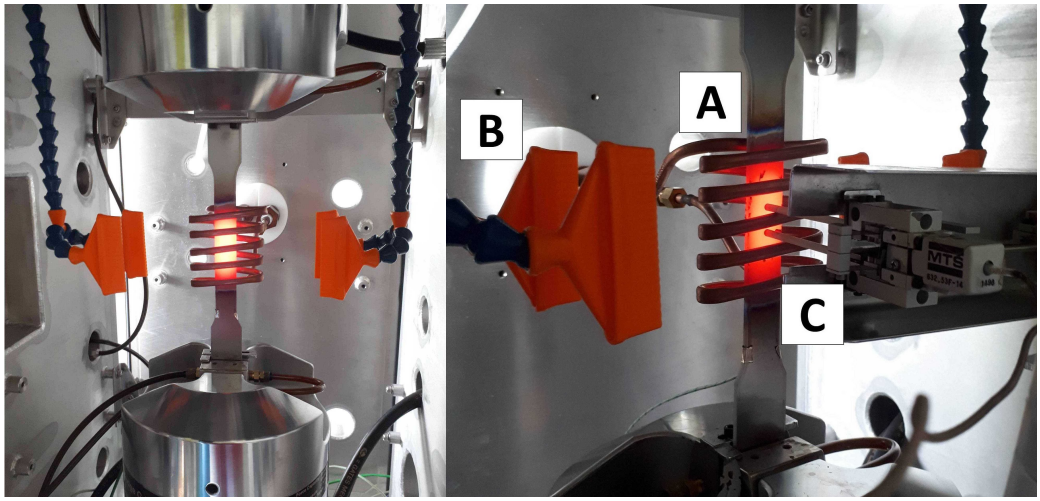

(a) **(b)**

Figure 2.22 – Picture of testing machine in (a) heat treatment and (b) mechanical testing conditions

- The maximum strain range was limited by the coil. It is not a big issue for C&U process conditions because the deformations undergone by the material are fairly small. However, it was not possible to impose SPF deformation before to test material in C&U conditions.
- The contact between the extensometer rods and the surface of the sample induces a contact force which is required to ensure appropriate measurement conditions. This force can produce creep deformation at high temperatures.

These specific features made mandatory to perform separately the heat treatment and the mechanical tests with the extensometer. The design and the implementation of the procedure is presented in the Section 2.4.

2.4 Preliminary testing

The influence of SPF process on material was investigated first. As the testing device is not able to perform large deformation tests, the influence of SPF deformation on the material behavior during C&U step cannot be investigated. However, it has been shown in the bibliography that the principal effect of SPF deformation on the material is related to grain growth, under both static and dynamic conditions, there might be cavity growth for very large strain out of the superplastic domain which has not been considered. Therefore, only the effect of temperature was reproduced to evaluate the SPF effects.

The Preliminary testing procedure was composed of three different sessions. These sessions, their objectives and main results are presented below. The whole description of the preliminary testing sessions are available in the Appendix A.2:

- Effect of SPF process

Samples were hold at SPF temperature for a set of time exposures from zero to 180 minutes. The objective was to observe at this temperature, how the microstructure behaves. Scanning Electron Microscope (SEM) analysis on samples revealed a significant grain growth at this

temperature. The average grain size of samples continuously increased along time exposure. An average time exposure of 100 min has been chosen for heat treating preparation procedure. This total value represents the averaged value of the re-heating time inside press plus the SPF cycle time.

- Effect of cooling rate

Complex mechanical tests composed of strain rate jump tensile test followed by creep tests under different forces were performed at 350, 650 and 770 °C on prepared samples. Different preparation procedures were tested. The objective of this session was to evaluate the effect of the cooling conditions of the process. Different samples preparation and mechanical loadings were applied so as to investigate the material behavior over a broad range of stresses, strain rates and microstructure conditions. The three temperatures of 350, 650 and 770 °C were selected to activate different deformation mechanisms, from viscoplastic to purely plastic mechanisms.

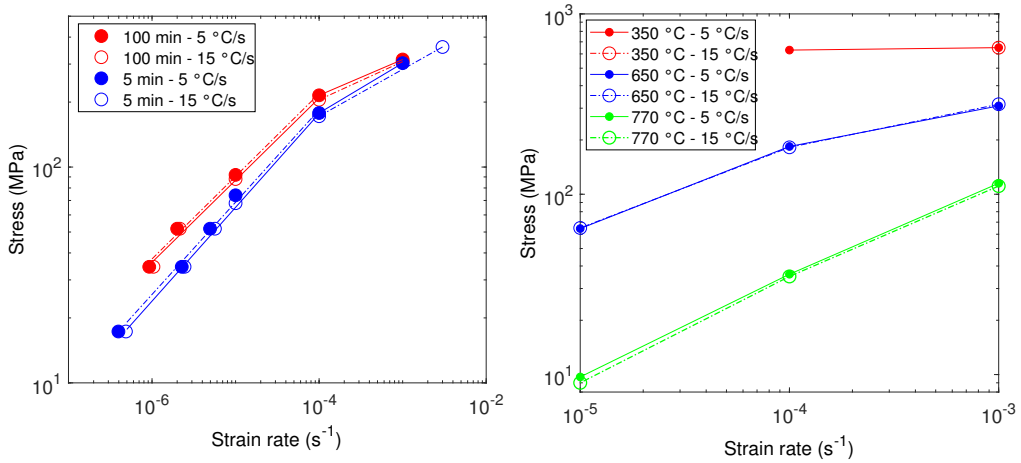

(a) **(b)**

Figure 2.23 – Log-log curve of stress vs. strain rate (a) influence of cooling rate and SPF time exposure at 650 °C (b) influence of cooling rate for different temperatures

The Figure 2.23a is a log-log plot of flow stresses versus strain rate at 650 °C. It highlights the higher influence of holding time at SPF temperature than cooling rate on the tensile properties. The Figure 2.23b is a log-log plot of flow stresses versus strain rate for the three temperatures. The specimens were previously hold during 100 minutes at SPF temperature. It confirms that the cooling rate has no significant impact on the mechanical properties in the process conditions.

- Influence of experimental procedure:

The thermal treatment of specimens at SPF temperature has to be performed without extensometer to avoid creep deformation due the force applied on the sample. Therefore the specimens were cooled up to ambient temperature to install the extensometer and then reheated to SPF temperature before cooling. The impact of this procedure (cooling and reheating) on microstructure was evaluated.
Three tests, with the same conditions than for the tests of the Figure 2.23b were performed without extensometer to avoid the problem of creep deformation, with and without a cooling at ambient temperature. The objective of this test is to validate the heat treatment procedure for final characterization session. The results confirms the conclusions of previous session.

Conclusion The heat treatments and mechanical tests which are presented in this preliminary testing session show some important points. Firstly, the time exposure at SPF temperature promotes significant grain growth. This is the principal parameter that affects not only microstructure, but also mechanical properties. Secondly, the material almost reveals none impact of the cooling rate on mechanical properties.

The heat treatment procedure for final design of experiment was established from these preliminary testing phases. The heat treatment is performed without extensometer to prevent from creep deformation. The specimen is then heated up to SPF temperature to reproduce an averaged cooling sequence. This cooling sequence is composed by a first cooling rate at 1.5 $°C.s^{-1}$ up to 850 °C and then a forced cooling rate at 7.5 $°C.s^{-1}$ until testing temperature. The Figure 2.24 shows the typical heat treatment procedure before mechanical tests.

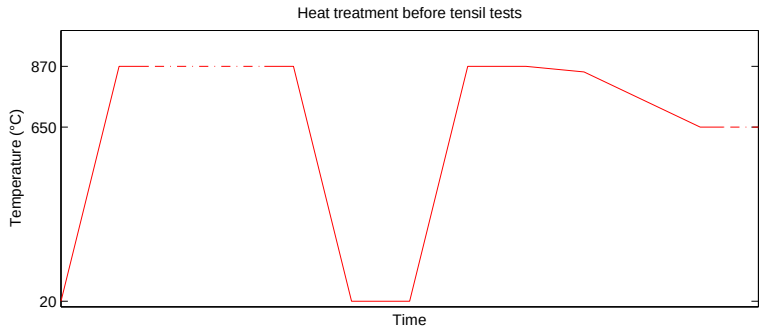

Figure 2.24 – Schematic temperature evolution during heat treatment preparation of mechanical tensile testing specimens

2.5 Final Characterization

Introduction

The objective of material characterization is to be able to reproduce the material behavior involved into the process through mathematical equations. Moreover, the objective of FE modeling of the process is to optimize the part cooling and removal from the mold after SPF, so that to decrease the obtained distortions after trimming operation. Thus, it is important to evaluate which are the thermo-mechanical loading at the origin of the distortions, and which mechanisms are at stake. There are several causes of distortions:

- Thermal stresses: these stresses are associated to low strain rate deformations, that are imposed by thermal gradient under heterogeneous cooling rate and complex geometry.
- Extraction induced stresses: the part removal is performed automatically with a machine that pull on a rigid frame on which the part is fixed. This operation can imposed high mechanical loading because of the part and mold interactions. One objective of the process optimization is to help the part removal operation by adapting cooling strategy in order to limit the stresses inducing plastic deformations.
- Residual stresses: the stress relieve occurs during trimming operation. These stresses are the consequences of the part deformations combined with heterogeneous material properties and stiffness of the part. In addition, the evolution of the elastic domain makes material modeling a complex issue because of hardening mechanisms and their evolution with temperature.

There are several material properties and behaviors involved in the generation of distortions:

- Elasticity - the Young modulus and yield stress evolution with temperature
- Visco-plasticity - the inelastic flow rule that relates the permanent deformations to an applied loading.
- Hardening - Softening - the capacity of material to increase or decrease the yield stress during plastic deformation.

The material characterization procedure aims to reproduced the different thermomechanical loadings to be able to evaluate the previously mentioned material behaviors.

2.5.1 Design of experiment

Two different tests inspired from the literature were performed. Both procedures were composed by tensile tests followed by relaxation tests. The first testing procedure (TP1), illustrated in the Figure 2.25a, is composed by two parts: a first strain rate jump test, then followed by a stress relaxation. Firstly, the jump tensile test is composed by six strain rates levels described in the Table 2.3. The first strain rate is relatively high to reach the first stress plateau faster. Each strain rate were applied for a deformation corresponding approximately to the data given in the 2.3. The deformations were adapted for each temperature in order to limit the maximum accumulated deformation. Indeed, the initial strain associated to $\dot{\varepsilon}_0$ evolves with temperature, while the maximum capacity of the machine is limited by the extensometer mounting inside the induction coil.

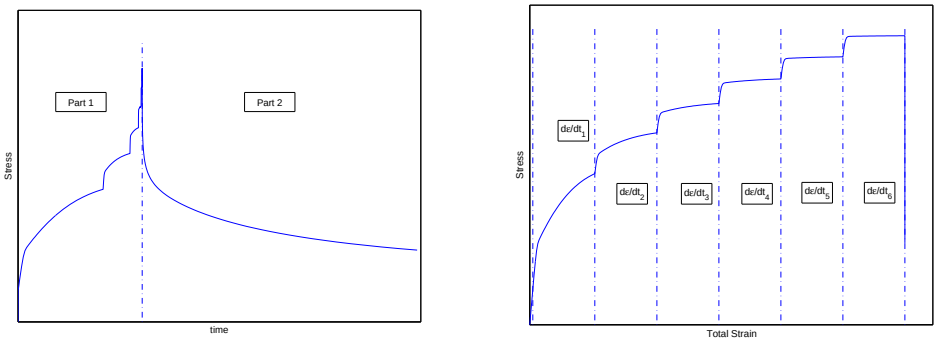

(a) **(b)**

Figure 2.25 – TP1: (a) stess-time and (b) stess-strain curves

	$\dot{\varepsilon}_0$	$\dot{\varepsilon}_1$	$\dot{\varepsilon}_2$	$\dot{\varepsilon}_3$	$\dot{\varepsilon}_4$	$\dot{\varepsilon}_5$	$\dot{\varepsilon}_6$
$\dot{\varepsilon}$ (s^{-1})	10^{-3}	$10^{-4.5}$	10^{-4}	$10^{-3.5}$	10^{-3}	$10^{-2.5}$	10^{-2}
ε (%)	$\approx \frac{k}{E}$	0.25	0.35	0.5	0.7	0.8	0.8

Table 2.3 – Jump test parameters of TP1: strain rates and associated strain

The second testing procedure (TP2), presented in the Figure 2.26a, is composed by a couple of tensile-relaxation tests. The first one, consists in deforming until few percents over the yield point in order to relax up to the true elasticity limit with no hardening effect. Indeed, there are different ways to assess the elasticity limit because of the complexity of phenomena that happens at plastic flow initiation. In our study, the true elasticity limit is considered instead of the conventional one that may contain viscosity and hardening phenomena. Then,

the second tensile test is performed at constant strain rate for few percents. Thus, the shape of hardening function is more easily exploitable than with the first procedure. The strain rate used for both tensile parts is equal to 10^{-4} s^{-1}.

The combination of both procedures enables to involve every specific behavior at different phase of the tests. Thus, it is easier to characterize a model in which the good property is affected to appropriate model parameter. Indeed, the difficulty of such viscoplastic material is that the viscosity can be assimilated to strain hardening (because of the exponential shape), and the softening due to static recovery mechanisms to viscosity effects for example.

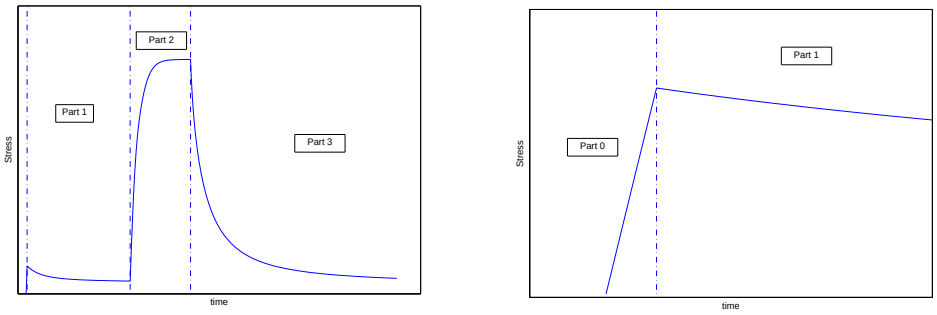

(a) **(b)**

Figure 2.26 – TP2: (a) full stess-time curve, (b) zoom on the Part 1

Both testing procedures were performed for different temperatures defined in table 2.4. The relaxation times were not the same for each test. Some values were adapted during the testing sessions. The values used for the relaxation times of tests 1 (t_R^1) and tests 2 (t_{R1}^2 , t_{R2}^2) are presented in the Table 2.5.

T (°C)	20	250	400	525	625	700	750	770	790	820	850	870
TP1	✓	✓	✓	✓	✓	✓	✓		✓	✓	✓	✓
TP2	✓	✓	✓	✓	✓	✓	✓	✓		✓		✓

Table 2.4 – Tested temperatures for each procedure

T (°C)	20	250	400	525	625	700	750	770	790	820	850	870
t_R^1 (s)	1210	1210	1210	610	310	310	185	/	185	185	185	185
t_{R1}^2 (s)	600	530	460	410	360	310	310	120	/	160	/	70
t_{R2}^2 (s)	1000	1000	850	650	500	280	280	280	/	280	/	280

Table 2.5 – Relaxation times of procedures

2.5.2 Results

For a better readability, only the shared temperature for both procedures will be presented. Indeed, the non-shared temperatures are located for high temperatures where the curves do not change too much, and they do not help to better understand the material behavior evolutions. However, the data have been used to characterize the material model in the next sections.

Experimental curves

The Figure 2.27 presents the untreated stress-time and stress-strain curves for both procedures. The tests at temperatures below 625 °C show oscillations (except for ambient tests for which heating is not activated during mechanical testing). It is due to the induction heating technology. Indeed, as explain in the Appendix A, the induction current is regulated by PID control loop, which was automatically adjusted by a specific procedure. The PID loop was not efficient for low temperatures.

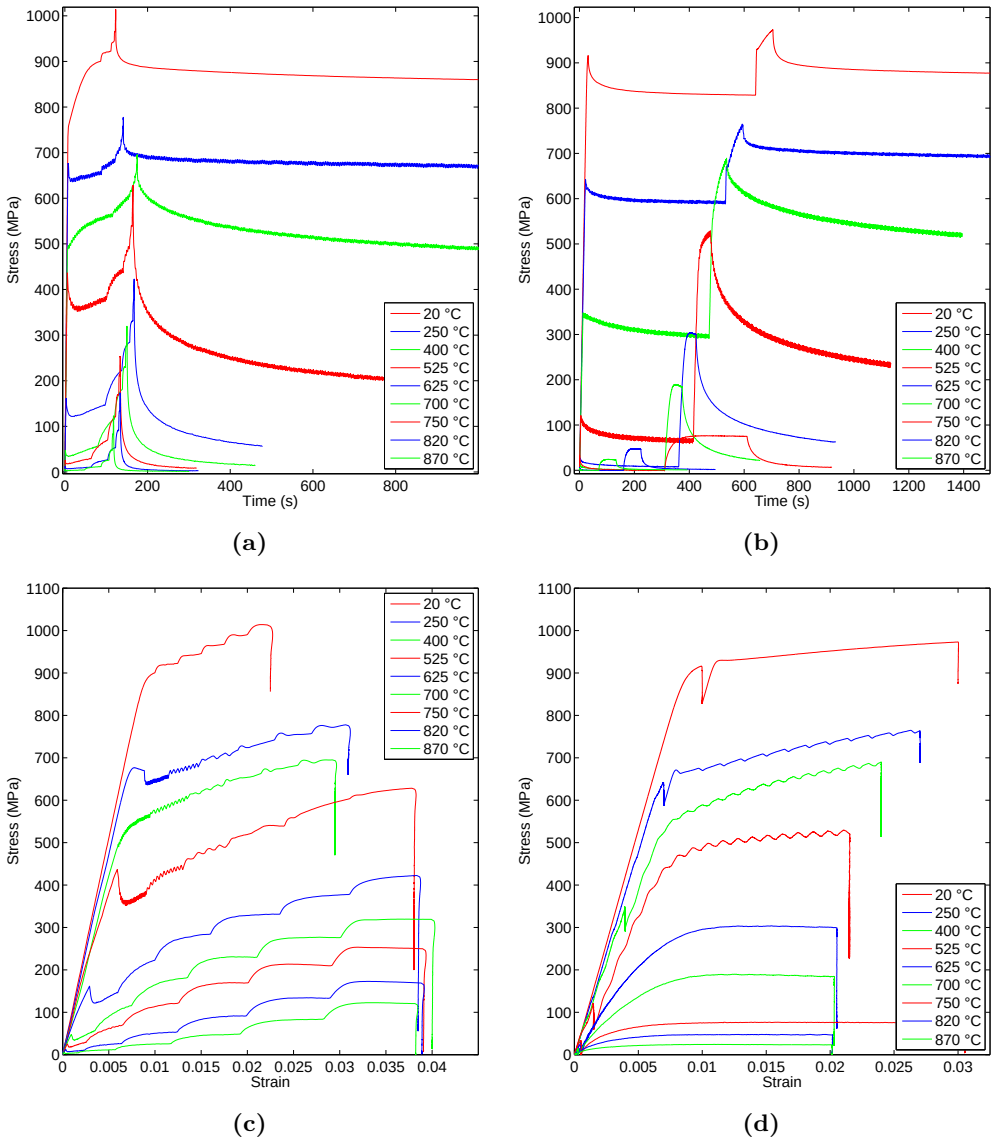

Figure 2.27 – Raw curves of TP1 (a) stress-time, (c) stress-strain and TP2 (b) stress-time, (d) stress-strain

Firstly, the results reveal a transition of material behavior between 525 and 625 °C. Indeed, the high temperatures curves present a high strain rate sensitivity (Figure 2.27c) and a saturated strain hardening effect (Figure 2.27d). On the contrary, the low temperatures reveal a large decrease of SRS with temperature, especially at 400 °C, and then a final rise at ambient temperature.

Then, these curves present a shape of strain hardening effect more linear, and the decrease of SRS moves on to an increase of hardening rate (slope of stress-strain curves).
Finally, the relaxation part of the Figure 2.27a and especially the Figure 2.27b show many differences in the stress relaxation shapes. The curves reveal a residual stress that confirms strain hardening phenomena, but also softening effects.

The next paragraphs describe each of the previously mentioned behavior in order to introduce material modeling aspects.

2.5.2.0.1 Yield stress

The Part 1 of TP2 is used to evaluate the true elasticity limit of the material. The Figure 2.28 shows the stress-time curves for this specific part of the test. The Figure 2.28a represents the temperature from ambient to 625 °C for which yield stress seems to be non-null. The Figure 2.28b shows the other temperatures which reveal null elasticity limits. The elasticity limits have been evaluated from this curves, and the values are used in the next paragraphs.

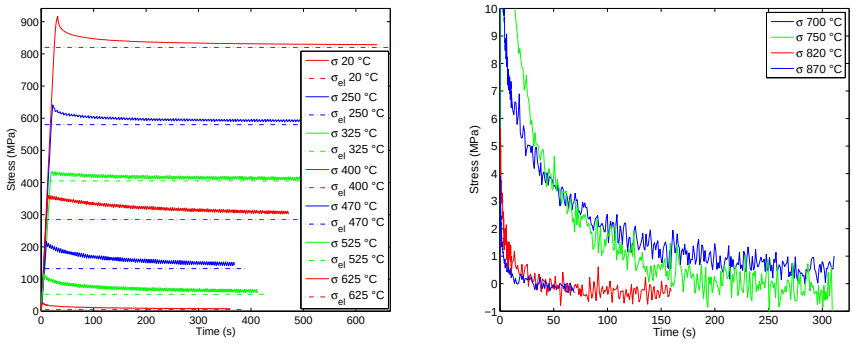

(a) **(b)**

Figure 2.28 – TP2 Part-1 :(a) yield stress estimation for non-null limits of elasticity and (b) for null limits of elasticity

2.5.2.0.2 Strain rate sensitivity

The SRS is related to the capacity of material to adapt flow stress depending on the strain rate. In general, this phenomena is directly related to viscous flow of dislocation in the material. It has been seen in section 2.2 that the stress exponent (the inverse of SRS exponent) depends on the deformation mechanisms that are activated for different temperatures and mechanical conditions.

❒ Jump tests part

The Figure 2.29 represents the low and high temperature curves of the part 1 of TP1. For the Figure 2.29a, the second tensile part of TP2 was added in order to highlight the SRS effects. The Figure 2.29a reveals that the SRS is not trivial to evaluate. Indeed, the TP2 curves are single tensile tests at 10^{-4} s^{-1}. The curves for 20 °C and 525 °C demonstrate a non null sensitivity despite the difficulty to evaluate the threshold for the last one. However, the curves for 250 °C and 400 °C seem to highlight no SRS when comparing with TP2 tests. This phenomenon for Ti-6Al-4V was already observed and described by [160, 8] as mentioned in the Section 2.2.

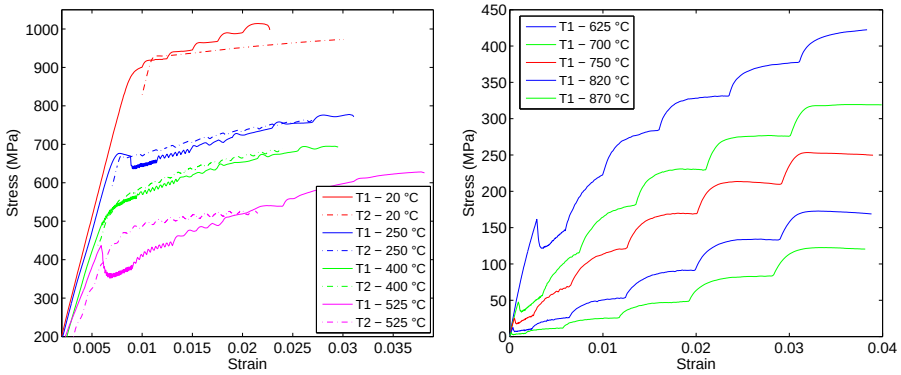

(a) **(b)**

Figure 2.29 – SRS effect (a) stress-strain curves of both procedures at low temperatures (b) stress-strain curves for jump test procedure at high temperatures

Concerning high temperature data, the Figure 2.29b clearly shows a high SRS. The values of asymptotic flow stress were estimated thanks to a qualitative method schematically described in Figure 2.30a. The Figure 2.30b represents the logarithmic stress-strain rate plot from the estimated flow stresses. The Figure 2.30c represents the associated evolution of m exponent with strain rate.

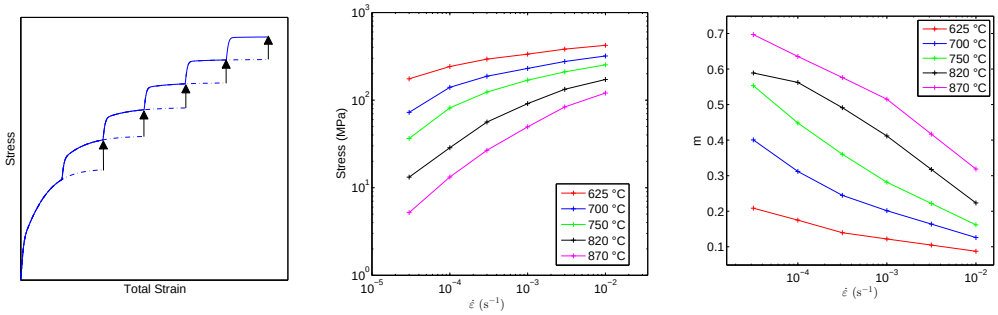

(a) **(b)** **(c)**

Figure 2.30 – Evaluation of SRS from TP1 data at high temperature: (a) flow stress evaluation method, (b) logarithmic stress-strain rate curves and (c) m exponent at hight temperatures

❒ Relaxation part

The stress relaxation part reveals the viscoplasticity properties of the material. Indeed, the constant tensile strain during the test enables to express the plastic strain rate as a function of stress rate as defined in the Equation (2.32). It is possible to express the SRS from relaxation curves by using the Equation (2.33). This method is highly dependent on the disturbances of stress-time data. The relaxation curves of TP2 part 2 were firstly filtered (Figure 2.31a and 2.31b), before to compute SRS exponent analytically.

$$\dot{\varepsilon}_t = 0 = \frac{\dot{\sigma}}{E} + \dot{\varepsilon}_{pl} \tag{2.32}$$

$$m = \frac{\partial ln(\sigma)}{\partial ln(\dot{\sigma})} \tag{2.33}$$

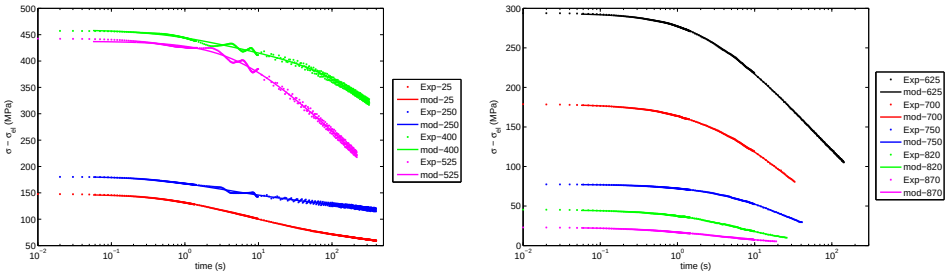

(a) **(b)**

Figure 2.31 – Stress relaxation curves of TP2 part 2: (a) low temperatures, (b) high temperatures

The SRS exponent is usually computed for high temperatures where the sensitivity is high. At high temperature, the elasticity limit is generally null, contrary to low temperatures. Therefore, the m exponent is replaced by m^* defined in the Equation 2.34 which enables to have comparable parameters. Normally, it would have been better to compute the SRS exponent with $\sigma_y = \sigma_{el} + R$ to be totally comparable. However, the value of strain hardening component is difficult to evaluate. In addition, the softening effect can influence this value during stress relaxation. Thus σ_y is taken equal to σ_{el}.

$$m^* = \frac{\partial ln(\sigma - \sigma_y)}{\partial ln(\dot{\sigma})} \tag{2.34}$$

The Figures 2.32 represents the SRS exponent versus strain rate curves for each tested temperatures. The m curves are highly non-linear contrary to the curves obtained from the jump tests. For the low temperatures curves (Figure 2.32a), the curves at 25°C and 525°C have globally higher sensitivity than other temperatures as depicted from raw curves. The curve at 400°C reveals a bell effect that is characteristics of higher temperatures.

For the high temperatures curves (Figure 2.32b), The bell's effect is enhanced while increasing the temperature. The order of bells superposition is not totally in accordance with jump tests, especially for 750 °C. However, this test is the only one which was not performed with the same strain rate than the others, and maybe the initial strain rate had not been fitted (ie. stress-time fitting) the same way than for others.
More globally the analyses of SRS show a high sensitivity for high temperatures that almost decreases until no sensitivity around 400 °C. Then, between 400 and 20 °C it finally rises while the temperature decreases such as observed on jump test in the Figure 2.29a.

2.5.2.0.3 Strain hardening

The TP2 part 2 is used to analyze the strain hardening behavior of the material. The data were split into "low" (ambient temperature to 525 °C) and "high" temperatures (625 to 870 °C). The Figures 2.33a and 2.34a represent the stress-strain curves adjusted by their initial stress and strain values at the end of first relaxation (σ_{ini} and ε_{ini}). Hence it is more convenient to analyze the data.

The Figure 2.33a represents the low temperatures hardening shapes. When the temperature increases, the hardening behavior passes from a quasi-linear to an exponential shape. The hardening rates were computed from filtered portion of stress-strain curves and plotted in the Figure 2.33b. The hardening rates evolution confirms that the hardening effect seems

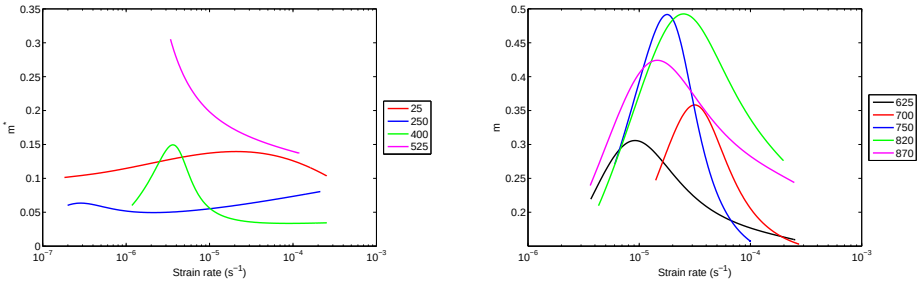

(a) **(b)**

Figure 2.32 – Stress relaxation curves of TP2 part 2 - SRS exponent: (a) m^* - low temperatures, (b) m - high temperatures

to be higher for temperature of 250 and 400 °C. In addition, the decrease of the hardening rate is more important at higher temperatures which confirms the tendency to switch to an exponential shape.

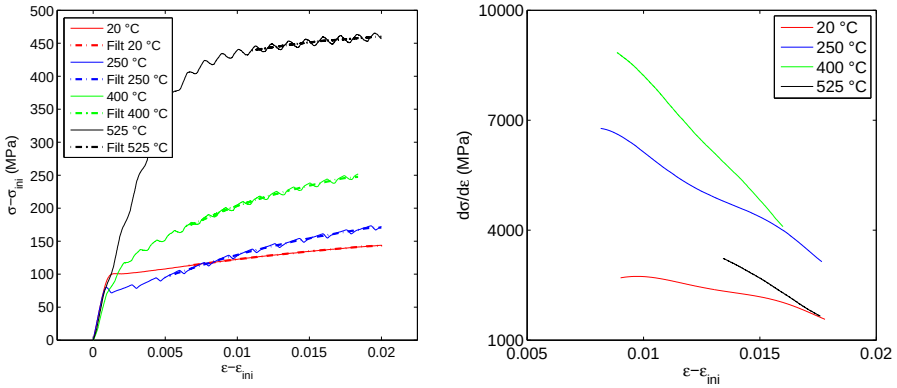

(a) **(b)**

Figure 2.33 – Strain hardening effect at low temperatures - (a) $\sigma - \sigma_{ini}$ vs. $\varepsilon - \varepsilon_{ini}$, (b) hardening rate computed with filtered curves vs. $\varepsilon - \varepsilon_{ini}$

The Figure 2.34a represents the high temperatures hardening shapes. There are several phenomena that can lead to this exponential shape. Exponential Voce equation can efficiently model the flow stress evolution in these configurations. However, this shape can also be associated to high viscosity. Nevertheless, the stress relaxation curves shown in the Figure 2.34b reveals that there are still residual stresses after hundreds seconds of relaxation, which means that strain hardening operated.

2.5.2.0.4 Softening

The Softening behavior is observable during relaxation tests. Indeed, stress relaxation is viscoplastic phenomena that produces conversion of accumulated elastic energy through blocked dislocations into plastic deformation when lower energy is required for dislocations to overcome obstacles.

The evolution of flow stress rate is proportional to plastic strain rate as defined in the Equation (2.32). The stress variation can be split into two contributions (Equation (2.35)

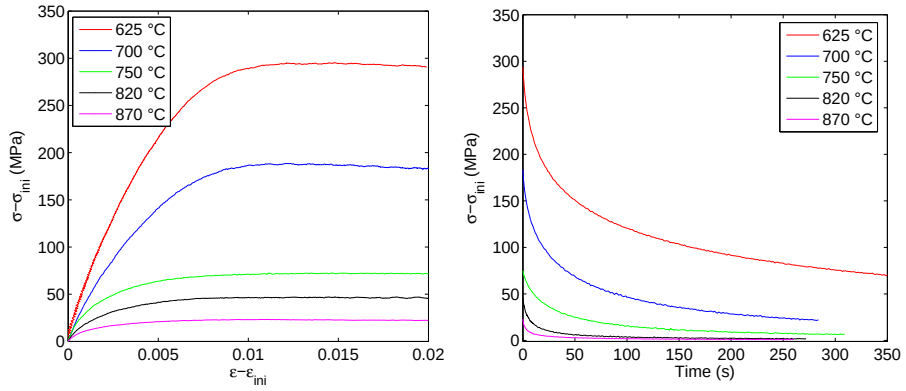

(a) **(b)**

Figure 2.34 – Strain hardening effect at high temperatures - (a) $\sigma - \sigma_{ini}$ vs. $\varepsilon - \varepsilon_{ini}$, (b) stress relaxation vs. time

where the viscous stress σ_v is defined in the Equation (2.36)). By using these equations, the stress variation is a function of viscous stress relaxation, and hardening variations. When the softening mechanisms work, it induces yield stress decrease, and consequently it induces plastic strain rate.

$$\frac{\partial \sigma}{\partial t} = \frac{\partial \sigma_v}{\partial t} + \frac{\partial R}{\partial t} = -E\dot{\varepsilon}_p \tag{2.35}$$

$$\sigma_v = \sigma - \sigma_{el} - R > 0 \tag{2.36}$$

The Figure 2.35 presents the superposition by temperatures of the three different relaxation steps of TP1 ($R1$) and TP2 ($R2_1$ and $R2_2$ respectively the first and second relaxation steps). The stresses are corrected by σ_{el}. The fact that softening and relaxation of viscous stress act at the same time makes difficult the analysis of the results.
Before to analyze softening, it is necessary to pay attention of potential strain hardening to be softened. The $R2_1$ curves were stretched up to a small percentage over elasticity limit. Thus, yield stress contribution due to strain hardening is supposed to be fairly weak. On the contrary, both curves $R1$ and $R2_2$ underwent plastic deformation until around 2 to 4 %.
The temperatures over 600 °C exhibit a stabilized flow stress regardless of plastic strain so that strain hardening reaches the asymptotic value. This might confirm that the softening mechanisms are highly active at these temperatures.
For the lower temperatures, there is a clear impact of the time on the stress relaxation, ie. the softening mechanisms in these cases. It is interesting to notice that there is a minimum softening rate for the temperature around 250-400 °C with an increase for the lower temperature so as for SRS behavior.

Behavior analysis

The mechanical testing procedures enabled to highlight every specific behaviors that are at stake during C&U step of the industrial process: elasticity, viscoplasticity, strain hardening and dynamic and static softening mechanisms.

The material testing has revealed two important transitions in the mechanical behavior. A first one which occurs around 625-700 °C, generates the appearance of the elasticity limit, strain hardening effect and a decrease of the strain rate sensitivity. This transition physically corresponds to an important change in α and β contents that conditions a transition of the deformation mechanisms. Indeed, the dislocation motion modes switch from high rate

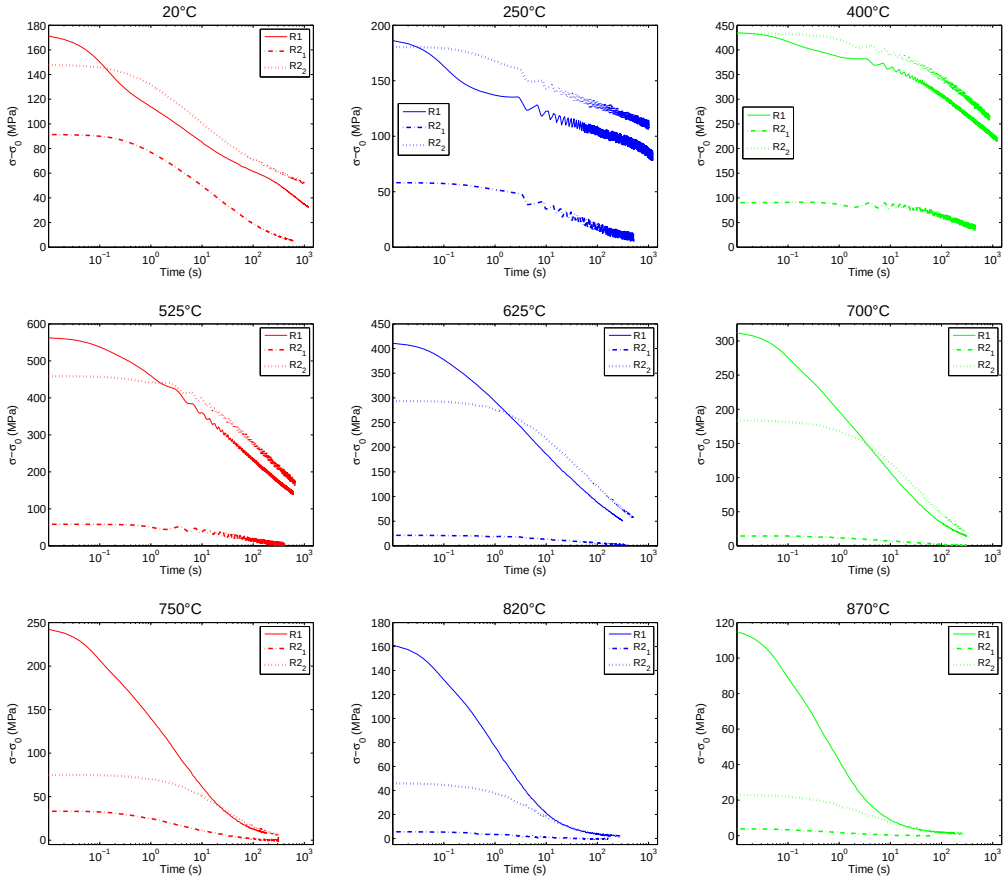

Figure 2.35 – Superposition of relaxation tests $R2_1$ from TP1, and $R2_1$ and $R2_2$ respectively from TP2 part 1 and 2 for each temperature

sensitive diffusion and dislocation creep to crystal plasticity because of high reduction of vacancy diffusion potential.

The second transition occurs around 400 °C. It impacts the SRS and hardening phenomena in an inversely proportional way. Indeed, the SRS decreases to a minimum around 400 °C while hardening rate is maximum. Then, SRS rises and hardening rate decreases.

2.6 Material model

The experimental data obtained from different thermo-mechanical tensile tests are the basis for material model identification. The literature provides different types of models to describe the behavior of Ti-6Al-4V alloy. There are two main classes of models:

- Microstructure-based model: these models are composed by equations that describe the evolution of internal variables such as dislocation density, the grain size, or voids density, etc., and their interactions together. These internal variables are related to macroscopic mechanical variables.
- Phenomenological model: the different mechanical phenomena are associated to specific non-microstructural variables. These models are mathematical expressions that enables to reproduce macroscopic behaviors.

Many authors developed material models that mix these two different approaches. Some of these models are presented in the Section 2.2. In this work, the selected approach is a phenomenological model based on a Lemaitre and Chaboche unified viscoplastic formulation [135]. However the power law was combined to an hyperbolic sine function such as Sellars and Stegart [126] formulation. An isotropic hardening law combining strain hardening and static recovery terms is used.

2.6.1 Constitutive equations

As defined above, the constitutive equations are used in the framework of Lemaitre and Chaboche unified viscoplastic model. Equation (2.37) defines the total strain tensor $\underline{\underline{\varepsilon}}^t$ as the sum of elastic $\underline{\underline{\varepsilon}}^{el}$, plastic $\underline{\underline{\varepsilon}}^p$ and thermal $\underline{\underline{\varepsilon}}^{th}$ strain rate tensors where the $\underline{\underline{\ }}$ notation refers to a 3x3 tensor.

$$\dot{\underline{\underline{\varepsilon}}}^t = \dot{\underline{\underline{\varepsilon}}}^{el} + \dot{\underline{\underline{\varepsilon}}}^{th} + \dot{\underline{\underline{\varepsilon}}}^p \tag{2.37}$$

The elastic deformation is considered isotopic, and related to the Cauchy stress rate tensor $\dot{\underline{\underline{\sigma}}}$ with the Hooke law defined by Equation (2.38) where ν, E, Tr and $\underline{\underline{I}}$ are respectively the Poisson ratio, the Young's modulus, the trace operator and the identity matrix.

$$\dot{\underline{\underline{\varepsilon}}}^{el} = \frac{1+\nu}{E}\dot{\underline{\underline{\sigma}}} - \frac{\nu}{E}Tr(\dot{\underline{\underline{\sigma}}})\underline{\underline{I}} \tag{2.38}$$

The thermal strain rate tensor induced by expansion is defined by the Equation (2.39) where α_{th} and $\dot{T}$ are the linear coefficient of thermal expansion and the cooling rate.

$$\dot{\underline{\underline{\varepsilon}}}^{th} = \frac{1}{3}\alpha_{th}\dot{T}\underline{\underline{I}} \tag{2.39}$$

The viscoplastic strain is associated to inelastic deformation. The viscoplasticity takes place when plasticity criterion is met. A Von Mises criterion is used as defined in the Equation (2.40) where $\overline{\sigma}$ and σ_y are the equivalent stress and the yield stress. The equivalent stress is computed by the Equation (2.41) where $\underline{\underline{s}}$ is the deviatoric stress tensor defined by the Equation (2.42) and $\underline{\underline{s}} : \underline{\underline{s}}$ is the sum of the term to term product of $\underline{\underline{s}}$.

$$f = \overline{\sigma} - \sigma_y \leq 0 \tag{2.40}$$

$$\overline{\sigma} = \sqrt{\frac{3}{2}\,\underline{\underline{s}} : \underline{\underline{s}}} \tag{2.41}$$

$$\underline{\underline{s}} = \underline{\underline{\sigma}} - \frac{1}{3}Tr(\underline{\underline{\sigma}})\underline{\underline{I}} \tag{2.42}$$

$$\sigma_y = k + R \tag{2.43}$$

The yield stress (defined by the Equation (2.43)) is composed by a first component k associated to true elasticity limit below which no plastic deformation takes place. k is dependent of initial microstructure and temperature. A second variable R is associated to strain hardening and softening phenomena. The R variable enables to take account of the impact of the plastic flow (motion and growth of the dislocations density) on the yield stress.

The viscoplastic strain rate tensor is defined deriving a viscoplastic potential Ω. The Equation (2.44) relates the viscoplastic potential to the viscoplastic criterion f where $\dot{p}$ represents the accumulated plastic strain rate.

$$\dot{\underline{\underline{\varepsilon}}}^p = \frac{\partial\Omega}{\partial\underline{\underline{\sigma}}} = \frac{\partial\Omega}{\partial f}\frac{\partial f}{\partial\underline{\underline{\sigma}}} = \dot{p}\frac{\partial f}{\partial\underline{\underline{\sigma}}} = \dot{p}\underline{\underline{n}} \tag{2.44}$$

The Equation (2.45) defined the viscoplastic function g that relates the viscoplastic strain rate (also called equivalent plastic strain rate $\dot{\bar{\varepsilon}}_p$) to a set of internal α^i and external β^i variables. These variables are usually microstructure parameters, macroscopic thermo-mechanical variables, or both.

$$\dot{p} = \dot{\bar{\varepsilon}}_p = g([\alpha^i], [\beta^i]) \tag{2.45}$$

Hereafter, each parameter of the constitutive equations is presented and characterized from the experimental data.

2.6.2 Elasticity domain

Concerning the elasticity domain, only the temperature influence is considered for typical thermal treatment and microstructure conditions of the process. The elastic properties (especially the elasticity limit) may be affected by different forming times or cooling rates but the model was supposed to be used in the process conditions for which no significant impact is partly demonstrated (see Section 2.4).

2.6.2.1 Young's modulus

The Young's modulus values were computed on several pieces of curves of both testing procedures for every temperatures. The Figures 2.36a and 2.36b show how the computation is made. Several values are obtained at different phases of the tests in order to have a representative value. Indeed, the Young's modulus is sometimes difficult to evaluate for low yield stress materials, especially at high temperature. The Figure 2.36c represents the averaged points of both procedures and the polynomial model obtained. The temperature evolution is defined by the Equation (2.46) with the next parameters: E_0=107392, E_1=35.334, E_2=4.084e-2 and E_3=1.004e-4.

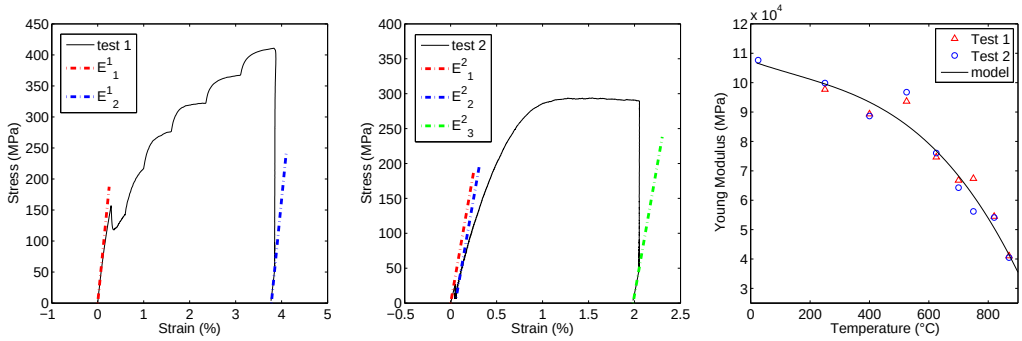

(a) **(b)** **(c)**

Figure 2.36 – Young modulus measurement zone on (a) TP1 and (b) TP2 types, and (c) model compared to experimental data

$$E(T) = E_0 - E_1 T + E_2 T^2 - E_3 T^3 \tag{2.46}$$

2.6.2.2 Limit of elasticity

The starting of plastic deformation during tensile tests is not obvious to define. Indeed, the change in stress rate is equivalent to the appearance of plastic deformation. However, the stress rate can be highly strain rate sensitive because of high SRS of the material. The first

tensile relaxation part of TP2 were performed to get this information. The Figure 2.37a shows tensile relaxation curves at the temperature for which there is a non-null limit (ie. the temperature $T < 700$ °C) and an qualitative estimation of k. The Figure 2.37b represents the estimated points and the evolution is defined from the Equation (2.47) where k_0=842, k_1=2.38e-8, T_k=700, γ_k=2.9.

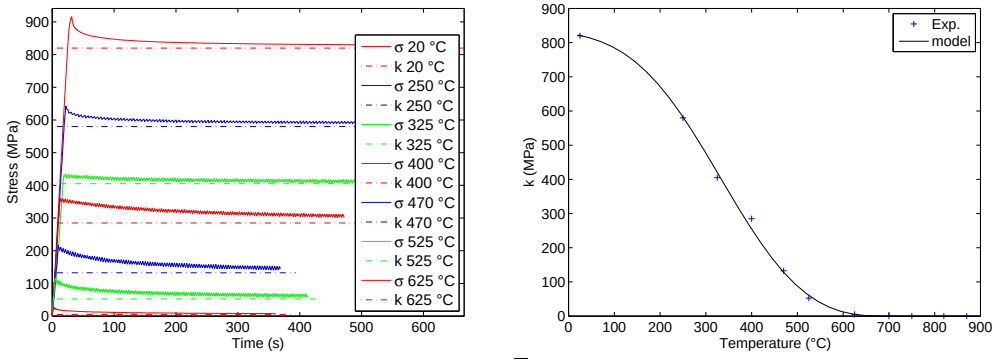

(a) **(b)**

Figure 2.37 – (a) Stress relaxation curves of TP2 part 1 with an estimation of k (b) Model vs. experiment of k variation as a function of the temperature

$$k(T) = \begin{cases} k_0 \left(1 - exp\left(-k_1 \left(T_k - T\right)^{\gamma_k}\right)\right) & if\ T \leq T_k \\ 0 & if\ T > T_k \end{cases} \tag{2.47}$$

2.6.3 Plastic domain

2.6.3.1 Viscoplastic function

As defined above, the chosen viscoplastic function is the Sellars and Tegart formulation defined by the Equation (2.48). It is a combination of hyperbolic sine and power law expressions. It has the advantage to promote a variable strain rate sensitivity instinctively with constant parameters. The Equation (2.49) defines the expression of SRS exponent for the presented viscoplastic function already defined in the Section 2.2.

$$\dot{\bar{\varepsilon}}_p = \dot{\varepsilon}_0 sinh\left(\beta \left\langle \sigma_v \right\rangle\right)^n \tag{2.48}$$

$$m = \frac{\left(\frac{\dot{\bar{\varepsilon}}_p}{\dot{\varepsilon}_0}\right)^{1/n}}{\beta n \overline{\sigma} \sqrt{1 + \left(\frac{\dot{\bar{\varepsilon}}_p}{\dot{\varepsilon}_0}\right)^{2/n}}} \tag{2.49}$$

The Figure 2.38a shows the evolution of m with the strain rate for different n values. The parameters used to plot these curves are E_0=5e-5, β=2e-2, k=10 and R=25. The Figure 2.38b taken from the Section 2.5.2 enables to confirm that hyperbolic sine is fairly well adapted contrary to constant SRS value of classical Norton Hoff power law.

The Viscous stress σ_v used in the viscoplastic function is defined by the Equation (2.50) where R and k are the hardening and elasticity limit functions. R is composed by two functions (see in the Equation (2.51)) H and S respectively corresponding to the hardening phenomena (Voce's type) related to the dynamic IDD evolution, and the softening phenomena due to static recovery. H and S are defined in a differential form. $\dot{H}$ is expressed in the Equation

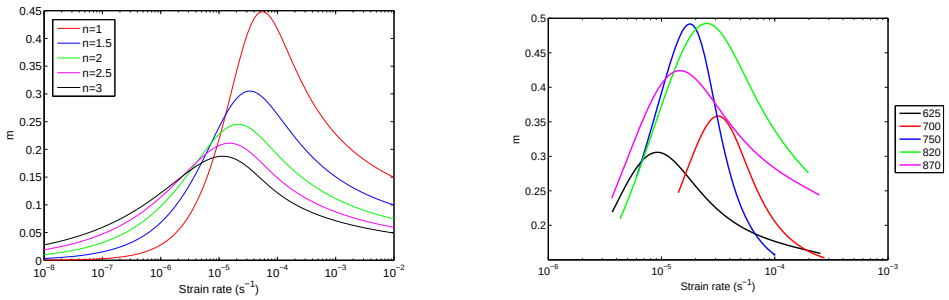

(a) **(b)**

Figure 2.38 – Comparisons of strain rate sensitivity exponent m: (a) model computed analytically, (b) experiment - high temperature

(2.52) where b and Q are material parameters respectively related to the rate of hardening and the threshold. $\dot{S}$ is defined by the Equation (2.53), γ and c are material parameters. The condition used for softening is that the effective stress is greater than the yield stress. This condition is set in order to avoid to totally remove the hardening component related to dislocation when no active stress is applied.

$$\sigma_v = \overline{\sigma} - R - k \tag{2.50}$$

$$\dot{R} = \dot{H} + \dot{S} \tag{2.51}$$

$$\dot{H} = b(Q - R)\dot{\overline{\varepsilon}}^p \tag{2.52}$$

$$\dot{S} = \begin{cases} -\gamma R^c & if\ \overline{\sigma} > k \\ 0 & if\ \overline{\sigma} \leq k \end{cases} \tag{2.53}$$

2.6.3.2 Characterization method

The performed testing procedures are complex as several behaviors interact simultaneously. Indeed, an important attention had been paid for defining an appropriate characterization procedure. It is described in details in the Appendix A.3. It consisted in computing stress-time curves for entire tests in order to take account of the behavior history. A Taylor's approximation method was used such as defined by the Equations (2.54) and (2.55) where every parameters of the model is involved. Each set of curves (both procedures) where simultaneously fitted for the same temperatures in order to attribute the adequate properties to the good phenomenological parameters.

$$\sigma\left(t + dt\right) = \sigma\left(t\right) + dt \times \dot{\sigma}\left(t\right) \tag{2.54}$$

$$\dot{\sigma}\left(t\right) = E\left(\dot{\varepsilon}_t\left(t\right) - \dot{\varepsilon}_p\left(t\right) - \dot{\varepsilon}_{th}\left(t\right)\right) \tag{2.55}$$

Several optimization algorithms were consecutively used to perform the characterization of model parameters. Indeed, a first Genetic Algorithm enabled to reach local minimum with large bounds. Then a bounded simplex method was used to refine the GA-based minimum. Finally, a non-bounded simplex method was used to find the optimal set of parameter from mathematical point of view. The last results might give non-physical parameters contrary to bounded methods. The cost function used in each optimization algorithm has been carefully

defined. The different part of both testing procedures are differently weighted in order to take account of the different scales in rate dependent behaviors. Moreover, the error accumulated during tensile part of tests is not imposed at the beginning of relaxation by correcting the stress gap.

This optimization procedure was performed first at each temperature separately. Several tuning steps were repeated in order to reveal physical and also mathematically realistic parameter variations. The Figure 2.39 represents a set of interpolation functions for the best parameters obtained by temperatures. Finally a global model has been characterized by optimizing the parameters' interpolation functions. Hereafter, only the final global model optimization is presented. The intermediate steps are presented in the Appendix A.4.

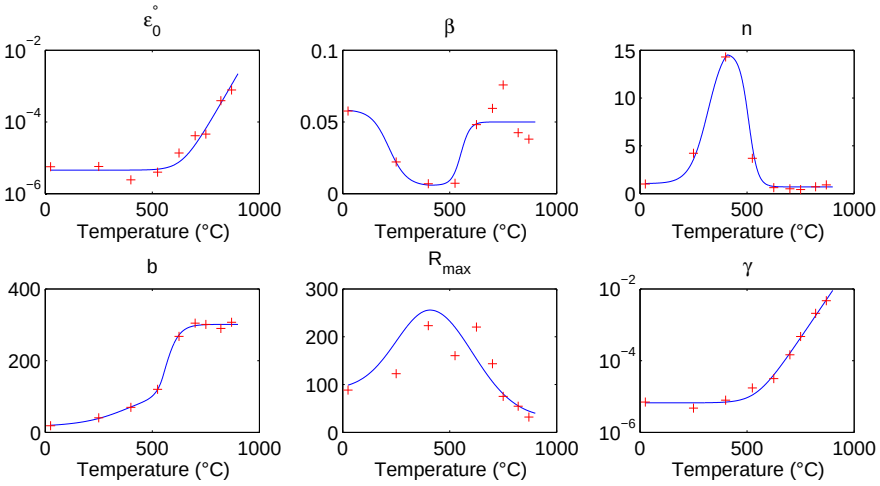

Figure 2.39 – Plot of temperature by temperature model coefficients with sets of interpolation functions

2.6.3.3 Results

For the global optimization, some additional data from anisothermal testing procedures presented in the next section is included in the set of tests data. The single difference for stress computation was that thermal strain rate was included into elastic strain rate computation. The coefficient of expansion had been measured previously for the different thermal pattern. The results are presented in the Appendix A.4.4. The Figure 2.40 shows the stress-time and stress-strain curves of model compared to experimental data.

The results for both low and high temperatures are fairly representative of experimental data on the whole range of temperature. The main gaps are concentrated at intermediates temperature between 400 and 625 °C where the mathematical non linearities of the model are strong. However the results are satisfactory. The Figure A.17 shows the parameters interpolation functions. The same temperatures for the transitions of behavior are used around 400°C for n and Q parameters. The parameters of the model are given in the Appendix A.4.3.

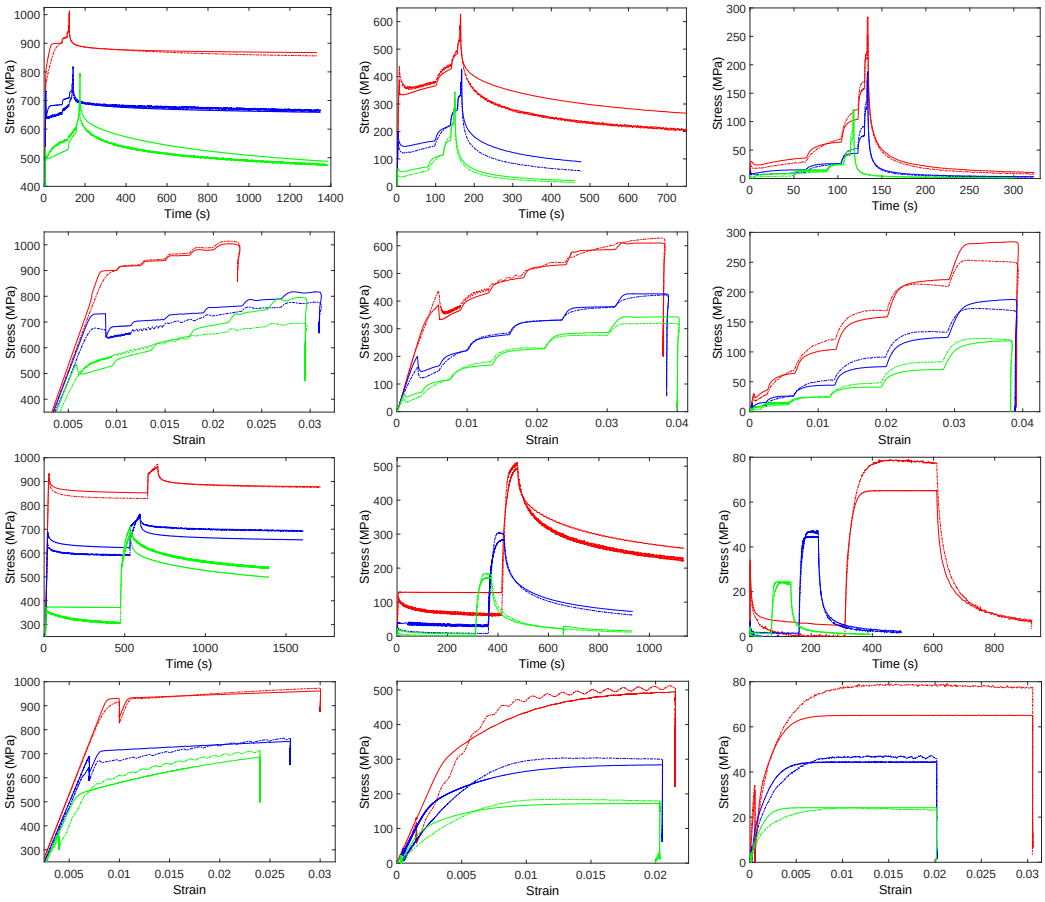

(a) 25 - 250 - 400 °C **(b)** 525 - 620 - 700 °C **(c)** 750 - 820 - 870 °C

Figure 2.40 – Final results: comparisons of model and experimental curves for TP1 and TP2

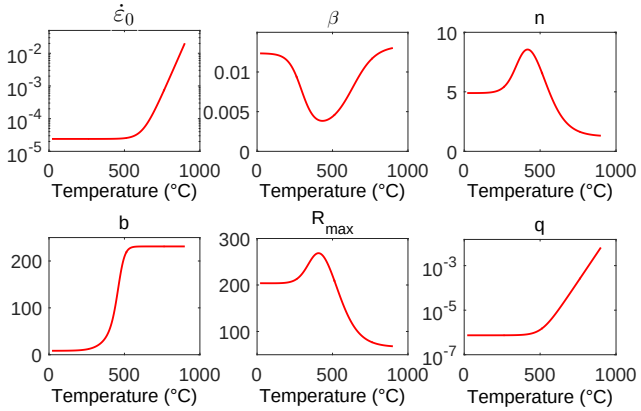

Figure 2.41 – Final results: model paremeters evolution with the temperature

2.6.3.3.1 Anisothermal tests

Some anisothermal tensile tests were performed in order to validate the model in varying temperature conditions such as the material undergoes in the process. Two different sessions were performed. The first one is composed by four different tests where the specimens underwent two different cooling rates and strain rates. The second session consisted in a test adapted from TP2 above the transition temperature of n and Q parameters mentioned in the previous paragraph at 470 °C. An anisothermal tensile test is conducted at 5.10^{-4} s^{-1} at the end of TP2 procedure under free cooling conditions.

❒ High temperature validation

The objective of this session is to mainly observe how the model behaves in anisothermal conditions, but also to verify the effect of cooling rate which had been neglected consequently to preliminary testing results. The test procedure (shown in the Figure 2.42) firstly consists in reproducing the same thermal treatment than for final characterization, then cooling slowly (as for free cooling inside press before rapid cooling) up to 850 °C. Then the two cooling rates at 3 and 7.5 °C.s^{-1} are imposed during 40 seconds. At the same time, the tensile test is performed. The Table 2.42a gives the procedure for the four tests.

Test	$\dot{T}$ (°C.s^{-1})	$\dot{\varepsilon}$ ($^{-1}$)	ε (%)
1	3	5.10^{-4}	2
2	3	5.10^{-5}	0.2
3	7.5	5.10^{-4}	2
4	7.5	5.10^{-5}	0.2

(a)

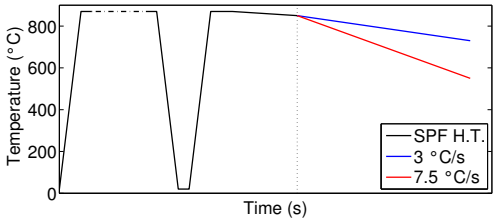

(b)

Figure 2.42 – Anisothermal tests: (a) test parameters and (b) heat treatment

The comparison of the model and the experimental data are given in the Figure 2.43. The curves with the upper stress level are those with ε=5.10^{-4} and the lower ε=5.10^{-5}. In the experimental condition, the cases with $\dot{T}$=3 °C.s^{-1} have data until around 700 °C whereas the numerical tests were extended up to the same temperature than the other cooling rate. The model give a better fit for the low cooling rate for both strain rate conditions. For the tests with $\dot{T}$=7.5 °C.s^{-1} the model under estimates the flow stress value. This may be due to dynamic phase transformation issues.

❒ Intermediate temperature validation

The objective of this second session is to observe how the model behaves in anisothermal conditions, in the range of strong non-linearity of the model. The test procedure (shown in the Figure 2.44a) is the same that for TP2 at 470 °C. However, at the end of second relaxation phase, the induction heating is stopped so that to create free cooling period during what the specimen is deformed at 10^{-4} s^{-1}. The temperature range during the anisothermal part of the test varied from 470 °C to 200 °C. Therefore the local decrease of SRS and other associated behavior in this temperature range are involved during the test.

The stress-strain curves of experimental and model data for the whole test are presented in the Figure 2.44b. The model is in good agreement with experimental data except for the first relaxation step. The absence of stress relaxation has also been observed in this range of temperature in the Section 2.5.2. It is related to the strong decrease of the SRS parameter.

The model for the anisothermal part presented in the Figure 2.44c fairly well reproduces the experimental curves. One important point is that none significant non-linearities are produced. Indeed, the mathematical transition defined in the model, especially for the n parameter, could produce detrimental non-linearities when crossing the critical transition temperature range, which is not the case.

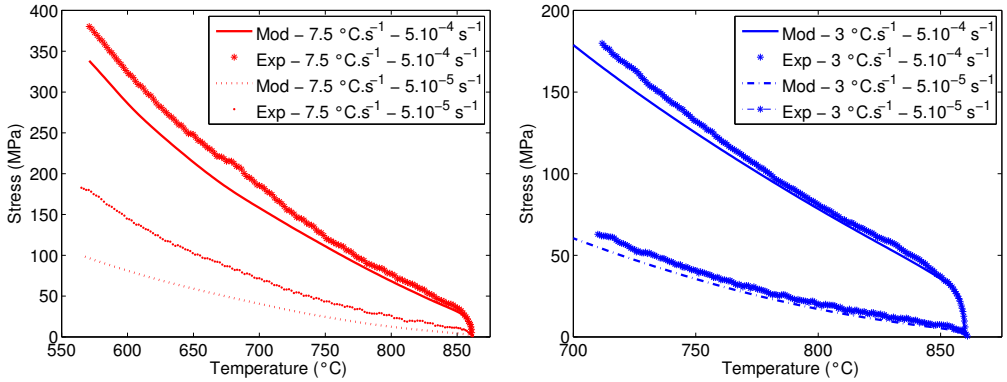

(a) **(b)**

Figure 2.43 – Anisothermal tests: stress-temperature curves: (a) 7.5 °C.s^{-1} and (b) 3 °C.s^{-1}

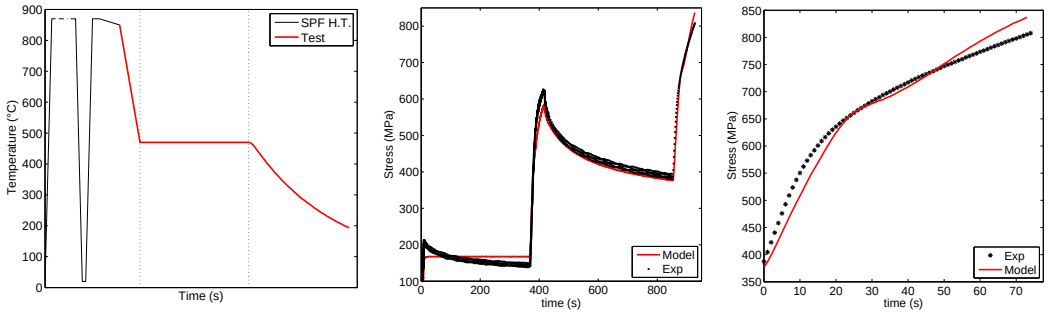

(a) **(b)** **(c)**

Figure 2.44 – Anisothermal validation - intermediate temperature:(a) heat treatment, stress-strain curves (b) full test (c) anisothermal portion

2.6.4 Discussion

The high non linearity of material behavior is a big issue for modeling purpose. Indeed, the most important difficulty that has been met is the local decrease of SRS closed to zero. Mathematically, when the SRS $m = 1/n$ tends to zero the equivalent stress is powered at $1/n \to \infty$. This effect is counterbalanced with the β coefficient. However, the consideration of the SRS decrease is limited in order to preserve the model from instabilities. That is why the model response for the tests at temperature around 400 °C is not as closed than others.

Regarding to the objective of process modeling, most of the constraints related to unloading step happen in the ranges of 600-900 °C so that the risk is limited. In the literature, few researches mentioned these singularities in SRS evolution with temperature. Surand [160] performed thermomechanical numerical simulations on samples with a material model taking account of this phenomenon. However, the definition of the model is still confidential.

For some curves at temperatures corresponding to the low SRS, the model response during the first relaxation of TP2 (for low viscous stress) does not seem to operate. For these conditions, ie. a low SRS combined with a low strain level (or dislocation density), the model is not well fitted. Indeed, a part of the stress, even low level, has promoted an increase of the dislocation density that is not described by the R variable and is not relaxed because of the stress exponent is limited to avoid too high non-linearities. It is traduced mathematically by a very long relaxation time when the viscous stress is close to yield stress.

From the material behavior point of view, this can come from two main reasons. Firstly, low stress based deformation mechanisms (like Harper-Dorn creep) can be activated for this range of temperature and stress. Secondly, the presence of low dislocation density at the beginning of the test may provide higher motion of dislocation and finally relaxation contrary to second relaxation part which comes after hardening phase. Supplementary tests might help to answer these questions.

Khraisheh et al. [159] used an additive formulation with several term contributions to separate the effect of different deformation mechanisms (defined in the Equation (2.56)). This method could be a way to improve the model response for low stress regime at this temperature range. However, the limit of such phenomenological model may be reached. Dislocation density based models would be more adapted to include such behaviors.

$$\dot{\bar{\varepsilon}} = \left(\frac{\bar{\sigma} - (k + R)}{C} \right)^{1/m} + C_i \bar{\sigma}^n \tag{2.56}$$

Beyond the accuracy of the model to fit experimental data, there are some hypothesis to discuss. Firstly, the model is based on a specific thermal treatment associated to a starting microstructure (typical grain growth). The heating and forming times that produce grain growth vary from a part to another. Additional tests must be performed to evaluate how the grain size modifies the behavior law. Indeed, the effect of grain size is generally related to long range obstacles and immobile dislocations. Therefore it may have an impact on elasticity limit through Hall-Petch relation, but also on hardening mechanisms.

Secondly, the effect of temperature variation hardening has been neglected. Some authors [161, 135, 162] used a differential terms that takes the influence of temperature history on hardening term such as defined in the Equation (2.57). Therefore, it is possible to consider the evolution of the influence of dislocation density. In the process conditions, some mobile dislocations can become immobile and generate additional hardening because the activation energy for motion is no longer sufficient. Some additional test could be conducted to evaluate the importance of such effect for typical thermomechanical path.

$$dR = \frac{\partial R}{\partial \dot{\varepsilon}} \dot{\varepsilon} + \frac{\partial R}{\partial \dot{T}} \dot{T} \tag{2.57}$$

2.7 Conclusions

The objective of this chapter is to characterize a material model able to reproduce the mechanical behavior of Ti-6Al-4V sheet after SPF. The finality of such material model is to reproduce numerically the mechanical behavior at stake during the process in order to get the cartography of deformation and residual stress at the end of the whole process for a specific cooling and unmolding procedure.

The bibliographic review has given an overview of the complexity of Ti-64 titanium alloy behaviors on the process range of temperature and the numerous parameters that may influence the material behavior during processing.

This complexity constrained to perform a preliminary testing session which had the objective to evaluate the impact of several parameters. The effect of SPF on microstructure and mechanical behavior has been investigated. The results have shown that the microstructure is impacted through grain size increase with a significant influence on yield stress such as noted in the literature.
It has been shown that the cooling rate after SPF is of second order of influence. Indeed, different mechanical tests performed on samples cooled at different rates from SPF temperature showed no significant difference regardless of the temperature or previous SPF preparation time.

A design of experiment was defined from the preliminary testing session. Two testing procedures were implemented so that to be able to involve every material behaviors and properties that need to be characterized. Elasticity, viscoplasticity and hardening-softening behaviors were promoted on the whole range of temperature. An hyperbolic sine law combined with power law is used to define the viscoplastic function. A Voce hardening model combined with a static recovery term are implemented into an isotropic Von Mises plasticity criterion.

A specific methodology has been developed and implemented to characterize the model ensuring the association of each behavior to the associated parameter of the model. Indeed, the design of the cost function and the iterative optimization procedure enabled to fit experimental curves with fine precision. Sets of interpolation functions were used to define temperature evolution of the model parameters. These functions have been defined from experimental observations in order to give sense to their evolution.

To conclude on this chapter, the model that has been characterized meet successfully the objective of process modeling. Indeed, not only the flow stress behavior is well reproduced but also the elastic domain and its evolution through hardening mechanisms that may promote residual stresses.

Chapter

3

Heat Transfers modeling

3.1 Introduction

3.1.1 Context

This chapter fits into the global approach of the modeling of the process. The heat transfers (HT) have an influence on material properties, and mechanical conditions during the process at different level. Indeed, the HT produce thermal stresses through material expansion which can generate plastic deformations. In addition, the part deformations may modify the contact interactions with the mold, especially the friction and clamping effects that can happen under material expansion, which at the end modify the conductive HT. Finally, the heat exchanges help the part to cool down to increase its mechanical properties to resists to the thermomechanical loading undergone during part removal from the mold.

Thus, the HT have a important role to ease unmolding sequence while ensuring the most limited deformations of the part. The difficulty resides in the material properties that are highly viscoplastic at these temperature with null limit of elasticity for temperature above 700 °C such as highlighted in the Chapter 2. In addition, the global environment of the press, the oven, and the mold requires a very long time to heat at forming temperature. The few amount of energy lost during unmolding phase requires a long heating time to recover the forming temperature. The control of HT during unmolding sequence is a hard compromise between the shorter cooling time, and a sufficient and adapted cooling to minimize thermomechanical stresses and part deformations.

3.1.1.1 Heat transfers

Today, AIRBUS uses an air jet blow cooling system which is time and space controlled. Nozzles are disposed above the part surface every fifty centimeters in order to scan the whole part. It is possible to activate specific nozzles before unmolding operation in order to select targeted areas. After a specific time, the automatic handling robot pulls on an extraction frame on which the part is fixed to remove the part from the mold. The pulling effort is limited to prevent deformation so that it is incrementally increased while cooling is performed. When the part is removed from the mold, it is disposed outside the press and naturally cooled down. The different phases of the unmolding sequence are already presented in the Section 1.1.3.1. The Figure 3.1 shows three configurations. The configuration 1 corresponds to the opening of the press. The configuration 2 corresponds to the blowing and the extraction operation. Finally, the configuration 3 corresponds to the natural cooling down outside the press.

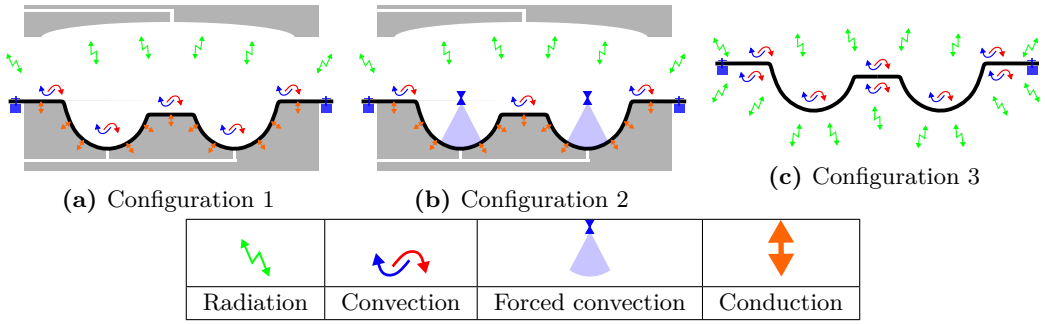

(a) Configuration 1 **(b)** Configuration 2 **(c)** Configuration 3

Figure 3.1 – Schematics of the different heat transfer configurations

❒ Conduction

Conductive HT happens between the different parts that are in contact: the formed part, the mold and the extraction frame. The interactions between the mold and the press environment are not considered in the thesis. Indeed, the mold is made of refractory steel that has a high thermal inertia and negligible temperature variations at its interface with the hot press.

❒ Radiation

Radiation HT mode is effective during the whole process. When the part is inside the press, it happens between every surface that are facing to the part, and the frame surfaces. The whole press environment provide radiative heat flux. A large energy is lost by radiation HT through the opened door of the press. When the part is outside, the assembly only exchange with ambient environment and itself.

❒ Convection

Convection HT mode is particularly complex and varying during the process. Indeed, at the beginning of the configuration 1, the air inside the press is approximately at SPF temperature. Some cold air goes inside whereas hot air leaves the press, and a complex flow produces natural convective HT. During the configuration 2, the air blowing produces forced convection on the top surface of part and a complex swirling flow inside the press. Finally, during the configuration 3, convective HT happens on both sides of the part and the frame.

3.1.1.2 Heat equation

The final purpose of this work is to implement a FE model. Therefore, the thermal analysis of the problem is briefly introduced to highlight the problematics of the chapter. The temperature variation during the process is obtained by solving the law of conservation of energy which derived from the first thermodynamic principle. The Equation (3.1) defines the integral form of this conservation law where V is the volume, ρ the density, $\dot{U}$ the rate of energy, r is a volume heat generation term and q is a surface HT term. This equation traduces that the energy variation of a volume is equal to the energy that is lost and the energy that is provided to this volume.

$$\int_V \rho \dot{U} dV = \int_V r dV + \int_S q dS \tag{3.1}$$

Inside a solid, thermal diffusion is governed by Fourier's law which is defined in the Equation (3.2) where q_λ is the surface heat flux at material volume boundary and λ the thermal conductivity. The heat equation is obtained in the temperature differential form (see Equation (3.3)) by combining the Equation (3.1) with the Equation (3.2). The microstructure transformation and plastic heat dissipation terms have not been considered in our context so that the r term is removed.

$$q_\lambda = -\lambda \nabla T \tag{3.2}$$

$$\rho C_p \frac{\partial T}{\partial t} = r + \nabla.(-\lambda \nabla T) \tag{3.3}$$

At material boundaries, the HT can happen through conduction, convection and radiation modes. In this case, the surface heat flux ($q = -\lambda \nabla T$) inside heat equation is replaced by the respective contributions. For conduction between two contacting surfaces, the heat flux $q_{cond}(1 \rightarrow 2)$ is defined in the Equation (3.4) where k_c is the conductance coefficient, and T_1 and T_2 the surface temperatures of surfaces 1 and 2. In this equation, k_c which is also equal to the inverse of the thermal contact resistance R_c, is an empirical parameter that encompasses material, geometrical, and process parameters.

$$q_{cond}(1 \rightarrow 2) = k_c(T_1 - T_2) \tag{3.4}$$

Then, radiation surface heat flux between two surfaces $q_{rad}(1 \rightarrow 2)$ is defined (3.5) (in the case of black body radiations) where ϵ is the total emissivity of the material, σ the Stephan-Boltzmann constant and $F_{(1\rightarrow 2)}$ is the view factor (VF). $F_{(1\rightarrow 2)}$ is the ratio of hemispherical projection of surface 1 regarding to surface 2 on total hemispherical surface. This equation is valid when both surfaces have an homogeneous temperature and emissivity. However, ϵ may vary as a function of material, geometrical, and process parameters.

$$q_{rad}(1 \rightarrow 2) = \epsilon \sigma F_{(1\rightarrow 2)}(T_1^4 - T_2^4) \tag{3.5}$$

Finally, the convection heat flux q_{cond} can be defined with the Equation (3.6) where h_c is the convection coefficient and T_f the fluid temperature. h_c is the result of the simplification of a complex fluid dynamic problem that involve the surface and fluid interactions and it depends on the fluid, the surface geometry and the process parameters.

$$q_{conv} = h_c(T_f - T) \tag{3.6}$$

Each heat flux contribution is a surface based term. These equations are fairly simple to implement, but they require to know the respective parameters k_c, h_c and ϵ and their evolutions regarding to the material, geometrical, and process parameters. A distinction is made between natural and forced convection coefficient respectively named h_c and h_{fc} when the differentiation is needed.

3.1.2 Problematics and objectives

The problematic of heat transfers in the context of the process lies in understanding how they occur and how they must be taken into account in the model. Regarding to the FE modeling purpose, it consists in defining k_c, h_c and ϵ for the various conditions and their dependencies on the material, geometrical, and process parameters. This implies to answer several objectives:

- The first objective has consisted in performing thermal measurement in operating conditions in order to characterize the heat transfers.
- The second objective has consisted in characterizing the parameters of the BC of each HT modes k_c, h_c and ϵ and their evolution during the different phases of cooling and unmolding process.

The HT parameters are associated to three modes that happen simultaneously with more or less intensity during the process. They may be material, surfaces quality, space and time dependent. A first bibliographic review was made to understand how these parameters behave in the process conditions, and how they are modeled in the literature.

3.2 State of the art

3.2.1 Radiative heat transfers

3.2.1.1 General considerations

The radiative HT operates by electromagnetic wave emission. Planck has largely contributed to the definition of the basic concept of heat radiation theory [163]. Indeed, every material emits or absorbs radiative energy depending on temperature and wave length. When an electromagnetic wave strikes on a surface, it is absorbed or reflected. Some materials, called black bodies, absorb the total wave energy such that they seem black for human eyes. The energy of radiative electromagnetic wave for black bodies has been given by Planck such as

defined in the Equation (3.7) where the L^0_λ is the spectral radiance which is the radiative energy per unit area of the body, per unit solid angle per unit wavelength, T the temperature, λ the wave length, c the speed of light, h the Planck constant and k the Boltzmann constant.

$$L^0_\lambda = \frac{2hc^2\lambda^{-5}}{exp(\frac{hc}{k\lambda T}) - 1} \tag{3.7}$$

The Stephan-Boltzmann's law relates the radiative power (or surface heat flux) ϕ^0_{rad} of a black body with the temperature as total emittance in the Equation (3.8) where σ is the Stephan-Boltzmann's constant. The emittance is the total hemispheric integration of radiance as defined in the Equation (3.9) where λ is the solid angle of the unit hemisphere.

$$\phi^0_{rad} = M^0 = \sigma T^4 \tag{3.8}$$

$$M^0 = \int_0^\infty M^0_\lambda d\lambda = \int_0^\infty \int_{\partial\Omega} L^0_\lambda d\Omega \; d\lambda \tag{3.9}$$

The emissivity of a surface is the parameter that relates the previously described theory of perfect black body to every surface for which radiative power is not totally absorbed. The energy that is not absorbed is either reflected or transmitted. The total hemispherical emissivity ϵ (generally called total emissivity) is defined in the Equation (3.10) as the ratio of total emittances of the surface and a black body. It exists additionnal emissivity quantities. The spectral directional emissivity $\epsilon_{\lambda,\Omega}$ is defined as the ratio of spectral directional radiances of a surface and a black body. In, addition, the spectral hemispheric emissivity ϵ_λ is defined as the ratio of spectral emittances of a surface and a black body.

$$\epsilon = \frac{\int_0^\infty M_\lambda d\lambda}{\int_0^\infty M^0_\lambda d\lambda} = \frac{\int_0^\infty \epsilon_\lambda M^0_\lambda d\lambda}{\sigma T^4} \tag{3.10}$$

The thermal heat flux leaving any surface ϕ_{rad} can be defined using the back body theory and the emissivity definition as given in the Equation (3.11).

$$\phi_{rad} = \sigma \epsilon T^4 \tag{3.11}$$

3.2.1.2 Emissivity

3.2.1.2.1 Parameter affecting emissivity

The emissivity is the key parameter of radiative HT. It is sensitive to many parameters that can be geometric, material, temperature and surface quality dependent [164]. The Figure 3.2a shows the evolution of directional emissivity for titanium as a function of angle and wavelength. There are clear variations according to both parameters. The Figure 3.2b presents emissivity variations for several surface finishing and oxidation conditions. The results highlight a strong impact of the oxidation state, and a slight influence of the surface finishing state.

Many authors investigated the emissivity properties of titanium alloys, especially the Ti-64 alloy, for infra-red temperature measurement purpose [165, 166, 167, 168, 169, 170]. In these studies, the spectral emissivity is of interest to recover temperature with the peak radiance intensity. Milosevic et al. [20] characterized the total hemispherical emissivity of Ti-64 for a various range of temperature between 780 and 1700 K. They proposed a fourth order polynomial model evolution with temperature represented in the Figure 3.3a. Pagan et al. [21] experimentally determined spectral and total emissivities under different oxidation conditions such as presented in the Figure 3.3b.

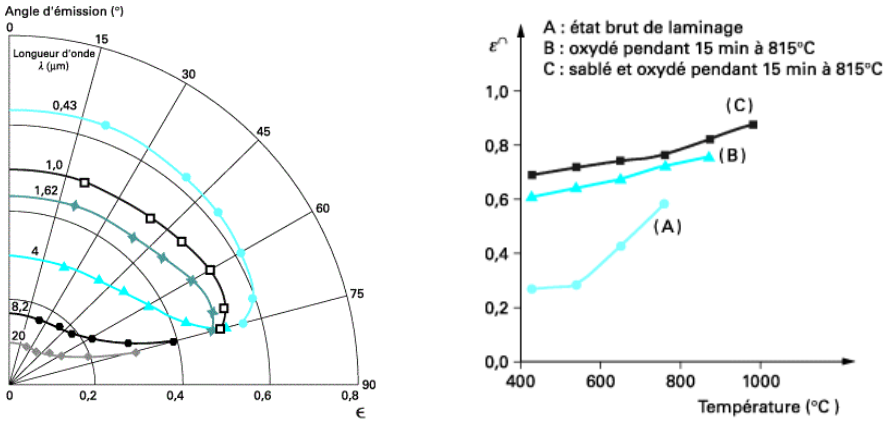

(a) **(b)**

Figure 3.2 – Evolution of emissivity properties: (a) effect of angle and wavelength on Ti-64, (b) effect of surface properties on Inconel 718 [19]

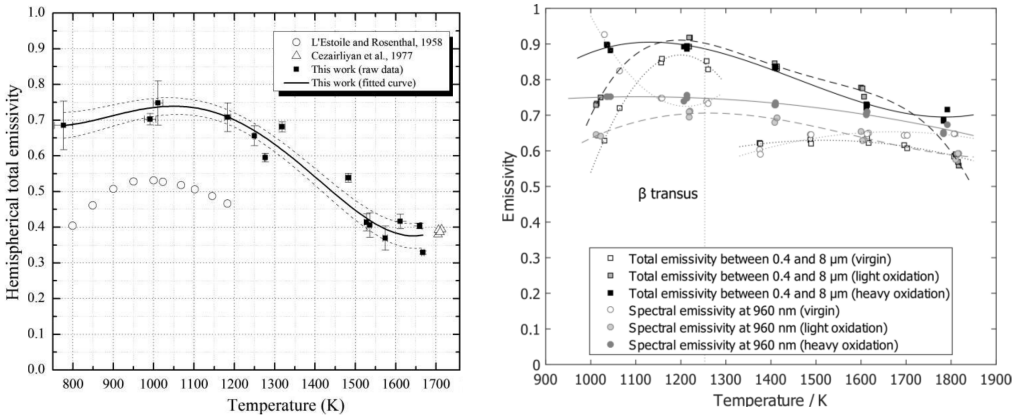

(a) **(b)**

Figure 3.3 – Hemispherical total emissivity of Ti-6Al-4V as a function of temperature (a) from Milosevic et al. [20] (b) from Pagan et al. [21]

A particular shape of emissivity variation seems to be emphasized from the Figure 3.3a and 3.3b for the heavy oxidized state. Indeed, the emissivity increases from the temperature around 1600-1700 K up to the 1100-1200 K and then slightly decreases for lower temperatures. However, the level of emissivity and its variation seems highly dependent of the tested sample and its oxidation state.

3.2.1.2.2 Effect of oxidation

The Figures 3.2b and 3.3b reveal the importance of the effect of oxidation on the emissivity for the Ti-64 alloy. The SPF process works at temperature around 900 °C where oxidation is likely to occur.

González-Fernández et al. [166] experimentally showed that the spectral emissivity decreases with wavelength and increases linearly with temperature on 500-1200 K accordingly to Plank's theory. They shows that thermal cycling modifies the spectral emissivities.

Li et al. [169] analyzed the evolution of the oxide thickness growth at different temperature and the impact on emissivity measurements. They highlighted that their spectral emissivity

measures were disturbed by reflection on oxide interface as a function of oxide thickness at some wavelength. Hagqvist et al. [167] also highlighted the evolution of radiative emitted energy due to the evolution of surface properties because of oxidation processes. They proposed to model emissivity as the sum of Ti-64 metal emissivity and the oxide layer emissivity as defined in the Equation (3.12). Oxidation is activated at temperature superior to an activation temperature T_{act}=810K. The normalized thickness rate $\dot{d}$ (with metal thickness) defined in the Equation (3.13) is proportional to the partial pressure oxygen P_{O_2} in the chamber multiplied by the normalized metal layer where the oxygen sites are supposed to be uniform into the thickness.

$$\epsilon = \epsilon_m + \epsilon_{Ti0_2} = \epsilon_m + k_1 d \tag{3.12}$$

$$\dot{d} = k_2 P_{O_2}(1-d) - k_3 d \langle T - T_{act} \rangle \tag{3.13}$$

3.2.1.2.3 Conclusions

The thermal radiation HT is globally driven by the emissivity parameter of a surface. It is sensitive to various parameters, mainly the temperature, the roughness, the oxidation and the coating properties. The most critical parameter seems to be the oxidation in the process case. The effect of Boron-Nitride (BN) lubricant coating may also have an impact on the emissivity not only intrinsically, but also indirectly through its anti-oxidation action.

3.2.1.3 Radiative heat transfers in FEM analysis

In hot stamping, the thermal radiation are important during the step of transfer of the blank into the stamping machine and after stamping operation. The sheet metal part exchanges heat with the environment but also with the dies. Most of the time, the limit temperatures (high temperature environment: dies, tooling, etc.) are considered homogeneous and constant [76, 171, 172]. Usually, the manipulation of the Equation (3.5) is generally made to get the form of the Equation (3.14) such as defined Equation (3.15). This formulation enables to define a global heat transfer coefficient (HTC) with the contribution of each HT mode inside. Sometimes it is even neglected [171, 35] considering the temperatures too low for radiation to have an impact.

$$q_{rad} = h_{rad}(T_1 - T_2) \tag{3.14}$$

$$h_{rad} = \epsilon\sigma F_{(1\to2)}(T_1^2 + T_2^2)(T_1 + T_2) \tag{3.15}$$

In some cases, a so-called radiation shape factor f is used [173, 172] to take account of the heterogeneous facing surface temperature such as defined in the Equation (3.16)

$$q_{rad} = h_{rad}(T_1 - T_2)f \tag{3.16}$$

However, for complex shapes, surface properties or temperature distributions, it may be necessary to use more complex modeling techniques. Inside heating furnace [174] or autoclaves [175] for example, a full computation of radiative HT may need to be computed. The numerical methods to compute thermal radiations are extremely complex [176]. Thermal radiations involve several coupled phenomena that require physical or mathematical simplifications that are currently not easily applicable in the context of thermo-mechanical analyses.

3.2.1.4 Thermal radiation boundary condition

The radiative heat flux between two surfaces can be simplified using the gray body radiation theory [177]. Gray body implies monochromatic emissivity. It is demonstrated in the

Section 3.6 that this condition is fairly respected for oxidized surface of the Ti-64 alloy. ABAQUS® HT analysis propose the cavity radiation BC that compute thermal radiation HT using this theory [178]. The radiative heat flux is computed with the Equation (3.17) where the VF F and the surfaces A_1 and A_2 are geometrical parameter that are computed numerically and ϵ_1 and ϵ_2 are the total emissivities. ϵ_1 and ϵ_2 need to be defined as a function for temperature and surface process quality (roughness, coating, etc.) and especially the effect of oxidation as mentioned above.

$$Q_{rad_{1\to2}} = \frac{\sigma(T_1^4 - T_2^4)}{\frac{1-\epsilon_1}{A_1\epsilon_1} + \frac{1}{A_1 F} + \frac{1-\epsilon_2}{A_1\epsilon_2}} \tag{3.17}$$

3.2.2 Natural convection heat transfers

3.2.2.1 General considerations

The convection coefficient is defined from the Newton's law of cooling (Equation (3.18)) as the ratio of surface heat flux q_{conv} and the temperature difference between environment gas T_∞ and the exchanging surface at the temperature T. This is a macroscopic description of the problem. At the interface, a local description of the HT can be obtained by the Fourrier's law (Equation (3.19)) where λ_f is the thermal conductivity of the fluid, and x_n is the coordinate normal to the surface. This formulation implies to know the temperature variation of the fluid at the surface.

$$h_c = \frac{q_{conv}}{T_\infty - T} \tag{3.18}$$

$$q_{conv} = -\lambda_f \left.\frac{\partial T}{\partial x_n}\right|_{x_n=0} \tag{3.19}$$

The Nusselt number is an dimensionless quantity that is used to quantify the HT intensity. It is defined Equation (3.20) where T^* ($=T/(T-T_\infty)$) and x_n^* ($=x_n/L_c$) and L_c are respectively the dimensionless temperature and normal to surface coordinate and the characteristic length which is a typical length of the convection problem. The average Nusselt number $\overline{Nu}$ (defined Equation (3.21)) is regularly used in convection HT problems.

$$Nu = \left.\frac{\partial T^*}{\partial x_n^*}\right|_{x_n^*=0} = \frac{hL_c}{\lambda_f} \tag{3.20}$$

$$\overline{Nu} = \int_S Nu dS \tag{3.21}$$

Convective flow can have different modes. Indeed, it can be natural or forced. Natural convection involves the buoyancy driven flows promoted by temperature differences. These buoyancy forces produce fluid motion and swirling of fluid that induce HT. Forced convection is guided by specific induced flow direction that leads the global fluid flow and HT. In both cases turbulences can be developed and increase the HT. The figure 3.4 presents two types of natural and forced induced turbulent flows. The mechanisms of turbulences in both cases are not detailed in this chapter. Only the relation between turbulence and HT is discussed. The forced convection case is approached in the Section 3.2.3.

As mentioned above, natural convection is a buoyancy driven flow. One way to determine convection intensity is to used Grashoff number Gr. It is the ratio of buoyancy forces and the viscous forces such defined in the Equation (3.22) where g is the gravitational acceleration, ΔT the surface and fluid temperature difference, L_c the characteristic length, β, ρ and μ are respectively the coefficient of thermal expansion, the density, and the the dynamic viscosity

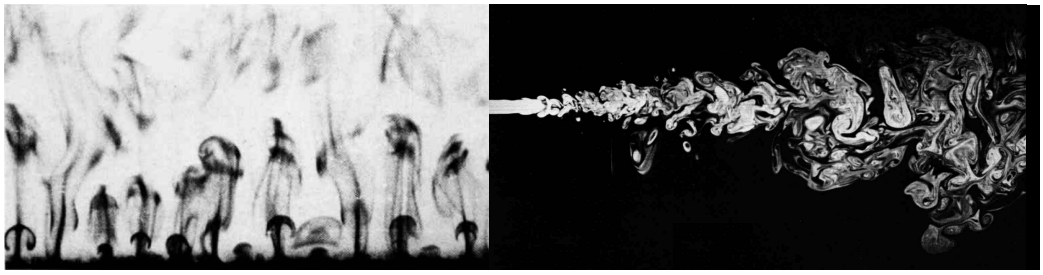

(a) **(b)**

Figure 3.4 – Turbulent flow visualization (a) buoyant thermal rising from heated surface (b) water jet [22]

at fluid temperature T_f ($T_f = (T_\infty + T)/2$).

$$Gr = \frac{g\beta\Delta T L_c^3 \rho}{\mu^2} \tag{3.22}$$

Gr number express ratio of the acting forces (buoyancy and viscous) that promote and limit the fluid motion in convective mode. When Grashoff number is very low, the temperature gradient does not produces motion of fluid and heat is exchanged by conduction. When Gr increases, convection follows a laminar flow. Then, at high Gr, a transition is reached and the flow becomes turbulent.

An other important dimensionless number is the Rayleigh number. It expresses the HT inside fluid. It is defined (Equation (3.23)) as the product of Grashoff and Prandtl numbers Pr. Prandtl number (Equation (3.24)) is the ratio of momentum diffusivity and thermal diffusivity. The Rayleigh number is regularly used to describe the fluid flow conditions for natural convection problems. The Figure 3.5 illustrates two different laminar and turbulent flows in the case of horizontal plates natural convection experiments for two Ra intensities [23] .

$$Ra = GrPr \tag{3.23}$$

$$Pr = \frac{\nu}{\kappa} = \frac{\mu Cp}{\rho} \tag{3.24}$$

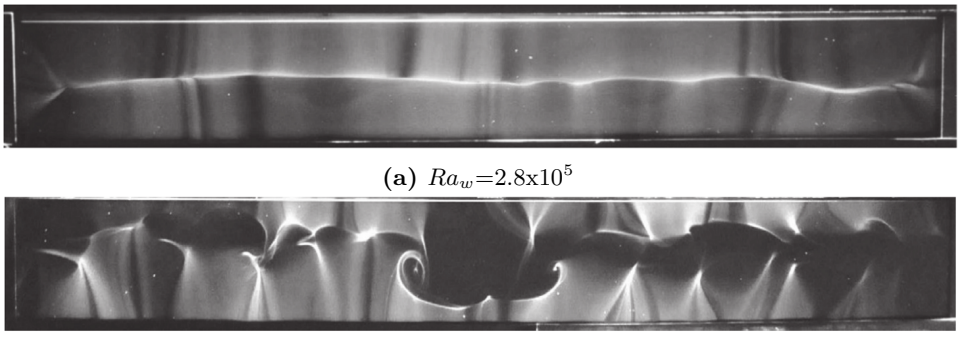

(a) Ra_w=2.8x10^5

(b) Ra_w=2x10^6

Figure 3.5 – Flow visualization of natural convection adjacent to upward-facing horizontal plate with (a) laminar (b) turbulent regimes [23]

In our process there are two main different natural convection configurations, when the part is inside and outside the press. The first configuration is rather complex because there are different surface temperatures and the temperature of the fluid is different inside and outside the press at the beginning. This case can be assimilated to open cavity which have been largely studied in the literature. The second configuration is sightly simpler because the fluid environment temperature is constant (the ambient environment temperature). It is most of the time (hot stamping analogous cases) assimilated to an horizontal plate which is a reference case.

As introduced in the introduction chapter in the Section 1.4, only the computational fluid dynamic (CFD) analysis is able to provide a fine description of the convection coefficients generated by the process. However, The open cavity and plates problems are briefly regarded to have estimation means of the convection coefficients in these cases.

3.2.2.2 Nusselt correlations: horizontal plates

The HT over hot horizontal plates can be divided into two different configurations (HT upwards and downwards from the plate regarding to the gravity direction) for which turbulent and laminar regimes can be differentiated. Most of the authors who worked on these configurations reported the same power laws based correlations such as defined in the Equation (3.25) where C and n are slightly varying coefficients that depends on experimental conditions.

$$\overline{Nu} = CRa^n \tag{3.25}$$

Some correlation laws are presented in the Equation (3.26) where the models ^{*1}, ^{*2} and ^{*3} respectively refer to the next references [24] [179] and [180].

$$Nu = \left\{ \begin{array}{lcll} 0.96R_a^{1/6} & Ra < 200 & *^1 & \\ 0.59R_a^{1/4} & 200 < Ra < 10^4 & *^1 & \\ 0.54R_a^{1/4} & 2.10^4 < Ra < 8.10^6 & *^2 & \} \ up \\ 0.13R_a^{1/3} & 8.10^6 < Ra < 1.6.10^9 & *^2 & \\ 0.58R_a^{1/5} & .10^4 < Ra < .10^6 & *^3 & \} \ down \end{array} \right. \tag{3.26}$$

The Figure 3.6a represents the Sherman Number Sh evolution for low Rayleigh. Sh is the mass transfer coefficient, which is equivalent to Nu number for isothermal plate convection. The Figure 3.6b represents Nusselt correlation with experimental results for upward natural convection for various rectangular plate dimensions and Length-to-width ratios. For both studies [24, 23], the authors managed to find a power law based correlation that works fairly well. Both correlations laws present a slope change associated to laminar-to-turbulent transition which do not happen for the same Rayleigh numbers. This is due to the chosen characteristic length that may differ according to the authors and change the Nu value without actually impacting the convection coefficient value.

Some studies reported the dependence of Nusselt number on plate inclination [180]. The authors determined a cosine dependence of the classical correlation laws such as defined in the Equation (3.27) in the case of horizontal plate natural convection facing downward.

$$\overline{Nu} = 0.56(Gr.Pr.cos\theta)^{1/4} \tag{3.27}$$

3.2.2.3 Nusselt correlations: open cavities

Cavities are one of the textbook case for natural convection heat transfers that has been largely studied for decades [25, 26, 27, 181, 182, 183]. In the context of SPF process, the use of side facing open cavity models for heat transfer analysis is fairly consistent. Indeed, the configuration of the press is a parallelepiped cavity which opens during the unmolding

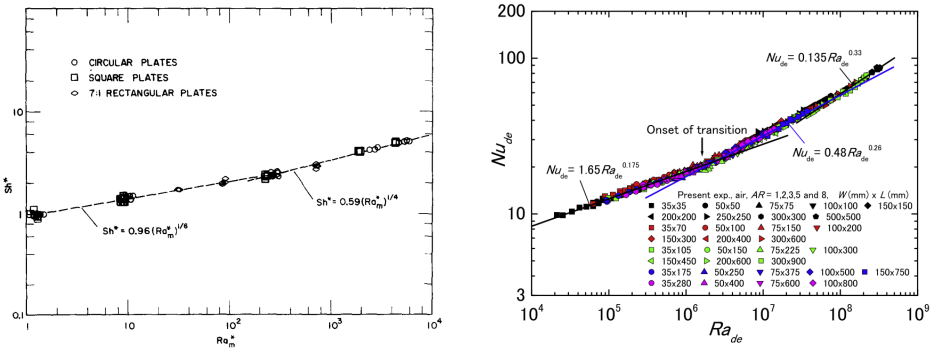

(a) **(b)**

Figure 3.6 – Two examples of Nusselt correlations with Rayleih numbers from (a) Goldstein et al. [24] and (b) Kitamura et al. [23]

procedure. The main difference with the industrial case is that there is a substantial warm volume inside (the mold and formed part) that disturbed the fluid flow. However, It is the most similar case from literature.

The Figure 3.7a schematically represents the configuration of exchanging surfaces for natural convection inside the press when the door is opened. The cavity geometry and the BC can widely vary in the literature according to the associated engineering application. Some authors investigated the influence specific factors on fluid flow, temperature, and cavity orientation [26, 181]; size, shape and position aperture [182, 183]. The Figures 3.7b, 3.7c and 3.7d represents the relevant cases from the literature with different configurations: open cavity, partially open cavity, partially open cavity with an internal source inside the cavity.

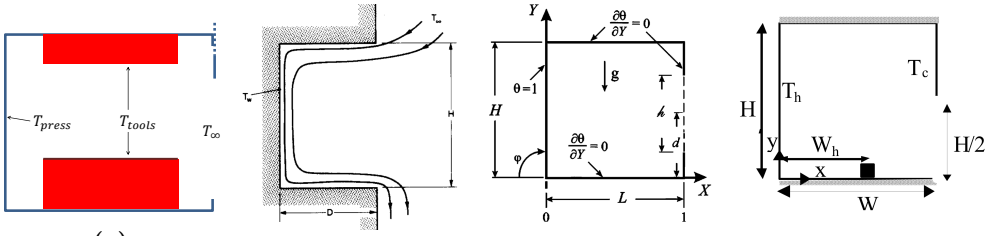

(a) **(b)** **(c)** **(d)**

Figure 3.7 – Schematics of (a) industrial press configuration for cavity convection analysis, three different near-SPF configurations of natural convection with (b) Open Cavity [25], (b) Partially opened cavity [26] and (c) Partially opened cavity with internal source [27]

There are four important aspects described in the literature that can influence the convection HT for SPF process: the cavity face of interest, the time evolution of convection flow, and the temperature impact on flow regime. These aspects are approach below:

❒ The face of the cavity

Penot [184] first and then Skok et al. [25] observed each faces of its cavity independently, and they measured the heat transfer for different Gr value for the opened cavity configuration such as defined in the Figure 3.7b. The Figure 3.8 represents the evolution of the averaged Nusselt number for bottom, vertical and top faces. The heat transfer decreases largely form the aperture to the vertical surface. The vertical surface has a small tendency to decrease up to top surface which has a Nusselt number clearly inferior to the others.

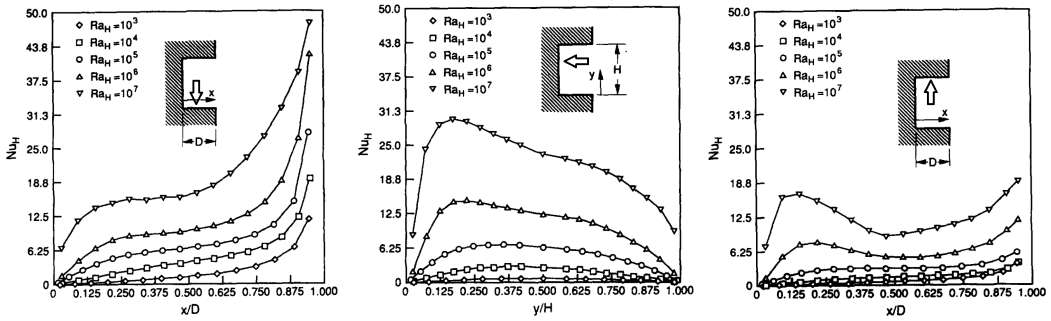

Figure 3.8 – Nu evolution along the each cavity faces for different Ra values [25]

❒ The time dependency

Some authors investigated numerically the evolution of convection flow during transient phase [28, 29]. They performed simulations for different Rayleigh value with small temperature differences (ΔT=0.1-10 K). The Figure 3.9a shows the time evolution of the global cavity averaged Nusselt number for several Ra values [29]. The values start fairly high and they subsequently converge to a steady state value. The Figure 3.9b compares the same evolution by faces for Ra=10^7 [28]. The convergence rate seems relatively equal as a function of the faces but dependent on the Rayleigh value.

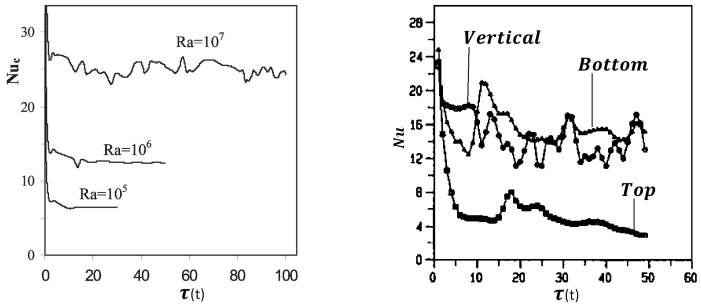

(a) **(b)**

Figure 3.9 – Time evolution of Nu as a function of (a) Ra [28] and (b) cavity faces [29]

❒ The temperature dependency

Large temperature differences have been particularly studied for cavity solar receiver applications. Clausing [185, 186] performed experimental tests with walls at high temperature between 725 to 1020 °C. He used a model for the Nusselt correlation proposed by Le Quere et al. [187] with an additional term ($\frac{T_s - T_\infty}{T_\infty}$) such as defined in the Equation (3.28). This additional term enables to consider the turbulent flows. Juarez et al. [188] also investigated large temperature differences. They tested numerically the influence of ΔT variation (from 10 to 500 K) for different Ra numbers (from 10^4 to 10^7). They proposed an other additional terms ε ($= \frac{T_s - T_\infty}{T_\infty}$) in their correlation model defined in the Equation (3.29).

$$\overline{Nu} = 0.82 Ra_H^{1/3} \left[-0.9 + 2.41 \left(\frac{T_w}{T_\infty} \right) - 0.5 \left(\frac{T_w}{T_\infty} \right)^2 \right] \tag{3.28}$$

$$\overline{Nu} = a + bRa^c + d\varepsilon^e + fRa^c\varepsilon^e \tag{3.29}$$

❒ The impact of an obstacle

Some authors [27, 189, 190] worked on the impact of internal source inside an open cavity presented in the Figure 3.7d. This type of configuration takes account of the perturbations produced by the obstacle, and also the forces generated by the heat source. Fontana et al. [189] compared the impact of heat source intensity inside a half-side-opened cavity for low Rayleigh values (Ra=10^3-10^5). The Figure 3.10 presents the stream lines for different R values which is the ratio of the internal source based Ra_i and external air based Ra_e (with Ra_e=10^5). The configuration where R=0 plays the role of a simple obstacle. Their temperatures are not comparable with the SPF process. However, it indicates that the swirling flows inside the cavity may be very complex especially for the transient phase during the furnace opening.

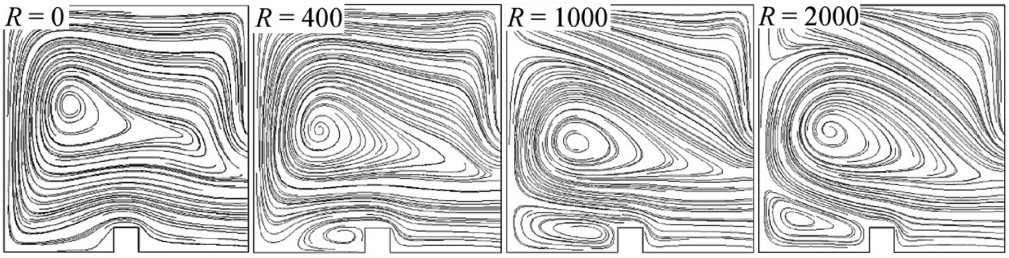

Figure 3.10 – Streamlines evaluated at Ra_e=10^5 for several R values [190]

3.2.2.4 Heat transfers in hot forming process

In the literature, especially for hot stamping, a basic convection heat flux is considered with the ambient environment. The experimental correlations based on literature from horizontal plates are used for convection on top and bottom surface of the sheet [76, 171, 172].

These correlation laws enable to estimate the average HTC in the case where geometries are comparable to flat plate. It is not as simple for SPF process for several reasons. Firstly, the local heat transfers are averaged, even though the size of the plate is large combined with a low thermal conductivity of Ti-64. This may lead to strong temperature heterogeneity. Secondly, the flat plate hypothesis can be far from reality in SPF process. Indeed, the geometry of the formed parts can have large depth distance with confined zone such as presented in the Figure 3.11 in the perpendicular plane of initial sheet metal. The part is clearly far from a plate. Finally, there is a strong influence of the high temperature surrounding environment (press, dies, frame tooling, etc.) onto the fluid. Therefore, the classical correlation model may not be applicable for such complex conditions.

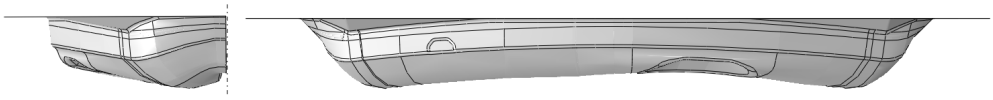

Figure 3.11 – CAD views of the longitudinal and lateral view of the nacelles of the A350-900 air Inlet

Many authors have investigated the heat transfers using CFD analysis inside industrial heating furnaces [191, 192, 174], autoclaves [175] or gas quenching furnaces [193, 194, 195, 196, 197]. The CFD simulation is used to compute convective heat transfers in such industrial context because of the complexity of fluid flow and geometries. In every case, the authors highlight strong distributions of convection coefficient [196, 197] that have an importance on the temperature computation and the effect on microstructure properties [197].

3.2.2.5 Natural convection boundary condition

It has been chosen to use CFD analysis to have an estimation of the convective heat transfer during the process. However, there are two different configurations, inside and outside the press, that require two different models for the boundary condition. For the inside-press configuration, the low temperature difference at the opening of the press, with a limited time to reach steady state before blowing is highly complex to simulate. Moreover, the low heat transfers produced by the small temperature difference as a limited interest compared to the huge investment.

Therefore, the Nusselt correlations for open cavity problems have been used for the inside-press natural convection coefficient. It has been taken homogeneous and varying from zero to a steady state value computed thanks to the Equation (3.28).

For the outside press convection configuration, CFD modeling was used to understand the convection modes operating during cooling. CFD analysis were performed to evaluate convection coefficient distributions. Then, basic constant, linear or bi-linear regressions over part surfaces were used to model convection coefficient so as to be easily implement in classical convection BC in the thermo-mechanical model.

3.2.2.5.1 CFD-based convection coefficients

As introduced in the Section 1.4 some authors worked on convection HT using CFD analysis on three main topics: furnace applications, autoclave and gas quenching processes. However, CFD analysis of external natural convection flows at high temperature differences such as post SPF ambient cooling phase has not been investigated in the literature. Thus there is not clear available work that validate a numerical methodology for computing HTC in the process conditions. Therefore, a feasibility study of the use of Abaqus-CFD solver to model natural convection flows in the process conditions is presented in Appendix C. It includes a bibliographic review on CFD FE analyses, the use of turbulence models and modeling practices. It includes also a comparative study of numerical and experimental results based on a similar case: horizontal plates natural convection. Finally, a sensitivity study of critical model parameters is presented to evaluate the relevance of using of CFD tool to estimate the convection coefficient variations over space and time for SPF application.

The conclusion of the numerical analysis enabled to validate a modeling methodology. The CFD models are build on several major hypothesis. The Reynolds-Averaged Navier-Stocke equations (RANS) with a turbulent k-ω SST model are solved with an incompressible flow analysis. A transient resolution is used with the fully implicit (backward-Euler) method until steady state for several sets of surfaces with homogeneous temperatures previously computed from solid HT analysis. This method enables to compute HTC at several intermediate times of cooling and then interpolate instead of computing full transient analysis on very long time period. Finally, simplified geometries are used to get structured meshes.

The Figure 3.12a shows the geometry of the fluid box of one experiment performed for HT characterization presented in the Section 3.4.2. It consists of a hot mold that cool down under natural cooling conditions. The Figures 3.12b and 3.12c show the mesh and a zoom on the mold surface for a central cutting view. The Figure 3.12d shows typical results obtained from CFD analysis. It is the superposition of temperature field and velocity vectors around mold zone in the steady state. Both fields are not symmetrical because of turbulences.

The Figure 3.13 shows the HTC h_c computed from normal to surface heat flux $HFLN$ ($h_c = (T_{mold} - T_\infty)/HFLN$) for the next three temperatures [50,450,850]°C. The contour plot seems very discontinuous which is due to the turbulences. A twenties of increment over around ten seconds after reaching the steady state are averaged in order to get representative value for each simulated temperatures.

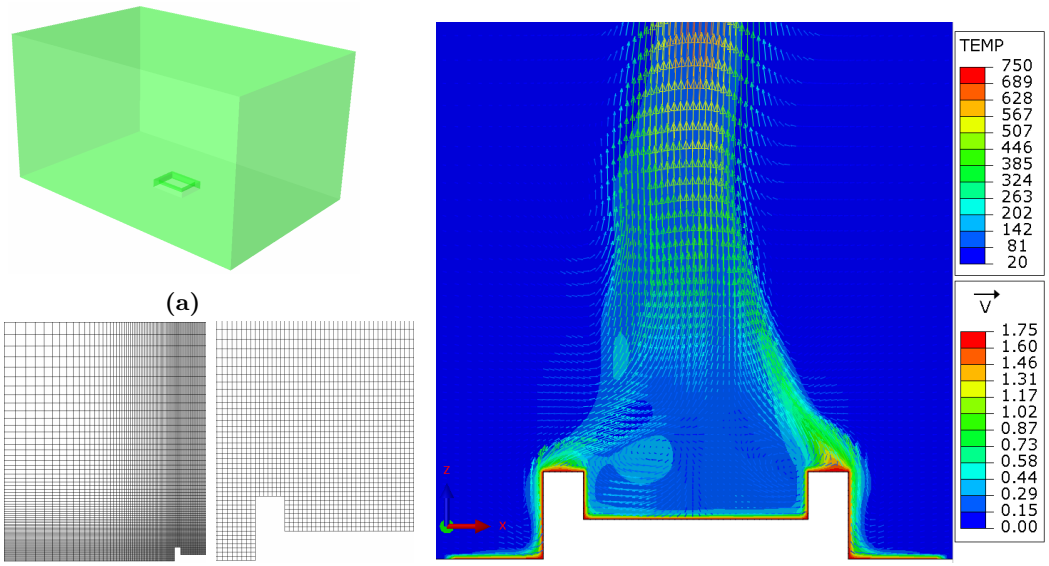

Figure 3.12 – CFD analysis of the Mold experiment: (a) fluid environment geometry, half of mesh representation on a cut-plane (b) scale 1, (b) zoom on the mold surface, (d) superposition of Temperature contour plot with velocity vector at 750 ° in steady state conditions

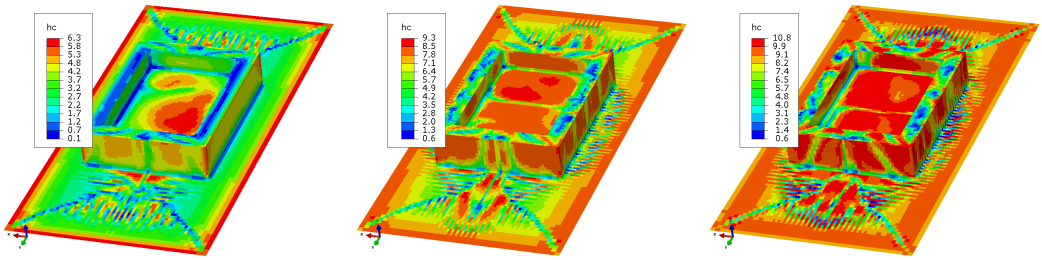

Figure 3.13 – CFD-based computed HTC for steady state conditions at several temperatures

The objective of using the CFD analysis is to obtain the distribution of h_c as a function of space and temperature. From these distribution a specific model of h_c such as given in the Equation (3.30) is defined. This way, the model is easily implementable in the FEM. The convection coefficient is defined as a function of time instead of temperature to avoid local temperature changes that would not be representative of real convection flow variations.

$$h_c = f(x, y, z, T) = g(x, y, z, t) \tag{3.30}$$

3.2.3 Forced convection heat transfers

3.2.3.1 General considerations

The industrial blowing machine is composed by a large number of nozzles that are equally distanced by around 25 cm. There are several type of nozzle geometry, but the present study focuses on round pipe nozzles of 8 mm diameters. The nozzle to part surface distance varies

according to the shape of the formed part, but it is fixed to 30 cm to the flash joint of mold. Some measurement were performed to determine the maximum and minimum flow rate (and associated averaged velocity at nozzle exit) in extrema process conditions. The velocities are in the range of 5-10 m.s^{-1} which correspond to Re=2600-5200.

The Forced convection problem is a very wide domain that groups a very large engineering field of applications. In the present case, we focus on the HT induced by air jet nozzle impingement on a hot surface. We need to define the HT coefficient induced by nozzle jets randomly disposed over a non-flat complex surface. The problem is even more complex because of the influences of nozzle jets on each others and the swirling flow influenced by specific geometry of SPF part. The problem has been treated as round nozzle jets impinging on horizontal flat plate in order to be simplified.

When a single jet induced by nozzle impinges on a surface, the fluid follows different phases that can be divided in several regions. The Figure 3.14 depicts the different regions that compose the jet [30]:

- The free jet Region: it is in this zone that the velocity profile is developed. The axial velocity decays while the turbulence level rises.
- The stagnation region: in this area, the fluid is strongly deviated because of the surface obstruction. The pressure and the HT is maximum in this area where the velocity gradients are very high.
- The wall jet region: it corresponds to the deviated flow that spreads along the plate. The thickness of the formed boundary layer increases with the radial distance.

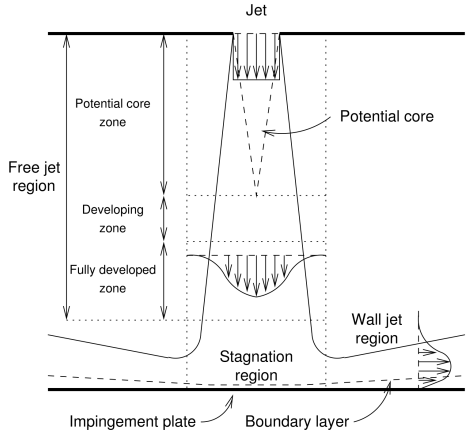

Figure 3.14 – Flow configuration of a round impinging jet with regions of different flow [30]

3.2.3.2 Parameters affecting Forced convection

There are several parameters that influence the development of the different mentioned zones of the jet flow. These parameters consequently influence the HT. Zuckerman and Lior [198] summarized these parameters and the models that have been developed these past decades:

- The Reynolds number - Re: it traduces the initial energy of the jet flow
- The ratio of nozzle to plate distance on its diameter - H/d: it defines the dimensionless distance for the velocity profile to develop
- The ratio of the radial distance from the stagnation point and the nozzle diameter - r/D

The influence Re number and H/d ratio has been largely studied around the impingement region for large range of values. The Figure 3.15 give the variation of Nusselt number with the r/D ratio for several H/d ratio and Re numbers [31]. It reveals two different behaviors. The first corresponds to an exponential-type decreasing shape while for the second, a secondary peak is observed while leaving the stagnation region. This second peak of heat transfer is more intense at high Reynolds number.

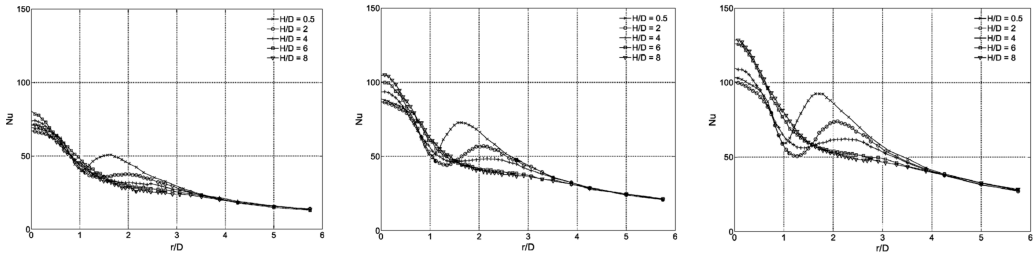

(a) **(b)** **(c)**

Figure 3.15 – Time averaged Nusselt number distributions for different H/D ration at several Reynolds number (a) 10000 (b) 20000 (c) 30000 [31]

3.2.3.3 Forced convection models

Mohanty and Tawfek [199] proposed three correlation laws associated to three experimental diameters 3, 5 and 7 mm. The Equation (3.31) gives the correlation law for the 7 mm diameter. The model is valid for $9 \leq H/d \leq 41.4$ and $7240 \leq Re \leq 34500$.

$$Nu_0 = 0.615 Re^{0.67} (\frac{H}{d})^{-0.38} \tag{3.31}$$

They also investigated the radial evolution for such experimental conditions. They proposed that the convection coefficient is constant around the stagnation point ($r/d \leq 0.5$), and then exponentially decreases up to a constant wall jet convection coefficient such as defined in the Equation (3.32).

$$\frac{h(r) - h_0}{h_1 - h_0} e^{-c(r/d)} \tag{3.32}$$

Tawfek [200] proposed an average definition of Nusselt number associated to a radial integration inside specific radius. He obtained a correlation law (Equation (3.33)) fairly consistent with the experimental data over different radius (valid for $2 \leq r/d \leq 30$, $6 \leq z/d \leq 58$ and $3400 \leq Re \leq 41000$) contrary to Mohanty and Tawfek [199] correlations.

$$\overline{Nu} = 0.453 Pr^{1/3} (Re)^{0.691} (z/d)^{-0.22} (r/d)^{-0.38} \tag{3.33}$$

The other major parameter in jet flow impingement HT is the multiple jet flow characteristics. When several jets impinge onto a plate, the wall jets may meet each other and the collision promotes flow deviations. Indeed, the influence of pitch (inter-distance between nozzles) was experimentally [32] and numerically [201, 32, 202, 203] studied. It is difficult to generalized the influence of multiple arrays because of the complexity of the possible configurations. However, it was proved that the pitch plays an important role in the HT amplitudes between nozzles. Reducing the pitch contributes to spread the Nusselt radial variation of single jet form such as defined in the Figure 3.16 [32]. Reducing too much the pitch can promote interaction of jets before impingement such that experimental correlations may be difficult.

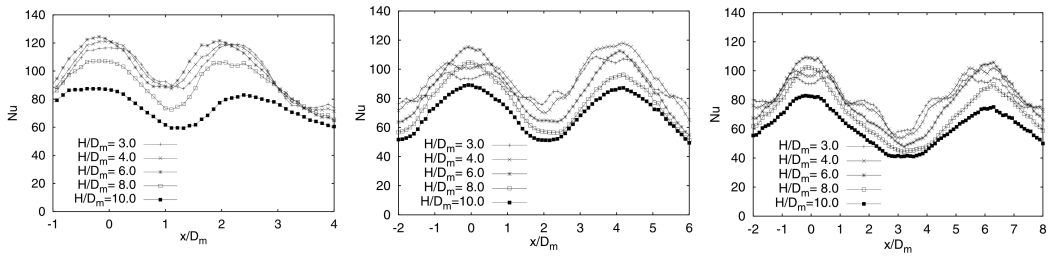

(a) (b) (c)

Figure 3.16 – Profiles of the local Nusselt number for all hexagonal configurations at Re=2.10^4 for contoured nozzles [32]

3.2.3.4 Forced convection boundary condition

The model for forced convection is based on the work of Mohanty and Tawfek [199]. It model consists in a constant value in the stagnation zone (considered for $r < d/2$ where d is the diameter of the pipe and r is the distance to the stagnation point), and beyond, a negative exponential decrease. The model is reminded Equation (3.34) where h_1 and h_0 are respectively the peak and the residual convection coefficients, and k_h a parameter.

$$h_{fc} = \begin{cases} h_1 & r \leq R \\ h_0 + (h_1 - h_0)e^{-k_h\left(\frac{r-R}{R}\right)} & r > R \end{cases} \tag{3.34}$$

3.2.4 Conductive heat transfers

3.2.4.1 General considerations

The HT that happen between two bodies in contact can follow different configurations. Indeed, the thermal contact resistance (TCR) implies that two bodies have a common contacting surface. When two bodies are in such configuration, the surface roughness produces series of local contact and cavities at the interfaces as described in the Figure 3.17a. However, contact resistance aspects can also take account of near surface contact HT that happens only through radiative and convective flux. The Figure 3.17b and 3.17c show the real and assimilated contact interface for TCR modeling where the blue, orange and green bodies respectively represent the continuous bulk solids participating to thermal diffusion, and the interface. The Equation (3.35) gives the conductive flux using TCR approximation where R is the TCR coefficient and k (=$1/R$) is the thermal conductance.

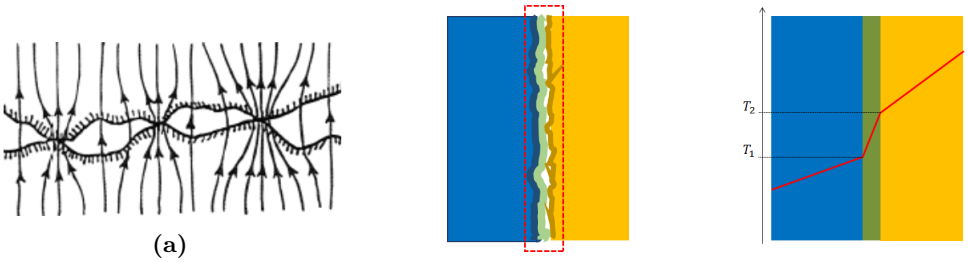

(a) (b) (c)

Figure 3.17 – Illustration of TCR problem (a) at roughness scale [33], (b) real configuration (c) model simplification

$$q_{cond} = \frac{T_2 - T_1}{R} = k(T_2 - T_1) \tag{3.35}$$

Most of conductance theories stand that the heat flux at interface can transfer through solid contacting surfaces and non contact cavities. Both possible ways to transfer heat produce two parallel contact resistances. The global HT coefficient k is defined as de sum of conductance coefficients of both media defined in the Equation (3.36) where k_c is in-contact term of conduction, and k_{nc} the non-contact term referring to radiative and conductive HT.

$$k = k_c + k_{nc} \tag{3.36}$$

3.2.4.2 Parameters affecting conductance

Yovanovich summarized four decades of research on thermal contact HT [204]. In this reference work, he detailed the different parameters that influence the contact conductance:

- The topology of the contacting surfaces: the main geometric parameters are the surface roughness R_a and asperity slopes m that influence the real surface in contact and the deformation under pressure behavior.
- The contact pressure P: the pressure between the contacting surfaces is at the origin of the deformations that promote an evolution of contact surface ratio.
- The gap thickness (δ_k): this parameter describes the average gap distance between the contacting surfaces.
- Thermal conductivity of the contacting materials (k_{eq}).
- The elastic properties: Modulus of elasticity of the contacting solids (E) This affects the elastic deformation of the contacting surfaces. The surface hardness (H) or yield strength (σ_0) of the contacting materials play also an important role. During high pressure, the surface topology evolves because of plastic deformations and the contact surface ratio varies.
- Average temperature of the interface (T_m): it influences the physical properties of the contacting materials.
- Interface properties: interstitial material, such as foil, coating or grease, placed between the two surfaces of the joint.
- Oxidation: the thermal contact resistance of a material increases when the surface is oxidized. The effect of oxide layers can be quite significant for flat surfaces.

For a couple of materials with specific surfaces properties, the main parameters that influence HT are the contact pressure first, and then the temperature of surfaces. The Figure 3.18 represents the conductance variation with the temperature at different contact pressure and R_a values for a AISI 304 stainless steel. The variations are significant according to pressure and temperature, whereas the shapes of temperature variation evolve with the surface roughness.

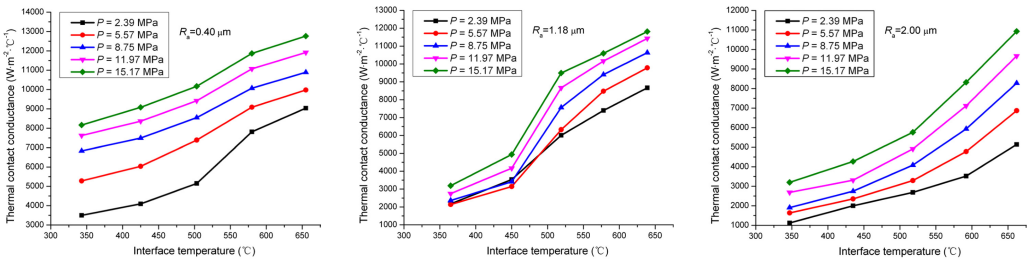

Figure 3.18 – Effects of contact pressure and interface temperature on TCC of a SUS 304 stainless steel: (a) R_a=0.4 μm, (b) R_a=1.18 μm, (c) R_a=2 μm [34]

3.2.4.3 Conductance models

3.2.4.3.1 Contact conductance

Cooper et al. [205] defined that the ratio of apparent contact surface A_r and total surface A_a is equal to the ratio of the pressure and the contact hardness H_c of materials (Equation (3.37)). From this relation, they defined a dimensionless contact conductance model that takes account of the effective RMS roughness σ ($=\sqrt{\sigma_1^2+\sigma_2^2}$), the effective mean asperity slope m ($=\sqrt{m_1^2+m_2^2}$), the effective thermal conductivity k_{eq} ($=2k_1k_2/(k_1+k_2)$), and the ratio of pressure and hardness defined in the Equation (3.38) where a_1 and b_1 are material constants. This model is commonly called the CMY model in reference to Cooper, Mikic and Yovanovic who created the model. This model fits experimental data with good agreement for different material and roughness properties with a_1=1.25 and b_1=0.95 [204].

$$\frac{A_r}{A_a} = \frac{P}{H_c} \tag{3.37}$$

$$\frac{k_c\sigma}{k_{eq}m} = a_1(\frac{P}{H_c})^{b_1} \tag{3.38}$$

The previously described model deals with plastic deformation of asperities. Mikić [206] defined a model based on the same formulation based on elastic regime where he replaced the hardness term and included effective Young Modulus E_{eq} ($1/E_{eq} = (1-\nu_1^2)/E_1+(1-\nu_2^2)/E_2$) such as defined in the Equation (3.39).

$$\frac{k_c\sigma_s}{k_{eq}m} = 1.551(\frac{P\sqrt{2}}{E_{eq}m})^{0.94} \tag{3.39}$$

Dou et al. [34] proposed a temperature correlation of the CMY model defined in the Equation (3.40) where T is the interface temperature, k_{eq} and H_c are taken at reference temperature T_0, and c_1, c_2 and c_3 are constants. This empirical relation worked fairly well for a SUS 304 stainless steel for a temperature range of 360 to 640 °C, a pressure range of 2.39 to 15.17 MPa and a roughness range of 0.025 to 2 μm.

$$\frac{k_c\sigma_s}{k_{eq}m} = c_1(\frac{T}{T_0})^{c_2}(\frac{P}{H_c})^{c_3} \tag{3.40}$$

3.2.4.3.2 Gap conductance

There are two gap scales: microgaps and macrogaps. The microgap conditions refers to in contact cavities formed by roughness asperities. Microgaps are sensitive to pressure. Macrogaps are formed when there is no positive contact pressure.

Usually, for conforming contact conditions, the heat transferred by conduction through solid thermal diffusion is largely superior to radiative and convective terms. In some cases, gap conductance can have an impact, especially at high temperature, the radiative HT are no longer negligible, particularly at low pressure when the contact term of conductance is lower. Liu and Shang [207] shows that under 850 K the radiative term has no impact.

Some authors proposed a model with the contribution of three modes simultaneously [208, 207] such as defined in the Equation 3.41 where k_f and k_r are the gas gap and the radiation gap conductance. Madhusudana and Fletcher [209] analyzed the effect of gap conductance through gas. They proposed that gas transfers heat through conduction because of low Grashoff number such that defined equation (3.43) where k_f^* is the fluid thermal conductivity

and δ the mean thickness of the gas gap. The effective thickness of the gap would be of the same order of magnitude as the surface roughness heights for microgap conditions. Liu and Shang [207] related the evolution of δ for positive pressure contact conditions such as defined in the Equation (3.43). The model can be extended for to macrogaps using δ=$\delta_0 + d$ where d is the peak-to-peak interface distance and δ_0 refers to the equivalent gas gap value at zero pressure.

$$k = k_c + k_f + k_r \tag{3.41}$$

$$k_f = \frac{k_f^*}{\delta} \tag{3.42}$$

$$\delta = 1.53\sigma(\frac{P}{H})^{-0.097} \tag{3.43}$$

A radiative conductance term k_r was used in some high temperature conduction case [208, 207] derived from Stephan-Boltzman heat flux relation. k_r is defined in the Equation (3.44) where C is a coefficient that depends on the surface emissivities and the (VF), σ_b is the Stephan-Boltzmann constant. C is defined (3.45) where F is the VF of surfaces, ϵ_1 and ϵ_2 are the surface emissivities.

$$k_r = C\sigma_b(T_1^2 + T_2^2)(T_1 + T_2) \tag{3.44}$$

$$C = \frac{1}{\frac{1-\epsilon_1}{\epsilon_1} + \frac{1}{F} + \frac{1-\epsilon_2}{\epsilon_2}} \tag{3.45}$$

3.2.4.4 Conductive heat transfers in FEM analysis

Some authors investigated the FEM of conduction heat transfers during stamping process. They generally defined the surface BC such as defined in the Equation (3.46) where h_{eff} is an effective HTC as the sum of the different modes contribution [76, 171, 35, 172].

$$q = h_{eff}(T_1 - T_2) \tag{3.46}$$

Shapiro used a contact pressure conduction model for stamping step [210]. He gave different contact pressure models available into LS-DYNA FE software. The models are given in the Equations (3.47) where a, b, c and d are constants, (3.48) where k_{gas}, λ and σ are respectively the gas and equivalent surfaces thermal conductivities and the equivalent roughness of parts surfaces and (3.49) where a, b, c and d are constants which are respectively polynomial, power and exponential law models.

$$h(p) = a + bP + cP^2 + dP^3 \tag{3.47}$$

$$h(p) = \frac{\pi k_{gas}}{4\lambda}\left[1 + 85\left(\frac{P}{\sigma}\right)^{0.8}\right] \tag{3.48}$$

$$h(p) = a\left[1 - exp\left(-b\frac{P}{c}\right)\right]^d \tag{3.49}$$

Martins et al. [35] chose to use a continuous model based on exponential functions that allow to work with both positive pressure and gap interface conditions represented in the Figure 3.19a. Thomas et al. [36] include a pressure and gap dependent TCR models (shown in the Figure 3.19b) in the simulation of hot tearing process. They introduced a radiation contribution using the gray radiation theory and a gas-gap term limited to the zero pressure conductance h_0 for near-zero gap values.

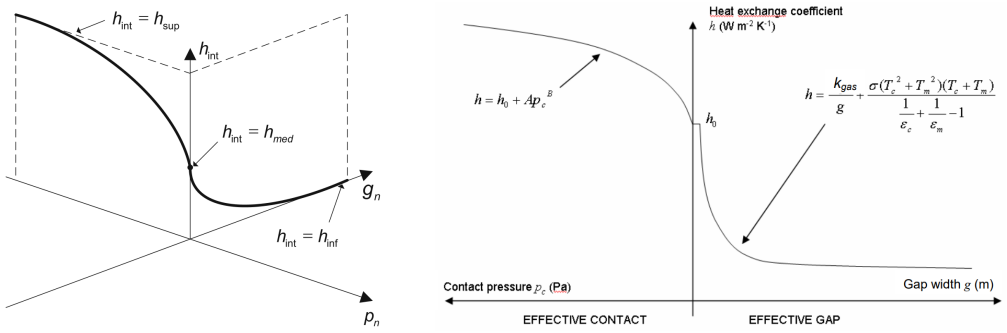

(a) **(b)**

Figure 3.19 – (a) interfacial heat transfer coefficient [35], (b) conductance model used in hot tearing process simulation [36]

3.2.4.5 Conductance boundary condition

The contact conditions during the cooling and unmolding operations are particularly varying. They switch from positive pressure conduction to radiative-conductive HT modes. In addition, the regular pressure order of magnitude described by standard models is most of the time superior to the process. Finally, the BN coating added to the high temperature pressure contact conditions during superplastic deformation may tend to reduce contact asperities and mitigate the effect of pressure on conductance.

ABAQUS® proposes to compute the gap radiation HT and conductance evolution with pressure and gap distance separately such as defined in the Equation (3.50) where k_c is the conductance and ϕ_{rad} the radiative flux defined in Equation (3.17). In the process case, the contact distance is considered closed to zero such that the VF are equal to one.

$$\phi_c = \phi_{rad} + k_c \Delta T \tag{3.50}$$

The gas-gap and pressure conductance is modeled with the parameter k_c defined in the Equation (3.51) build from the model given in the Figure 3.19b. It is simplified compared to literature's models to ease the computation and the characterization work. k_0 is a surfaces parameter, λ_{air} is the thermal conductivity of air, and δ_0 ($= \lambda_{air}/k_0$) is a parameter adjusted such that to get a continuity between closed to open contact transition.

$$k_c = \begin{cases} k_0 (P/P_{ini})^{0.95} & P > P_{ini} \\ k_0 & 0 < P \leq P_{ini} \\ \lambda_{air}/(\delta + \delta_0) & \delta > 0 \end{cases} \tag{3.51}$$

The pressure dependency is firstly considered constant for low pressure ($P \in [0, P_{ini}]$ - P_{ini}=0.01 MPa) and then obeys to classical formulation as defined in the Equation (3.51). This way, the non-linearity and convergence issues related to open-to-close contact transitions produced during cooling are limited.

A tabular definition of the pressure and gap conductance model is used for convergence reasons. It is defined independently from the k_0 parameter using the normalized definition as shown in the Figure 3.20b. The normalized pressure and distance are defined in the Equation (3.52). The definition of the tabular model presented in the Table 3.1 has the advantage to get only one parameter: k_0.

$$k^* = \frac{k_c}{k_0} = \frac{1}{1 + \delta^*} \quad with \quad \delta^* = \frac{\delta}{\delta_0} = \frac{\delta k_0}{\lambda_{air}} \tag{3.52}$$

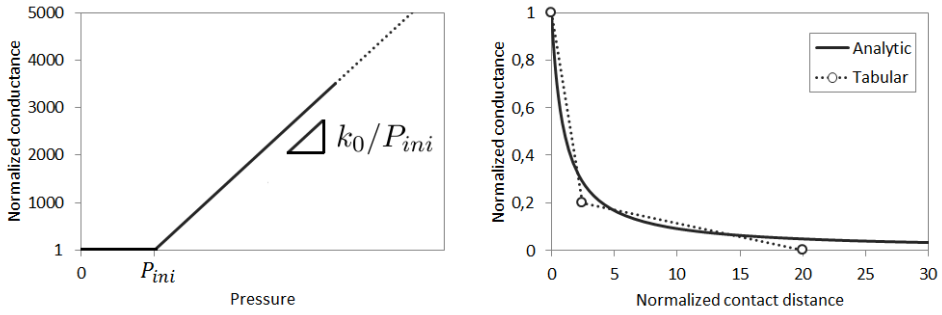

(a) **(b)**

Figure 3.20 – Graphs of the normalized conductance model as a function of (a) pressure and (b) normalized distance

gap		pressure	
0	k_0	0	k_0
$2.5{*}\delta_0$	$k_0/5$	P_{ini}	k_0
$20{*}\delta_0$	0	50	$(k_0/P_{ini}){*}50$

Table 3.1 – Tabular definition of pressure-gap conductance model

3.2.5 Conclusions

The principal objective of this chapter was to characterize the parameters of the BC models for the four modes (natural and forced convection, conduction and radiation) so that to implement them into the FE model. The literature review has given an overview of the different HT modes, how they evolve, what are their parameters of influence and what kind of model could be used for the SPF process purpose. The important points are summarized below and criticized regarding to SPF process. Then, sub-objectives are detailed to introduce the methodology employed to answer the principal objective:

3.2.5.1 Radiation

The radiative HT is the consequence of electromagnetic wave radiation emission and absorption. The capacity of emitting and absorbing thermal radiation is relative to the surface emissivity. It is material, temperature, surface, direction and wavelength sensitive. The characterization of emissivity of various materials including Ti-64 were performed for various conditions of temperature roughness and oxidation. Some models exists to take account of emissivity variations.
The objective concerning thermal radiations was to evaluate emissivity and its variation for the process conditions of temperature and oxidation such as defined in the Equation (3.53) where d represent the oxide layer thickness. Indeed, Ti-64 sheets are coated with BN lubricant that modify emissivity and oxidation process. In addition, the emissivity properties of surrounding environment such as tooling and press had to be also investigated.

$$\epsilon = f(T, d) \tag{3.53}$$

3.2.5.2 Natural Convection

There are two different configurations during the cooling process that produced different convection flows. Inside press, the fluid flow is specific to cavity flow that promote swirling effect and an important variation of convection coefficient along walls because of temperature

variation of the fluid during the travel inside the press. Then, the configuration of the massive mold and the heating platens promote turbulences due to the temperature difference with the rest of the press. Finally, most of the literature cases focus on an initial cold environment so that the time variation of the convection coefficients are opposite to SPF process configuration where it starts from low value at press opening. The used model has the form of the Equation (3.54) where h_0 represents the transient effect during opening of the press' door, and h_1 the steady state value of h_c for the process conditions.

$$h_c = h_0(t) * h_1(Ra, T) \tag{3.54}$$

Outside the press, the literature on natural convection over horizontal plates gives a global evaluation of HT coefficient and its sensitivity to flow regimes. However, the complexity of geometry with confined zones and non-flat geometries make difficult to evaluate local HT coefficients. Moreover, the high temperature of SPF case has not been investigated in the literature, especially for such high Rayleigh numbers that promote turbulences.
The objective concerning the natural convection coefficient (NCC) was to defines first an experimental procedure that promote various representative convection regimes. Then, a strategy for high temperature measurements had to be developed to get thermal data for the NCC characterization and numerical correlations. Finally, the NCC has to be modeled as a function of space and time (Equation (3.55)) based on CFD simulations results to fit the experimental data.

$$h_c = f(t, x, y, z) \tag{3.55}$$

3.2.5.3 Forced Convection

The forced convection problem was largely investigated regarding to jet impingement HT. The influence of the velocity, the nozzle-to-plate distance, the pitch between nozzles for multi-jet impingement were mainly investigated on flat plate. Some models exist to define associated HTC. The model developed by Mohanty and Tawfek [199] seems the most adapted to the process conditions (dimensions and flow regime).
The objective concerning blow cooling was to characterize the mentioned model and propose an adaptation for non flat geometries and multiple nozzles such as defined in the Equation 3.56 where g_{fc} is a correction function.

$$h_{fc} = \left[h_0 + (h_1 - h_0)e^{-k_h\left(\frac{r-R}{R}\right)}\right] * g_{fc}(x, y, z) \tag{3.56}$$

3.2.5.4 Conduction

During thermal conduction HT, every mode plays a role. The real contact interface is composed by contacting points and cavities formed by asperities. Conduction at contacting point is sensitive to temperature and thermal diffusion properties of materials. The convection inside the roughness cavities (named gas-gap conduction) is made by convection through the air and also radiation between the cavities' surfaces. The global conductance coefficient varies as a function of surface ratio of contacting points and the total surface. This variation is controlled by the contact pressure and the materials resistance to deformation (Young modulus or hardness). Some models takes account of roughness and asperities parameters. In SPF process the thermal stresses induced during blow cooling produces heterogeneous contact conditions with positive pressure and positive gap configurations. Moreover, BN used for lubrication plays a role into conduction HT.

The objective concerning conductance model was to perform experiments that reproduced the different configurations of contact with representative surface conditions (roughness and BN coating). Then the radiative-conductive conductance model defined in the Equation (3.50) had to be characterized especially the k_0 parameter defined in the Equation (3.51).

3.3 Strategy for the heat transfer characterization

3.3.1 Characterization issues

There are different methods to determine HT coefficients. Some laboratory experiments exist for each mode. They usually propose to measure temperature or heat flux variation in controlled condition to obtained HTC from simplified heat equation. However, the simplification or even suppression of some industrial operating conditions are discussed below:

❒ Radiations

The measurement of emissivity is usually made on prepared samples at various temperature and heat treatments inside controlled environment (Argon, air, etc.) and temperature. This type of experiment enables to get spectral emissivity by comparing to black body radiation measurement. The total emissivity is obtained by measuring the spectral emissivity for various wavelength in the near peak wavelength of a temperature. However, the heterogeneity of surfaces are difficult to reproduce on laboratory samples. Indeed, during SPF the sheet metal undergoes heterogeneous deformations and loading conditions that modify the metal surface and the layers of BN lubricant and its potential oxidation barrier effects so that emissivity may significantly vary on the surface.

❒ Convection

HT measurements can be performed on flat plate or curved plate surface, at various orientation under various flow regime conditions and temperatures. However, in the industrial case, the fluid flow is influenced by the surrounding environment such as hot press, handling robot, etc., that modifies the fluid temperature and flow. Simple shapes in laboratory environment are preserved from such perturbations. Moreover, convection HT induced into the laboratory configurations for specific surface cannot be transferred to an equivalent surface if the surrounding surfaces are fully different than the experimental configuration.

❒ Conduction

It exists several widespread laboratory experiments such as "bolted joint" of "cylinder joint" experiments that focuses on positive pressure contact conditions. However, as explained in Section 3.2.5, the contact conditions (pressure and gap at interface) varies along the process. In addition, the BN coating is heterogeneous so that it influence a lot the contact resistance. A sensitivity study to BN coating would have to be performed.

3.3.2 Characterization method

The industrial configurations for each mode are so complex that they would impose to make varying too much parameters to get fully characterized. Therefore, it was chosen to perform the major part of the characterization experiments in industrial conditions. However, there are several constraints in the industrial environment. Indeed, There is no possibility to instrument the industrial machines with measurement means for complexity of warm environment, cost and availability reasons. Therefore, the first objective mentioned in the Section 3.1.2 has actually consisted in designing a laboratory mean to reproduce and measure the heat transfers that occur during the industrial process.

This tooling is composed of a complete SPF tooling (mold and extraction frame) with formed parts in order to get strictly the same conditions of the industrial process. The mold and the parts were previously prepared (surface finishing and BN coating) and several parts were formed at AIRBUS on an industrial SPF press. The Mold and the formed parts were then

transferred to the laboratory where a SPF process-based furnace have been used to re-heat parts and tooling equipped with a thermal instrumentation.

Therefore, most of the characterization issues mentioned above are circumvented by having industrial conditions for the laboratory experiments. However, the characterization of thermal BC model is not as trivial as with the laboratory experiments.

The characterization of HT was performed in several steps as explained in the Figure 3.21:

- Prototyping: this step consisted into the design and the manufacturing of a complete tooling. Then several parts were formed to get samples for characterization purpose.
- Experimentation: several experiment were designed in order to promote different HT configurations. The design of experiments was carefully developed to isolate one HT mode over others to ease its characterization. The experiments were performed with various means of local and field measurements of the temperature.
- Characterization: an inverse analysis method was used for the HT characterization. The data from field and local measurements were post treated and used to compare and fit the thermal BC.
- Adaptation: the differences between the HT that were characterized on prototype tooling configuration and industrial case have to be evaluated. Some modification of the BC models are proposed in the Chapter 4 to be used for industrial case.

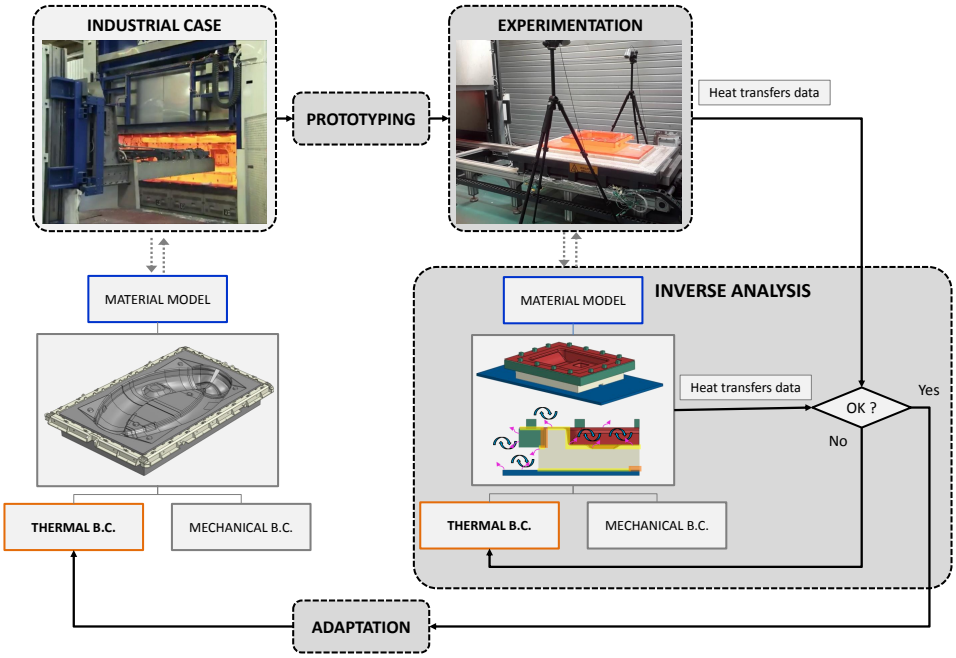

Figure 3.21 – Schematic of characterization steps

These several steps are detailed in the next sections of the chapter, except for the adaptation which is presented in the Chapter 4. In addition to these characterization on prototype tooling, independent emissivity measurements were performed on several surface quality from formed part.

3.4 Design of Experiments

The design of the experiments was built on several instrumented heating and cooling procedures on an industrial tooling with formed parts. These tests were performed using a

laboratory oven. The tooling had to be adapted to the size constraints of the furnace. In this section, the testing machine, the tooling and the design of the experiments are detailed.

3.4.1 Testing machine

The laboratory equipment is a resistance heating furnace. It is composed by a movable platform (the shuttle) that shift along a rail in the horizontal direction. The tooling is disposed at the center of the shuttle. The motion of the shuttle is automatically controlled from heating point to the end of rail. The second part of the furnace (the bell), which is composed by the resistance heaters, is movable in the vertical direction. The system is controlled by an automaton that enables to impose heating profiles. The temperature is enslaved thanks to environment thermocouples inside the furnace. The Figure 3.22a represents the different parts described above.

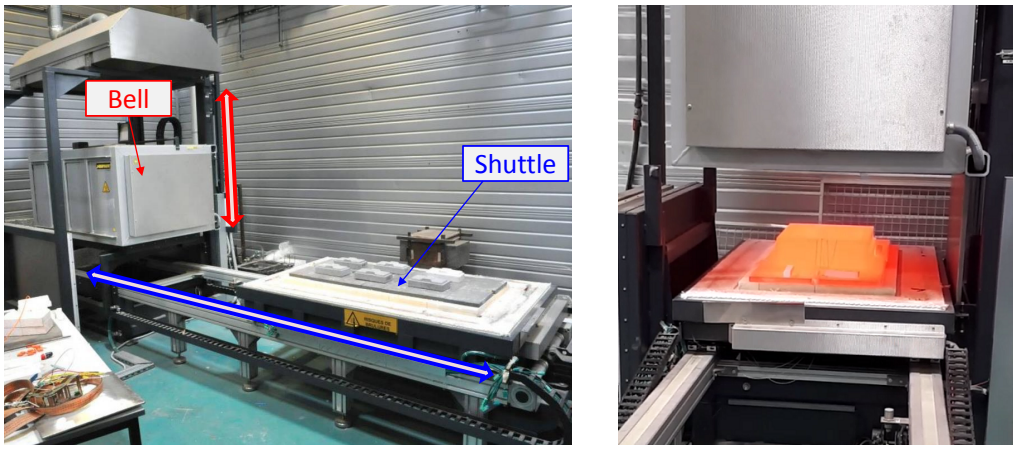

(a) **(b)**

Figure 3.22 – Picture of equipment: (a) the shuttle outside (b) the bell is opening at high temperature

The shuttle has an usable area of 1,2x0.70 m^2 with a maximum height of 0.8 m. The furnace can reach a maximum temperature of 1380 °C. The exit procedure consists in a first vertical opening of the bell (3 s), followed by the horizontal displacement of shuttle (5 s). The Figure 3.22b represents the maximum height position of the bell. The procedure is not modifiable such that the furnace do not give the possibility to reproduce the side-open cavity configuration of the inside press natural cooling operation.

3.4.2 Design of prototype

The size of the testing machine made difficult to find existing SPF die to use for our experiments. Indeed, the size of industrial parts are larger than the shuttle size. There was the possibility to use an existing prototype die that had already been used for SPF thermal study [62] as shown in the Figure 3.23a. A first numerical study of the forming feasibility with the present die was performed. The numerical results showed that the mold shape was to much complicated to ensure superplastic forming conditions. A second numerical analysis enabled to propose mold modifications to be able to form such as presented in the Figure 3.23b. Once the final surface of SPF die was fixed, some modifications of the geometry and additional tooling (extraction frame and top SPF die) were designed accounting of the press environment and the process constraints. The Figure 3.23c shows the CAD definition of the tooling assembly.

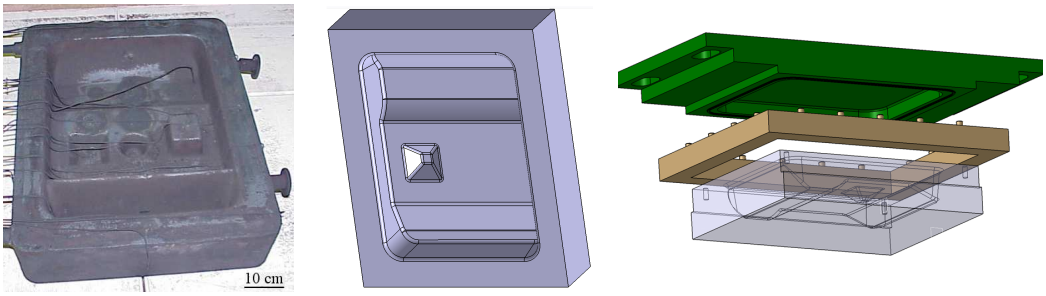

(a) **(b)** **(c)**

Figure 3.23 – Prototype tooling: (a) initial geometry, CAD views of (b) the modified mold and (c) the entire SPF dies assembly

The different manufacturing operations were defined in partnership with the mechanical workshop department of AIRBUS Saint-Eloi plant in Toulouse. The material of the SPF die was a SP50 alloy (Nickel-Chrome-based refractory alloy from Aubert & Duval). The hole was sealed with inconel 625 and the extraction frame and top die were manufactured from an old SPF die made of X40CrNi alloy. The three parts are presented in the Figure 3.24. The thermo-physical properties of the different materials are given in the Appendix D.1.

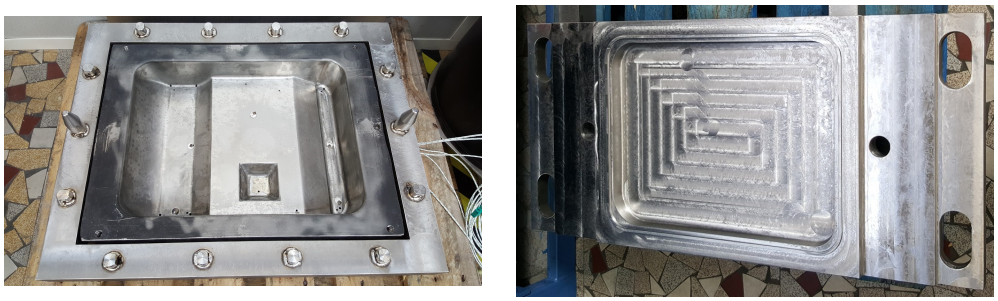

(a) **(b)**

Figure 3.24 – Picture of (a) mold and extraction frame and (b) top mold for SPF forming

Five parts were formed using a pressure cycle computed using the method developed by Rollin et al. [60]. A BN coating was applied on the surface of the dies and on each side of blanks. The objective is to decrease friction for the side in contact with the mold, and to limit oxidation on the other side. The parts were formed with and without BN coating on the gas pressure side. Thus, two surface conditions were available for radiation BC characterization. One with highly oxidized upper surface, and the other with a limited oxidation layer.

3.4.3 Design of instrumentation

Three different instrumentation means were used for each experiment: thermocouples, a pyroreflectometer and a thermal camera. Each measurement mean presents advantages and weaknesses. They are highlighted below regarding to the need and the experimental constraints:

❒ Thermocouples

Thermocouples have a considerable advantage compared to radiation-based measurement methods. They give a true temperature information. Indeed, once the thermocouple is

welded, no prior calibration and supplementary material properties (such as emissivity) are required to exploit the obtained data. However, the main drawback is that they require to be welded a-priori, and the manipulation of the part is limited by the cables. Moreover, the junction of thermocouples can be influenced when high flux are imposed such like during air-jet impinging forced convection, even when it is protected by an insulation.
The thermocouple that were used are 0.3-0.5 mm wire diameters type K with fiberglass-based sheath protection. A high temperature cement Omega Bond™ 700 was used to protect welded junction mechanically and from external disturbing heat flux such like blowing. The thermal conduction properties of cement is around 0.75 $W.m^{-1}.K^{-1}$ compared to around 12 $W.m^{-1}.K^{-1}$ (between 20-900 °C) for Ti-64. Aluminum adhesive tapes were disposed to prevent from motion during shuttle displacement and preserve the welds. Some thermocouples welded on the part surface are shown in the Figure 3.25a.

❒ Pyroreflectometer

The use of pyrometry and reflectometry measurements on a single point enables to get true temperature at these point independently from the influence of the emissivity value and its variations. This measure in a good alternative to thermocouples when high flux can disturb measured data. In conjunction with thermal camera data at measurement point, it is possible to obtained emissivity information. However, the pyro-reflectometer is composed by two lasers that require to be focused to get reflection information. Thus, the pointed surface needs to be fix during the experiments. The pyrorefletometer and its lasers are represented in the Figure 3.25b.

❒ Thermal camera

A thermal camera gives the radiance temperature by comparing to radiance signal calibrated on a black body. It has the weakness to need emissivity information to get the true temperature, yet, it has a strong advantage to record field data. In conjunction with thermocouple, pyroreflectometry or additional emissivity measurement (with spectrometer) the camera provides temperature field on the measured surface. The equipment was a near infra-red (NIR) camera sensor fitted with 1.55 μm passband filter. It was calibrated with black body in the temperature range between 500 °C and 800 °C. The Figure 3.25c shows a thermogram obtained from the camera that highlights the gradient of temperature thanks to the brightness contrasts.

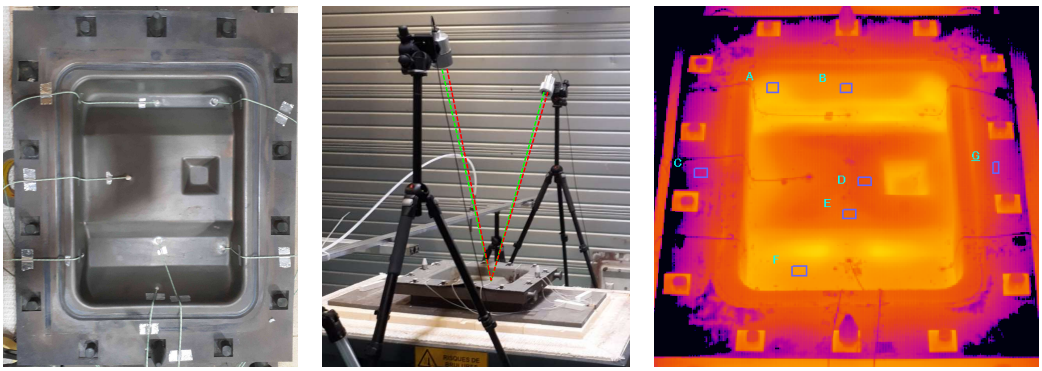

(a) **(b)** **(c)**

Figure 3.25 – Picture of (a) the formed part equipped with thermocouples (b) the pyro-reflectometer installation (c) the thermal radiation intensity field from thermal camera

3.4.4 Design of testing procedures

3.4.4.1 Heat transfers operating ranges

The HT at part surfaces are a combination of convection, radiation and conduction (at contact interfaces) modes. The design of experiments must help to isolate a specific mode over others to characterize the HT coefficients more easily. In order to evaluate the operating range for each mode, an estimation of associated heat flux was performed using extreme transfer conditions. Indeed, except for conduction phenomena which refers to surface temperature difference at interface, radiation and convection heat flux intensities can be compared at a specific surface temperature.

In the frame of experiments performed on the prototype tooling at ambient temperature cooling conditions, the radiation, the natural and forced convection heat flux can be estimated as follow:

- Radiation: the Figure 3.26a represents the sum of viewing factors of the shaped surface of the part computed by ABAQUS® . By considering that the part is cooling at a constant temperature, a minimum and a maximum radiative heat flux can be estimated using a constant emissivity (taken at 0.85 for oxidize surfaces) with the Equation (3.5). A spectra of operating radiative flux is represented in the Figure 3.26b in red with logarithmic y-axis variations.
- Natural convection: its spectra (in blue) is computed using the Nusselt correlation of the Equation (3.26) with extreme values for the film temperatures (between 50 and 440 °C) and the characteristic length (the part alone or the whole shuttle surface). The obtained extrema values of convection coefficients are 3.75 and 10 $W.m^{-2}.K^{-1}$. The associated heat flux spectra is represented in blue in the Figure 3.26b.
- Forced convection: its spectra (in green) is computed using the Nusselt correlation of the Equation (3.31) at H/d=50, and a Reynolds number computed with fluid velocity of 5-10 $m.s^{-1}$ (obtained from flow rate measurements). The HTC values are considered at stagnation point around 80 and 135 $W.m^{-2}.K^{-1}$.

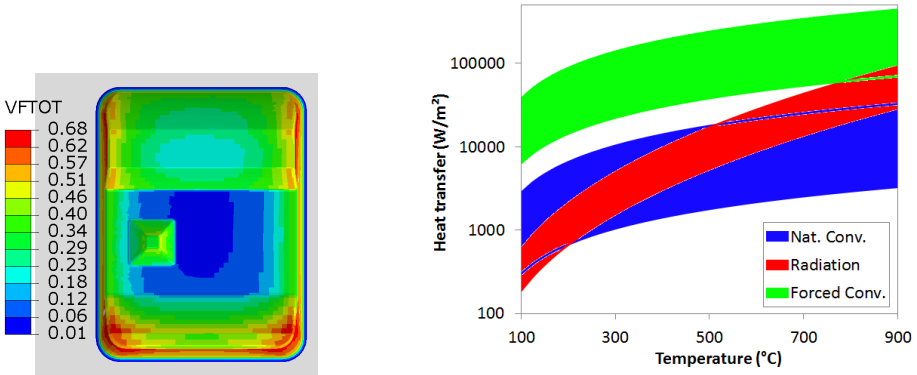

(a) **(b)**

Figure 3.26 – (a) view factors of the part surface, (b) heat flux spectrum comparison

The Figure 3.26b clearly shows that the forced convection is much more intense than both other modes on the whole range of temperature. Therefore, any kind of experiment where blow convection is reproduced may enable to isolate its effect. Concerning convective and radiative flux, both contributions seem equivalent with a slight superior effect for radiation at high temperatures. Indeed, for the temperature between 700-900 °C, the radiation mode is globally higher. However, the low viewing factor values in the corner regions may promote lower radiative heat flux than convection mode whatever the temperature range. Therefore,

the characterization of both modes can not be performed totally isolating one from each other. A solution has been to promote two different convection flows around the geometry while keeping the same radiative configuration (ie. the same geometry and surface conditions).

Concerning conduction HT, the Figure 3.27 represents the evolution of the heat flux generated by conduction as a function of pressure and gap for a specific configuration. Indeed, it corresponds to two surfaces such as part and die respectively at 800 and 850 °C for which the zero pressure conductance value has been estimated at 200 $W.m^{-2}.K^{-1}$ from low pressure data of the literature [211]. Both sides of the zero pressure-gap axis is computed with pressure and radiative-gas gap conductance model (at constant temperature properties) with the Equation (3.41). The heat flux is divided by five for the contact conditions from 2,5 MPa up to 2,5 mm according to literature models. Therefore, variation of contact conditions promoted by thermal stresses are supposed to highlight the conductive heat flux variations. One difficulty is to evaluate these conduction heat flux gradients from the upper side temperature information which is influenced by thermal diffusion through the thickness heterogeneously distributed on the part.

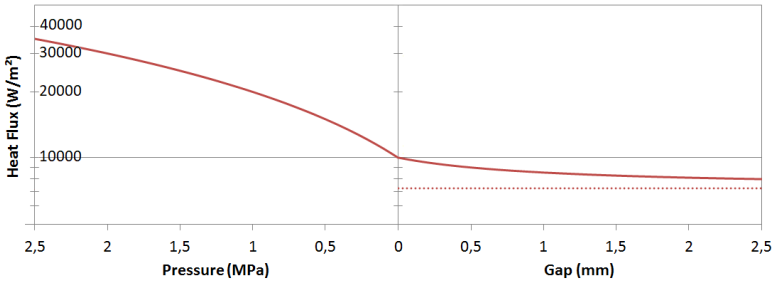

Figure 3.27 – Evolution of conduction heat flux model as a function of pressure and gap distance at interface for specific contact conditions

3.4.4.2 Experiments configurations

A total of six different configurations were defined to characterize and validate the the HT BC. A first configuration was used to develop the global methodology, especially regarding measurement issues. Then, two configurations without contact interfaces were used to fix thermal radiation and natural convection. A fourth configuration mixing every modes were used for forced convection and conduction HT characterization. A fifth configuration was used to validate the different models without isolating a mode over others. This configuration was used with and without BN coating to test its influence on the upper surface. A last configuration enabled to perform unmolding procedure with a natural cooling at ambient temperature such as for the outside press natural cooling phase. Each configuration consisted in a pre-heating procedure composed by four hours heating ramp up to 870-900 °C followed by a two hours plateau, and then various cooling conditions. Each experiment is presented below:

❒ The "development" experiment

This experiment consisted in testing the use of different means of measurement: the effect of the heating procedure and the motion of the shuttle on the thermocouple resistance; the behavior of the pyro-reflectometer and the NIR camera (respectively shown in the Figure 3.28a and 3.28b) during the experiment. Some points were important to be questioned regarding to the position of means, their orientation regarding to the measured surfaces and some details related to the technologies. Moreover, an important aspect consisted in observing how the part filled back into the mold after heating. Indeed, the initial condition of the tests is an important point to pay attention for thermal contact characterization.

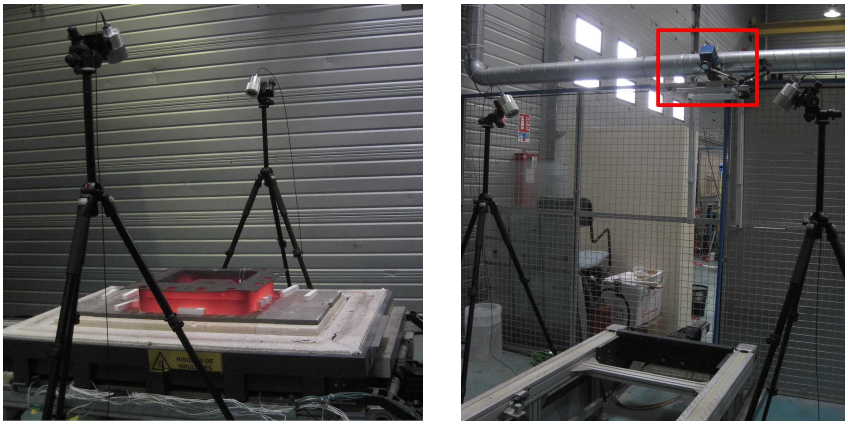

(a) **(b)**

Figure 3.28 – Pictures of the development experiment focused on (a) the pyroreflectometer and (b) the NIR camera

❒ The "Mold" experiment

This experiment consisted of using only the SPF die in order to promote natural convective and radiative HT without conduction between the mold and the part. The surface of interest was the forming shape of the die. During the experiment, there were also HT with shuttle by radiation and conduction. The contact conditions at mold and shuttle platen was considered staying quite homogeneous and constant along the experiment due to the weight of the mold.

This experiment had two objectives. The first one concerns the effect of the forming shape on the radiative flux and the convection flow. Indeed, except the surface emissivity, the HT configuration at this surface is supposed to be fairly identical to the configuration with the part. The advantage of this case is that the unknown of part-mold conduction is removed. The cooling of die was performed over long period up to reach ambient temperature in order to go all over the temperature range and the operating range of both modes. A second objective is to characterize in a fairly simple case the HT of the mold with the surrounding shuttle environment.

A picture of the configuration is given in the Figure 3.29a. It shows that the die was particularly oxidized outside the forming shape which was protected by BN coating. Five thermocouples were fixed as shown in the Figure 3.29b on a CAD representation. The different thermocouples were arranged according to specific orientations (vertical, horizontal, inclined) and locations (exterior, joint surface, inside forming shape) to evaluate the effect of radiative and convective flux at this positions.

❒ The "Part-Frame" experiment

This configuration is presented in the Figure 3.30a. The assembly is composed by the part and the frame which is placed on ceramic bars to elevate it and let air flows downward the part. During the experiment, the part was mainly subjected to radiative and convective HT. The BC at the upper surface are closed to the Mold experiment conditions. Thus it is possible to fix radiation and convection HT in conjunction with the Mold experiment.

In addition, the possibility for air to flow downward to the part enables to get analogous situation when the industrial part is cooling outside to the press. In this case the heat flux is more complex than the Mold experiment. In addition to downward air flow, thermal radiation operates between every parts and the environment.

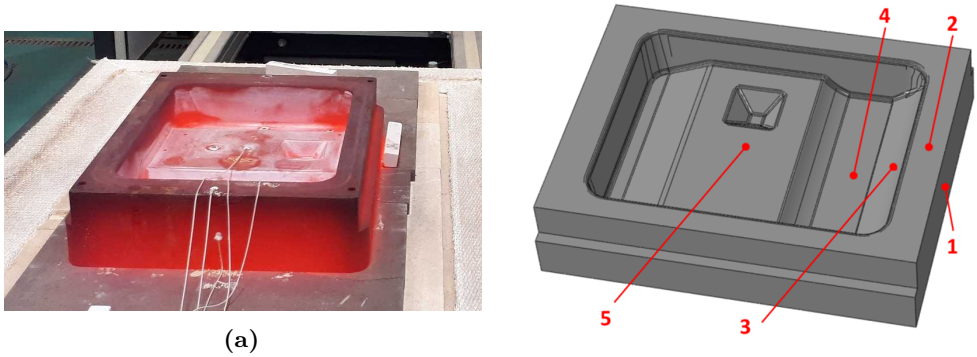

(a) (b)

Figure 3.29 – Mold experiment: (a) picture at high temperature, (b) CAD view with the thermocouple positions

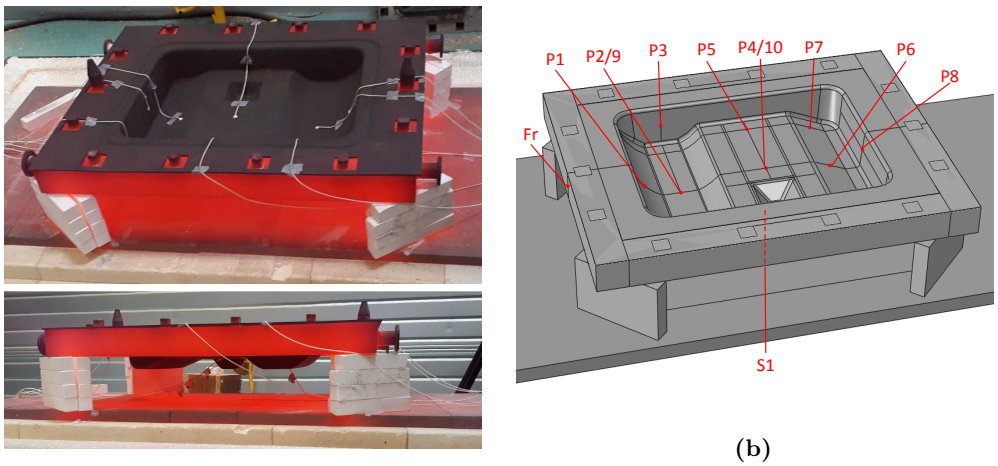

(a) (b)

Figure 3.30 – Part-Frame experiment: (a) picture at high temperature, (b) CAD view with the thermocouple positions

Eight thermocouples were placed at various position with different orientations upward, but also downward (thermocouples P9 and P10) such as seen in the Figure 3.30a and schematically presented in the Figure 3.30b. The thermocouples P9 and P10 are located on the same position at the opposite side of the thermocouples P2 and P4. A thermocouple S1 is also fixed on the shuttle at the center below the part.

❒ "Mold-Part-Frame"

This configuration presented in the Figure 3.31a was used to perform several types of experiment. It was used to perform air jet blowing operation as presented in the Figure 3.31b, and also natural cooling experiments with the BN impact evaluation. The same thermocouples location was used for each experiment as shown in the Figure 3.31c.

- "Blowing" experiment

This configuration had two combined objectives: firstly to determine the HTC for typical single nozzle blow cooling operation, and then characterize the thermal conductance model. Indeed, the air jet impinging the part is supposed to generate an intense cooling and

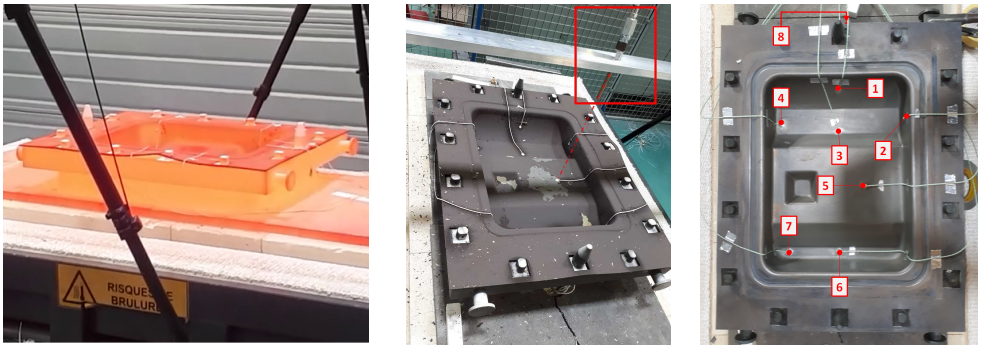

(a) **(b)** **(c)**

Figure 3.31 – Mold-Part-Frame experiment: (a) picture at high temperature, (b) the blowing system and (b) the thermocouple position

significant thermal gradient that would produce an expansion of the sheet. Thus, strong heterogeneous contact conditions could be induced which would exacerbate the influences of contact resistance heterogeneity at the mold-part interface. The nozzle was placed at 30 cm above the thermocouple P5. The cooling procedure was composed by several blowing sessions of around 20-30 seconds broken with natural cooling phases. By this way, the conductive heat flux generated by temperature differences between part and mold were activated.

- "Natural convection" experiment

This experiment consisted in natural cooling during around ten minutes. Two surface preparations were tested: with and without BN coating. The objective of these experiments was to validate the different boundary conditions determined through the dedicated experiments. The use of both surface preparations enables to evaluate the impact of such parameter.

❒ Unmolding

This experiment consists in using the "Part-Frame" based configuration to test the effect of natural cooling with none influence of shuttle onto the bottom surface of the part such like during the outside press natural cooling. The part removal operation was performed with a hoist system hanged to the frame (Figure 3.32a) and then placed on beams (Figure 3.32b) set beforehand so that to identically place back the part.

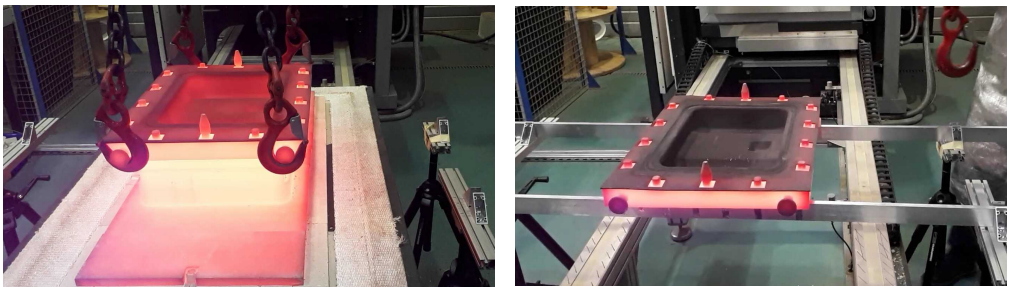

(a) **(b)**

Figure 3.32 – Picture of the Unmolding experiment: (a) during the handling of the frame, (b) after repositioning

It was not possible to weld thermocouples neither to use the pyroreflectomer, only the camera was able to give temperature data. Indeed, the motion of part made difficult to replace at

the exact same position to get intersection of lasers of pyroreflectometer at the same point. In addition the thermocouples wires had to pass by the shuttle channels that prevent the unmolding operation.

3.4.4.2.1 Discussion

The definition of an adapted design of experiments is crucial to answer the global objective of thermal characterization. It was chosen to use an modified SPF die as laboratory prototype tool to have industrial conditions. This solution enabled to free form industrial problematics that make very complex the condition of HT to reproduce with usual laboratory experiments. A set of experiments from which HT were more or less isolated were defined from the HT operating range. Therefore the identification of thermal boundary conditions through inverse analysis was simplified.

3.5 Experimental results

A large number of experiments and associated data were obtained. In this section, the principal results that are used for the characterization of boundary conditions are presented.

3.5.1 Development experiment

As introduced in section 3.4.4, a first experiment was used to test several details of the methodology such as:

1. The heating procedure: the programming of heating, the thermal response, the opening of the bell and the displacement of shuttle. Take care of the timing and the good maintaining of the part assembly and the THC during the shuttle displacement.
2. The measurement means: test the different means of instrumentation (THC, pyroreflectometer and camera).
3. The part and die fitting back: evaluate if the positioning of the part inside the mold is identical to the initial conditions of the end of forming before cooling and unmolding steps.

The presentation of the results has been placed in the Appendix B.1 in order to alleviate the quantity of experimental results in this section. Only the conclusion are presented below.

The first objective have been fully met. Indeed, the heating procedure and the equipment displacement worked perfectly. However, an electric disturbance modified THC signal during part of heating phase with none impact during cooling procedure. In addition, one of the welded THC showed a noisy signal that was probably due to a poor welding joint. A particular attention to the welding preparation was paid for the other tests.

Concerning the measurement means, the agreement between THC and camera was demonstrated, as well as for the camera and the pyroreflectometer. A good confidence was shown in the measurement by NIR camera, especially in the oxidized state. At the beginning, the values were underestimated but the emissivity value provided by the pyroreflectometer allows a correction a posteriori. The pyroreflectometer did not work optimally because the reflectivity measurement was not possible. I was probably due to a variation of height of the sheet in between the laser setting before and after heating. However, it enabled to evaluate the "grey" condition of the material in the process conditions.

Finally, the spot THC placed at the surface of the mold confirmed that the part was in contact at the starting of the furnace opening. Therefore, the SPF conditions were respected and initial conditions for characterizing the HT were acceptable.

3.5.2 The Mold experiment: natural cooling

The objective of this experiment was to get temperature data in a configuration with no effect of part-mold conduction, but only convective and radiative HT. The mold-platen conduction has obviously an impact on the temperature evolution, but over a long period of time and with fairly well-known contacting conditions contrary to the part-mold interface.

3.5.2.1 Temperature measurements

This experiment was performed on a long period to let the mold cooling down to the room temperature. The Figure 3.33 shows the logarithmic time evolution of the temperature of the THC during the whole test. The graph shows disparities of temperature according to the position inside or outside forming shape. The THC 2, which has a null view factor regarding to mold surface has the highest cooling rate at high temperature. This confirms the importance of thermal radiation for this range of temperatures.

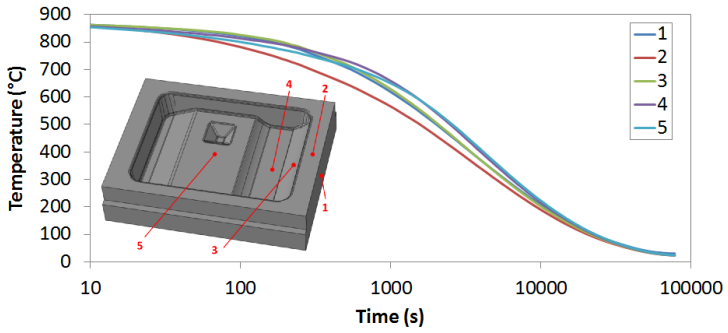

Figure 3.33 – Mold exp.: evolution of temperature of thermcouples during experiment with associated position on CAD representation

The Figure 3.34b compares the curves of THC and camera extracted temperature during the first thousand seconds. The Figure 3.34a represents the positioning of camera extraction zones. Some points are located around the THC position, the square D is located at pyrometer position (represented in green) and some other zones are retained for characterization issues. The comparison of THC and camera seems to be accordant, contrary to the pyrometer and camera (Figure 3.34c). Indeed, the pyrometer curve seems to deviate from the camera curve while they are both radiance temperatures at the same wavelength. This phenomenon may be a consequence of the lost of signal power (because of low emissivity values) to which the pyrometer is more sensitive.

3.5.2.2 Analysis

Emissivity evolutions were computed from the curves of the Figure 3.34b by considering THC data as the true temperature. The Figure 3.35a shows the curves of the computed emissivities for each THC. There are large differences and non physical values (>1). However, there is the same tendency to increase during the experiment for every position. The emissivity curves obtained from THC 1 and 2, which are both outside from the forming shape are globally higher than two others. This is probably due to the BN layer which is still present in the forming shape area and has an inferior emissivity than oxidized surfaces such as observed in the Figure 3.35b.

Local spectral emissivity measurements performed with a portable BRUKER Fourier-transform infrared spectometer at the point indicated in the Figure 3.34a are presented in the Figure 3.35c. The results confirmed strong emissivity differences in between 0 to 0.8.

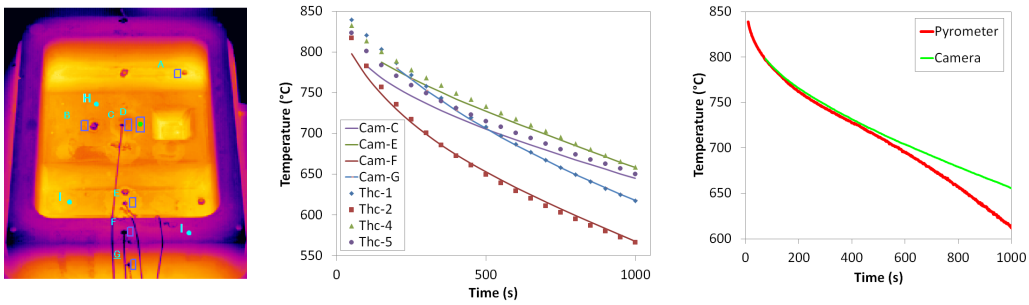

(a) (b) (c)

Figure 3.34 – Mold exp.:(a) camera picture with extraction points - comparison of temperature data from (b) camera and THC (c) camera and pyrometer

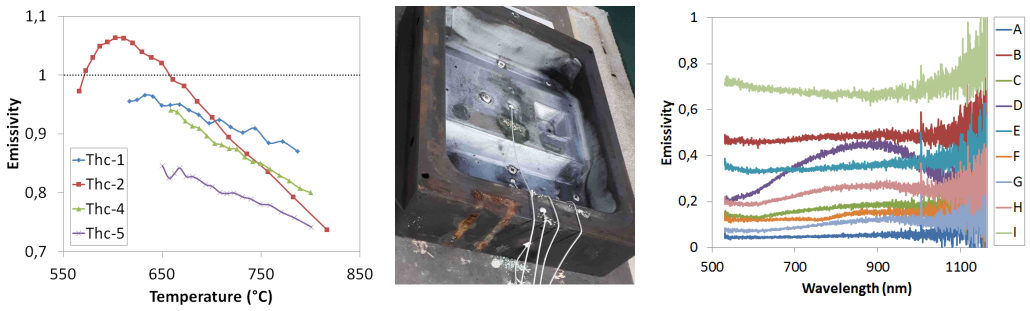

(a) (b) (c)

Figure 3.35 – Mold exp.:(a) computed emissivities, (b) picture of cold mold after the experiment and (c) spectral emissivity measurements

The Figure 3.35b shows the state of mold at the end of the experiment. The surface quality remained highly impacted by the experiments compared with initial state after forming, which can explains the emissivity gradient measured with the camera and the spectral measurements.

3.5.2.3 Conclusions

The analysis of the temperature measurements have shown that the emissivity of the mold surface was to highly heterogeneous probably because of the surface degradation (stop off, wears, oxidation, etc.). In addition, the pyrometer data shows a deviation of temperature compared to the camera data. Therefore, the non contact measurement data are not relevant and only the THC data were used for the characterization presented in the Section 3.6.3.1.

3.5.3 The Part-Frame experiment: natural cooling

The objective of this experiment was to get temperature data in a configuration with no effect of part-mold conduction such just like the Mold experiment. Moreover it promoted different convective and radiative heat flux distributions over the part. Therefore, this second configuration enabled to get additional temperature data for the characterization of both radiative and convective boundary condition which were not possible to simply isolate from each other. As for the Mold experiment, there are conduction HT between the ceramic bars with the frame and the platen and the frame with the part. However, their effect is quite limited on the formed shape area of the part. In addition, they can be considered in the simulation using hypothesis to performed the characterization using the inverse analysis.

3.5.3.1 Temperature measurements

This test consisted into natural cooling conditions during around 10 minutes after the shuttle exit of the furnace. During the experiment, some THC did not resist to the thermomechanical conditions. The Figure 3.36a represents the time evolution of the temperature for all THC. The THC 2 did not give any data during cooling. Moreover, the THC 4, 1 and 5 no longer gave data after the 80 first seconds such as seen in the Figure 3.36b.

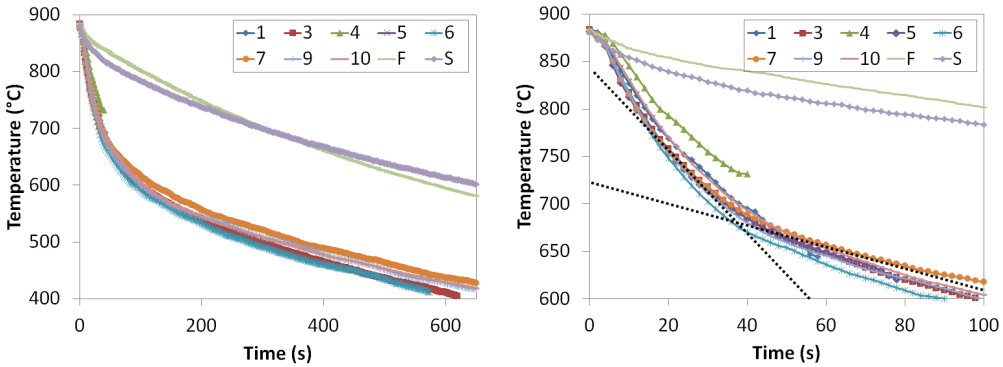

Figure 3.36 – Part-Frame exp.: THC data - temperature vs. time curves (a) full experiment, (b) t<100 *s*

The THC data show some interesting points. Firstly, the two THC fixed on the shuttle and the frame cooled much slowly than the part which is much less massive. However, the shuttle THC cooled faster than the frame during the 40 first second, and then the tendency is inversed. This change in the thermal behavior regarding temperature response is also observed for the part THC as represented in the Figure 3.36b with dotted lines which traduce a slope change. This change is more or less continuous according to the position over the surface.

Concerning the camera, the temperature for some positions indicated in the Figure 3.37b, are plotted in the Figure 3.37a and a zoom is made on the 90 first seconds in the Figure 3.37c. The same phenomena is observed with camera data. However, the position C, which is located at the joint plane above the frame contact surface, obviously cools much slowly, but also does not present the slope change.

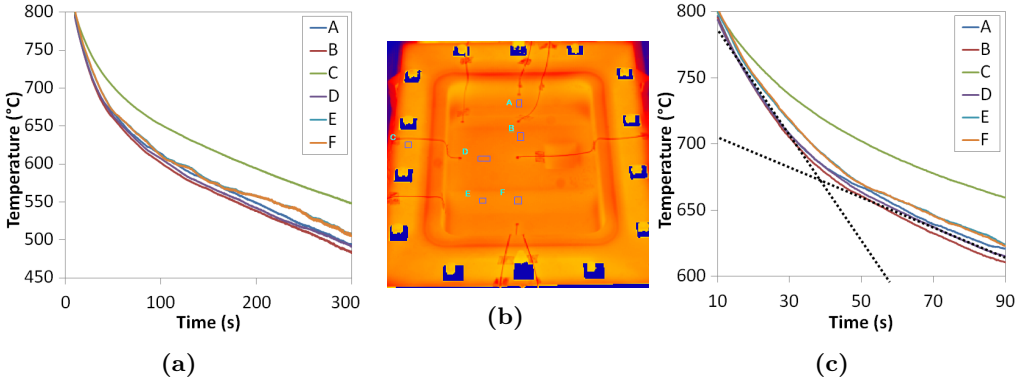

Figure 3.37 – Part-Frame exp.: NIR camera data (a) temperature versus time, (b) extraction zones on temperature histogram, (c) focus on the temperature slopes change

3.5.3.2 Analyses

The emissivities at THC were computed using the same method than for the previous experiment. Camera data were extracted very close to the THC 4, 5, 6 and 7 which were visible with the camera. The Figure 3.38a shows the emissivity variations at the associated THC position. The emissivity values approximately started from the same value (ϵ=0.6-0.7) and then varied heterogeneously regarding their position. The values above one have no physical sense. However, the shape of the curves are similar. The emissivities increased first and tended to reach a plateau. This phenomena might be related to the oxidation mechanisms that are active above 600 °C for these materials.

The Figure 3.38b presents a comparison between camera and pyrometer. The camera curve deviates around 500 °C which corresponds to the lower range of the calibration temperature of the camera. The shape of curves ar fairly identical, yet a gap difference is noticeable from around 50 seconds. This might probably be due to part deformations such as for the development experiment.

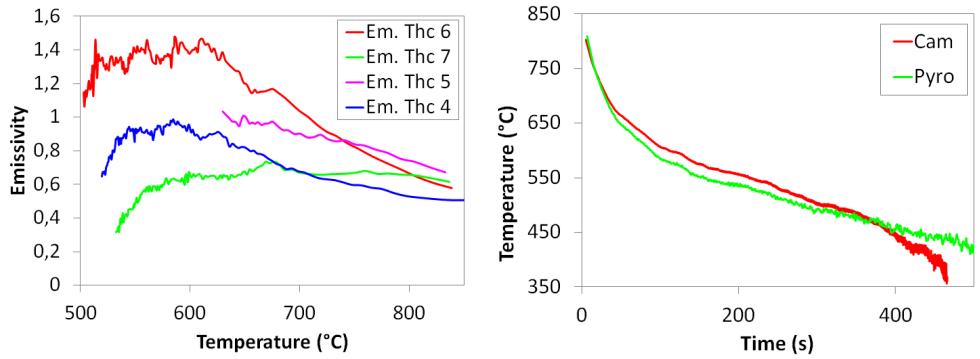

(a) (b)

Figure 3.38 – Part-Frame exp.: (a) emissivity variation with temperature computed from thermocouples-camera data, (b) comparison of pyrometer and associated camera data

3.5.3.3 Conclusions

The results of this experiment gives a good correlation between contact and non contact measurements. However, the emissivity computation gives different variations during the test. Nevertheless, the heterogeneity is less disparate than for the Mold experiment and tended to reveal an increasing evolution from 0.6-0.7 up to a plateau value closed to 1. As for the Mold experiment, only the THC data were used for the characterization presented in the Section 3.6.3.2.

3.5.4 The Mold-Part-Frame experiment: blowing

The objective of this experiment was double. Firstly, it was used to obtain temperature field produced by air blowing on a hot part in the industrial conditions to characterize a forced convection model. Then, the effect of this rapid cooling was supposed to produce part deformations which should lead to an evolution of the contact conditions at the part-mold interface. The evolution of the temperature field promoted by these varying contact conditions was used to characterized the conductance model.

3.5.4.1 Temperature measurements

The procedure of the blowing experiment is composed by successions of natural and forced cooling of different periods. The Figure 3.39a shows the temperature curves from the THC during the whole test. The THC 3 did not give data. The procedure was composed by seven blowing sessions after what temperature tended to heat back at an asymptotic value.

The Figure 3.39b represents the averaged temperatures curves of welded and spot THC (presented in the Section 3.5.5) in the case of natural convection and blow cooling experiments. This graph shows that the mold was almost not impacted by forced convection. Indeed, the asymptotic curves at each blow session seem to coincide with natural convection curve. On the contrary, the part temperature is largely impacted at each blow session. However, the asymptotic curve at the end of experiment has only 15 °C less from natural convection curve. This is most likely due to the massiveness of mold that control the part temperature through conduction HT.

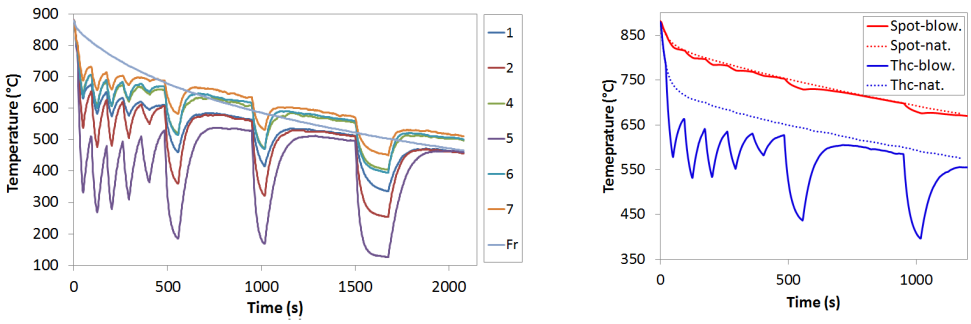

(a) **(b)**

Figure 3.39 – Mold-Part-Frame exp.: comparison of temperature data from (a) thermocouples (b) averaged temperatures of upward-welded and downward-spot THC during natural convection and blowing experiments

The Figure 3.40a gives the temperature curves of zones of the part extracted such as presented in the Figure 3.40b. For the temperatures lower to 450-500°C, there are deviations until discontinuities of curves. The A, B, D and E curves seem to have the same kind of evolution than THC. The zone F seems to have a different behavior during the post blowing phase especially after the sixth session. Comparatively, the zone B which has approximately the same level of temperature seems to be preserved from this phenomenon. This is probably due to the thermal contact conditions that were different for both zones.

Concerning the zones C and G that are located in the joint plan, they are fairly less impacted by the blowing jet. A slight difference is observed between both zones that are symmetrically disposed. This is due to a deformation of the part that limits the thermal conduction with the frame. The deformation is visible near the pocketed zone in dark in the Figure 3.40b.

The Figure 3.41a shows an example of profile data (extracted from the line represented in the Figure 3.40b) at several time during the first blowing session. The Figure 3.41b shows the same profile which are adjusted by the maximum temperature of the profile (ΔT=T-max(T)). These curves highlight that the temperature gradient increased between the two first times and then slightly decreased.

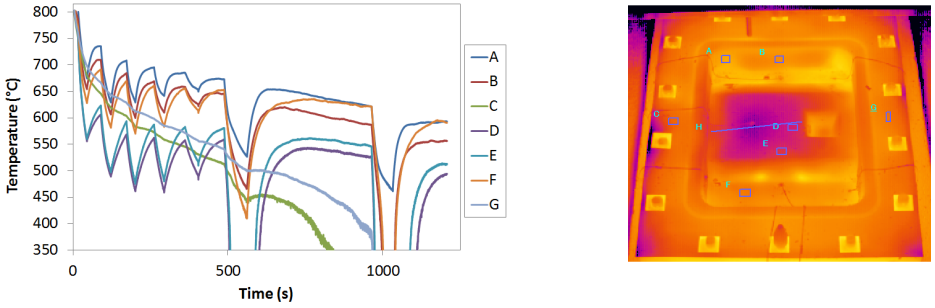

(a) (b)

Figure 3.40 – (a) radiant temperature vs. time evolution during blowing experiment from NIR camera data, (b) position of extraction zones on NIR camera colored histogram of temperature

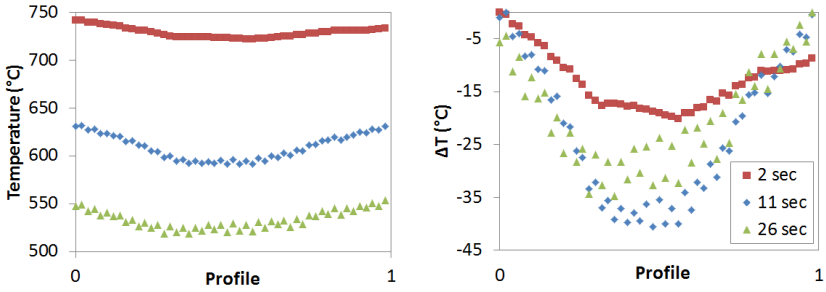

(a) (b)

Figure 3.41 – radiant temperature variation on profile extracted from NIR camera (a) unscaled, (b) scaled on maximum temperature

3.5.4.2 Analyses

A zoom on the first blowing session is presented for THC and camera data in the Figure 3.42 with the same temperature scales. Both graphs confirm that under forced convection, the THC are influenced by the external heat flux even with the low-conductive cement disposed onto the THC welds.

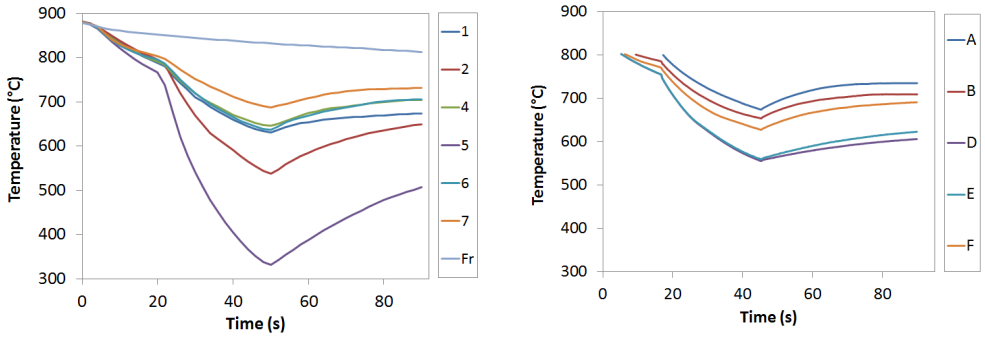

(a) (b)

Figure 3.42 – Comparison of the temperature evolution during the first blowing session for (a) thermocouples, (b) camera

3.5.4.3 Conclusions

It was seen that the effect of blowing on the THC did not give a valid temperature data. Therefore, during blowing, only the camera data have been used. However, the camera data had been calibrated for temperature in between 500 and 800 °C. Thus, for the first natural cooling phase, the THC has been used, and the camera for the rest. Some profile such as those presented in the Figure 3.41 have been extracted to cover the impinging zone from which the forced convection model is characterized in the Section 3.6.4.

A difference between pyrometer curves and associated camera zone from the beginning of the first blowing session happened. This was again probably due to the deformation of part under high cooling rate. Thus, the curve from pyrometer data is not presented and was not used for characterization purpose.

3.5.5 Mold-Part-Frame experiment: natural cooling

The aim of this experiment was to validate the different boundary conditions characterized from the results of each previously described experiment in a configuration where each radiation, convection and conduction HT were involved. Two surface conditions were tested for the superior surface of the part (with and without BN coating) in order to have two different emissivities and analyze the sensitivity of the FE model to this parameter. The first objective of BN coating is to reduce friction phenomena. In addition, it has the effect to modify the emissivity of the surface and also to prevent from oxidation. Indeed, the oxidation effect as an impact on emissivity variation at high temperature, thus, BN is supposed to modify radiative HT.

3.5.5.1 Temperature measurements

A new BN coating was applied on a part in the laboratory. The formed part was previously cleaned from oxide chips coming from forming phase in order to return in the condition before forming. However, the coating was not applied in conditions that it could resist at high temperature during the furnace heating and cooling step. Indeed, the drying time was not respected such that the coating produced chips that detached from the part such as presented in the Figure 3.43a.

The Figure 3.43a represents two pictures of the part and BN coating at the end of the experiment. At the beginning of the cooling phase, the coating was still in good conditions. It is the effect of high cooling rates that produced its detachment. The Figure 3.43b and 3.43c represent thermal camera images of the BN and without BN (wBN) case. The BN case shows significant discontinuities of thermal radiations over the surfaces. They may be related to emissivity disparities due to oxidation, but also a rapid cooling of detached oxide layers.

The Figure 3.44a shows the curve of temperature from THC for wBN case. These experiments were performed with the same THC than blowing test. That is why THC 3 has no associated data. There is a high gradient of cooling rate during the first 150 seconds while for the rest of the test, the variations are small.

The Figure 3.44b represents the temperature difference ΔT between BN and wBN cases (Δ T=T_{BN}-T_{wBN}). This graph highlights firstly that the BN painting has an impact on thermal response for identical cooling procedure. Secondly, the temperature differences go increasingly between zero and around 300 seconds, and then it stays approximately constant until decreasing during the third part of the experiment. This phenomena seems to follow the transition of HT mode from radiation-dominated to convection dominated. In a first time the difference of emissivity made the temperature difference to increase, then it stagnated because of identical convection flow. Finally, the thermal conduction controlled by the temperature of the mold made the parts temperature to converge.

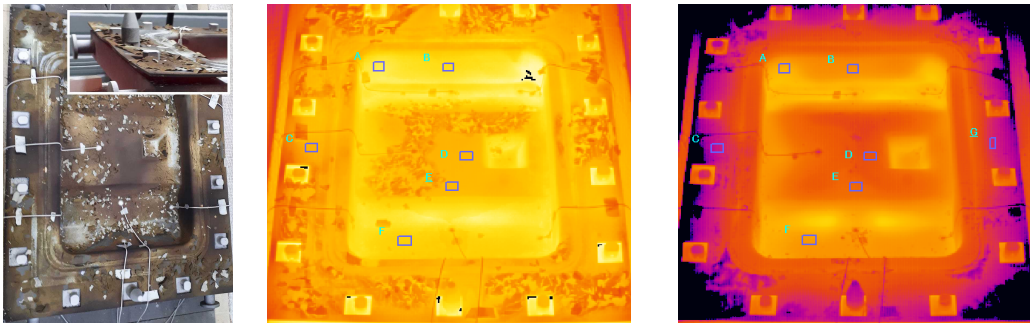

(a) **(b)** **(c)**

Figure 3.43 – (a) picture of Part after BN coated experiment, temperature histograms from the NIR camera for both coating conditions (b) with BN and (c) without BN

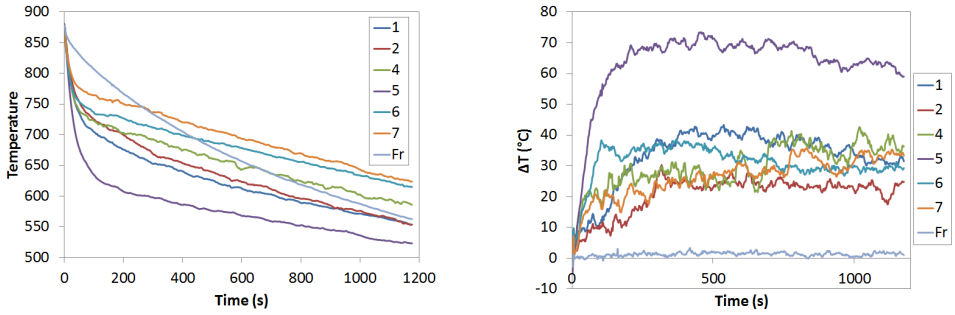

(a) **(b)**

Figure 3.44 – Thermocouples-based data (a) temperature vs. time from without BN experiment and (b) temperature difference ΔT (=T_{BN}-T_{NoBN}) between both coating

The Figure 3.45a represents the temperature data obtained with the camera for BN case. Some large variations can be observed especially for the zone D. They are due to the BN chips detachment. The Figure 3.45b shows the same ΔT variations during the test. In this case the data observed from the camera are radiance temperatures. Therefore, the BN case temperatures are under estimated because of a lower emissivity which globally produces negative ΔT values.

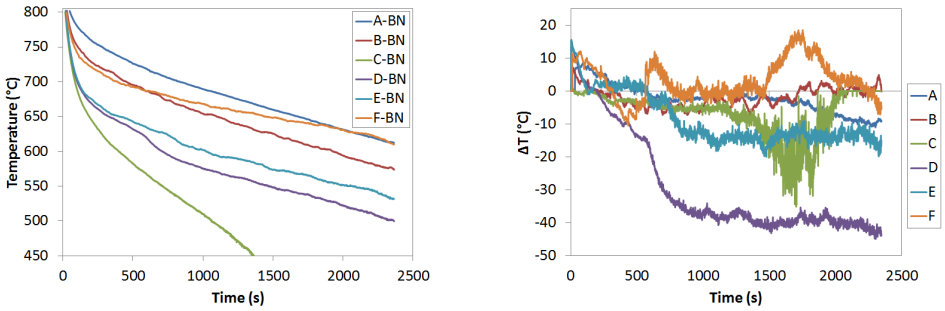

(a) **(b)**

Figure 3.45 – NIR camera-based data (a) temperature vs. time from without BN experiment and (b) temperature difference ΔT (=T_{BN}-T_{NoBN}) between both coating

3.5.5.2 Conclusions

Both the THC and camera data gave exploitable results for the two surfaces conditions. However, the potential emissivity heterogeneity once again made difficult to exploit the camera data. Therefore, only the THC data were used for the validation of the BC presented in the Section 3.6.4

3.5.6 Unmolding experiment

The objective of this experiment was to get additional temperature data in a configuration where no conduction occurred and the thermal radiation would have been better mastered contrary to the Part-Frame experiment. Indeed, in the Part-Frame configuration, the part exchanges heat by radiation with the platen and the ceramic bars, and the convective flux is more complex than the unmolding experiment for characterization purpose.

3.5.6.1 Temperature measurements

This experiment was only instrumented with IR camera as described in the Section 3.4.4. The temperature decrease that happened in between furnace opening and part re-positioning after unmolding step was too large. Indeed, The figure 3.46a, 3.46b and 3.46c show the different temperature histograms respectively before part removal, during and few seconds after being repositioned. The purple tones mean that radiant temperatures of part are lower to 500 °C which is the limit of camera calibration. Therefore none exploitation of this experiment was possible.

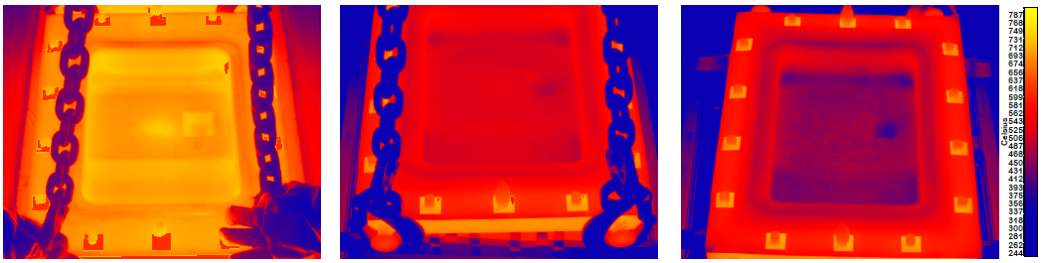

(a) **(b)** **(c)**

Figure 3.46 – Temperature histogram pictures from NIR camera (a) before part removal, (b) during part raising and (c) after few second repositioned

3.5.7 Discussion

Globally, the different experiments that were performed gave important data for thermal BC characterization. However, an important issue was met regarding pyroreflectometry. No reflectivity could have been measured mainly because of part deformation that disturbed the lasers coincidence. Indeed, the reflectivity measurement coupled with pyrometer data would have enable to get true temperature and a value of emissivity as a function of temperature and oxidation (by coupling with camera data).

Nevertheless, THC data enabled to get confident temperature data considered as true temperature. Emissivity variations have been evaluated using THC and camera data for the different experiments. The mold experiment showed a strong variation of its emissivity such that non contact data cannot be used for the characterization. Concerning the other experiment measuring Ti-64 surface temperature, the camera data seems better confident.

The THC data were mostly chosen for characterization rather than camera data because of the dependency on the emissivity unknown which was heterogeneously distributed. Nevertheless, the camera was needed for the blowing experiment instead of THC that were not exploitable during the blowing phase. That is why, additional spectral measurement were performed to evaluate to total emissivity values to use for radiative boundary conditions. The spectral measurement methodology and results are presented in the next section.

Considering the emissivity and thermal radiation obtained by this way, the mold and Part-Frame experiments were used to characterize convection. The Blowing experiment was used to characterize both the forced convection and conduction thanks to first blowing session. The Mold-Part-Frame experiments were used to validate the different BC models.

3.6 Heat Transfers Characterization

3.6.1 Strategy

As mentioned above in this chapter, the complexity of characterizing the BC associated to the three modes resides in their concomitant operating ranges. Several experiments were carefully designed to solve this issue and to get the adequate temperature data to characterized the BC models through an inverse analysis technique.

❒ Natural convection and thermal radiation

The experimental results presented in the Section 3.5 highlights that a significant heterogeneity exists regarding the emissivity properties of the mold but also for the part. This heterogeneity bring an additional difficulty to the characterization problem. Therefore, specific emissivity measurements have been performed on representative samples presented in the Section 3.6.2.

In addition, the natural convection models are computed from a priori CFD analyses. The results of these simulations are detailed in the Section 3.6.2 for the Mold and Part-Frame configurations for which the natural convection is of first order.

The results obtained in this preliminary characterization phase are used in the first step of characterization. Because of the mentioned heterogeneity of emissivity and the fact CFD models are build on simplified geometry, the BC models are then refined in additional steps to get optimized temperature responses.

❒ Forced convection and contact conduction

In this case, the procedure is slightly different because both modes happened with distinct order of magnitude. Indeed, the first blowing phase produced a high cooling of the part, and then the rise of the temperature is the consequence of conduction phenomena directly impacted by the deformation promoted by thermal stresses (consequent to the blowing). However, the thermal response during the blowing phase is also conditioned by the conductive heat transfers from the mold that tend to limit the cooling down.

Therefore, the characterization was made using several steps. The first step was used to evaluate the conductance model using the results of the first natural cooling phase before blowing. Then, the forced cooling model was evaluated using the first blowing phase. Finally, a last step was used to refine both the conductance and the forced convection model that have demonstrated a strong coupling.

3.6.2 Preliminary characterization

3.6.2.1 Thermal radiation

3.6.2.1.1 Theory

The parameter that matters in the thermal radiation is the total emissivity. It is related to the spectral emissivity such as defined in the Equation (3.57) where L^0_λ is the black body spectral radiance which is defined with Plank's law. It is necessary to know the spectral emissivity on a wavelength range ($\lambda \in [\lambda_A - \lambda_B]$) that covers the effective emitting wavelength of the targeted temperature range. This range is usually taken in between 1-20 μm which corresponds to radiative intensity spectra for the process temperatures.

$$\epsilon \backsimeq \frac{\int_{\lambda_A}^{\lambda_B} \epsilon_\lambda L^0_\lambda \, d\lambda}{\int_{\lambda_A}^{\lambda_B} L^0_\lambda \, d\lambda} \tag{3.57}$$

Spectral emissivity measurements have been performed at ambient temperature only. The bibliographic review showed that emissivity is much more dependent on surface properties (especially oxidation layer) than temperature (for constant surface properties). Thus, the total emissivity was computed considering no influence of the temperature on the spectral emissivity.

3.6.2.1.2 Results

Spectral emissivity variation was measured using a BRUKER Fourier-transform infrared spectrometer. Two different detectors InGaAs and DLaTGS were used to cover 1-20 μm wavelength range. Three samples were cut from a formed part at different positions representative of the post SPF surface conditions for both with and without BN coating conditions. The Figure 3.47a represents the averaged curves of spectral emissivity with standard deviation bars for both surface qualities. The samples with BN present globally a lower emissivity between 0.4 and 0.75, and are much varying with the wavelength than the other. The sample without BN coating presents fairly small variations, between 0.75 and 0.9, which seems to confirm the grey body observation made from the results of the Development experiment in the Appendix B.1.0.2.

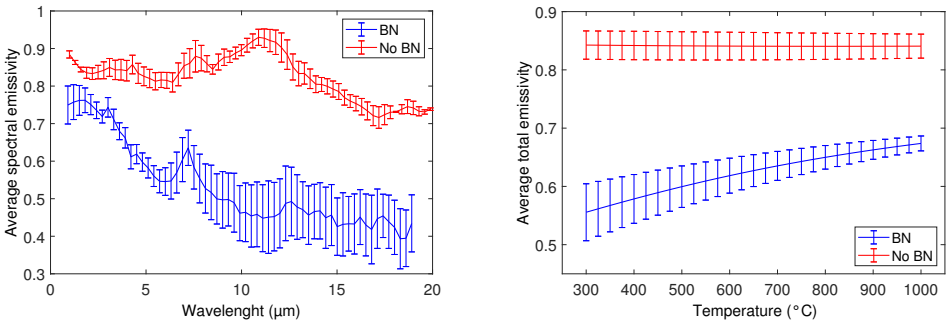

(a) **(b)**

Figure 3.47 – Comparison of emissivity with and without BN coating: (a) spectral emissivities, (b) computed total emissivities

The Figure 3.47b shows the total emissivity variations for both coating conditions after computation and filtering. The differences between both surfaces conditions are similar than observed for spectral emissivities.

3.6.2.1.3 Discussion

The obtained total emissivity without BN coating does not correspond to the values computed from the results of the Development experiment. Indeed, in the experimental cases, the emissivity seemed to increase from a value around 0.6-0.8 until to reach a plateau around 0.8-1.

This difference of behavior might have several origins. Firstly, the total emissivity obtained from measurement is based on the assumption that the spectral emissivity is not temperature sensitive which may not be correct. In addition, The literature review has shown that the oxide growth has the consequence to increase the total emissivity, which may be at the origin of the increase during the experiments. Finally, it can be a combination of both. Indeed, the emissivity of the oxide layer formed at the furnace opening may have such temperature sensitivity.

Regardless to the origin of the observed increase of emissivity, it is contained in between 0.8 and 1 for the parts without BN coating and 0.55 and 0.7 with BN. For the inverse analysis, The total emissivity was firstly considered constant in range of 0.8-1, and varying emissivities were also tested.

3.6.2.2 Natural convection

In this section, the models used for the CFD computations are not presented but they are detailed in the Section 3.2.2.5 and the Appendix C. The focus is only made on the process conditions, the results in terms of HTC, and how the associated models were designed for the two experimental configurations.

3.6.2.2.1 Mold experiment

❒ Model

The experimental curves at the different thermocouples on the mold (seen in the Figure 3.48a) show that the global temperature of the mold was fairly homogeneous. The maximum deviation with the average curve is about 60 °C maximum and an average deviation inferior to 14 °C. Therefore the temperature of the mold and shuttle surfaces were considered homogeneous for the CFD simulations. A set of temperatures between 850 °C and 50 °C was modeled each 50 °C in order to evaluate the convection coefficient over the whole temperature range. The mold experiment was simplified for CFD modeling issues as showed in the Figure 3.48b and 3.48c.

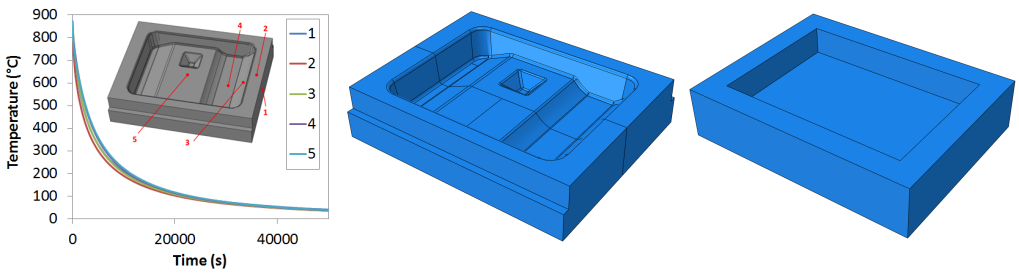

(a) **(b)** **(c)**

Figure 3.48 – Mold experiment: (a) THC temperature vs. time curves, CAD view of (a) Mold and (b) Simplified Mold

❒ Results

The Figure 3.49 shows the distribution of the HTC h_c computed from the normal to surface heat flux HFLN ($h_c = (T_{mold} - T_\infty)$/HFLN) for the next three temperatures [50,450,850]°C. The contour plot seems very discontinuous which is due to the turbulences. A twenties of increment over around ten seconds after reaching the steady state were averaged in order to get representative values for each simulated temperatures.

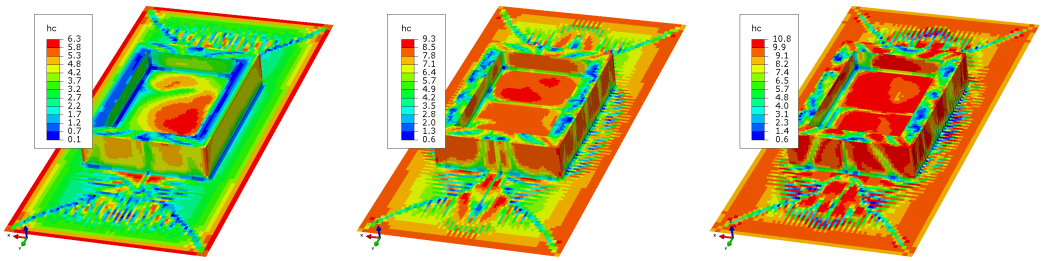

(a) 50°C **(b)** 450°C **(c)** 850°C

Figure 3.49 – CFD-based computed HTC for steady state conditions at several temperatures

❒ Convection coefficient modeling

The averaged results of HTC brought out several surfaces with fairly homogeneous values at every computed temperatures. The Figure 3.50a represents the computed HTC as a function of temperature for the mentioned surfaces associated by colors with the mold representation. There is a significant difference between the joint surface of the mold in yellow, and the rest. The yellow surface has a lower convection coefficient, which is even noticeable in the Figure 3.49. The Figure 3.50b highlights this difference when the vertical surfaces respectively inside (green and turquoise) and outside (brown and red) the mold are averaged.

It was chosen to define the convection coefficient as a function of time instead of temperature to avoid local temperature changes that would not be representative of real convection flow variation. The Figure 3.50c gives the graph of time evolution of the HTC and the associated fitting curves. The model 1 is defined in the Equation (3.58) where h_0=2.2 and h_1=6. The model 2 is defined by scaling the model 1 with a factor 0.725.

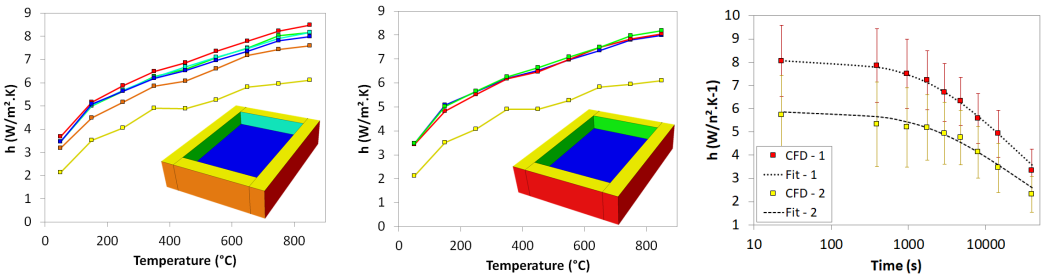

(a) **(b)** **(c)**

Figure 3.50 – Averaged HT coefficient variations associated to (a) 1^{st} (b) 2^{nd} surface definition, comparison of CFD based HTC and the model as a function of time

$$h = h_0 + h_1 exp(-2.10^{-3} t^{0.62}) \tag{3.58}$$

The h_0 and h_1 coefficients are the parameters used to fit the temperature curves in the Section 3.6.3.1. In the first step of optimization, the parameters are taken as obtained from CFD analysis. In a second step, the h_1 parameter was tuned to adjust the heat flux while preserving the decreasing behavior of h_c.

3.6.2.2.2 Part-Frame experiment

❒ Model

The geometry simplifications for the CFD analysis are shown in the Figure 3.51. Contrary to the Mold experiment, the differences in the massiveness of parts and their associated thermal responses made necessary to take account of the heterogeneous temperatures of the part surfaces. An a-priori simulation was used to evaluate the temperature heterogeneity of the parts during the experiment using literature hypothesis (horizontal plates based correlations) for the convection coefficients.

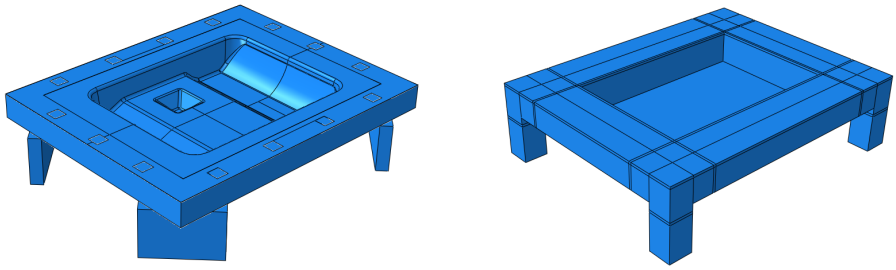

(a) **(b)**

Figure 3.51 – CAD view of (a) Part-Frame assembly and (b) simplified geometry

The Figure 3.52a shows the temperature field obtained with the a-priori simulation after 250 seconds outside the furnace. The white points represent several locations over the different parts which were used to evaluate the temperature heterogeneity during the experiment. The Figure 3.52c is a graph comparing temperature evolutions from experimental data and simulation. The filled lines (blues and red) with markers correspond to average thermocouples data (part and shuttle plus frame). The dotted lines correspond to the averaged nodal temperatures with error bars (± the standard deviation) from the simulation using previously mentioned white points. Three different temperature zones were defined as represented in the Figure 3.52b.

This preliminary study of temperature evolution enabled to confirm a good agreement of simulation with literature data. Moreover, it is possible to define sets of temperatures at different times of the experiment (represented by the black lines with rounds markers in the Figure 3.52b). These temperature sets (given in the Table 3.3) have been used in the CFD analysis.

Homogeneous surface temperatures	t_0	t_1	t_2	t_3	t_4	t_5
Part	880	755	660	604	544	475
Frame - Shuttle (ins)	880	855	835	803	749	612
Shuttle (out)	880	850	817	773	700	596

Table 3.2 – Definition of the sets of homogeneous surface temperatures (°C) for CFD simulations

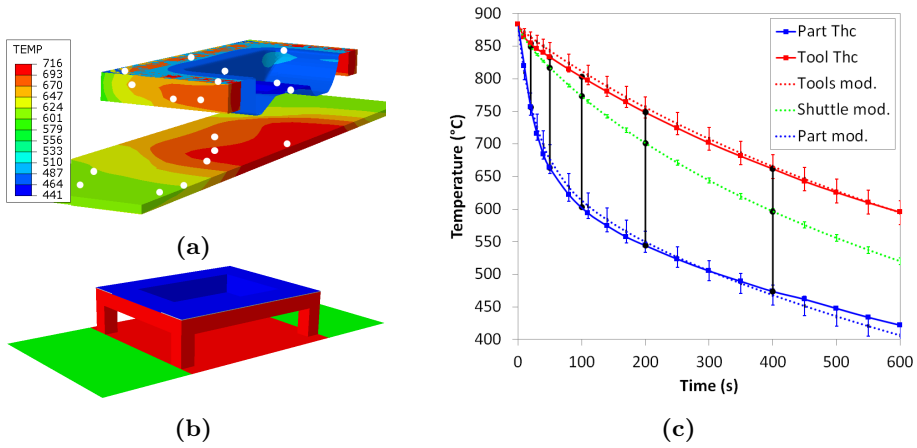

Figure 3.52 – A-priori thermal simulation results (a) temperature field and markers, (b) surface BC simplifications for CFD analysis and (c) comparison of simulated and experimental temperatures

❒ Results

The Figure 3.53 shows the steady state normal heat flux HFLN extracted from CFD analysis fot t_2 set simulation. The HTC values are not given because of the heterogeneous temperatures of the shuttle. The high level of fluid temperature near the bottom surface of part mentioned above is traduced by a negative HT (Figure 3.53a). Except for the near bottom part surfaces (part and frame) and the inside shuttle surface, there are turbulences that promotes heterogeneous HT. For the computation of exploitable HTC values, a twenties increments over around ten seconds after reaching steady state were averaged in order to get representative values.

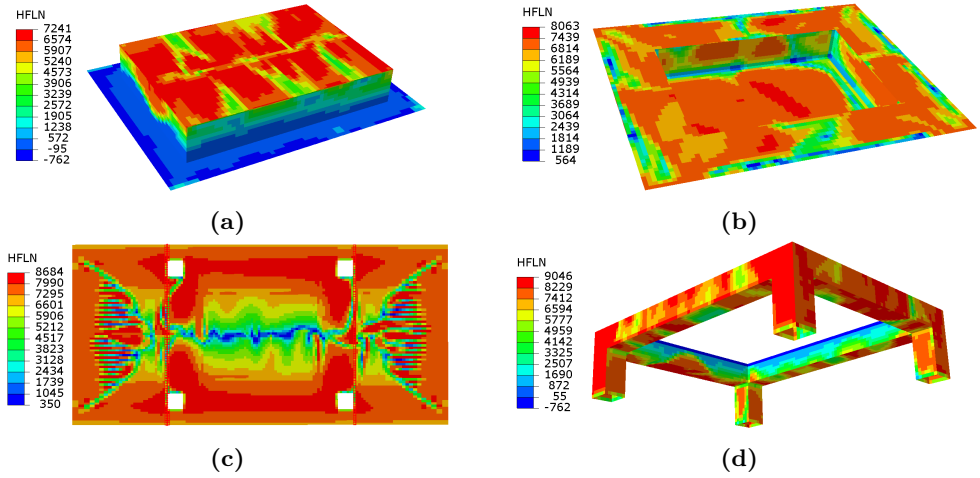

Figure 3.53 – Normal heat flux fields (W.m^{-2}) from CFD simulation at time t2 for (a) the bottom and (b) top surface of part, (c) platen and (d) frame

❒ Convection coefficient modeling

The results of CFD analyses of the six sets of surfaces temperatures enabled to split the surfaces of the geometries according to their associated h_c variations as represented in the Figure 3.54. The turquoise, red, blue and green colors are respectively affected to the part

top, the part bottom, the frame and the shuttle surfaces. For each colors, several shades are used to distinguish the split surfaces accordingly to their homogeneous variation of h_c. In addition, a distinction is made between surfaces perpendicular to x and y axis. Indeed, the effect of the rectangular shapes of part and the shuttle promote different fluid flows on both sides of the assembly.

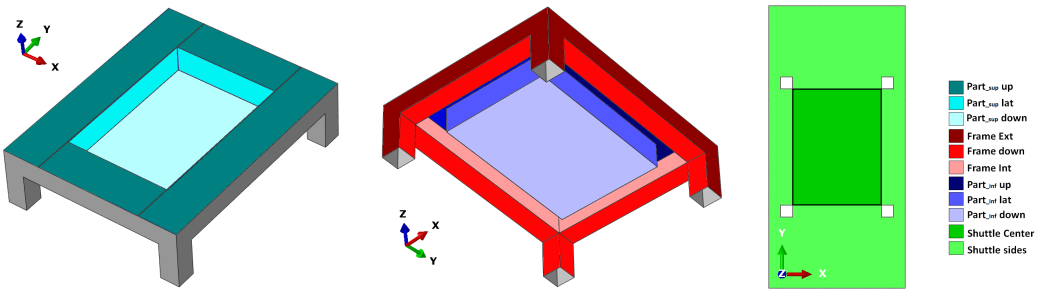

(a) Part top **(b)** Frame, part bottom **(c)** Shuttle

Figure 3.54 – Representation of split surfaces based on HTC variations

The evolution in space and time of the h_c distribution is rather complex to represents. Therefore the surface averaged evolutions of h_c is plotted in the Figure 3.55 as a function of the surfaces given in the Figure 3.52 for simplicity reasons.

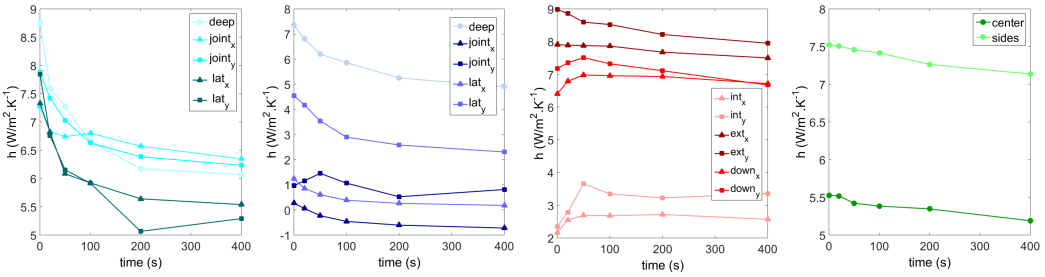

(a) part - top **(b)** part - bottom **(c)** shuttle **(d)** frame

Figure 3.55 – Time evolution of space-averaged HTC for split surfaces (Figure 3.54)

The behavior of the part is globally different between the bottom and the top surface. A rapid decrease of h_c is observed for the high and positive value of the part which is a consequence of its rapid cooling of contrary to the shuttle and the frame that are more massive. It is interesting to notice that the rapid temperature decrease of the bottom surface of part in the confined region closed to the frame produce a negative h_c value. It is the consequence of the higher temperature of the frame that heat up the air above the part temperature in this region.

The models used to described h_c distribution for each surface are not considered homogeneous. They are composed by constant, linear or bi-linear functions of surface coordinates to reproduce the most accurately the h_c distributions. The Figure 3.56 shows an example of h_c fit for the bottom part surface (at the temperatures set t_0).

For the optimization of the h_c models, it was not possible to refine the 2 to 5 parameters of the models for each split surfaces. It would have been too much time consuming, and it would have not respected the fluid mechanics that determined the original functions. Therefore, a simple weighting coefficient was tested for the h_c models so that to keep a logic in the h_c evolution.

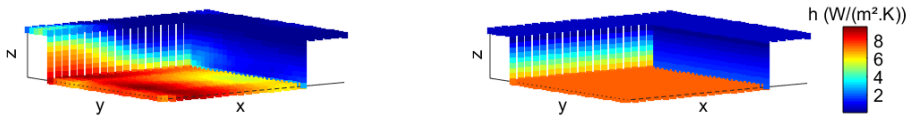

(a) (b)

Figure 3.56 – Comparison of HTC for bottom surface of part at time t0 based (a) CFD analysis and (b) fitted model

More globally, the h_c values obtained from CFD seems to match with the values computed from Nusselt correlation laws in the Section 3.4.4.1. However, the CFD analysis of horizontal plates results compared to the literature data revealed that a under-estimation of the h_c value can be made for the non-turbulent flows. Untreated models were used in first approximation, and then a tuning of the h_c function was made to refined the temperature responses.

3.6.3 Inverse analysis: natural convection and radiation

The method of characterization is based on an inverse analysis technique. The objective is to fit some temperature curves associated to the different measurement technologies. The optimization of the numerical results has been performed using parameters of models implemented in thermal BC. In first approximation, these parameters were estimated from bibliography and a-priori characterization. Then, their optimization have been performed through several steps including sensitivity analysis and finally optimum finding.

Several FE models were build to reproduce the experiments. There are three different assembly configurations: Mold, Part-Frame and Mold-Part-Frame. There are presented in the Figure 3.57. The two first were computed through pure thermal analysis because the HT were not impacted by the parts deformations. The third model was used to model blowing and natural cooling experiment. Both cases involve thermal contact HT that are sensitive to pressure and gap evolution at the interface. Therefore, this model was computed with a coupled temperature displacement analysis. The definition of each model is briefly defined below from the thermal point of view. More details about the FEM and the implementation of such models are available in the Chapter 4 which is dedicated to the FE model developed for the industrial case.

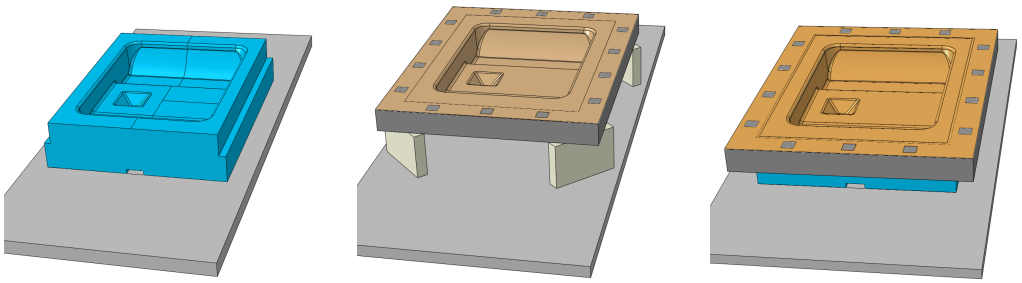

(a) (b) (c)

Figure 3.57 – Cad views of the models used for the inverse analyzes (a) Mold, (b) Part-Frame and (c) Mold-Part-Frame experiments

3.6.3.1 Mold experiment

The objective of the mold experiment is to characterize the radiative and convective BC models. A three steps characterization was performed to achieve an acceptable fit. The thermal boundary conditions for the model are presented below.

3.6.3.1.1 Model

❒ Radiation BC

The emissivity of the mold was taken at ϵ_{mold}=0.85 referring to emissivity computation based on camera and thermocouple comparisons in the Section 3.5. The emissivity of the shuttle's platen was fixed at 0.8.

❒ Convection BC

The Equation (3.58) with h_0=2.2 W.m^{-2}.K^{-1} and h_1=6 W.m^{-2}.K^{-1} is used for the convection coefficient of every surfaces.

❒ Conduction BC

The thermal conductance between mold and platen was fixed at 500 W.m^{-2}.K^{-1}. It corresponds to rough surfaces with stainless steel contact conditions at around 1 MPa which corresponds approximately to the stress promoted by gravity [211]. The material of the mold is a SP50 Aubert & Duval alloys with thermal conductivity around 10-25 W.m^{-2}.K^{-1} for in the temperature range of 20-900 °C, which is equivalent to SS304 used in the work of Milanez et al. [211].

The positions of the thermocouples are reminded in the Figure 3.58

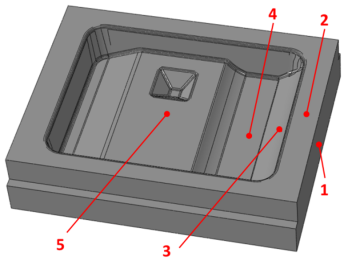

Figure 3.58 – Mold experiment: representation of the THC positions

3.6.3.1.2 Results: step 1

The Figure 3.59a shows a comparison between thermocouple data and model temperatures with a logarithmic time evolution. The Figures 3.59b and 3.59c represents respectively the evolution of the temperature difference Δ ($=T_{thc}$-T_{mod}) with logarithm of time and the temperature. The variations of the Δ curves show two type of behaviors. Firstly they have distinct types of variations during the 500 first seconds. Then every curves describes the same bell's shape that seems to correspond to a temperature dependency.

These observations indicates two possible errors in the definition of boundary conditions. The first temperature difference behaviors can come from an heterogeneous convection heat distribution on the surface. The second one suggests that there could have a variation of emissivity as a function of temperature. However, the homogeneity of the mold temperature does not enable to clearly distinguish the causes of these singularities.

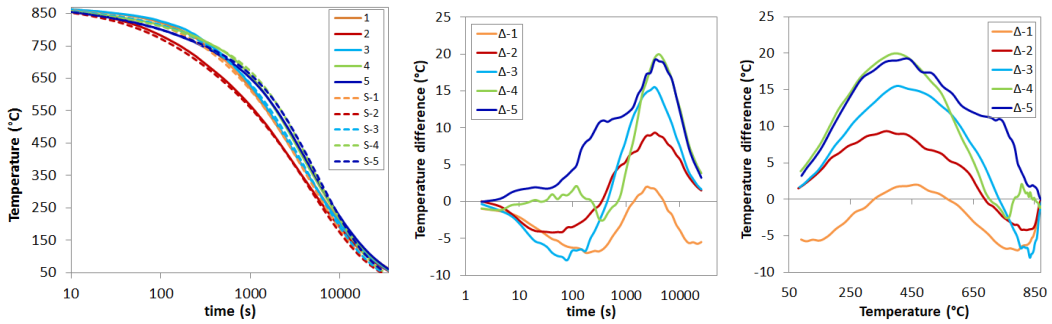

(a) (b) (c)

Figure 3.59 – Mold experiment: (a) temperature vs. log. time, temperature difference Δ as a function of (b) log. time and (c) temperature

3.6.3.1.3 Results: step 2

The strategy for the characterization of both the mold emissivity and the NCC evolution has been made into two steps. Firstly the sensitivity of both BC parameters were tested to evaluate their impacts independently. Then, the parameters were optimized. The testing values for mold emissivity were taken homogeneous and constant between 0.85 and 1 such as computed from camera and thermocouple data (Figure 3.35a). Concerning the convection model (plotted in the Figure 3.50c as a function of temperature), the temperature difference variations seem not to correspond to the model variations. However, a variation of the h_1 parameter of the model (Equation (3.58)) was tested to evaluate its influence.

The Figures 3.60 and 3.61 show respectively the temperature difference sensitivity to mold emissivity and the h_1 parameter of h_c model. The variation of the temperature difference is not reduced but rather transferred on the temperature axis during the variation of the NCC. On the contrary the mold emissivity seems to be the parameter that produce a change in the variation of curves shapes.

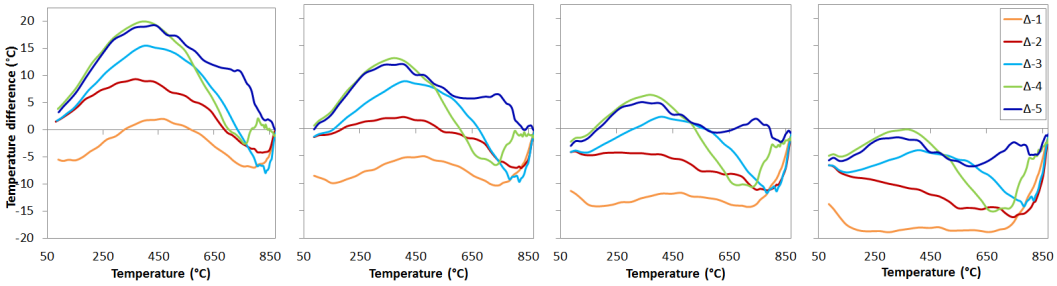

(a) (b) (c) (d)

Figure 3.60 – Temperature difference sensitivity with mold emissivity (a) 0.85, (b) 0.9, (c) 0.95, (d) 1

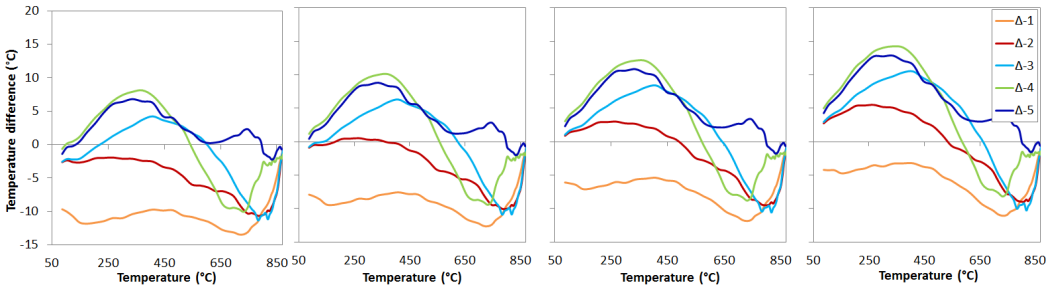

(a) (b) (c) (d)

Figure 3.61 – Temperature difference sensitivity to h_1 parameter of the h_c model (a) 6.15, (b) 5.65, (c) 5.15, (d) 4.65

3.6.3.1.4 Results: step 3

The emissivity curves computed in Section 3.35a give a specific tendency of the emissivity variation. The data are not available below 600 °C, yet the evolution seems to reach a plateau or even to reduce. Two different emissivity variations have been defined using the computed curves with a first increase and then a plateau or a decrease of the emissivity. The Figure 3.62 shows the Δ curves from these computations associated to emissivity variations. The results shows a improvement with the plateau based variation of emissivity.

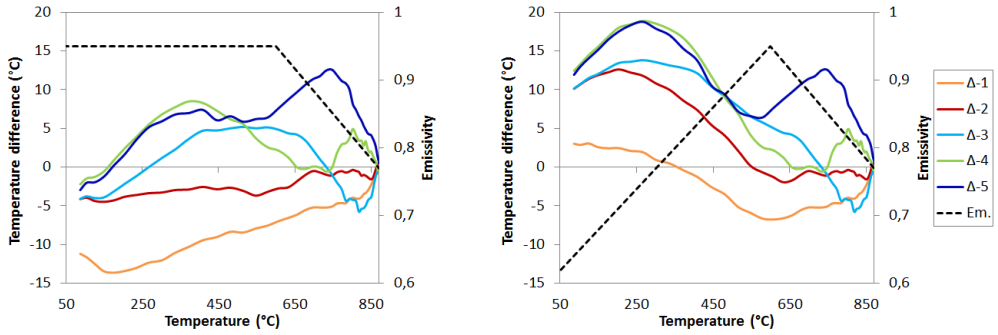

(a) (b)

Figure 3.62 – Temperature difference sensitivity to emissivity variation (a) plateau and (b) decreasing based emissivities

3.6.3.1.5 Discussion

The global results of the simulation are fairly in agreement with the thermocouples data. The higher sensitivity on emissivity highlight that a varying emissivity with temperature for the mold might be a better hypothesis. The emissivity computed from experimental camera and thermocouple measurement seems to give a good tendency. However, high temperature emissivity measurements should be performed to confirm. Indeed, this hypothesis may be actually the consequence of an other phenomenon.

Concerning natural convection, the CFD simulations give a good evolution of the average value of the NCC. However, the simplifications of the geometry may be at the origin of the observed deviation of the Δ curves. As for emissivity, this should be confirmed with simulations with the exact mold geometry.

Nevertheless, the temperature differences are contained in a gap smaller than more or less ten degrees on a simulation time of around twelve hours, which is satisfactory. However, the computation time for varying emissivity models is around ten times superior than the constant one. This is due to the radiosity matrix that need to be re-computed as a function of emissivity changes. For the rest of the inverse analysis computations, a constant and homogeneous value of emissivity (ϵ_{mold}=0,9) is taken with which the results are the best.

3.6.3.2 Part-Frame experiment

For this experiment, the principal HT happen through convection and radiation as for the Mold experiment. However, conduction HT occur at different interfaces. Each mode and the concerned surfaces is described below.

3.6.3.2.1 Model

❒ Radiation BC

The emissivity of frame have been taken equal to mold (refractory metal with highly oxidized surface). The part emissivity was considered constant with temperature and estimated at 0.85 from spectrometry measurements.

❒ Convection BC

The NCC model computed from CFD analysis are used for the first step of the characterization. Contrary to Mold experiment, NCC models have shown very different values and variations with time as a function of the surfaces. A simple global weighting function was used to scale the NCC model for the optimization.

❒ Conduction BC

Several conductances were defined at three different interfaces: ceramic bars-frame, ceramic bars-shuttle platen and frame-part. The two first were considered as constant contacting surface condition because of the weight of the frame and part assembly. On the contrary, a radiation based HT is considered for part-frame interface because the part deformations did not allow perfect contact at the interface. The convective part of gas-gap condition was neglected. The conductance coefficient of 500 $W.m^{-2}.K^{-1}$ was taken for frame-ceramic and ceramic-platen. A constant value of 100 $W.m^{-2}.K^{-1}$ was taken for the pressure based conductance for the part-frame interface.

The positions of the thermocouples are reminded in the Figure 3.63

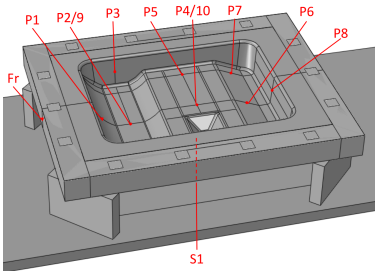

Figure 3.63 – Representation of the Part, Frame (Fr) and Shuttle (S) thermocouples

3.6.3.2.2 Results: step 1

The Figure 3.64a shows the comparison of experimental and numerical results of the step 1. There is a clear difference of the temperature variation of the frame and platen thermocouples with those of the part. The Figures 3.64b and 3.64c show the Δ curves for every thermocouples respectively as a function of time and temperature. As for the Mold experiment, the part thermocouples show a common bell's shape variation except for the frame and shuttle THC.

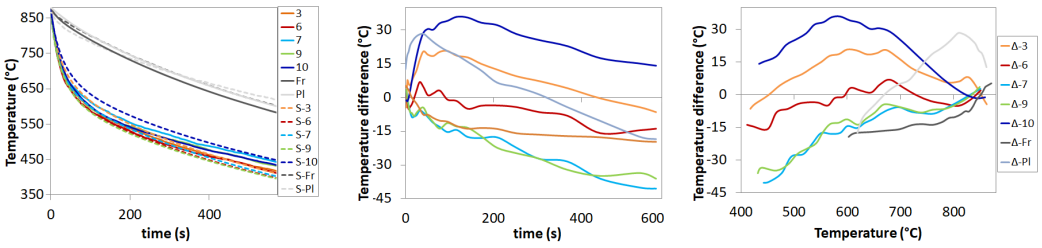

(a) **(b)** **(c)**

Figure 3.64 – Part-Frame experiment: (a) temperature vs. log. time, temperature difference Δ as a function of (b) log. time and (c) temperature

However, contrary to Mold experiment, the bell's shape variation seems to corresponds to a time evolution. Indeed, the platen thermocouple is not synchronized with the temperature in the Figure 3.64c. The origin of the shape of the temperature difference might rather come from convection phenomenon. Indeed, in the Section 3.5.3.1 the experimental results have shown a change in the cooling rate that seemed to come from a transition in the convection flow from a transient to a steady state.

The THC 9 and 10 are located on the bottom surface of the part. Their curves have different shapes while they have viewing factors at 0.96 and 0.965 respectively. Therefore, the difference comes most likely from the convection BC. The simplified geometry used for CFD analysis does not take account of part to plate distance which changes for both position for the real geometry. This may lead to a different convection flow and finally different HTC.

3.6.3.2.3 Results: step 2

So as for the Mold experiment, two sets of simulations with a variation of emissivity and NCC are tested to find the optimized parameters in a third time.

A explained above, a variable weighting function was applied on the CFD based h_c models. It is defined in the Equation (3.59) where h_{CFD} is the CFD-based NCC and α_h the parameter of the weighting function. α_h was tested with the values 0.4, 0.6 and 0.8. The Figure 3.65 gives the associated weighting function variation with time.

$$h_2 = h_{CFD} * (\alpha_h + (1 - \alpha_h)e^{-0.01t}) \tag{3.59}$$

The Figures 3.66 and 3.67 give respectively the temperature difference versus temperature for the emissivity and weighting coefficient variations. Increasing the emissivity seems to decrease the amplitude of the temperature difference, especially for the THC 10. The best results are obtained for ϵ=0.9. Concerning the weighting coefficient, decreasing the k_0 value seems to straighten up the temperature difference for THC 3, 6, 7 and 9 but no significant impact on THC 10 is observed. This correction corresponds to a decrease of the convection HT intensity such as observed on experimental curves in the Figure 3.64a.

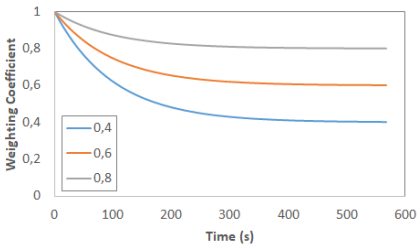

Figure 3.65 – Evolution of weighting coefficient

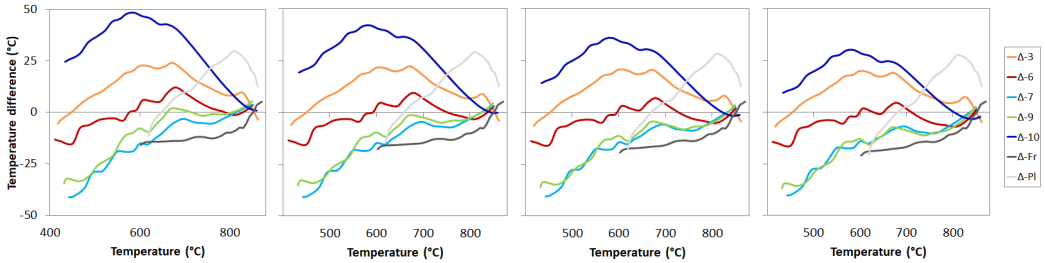

(a) ϵ_{part}=0.75 **(b)** ϵ_{part}=0.8 **(c)** ϵ_{part}=0.85 **(d)** ϵ_{part}=0.9

Figure 3.66 – Temperature difference sensitivity with part emissivity

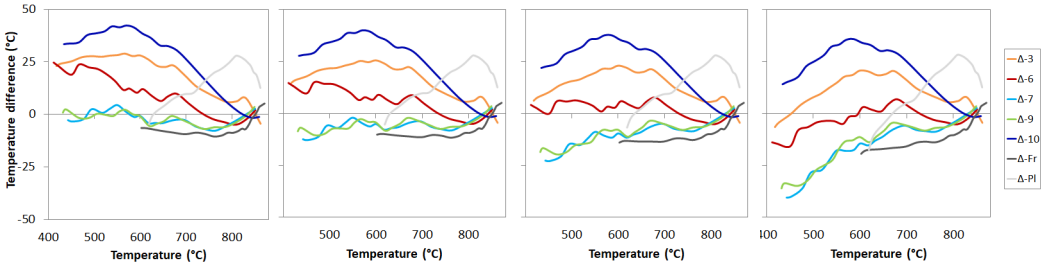

(a) k_0=0.4 **(b)** k_0=0.6 **(c)** k_0=0.8 **(d)** k_0=1

Figure 3.67 – Temperature difference sensitivity with NCC variation

3.6.3.2.4 Results: step 3

As for the mold experiment, a variable emissivity was tested with the best weighting coefficient (α_h=0.5). The Figure 3.68 gives the temperature difference curves for the optimized parameters.

The error is contained in a -10 °C and +30 °C. There might have been possible to improve the response of the numerical model to better fit the experimental curves. However, the optimization approach could not be reproduced in another case such as the industrial cooling. One important aspect has been to understand that the model is significantly sensitive to the emissivity changes during the cooling phase.

3.6.3.2.5 Discussion

Contrary to mold experiment, the sensitivity of the model to the emissivity at the thermocouple positions was rather limited. This might be due to the thermal radiation with the platen that would balance the radiative HT with environment at room temperature.

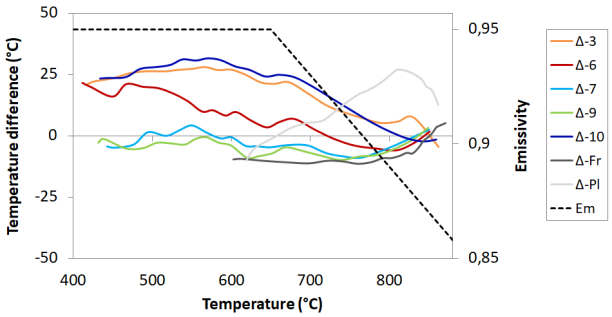

Figure 3.68 – Temperature difference for the optimized BC

Regarding NCC, the sensitivity is higher. The global temperature difference can be corrected by reducing the convection through the weighting coefficient. This means that the initial CFD based coefficients are not in good agreement. For example, when α_h=0.8, It seems to suit better for THC 6 while α_h=0.6 is better for THC 7 and 9. However, THC 6 and 7 belong to the top surface of part (as described in the Figure 3.54a) for which the NCC was defined homogeneous based on CFD results and simplifications. The corner effect of the confined zone of THC 6 compared to 7 should promote a NCC gradient. The same conclusion may be taken for THC 9 and 10 as explain above. The simplification of the geometry may be one reason of the obtained temperature differences.

The final simulation with varying emissivity seems in a good agreement with the experimental temperatures, but also with the emissivity variation shapes computed from experiment. This may confirms that oxidation occurs even after the heating time once the part is cooling down outside the furnace as discussed for Mold experiment. Indeed, the parts after forming were so oxidized that a cleaning was performed to remove the fragile oxide layer to ease THC welding. By doing so, an new oxide layer might have been created during the experiment. The increase of emissivity with oxidation for ti-64 has been demonstrated in the literature [169, 21].

3.6.4 Inverse analysis: forced convection and conductance

The objective of this experiment was to fit the forced convection and conductance models. A single blowing sequence was modeled. It is composed by three phases: natural cooling (16 s), blowing (28 s) and a final natural cooling (40 s).

A pure HT analysis was used in first approximation to estimate first sets of BC parameters. Then it was modeled with fully coupled thermal displacement analysis in order to consider the evolution of the contact conditions during the experiment. The material behavior was considered thermo-elastic and the initial contact with the mold taken perfect.

3.6.4.1 Model

❒ Radiation BC

For HT analysis, the cavity radiation BC, described in the Section 3.2.1.4, is used with a 0.9 homogeneous and constant emissivity for the part, mold and frame. For coupled analysis, ABAQUS® does not propose VF-based thermal radiation BC. To circumvent the problem, a radiative flux was imposed thanks to a previous HT analysis that was used to evaluate the VF and approximate temperature evolution, and finely the radiative heat flux. This method has been called "weak radiative" method (WRM). The Appendix B.2 explains how

it is implemented into the model. A comparative analysis is presented. The WRM gives relevant results and presents almost no differences on temperature fields compared to cavity BC for the tested case.

❒ Natural Convection BC

For this experiment, natural convection operates around 16 seconds before the activation of blow cooling, and 40 seconds after the end of blowing. During these periods, the convection flow have not the time to establish a steady state how it is computed with CFD modeling procedure. The convection have been considered homogeneous during the natural cooling phases. Exponential decreasing functions are used to model the transition phase from forced convection to natural. It is used after blowing, but also at the beginning of the experiment, when the shuttle is moving at 1 m.s^{-1} during 3 seconds. The Figure 3.69a represents schematically this evolution where the initial NCC value starts at 20 W.m^{-1}.K^{-1} and then goes to a "limit" value of 7.5 W.m^{-1}.K^{-1} such as obtained from CFD analysis at the beginning of Mold and Part-Frame experiments.

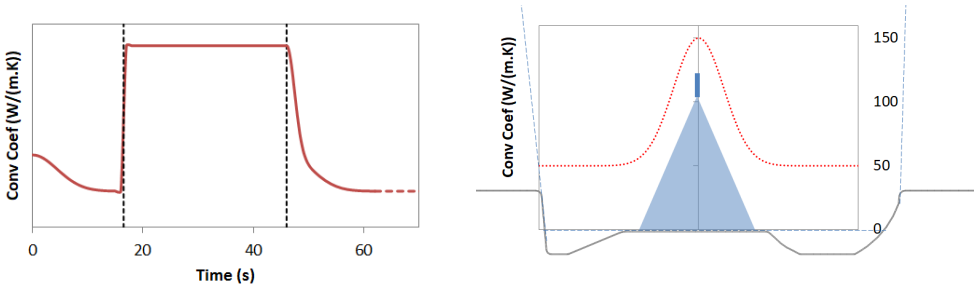

(a) **(b)**

Figure 3.69 – Schematic representation of the convection coefficient variation with (a) time and (b) space

❒ Forced Convection BC

The used model has been defined in the Section 3.2.3.4 and is reminded in the Equation (3.60). h_{fc_0}, h_{fc_1} and $k_{h_{fc}}$ are the parameters to fix. In a first approximation, they were fixed using literature [199] with h_{fc_0}=150 W.m^{-1}.K^{-1}, h_{fc_1}=50 W.m^{-1}.K^{-1} and $k_{h_{fc}}$=0.179.

$$h_{fc} = \begin{cases} h_{fc_1} & r \leq R \\ h_{fc_0} + (h_{fc_1} - h_{fc_0}) e^{-k_{h_{fc}}(\frac{r-R}{R})} & r > R \end{cases} \tag{3.60}$$

The Figure 3.69b represents schematically the superposition of a cutting view of the part and the curve of convection coefficient evolution. A reduced value of the residual forced convection is considered on the joint plane at 80% of the h_{fc_0} value.

❒ Conduction BC

The used model has been defined in the Section 3.2.4.5 and is reminded in the Equations (3.61) and (3.62) where the only parameter to characterize is k_0. Indeed, P_{ini} was fix to 0.01 MPa and P, δ and λ_{air} are respectively the contact pressure, the gap distance and the thermal conductivity of air.

$$\phi_c = \phi_{rad} + k_c \Delta T \tag{3.61}$$

$$k_c = \begin{cases} k_0 (P/P_{ini})^{0.95} & P > P_{ini} \\ k_0 & 0 < P \leq P_{ini} \\ \lambda_{air}/\delta(1 + k_0/\lambda_{air}) & \delta > 0 \end{cases} \tag{3.62}$$

It was not as obvious to evaluate the k_0 value from the literature. Indeed, the loading conditions, the materials, the surface quality or the temperature conditions made difficult to find out conductance data in the literature.

Therefore, the characterization has been achieved in three steps. The first step consisted in evaluating a k_0 value during the first natural cooling phase independently from forced convection model. Both pure HT and coupled analysis were performed to evaluate the impact of contact distance onto the temperatures.
Then, the whole experiment has been used to evaluate the three parameters of the forced convection model h_{fc_0}, h_{fc_1} and $k_{h_{fc}}$. A numerical design of experiments based on extrema values of the three parameters was performed using pure HT analysis.
Finally, a last step enabled to characterized optimized parameters for both conductance and forced convection models.

For the first natural cooling step, the THC data have been used while those of the camera for the rest of the experiment because of the detrimental influence of blow cooling on measurement as shown in the Section 3.5.4. The position of both are reminded in the Figures 3.70a and 3.70a. In addition, some points on two profile lines X and Y (referring to their directions) given in the Figure 3.70c were used to characterize the forced convection model. The two lines intersect at the impinging point of the nozzle.

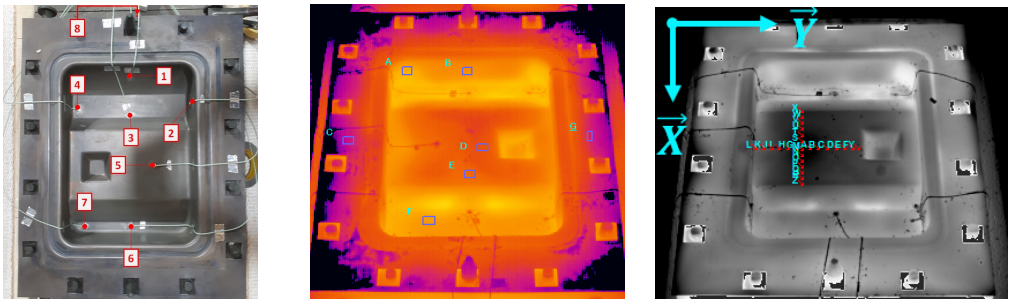

(a) **(b)** **(c)**

Figure 3.70 – Representation of the position of (a) the thermocouples and (b) camera measurement point and (c) camera profiles

3.6.4.2 Results: step 1

The Figure 3.71a shows the temperature evolution at thermocouples positions for data from the experiment and various k_0 values between 0 and 500 W.m^{-2}.K^{-1}. The curves seems to show a better fit for the low k_0 values in between 0 and 100 W.m^{-2}.K^{-1} except for the THC-7. It is located on a corner of the formed shape in a confined zone. The conclusions on the characterization of NCC for the Mold and Part-Frame experiments have highlighted the heterogeneity of coefficient that can be over-estimated for such confined zones. It is once more confirmed.

The Figures 3.71b and 3.71c respectively show the temperature and contact distance at thermocouples positions for the coupled simulations. In this case, the conductance model considered of the contact distance evolutions and the contact pressure (negligible in the experimental case). The difference of temperature compared with uncoupled analyses is almost zero. This is due to the limited contact distance generated during this phase of cooling (δ <0.2 mm). The k_0 sensitivity analysis performed on this first cooling phase has revealed that the conductive HT related to the k_c contribution seems rather limited

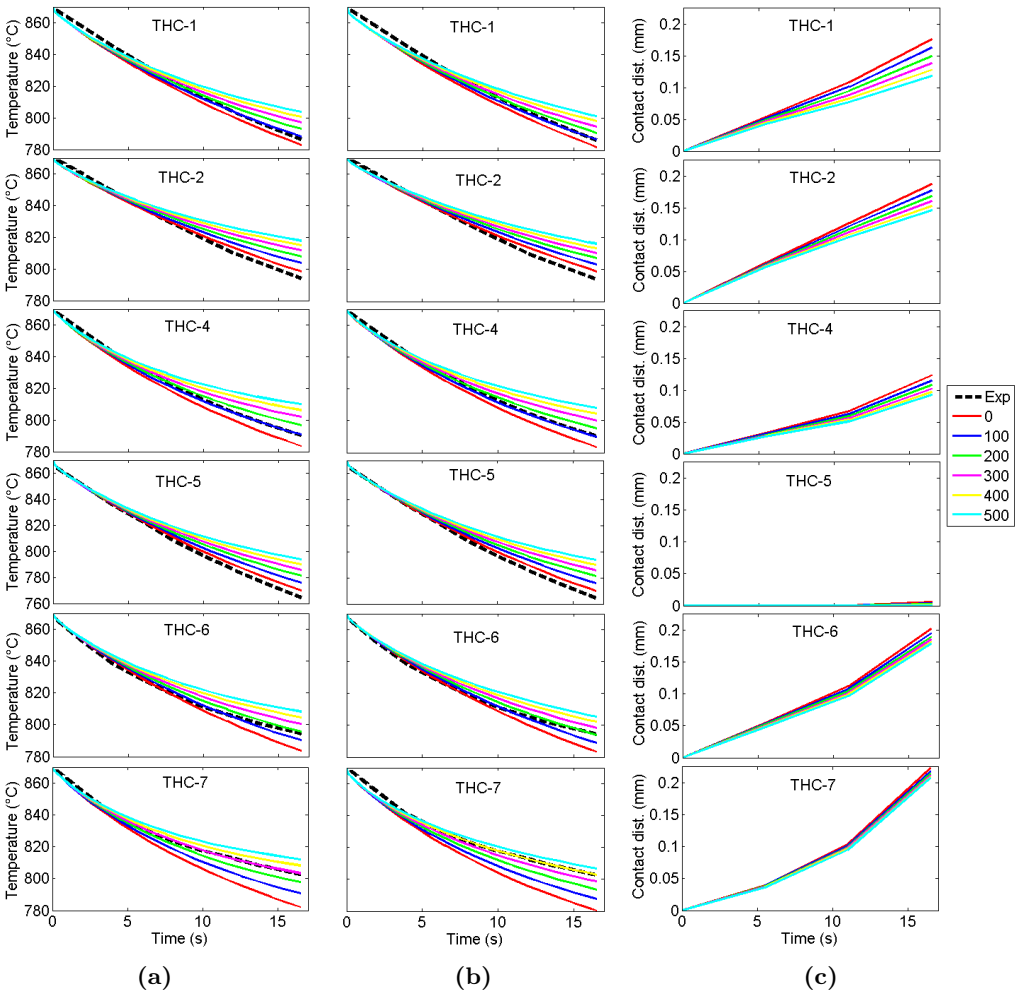

Figure 3.71 – Temperature evolution of thermocouples during STEP-1: effect of conductance coefficient (a) heat transfer and (b) coupled analysis, (c) contact distance evolution

3.6.4.3 Results: step 2

For the second phase, the complex coupling between forced convection and conduction models led to investigate it first through a simple design of experiments. The parameters of the forced convection model have been tested using two side values presented in the Table 3.3. These sets of test cases were computed with uncoupled HT analysis with two constant conductance values: 0 and 100 $W.m^{-2}.K^{-1}$. The HT analysis were used expecting that the conductance coefficient would be in between both tested values. Indeed, the result of the phase 1 simulations have shown that the conductance coefficient k_0 seems quite low in between the tested values 0 and 100 $W.m^{-2}.K^{-1}$.

Test case	1	2	3	4	5	6	7	8
h_{fc_0} ($W.m^{-1}.K^{-1}$)	50	50	100	50	100	50	100	100
h_{fc_1} ($W.m^{-1}.K^{-1}$)	150	150	150	250	150	250	250	250
$k_{h_{fc}}$ ($W.m^{-1}.K^{-1}$)	0.1	0.2	0.1	0.1	0.2	0.2	0.1	0.2

Table 3.3 – Design of experiments for the sensitivity analysis on forced convection coefficient model parameters (Equation (3.60))

Contrary to the first cooling phase, the simulation results are compared to the camera data because of the influence of cooling on measurement as explained in Section 3.5.4. The Figures 3.72a and 3.72b respectively show the comparisons of camera data and simulation for k_0=0 and k_0=100 W.m^{-2}.K^{-1}. There are one interesting point that stand out from these graphs. The case with k_0=0 W.m^{-2}.K^{-1} seems to suit better for the point CAM-B, CAM-D and CAM-E while the two others fit better for k_0=100 W.m^{-2}.K^{-1}. However, except for the cases 3, 5, 7 and 8 for which the cooling seems globally too high, the zero conductance seems to fit fairly better the experimental results. The previously mentioned cases are those with the high side value for h_{fc_0}.

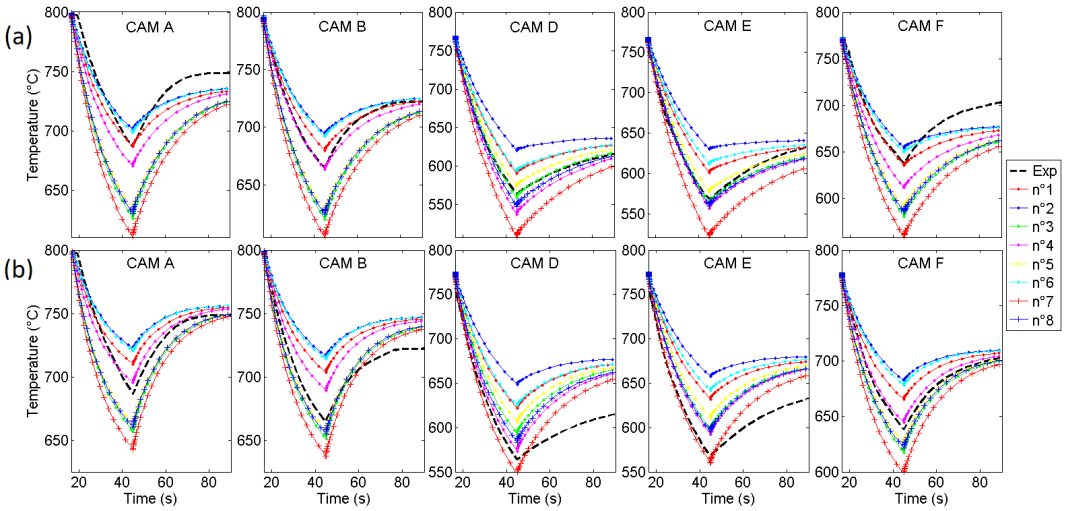

Figure 3.72 – Temperature curves at camera position: comparison of forced convection test cases with uncoupled analysis for (a) k_0=0 W.m^{-1}.K^{-1} and (b) k_0=100 W.m^{-1}.K^{-1}

The Figure 3.73 shows the comparisons of camera profile (Figure 3.70c) and simulation results at three times (t=[2,7,21] s) from the start of blowing for k_0=0 and k_0=100 W.m^{-2}.K^{-1}. The first thing to notice is that there are almost no difference between both k_0 value compared to camera points. There is no difference in the shape of the temperature profile but a slight change in the values. There are three cases that fit quite well the profiles: the cases 4, 7 and 8.

The global results of this design of experiments shows that the conductance between part and mold seems close to zero. This means that radiative HT in gap conductance is of the first order. The case 4 is the better configuration with the low side value of h_{fc_0} and $k_{h_{fc}}$ and the high side value for h_{fc_1}. Nevertheless, the convection intensity is over estimated for the camera points A and F. One possibility concerning CAM-F would be the plateau effect that limits the air flow for lower vertical positions as described in the Figure 3.74. Concerning CAM-A which is above the plateau plane, it is not easy to justify the difference. Else, the point A which is closed to the corner of the rectangular geometry might have produced a side effect that limit air flow compared to CAM-B position closed to the center of symmetry.

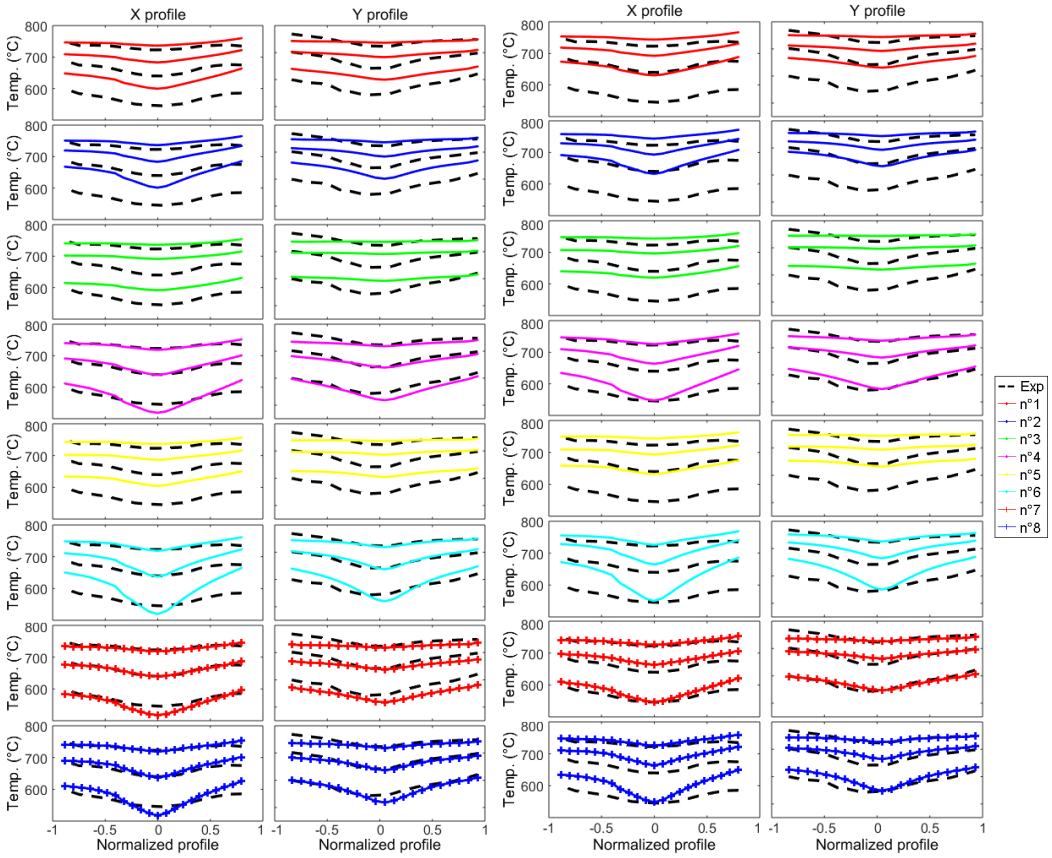

Figure 3.73 – Temperature profile at blowing times t=[2,7,21]s : comparison of forced convection test cases with uncoupled analysis for (a) k_0=0 W.m^{-1}.K^{-1} and (b) k_0=100 W.m^{-1}.K^{-1}

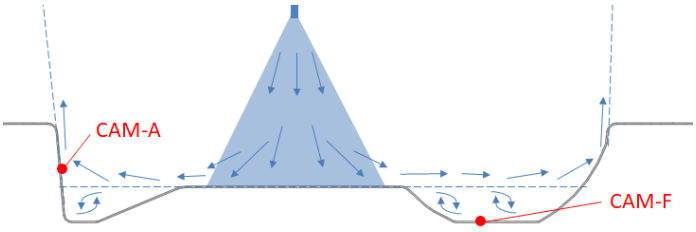

Figure 3.74 – Schematic representation of forced convection flow

3.6.4.4 Results: step 3

The last step of characterization consisted in optimizing the parameter of the test case 4. Indeed, there are several aspects that could be improved concerning the temperature profile and time evolution curves. Only the best optimized parameters and associated results are presented. The improvements consisted in:

- Decrease the $k_{h_{fc}}$ parameter to minimize the amplitude in the temperature profile curves.
- Implement a scaling factor that take account the plateau effect mentioned before as defined in the Equation (3.63) where α (=0.25), β (=1) and z_{plat} are respectively parameters of the model and the plateau vertical coordinate.
- Set h_{fc_0} and h_{fc_1} values
- Use k_0=0 W.m^{-2}.K^{-1} which means to consider only the gap radiation effect.

$$h_{fc2} = h_{fc} \begin{cases} 1 & z \geq z_{plat} \\ 1 - \alpha \left[1 - e^{-\beta(z - z_{plat})/z_{plat}}\right] & z < z_{plat} \end{cases} \tag{3.63}$$

The Figure 3.75 shows the temperature and contact distance evolution for the camera points. The opt and opt* curves are respectively the original data from simulation and the latest ones corrected with the temperature gap at the end of the blowing phase. Introducing the opt* curves enables to evaluate the post blowing phase freeing from previously induced error due to first natural cooling and forced convection. The results are fairly good for CAM B, D and E such as previously. Concerning CAM A and F, the cooling is still too much high. The contact distance should have shown a close gap at these two point which would promote conduction HT and slow down cooling such as observed experimentally. However it is the contrary, which either confirms that the contact HT is negligible (k_0=0 W.m^{-2}.K^{-1}), or that the computed contact distances is not representative of experimental ones.

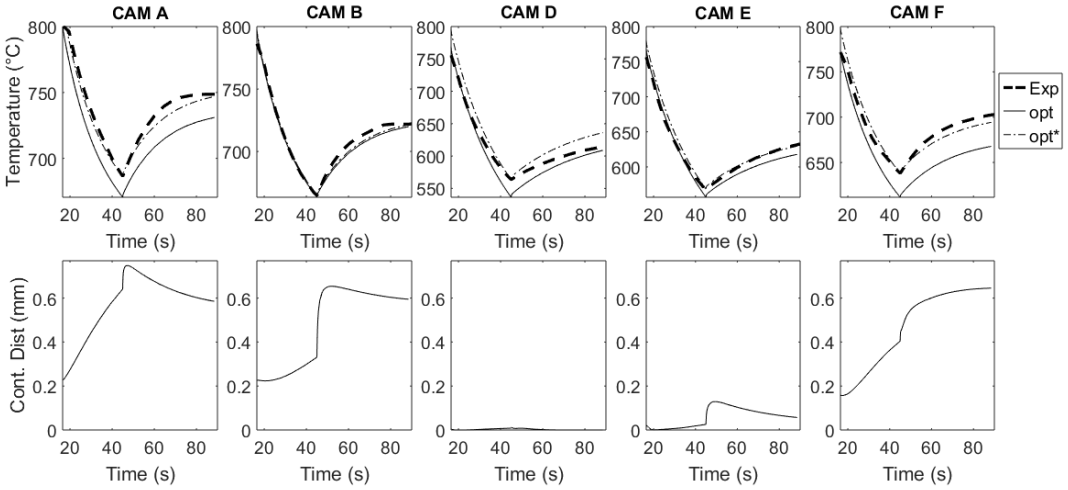

Figure 3.75 – Temperature curves at camera points for the optimized BC parameters

The profile curves shown in the Figure 3.76 still have a high amplitude especially for the last time on X profile. However, the temperature difference does not exceed 30 °C which remains acceptable for such hard cooling conditions.

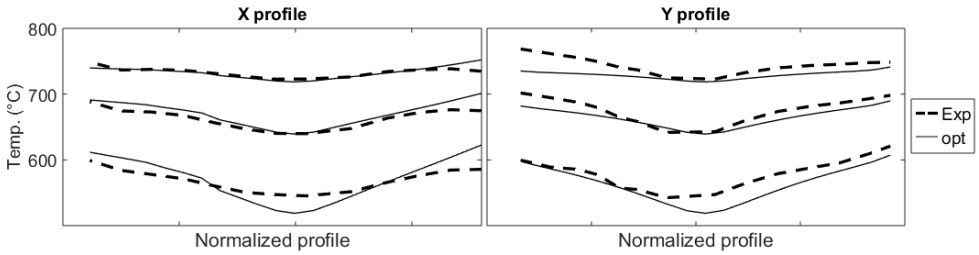

Figure 3.76 – Temperature profiles for the optimized BC parameters

3.6.4.5 Discussion

This experiment is used to characterize the conductance and the forced convection model. Both associated BC models have been characterized and gave an acceptable fit of experiment data. However, it remains some non-negligible differences that might happen or even be amplified in the industrial process conditions.

It may be due to uncertainties concerning the hypothesis taken for the experiments and the models especially regarding contact HT that affect consequently the cooling induced by forced convection. Indeed, the formed part has been considered in perfect contact conditions at the beginning of the experiments. This was verified for the design experiment (see in the Appendix B.1). However, it has undergone successive cooling and removing operations after forming which may promote deformations. That is why the initial contact condition might have been heterogeneous at the start of the tests contrary to those used numerically.

In addition, a constant and homogeneous emissivity has been considered during the simulation. However, the effect of blowing might have increased the oxidation rate and finally the emissivity distribution of the part. It was observed that some chips of oxide layer peeled away from the part surface in the impinging zone. The thickness of these chips was bigger than for the rest of the surface.

It is not easy to characterize simultaneously two phenomena which interact with each other. In our case, it is also complex because natural convection and thermal radiation are not perfectly described. Finally, it is even more complex when the contact condition at the interface might have not been well described at the beginning but also during the simulation. Indeed, the deformation of the part is a consequence of the material behavior (supposed thermo-elastic) and the cooling conditions that are dependent of the deformations. It would have been better to carry out the blowing operation independently of the sheet-mold contact, with the mold only for example. Then, it would have been easier to characterize the conductance model.

3.6.5 Validation: Mold-Part-Frame experiment

The definition of the model for the validation experiments is exactly the same than for the blowing experiment except for the forced convection BC. No CFD analysis were performed for this experiment. Indeed, the geometrical configuration of the experiment is near from the Mold and the Part-Frame experiments. Therefore both convection model have been used and compared. In addition, a value of ϵ_{BN}=0.65 referring to the measured emissivity seen in the Figure 3.47b was used to simulate the Mold-Part-Frame experiment with BN coating.

The Figure 3.77 gives the comparison of the experimental data and the model for the Mold-based and Part-Frame-based NCC for the simulation with and without BN coating.

The results are better for the experiment without BN coating. It is probably due to the part emissivity value that comes from BC characterization. Indeed, except for the THC 5

which has an significant gap (around 80 to 100 °C), the other are contained into more or less 25 °C degrees for the Mold-based NCC. The Part-Frame based NCC model gave slightly worst results than Mold based configuration. This is probably due to absence of the mold in the case of Part-Frame configuration that produced a convection flow too far from the Part-Mold-Frame configuration.

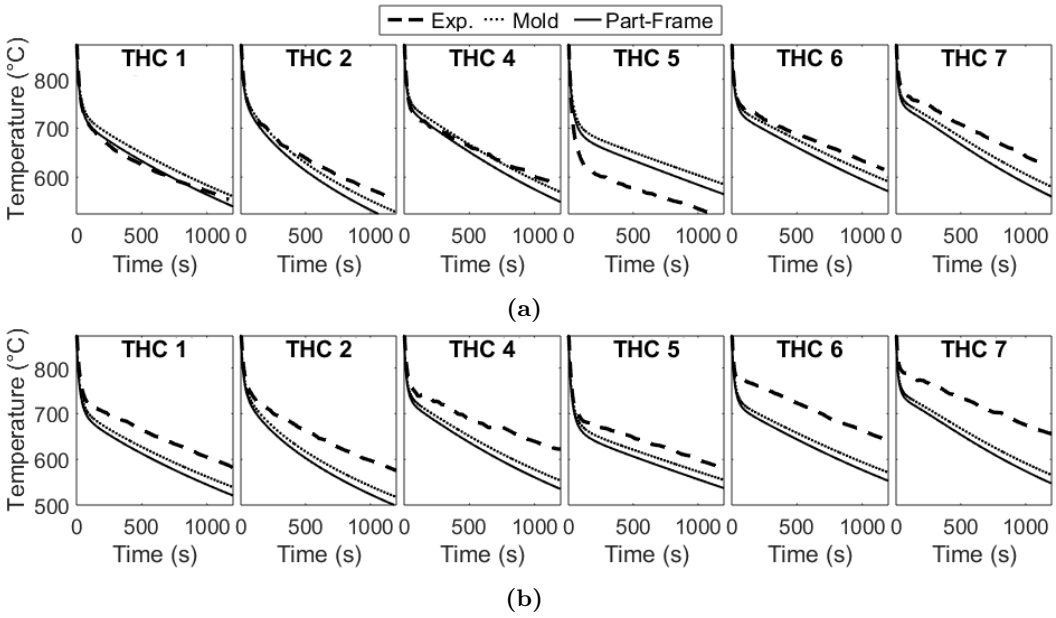

Figure 3.77 – Temperature evolution at thermocouples position for the validation experiment: comparison of the CFD-based NCC from Mold and Part-Frame experiment (a) without BN and (b) with BN

For the experiment with BN coating, the temperature curves are globally farer than the other experiment. They are two types of temperature behavior. The THC 1, 2 and 4 seems to have a varying error that growths as a parabola, while the others have an obvious constant or linearly varying error from the first seconds of the test. However there is no correlation between their positions and the difference in the behavior that can indicate an error in the affected boundary conditions. Indeed, the THC 4 and 7 are located in a corner in a confined zone for which radiative and convective HT are likely to be equivalent. The THC 5 and THC 6 and 7 are totally different in their positioning and their associated radiative and convective BC. However their behaviors are not consistent.

3.6.6 Discussion

The use of the characterized BC have given fairly good results, particularly using parameters which were not totally adapted to the validation configuration, especially for the NCC models. In addition, the successive experiments on the part had probably produced an evolution of surface properties for emissivity, but also deformation that had modified the initial contact conditions for conduction HT.

The BN painting used for our experiment that was placed before the test on a cleaned surface was different than the one applied in AIRBUS. This might indicate that both coating have not the same properties. Indeed, the BN coating seems to limit the cooling rate compared to the simulation computed with the value obtained from emissivity measurement on AIRBUS coating.

3.7 Conclusion

The objective of the chapter was to characterize the HT in the process conditions so that to defined models for the thermal BC through the h_c, k_c and ϵ parameters. This objective is aligned with the global objective of the thesis. Indeed, the thermal BC have been defined to be part of the thermomechanical model in order to reproduce the impact of cooling and part removing phase on residual stresses and geometrical distortions of SPF parts.

A small scale industrial SPF tooling was chosen for the characterization to be as closed as possible than the industrial conditions. Indeed, there is a high variability of HT conditions such as contact conditions, convective flow and surface conditions for radiations. It would have been difficult to perform consistent laboratory characterization transferable to industrial simulations. The SPF tooling was composed by a forming die, a top die and an extraction frame in order to reproduce the exact process conditions. Several parts were formed on an industrial press in AIRBUS and some of them used for further experiments in a laboratory furnace to test various cooling conditions.

Several cooling experiments in a SPF type furnace were performed in various conditions to uncoupled HT modes and ease the BC characterization. A movable shuttle was used to pass from the furnace to an ambient cooling environment. Thermocouples and non-contact measurements such as pyroreflectometer and infra-red camera were used to perform thermal measurement during the experiments. The next configurations were tested: the mold only (Mold), the part and the frame in elevated position to reduce the ambient cooling step of the process (Part-Frame), the mold with the part and the frame (Mold-Part-Frame). A first experiment with the mold and a part was used to implement and validate the measurement means in the operating conditions. The Mold and Part-Frame experiments were used for convection and radiation BC characterization because no first order contact HT was involved. Then, the Mold-Part-Frame configuration was used first with a blowing system with an industrial nozzle to reproduce forced convection step. This experiment was used to characterize both the forced convection and conductance models. Then it was used to evaluate the validity of the thermal BC previously characterized with two coating conditions (with and without BN coating). A last experiment which consisted in reproducing the part removing operation was performed but no usable thermal measurement were obtained. Additional spectrometry measurements were performed in different post SPF surface conditions to get emissivity data for thermal radiation.

Inverse analyses were used with FE models of the experiments to characterized BC models. For radiation BC, a full radiative computation including view factors computation based on grey-body radiation theory was used with the emissivity as the parameter to optimize. Concerning, natural convection HT, none existing analytical correlation might be used in the SPF context with high temperature external natural convection flow. CFD analyses were performed for both Mold and Part-Frame configurations. Convection coefficient models were defined using simple constant, linear of bi-linear function of space from CFD simulation results. The forced convection model was taken from the literature. Finally a radiative-convective-conductive model was adapted from the literature. A tabular definition was adopted using a single parameter for convective-conductive contribution and the emissivity of parts for near contact radiation HT.

The characterization of parameters of the BC models were performed in several steps. Indeed, a first step consisted in testing the literature and a-priori characterization based parameters. Then a second step consisted in a sensitivity analysis of the involved parameters. Despite the fact several configurations were used to uncouple as much as possible the HT modes, the effect of parameters was not trivial. A final step was used to find optimum parameters for the models. The methodology and obtained values of BC models were applied to the Part-Mold-Frame experiment to evaluate their validity in an experiment with all mixed modes of HT.

The global results of the characterization was fairly good for the Mold and Part-Frame experiment for which dedicated CFD analyzes were performed. The best results with optimized BC are obtained with a varying emissivity. However, the initial CFD based parameter did not give a perfect fit, especially for Part-Frame experiment which is the complex one in terms of fluid flow. Indeed, the geometry simplifications or the simplification of the CFD model itself might have generated errors.
For the blowing test, a conductance model without gas-gap conduction and only contact radiation HT enables to give good results. However, the initial contact conditions at the beginning of the experiment are questionable due to the multiple heating-cooling phases undergone by the part. In addition, the in-contact conditions (ie. with positive pressure) of the conductance model have not been really involved, only through the gravity effect. However, the industrial conditions are harder when parts clamp onto the mold during blow cooling for example. Thus, conductive HT may be erroneous in this case. Nevertheless, during industrial cooling the part and mold are in contact inside the furnace where the radiative HT are totally different. The high temperature inside furnace environment preserves from cooling so that the temperature difference is rather limited such as the potential conductive HT errors until blowing phase.
The validation case gave acceptable results but with significant temperature gaps especially in the case with BN coating. It might comes from a combination of errors such as heterogeneous emissivity and convection and also initial contact conditions that are not well described in the model.

To conclude, the thermal boundary conditions input in the models gave fairly good results. However, some points may be improves regarding the methodology and modeling hypotheses:

- CFD analyzes should be performed without geometrical simplification. A compressible conditions should be tested to evaluate the influence of density variations for such high temperature turbulent convection cases.
- Two distinct experiments should be performed to characterize forced convection and conductance models. Using the mold configuration would be better for blow cooling test and a dedicated tests with well-known initial conditions for conductance test.
- The simulation of the different cooling operations undergone by the part using the thermo-elastic-viscoplastic model characterized in the Chapter 2 should help to better reproduce the initial contact conditions of experimental tests.
- Concerning the possible heterogeneity of emissivity, an additional characterization might be performed at several strain levels to evaluate a possible correlation with oxidation or alpha-case layer, and finally the emissivity.

Chapter

4

Simulation of the process

4.1 Introduction

4.1.1 Context

The aim of using FEM analysis of the process is to tackle the complex issues that are not possible to solve plainly, with experimental or analytical methods. Moreover, it can be a

mean to reduce experimental campaigns that may be long and expensive. The most critical issue regarding SPF concerns the sheet metal working operations that are required to fit part geometry into assembly tolerances. This issue may be a consequence of several possible causes:

- The cooling procedure: there is no analytical or numerical approach to determine the ideal cooling strategy to adopt (the blowing zones, the blowing time, the sequence, etc.). It is empirically defined activating or deactivating nozzle such as represented in yellow in the Figure 4.1a
- The extraction procedure: two strategies are regularly tested with the handling robot. The robot either imposes a vertical effort impulse up to a target value and maintains the force or it removes the effort between each iteration. The effort is transmitted through the frame thanks to four arms at each lateral side as represented in purple in the Figure 4.1a. The Figure 4.1b shows the force evolution during a four maintained impulses extraction procedure applied after the forming of a nacelle of air inlet of the A350-1000 plane.
- Handling frame fastening: the part is fixed on the frame before forming through laser cut holes and cotter pins that block the vertical displacement such as shown in the Figure 4.1c. Some other holes in which obstacles fill into, limit the part flowing in the perpendicular direction to the frame profile especially during the forming step.
- Handling frame deformations: the frame used to extract the part thanks to the handling robot deforms through the thermo-mechanical stress undergone during the repeated processes.
- The degradation of parts conformity during batches: the first parts are produced with no major problems while, it is more and more difficult to remove parts from the mold throughout the rest of the batches.

The scope of the project is limited to the study of the impact of cooling and unloading (C&U) procedure. Indeed, the cooling strategy, if optimized, is supposed to ease part removal operation. Thus, every other issues can be partly or totally solved. Indeed, the degradation of production such as to frame deformations are probably due to the high stresses promoted by friction between the part and the mold. In both cases, the boron nitride (BN) lubricant may debase and consequently increase friction and the induced stresses during the part removing operation.

One major issue concerning the simulation purpose is the absence of experimental data to compare with. Indeed, no real traceability of part distortions associated to key process parameters have ever been performed in AIRBUS plant because of the difficulty to evaluate the distortions from geometrical measurements. There are many temperature measurements in the furnace itself, and also at some positions inside the dies. They are used to allow the beginning of forming cycles that require a specific temperature range for superplasticity. However, these data concerns positions too far from the surface, and does not enables to compare with temperature field from the simulation.

The only data that can be used for comparison of the numerical and experimental results come from the pulling robot. The Figure 4.1b shows typical pulling force evolution during multi-pulse removing operations of the nacelles of air inlet for the A350-1000 plane.

This curve concentrates a very large amount of information. Indeed, the evolution of the force after each iteration is the consequence of the stress relaxation and therefore of the material behavior. The material properties are strongly dependent on the evolution of the temperature, and so, on the thermal exchanges undergone during the cooling procedure. Then, the number of iterations is necessarily a consequence of the general deformation of the part and the components of friction forces (adhesion) which oppose to the extraction.

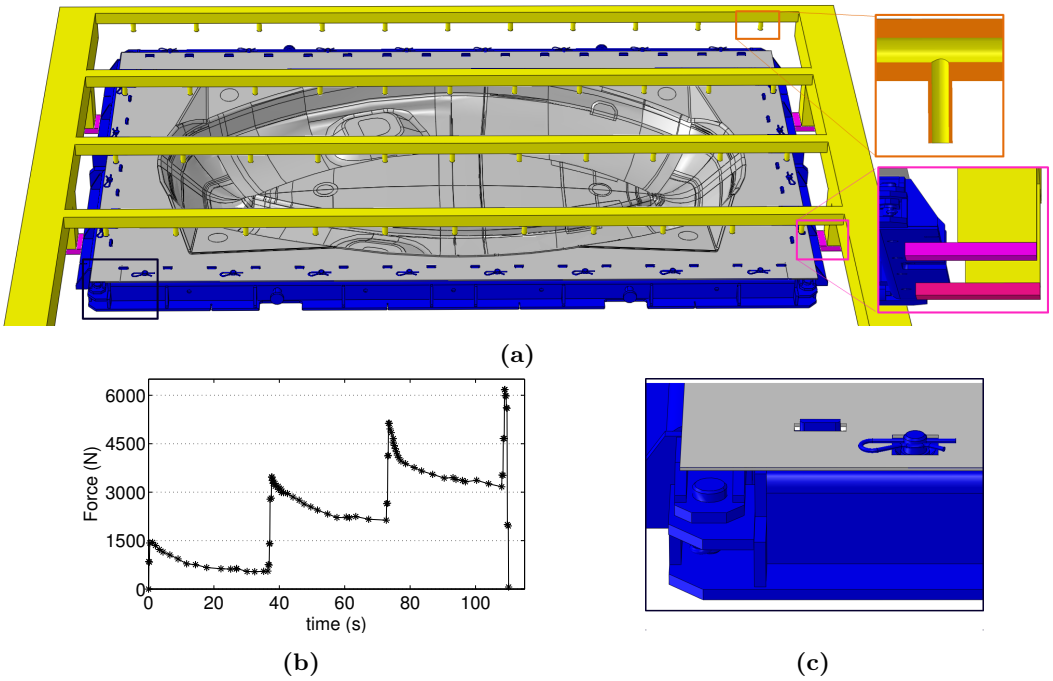

Figure 4.1 – (a) cad view representing the part, frame and handling robot environment, (b) curve of the pulling force vs. time during extraction sequence of a A350-1000 nacelles of air inlet and (c) zoom on the frame-part fastening

In the example of the Figure 4.1b, the part required four pulse to be removed from the mold. The difficulty of removing the part from the mold is experimentally analyzed by the number of pulse iteration. The average number of pulses needed to extract the part is around two or three which corresponds to 3000-4500 N. However, it can change according to numerous parameters that may come from BN lubricant degradation throughout batches, but also from the accumulated variability involved in the process such as blank thickness tolerances ($\pm 10\%$) or the temperature heterogeneity, and so on. The only certainty is that shop floor operators and sheet metal workers confirm that the changes in the cooling procedure significantly influence the final distortions.

4.1.2 Problematic and objectives

The problematic of this chapter can be summarized into a single question:
Which thermomechanical FE model has to be implemented in order to optimize the cooling strategy ?

This problematic gives rise to several objectives:

- The first objective consists in implementing a FE model that enables to reproduce the effect of the process parameters on the distortions of part through the transposition of the industrial HT and mechanical conditions into numerical boundary conditions.
- The second objective is to develop a method to optimize the cooling strategy so that to minimize final distortions after the trimming operation.

4.1.3 Strategy

The process modeling is applied on an industrial part: a portion of the nacelles of the air inlet of A350-900 reactors such as presented in the Figure 4.2a.

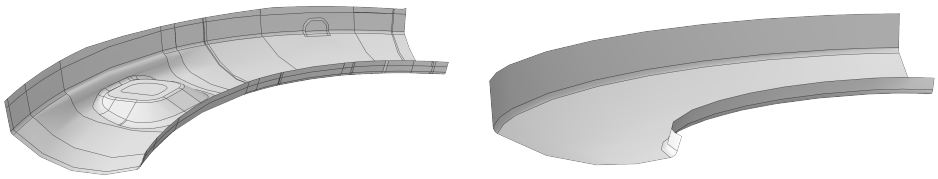

(a) **(b)**

Figure 4.2 – CAD views of air inlet geometry: (a) industrial part, (b) simplified geometry

In the first part of the chapter, the FE model is fully described, the mechanical BC, the contact interactions and the adaptation of the thermal BC characterized in the Chapter 3 for the industrial process environment.

Secondly, the results of the model are presented for the cooling strategy used in the shopfloor. The evolution of thermo-mechanical quantities is depicted for each part of the model during the whole process simulation. The pulling force and distortions are discussed. The confrontation of the force curves resulting from the simulation with experimental one suggested that some of the numerical parameters might generate errors in the evolution of the pulling effort which is a reference indicator.

Then, a simplified model is used to analyze the sensitivity of the model parameters impacting the effort curve: the numerical contact damping tool and the friction parameter. Indeed, the numerical damping which is required for the convergence of the high non-linearity of such process simulation. The model uses a simplified geometry presented in the Figure 4.2b and some simplifications of the industrial process. This analysis demonstrates a strong effect of the numerical contact damping that may be detrimental for the solution in terms of efforts and deformations generated by the C&U procedure. Then the effect of the contact control is tested on the industrial geometry.

On the basis of these results, an optimization of the cooling strategy is carried out on the simplified model. The parameters of this optimization are the blowing time, and the affected zones. Different combinations have been tested and the analysis of the force curves and the part deformations is made. This study is carried out for different data setting cases. Two contact damping conditions are used so as to assess the impact of this very sensitive parameter on the optimization results. Moreover, two part-frame clamping conditions are tested: either fixed or plane displacement free conditions. Indeed, both fastening conditions corresponds to the simplifications of the industrial conditions.

Finally, a discussion is proposed regarding to the model, the optimized strategy, and the investigations to perform in order to improve the model and the process.

4.2 Description of the model

4.2.1 Modeling procedure

The numerical procedure that has been employed to reproduce the process is composed by three different resolution schemes which correspond to particular thermomechanical conditions. Indeed, it is composed first by the SPF step which is computed with an isothermal viscoplastic numerical model. Then the whole C&U step is computed with a fully coupled temperature displacement procedure with a viscoplastic integration scheme. Finally the trimming is computed with a static procedure considering that no viscoplastic phenomena occur during this operation. These three procedures are described in the next paragraphs.

4.2.1.1 SPF

The SPF process simulation is performed considering a homogeneous and constant temperature of 870 °C. The mold is considered rigid. The airtightness is ensured by a closing effort applied on the upper die which is transmitted to a sealing seam at the dies interface. This is traduced by a zero horizontal displacement which is imposed to the blank. The forming pressure is applied on the superior surface located inside sealing zone. The process is finished once the whole die surface is filled by the sheet metal.

The step is computed thanks to *Visco step resolution scheme on ABAQUS® [212] which solve a large deformation problem. A symmetrical configuration is used such as shown in the Figure 4.3a which represents half of the real geometries. The die is considered rigid. A Norton Hoff material model (Power law model [212]) is used. A Coulomb's friction law (μ=0.1) is implemented through a penalty contact algorithm. The pressure evolution is computed thanks classical pressure band algorithm proposed by ABAQUS® [212] coupled with a statistical strategy developed by Rollin et al. [60]

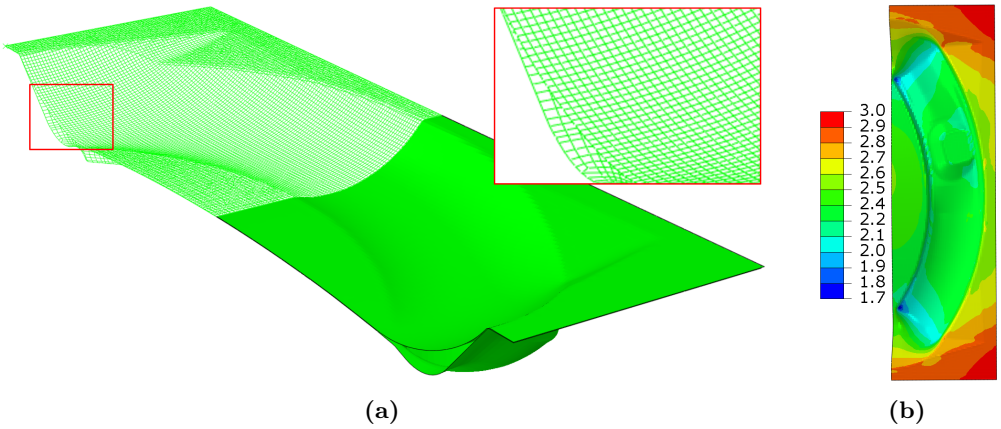

Figure 4.3 – SPF model: (a) meshed geometries, (b) thickness field (mm)

The SPF model is not much detailed in the manuscript. The mechanical equations and numerical solving method are an exception of the one presented below concerning the coupled temperature-displacement model. The thickness field (shown in the Figure 4.3b) is extracted from nodal position of the final mesh. It is then transferred onto the mesh of C&U simulation.

4.2.1.2 Cooling & Unloading

The different phases that composed part removing operation are divided in sub-step that are defined by thermal and mechanical BC variations. The evolution of thermal BC have been described in the Section 1.1.1 and reminded hereafter. The Figure 4.4 shows CAD views of both inside and outside configurations of the process:

1. The press' door opening: the initial steady state conditions (considered homogeneous at the forming temperature - 870°C) move to an open-cavity-based convection and radiation type.
2. The air blowing: the multi-jet blowing induced thanks to the robot (in yellow) is modeled through a forced convection BC activated during a specific time (around 30 seconds).
3. The extraction effort: the handling robot (in yellow) applies an effort onto the frame (in blue) in Z-axis direction thanks to four handling arms (in purple) located 2-by-2 at both sides of the frame. The robot induces a constant speed until a maximum force instruction.

4. The transfer: the part is transferred outside the press once it is removed from the mold. The air blowing is stopped. The convection and radiation heat transfers pass from warm open cavity to external natural based cooling conditions.

5. The ambient cooling: the part with the frame cooled down to the ambient temperature (right side of the Figure 4.4).

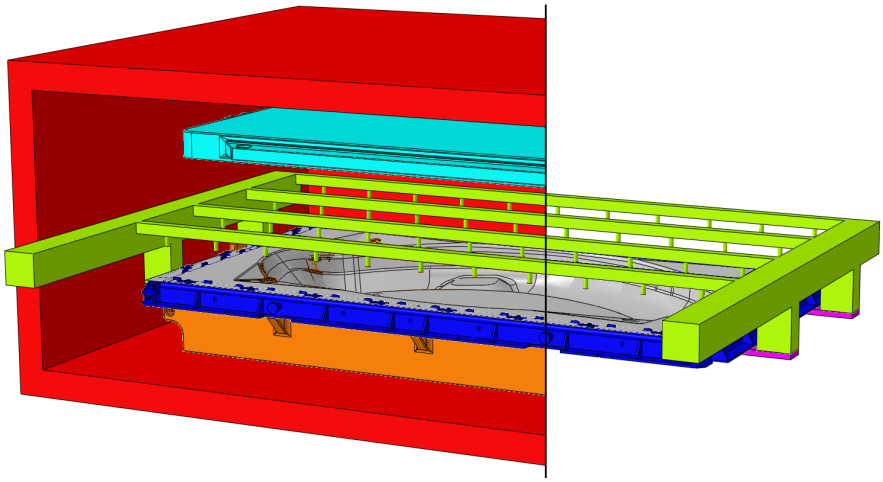

Figure 4.4 – Cooling and removing operation: 3D cad view with steps l to 3 (left side) and steps 4 and 5 at (right side)

The mechanical BC mainly resides in the contact conditions, the connections between the part and the frame and the way that the extraction effort is applied on the frame to extract the part.

At the beginning of cooling, the contact between part-tool and part-frame is supposed to be perfect with zero gap and small pressure induced by gravity. The temperature of the mold, the part, and the frame is considered at SPF target temperature. In reality, the frame is probably at a lower temperature because it is heated thanks to radiant heaters and it does not receive the conductive flux from platen contrary to dies.

The whole cooling and unloading steps are computed with strong temperature displacement coupling to take account of the evolution of contact conditions at part-mold interface during cooling. The different HT are imposed trough variable HTC and limit temperatures that take part into BC equations. The material model obtained from characterization described in the Chapter 3 is implemented through a CREEP user subroutine. This ABAQUS® subroutine proposes to define viscoplastic strain increment as a function of temperature, strain, effective stress and some other parameters like user state variables [213].

4.2.1.3 Trimming

The trimming operation is performed with laser or plasma cutting machines. Numerically, it is performed by element set removing and static equilibrium computation to evaluate the stress relief. The Figure 4.5 shows the CAD geometries before and after the element set removing. The hypothesis that the heat produced by the process has no influence on residual stress is taken. Moreover, it has been considered that no plasticity occurs during stress relief so that static step resolution scheme is valid.

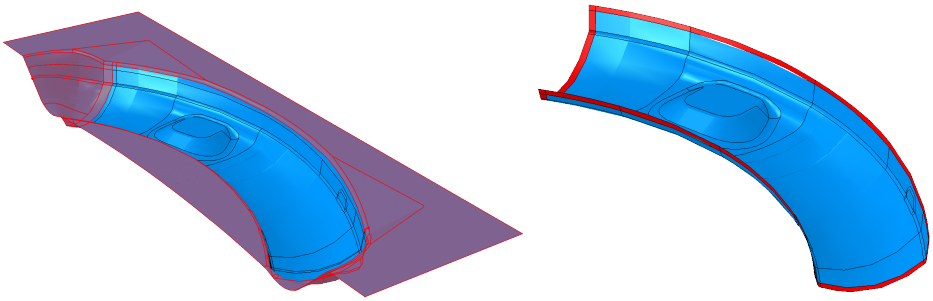

(a) (b)

Figure 4.5 – CAD views of the SPF part: (a) before, (b) after the trimming step

4.2.2 Problem and geometries simplifications

4.2.2.1 Problem simplifications

In the simulation of the C&U process, the system evolves when the part is transferred from inside to outside the press. Indeed, the surrounding environment switches from a hot press to an exterior environment at the workshop temperature. In addition the mold and its interactions with the part are removed. Both configuration of the system are presented in the Figures 4.6a and 4.6b. The colors used in these schematic representations refer to the colors of the Figure 4.4.

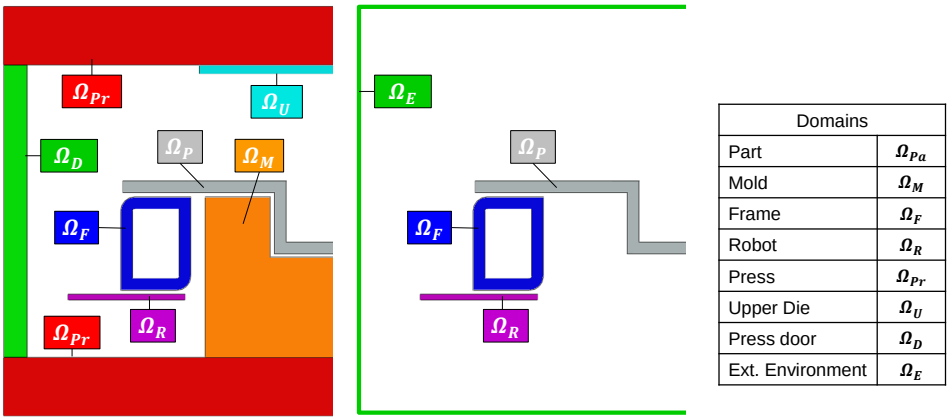

Domains	
Part	Ω_{Pa}
Mold	Ω_M
Frame	Ω_F
Robot	Ω_R
Press	Ω_{Pr}
Upper Die	Ω_U
Press door	Ω_D
Ext. Environment	Ω_E

(a) (b)

Figure 4.6 – Domains definition: (a) inside, (b) outside the press' configurations

The different domains defined in both figures are not all considered in the simulation as solid parts but some of them are simply taken into account through boundary conditions. Indeed, the domains that are included in the simulation are represented in the Figures 4.7a and 4.7b for the inside and outside configurations respectively.

The press and the upper die are not modeled in the simulation because their interactions with the part are supposed unaffected by the C&U process. Actually, it is not the case. Indeed, the exchanges through the open door and with the cold air brought during the blowing operations affect the temperature distribution of the press and the upper die. However, their range of temperature variations are fairly low compared to the part because they are refractory concrete and steel materials that resist to the temperature changes.

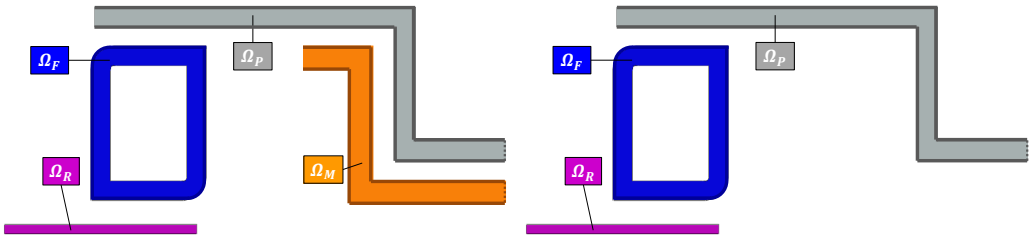

(a) **(b)**

Figure 4.7 – Domains definition after simplifications: (a) inside, (b) outside the press' configurations

The Figure 4.8 gives the variation of the averaged temperatures of the control thermocouples used in the tooling and the press during a complete forming sequence (loading, heating, forming, cooling and unloading). The temperature of the upper die has almost no variation while the range of the lower die and the platen is of 30 degrees. Moreover, the platen thermocouples are located closed to the heating elements included in the platens which generates a higher temperature range. However, the temperature at the surface of the press which is involved in the heat transfers is lower. Therefore, they are directly considered in the simulation trough the thermal radiation BC, and indirectly in the convective BC with homogeneous temperature taken from the experimental curves.

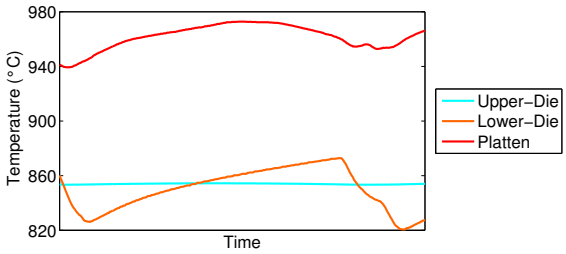

Figure 4.8 – Averaged temperature evolution of tooling during a whole SPF cycle

Concerning the mold, its temperature variation is also rather limited during the process. The heat transfers between the mold and the part could be simply considered through a heat transfer coefficient with a rigid mold surface. However, it is directly involved into complex conduction heat transfers that depend on the gap and pressure conditions at the interface. In addition, the heterogeneity of the mold temperature, even limited, influence the heat flux with the part. Therefore, the mold has been considered as part of the thermomechanical system and included in the model.

Finally the geometry of the robot is not considered in the model. Indeed the interactions of its structure has been neglected to simplify the problem from the thermal and mechanical point of view. The arms that transmit the pulling efforts are modeled using perfect rigid surface because of the high rigidity of the handling system.

4.2.2.2 Geometry simplifications

The different parts of the model are meshed using shell elements. The shell elements problematics are discussed later in the Section 4.2.5.1. In this section, only the geometrical aspects are approached. The 3D real geometries have been simplified such as represented in the Figure 4.9. The parts are partially represented to make out the hidden mold. A

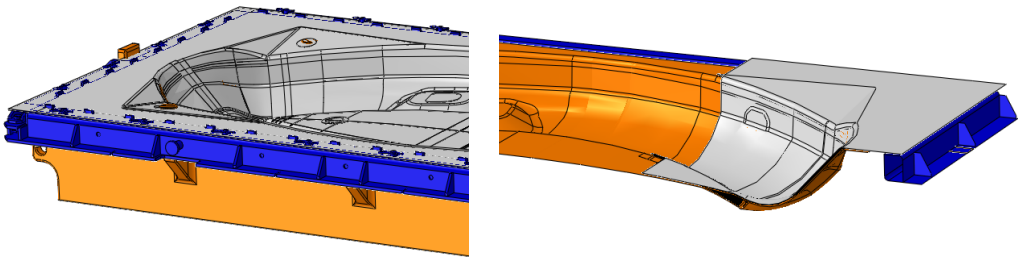

(a) (b)

Figure 4.9 – CAD views of the assembly with the frame, and the bottom mold and the formed part (a) 3D CAD and (b) shell based simplified assemblies

symmetry condition is used in the model such that half of the geometries are considered as explained above.

The sheet metal part fulfill the shell usage condition that requires one very small dimension compared to the two other. Concerning the mold, the condition is clearly not respected. However, the massiveness of the mold which limits the changes of temperature and its high strength at the process temperatures almost make it rigid. Therefore, it has been chosen to model it with thick shell elements to limit the computation time. The Figure 4.10 shows a 3D central cut view of the industrial mold and the simplified shell-based geometry. A thickness of 100 mm was taken for the shell-based section of the mold. Double arrows of 100 mm are positioned from the upper surface of the industrial geometry in the Figure 4.10a to highlight the shell-based hypothesis.

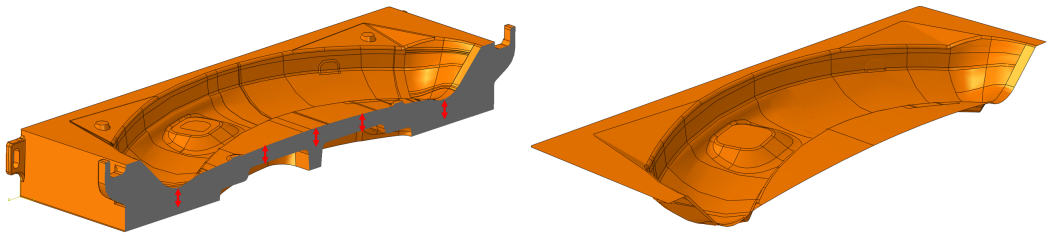

(a) (b)

Figure 4.10 – CAD views of the mold: (a) industrial and (b) simplified geometry

The extraction frame is also modeled with shell elements. The geometry is rather complex such as shown in the Figure 4.11a. The simplified geometry used in the model shown in the Figure 4.11b only considers the structural elements of the frame.

4.2.3 Physical equations

The equations that govern the evolution of thermomechanical quantities are independent of the FE method and the model. However, they are applied to a system composed by different domains limited by boundaries that have specific thermo-physical properties. In the present model, only the solid continuum domains are considered. Nevertheless, the fluid are also considered in the CFD simulation that are used to evaluate the convection coefficient distribution.

The Figures 4.12 schematically represents the boundaries and the interfaces of the model domains respectively denoted $\partial\Omega$ and Σ for the inside and outside configurations. The

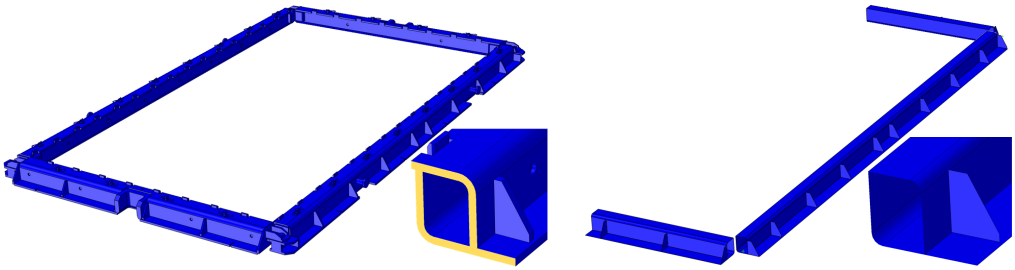

(a) (b)

Figure 4.11 – CAD views of (a) the extraction frame with zooms on the pivot connection and frame cut section (b) shell-based simplified model

identified colors of the interfaces correspond to domains and associated boundaries involved in thermal or mechanical boundary conditions. These conditions are detailed in the next paragraphs.

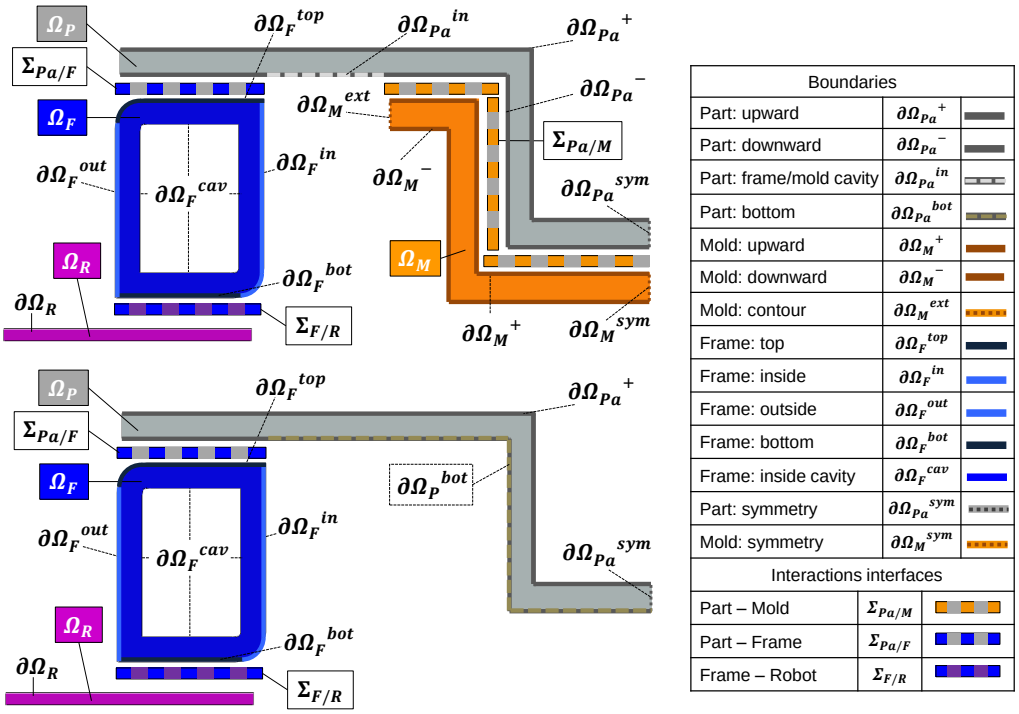

Figure 4.12 – Definition of boundaries and interfaces of the domains

4.2.3.1 Mechanical equations

The equations involved in such problems result from the fundamental principle of dynamics defined in the Equation (4.1) applied to the deformable domains Ω_{def} $(= \Omega_{Pa} + \Omega_M + \Omega_F)$ where $\underline{\underline{\sigma}}$ is the Cauchy stress tensor, ρ the material density and $\overrightarrow{g}$ the gravity force. $\underline{\underline{\sigma}}$ is defined as a third order tensor that fully defines the stress state of a material point of a domain. Each terms of the tensor corresponds to normal and tangential stresses that balance the material domain. It is through this term that the material behavior law in introduced.

$$\overrightarrow{div}\left(\underline{\underline{\sigma}}\right) + \rho\overrightarrow{g} = \overrightarrow{0} \ \forall M \in \Omega_{def} \tag{4.1}$$

4.2.3.1.1 Behavior equations

In the present work, an additive decomposition of the strain and strain rate tensor is used. It consists in defining the total strain rate tensor $\dot{\underline{\underline{\varepsilon}}}$ as the sum of the deformation contributions. The Equation (4.2) defines the $\dot{\underline{\underline{\varepsilon}}}$ for the different domains of the model where $\dot{\underline{\underline{\varepsilon}}}^{el}$, $\dot{\underline{\underline{\varepsilon}}}^{vp}$ and $\dot{\underline{\underline{\varepsilon}}}^{th}$ are respectively the elastic, the viscoplastic and the thermal strains rate tensors.

$$\dot{\underline{\underline{\varepsilon}}} = \begin{cases} \dot{\underline{\underline{\varepsilon}}}^{el} + \dot{\underline{\underline{\varepsilon}}}^{vp} + \dot{\underline{\underline{\varepsilon}}}^{th} & \forall M \in \Omega_{Pa} \\ \dot{\underline{\underline{\varepsilon}}}^{el} + \dot{\underline{\underline{\varepsilon}}}^{th} & \forall M \in \Omega_M + \Omega_F \end{cases} \tag{4.2}$$

In the case of the infinitesimal theory the total strain rate tensor is related to the gradient of velocity of the material such as defined in the Equation (4.3) where $\dot{\underline{\underline{F}}}$ and $\dot{\underline{\underline{F}}}^T$ are second order tensors of the velocity gradient of a material point and its transpose.

$$\dot{\underline{\underline{\varepsilon}}} = \frac{1}{2}\left(\dot{\underline{\underline{F}}} + \dot{\underline{\underline{F}}}^T\right) \ \forall M \in \Omega_{def} \tag{4.3}$$

The elastic strain rate tensor can be related to the Cauchy stress rate tensor thanks to the Hooke's law such as defined in the Equation (4.4) where $\underline{\underline{C}}$ is the Hook's tensor or the elastic stiffness tensor which is a 9x9 tensor that can be simplified in the case when $\dot{\underline{\underline{\varepsilon}}}^{el}$ and $\dot{\underline{\underline{\sigma}}}$ are symmetrical and the material is isotropic into the Equation (4.5) where E and ν are the Young modulus and the Poison ratio that both may depend on temperature and $\underline{\underline{I}}$ is the second order identity tensor.

$$\dot{\underline{\underline{\varepsilon}}}^{el} = \underline{\underline{C}}^{-1}\dot{\underline{\underline{\sigma}}} \ \forall M \in \Omega_{def} \tag{4.4}$$

$$\dot{\underline{\underline{\varepsilon}}}^{el} = \frac{1}{E}\left[(1+\nu)\dot{\underline{\underline{\sigma}}} - \nu Tr(\dot{\underline{\underline{\sigma}}})\underline{\underline{I}}\right] \tag{4.5}$$

The viscoplastic strain rate tensor is related to the viscoplastic function $\dot{p}$, the plasticity criterion f_{vp} and the Cauchy stress tensor such as defined in the Equation (4.6). The definition of the $\dot{p}$ function and the characterization of its parameters for the Ti-6Al-4V alloy is described in the Chapter 2.

$$\dot{\underline{\underline{\varepsilon}}}^{vp} = \dot{p}(\underline{\underline{\sigma}}, \dot{\underline{\underline{\varepsilon}}}^{vp}, \underline{\underline{\varepsilon}}^{vp}, T)\frac{\partial f_{vp}}{\partial \underline{\underline{\sigma}}} \ \forall M \in \Omega_{Pa} \tag{4.6}$$

Finally, the thermal strain rate tensor is related to temperature rate $\dot{T}$ and the isotropic coefficient of thermal expansion α_{th} such as defined in the Equation (4.7).

$$\dot{\underline{\underline{\varepsilon}}}^{th} = \alpha_{th}\dot{T}\underline{\underline{I}} \ \forall M \in \Omega_{def} \tag{4.7}$$

The thermophysical properties of the part, mold and frame material that have been used in the model are provided in the Appendix D.1.

4.2.3.1.2 Interface interactions

The different domains of the system are constrained between each other through contact interactions or specific couplings that both impose specific force and/or displacement relations at their boundaries

- ❒ Contacts

There are three mechanical contact interfaces in the model: the part-mold $\Sigma_{Pa/M}$, the part-frame $\Sigma_{Pa/F}$ and the frame-robot $\Sigma_{F/R}$ interfaces.

The mechanical contact is governed by a normal and a tangential behavior. The normal behavior refers to the contact pressure-overclosure relationship. An augmented Lagrange method is used. This contact algorithms is related to the FEM specific to ABAQUS® software. It is briefly described in the Section 4.2.5.2. This method enables to compute the contact pressure as a function of underlying element stiffness.

Concerning the tangential shear stress, it is computed using a Coulomb friction model. It defines the critical shear stress τ_{crit} at which sliding of the surfaces starts as a fraction μ of the normal contact stress σ_n such that $\tau_{crit} = \mu\sigma_n$. The Coulomb model defines sticking conditions if the contact shear stress is below the critical one while sliding occurs when it is reached such that defined in the Equation 4.8 where $\gamma_{eq}=\sqrt{\gamma_1^2+\gamma_2^2}$ and $\tau_{eq} = \sqrt{\tau_1^2+\tau_2^2}$ with γ_1, γ_2, τ_1 and τ_2 are respectively the contact slip rates and shear stresses in the local direction.

$$\forall M \in \Sigma \ , \ \left\{ \begin{array}{ll} \dot{\gamma}_{eq} = 0 & \tau_{eq} < \tau_{crit} \\ \dot{\gamma}_{eq} > 0 & \tau_{eq} = \tau_{crit} \end{array} \right\} \tag{4.8}$$

The values of friction coefficients for the different interfaces are defined in the Table 4.1. The value of the interface $\Sigma_{Pa/M}$ is the same than used for the forming step. The value of the interface $\Sigma_{Pa/F}$ is set to 0.2 because of the coarse surface quality of the frame and the absence of BN coating. Finally, no friction is considered between the robot and the frame.

$\Sigma_{Pa/M}$	$\Sigma_{Pa/F}$	$\Sigma_{F/R}$
0.1	0.2	0

Table 4.1 – Coulomb friction coefficients

❒ Kinematic coupling

They are several coupling interactions. The pivot connections between the frame's profiles are modeled using coupling between edges at the ends of frame profiles and respective reference points themselves constraint with a pivot based kinematic coupling as shown in the Figure 4.13. Their mechanical coupling is defined in the Equation (4.9) where $\mathcal{V}\left(\Omega^1_{F_{long}}/\Omega^1_{F_{lat}}\right)$ is the kinematic screw relation at the reference point R^1 in its local coordinate system $\mathcal{R}_{R^1_p}$ represented in the Figure 4.13b where ω_3 is the available rotation around the direction $\overrightarrow{e}_3$ of $\mathcal{R}_{R^1_p}$. The same coupling also exists for the second lateral frame's profile.

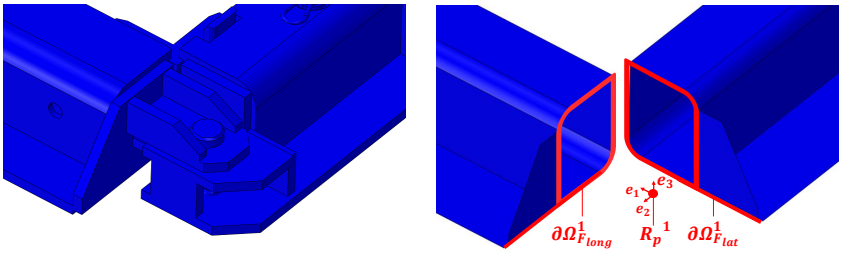

(a) **(b)**

Figure 4.13 – Frame's profiles pivot fastenning (a) industrial CAD view, (b) model representations

$$\forall M \in \partial\Omega^1_{F_{long}} \cup \Omega^1_{F_{lat}} \ , \ \mathcal{V}\left(\Omega^1_{F_{long}}/\Omega^1_{F_{lat}}\right) = \underset{R^1_p}{\left\{ \begin{array}{ll} 0 & 0 \\ 0 & 0 \\ 0 & \omega_3 \end{array} \right\}}_{\mathcal{R}_{R^1_p}} \tag{4.9}$$

A second type of coupling concerns the fastening systems that clamp the part onto the frame. They are modeled using ABAQUS® fasteners as represented in the Figure 4.14. These fasteners fix the degrees of freedom of the nodes belonging both surfaces included into a radius around a reference point. These reference points correspond to the cut zones where the part is clamped with cotter pins. Each reference point has its local coordinate system

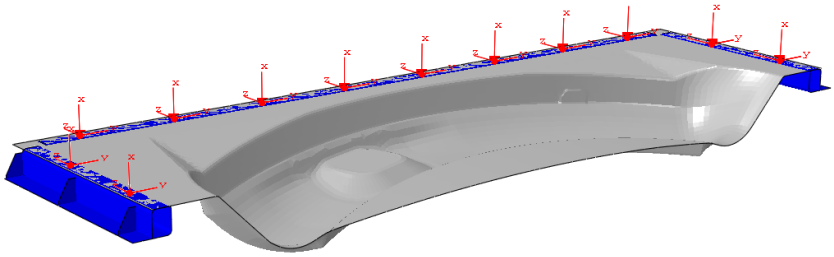

Figure 4.14 – Representation of part-frame fastening locations

and coupling constraints defined in the Equation (4.10) where M_0, R_{crit} are respectively the initial position of point M that belongs to ${\partial\Omega_F}^{top}$ or ${\partial\Omega_{Pa}}^{-}$ and the critical radius for wich the fastening coupling is active. The terms v_2 and v_3 are velocity components that becomes null if the maximum critical distance is reached. This distance estimated at ±10 mm corresponds to the large tolerance of laser cutting that allows small displacements in the contact plane.

$$\forall M \in {\partial\Omega_F}^{top} \cup {\Omega_{Pa}}^{-}, \text{ if } \|\overrightarrow{M_0 R_p^i}\| < R_{crit} \ , \ \mathcal{V}\left({\Omega_F}^{top}/{\Omega_{Pa}}^{-}\right) = \underset{R_p^i}{\left\{ \begin{array}{cc} 0 & \omega_1 \\ v_2 & 0 \\ v_3 & 0 \end{array} \right\}}_{\mathcal{R}_{R_p^i}} \tag{4.10}$$

4.2.3.1.3 Boundary conditions

During the whole simulation, a mechanical symmetry boundary condition is applied on the node shown in the Figure 4.15.

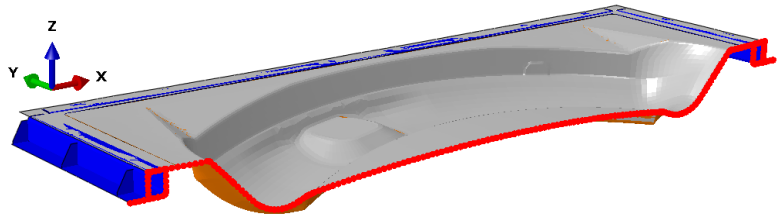

Figure 4.15 – Representation of symmetry boundaries (in red) of the model

The mechanical boundary conditions do not significantly evolve throughout the steps of the model. There are slight evolutions that are mainly based on numerical contact purpose. A summary of their evolution is given in the Figure 4.20. In the left column is given the time scales for each steps of the simulation. In the right columns are detailed the different numerical steps. The grey dark ones are real phases existing in the process while the light grey ones are pure numerical steps that are used for contact transitions states. In the central columns are given the evolution of mechanical BC. The detail of the mentioned conditions is presented in next paragraphs.

❒ Opening of the press and blowing steps

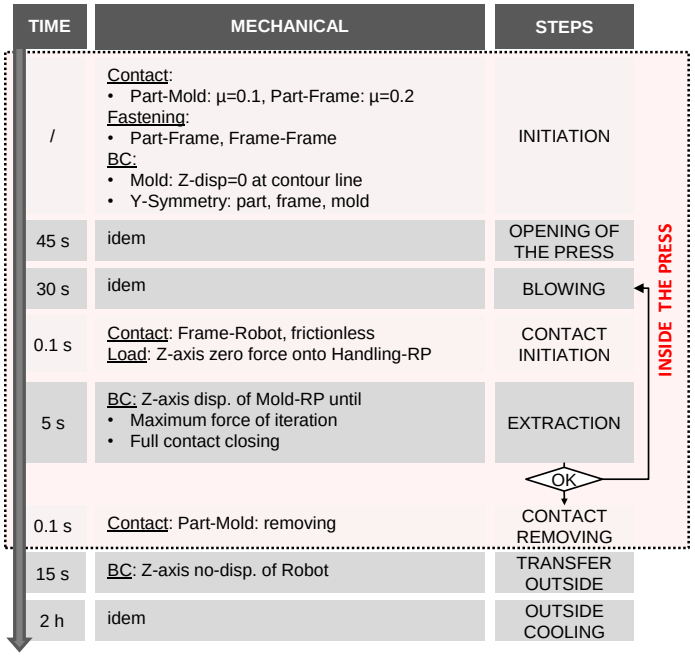

Figure 4.16 – Description of mechanical BC evolution during process simulation

During the two first steps of natural cooling phases and the first blowing, there is a first zero displacement BC imposed in the z-axis direction on the contour line of the mold such as represented in the Figure 4.17. In addition, the displacements of a single central node of the symmetry line are fixed in the perpendicular plane of the symmetry axis.

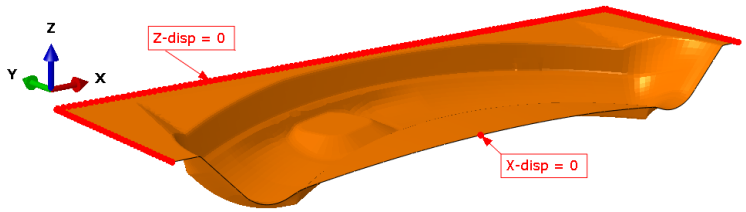

Figure 4.17 – Representation of the mold nodes (in red) involved in displacement boundary conditions

Another BC concerns the frame. Indeed, it is placed on several support elements of the mold such as highlighted in the Figure 4.18. This support is traduced by a zero-displacement of the ${\partial\Omega_F}^{bot}$ surface boundary in the z-axis direction.

❒ Extraction steps

At the beginning of the extraction steps, there is a transition in the BC that control the z-axis displacement of the frame. The zero-displacement of the ${\partial\Omega_F}^{bot}$ surface boundary is removed. The contact at the frame-robot interface is activated. A zero-displacement of the $\partial\Omega_R$ surface boundary in the z-axis direction is imposed such as shown in the Figure 4.19.

During the extraction process in AIRBUS, the robot imposes a vertical displacement at 30 mm/s through its arms that generate efforts onto the frame to remove the part from the

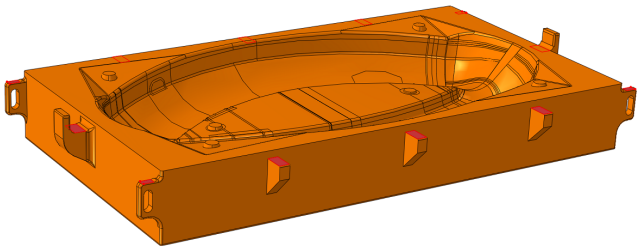

Figure 4.18 – 3D CAD view of the industrial mold: highlighting of the frame's support zones

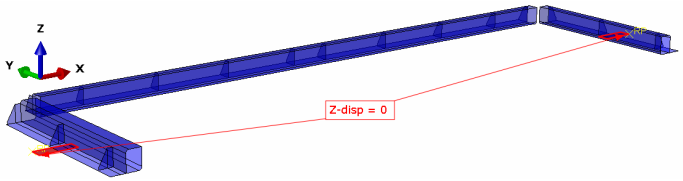

Figure 4.19 – Representation of the robot's arms dispacement boundary conditions

mold. The displacement is induced until the applied effort reach a maximum value. Once it is reached, the displacement is stopped and an additional blowing step is performed. The maximum robot effort value is incrementally increased by 150 kg for this part. At the first force impulse, the weight of the part and the frame are added to the maximum force.

In the model, the relative displacement is imposed to the mold instead of the the robot for numerical reasons that are discussed later in the chapter. Indeed, it limits the viscous forces introduced by the numerical damping necessary to help the convergence of the model. The z-axis velocity is imposed on the contour line of the mold through a user subroutine that stops the displacement once the maximum force is reached.

❒ Transfer and outside cooling

During the steps that follow the extraction, there is no modification of the BC. However, the mold is removed from the simulation so as to the associated interfaces and BC.

4.2.3.2 Thermal equations

The evolution of the temperature field of an environment is obtained by solving the heat equation at a material point as defined in the Equation (4.11). The thermo-physical parameters ρ, c and λ are respectively the density, the heat capacity and the thermal conductivity of the material and are all temperature dependent as defined in the Appendix D.1. In a coupled system, this equation is solved in parallel to the mechanical equations such that the influence of the temperature on material behavior is considered.

$$\rho c \frac{\partial T}{\partial t} = -div(\lambda \overrightarrow{grad}(T)) \; \forall M \in \Omega_{def} \tag{4.11}$$

This equation governs the temperature evolution inside a domain. At its boundaries, there are three different heat transfer modes which are commonly involved: the radiative, conductive and convective transfer modes. Contrary to the mechanical part of the equations, the idea of boundary, and interface is more complex for the thermal point of view. For instance, the radiative transfer at the interfaces of the part and the press' environment becomes a boundary condition because of the taken simplifications of the problem as described in the

Section 4.2.2.1. Therefore, the general heat equation at the boundary is presented hereafter, and later detailed in the Section 4.2.4.

4.2.3.2.1 Boundary conditions

At the boundaries of a domain, the thermal diffusion term may be balanced by different contributions that can be radiative ϕ_{rad}, convective ϕ_{conv} and conductive ϕ_{cond} flux as defined in the Equation (4.12) where x is the coordinate in the direction normal to the boundary surface. These equations need to be adapted regarding to the interfaces and boundaries involved in the HT such as defined in the Figure 4.12. They are detailed in the next paragraphs.

$$-\lambda \left.\frac{\partial T}{\partial x}\right|_{x=0} = \begin{cases} \phi_{rad} \\ \phi_{conv} \\ \phi_{cond} \end{cases} \quad \forall M \in \partial\Omega \tag{4.12}$$

4.2.4 Thermal boundary conditions

The thermal boundaries and contact conditions evolve throughout the steps of the model. A summary of their evolution is given in the Figure 4.20 such as presented for the mechanical part of the model. In the thermal case, there are changes at every step except for the contact initiation of the robot and the frame for which no conduction HT are defined. The detail of the mentioned conditions is presented in next paragraphs.

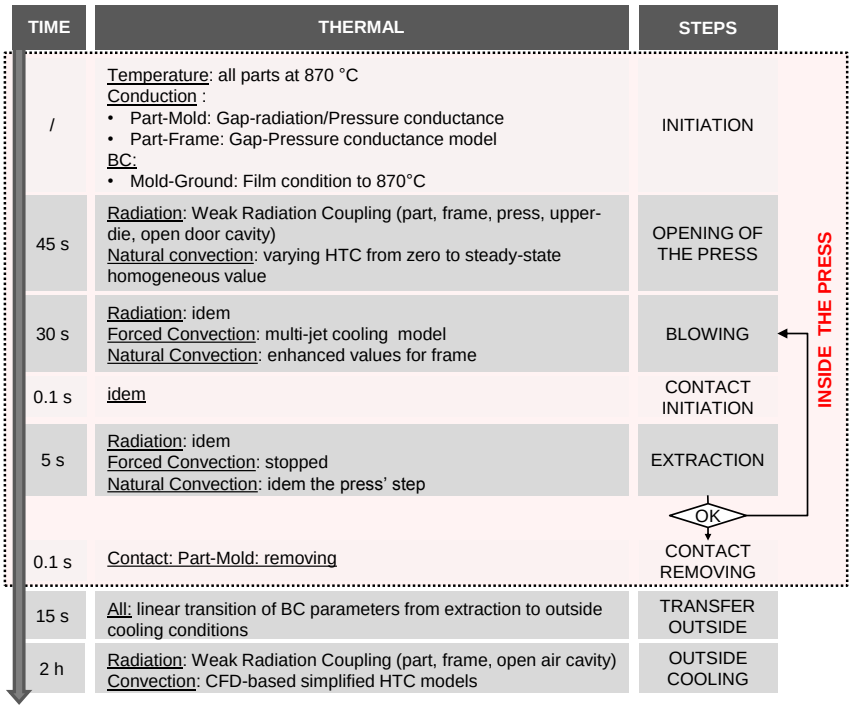

Figure 4.20 – Description of thermal BC evolution during process simulation

4.2.4.1 Radiation

The different boundaries of the model that exchange heat by thermal radiation are defined in the Figure 4.21 where each defined interface Σ may involved several exchanging boundaries.

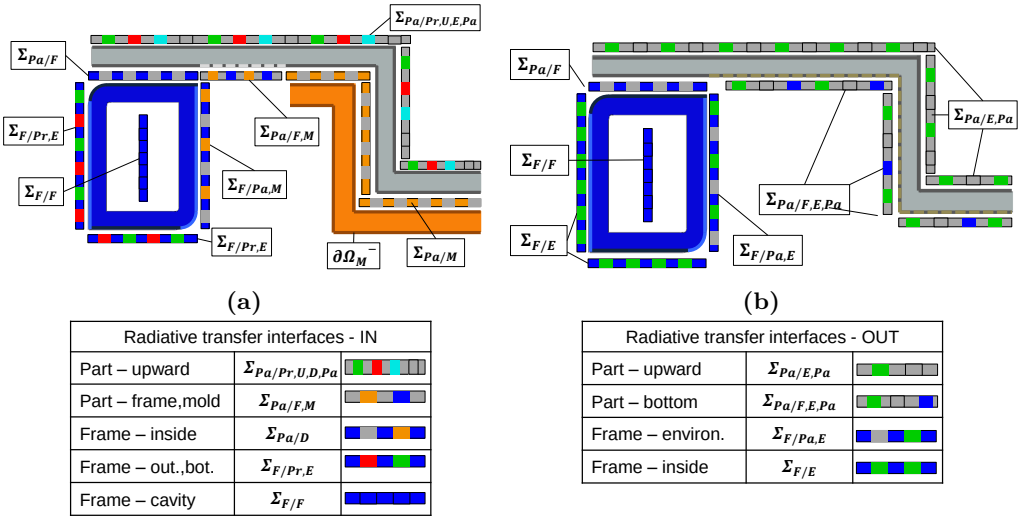

Radiative transfer interfaces - IN	
Part – upward	$\Sigma_{Pa/Pr,U,D,Pa}$
Part – frame,mold	$\Sigma_{Pa/F,M}$
Frame – inside	$\Sigma_{Pa/D}$
Frame – out.,bot.	$\Sigma_{F/Pr,E}$
Frame – cavity	$\Sigma_{F/F}$

Radiative transfer interfaces - OUT	
Part – upward	$\Sigma_{Pa/E,Pa}$
Part – bottom	$\Sigma_{Pa/F,E,Pa}$
Frame – environ.	$\Sigma_{F/Pa,E}$
Frame – inside	$\Sigma_{F/E}$

Figure 4.21 – Schematical definition of the radiative interfaces (a) inside, (b) outside the press and the legend

The problem is extremely complex in its geometrical definition, but also because of the heterogeneous temperature of the different surfaces.

There are three different radiative BC applied in the model which correspond to the type of boundaries involved in the HT. There are radiative transfers at the interfaces with the press and exterior environment: $\Sigma_{Pa/Pr,U,E,Pa}$, $\Sigma_{F/Pr,E}$, $\Sigma_{F/Pa,M}$, $\Sigma_{Pa/F,M}$, $\Sigma_{Pa/F,E,Pa}$, $\Sigma_{Pa/E,Pa}$, $\Sigma_{F/Pa,E}$ and $\Sigma_{F/E}$. These radiative BC are modeled using the weak radiation method (WRM) developed below. Then, there are the HT at the contact interfaces $\Sigma_{Pa/F}$ and $\Sigma_{Pa/M}$ which are considered using gap radiation model. Finally, there are HT inside the frame's profiles cavities $\Sigma_{F/F}$. These three types of BC are detailed below.

4.2.4.1.1 Weak radiation method

The WRM consists in using an approximation for the radiative heat flux computation of surfaces which have homogeneous temperatures and emissivities. The classical gray body radiation theory gives the radiation HT received by a surface $\partial\Omega_1$ from a surface $\partial\Omega_2$ respectively at a temperature and emissivity $T_{\partial\Omega_1}$, $\epsilon_{\partial\Omega_1}$ and $T_{\partial\Omega_2}$, $\epsilon_{\partial\Omega_2}$ with the Equation (4.13) where $F_{\partial\Omega_2\to\partial\Omega_1}$ is the VF of the surface $\partial\Omega_2$ regarding to the surface $\partial\Omega_1$. It corresponds the projected surface on a unit surface hemisphere for which the center is the center point of the element such that the total VF of a surface is one.

$$\phi_{rad}(\partial\Omega_2 \to \partial\Omega_1) = \frac{\sigma(T^4_{\partial\Omega_2} - T^4_{\partial\Omega_1})}{\frac{1-\epsilon_{\partial\Omega_1}}{\epsilon_{\partial\Omega_1}} + \frac{1}{F_{\partial\Omega_2\to\partial\Omega_1}} + \frac{1-\epsilon_{\partial\Omega_2}}{\epsilon_{\partial\Omega_2}}} \tag{4.13}$$

The Equation (4.14) give the approximated heat flux $\widehat{\phi^M_{rad}}(\partial\Omega)$ received by a material point M at temperature T and an emissivity ϵ with a surface $\partial\Omega$ which have a homogeneous temperature $T_{\partial\Omega}$ and emissivity $\epsilon_{\partial\Omega}$ as defined with the WRM method. $F^M_{tot}(\partial\Omega)$ is the total viewing factor of the surface $\partial\Omega$ with the point M. In ABAQUS® , the total viewing factor $F^{el}_{tot}(\partial\Omega)$ can be computed using the sum of the element-element viewing factor F_{el/el_i} between the concerned element el and the elements el_i belonging to constant temperature

surface $\partial\Omega$ such as defined Equation (B.4).

$$\forall M_{\partial\Omega} \in \partial\Omega,\ \text{if}\ \{T = T_{\partial\Omega},\ \epsilon = \epsilon_{\partial\Omega}\},\quad \widehat{\phi_{rad}^{M}}(\partial\Omega) = \frac{\sigma(T_{\partial\Omega}^4 - T^4)}{\frac{1-\epsilon_{el}}{\epsilon_{el}} + \frac{1}{F_{tot}^{M}(\partial\Omega)} + \frac{1-\epsilon_{\partial\Omega}}{\epsilon_{\partial\Omega}}} \tag{4.14}$$

$$F_{tot}^{el}(\partial\Omega) = \sum_{el_i \in \partial\Omega} F_{el/el_i} \tag{4.15}$$

This approximation has been used considering constant and homogeneous emissivity (ϵ=0.9) for the part, mold and frame. This emissivity value has given an acceptable fit of the experimental tests in the Section 3.6. The viewing factors have been computed thanks to a-priori HT analysis using multiple configurations. The temperature of the part, the frame, the press' walls, the upper dies and the exterior environment have been considered homogeneous to reduce the number of viewing factors configurations. The computation of the radiative heat flux BC $\phi_{rad}^{M\in\partial\Omega_{Pa}{}^{+}}$ at the upward surface ${\partial\Omega_{Pa}}^{+}$ is given in the appendix D.2 as an example. This method has been applied for every surface involved in the radiative interfaces for both inside and outside geometrical configurations as defined in the Figure 4.21.

4.2.4.1.2 Gap radiation

At the contact interfaces $\Sigma_{Pa/F}$ and $\Sigma_{Pa/M}$, the HT is a combination of conduction at contacting points, and convective-radiative transfers for the rest of the non-contact area of the interface. The radiative part is modeled using a gap-radiation model such as defined in the Equation (4.16). In our case, the equation is simplified because the emissivity ϵ is the same for the part, the mold and the frame, and the viewing factor is taken perfect (F=1).

$$\phi_{rad}^{cond}(\partial\Omega_2 \to \partial\Omega_1) = \frac{\sigma(T_{\partial\Omega_2}^4 - T_{\partial\Omega_1}^4)}{\frac{1-\epsilon_{\partial\Omega_1}}{\epsilon_{\partial\Omega_1}} + \frac{1}{F_{\partial\Omega_2\to\partial\Omega_1}} + \frac{1-\epsilon_{\partial\Omega_2}}{\epsilon_{\partial\Omega_2}}} = \frac{\epsilon\sigma(T_{\partial\Omega_2}^4 - T_{\partial\Omega_1}^4)}{3-2\epsilon} \tag{4.16}$$

4.2.4.1.3 Frame's profiles cavity radiation

Another radiative boundary condition is defined for the surface inside the frame's profiles ${\partial\Omega_F}^{cav}$. Indeed, the heat transfers inside the cavity of the profiles tends to balance the temperature of the surfaces. An average-temperature radiation BC is used to take account of the heat transfers. It consists in using the average temperature of the cavity $\langle T_{\partial\Omega_F{}^{cav}}\rangle$ as the limit temperature of a classical surface radiation BC as defined in the Equation (4.17).

$$\phi_{rad}^{cav}({\partial\Omega_F}^{cav}) = \epsilon\sigma(\langle T_{\partial\Omega_F{}^{cav}}\rangle^4 - T^4) \tag{4.17}$$

4.2.4.2 Conduction

Thermal contact HT are defined for the part-mold $\Sigma_{Pa/M}$ and the part-frame $\Sigma_{Pa/F}$ interfaces. It is a combination of conduction, convection and radiation HT. The radiative part of the transfer is defined in the Section 4.2.4.1.2. Both other contributions are commonly included inside a conductance k_c such as defined in the Equation (4.18).

$$\phi_{cond}(\partial\Omega_2 \to \partial\Omega_1) = k_c(T_{\partial\Omega_2} - T_{\partial\Omega_1}) \tag{4.18}$$

The conductance model obtained from characterization and presented in the Section 3, only considers a radiative contribution. However, the industrial process involves higher contact pressure values contrary to the experiments performed on the prototype tooling.

Indeed, the high pulling efforts observed in the shopfloor are produced by high shear contact stresses because of friction. Therefore, the hypothesis of a negligible conductive contribution of the conductance model is likely to be wrong. Thus, a contact contribution k_c of the conductance model is considered such as defined in the Equation (4.19) where k_0, P_{ini} and a are parameters of the model. k_0 is taken equal to 100 W.m^{-2}.s^{-1} which is the non-null value tested in the Section 3.6.4 for which the results are fairly good. P_{ini} and a are respectively taken at 0.01 MPa and 0.985 such as in the Section 3.6.4.

$$k_c = \begin{cases} k_0(P/P_{ini})^a & P > P_{ini} \\ k_0 & 0 < P \leq P_{ini} \\ 0 & \delta > 0 \end{cases} \tag{4.19}$$

This model is based on the famous MYC model developed by Mitikc, Yovanovic and cooper [205] considering conductivity, roughness and hardness properties homogeneous and independent of the interface temperature.

4.2.4.3 Convection

4.2.4.3.1 Natural convection: inside the press

The inside convection flow is very complex. The air goes inside the press by the door flowing through complex paths influenced by the tooling geometries. However, the associated heat transfers are fairly low during the transition phase until forced cooling experiment. Indeed, the air inside the press is at the press environment temperature at the beginning of the door opening such that the convection HT start to zero and then increase while the cold air goes inside. That is why a simple approximation is made considering that it has no significant impact. The convection coefficient starts from zero and goes up to a homogeneous value of 1 W.m^{-2}.K^{-1} with a smooth transition. The non-symmetry of the press configuration is not taken into account. This BC is applied on the next surfaces: $\partial\Omega_{Pa}{}^{+}$, $\partial\Omega_F{}^{out}$, $\partial\Omega_F{}^{bot}$, $\partial\Omega_F{}^{in}$.

4.2.4.3.2 Natural convection: outside the press

This section have been addressed with the methodology based on CFD simulations developed on horizontal plate natural convection described in the Appendix C. This method consists in performing CFD analyses of the configuration with simplified geometries in order to compute an approximated distribution of the convection coefficient on the different surfaces. These simulations are computed for several temperature conditions that correspond to different time of the cooling phase to take account of the impact of the temperature on the fluid flow. Then, the distribution of the convection coefficient is modeled as a function of time and space using approximated analytical relations.

The method has been applied on the industrial geometry in the configuration outside the press is presented in the Appendix C.5. The results of this work gives various functions that describe the space distribution with constant, linear, bilinear space evolution function that vary during the process.

However, further results in the Section 4.3.2 show that no plastic deformations occurs during this step. Therefore, the convection coefficient obtained from CFD analysis has been homogenized to simplify the problem. The Figure 4.22 gives the temperature and time evolution of the HTC affected to the top and bottom surfaces of the part and the exterior surfaces of the frame. In the model, the time evolution of the convection coefficient is preferred in order to avoid local evolutions of the coefficient that would not have an impact

on the global fluid flow. There is a significant difference between the bottom and top surface of the part. The HTC values are fairly low because the path of the air is continuously affected by the hot parts that heat the air and limit the HT.

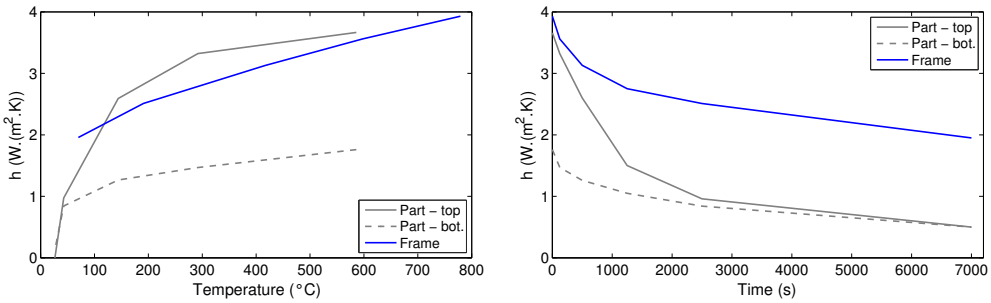

Figure 4.22 – Homogenized convection coefficient based on the CFD simulation (a) temperature and (b) time evolution

4.2.4.3.3 Forced convection

The model used to define the space distribution of the forced convection coefficient (FCC) is based on the model characterized in the Section 3.6 from the prototype testing experiments (given in the Equation (3.34)). However, it is adapted for a single circular nozzle impinging perpendicularly to a flat plate at a specific distance. In the industrial case, the impinged surface may be circular (convex or concave), inclined, at varying distance and many nozzles are used simultaneously. Therefore the shape of the distribution is likely to be influenced by the mentioned parameter, but also by the interactions of the several residual flows that are influenced by the surrounding shapes around the impinging zones.

$$h(r, z_0) = \begin{cases} h_0 & < R \\ h_0 \; e^{-k_0 \frac{r-R}{R}} & r \geq R \end{cases} \tag{4.20}$$

Two modifications have been implemented to the initial model characterized for the testing conditions such as reminded in the Equation (4.20) where z_0 is the distance between the nozzle and the surface for the blowing experiment. The first modification consists in considering the distance z between the nozzle and the impinged surface. Tawfek [200] demonstrated that the average Nusselt number is proportional to the inverse of the distance to a power 0.22 so that the FCC can be modified such as proposed in the Equation (4.21).

$$h(r, z) = h(r, z_0) \left(\frac{z_0}{z}\right)^{0.22} \tag{4.21}$$

The second modification concerns the shape of the distribution that may influence by the impinged surface. The assumed hypothesis is that the heat flux is conserved regardless of the shape of the surface. It is traduced by the Equation (4.22) in the case of $z{=}z_0$ where k_0 is the k parameter obtained from characterization.

$$\overline{h} = \int_0^\infty h(r)dr = h_0 R(1 + 1/k_0) \tag{4.22}$$

Using the hypothesis of heat flux conservation combined with the Equation (4.22), a variable definition of k is proposed in the Equation (4.23).

$$k(z) = 1/\left(\frac{1 + 1/k_0}{\left(\frac{z}{z_0}\right)^{-0.22}} - 1\right) \tag{4.23}$$

The Figure 4.23 shows the comparison of the initial and the modified models applied onto a surface with a varying distance such as for industrial case. The improved model highlights a slight decrease of the coefficient in the z-axis.

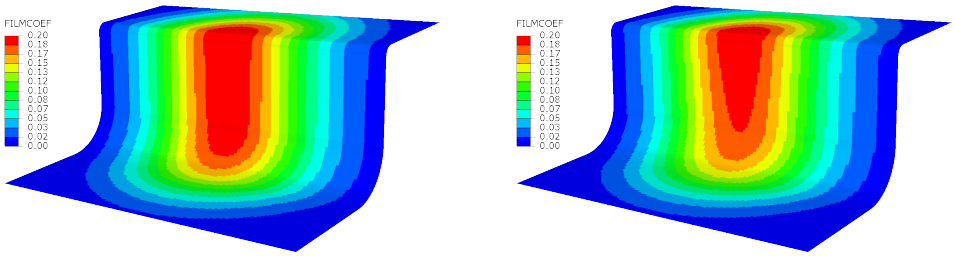

(a) **(b)**

Figure 4.23 – Forced convection coefficient model on varying H/d ratio (a) geometry, (b) unscaled model and (c) z-scaled model

The Figure 4.24 gives the industrial strategy for the blowing configuration and the associated distribution of the FCC.

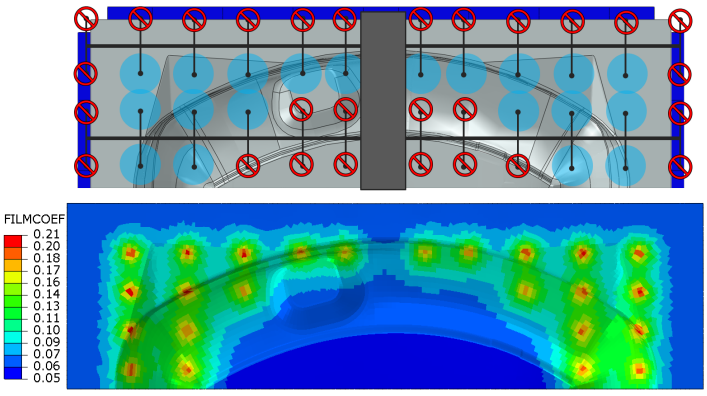

Figure 4.24 – Blowing strategy and associated FCC model ($mW.mm^{-2}.K^{-1}$)

4.2.5 Finite element method

In this section, a brief description of the structure of such numerical model is made. Only the general concepts and the associated problematics regarding to the process are approached. Some additional details are given in the Appendix D.3.

The FEM enables to solve partial differential equations such as thermal and mechanical equations on complex 2D and 3D problems. The method consists in subdividing a continuous system into finite elements that constitutes a mesh discretization of the system. The mathematical formulation of the problem is modified so that to obtain a linear system of

equations easier to solve numerically. The simplifications are based on the variational (also called "weak") formulation based on the Galerkine method which enables to transform the continuous problem in a discrete one.

It is possible to define an approximated solution of one equation as linear combination of interpolation functions (defined for each finite elements) like polynomials (usually first or second order) functions. Once the problem is described with the variational form, it can be written under a matrix form and finally solved with a numerical algorithm. Some more details on the FEM are presented in the Appendix D.3.

In the developed model, an implicit resolution of the fully coupled temperature and displacement equations are performed using the Newton-Raphson algorithm. The time integration is based on an automatic scheme that use either explicit or implicit integration based on plasticity and stability criteria. The explicit integration stability is based on a the maximum difference in the creep strain increment that has been fixed at 1%.

4.2.5.1 Element discretization

For this sheet metal forming process, quadrangle shell elements are used to take advantage of their lower time computation compared to 3D continuum elements. Indeed, the low thickness of the sheet metal parts enables to use the shell theory. the section integration is made using five points in the thickness with the Simpson's rule. On the contrary, the mold and the frame's profiles does not respect the thin shell theory, especially the mold. In this case, ABAQUS® uses thick shell theory when the thickness is superior to 1/15 of a characteristic length of the element.

The coupled temperature-displacement continuum shell elements in Abaqus have continuum shell geometry and use linear interpolation for the geometry and displacements. The temperature is interpolated linearly as well. First order integration (for mechanical quantities) elements with a reduced integration are used (S4RT elements). The reduce integration uses a single integration point located at the element's centroid for first order element. It limits the number of integration points, and it uses the more accurate "uniform strain" formulation [214].

A portion of the meshes of the three different geometries are presented in the Figure 4.25. They are composed by S4RT or S3RT temperature displacement coupled shell elements as discussed in the Section 4.2.5.1.

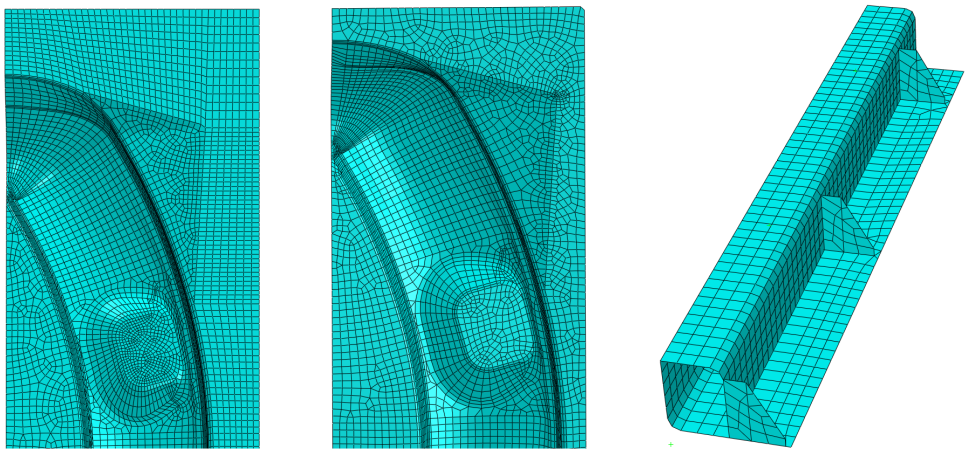

(a) **(b)** **(c)**

Figure 4.25 – Mesh views: (a) Part, (b) Mold and (c) Frame

The total number of elements is 9371 and 7972 respectively for the part and the mold. The part has much refine mesh precision compared to the mold in order to be able to well describe the deformation undergone during the simulation. The extraction frame is divided into two lateral profiles which are half the real geometries (because of the symmetry) and a longitudinal one. They have respectively 1350 and 4534 elements. The total number of element in the model is 23227

4.2.5.2 Contact resolution

The heat conduction and friction forces generated through the contact at the part interfaces during cooling phase are the root causes of part distortions. Therefore, the contact resolution has to be carefully implemented. The contact modeling consists into different numerical methods/algorithms that governs the resolution of the thermal and mechanical quantities at the interface: contact tracking method, surface contact discretization and the contact enforcement method.

In our case, a path-based tracking algorithm within a finite sliding approach (surface-to-surface contact discretization) is used with an augmented Lagrangian method to solve the mechanical contact interactions. The contact resolution consists in solving the contact pressure that balances the system as a function of node/surface penetration. The path-based tracking algorithm algorithm carefully considers the relative paths of points on the slave surface with respect to the master surface within each increment. The surface-to-surface discretization enables to better take account of penetration of nodes with reasonable mesh refinement differences. The augmented Lagrangian method has a low penetration tolerance that provides a much precise contact resolution with less approximation. Some more details on these aspects are available in the ABAQUS® documentation [215, 216].

4.2.5.3 Damping

In order to solve non-linear problems, ABAQUS® provides tools to improve the stability of numerical schemes. Numerical damping may be introduced at a global scale of the problem but also at the contact scale. Global or general damping might help to solve material or geometrical non-linearities while contact damping (called contact control in ABAQUS®) provide the capability to prevent rigid body motion at contact interface during opening and closing of contact. The latest is highly important for the process problematics that involve contact friction and evolving contact conditions from closed to opened along the simulation. However, both are required to help convergence of such non-linear problems.

The issues of such numerical damping is that they might bring significant error if they are not carefully used . Indeed, both tools are based on the same principle. Viscous forces are introduced in the forces' equilibrium equation with the form of the Equation (4.24) where M^* is an artificial mass matrix calculated with unity density, c is a damping factor, v is the vector of nodal velocities.

$$F_v = cM^*v \tag{4.24}$$

Both coefficients for global and contact based damping are automatically computed regarding material, mechanical and geometrical properties. However, the computed value is not always adapted and ABAQUS® introduce a scaling factor to adapt the stabilization level to the problem. One important aspect is to ensure that the viscous damping energy and the contact damping stress respectively introduced by global and contact damping remain below a few percentage of the internal energy and the contact stresses (ABAQUS® recommends 5%).

4.3 Results

The results presented in this section correspond to the the model described in the Section 4.2 with the blowing strategy of the Figure 4.24. As mentioned in the introduction of the

chapter, a strong influence of the numerical contact damping has been observed. An analysis of its impact on the pulling force during part removing and the final deformations of the part is presented in the Section 4.4. It has been highlighted that it generates anomalous damping stresses that oppose to the contact opening.

For this section, two different values of the contact damping factor (CDf) are assigned to limit the artificial forces promoted by this numerical tool in the zones where they may be critical. The Figure 4.26 shows a first zone highlighted in red for which the factor is higher (CDf=1e-3). A lower factor (CDf=1e-6) is used for the rest of the contact surface of the part. The lower value is affected on the surfaces almost horizontal for which normal contact stresses have no sense and artificially increase the necessary forces to remove the part from the mold.

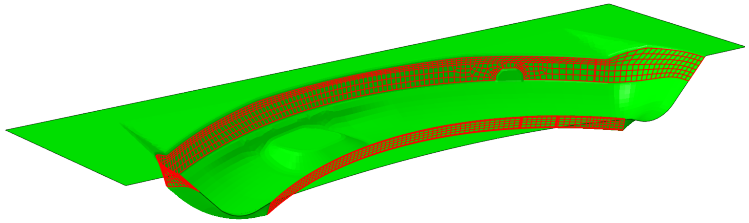

Figure 4.26 – Representation of the split surfaces for contact damping attribution

In order to present easily the results of the simulation, several specific times are described in the Figure 4.27b. These times correspond to the end of press' opening t_1, blowing $t_{2,i}$, peak force $t_{2,i}$(F) and ambient cooling steps t_3 and t_3(X). The t_3(X) time point represents a specific time of X seconds after the transfer of the part outside in the ambient cooling conditions. The duration of each step is given in the flowchart of the Figure 4.27b.

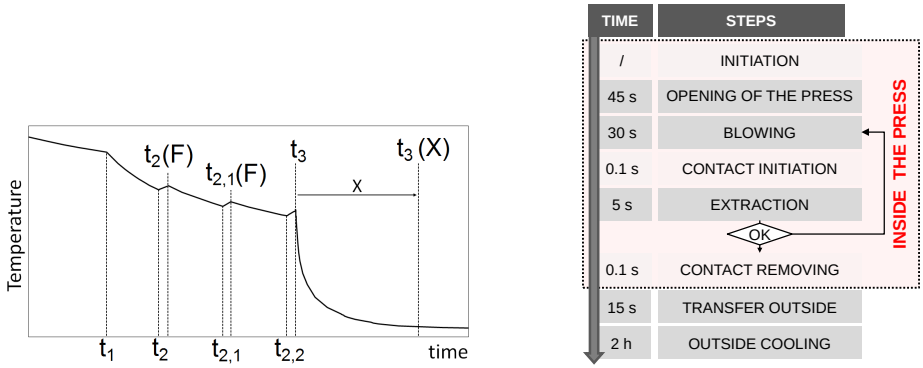

Figure 4.27 – Schematic representation of specific time of the process on (a) Temperature evolution, (b) Flowchart

Finally, the isovalues that are shown in this section are associated to the mid-side integration point in the section of the shell elements except if it is precised.

4.3.1 Thermal results

The first important aspect of the process is the temperature variations. They are described separately for each part of the assembly. Some nodes have been selected to highlight the various temperature evolution in specific zones of the parts subjected to different thermomechanical loading.

4.3.1.1 Part

The Figures 4.28a, 4.28b, 4.28c and 4.28d show the temperature distributions at the times t_1, t_2, t_3 and $t_3(1000)$. The Figure 4.28e gives the temperature evolution during the whole simulation at the nodes N_1, N_2, N_3 and N_4 highlighted on the geometries of the temperature distribution figures.

The Figure 4.28a highlights the non-symmetry of the radiative heat flux through the open door. Indeed, the temperature decrease reaches more than fifty degrees while the deep zone is preserved from radiative HT through the open door and its temperature decrease is limited to thirty degrees. In , the top corner zones have a lower temperature. It is a consequence of the absence of frame (modeled with coupling interaction) in these region. It is not the case with the real tooling but this area cannot influence the final distortions of the part.

The Figure 4.28b clearly shows the effect of the local cooling imposed by the nozzles. The temperature in the affected zones decreases up to 559 °C. It makes a maximum difference of around 285 °C in thirty seconds which corresponds to an average cooling rate of 9.5 °C.s^{-1}. The minimum cooling rate is around 1.7 °C.s^{-1} in the central dome zone. The Figure 4.28e highlights the gradient of cooling rate especially for the node N_4 for which the temperature gap with the other nodes increases throughout the three blowing phases. The central bar of the robot that has a strengthening role (Figure 4.24) produces a gap in the affected zone.

The temperature field at time t_3 in the Figure 4.28c shows that once the blowing stops, the localization of cooling tends to be homogenized. This phenomena can be observed on the time evolution at the end of each blowing steps. The temperature increases which is a consequence of thermal diffusion, but also the radiative and conductive heat transfers that tends to heat back the part at the press and the mold temperature.

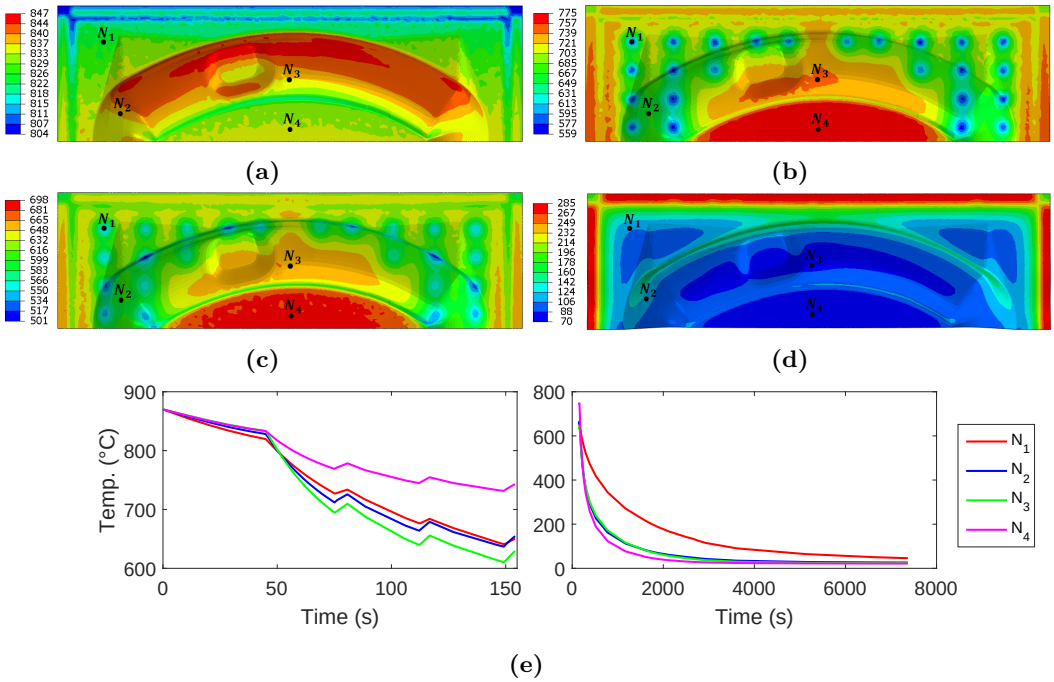

Figure 4.28 – Temperature field of the part at time (a) t_1, (b) t_2, (c) t_3 and (d) $t_3(1000s)$, nodal temperature-time curves inside (left) and outside (right) the press (e)

Finally the outside cooling leads to two zones which have a temperature almost homogeneous: the frame area and the rest (Figure 4.28d). The conduction with the frame maintains the

temperature of the part higher than the rest as clearly seen in the Figure 4.28e with the node N_1 compared to the others. After 1000 seconds of cooling outside the press, the maximum difference of the part temperature is 215 °C between the zone in contact with the frame and the central dome zone.

4.3.1.2 Mold

The Figures 4.29a, 4.29b and 4.29c show the temperature distributions of the mold at the times t_1, t_2 and t_3. The Figure 4.29d gives the nodal temperature curves of the N_1, N_2, N_3 and N_4 located at the same positions than for the part. The distribution of the temperature has the same shape than the part. However, the temperature decrease is much smaller: between 10-22 °C, contrary to 130-250 °C for the part such as confirmed in the Figure 4.29d.

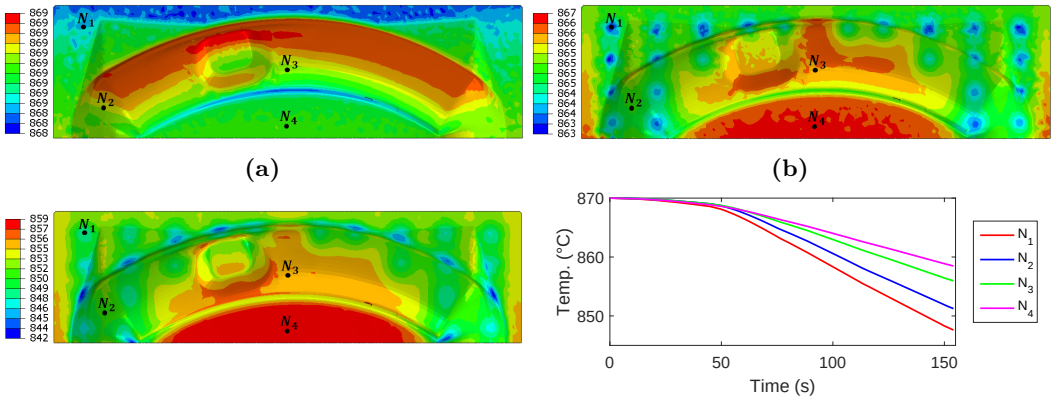

Figure 4.29 – Temperature field of the mold at time (a) t_1, (b) t_2, (c) t_3 and (d) nodal temperature-time curves inside the press

4.3.1.3 Frame

The Figure 4.30 shows the temperature distributions of the frame at the times t_1, t_2, t_3 and $t_3(2500)$. There are large temperature gradients as a function of the sides of the frame profiles and the profiles themselves. At the end of the opening of the door, there is a temperature gap of 50 °C between the coldest zones facing the door and the hottest facing the mold (Figure 4.30b). This gap rises to 60 °C at the end of first blowing phase (Figure 4.30b), end even more than 80 °C (Figure 4.30c) at the end of the third blowing phase.

The gradient of temperature changes when the frame is outside the press (Figure 4.30d). When the frame is outside the press (Figure 4.30d), The bottom side of the frame profiles is colder because of the changes in the radiative HT. Indeed, the part limit the heat transfer with the ambient environment on the top side while it is facing to the cold environment on the bottom side.

The Figure 4.31 highlights some nodes used for the longitudinal and lateral profiles of the frame. Indeed, five nodes (N_1, N_2, N_3, N_4 and N_5) have been selected on both profiles in order to highlight their difference in the thermal behavior especially inside the press as observed in the Figure 4.30. The Figure 4.32 gives a comparison of the the nodal temperature curves inside the press for the longitudinal and lateral frame profiles. The temperature difference rises to around 100 °C and 50 °C respectively for the longitudinal and lateral profiles which is pretty high. It confirms the observation made on the Figure 4.30.

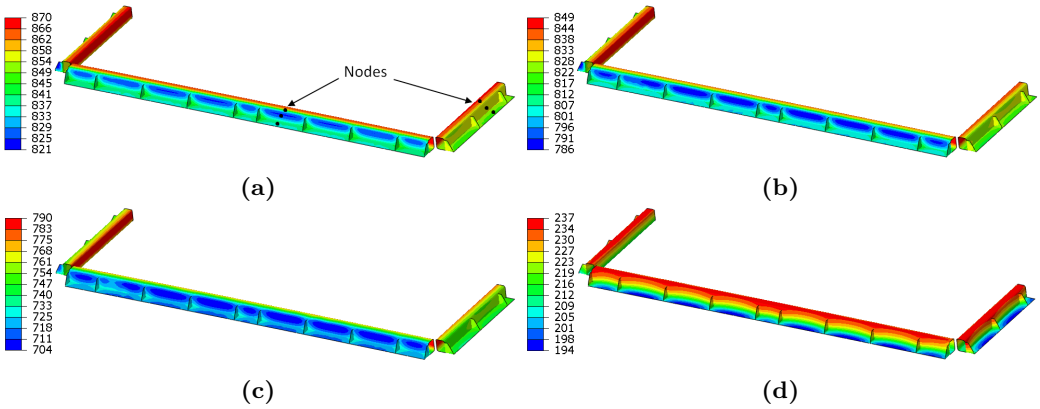

Figure 4.30 – Temperature field of the frame at time (a) t_1, (b) t_2, (c) t_3 and (d) t_3(2500s)

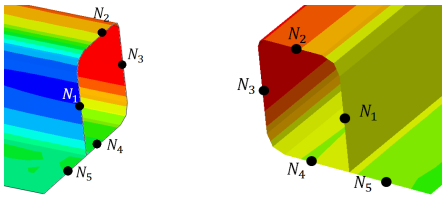

Figure 4.31 – Representation of the nodes used for temperature plots on the longitudinal and lateral frame's profiles from the Figure 4.30a

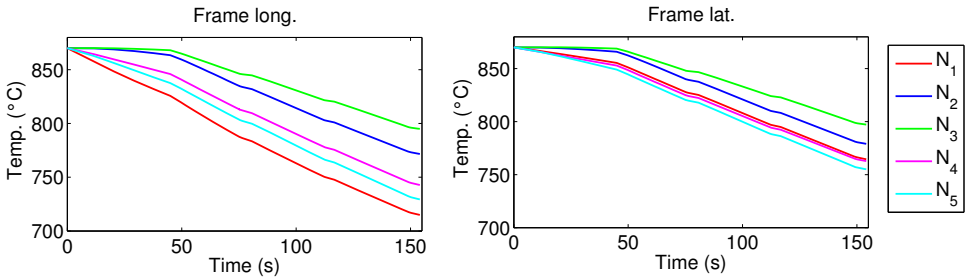

Figure 4.32 – Temperature evolution of the frame inside the press for the longitudinal (left) and lateral (right) profiles

4.3.1.4 Comparison

The Figure 4.33 shows the evolution of the mean temperature (averaged at N_i nodes presented above) of each part. It highlights the global differences between part and mold inside the press due to the conductive heat transfers, and between the part and frame outside the press.

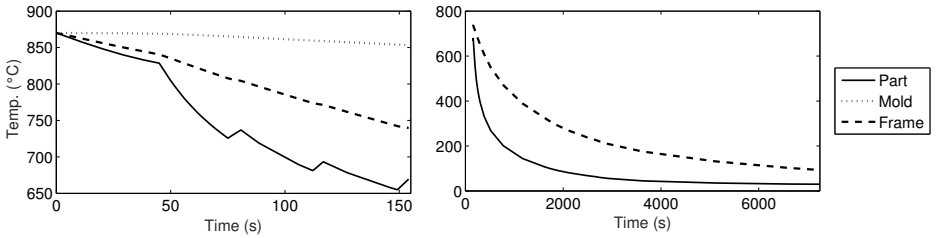

Figure 4.33 – Mean temperature evolution during the process inside (left) and outside (right) the press

4.3.2 Thermo-mechanical results

The thermal stresses just like the mechanical loadings imposed by the pulling robot have a strong impact on the unloading process and the final distortions of the part. In this section, the thermomechanical quantities are analyzed throughout each step of the simulation for the part and the frame respectively in the inside and outside configurations. The mold is not included in the mechanical analysis because of the geometrical hypothesis that deforms the results, and the low temperature variations that limit the associated thermal stresses.

4.3.2.1 Part

4.3.2.1.1 Inside the press

The Figure 4.34 gives a comparison of the logarithmic equivalent plastic strain and Von Mises stress fields at the times t_1, t_2, and $t_3(7200)$. The scale of the plastic strain is the same for the three isovalues: $\varepsilon \in [1e^{-5}, 1e^{-3}]$ s^{-1}. This figure highlights that the major part of plastic deformation is produced during the first blowing phase before pulling. This might be due to the increase of the yield stress at lower temperatures that limit the plastic deformation.

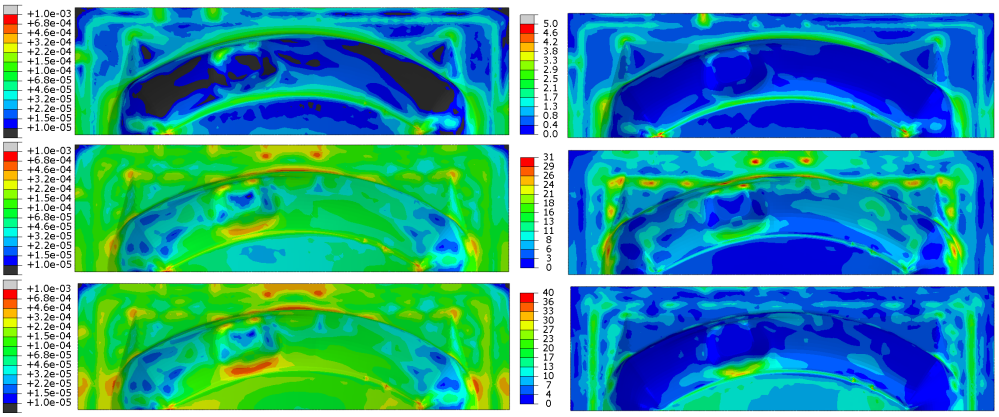

(a) Plastic Strain **(b)** Von Mises Stress (MPa)

Figure 4.34 – Equivalent plastic strain and Von Mises stress fields at time t_1, t_2, t_2(peak), $t_{2,1}$ and $t_3(7200)$ respectively from up to down

The Figures 4.35a and 4.35b give respectively the plastic stain field before and at the peak force impulse for the first and second iterations with the same scales ($\varepsilon \in [1e^{-5}, 1e^{-3}]$ s^{-1}). The extraction force seems to have none effect on the plastic deformation of the part contrary to the cooling that produces a slight increase of the strain level.

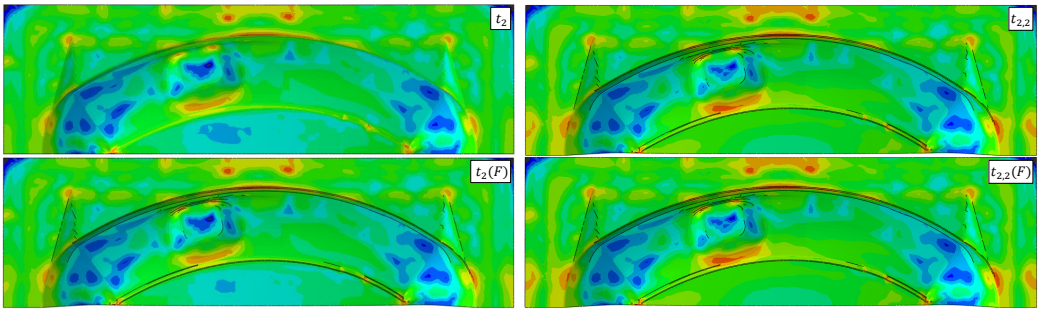

(a) t_2/t_2(F) **(b)** $t_{2,2}/t_{2,2}$(F)

Figure 4.35 – Equivalent plastic strain field (scale:[1e^{-5},1e^{-3}] s^{-1}) at time (a) t_2 (top) and t_2(F) (bottom),(b) $t_{2,2}$ (top) and $t_{2,2}$(F) (bottom)

The Figure 4.36 shows a comparison of the pulling force curve with the experimental one. The gravity load is subtracted to the total load. The numerical results lead to a total contact opening at the third impulse contrary to the fourth impulse for the experimental process. However, in the numerical cases, the force seems to relax until zero effort which does not correspond to a material based relaxation. Indeed, this phenomenon is due to the effect of the numerical contact damping that introduce viscous damping stresses that oppose to the contact opening.

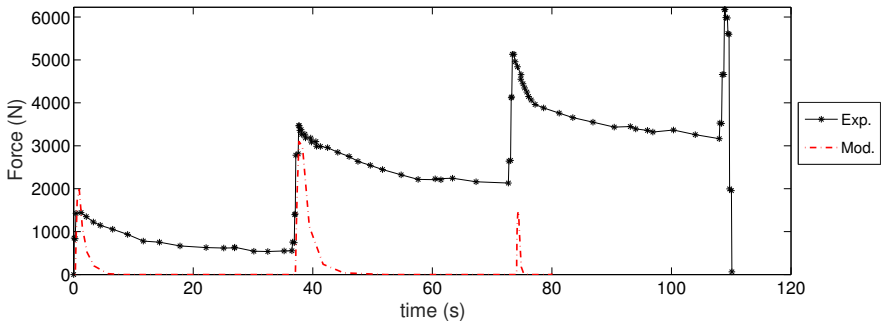

Figure 4.36 – Comparison of the experimental and model based pulling force curves

Actually, there is no friction forces that should have produced a non-null relaxed force because of stick contact conditions. A analysis of the effect of the numerical contact damping is made in the Section 4.4.

4.3.2.1.2 Outside the press

It has been shown that the plastic strain no longer evolves once the blowing is stopped. However, it is interesting to have a look on the evolution of the thermomechanical loading during the outside cooling. The Figure 4.37 gives a comparison of the temperature and Von Mises stress distributions at several times outside the press. There is a global increase of the stress field in the zones of the fastening with the frame. The Von Mises stress reaches 250 MPa at the intermediate times that seems to correspond to the highest temperature difference between part and frame's zone. The effect of part to frame connections produced a specific stress map as seen particularly for the time $t_3(1000)$. This phenomena is a consequence of the expansion of the part that comes earlier than the frame due to its thermal inertia. This might be one origin of the frame distortions.

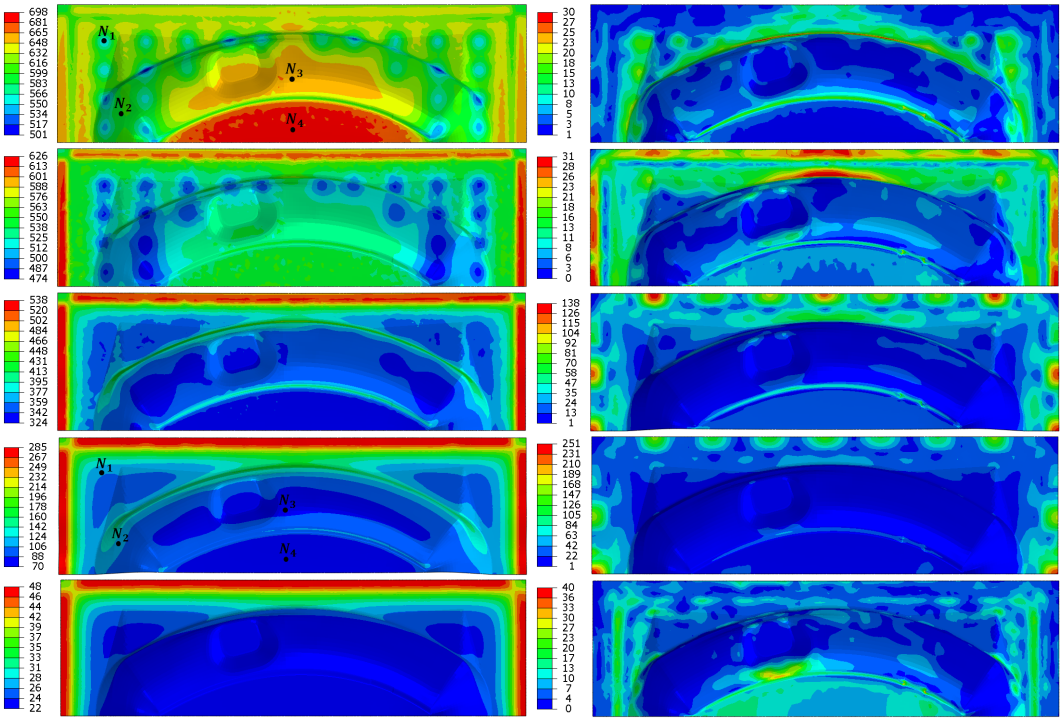

(a) Temperature (°C) **(b)** Von Mises Stress (MPa)

Figure 4.37 – Temperature and Von Mises stress fields at time t_3(0s), t_3(28s), t_3(125s), t_3(1000) and t_3(7200) respectively from up to down

4.3.2.1.3 Evolution during the process

The Figure 4.38 summarizes the thermomechanical values with the evolution of temperature Temp., the Von Mises stress σ_{VM}, the equivalent plastic strain rate $\dot{\bar{\varepsilon}}_{pl}$ and the equivalent plastic strain $\bar{\varepsilon}_{pl}$ evolution for the selected nodes of the part (reminded in the temperature isovalues of the Figure 4.37) for the three steps: 1 - natural cooling, 2 - forced cooling and removing and 3 - outside cooling.

In these graphs, it is interesting to notice that plastic deformations start from few seconds after the opening of the press. The strain rates are fairly low ($\dot{\bar{\varepsilon}}_{pl}$<1e^{-6} s^{-1}) during the step 1. Then, the major part of plastic deformation is generated during the step 2. The strain rates increase and reach a maximum value of around 1e^{-5} s^{-1} for the node N_1 which has the highest cooling rate of the selected nodes.

During each force impulse, the blowing is stopped and the stresses and plastic strain rates decrease. This confirms that the cooling is of first order importance compared to the pulling force. The nodes N_1 and N_2 no longer follow plastic deformation after the first blowing phase because they are subjected to a higher cooling rate than the two others. Their temperatures decrease respectively below 600 °C and 700 °C for which the limit of elasticity is no longer null. The nodes N_3 and N_4 keep deforming during all the blowing steps inside the press. At the end of the third blowing phase, the maximum plastic deformation is reached by the node N_3 with 1.2e^{-4} which is fairly low. In addition, the highest deformation is not the node N_1 with the highest cooling rate but the node N_3 which is the node located in the deep zone of the useful portion of part. This is probably related to the thickness distribution which is lower in this zone.

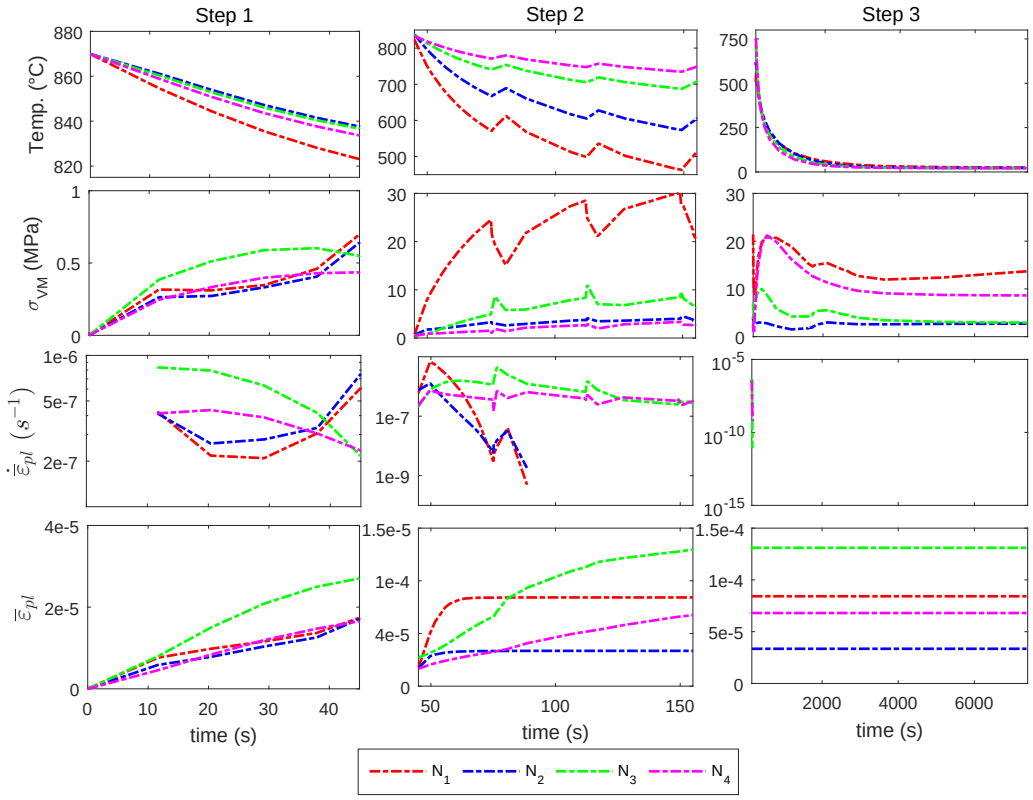

Figure 4.38 – Temperature, Von Mises stress, Plastic strain rate and plastic strain curves of the part's nodes for the steps 1 (natural cooling inside the press), 2 (forced cooling and part removing) and 3 (outside cooling)

Finally, there is none plastic deformation during the cooling outside the press such as observed above. The stresses stay rather low (σ_{VM}<30 MPa) because the nodes are not located in the areas near from the part-frame fastening zones.

4.3.2.2 Frame

The material behavior of the frame is thermo-elastic such that no plasticity may occur during the simulation. However, it is shown in the Section 4.3.1.3 that the temperature gradient of the frame reaches high values such that it might be detrimental and produces distortions.

The Figures 4.39a and 4.39b give the temperature(°C), the displacement vectors and Von Mises stress of the frame respectively at times t_3 and $t_3(2500)$. The geometry are scaled with a factor of x25 for the displacement and stress figures to highlight the deformation tendencies.

There is a clear influence of the temperature gradient of the frame that produces significant deformations. At the end of the third blowing phase, when the temperature gradients are the highest, the maximum displacement reaches more than 10 mm in the center of the longitudinal profile. After 2500 seconds outside the press, the temperature gradients promotes a z-axis displacement up to more than 3 mm, still in the center of the longitudinal profile. The frame deformations might affect the part distortions, but also permanent deformations of the frame. Indeed, the Von Mises stress distribution at the time t_3 reaches 350 MPa when the temperature is around 750 °C. At the time $t_3(2500)$, the stress reaches 1220 MPa when the temperature is around 215 °C. The Incolnel 718 superalloy has good properties at high

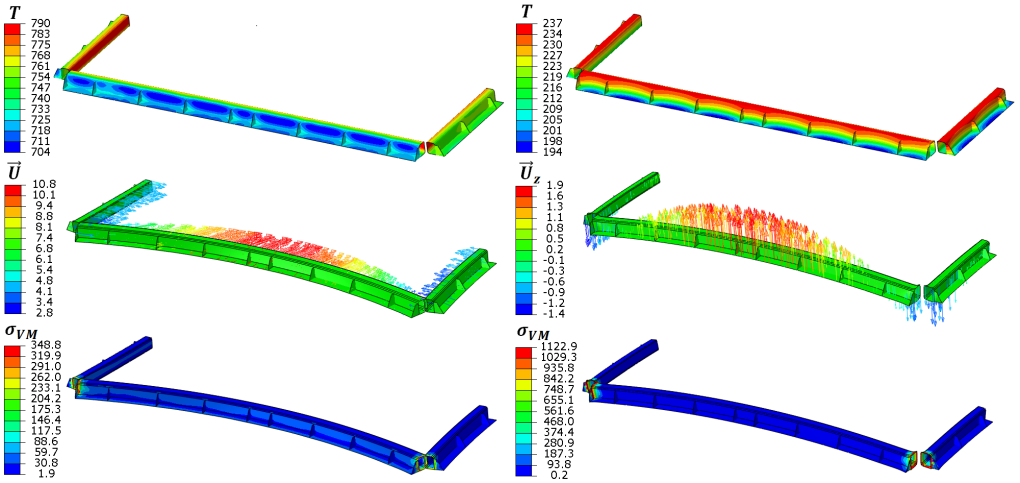

(a) t_3 **(b)** $t_3(2500)$

Figure 4.39 – Temperature field (°C), scaled displacement vectors (mm) and scaled Von Mises stress (MPa) of the frame at times t_3 and $t_3(2500)$ - scale factor x25

temperatures, a quasi-static yield stress around 800 MPa and 1100 MPa respectively at 750 °C and 215 °C which may produce plastic deformations [217].

4.3.3 Distortions and residual stresses

The Figure 4.40 gives the local orientation of the part. The Figure 4.41 gives the Von Mises stress and the stress components at the mid-side integration points before and after the trimming operation.

The σ_{22} and σ_{12} components are fairly low compared to the σ_{11} before trimming. Indeed, the main residual stresses are compressive stress ($\sigma_{11}<0$) located in the interior radius of the part. The Figure 4.42 represents the scaled displacement field (scale factor x100) generated by the residual stresses compared to the end of process geometry superposed with the non-deformed mesh. The interior of the air inlet seems to twist symmetrically from each side of the yOz plane around the z-axis. It is the consequence of the compressive stresses mentioned above. This defect is usual in AIRBUS plant and is called the "bending" defect.

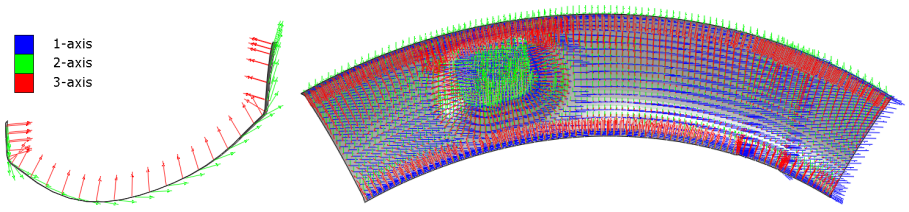

Figure 4.40 – Local orientations of the part

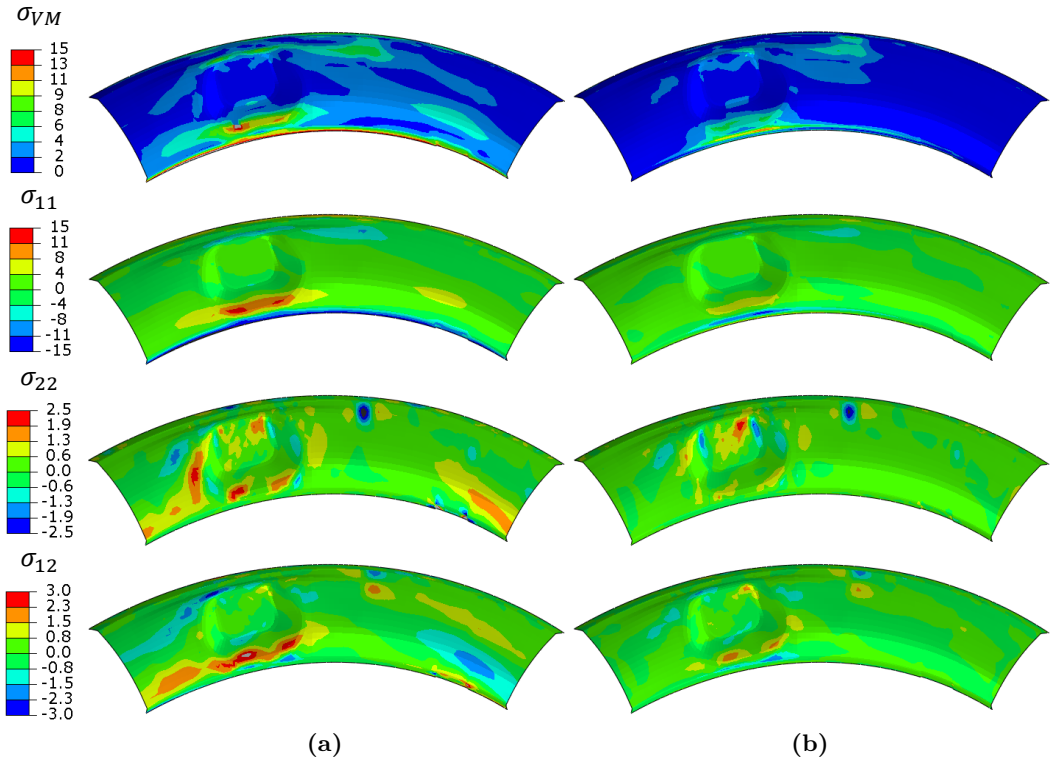

Figure 4.41 – Residual Von Mises and stress components (a) before and (b) after trimming operation (MPa)

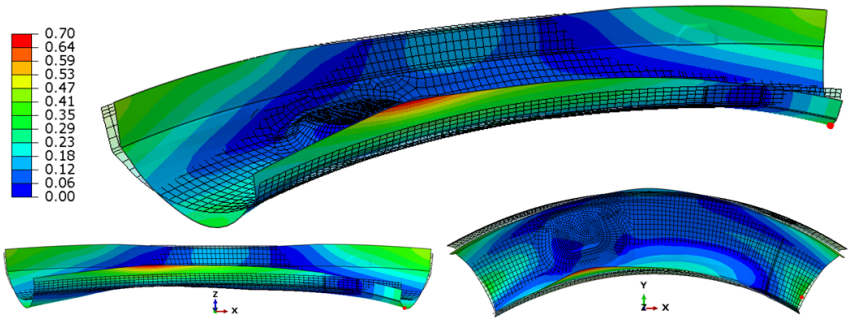

Figure 4.42 – Superposition of the deformed part (x100 scale factor) and the pre-trimming mesh with the norm of the displacement vector field (mm)

The evaluation of the distortion are analyzed using the mean distance computation $\mathcal{D}$. The deformed geometry is superposed on the theoretical one using a reference node, a plane and a direction such as presented in the Figure 4.43a. The chosen element corresponds to a functional zone of the workpiece that have specific tolerances. The mean distance of the part $\mathcal{D}$ is computed for the three superposition configurations as defined in the Equation (4.25) where $\left\|\overrightarrow{M^0_{n_i} M^j_{n_i}}\right\|$ is the nodal gap distance as illustrated in the Figure 4.43a.

$$\mathcal{D} = \frac{1}{N} \sum_{n_i}^{N} \left\| \overrightarrow{M^0_{n_i} M_{n_i}} \right\| \tag{4.25}$$

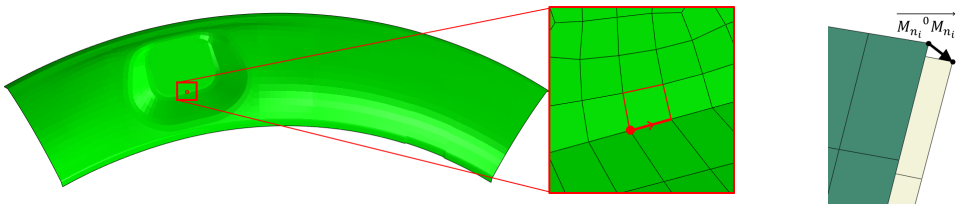

(a) (b)

Figure 4.43 – Representation of the (a) reference element used for mean distance computation (b) nodal gap distance for one node

The Table 4.2 give the mean distance, its standard deviation (% of the mean distance) and the maximum distance. The maximum distance is located at the node indicated in the Figure 4.42. The maximum displacement on the Figure 4.42 is fairly lower than the value of the 4.2. Indeed, the displacement field is directly computed from the stress relief regarding to the deformed geometry while the maximum displacement of the table is computed regarding to the theoretical geometry after re-positioning the part on the referenced element.

$\mathcal{D}$ (mm)	R.S.D($\mathcal{D}$) (%)	max dist. (mm)
1.034	63.5	3.143

Table 4.2 – Average, standard deviation and maximum value of nodal distance with the theoretical part geometry

4.3.4 Discussion

In this section, the simulation of the industrial process have shown plenty of interesting results.

Globally, the simulation gives an overview of the global temperature evolution and the consequence in terms of thermal stresses induced on the part but also on the tooling. One important aspect concerns the importance of the blowing phase. It is seen that it produces the major part of the plastic deformations which demonstrate the importance of the blowing strategy. Then another important aspect is the effect of the asymmetric HT through the open door, especially the radiative HT. Indeed, the frame cooling is highly influenced by the thermal radiation with the environment which generates bending of the frame's profiles. Finally, the distortions obtained at the end of the process after trimming are in agreement with the typical distortions obtained in the plant. However, the distortion measurements directly depends on the method, and the reference that is taken for measuring.

The model gives satisfaction regarding to the objectives of the chapter. However, two details have questioned the validity of the model: the absence of plastic deformation during the force impulse the absence of sticking contact conditions observed from the force curves comparisons. These aspects highlight an issue regarding to the numerical processing of contact. Indeed, experimentally, it is an evidence that friction phenomena occur during the extraction process. It is clearly seen by the shopfloor workers but also in the force curve.

Therefore, a sensitivity analysis of the model on two parameters that might affect the contact, the force curves and finally the distortions has to be conducted.

4.4 Sensitivity analysis

As introduced in the previous section, there might be an issue regarding the consideration of the friction at the part-mold interface. This problem leads to the absence of sticking

phenomenon that happens at the part-frame contact interface during the vertical displacement imposed by the robot on the frame.

In order to investigate how the model behaves during contact, a sensitivity analysis has been performed on two parameters that are part of the contact resolution. The first parameter is the contact damping factor which is purely numerical. The second one is the value of the coulomb friction coefficient which has rather a physical meaning. The impact of both parameter are analyzed quantitatively through the pulling force curves and also qualitatively through the plastic deformation.

4.4.1 Simplified model

A simplified model is used for the sensitivity analysis. The geometries of the part, the mold and the frame have been copied on the industrial ones. The Figure 4.44 represents the assembly of the mold, the part, the frame and a robot arm. It is quarter of the initial geometry with a double plane symmetry.

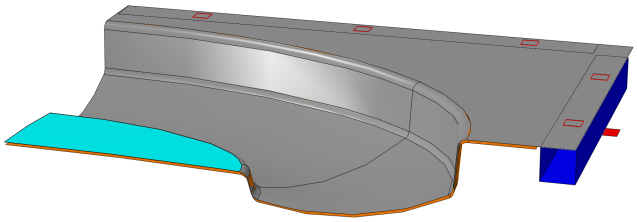

Figure 4.44 – Simplified model: CAD view of the assembly

The modeling approach is the same than for the industrial case except for forced convection model and the extraction procedure which have been simplified. The central dome area (in turquoise in the Figure 4.44) has been considered to be cooled through a constant forced convection coefficient of 200 $W.m^{-2}.K^{-1}$ with a residual semi-forced convection coefficient of 50 $W.m^{-2}.K^{-1}$ on the rest of the part surface. By targeting the dome areas, it enables to enhance the effect of male-female clamping of the part and the associated friction. In addition, the part-frame fastening is simplified. A condition of "rough" surface contact (no relative motion, no separation) is defined for the area corresponding to industrial fastening (red square above frame surface in the Figure 4.44).

The extraction of the part is performed after 30 seconds of blowing with a single impulsion until part removing to generate identical cooling procedure. The Figure 4.45 gives the time variation of the robot arms displacement. There is a first displacement step at 50 mm/s during 3 seconds and then 2 seconds waiting. The extraction efforts and the qualitative part deformations are used to analyze the impact of both the contact damping factor and the friction coefficient parameters.

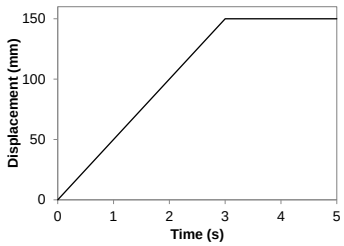

Figure 4.45 – Simplified model: robot diplacement curve

In a first approach, the displacement imposed by the robot was applied onto the frame to reproduce the real process. However, this method generated important additional viscous stress because of part and frame rigid body motion. Therefore, the relative extraction displacement was applied to the mold with z-axis fixed hanging points of the frame. High viscous stresses are applied onto the mold because of the associated mass but without any impact on the extraction.

4.4.2 Contact damping

As mentioned in the Section 4.2.5.3 the contact damping may have a detrimental effect if it is not well set. However it is required to converge. Six different values were tested at the beginning of the extraction step from 10^{-1} to 10^{-6} for the CDf. This factor is multiplied to a contact damping value generated automatically based on the stiffness of the underlying mesh and the time step size [218].

The Figure 4.46 represents the pulling force evolution during the 5 seconds of linear displacement of the robot. The right graph is a zoom of the left one on the lowest forces level. There are two major impacts on the force curves. The first one is the increase of the peak force. Indeed, the ratio of the difference of the peak force and the gravity load is around three when the CDf ratio is of ten. The CDf $1e^{-4}$ gives a peak force around 1500 N which corresponds to 1/4 of the usual value obtained for the industrial air inlet (2 impulses of 150 kg plus 300 kg of weight). The second effect concerns the evolution of the force after the peak. For the highest values $1e^{-1}$ and $1e^{-2}$, the force does not monotonically decrease until the mass load. There is an inflexion point which happens at the end of the robot displacement.

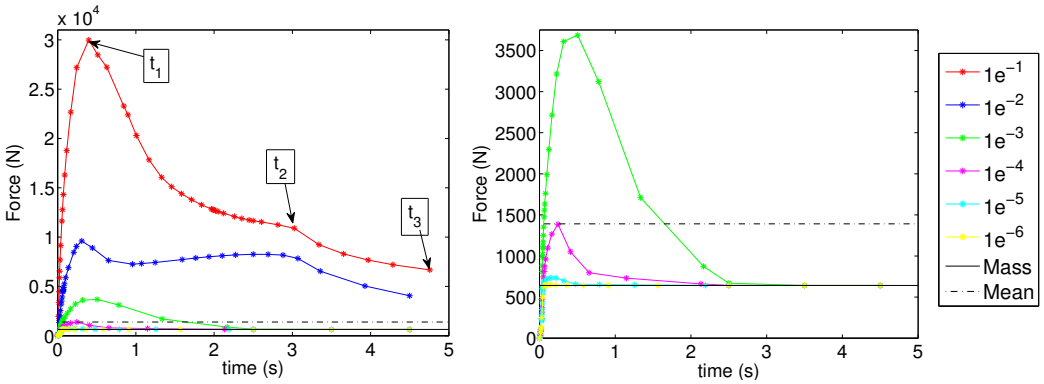

Figure 4.46 – Evolution of the pulling force during the removing operation - influence of the CDf - all curves (left) and a zoom on low CDf values (right)

In order to understand how the contact damping influences the contact stresses, the contact damping stresses have been analyzed, especially the normal component (CDPRESS). The Figure 4.47 shows the CDPRESS field at the peak stress time for CDf values of 1e-1, 1e-3 and 1e-5. The contact damping produces a negative contact stresses that force against the contact opening. These contact stresses are clearly artificial and disturb the response of the model regarding the forces but more globally of part deformation.

The Figure 4.48 gives the plastic strain fields at the end of the robot displacement (150 mm) for each CDf. The deformed geometry is completely different in the case with CDf=0.1 for which the CDPRESS components have held the part back into the mold throughout the robot displacement. The Figures 4.47 and 4.48 clearly shows the high sensitivity of the model

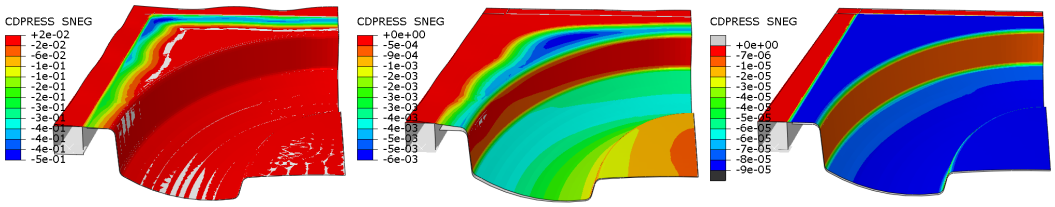

(a) CDf=1e^{-1} **(b)** CDf=1e^{-3} **(c)** CDf=1e^{-5}

Figure 4.47 – Contact damping stress field at the peak pulling force

to the CDf parameter which leads to non-physical results especially pronounced for CDf=0.1.

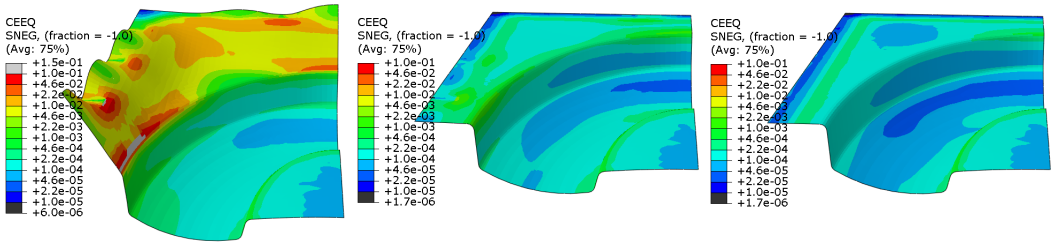

(a) CDf=1e^{-1} **(b)** CDf=1e^{-3} **(c)** CDf=1e^{-5}

Figure 4.48 – Equivalent plastic deformation field at the end of the robot displacement (150 mm)

The Figure 4.49 gives the CDPRESS field at the three times t_1, t_2 and t_3 represented in the Figure 4.46a. The figure highlights the fact that the decrease of the force curve is the consequence of the displacement of the contact opening zone and its surface reduction.

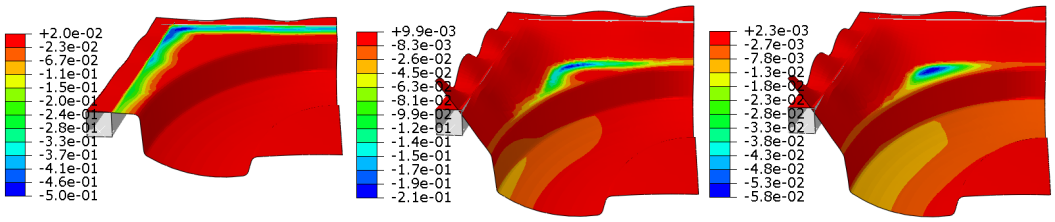

(a) t_1 **(b)** t_2 **(c)** t_3

Figure 4.49 – Contact damping stress field at the peak pulling force

This results fully question the consideration of the friction forces in the model. Indeed, the logic would impose to reduce to a minimum the artificial forces that modify the solution of the model. However, reducing the CDf seems to annihilate the friction forces which is not consistent with the experimental observations. Therefore, most of the next simulations include the analysis of the effect of CDf parameter.

4.4.3 Friction coefficient

A simple Coulomb's friction law is used in the model. The friction coefficient μ=0.1 of the law is calibrated so that to get good thickness predictions during the forming phase. However, this model for slipping contact condition might not be relevant for stick contact

conditions. In addition, the part and mold surface properties are pretty inhomogeneous and varying along forming batches. Indeed, the BN coating degrades because of localized friction phenomena at high pressure and thermal stresses. In addition the mold lubricant coating which is applied before the first forming is not recharged during a batch so that friction conditions evolve at each forming. Therefore, it is important to analyze the sensitivity of the model on this parameter not only to evaluate the criticality of the coefficient error, but also its variation along batches.

The effect of the Coulomb's friction coefficients has been analyzed by testing the next three values 0.1, 0.3 and 0.5. The three cases have been tested using four acceptable contact damping factors (1e-3, 1e-4, 1e-5 and 1e-6). The objective of testing the friction coefficients values for several CDf is to evaluate if the sensitivity of the model to friction varies with the contact damping stresses.

The Figure 4.50 shows the curve of the force evolution during the removing phase. There is clearly no impact of the friction coefficient on the pulling force curves. This confirms that the contact damping tool inputs non realistic forces that highly influence the global removing process. It is clear that the negative forces, normal to the contact surfaces, have no physical sense. They modify the response of the model to specific process conditions, however, it is required to get convergence.

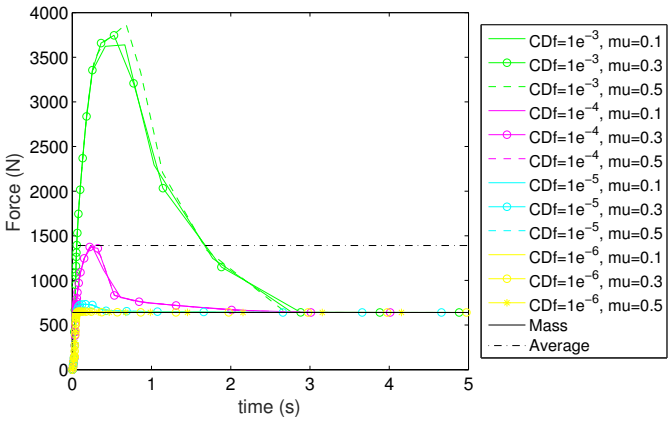

Figure 4.50 – Evolution of the pulling force during the removing operation - influence of μ and the CDf values

A solution is to assign different values of CDf as a function of the surfaces. In the case of the simplified model, the horizontal surfaces should not be involved in friction due to their perpendicular direction to the pulling force. The Figure 4.51a represents the exterior lateral surface that has been selected as the rubbing zone during pulling. Several CDf values have been attributed to this surface while the others were fixed at 1e-6. The Figure 4.51b gives the force evolution for the mentioned cases for two friction coefficient values (0.1 and 0.2). There is a clear reduction of the force level of 2 to 3 times less in the respective conditions of the Figure 4.46. However, the pulling force is still non-sensitive to the friction coefficient. This confirms that the generated force might be purely artificial.

4.4.4 Discussion

It has been seen in this section that the model is highly sensitive to numerical contact damping proposed by ABAQUS® . The CDf tool is necessary to get convergence for such problems with lot of contact closing-opening transitions due to the thermal stresses and the pulling effort.

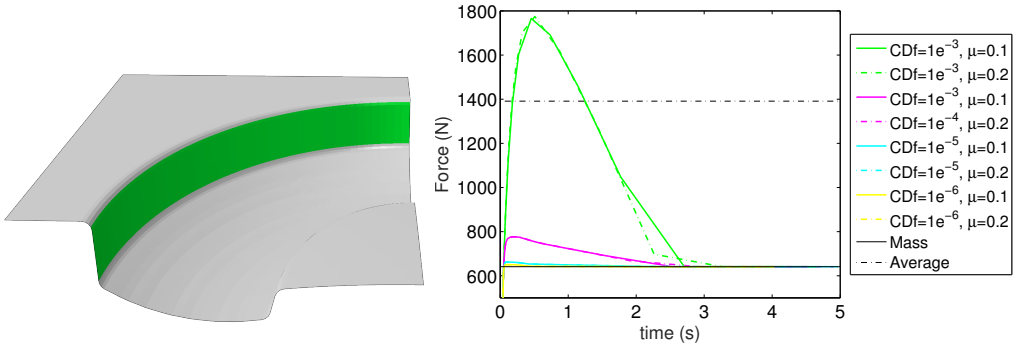

(a) **(b)**

Figure 4.51 – (a) lateral exterior surface, (b) evolution of pulling force during removing operation - influence of the CDf of the lateral exterior surface with mu=[0.1;0.2]

The contact damping introduces negative contact stresses to limit contact opening situations. The problem besides the overestimated pulling effort is that it influences wrongly the effect of a cooling strategy on the part deformations. Indeed, the contact damping stress path follow the contact opening zones. These zones are at the beginning located very closed to the frame that transmits the pulling effort and then glides up to the lateral surface. For high contact damping factors, the optimized cooling strategy might be the one which strength the previously mentioned zone whereas it might be different for low CDf values.

One tested solution is to affect various contact damping factors to limit non physical contact conditions. By selecting a-priori the surfaces likely to rub, it inevitably influences the contact pressure and the associated "friction" stresses. On the contrary, a specific cooling strategy is supposed to produce a particular thermal stress field and the associated deformation of the part. These deformations modify the contact pressure distribution between the part and the mold. Therefore, it is questionable to a-priori select the friction surfaces if the objective is to optimize the cooling strategy.

One other tested solution is to reduce to the minimum the contact damping factor to avoid any artificial forces. In this case, the model generates none friction. This might come from wrong hypothesis of the initial contact conditions, or the contact friction model which is not adapted for the process purpose.

4.4.5 Effect of contact damping on the industrial geometry

The sensitivity study on the simplified model has not given full confidence in the model definition and the associated results, especially regarding the effect of the contact damping. Therefore, a final analysis on the effect of contact damping factor with the industrial geometry has been made to ensure that the problem comes from the model and not from the simplification of the geometries. Four CDf (1e-3, 1e-4, 1e-5 and 1e-6) were used on the whole surface (no surface distinctions) with the industrial cooling. The Figure 4.52 gives a comparison of the pulling force curves. The left graph shows the successive iterations of the force impulses. The cases with a CDf of 1e-3 and 1e-4 require respectively 2 and 3 iterations to be removed from the mold while both other cases do not reach the first force impulse such as highlighted on the right graph.

The Table 4.3 gives the mean distance, its standard deviation and the maximum distance for every tested case. The values are approximately identical. It seems that the use of the contact control when using a maximum pulling effort limits the plastic deformation on the trimmed geometry.

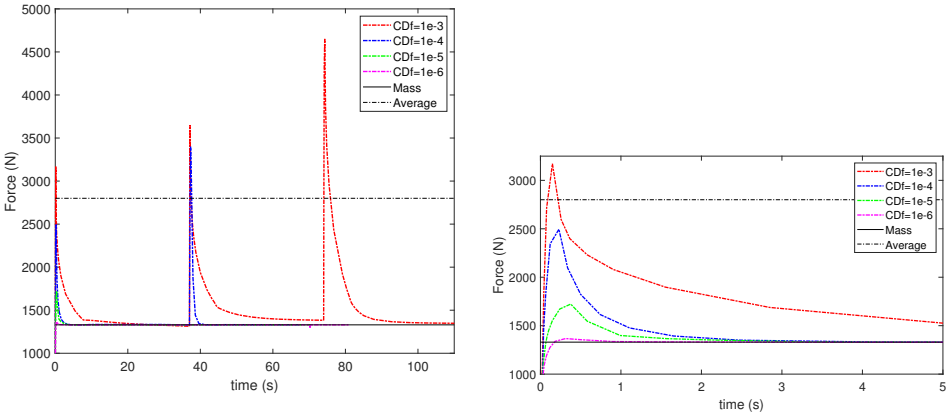

Figure 4.52 – Pulling force evolution with contact damping factors (a) whole force pulses and (b) zoom on the first pulse

CDf	$\mathcal{D}$ (mm)	R.S.D($\mathcal{D}$) (%)	max dist. (mm)
1e-3	0.272	73.7	0.955
1e-4	0.218	77.9	0.926
1e-5	0.256	77.8	0.857
1e-6	0.256	77.9	0.855

Table 4.3 – Average, standard deviation and maximum value of nodal distance with theoretical part for the tested CDf

The distortions data of the Table 4.2 in the Section 4.3.4 with $\mathcal{D}$=1.034 mm is superior compared to the Table 4.3. They are obtained for a different contact control assignment method with a low value (CDf=1e-6) on the near-horizontal surfaces and a high value (CDf=1e-3) for the rest. In this case the bending effect, highlighted in the Figure 4.53, produces plastic deformations near the useful portion of the part and lead to residual stresses in this region. On the contrary, the homogeneous CDf assignment produces the plastic deformation near from the frame.

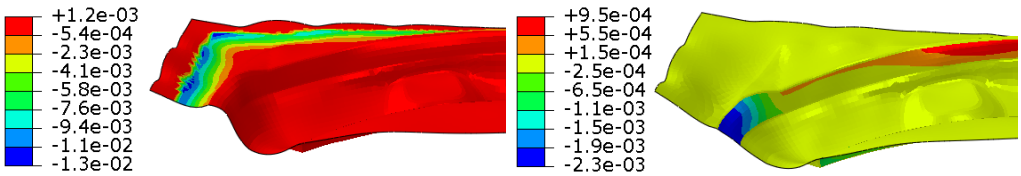

Figure 4.53 – CPRESS field at the peak force of the first impulse on a scaled geometry (a) homogeneous CDf=1e-3 and (b) heterogeneous CDf=[1e-6;1e-3] assigment (scale x50)

To conclude, the contact damping has a strong impact on the final solution of the model not only on the force curve, but also on the plastic deformation produced during part removing. In addition, the friction stresses observed experimentally do not seem to be reproduced in the model. The phenomenon may come from the contact formulation or from the initial conditions at the part-mold interface that are not adapted to the problem

4.5 Optimization of the cooling strategy

In this section the influence of the blowing strategy is analyzed to be optimized regarding to the final geometry of the trimmed part but also to the pulling force. Four different blowing strategies were tested as described in the Figure 4.54. The "Part" strategy consists in applying forced convection on the equivalent surface that is trimmed in the industrial process. The "Ext" blowing consists in cooling the exterior zone that is fasten on the frame and which enables to transmit the extraction effort to the rest of the part. The "Dome" strategy is the worst experimental case because it promotes the clamping of the part on the die. Finally, the "optim" strategy corresponds to the experimentally optimized blowing that gives the least distortions on the industrial part. Three blowing times of 15, 30 and 45 seconds were also tested.

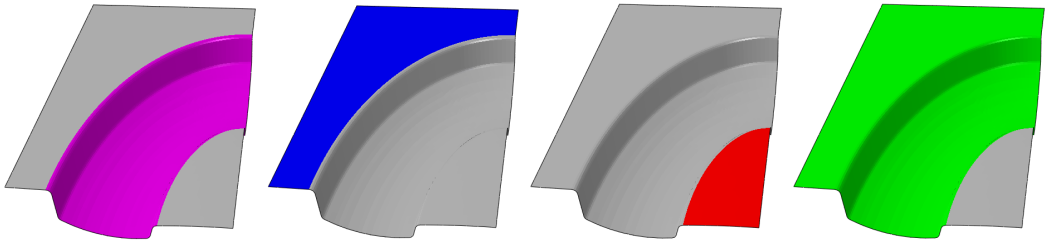

(a) "Part" **(b)** "Ext" **(c)** "Dome" **(d)** "optim"

Figure 4.54 – Representation of the tested blowing zones

The analysis of the blowing strategies has been carried out for two types of part to frame fastening connections: a fully clamped BC (fixed) as used for sensitivity study, and a contact plane displacement free (plane-free). The objective of using both fastening conditions is to evaluate the sensitivity of the model to this parameter for which the industrial process is in between. Indeed, the industrial fastening does not allow perpendicular to the contact plane displacement while a small displacement is allowed in the contact plane until it stops.

The sensitivity study have shown the limits of the model regarding to the consideration of the friction forces during part removing operation. Therefore, each tested case has been computed for two homogeneous CDf (1e-3 and 1e-6) in order to evaluate if the numerical contact damping factor influences the blowing strategy.

4.5.1 Method

The same procedure than for the sensitivity analysis is used for the optimization. The real process imposes an iterative maximum pulling force to limit part deformations during the removing step. However, it would have been too much complex to optimize a multi-step pulling sequence with various parameters that are currently highly influenced by the numerical contact damping. Therefore, a single pulling effort pulse has also been imposed, followed by an ambient cooling and finally the trimming operation.

The geometrical distortions are evaluated using the trimmed mesh and the initial mesh of the part corrected by its expansion. Both meshes are superposed into three different configurations as represented in the Figures 4.55a and 4.55b taken at different positions on the symmetry plane . The mean distance of the part $\mathcal{D}$ is computed for the three superposition configurations as defined in the Equation (4.26) where $\left\|\overrightarrow{M^0_{n_i} M^j_{n_i}}\right\|$ is the nodal gap distance as illustrated in the Figure 4.55c.

$$\mathcal{D} = \sum_{j}^{3} \left[\frac{1}{N} \sum_{n_i}^{N} \left\| \overrightarrow{M^0_{n_i} M^j_{n_i}} \right\| \right] \tag{4.26}$$

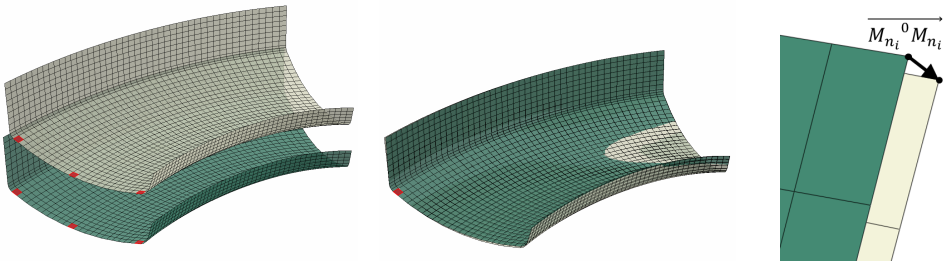

(a) **(b)** **(c)**

Figure 4.55 – (a) Superposition elements (in red), (b) superposed parts on one element and (c) nodal gap distance for one nodes

4.5.2 Results

4.5.2.1 Part-Frame fastening: fixed

The Figure 4.56 gives a comparison of the pulling force curves for both CDf values. The Figure 4.56a shows that the blowing strategy has none impact on the pulling force with CDf=1e-6. In addition, the displacement of the robot provides absolutely none friction forces such that the force curves reach the mass load once the whole surface is not supported by the mold anymore. On the contrary, 4.56b shows that when CDf=1e-3, the force curves reach a maximum around 3000-3500 N an then decrease up to the mass load. The minimum peak force is obtained by blowing 30 seconds on the dome zone while the maximum is obtained with a blowing of 45 seconds on the exterior zone. However, the differences are not really significant.

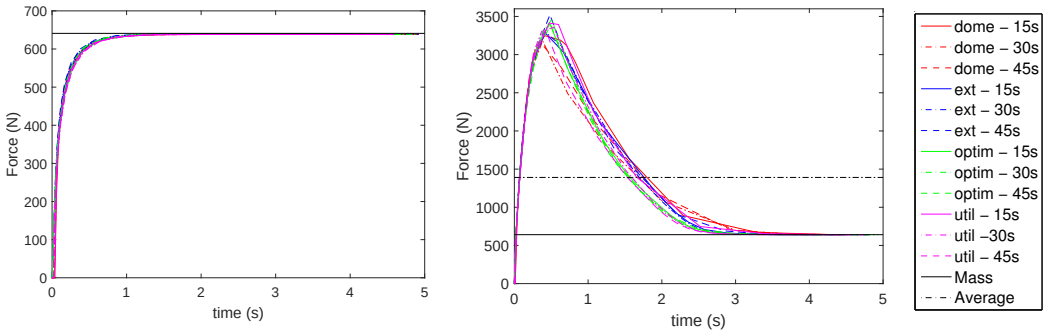

(a) **(b)**

Figure 4.56 – Pulling force curves: influence of the blowing strategy with (a) CDf=1e-6 and (b) CDf=1e-3 for fixed part-frame fastening connexions

The Figure 4.57 shows bar graphs that highlight the influence of the tested conditions on the relative mean distance $\mathcal{D}/\mathcal{D}_{max}$ where $\mathcal{D}_{max}$ (=1.74 mm) is the maximum mean distance obtained with the CDf of 1e-6. The bar colors refer to the blowing strategies such as given in the Figure 4.54 and the color intensity of the bars refers to the blowing times (15, 30 and 45 seconds). The most detrimental is obtained with 15 seconds of exterior blowing with both CDf. Contrary to the force curves, the contact damping has no significant effect. Indeed, the influence of the blowing strategy has a impact on the mean distance inferior to 8%.

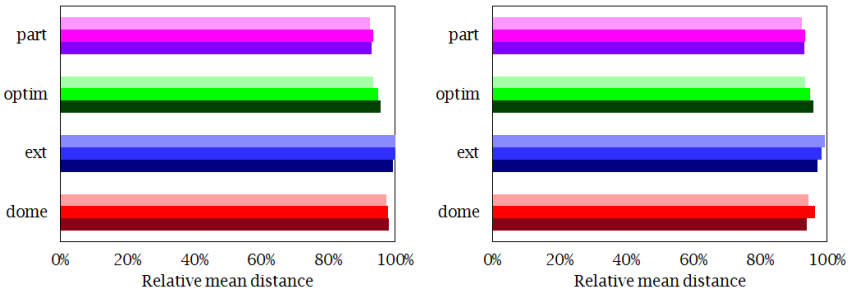

(a) **(b)**

Figure 4.57 – bar graph of the mean gap distance $\mathcal{D}$: influence of the blowing strategy with (a) CDf=1e-6 and (b) CDf=1e-3 for fixed part-frame fastening connexions

4.5.2.2 Part-Frame fastening: plane-free

The Figure 4.58 gives a comparison of the pulling force curves for both CDf values. As for the fixed conditions, there are none impact of the blowing strategies on the force curves for the CDf 1e-6. The same shape and force order of magnitude than for fixed conditions are also obtained with CDf=1e-3 except for the highest peak force obtained with 30 seconds blowing on the optim zone.

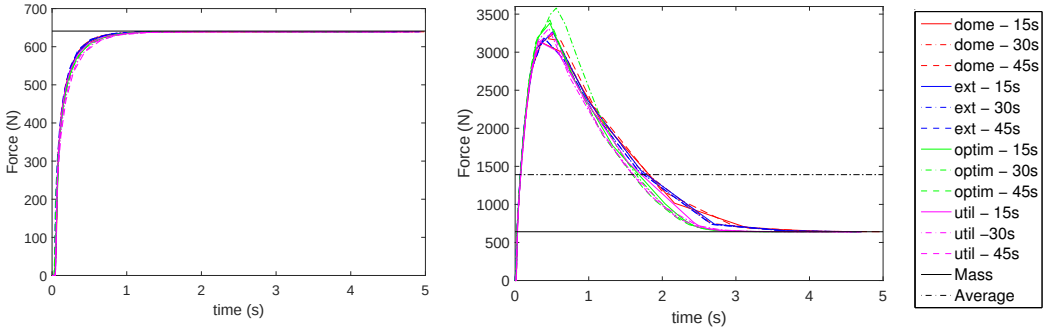

(a) **(b)**

Figure 4.58 – Pulling force curves: influence of the blowing strategy with (a) CDf=1e-6 and (b) CDf=1e-3 for plane-free part-frame fastening connexions

Concerning the impact on the means distance, the Figure 4.59 shows the relative mean distance $\mathcal{D}/\mathcal{D}_{max}$ still computed with $\mathcal{D}_{max}$=1.74 mm. A significant impact of the blowing strategy is produced in these conditions contrary to fixed fastening. However, there is still no significant effect of contact damping on the distortions results. For both CDf, the exterior cooling gives the best results with the less blowing time while the dome blowing give the worst distortions with $\mathcal{D}_{ext\text{-}15s}$=0.68 mm. The optim blowing, which gives the best results experimentally, is the second best strategy.

4.5.3 Discussion

Several interesting results are obtained in this section. The objective was to evaluate an optimized blowing strategy analyzing two indicators: the extraction effort and the final distortions after trimming. Four different blowing zones and 3 activation times were tested. These twelve cases were computed in four modeling conditions, two CDf (1e-3 and 1e-6) and two part-frame fastening conditions (fixed on contact plane free displacement).

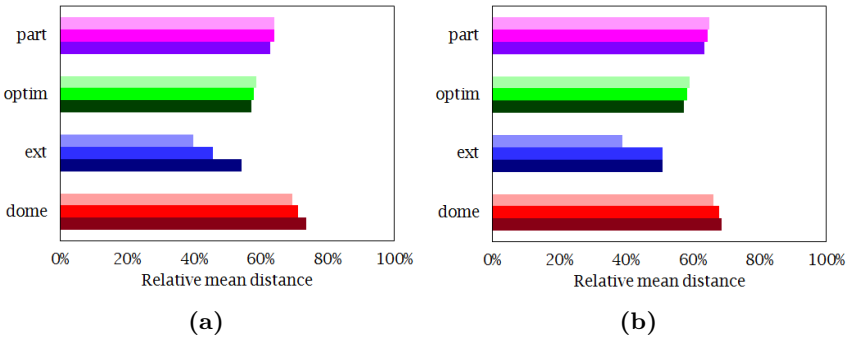

Figure 4.59 – bar graph of the mean gap distance $\mathcal{D}$: influence of the blowing strategy with (a) CDf=1e-6 and (b) CDf=1e-3 for plane-free part-frame fastening connexions

❒ Effect of the blowing strategy on the pulling effort

There is none sensitivity on the removing force regardless of the four modeling conditions. This highlights that the force evolution is not a good indicator in the modeling conditions. Indeed, the sensitivity analysis has shown that the total force was not the effect of shear stress produced by friction but contact damping stresses. Consequently the contact damping stress seems not significantly influenced by the blowing strategies.

❒ Influence of the fastening conditions on the distortions

The plane-free condition produces an average of 60% less distortions than for fixed fastening. This is probably due to the global expansion of the part produced regardless of the blowing strategy that generates a global tensile loading on the fasteners in the case of fixed conditions.

Then, there is a clear impact of the fastening condition, not only on the global $\mathcal{D}$ values but also on the sensitivity to blowing strategy. Indeed, in one case, the exterior cooling generates the least deformations, while it is the maximum in the other case. In the fixed condition, it is also probably a consequence of thermal expansion. Indeed, the exterior cooling promotes high thermal stresses at the global scale, but also in between each fasteners that generates plastic deformation. On the contrary, for the plane free condition, by cooling the exterior zone enables to strengthen the zone that transmits the robot efforts and support the weight of the part. Therefore the plastic deformations are limited

❒ Effect of the blowing strategy on the distortions

The results obtained with plane-free conditions are more consistent with the industrial process. Indeed, there is a significant effect of cooling on distortions. In addition, the dome strategy gives the worst distortions such as experimentally. This might confirms that allowing in contact plane displacement instead of blocking is a good hypothesis.

However, the fact that the exterior cooling gives the least distortions might be a consequence of the nearly absence of friction stress considered in the model. Indeed, if the friction forces were modeled, the exterior blowing strategy would finally lead to more plastic deformation in the useful zone of the part due to its lower yield stress (higher temperature). On the contrary, the optim strategy would behave better due to the cooling on both the exterior and the useful portion of the part.

To conclude, the optimization of the blowing strategy cannot be considered as completed. Indeed, the friction forces produced by the blowing strategy seems experimentally the most critical issue. Therefore, the optimization has to be performed with a model that considers rightly the effect of friction during the part removal phase. However, the obtained results are interesting indications that may be useful to optimize the final shapes of air inlet parts when the BN lubricant coating has perfect properties.

4.6 Conclusion

One first objective of this chapter was to implement a FE model that enables to reproduce the effect of the process parameters on the distortions of part through the transposition of the industrial heat transfers and mechanical conditions into numerical boundary conditions.

Implementation of the model

The whole process constituted by the forming stage, the thermo-mechanical effect of cooling inside and outside the press, and the final laser trimming operation is modeled. Therefore, it is possible to evaluate the effect of process parameters directly on the part distortions. The SPF step is modeled in a previous phase from which the thickness distribution of the formed part is obtained for the rest of the coupling and unloading phase. Then, a fully coupled temperature-displacement implicit resolution scheme has been chosen to take account of the coupling of part deformation and heat transfers during the cooling process. During the C&U steps, the evolution of thermal and mechanical boundary conditions are transposed from the industrial process. At the end of the outside cooling phase, the part trimming is modeled computing the residual stress relief of the final geometry.

The C&U model has been built using simplification hypotheses. Indeed, only the part, the frame and the mold are modeled as continuum domains. The press' environment (the platens, the upper die, the press' walls and door) and the robot are considered through thermal and mechanical boundary conditions. Then, every parts are modeled with shell elements based on the shell theory and considered as deformable with variable temperature. The mold and frame have been considered with a thermo-elastic mechanical behavior while the part involves also viscoplastic deformation based on the model developed in the Chapter 2.

Some mechanical BC have been built to transpose the most accurately the conditions of the process such as the robot arms displacement during extraction step or the part-frame fasteners for instance. The thermal BC have been adapted from the characterization presented in the Chapter 3 for the industrial conditions. An uncoupled method has been develpped (called weak radiation method) to take account of the complex radiative HT in the inside and outside configuration. It is based on the grey radiation theory and a-priori thermal analyses to compute the viewing factors of the different geometries. The natural convection HT were modeled using basic assumptions inside the press while CFD simulations were used to define convection coefficient function dependent on space and time for the outside configuration. The forced convection HT during blowing has been adapted from the Chapter 3 including a dependency to the impinged geometry. Finally, the conductance model has been taken from the Chapter 3 including a gap radiation, and a pressure dependent conductance coefficient.

Model results

The model has been applied on the industrial geometry of the nacelles of air inlet of the A350-900 plane. The blowing strategy used in the plant was tested. The results have given overview of the global temperature evolution and the consequence in terms of thermal stresses induced on the part but also on the tooling. It was shown that plastic deformation mainly occurs during the first blowing phase, and none deformation appears when the part cooled outside the press. The form of the distortions obtained after trimming are in good agreement with the typical shapes obtained in the shopfloor. Nevertheless, no exploitable experimental data enabled to compare the results of the simulation either in terms of temperature or deformation of the part.

However, the confrontation of the pulling force curves with the experimental data highlighted a numerical issue regarding the contact resolution, especially the consideration of friction

stresses. The sensitivity of the model on two parameters affecting the contact has been analyzed on a simplified modeling procedure. It has been shown that the model has a very high sensitivity on the contact damping factor regarding the pulling effort and the final distortions. On the contrary, the friction coefficient of the Coulomb model has none impact. The conclusion of this analysis was that no real friction stresses are involved in the model. Indeed, the effort and the induced distortions are purely artificially produced by the contact damping stresses. That is why the CDf, which is required to converge, has to be carefully set. Indeed, it may deform the behavior of the model subjected to a particular blowing strategy.

The second objective of this chapter was to implement a method to optimize the blowing strategy so that to minimize the final distortions.

Optimization of the blowing strategy

The optimization of the blowing strategy has been performed by testing four blowing zones and three blowing times. This numerical design of experiment was tested for two part-frame fastening conditions, and two contact damping factors in order to evaluate how the model behave for these different parameters.

The first interesting point was that the blowing strategy has none impact on the pulling force curves. The force is only impacted by the damping stresses which seems not impacted by the thermal stresses but rather by the contact closing/opening path. Then, the global distortions and the behavior of the model regarding to the blowing strategy is influenced by the tested fastening conditions. The fixed fastening condition tends to limit the displacement to accommodate the global material expansion that finally produces more distortions. Finally, the plane-free displacement fastening condition gave distortions tendencies that seems more in agreement with tendencies in AIRBUS than the other one. A blowing on the exterior zone closed to the part-frame contact and on the useful portion of the part gave the least distortions such as experimentally.

However, the results of this optimization are not complete. Indeed, the friction forces being not considered, the real effect of the thermal stresses produced by a strategy may be completely different. The present results are interesting indications that may be useful to optimize the final shapes of air inlet parts when the BN lubricant coating has perfect properties such like for the first forming of a batch.

Chapter

5

Conclusion

5.1 General conclusion

The work of this PhD thesis has been performed for AIRBUS commercial aircraft division in the frame of Ti-64 titanium alloy parts manufactured thanks to the SPF process. The objective was to optimize the part cooling and removal operations after SPF process to minimize the additional reworking manufacturing steps required to take back the geometrical distortions, especially the sheet metal working. The use FEM analysis has been chosen to reproduce the thermomechanical loading encountered by parts during the cooling and unmolding steps. The challenge of such model is to obtain the plastic deformations and the accumulated residual stresses during the whole manufacturing process that are the base of geometrical distortions after the trimming operation.

In the thesis, two first steps of characterization were performed, one on the material behavior of the Ti-64 alloy and a second on the heat transfers encountered by the part in the press environment (press, dies and tools) during the process. Both steps aimed to defined equations and models to implement in a FE model of the process. The last step of the PhD consisted in building a model of the process on ABAQUS® FE software able to reproduce and minimize the residual distortions of the formed part.

5.1.1 Material modeling

The study of the material behavior aimed to build a rheological law able to reproduce the right deformation and stress state as a function of macroscopic parameters such the as the temperature, strain rate, strain, etc.

A first bibliographic review aimed to understand which kind of model to use to reproduce the material behaviors involved during the process. This allowed us to highlight that the large temperature range of the process (20-900 °C), the high and heterogeneous cooling rates (0-20 °C.s^{-1}) and the large deformations (until 50%) undergone during SPF process implies a large spectra of deformation mechanisms in various microstructure conditions that made very complex the material modeling and the experimental investigations required for its characterization.

A preliminary testing session was performed to understand the influence of the various parameters in processing conditions in order to discriminate the first order material modeling parameters. This session consisted in testing the influence of the cooling rate on different forming state through tensile tests at different temperature and strain rate in the process range. These tests had a significant influence on the grain growth that influenced the mechanical properties during cooling while the cooling rate was of second order influence in the tested conditions. Following this session, a preparation procedure was defined for the final characterization.

The final testing procedure was composed of a first preparation heat-treatment based on the SPF process followed by two different tensile tests based on complex tensile-relaxation steps. These procedures have been designed to be capable to reproduce the various material behaviors encountered during the process that may finally affect the distortions such as elasticity, plasticity, strain-rate sensitivity, hardening and softening behaviors.

A material model based on an hyperbolic sine law coupled with a phenomenological yield stress model based on isotropic hardening-softening evolution was characterized. The model reproduces fairly well the material behavior not only through the tensile test curves, but also anisothermally. Indeed, anisothermal tests were performed at critical temperature where the behavior and the model are respectively highly varying and non-linear, and the model responded fairly well.

5.1.2 Heat transfers modeling

The evolution of the temperature of the part is a crucial aspect in the simulation of the process. Indeed, it controls the evolution of the material behavior and the thermal stresses produced by the expansion of the material. The temperature evolution is a consequence of the heat transfers. During the part removal operation, there are a complex combination of thermal radiation, convection, forced convection and conduction heat transfers. Each transfer mode occurs at a specific phase of the process, however they are concomitant which made complex their characterization.

A first bibliographic review of the equations and parameters that enables to model each HT mode was made for the various process conditions. Three major parameters have stood out from this review: the sheet metal emissivity ϵ for radiation, the convection coefficient h_c, and the conductance coefficient k_c. Various laws associated to the three parameters evolution as a function of the process parameters were presented.

The second step of the work consisted in designing an experimental procedure to characterize or validate the various parameters of the thermal BC models to implement in the simulation. It was chosen to use a small-scale industrial SPF tooling for the experiments. Several parts formed in industrial conditions were used in a laboratory furnace equipped with different measurement means. Various experimental configurations were tested to isolate heat transfer modes from others to ease the characterization.

An inverse analysis was used to fit the model parameters of the different BC. These BC models and usual parameters were taken from the literature, except for the natural convection coefficient. CFD simulations were computed first, and basic functions were used to model the

space and time evolution of the coefficients based on the CFD results. Two first testing configurations were simulated to fit the radiation and convection models. A second configuration involving a blowing system was used to fit the forced convection and conductance models. A last configuration enabled to validate every HT mode in a non-isolated configuration.

The temperature behavior of the models with the final characterized BC were fairly good compared to the experimental data. Indeed, the temperature differences between experimental and numerical results did not exceed 25 °C with an average difference around 5-10 °C at each thermocouple during the whole natural cooling experiments. For the blowing experiment the temperature difference was less than 25 °C except for two thermocouples (below 40 °C) which is fairly good for such high cooling rate induced by the blowing equipment. The validation experiment gave also good results in the same coating condition (without BN) than for the characterization. However, the temperature results of the simulation for the validation experiment (with BN coating) were not representative with around 50-100 °C below the experimental results. This was probably due to the difference between the BN applied for the experiment on a formed part and the experimental post-formed surface quality from which the characterization of the BN had been performed.

5.1.3 Simulation of the process

The implementation of a model able to optimize the post forming operations to minimize the final distortions implied to consider every phase, element and parameters of the process that could affect the distortions. It led to introduce the forming phase and the final trimming operation in the scope of the FEM analysis. Indeed, the forming process produces a specific thickness distribution and the trimming operation releases the residual stresses so that both are required to get the final distortions of a part.

A strong temperature displacement coupling has been used to take account of the evolution of heat transfers throughout the part deformations, especially for conduction purpose. The whole simulation is constituted by a first natural cooling step inside the press, then a blow cooling phase followed by successive extraction steps until unmolding and finally a last ambient cooling outside the press. The industrial strategy for C&U parameters was simulated. The temperature but also mechanical results have shown various interesting points for optimization purposes. Indeed, among others, it has shown that the major part of plastic deformation occurs before the end of the first blowing phase, or that the temperature gradients inside the extraction frame produce very high stress and deformations that may be detrimental for itself and the formed part, etc.

A sensitivity analysis of the model performed on several parameters of the model has highlighted that the contact damping tool, necessary for convergence, has a critical influence on the solution. The pulling extraction effort and the final distortions are impacted by the contact damping factor (CDf). An optimization of the blow cooling strategy has been performed on a simplified industrial geometry for two CDf and two part-frame fastening conditions. The main conclusion was that the location of the blowing has an insignificant effect compared to the mechanical fastening between the formed part and the extraction frame regardless to the CDf. This is a good indication of improvement for the part-frame fastening systems. In addition the results have confirmed the detrimental effect of the contact damping tool. Indeed, it produced either non-physical contact stresses for high CDf like in the sensitivity study or none contact stress for low CDf. The latest case has globally questioned on the part-mold friction phenomena observed experimentally.

The material behavior and heat transfers models obtained from the characterization were included in the simulation of the process. The developed FE model gave interesting and important results of the impact of the thermomechanical loading undergone during the C&U steps of the process. Two specific blowing strategies highlighted lower distortions than others. These strategies seemed in agreement with industrial tendencies. However, some

improvement at different level of the model are needed to be fully confident in the results that currently suffer from uncertainties. Therefore, some ideas of prospective work are proposed below to get the work done in this PhD deeper.

5.2 Prospective

5.2.1 Material modeling

The material model characterized in the Chapter 2 is totally satisfactory regarding to the objective of the thesis. However, one hypothesis taken at the outcome of the preliminary testing session might be questioned. Indeed, it has not been chosen to consider the dynamic effect of phase transformations during cooling. Nevertheless, the tensile tests comparing direct and temperature-stabilized tensile tests after cooling, and the anisothermal tests have highlighted an impact on the mechanical properties. This might come from a phase transformation delay promoted by the high cooling rates.

It would be interesting to characterize a model such as the one developed by Robert [70] which uses multi-phase description of the mechanical behavior. This kind of model would enable to take account of the effect of the variation and the heterogeneity of the cooling rate over the part, especially during blowing inside the press onto the phase transformations that determine the mechanical behavior.

In addition, no anisotropy of the material has been considered. Indeed, the Ti-64 grade 5, which corresponds to equiaxed microstructure with fine grains, do not exhibit anisotropy at high temperature during SPF. However, the beta phase which is intrinsically anisotropic (Hexagonal-close-packed structure), might promote anisotropic behavior especially into its secondary alpha phase morphology. Sirvin et al. [219] have shown the importance to consider the anisotropy of the Ti-64 at intermediate temperatures (400-500 °C). They also highlighted the importance to account for the kinematic hardening that exhibit better fit of their experimental results. Both mechanical behaviors, anisotropy and kinematic hardening, have not been considered in the present work for simplicity reasons, but also because of the small deformations undergone by the parts during the post forming steps of the process. However, some investigations would be necessary to ensure to use the adequate material model.

5.2.2 Heat transfers modeling

The complexity of the HT that occur during the process made complex to characterize and implement into the FE model in the frame of a single PhD thesis. There still are work to do on each HT mode in order to get more accurate description of the temperature during cooling down.

Concerning radiative heat transfer, the WRM works fairly well. However it is totally dependent on the emissivity parameter that has been difficult to characterize. Indeed, the emissivity seems to vary regarding to the several parameters that are difficult to master thanks to the simulation. The oxidation process after forming is influenced by the BN coating layer that is itself dependent on the forming phase (contact pressure and the thinning of the part), and the initial coating thickness obtained from painting. A deeper description of the emissivity variations for different thinning ratio, post forming preservation state, cooling rate and temperature conditions would be a first work to better consider the radiation HT into the model.

Concerning natural convection, the approach based on the CFD analyses has shown fairly interesting results. However, the simplifications of the used geometries and the model assumptions probably generated errors. In addition, this method was applied for the outside

press cooling configuration while the major part of the plastic deformation seems to occur inside the press. Some additional CFD analyses should be performed in both configurations with the right geometry and the best modeling assumptions to describe the convection flows in the high temperature conditions (compressible flow).

The forced convection model has been characterized with a single nozzle impinging onto a perpendicular planar surface which is the most simple case. The blowing phase during post SPF cooling involves complex surface with multi-nozzles blowing at different height of the surface and inter pitch distances. Therefore, the modeling conditions are probably far from the real convection HT. Some additionnal characterization should be done in conditions closer to the industrial ones to better reproduce the forced convection HT that are incidentally the highest heat flux produced during the cooling process.

Finally, the characterized conductance model has shown better result by neglecting the contact based term k_0. This was probably a consequence of the initial contact conditions of the experiment and maybe also because of the geometry of the formed part that was not favorable to friction (and clamping) between part and mold. In the industrial conditions, it regularly happens that the part is clamped onto the mold because of the thermal stress that promote expansion. When it is the case, the involved contact pressures, especially during the pulling phase, produce high conduction HT that are currently not well described in the model. Some additional experiments involving the various contact conditions (pressure, temperatures, surface conditions) should be conducted to improve the conductance model.

5.2.3 Simulation of the process

The major point to improve in the model concerns the contact resolution, not only for friction purpose, but also for conduction HT as discussed above. Indeed, it has been demonstrated that the necessary contact damping may generate non physical contact stresses that can be wrongly assimilated to friction.

This lead to work on two aspects. The first concerns the contact resolution method that need to be investigated. Is the resolution scheme behind the absence of friction or not ?
The second concerns the initial part-mold contact conditions at the end of forming. Indeed, they have been considered perfect (zero gap and zero pressure at part-mold interface). However, at the end of the forming stage, the removing of the forming pressure produce a deformation of the mold, even very small, that may generate a positive contact onto the part. This deformation can be at the origin of the friction phenomena during the part removal operation. These two aspects need to be investigated to involve the right friction phenomena that occur industrially into the simulation.

In addition, there are various optimization points that can be henceforth conducted:

- The frame deformations: it has been seen that the temperature gradients generate significant deformations that may finally produce permanent deformations. Its geometry could be optimized to limit the deformation or limit the temperature gradient.
- The part-frame fastening systems: it has been seen that the fastening conditions have a major effect on the final distortions. The position, the number and the degrees of freedom could be tested numerically to optimize their design.
- The robot pulling method: currently, the robot arms only pull on the two sides of the frame. A more homogeneous distribution of the pulling efforts could be tested.

Appendices

Appendix

Material modeling

A.1 Material testing equipment

A.1.1 Induction coil

A new coil was design using the geometry of a previous one which was working for the targeted temperatures but the temperature gradients generated in the flat specimens were not acceptable. Indeed, the shape of the coil was not regular because of a hand-made manufacturing process. Therefore, a new coil was designed with equivalent dimensions of the existing coil. A template pattern system was designed to help the coil shaping such as shown in the Figures A.1a and A.1b. The pattern system was manufactured by 3D printing with a high strength polymer material to resist to the significant shaping stresses due to the strain hardening properties of copper. It was designed so that to be able to separate both

parts once the coil is entirely formed. The Figure A.1c represents the coil working during a high temperature test.

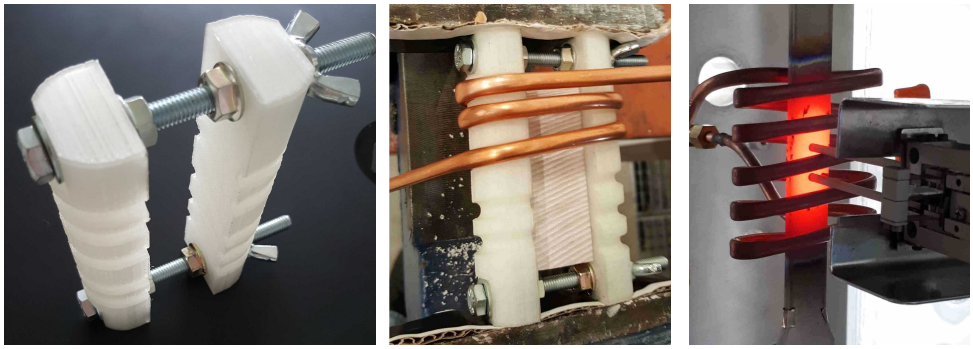

(a) **(b)** **(c)**

Figure A.1 – Coil manufacturing process: (a) pattern system, (b) shaping process and (c) high temperature test

A.1.2 Cooling system

The high cooling rates of the process require a system able to reproduce these conditions during mechanical testing. The natural cooling conditions were not sufficient to reach the 15 °C.s^{-1} required for the testing. Therefore, an additional heat flux had to be induced. Several systems using air blowing were handmade with copper tubes. The different configurations are schematically presented in the Figure A.2 where the schematic views of each case (Figures A.2a, A.2c and A.2f) are respectively associated to the real configurations in the Figures A.3a, A.3b and A.3c.

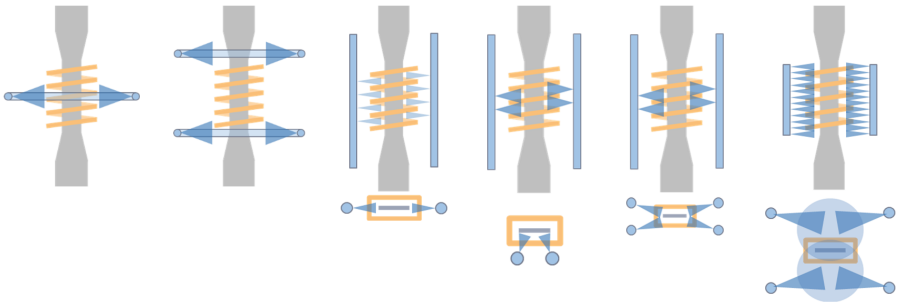

(a) **(b)** **(c)** **(d)** **(e)** **(f)**

Figure A.2 – Schematic representations of the tested cooling systems

The efficiency of the devices was evaluated through the temperature gradients produced during cooling. They were measured thanks to four thermocouples placed on both sides of the center of the sample spaced by 10 mm each such as represented in the Figure A.4a where the dimensions are in millimeters. The Figure A.2 sorts from left to right the less efficient to the best cooling device. The last configuration gives the best results because the air flow is not directly impinging on the surface of specimen. Indeed, the impact of both flux are shifted on both sides so that to create a kind of mist such as represented is the Figure A.2f. Therefore, the localization of heat flux that happened on the other configurations is limited. The system is connected to a 6 bars compressed air network. Two pressure limiters are placed before each side to ensure symmetrical cooling.

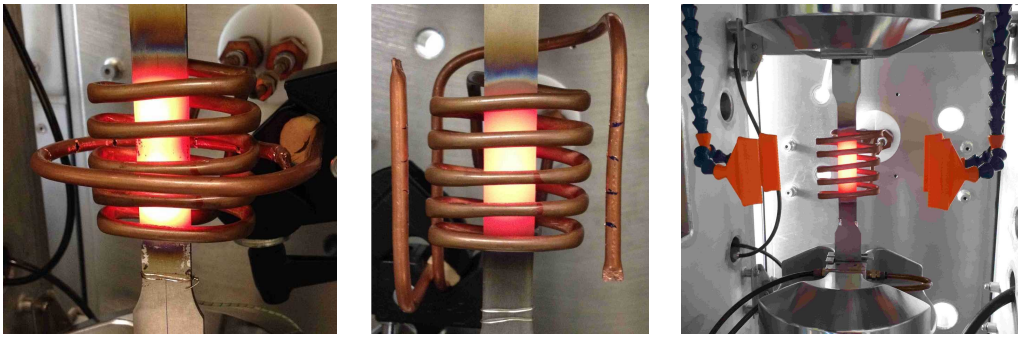

(a) (b) (c)

Figure A.3 – In service pictures of the(a) a, (b) c and (c) f cooling systems presented in the Figure A.2

A.1.3 Temperature gradient

The measurement of the temperature gradients was performed for a multi-stages temperature test. The Figure A.4a shows the temperature pattern followed during the test. A first heating to 870 °C is followed by six stages at 800, 700, 600, 500, 400 and 250 °C. The cooling rate to reach a new stage is -7.5 °C.s^{-1}. The Figure A.4b shows the first transition between 870 °C.s^{-1} and 800 °C.s^{-1}.

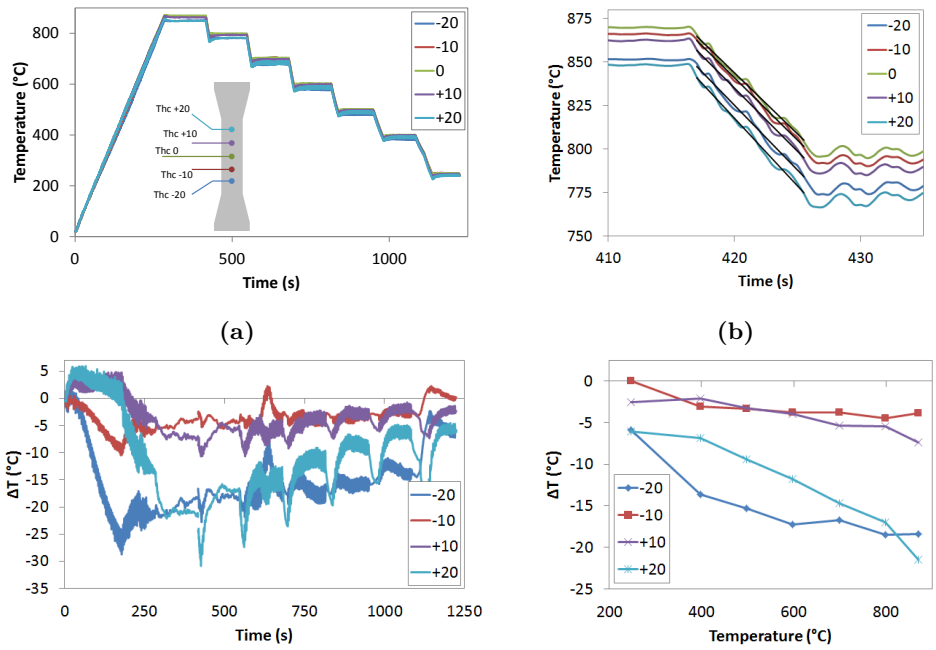

Figure A.4 – Temperature-time evolution of the gradient thermocouples (a) full test, (b) zoom on first cooling, (c) temperature gap and (d) stabilized temperature gap as a function of temperature

The Figure A.4c shows the evolution of the temperature gap with the control thermocouple "0" ($\Delta T = T_i - T_0$) for each thermocouple. A peak gap is produced at each stage transitions and followed by a decrease of the gap after a stabilization phase. The Figure A.4d gives the

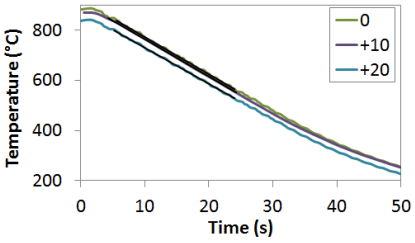

(a)

$\dot{T}$	Thermocouples				
(°C.s^{-1})	-20	-10	0	+10	+20
-7.5	-7.4	-7.1	-7.0	-7.3	-7.7
-15	/	/	-14.9	-14.8	-14.5

(b)

Figure A.5 – (a)temperature-time evolution of the gradient thermocouples for -15 °C.s^{-1}, (b) cooling rate responses of the different thermocouples for two setpoints

evolution of the stabilized gap as a function of testing temperature. These curves ensure that the maximum temperature deviation inside the useful portion of specimens is inferior to fives degrees during mechanical testing. In addition, the maximum distance between extensometer rods cannot exceed 15 mm (nominal distance 12 mm plus 24 %) which is equivalent to ±7.5 mm, which ensures a lower gradient.

An other important aspect concerns the gradient of cooling rate during the cooling phase. Indeed, it is important to ensure that the material followed an homogeneous cooling to analyse the effect of microstructure transformations on mechanical properties. Two cooling rate values were tested, the same than for the previous tests (-7.5 °C.s^{-1}), and also -15 °C.s^{-1} which corresponds to the preliminary testing case. The Figure A.5a shows the evolution of 0, +10 and +20 thermocouple during the cooling from 870 up to ambient temperature. The +10 and +20 thermocouples broke during this test contrary to the case with the lower cooling rate. The same type of curves is used for the -7.5 °C.s^{-1} case to compute experimental cooling rates from linear regressions. The Table A.5b gives the obtained values. The setpoints are fairly well respected so that even with a small gradient of temperature, the material underwent an homogeneous cooling rate.

A.2 Preliminary testing

A.2.1 Effect of SPF process

The time exposure at SPF temperature is related to two different steps encountered in the industrial process: the heating after loading the blank inside the press and the forming cycle. The heating phase can evolve depending of the time required to remove the part of the previous forming. The forming cycle depends on the geometry and the thickness. The influence of the time exposure was investigated through SEM analysis of a batch of samples that have been held at SPF temperature inside a furnace for different times. Table A.1 gives the time exposure associated to samples, and Figure A.6 illustrates the induced microstructures for each case. Each sample were cooled in the same conditions at ambient temperature.

Sample	(a)	(b)	(c)	(d)	(e)	(f)	(g)	(h)	(i)
Time (min)	0	5	15	30	60	90	120	150	180

Table A.1 – Design of experiment: time exposure at SPF temperature

The samples were analyzed with a NOVA nanoSEM 450 Scanning Electron Microscope with a ×2000 magnification factor. The micrographs were performed with back scattered electron detector, at 8.0 kV beam voltage, 5.0 mm working distance with a beam deceleration mode

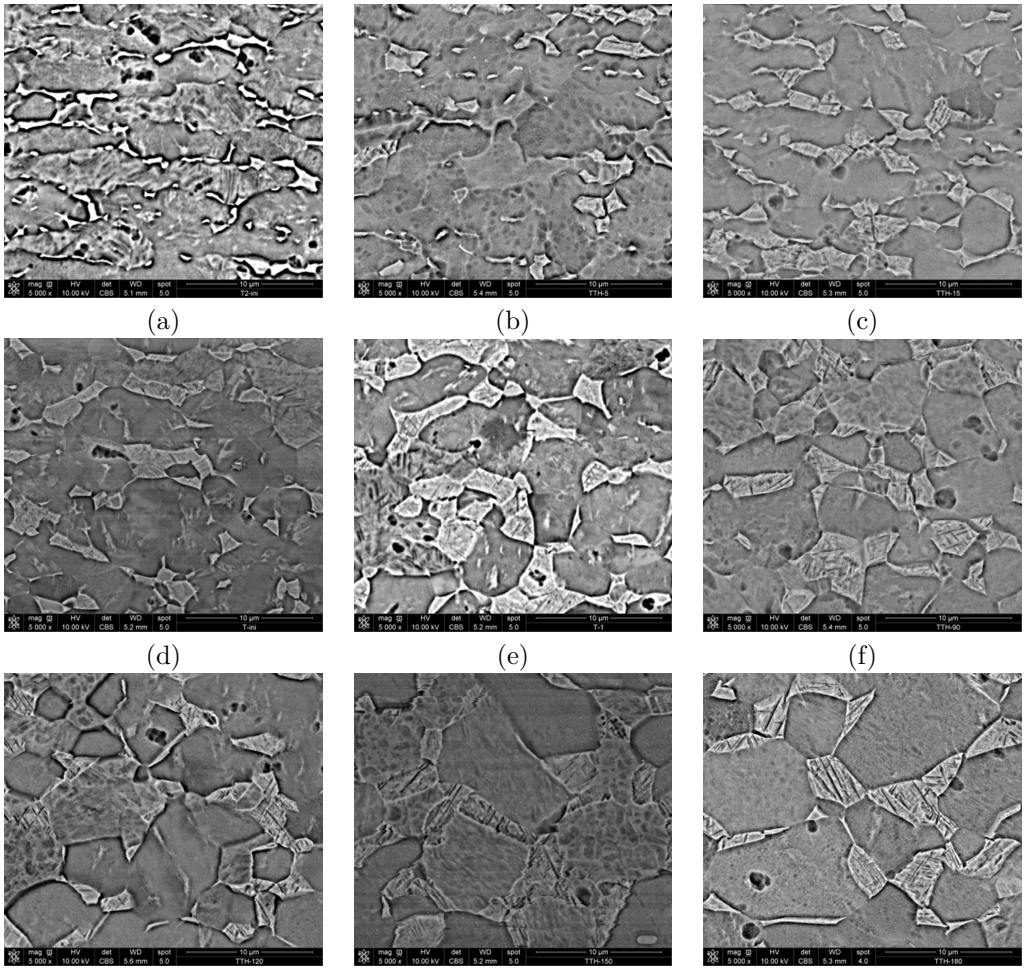

Figure A.6 – Micrographs of Ti-6Al-4V samples (x5000 magnification) heated during different time exposure (defined in table A.1)

which bring topological details of the surface. The SEM analyses reveal that a strong static grain growth occurs during holding at SPF temperature. No grain size measurement was made but it is easy to notice that the grain keep growing along time exposure. This results show that time exposure at SPF temperature has a real impact on the microstructure.

A.2.2 Effect of cooling rate

The objective of this session is to test the impact of the cooling rate and the time exposure on the material behavior. The Figure A.7a shows a schematic of the ideal heat treatment to perform before mechanical testing. However, the detrimental effect of the extensometer at high temperature made it necessary to equip with the extensometer after the heat treatment. Therefore the heat treatment differed from the one met during the process as described in the Figure A.7b.

The different tested values of cooling rates were defined with extrema values of the cooling rates imposed during the forced cooling phase of the industrial process. These values of 5 and 15 °C.s^{-1} were estimated with a blowing experiment conducted in the laboratory with an equipment similar to the AIRBUS device.

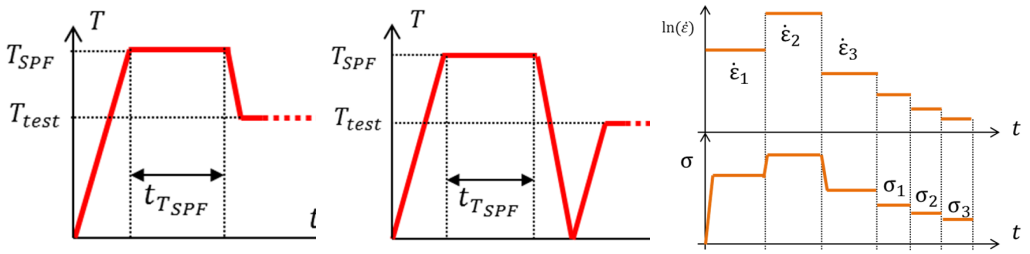

Figure A.7 – Schematic of the heat treatment (a) version 1, (b) version 2 and (c) description of mechanical loading

Step 1		Step 2	
$\dot{\varepsilon}$ (s^{-1})	ε_t (%)	F (kN)	t (s)
10^{-4}	2/2.5/3	3	200
10^{-3}	0.75/1/1.25	2	300
10^{-5}	0.25/0.75	1	500

Table A.2 – Parameters of testing procedure of 2^{nd} session part 1

A.2.2.1 Grain size influence

A.2.2.1.1 Description

This 2^{nd} session is divided into two parts. The first part consisted in comparing the effect on mechanical behavior of two different cooling rates and times exposure at SPF temperature with a total of four different configurations. By comparing two time exposures, the objective was to evaluate if the potential effect of rapid cooling would be dependent on grain size especially regarding phase transformation kinetics. In first approximation, a test temperature of 650 °C was chosen so that the remaining phase transformation below was very low to limit the effect of the heat treatment discussed above on the mechanical properties.

The mechanical part of the procedure was composed by a multi strain rate tensile test first, and then followed by a multi-load creep test in order to get lower strain rates behavior. The Table A.2 and the Figure A.7c describe the different steps of the procedure.

A.2.2.1.2 Results

The Figures A.8a shows the stress strain curves of jump tests. Unfortunately, the deformation range for each strain rate was not identical, but the curves clearly shows some differences between heat treatments. Indeed, even if flow stresses of low strain rate is not reached for all curves, the graph denotes superior values for long time exposure compared to small times at strain rates of 10^{-4} and 10^{-5} s^{-1}. On the contrary, the cooling rates seem to have no impact on flow stress, except a small difference for the lowest strain rate on long time exposure specimens.

Concerning the creep test curves presented in The Figures A.8b, the long time exposure tests present lower creep strain values which confirm what is obtained for the tensile tests. The creep strain rate seems to be approximately equal for the same time exposures.

The Figure A.8c is the a log-log graph of stress versus time which summarizes the results of the tests. The end values of creep tests for long time exposure are plotted on the graph even if the creep strain rate were not stabilized. Again, it confirms that for the temperature of 650

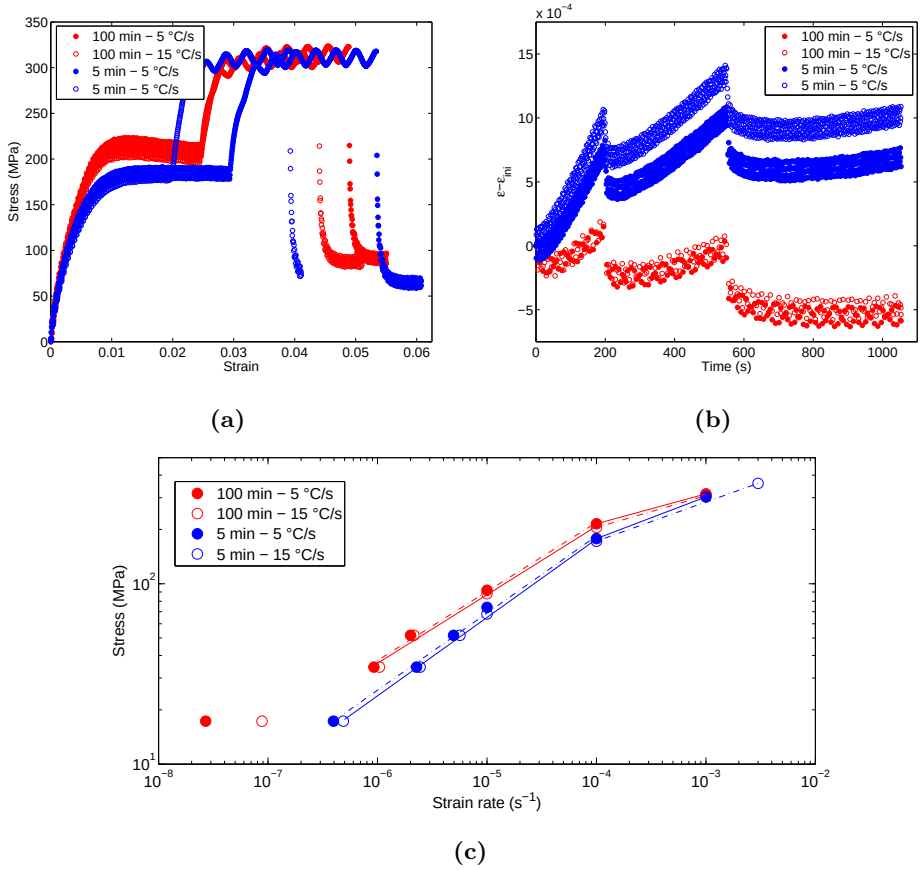

Figure A.8 – Results curves of 2^{nd} session part 1: (a) jump tests, (b) creep tests, (c) log-log curve of stress vs. strain rate

°C, the time exposure has a significant effect on material properties while the cooling rate parameter seems to be negligible. The Table A.3 shows the relative flow stress differences (computed with the Equation A.1) between long and short time exposures for low cooling rate data. The table shows that the differences rise to 20% at low strain rate while no significant difference happens for 10^{-3} s^{-1}. This is probably due to the deformation mechanisms at high strain rate that are less dependent on grain size than for low strain rates. Another interesting point is that the creep strain differences that can be observed between cooling rates for low time exposure become almost null for SPF representative long time exposures.

$$\underline{\Delta} X_{A/B} = \frac{X_A - X_B}{X_A} \tag{A.1}$$

$\dot{\varepsilon}$ (s^{-1})	10^{-5}	10^{-4}	10^{-3}
$\underline{\Delta}\sigma_{100/5}$ (%)	19.6	17.2	3.8

Table A.3 – Relative flow stress difference between 5 and 100 min of time exposure with a cooling rate of 5 °C.s^{-1}

A.2.2.1.3 Conclusion

The objective of these tests was to evaluate the effect of grain growth, as a SPF consequence, on mechanical behavior during the unmolding process. Thus the extrema cooling conditions were applied to two types of heat treatment in order to promote the possible transformation which can generate changes in the material behavior. The results have shown that Ti-6Al-4V is significantly impacted by the time exposure at SPF temperature at the tested temperature of 650 °C. On the contrary, the cooling rate did not seem to promote differences in the flow stress behavior at the tested temperature.

A.2.2.2 Temperature influence

A.2.2.2.1 Description

The second part consisted in testing the effect of cooling rate at different temperatures. For this session, the samples were only heat treated with a long time at SPF temperature. Indeed, the results of the previous session have shown the strong influence of time exposure at SPF temperature on mechanical properties. A time of 100 minutes was used to reproduce a representative industrial procedure.

The same procedure than previous session for mechanical tests were used. Only the jump test was used and three temperatures of 350, 650 and 770 °C were compared. For this session, the strain rate were started with 10^{-3} s^{-1} instead of 10^{-4} s^{-1} to consider the maximum possible effect of rapid cooling on phase transformation. The time before the mechanical loading after the heat treatment was ten seconds in order to let the temperature getting homogeneous, but also to limit the further microstructure changes.

A.2.2.2.2 Results

The Table A.4 summarizes the flow stresses data obtained from the tensile tests. At 350 °C, the SRS is not significant Therefore the tests were not performed at all strain rates. The comparison of flow stresses for the tests conducted at 5 and 15 °C.s^{-1} clearly shows that the differences are fairly small.

Temperatures (°C)		350		650		770	
Cooling rates (°C.s^{-1})		5	15	5	15	5	15
$\dot{\varepsilon}$ (s^{-1})	10^{-3}	650	650	309	315.5	115	111
	10^{-4}	630	/	184	182	36	35
	10^{-5}	/	/	64.5	65	9.7	9

Table A.4 – Priliminary testing 2^{nd} session part 2: flow stresses results (MPa)

The Figure A.9 is a log-log plot of flow stresses versus strain rate. The graph confirms the data of the Table A.4. The relative flow stress difference (computed by Equation (A.1)) for each temperature is presented in the Table A.5. The differences are almost null for 650 °C, and does not exceed 3.5% except for low strain rate with 7.2% which remains fairly low.

	$\dot{\varepsilon}$ (s^{-1})	350	650	770
$\underline{\Delta}\sigma_{15/5}$ (%)	10^{-3}	0	2.1	-3.5
	10^{-4}	/	-1.1	-2.8
	10^{-5}	/	0.8	-7.2

Table A.5 – Relative flow stress difference between 5 and 15 °C.s^{-1} cooling rates

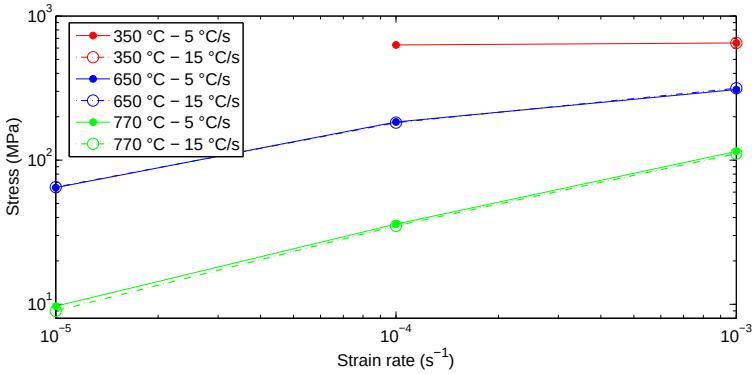

Figure A.9 – Loglog curve of stress vs. strain rate for the three tested temperature

At the end of each mechanical tests, the samples were cooled down up to ambient temperature at the maximum capacity of cooling system. Then, specimens were cut perpendicular to longitudinal direction and prepared for SEM analysis. The Figure A.10 represents the micrographs of each mechanical tests. The objective of these microstructure analyses is to draw qualitative conclusion on the absence of effect of the cooling rate on mechanical behavior.

The micrographs do not show significant differences. However, the phase transformations induced by the rapid cooling at the end of the test might have influenced the microstructure. The main difference resides in the beta transformed proportion which seems to be slightly higher at 5 °C.s^{-1}. This confirms the results of mechanical properties. Indeed, the α phase is the harder phase, and the tests conducted after the lower cooling rates showed a slightly higher flow stress.

A.2.2.2.3 Conclusion

The conclusion of this 2^{nd} session of preliminary testing is that the cooling rates imposed during the forced cooling step of the industrial process have no significant influence in the condition of the characterization procedure. This does not mean that cooling rate have none effect on the material, but in the process conditions of temperature, cooling rates, and mechanical loading, the influence of the cooling rate on mechanical behavior is negligible.

A.2.3 Influence of the experimental procedure

A.2.3.1 Description

The conclusions drawn in the previous section are based on a heat treatment that do not represent the exact thermal history of the material during the process. Therefore, it is important to verify if this difference does not change the consequences of tested parameters, especially the absence of impact of the cooling rate.

The difficulty to perform the heat treatment is related to the installation of the extensometer which is not possible during a long time exposure. For comparison issues, the tests performed in the 2^{nd} session on the temperature influence were reproduced without extensometer, and controlled by crosshead displacement. Three constant velocities were used so that to obtain the same nominal strain rates.

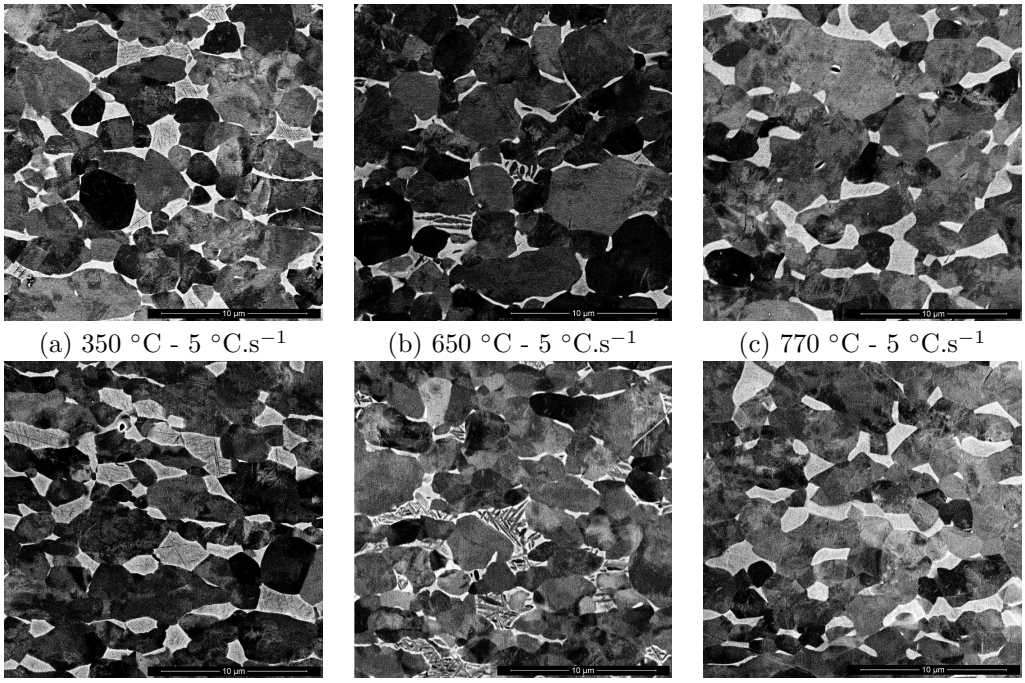

(a) 350 °C - 5 °C.s^{-1} (b) 650 °C - 5 °C.s^{-1} (c) 770 °C - 5 °C.s^{-1}

(d) 350 °C - 15 °C.s^{-1} (e) 650 °C - 15 °C.s^{-1} (f) 770 °C - 15 °C.s^{-1}

Figure A.10 – Micrographs of specimens cut on samples of preliminary testing 2^{nd} session - part 2

A.2.3.2 Results

A mistake were made to reproduce the same loading procedures for 650 °C tests. Indeed, the displacement associated to each cross-head speed is not the same. It is still possible to analyze the curves by translating the portion so that the flow stresses coincide. Indeed, the fact to decrease the strain rate produces a sort of relaxation, and the stress rate is supposed to be the same at the same stress level, except if the strain hardening would affect flow stress relaxation behavior. The Figures A.11a and A.11c show the stress-displacement curves of raw data. The Figures A.11b and A.11d are zooms on plastic zones of initial curves, with a superposition of both portions of curves for 10^{-4} and 10^{-5} s^{-1} on 650 °C. The results for 350 and 650 confirm that cooling rate does not impact the flow stress behavior more than 0.5 %, except for the lowest speed which does not exceed 1.5%.

A.2.4 Conclusion

The preliminary testing sessions were performed in order to get an estimation of the first order parameters that influence the material behavior. Indeed, the bibliographic review showed that the Ti-6Al-4V alloy presents a complex behavior highly sensitive to processing conditions. Therefore, it was important to investigate how the SPF process influences microstructure and mechanical behavior. The bibliographic review also highlighted the important role of cooling rate on microstructure transformations and mechanical behavior evolutions.

The effect of SPF process were simply reproduced by heat treating the samples at SPF temperature. This hypothesis is valid, because the main consequence of SPF on microstructure is grain growth (excluding void nucleation and growth that happened for higher strain rates and-or strain ranges). Indeed, superplastic deformation mechanisms are supposed to preserve from modifications of microstructure morphology. Only the dynamic grain growth is supposed

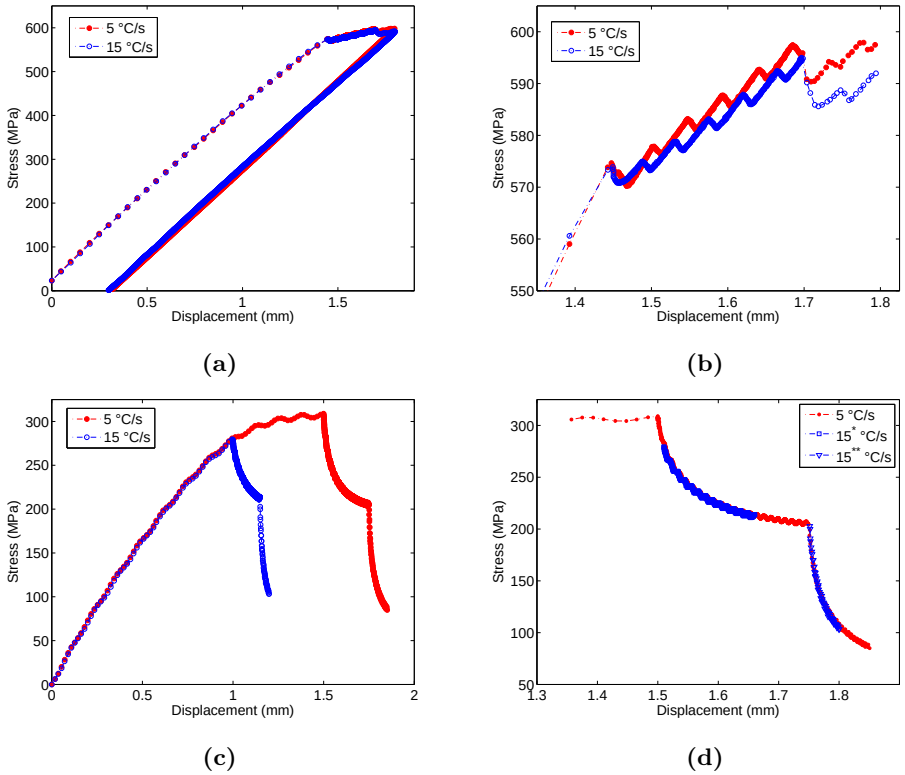

Figure A.11 – Preliminary testing session 3, stress-displacement curves: a) 350 °C, (b) 350 °C - zoom, (c) 650 °C and (d) 650 °C - zoom

to happen. The impact of cooling rate (in the range of the process) on mechanical properties were evaluated at different temperatures and mechanical loading.

The heat treatments and mechanical tests showed some important points:

- The time exposure at SPF temperature promotes significant grain growth. This is the main parameter that affects not only the microstructure, but also the mechanical properties. Indeed, the comparison made at 650 °C showed a flow stress difference between 17-20% for low strain rate at 10^{-5} and 10^{-4} s^{-1} and 4 % at 10^{-3} s^{-1}.
- The material reveals no significant dependency to cooling rate. The maximum flow stress difference between both tested cooling rates was around 7% for low strain rate ($\dot{\varepsilon}$ =10^{-5} s^{-1}) at 770 °C. The micrographs of tested samples showed small differences in effective α phase grain diameters. The higher cooling rate tests led to slightly lower α phase grain sizes corresponding to lower flow stresses.
- The testing procedure was validated at 350 and 650 °C. Indeed, the comparison between final procedure and ideal procedure almost presents no difference ($\underline{\Delta}\sigma_{15/5}$ <1.5%)

The potential errors than can be made by excluding cooling rate effect from material characterization and modeling is reinforced by one point. In the industrial process, the material is never cooled down before a first free cooling inside the opened furnace to let inserting the cooling robot. Thus, the first free cooling phase is characterized by a limited rate (between 0-2 °C.s^{-1}). Therefore, the potential effect of rapid cooling on microstructure and mechanical properties is limited because at these temperatures, the β phase proportion passes from around 50% at 870 °C to 25% at 800 °C.

A.3 Model characterization: method

A.3.1 Stress computation

The fitting method was performed by comparing stress-time curves. These curves were computed thanks to a first order Taylor's approximation as defined in the Equation (A.2a). The Equations (A.2b) and (A.2c) enables to express the stress time curve as a function of whole model parameters.

$$\sigma\left(t+dt\right)=\sigma\left(t\right)+dt\times\dot{\sigma}\left(t\right) \tag{A.2a}$$

$$\dot{\sigma}\left(t\right)=E\left(\dot{\varepsilon}_t\left(t\right)-\dot{\varepsilon}_{vp}\left(t\right)\right) \tag{A.2b}$$

$$\dot{\varepsilon}_t\left(t\right)=\frac{\left(l(t)-l(t-dt)\right)}{l_0}\frac{1}{dt} \tag{A.2c}$$

This procedure is incremental, and at each increment is computed $\sigma\left(t+dt\right)$, and then $\dot{\varepsilon}_p(t+dt)$ is updated thanks to the Equations (A.3a), (A.3b) and (A.3c)

$$\dot{\varepsilon}_p(t+dt)=\dot{\varepsilon}_0 sinh\left(\beta\left\langle\sigma_v(t+dt)\right\rangle\right)^n \tag{A.3a}$$

$$\sigma_v(t+dt)=\sigma(t+dt)-\left(R(t)+dt\times\dot{R}(t)\right)-k \tag{A.3b}$$

$$\dot{R}(t)=\begin{cases} b(Q-R(t))\dot{\varepsilon}_{vp}(t)-\gamma R(t)^c & if\ \sigma(t)>k \\ 0 & if\ \sigma(t)\leq k \end{cases} \tag{A.3c}$$

This procedure for stress-time has the advantage to include the effects of elastic, viscoplastic and hardening phenomena at the same time instead of isolating each behavior at the risk of forgetting some dependencies. However, the method presents several drawbacks:

- The errors are accumulated all along a test fitting. If a specific material behavior occurs a the end of the testing procedure, it can be difficult to characterize it if the rest of the curve is not well fitted. For example, if the stress value at the end of the tensile part of a test is superior to the experimental data, the hardening behavior may be overestimated. This also may produce the overestimation of softening parameter to minimize the gap between the model and the experiment.
- Some effects are time dependent, and the experimental data have not the same acquisition parameters for each part of testing procedures.

A.3.2 Cost function

A specific cost function was defined to answer both previously mentioned risks. The first objective was to combine the cost functions of both testing procedures by adding each cost functions. Then the deviations are differently computed for tensile and relaxation parts of the test (Equation (A.4)). Weighting coefficients α are applied in order to attribute a different order of importance as a function of strain rate or relaxation time. The Equation (A.5) defined CF^i as the sum of stress and stress rate relative mean square deviations CF_S^i and CF_{dS}^i, weighted by a coefficient k. CF_S^i and CF_{dS}^i are defined in the Equations (A.6) and (A.7) where σ_ϵ and $\dot{\sigma}_\epsilon$ are threshold values to prevent from a zero division for high temperature tests and stabilized flow stresses. The weighting coefficients k_T and k_R are defined in the Equations (A.8) and (A.9) where $\dot{\varepsilon}_\epsilon$ and t_ϵ are also threshold values that enable to adapt weighting. The threshold values used for cost functions are presented in the Table A.6.

$$CF=\frac{\alpha_T}{N_T}\sum_i^{N_T}CF_T^i+\frac{\alpha_R}{N_R}\sum_i^{N_R}CF_R^i \tag{A.4}$$

$$CF^i = \left(CF_S^i + CF_{dS}^i\right) \times k \tag{A.5}$$

$$CF_S^i = \frac{\left(\sigma_{exp}^i - \sigma_{mod}^i\right)^2}{\left|\sigma_{exp}^i\right| + \sigma_\epsilon} \tag{A.6}$$

$$CF_{dS}^i = \frac{\left(\dot{\sigma}_{exp}^i - \dot{\sigma}_{mod}^i\right)^2}{\left|\dot{\sigma}_{exp}^i\right| + \dot{\sigma}_\epsilon} \tag{A.7}$$

$$k_T = -ln\left(\dot{\varepsilon}_t^i + \dot{\varepsilon}_\epsilon\right)^{\gamma_T} \tag{A.8}$$

$$k_R = \left(\frac{1}{t^i - t_R^0 + t_\epsilon}\right)^{\gamma_R} \tag{A.9}$$

σ_ϵ	$\dot{\sigma}_\epsilon$	t_ϵ	$\dot{\varepsilon}_\epsilon$	γ_T	γ_R
1	1	0.1	1e-7	0.15	0.25

Table A.6 – Parameters of the cost function

One important issue of fitting a model on complex tests is that the error which is accumulated along model computation may be compensated mathematically with wrong behavior. Therefore, the computed stress and hardening values are corrected at the beginning of relaxation phases to overcome the problem. Indeed, when the initial stress value used for Taylor's method computing is adjusted to experimental value, the hardening parameter R needs to be adjusted as defined in the Equation (A.10). In this adjustment technique, every parameter is well known except $\dot{\varepsilon}_{exp}^{pl^i}$ which is computed thanks to the Equation (A.11) where $\dot{\sigma}_{exp}^{pl^i}$ is directly estimated from stress-time curves.

$$\begin{cases} \sigma_{mod}^{*i} = \sigma_{exp}^i \\ R_{mod}^{*i} = \sigma_{exp}^i - k - \frac{1}{\beta} asinh\left[\left(\frac{\dot{\varepsilon}_{exp}^{pl^i}}{\dot{\varepsilon}_0}\right)^{1/n}\right] \end{cases} \tag{A.10}$$

$$\dot{\varepsilon}_{exp}^{pl^i} = \begin{cases} \dot{\varepsilon}_{exp}^{t^i} & if\ \dot{\sigma}_{exp}^{t^{i-1}} = 0 \\ \dot{\varepsilon}_{exp}^{t^i} - \frac{\dot{\sigma}_{exp}^{t^i}}{E} & if\ \dot{\sigma}_{exp}^{t^{i-1}} > 0 \end{cases} \tag{A.11}$$

A.3.3 Optimization method

According to the large range of temperature, and the strong non-linearity of the problem, the optimization were performed in several steps with MATLAB® minimization functions. Most of large problem of material characterization were performed by Genetic Algorithm (GA) [220, 146, 221, 222, 223]. Indeed, GA enables to get global objectives of strongly non-linear problems.

A first Genetic Algorithm were used with wide bounds. This step was repeated three times in order to increase the chance to get global minimum. Indeed, the GA algorithm includes randomized parameter generation that can promote different solution for weak generation and population size number [224]. The better solution is consequently used with a constraint and unconstrained fmincon and fminsearch MATLAB® algorithms. The parameters used for each algorithm are defined hereafter:

- GA: The set of GA parameters used for this research is as follows: population size - 5xn_p (n_p : noumber of parametes of the optimization), number of generations - 50, crossover rate 0.95, mutation rate 0.01.
- Fmincon: The algorithm used was the interior-point' method without hessian function. The MATLAB®'s defaut parameters were used with 150 maximum iterations.
- Fminsearch: the algorithms used were mixed between 'reflect', 'contract inside/outside', 'expand' and 'initial simplex methods. The MATLAB®'s defaut parameters were user with 250 maximum iterations.

The Figure A.12 schematically represents the sequence which was performed where P_i and CF_i represent the best fit parameters vector and cost function for each algorithm. The Figure A.13 shows the evolution of cost function using the optimization procedure for the 750 °C experiments. The interest of using this sequence of algorithms is to reach a global minimum with GA algorithm, then refine the solution according to physically acceptable bounds, and finally obtain the better solution from mathematical point of view with unconstrained algorithm.

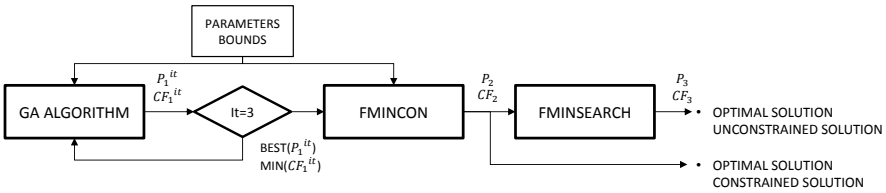

Figure A.12 – Schematic of parameters optimization procedure

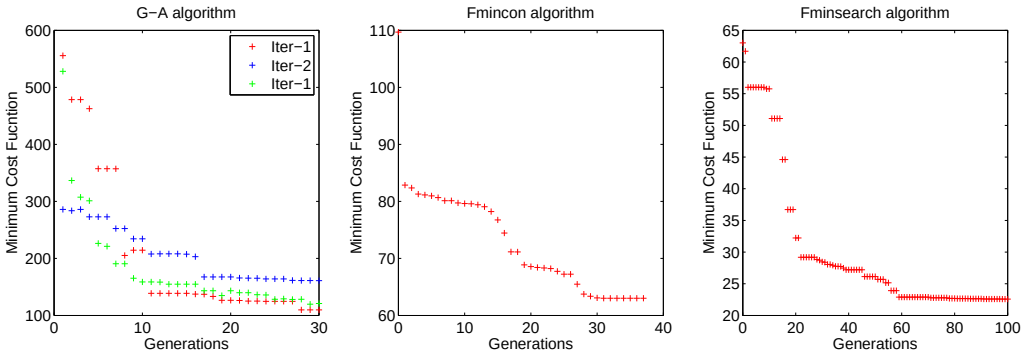

Figure A.13 – Evolution of cost functions through parameters optimisation whith multiple GA, fmincon and fmin search algorithms (example for 750 °C experiments characterization)

The complexity of the problem was first to give degrees of freedom to the parameters. Then, it was important to impose the variation range and the temperature evolution to certain parameters to get physical sense. This were manually made by adjusting the bounds as described in the Figure A.14. Both the unconstrained and constrained optimized parameters were used to adjust some bounds in order to fit the curves with physical meaning.

A.4 Model characterization: results

The characterization of the model was performed in two steps. The first step consisted in finding the best fitting set of parameters, temperature by temperature. The second step was

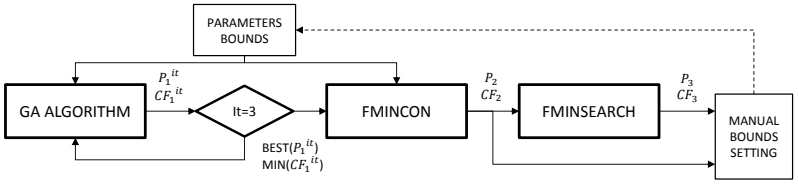

Figure A.14 – Schematic of parameters optimization procedure with bound adaptation

performed on the whole range of temperature using interpolation functions depending on temperature for each parameter.

A.4.1 Fit by temperature

The comparison of experiment and model are plotted as stress-time and stress-strain curves in the Figure A.15. For description issues, the temperatures between 25-400 °C, 525-700 °C and 750-870 °C are respectively called "low", "medium" and "high" temperature curves.

The low temperature curves show a fairly good fit of experiment data. However, there are some gaps on relaxation curves particularly for 250 and 400 °C. Indeed, the stress rates for TP1 Figures are almost good but there are small gaps due to the error generated during tensile part. Concerning TP2, for low and medium temperatures, the stress is not relaxed during first relaxation part of temperature of 400 and 525 °C. This is due to a too low viscous stress combined with a very low SRS which generates very low strain rate. In addition, softening is non-working because mathematically it depends on hardening value which is small because of small deformation. The high temperature curves also show a good fit of experiment data. The relaxation of stresses also shows some gaps but only for TP1 for high strain rate during jump tests. The SRS exponent n, or the viscosity parameter β might be strain or hardening dependent. Indeed, the dislocation density creates an important quantity of potential obstacles for plastic deformation.

The optimized set of parameters are plotted as a function of temperature in the Figure A.15d and A.15e.

A.4.2 Interpolation functions

Different functions were established to model the parameters evolution with temperature. The mathematical expressions were chosen to fit approximately the best fit parameters obtained temperature by temperature. The initial expressions have been gradually improved as optimizations were performed. The Equations (A.12) to (A.17) define the different interpolation function of $\dot{\varepsilon}_0$, β, n, Q, b and γ. $\dot{\varepsilon}_0$ and γ are modeled with exponential evolution with initial value at 0 °C.

$$\dot{\varepsilon}_0 = \dot{\varepsilon}_{00} + \dot{\varepsilon}_{01} exp(\dot{\varepsilon}_{02} T) \tag{A.12}$$

$$\frac{1}{\beta} = \beta_0 + \beta^*(T) f_1(T) \tag{A.13}$$

$$n = n_0 + n^*(T) f_1(T) \tag{A.14}$$

$$Q = Q_0 + Q^*(T) f_1(T) \tag{A.15}$$

$$b = b_0 + (b_1 - b_0) f_2(T) \tag{A.16}$$

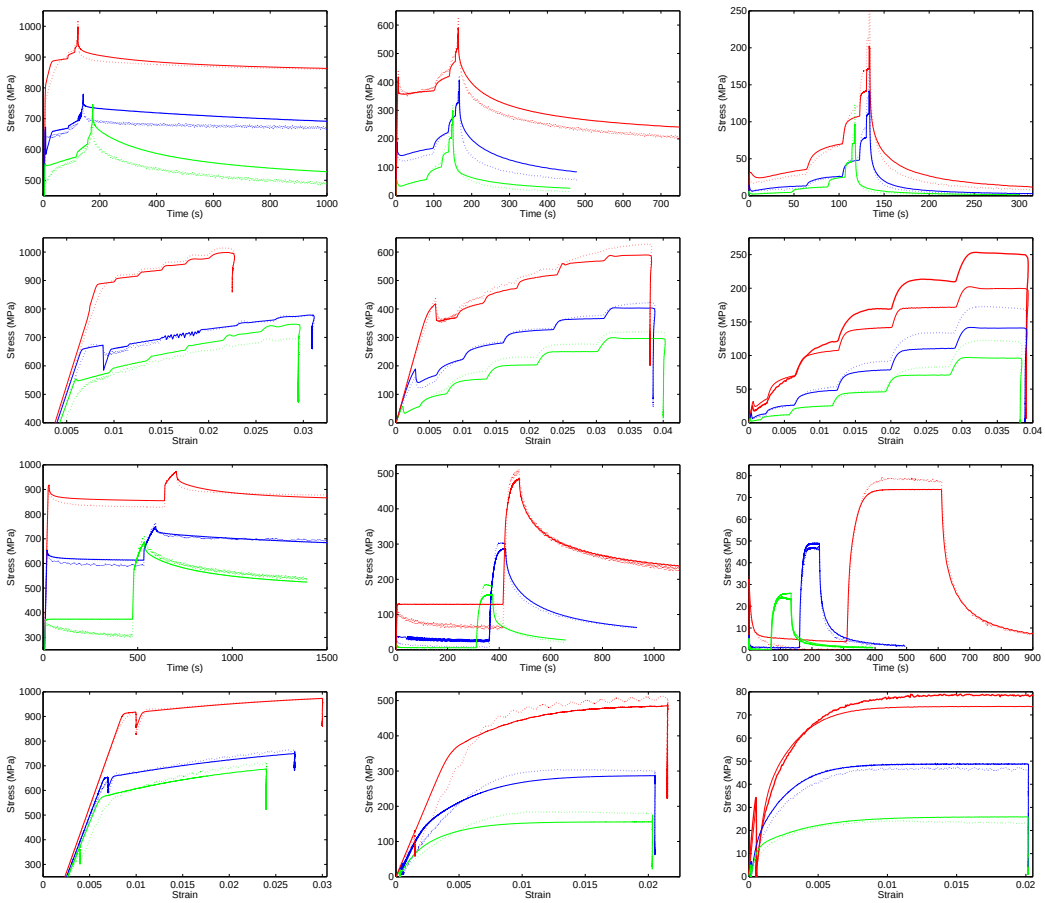

(a) 25 - 250 - 400 °C **(b)** 525 - 620 - 700 °C **(c)** 750 - 820 - 870 °C

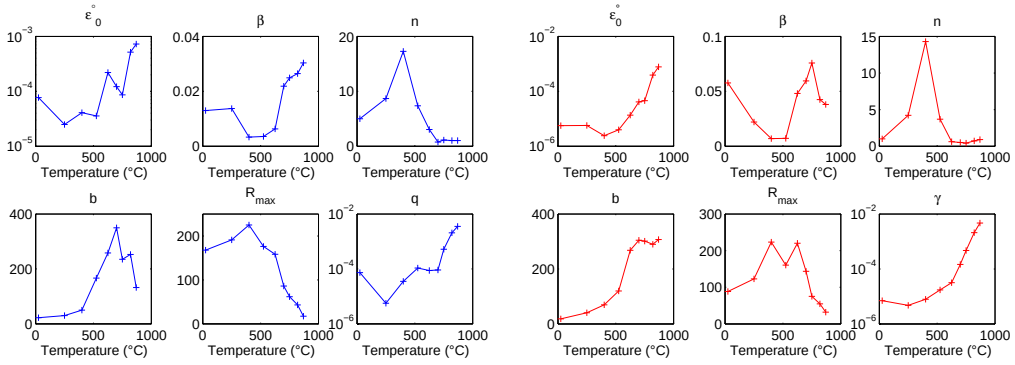

(d) **(e)**

Figure A.15 – Comparisons of experimental data and temperature by temperature model for TP 1 and TP2 with stress-time curves and stress-strain curves (a) to (c) and the temperature by temperature optimized parameter of (d) TP1 and (e) TP2 as a function of temperature

$$\gamma = \gamma_0 + \gamma_1 exp(\gamma_2 T) \tag{A.17}$$

β, n, Q and b parameters are modeled with additional functions f_1 and f_2 called threshold transition (TT) functions defined respectively in the Equations (A.18) and (A.20). The f_2 TT function enables to create thresholds transitions with variable rate of transition with α_{T2} the temperature dependent parameter of the hyperbolic tangent function (defined in the Equation (A.21)). Concerning f_1 TT function, the parameter which is temperature dependent inside the function is the upper threshold that vary according to another TT function (defined (A.19)) where δ can be replaced by β, n and Q.

$$f_1(T) = \left[1 - th\left(\alpha_{T1}\left(T - T^1_{trans}\right)\right)\right]/2 \tag{A.18}$$

$$\delta^*(T) = \delta_1 + \frac{\delta_2 - \delta_1}{2}\left[1 - th\left(-\alpha^*_{T1}\left(T - T^{1*}_{trans}\right)\right)\right]/2 \tag{A.19}$$

$$f_2(T) = \left[1 - th\left(-\alpha_{T2}(T)\left(T - T^2_{trans}\right)\right)\right]/2 \tag{A.20}$$

$$\alpha_{T2}(T) = \alpha^-_{T2} + \frac{\alpha^+_{T2} - \alpha^-_{T2}}{2}\left[1 - th\left(-\alpha^*_{T2}\left(T - T^2_{trans}\right)\right)\right] \tag{A.21}$$

The Figure A.16a and A.16b shows the evolution of such functions with temperature. The parameters used to plot the curves were fixed to highlight functions variations. This formulation enables to model the effect of material behavior transition including an evolution of rate transition for each behavior. The temperature associated to the transitions of material behavior T^1_{trans} and T^2_{trans} are the same used for β, n and Q.

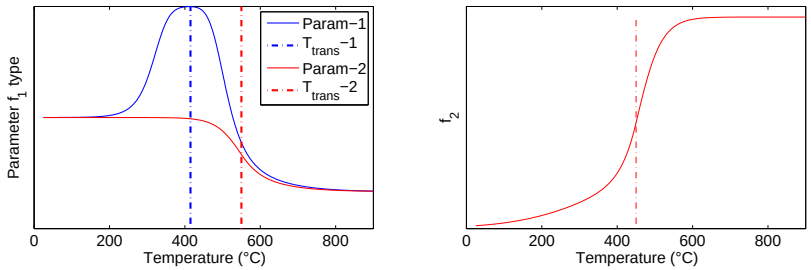

(a) **(b)**

Figure A.16 – Plot of temperature transition functions: (a) f_1 types (b) f_2

The use of such functions for the variation of n and Q corresponds to experimental observations. Indeed, the null SRS such like the more important hardening properties locally occurs around 400°C. However, concerning β, it is related to mathematical issue. Indeed, the increase of exponent n needs to be compensate to limit non-linear effects related to mathematical issue. This model requires a set of 26 parameters to define the viscoplastic function with hardening model.

A.4.3 Final Model

The Figure A.17 shows the parameters interpolation functions. The parameters of the model are presented in the Tables A.7, A.8 and A.9.

$\dot{\varepsilon}_{00}$	$\dot{\varepsilon}_{01}$	$\dot{\varepsilon}_{02}$	β_0	β_1	β_2	n_0	n_1	n_2
2.4e-05	6.5e-12	0.0243	75	5.9	296	1.248	3.652	10.93

Table A.7 – Parameters of the global model: viscoplastic function

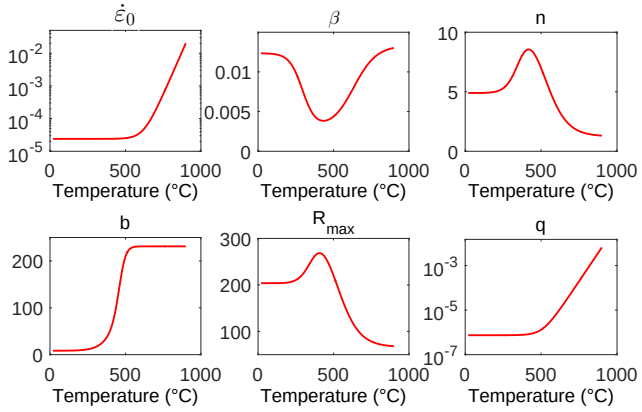

Figure A.17 – Evolution of parameters of the global model

b_0	b_1	Q_0	Q_1	Q_2	γ_0	γ_1	γ_2	c
8.4	231.1	66.4	137.6	291.46	7.46e-07	4.87e-12	0.0236	2.43

Table A.8 – Parameters of the global model: hardening-softening function

α_{T1}	T^1_{trans}	α^*_{T1}	T^{1*}_{trans}	T^2_{trans}	α^-_{T2}	α^+_{T2}	α^*_{T2}
6.58e-3	511.6	0.0117	359.9	447.8	1.06e-2	0.025	0.01

Table A.9 – Parameters of the global model: TT functions

A.4.4 Expansion coefficient

In order to evaluate the effect of thermal expansion during anisothermal tests, a control test were defined for both 3 and 7.5 °C.s^{-1} cooling rates in the same post heat treatment conditions. A no force condition were applied during tests in order to measure the effect of expansion only. The thermal expansion coefficient was computed thanks to the Equation (A.22) where ε_t is the total strain measured by extensometer which is equal to thermal strain. The results are shown in the the Figure A.18.

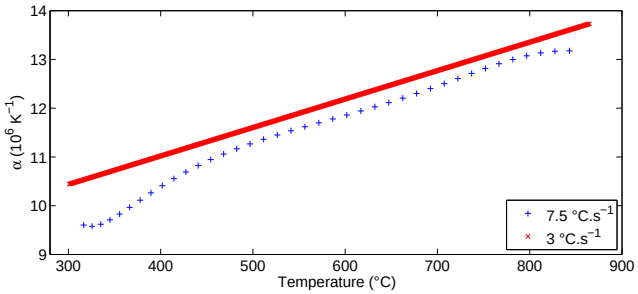

Figure A.18 – Evolution of expansion coefficient under 3 °C.s^{-1} and 7.5 °C.s^{-1}

$$\alpha = \frac{\varepsilon_t^{i+1} - \varepsilon_t^i}{T^{i+1} - T^i} \tag{A.22}$$

The evolution with temperature seems fairly identical with a small gap in the range of 850-450 °C. The curve computed from 7.5 °C.s^{-1} test reveals a slope variation at lower temperature. A linear evolution of the coefficient of thermal expansion was defined from these curves which

is considered independent of thermal treatment. The model is defined in the Equation (A.23) with α_0=8.55e-6 K^{-1} and α_1=5.834e-9.

$$\alpha = \alpha_0 + \alpha_1 T \tag{A.23}$$

Appendix

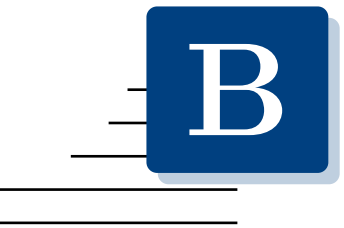

Heat Transfers modeling

B.1 Development Experiment

A first experiment was used to test different details of the methodology such as:

- The heating procedure: the programming of heating, the thermal response, the opening of the bell, the displacement of shuttle. Take care of the timing and the good maintaining of the parts assembly and the thermocouples during the motion of shuttle.
- The measurement means: test the different means of instrumentation (thermocouples, pyro-reflectometer and camera).
- The part and die fitting back: evaluate if the positioning of the part inside the mold was identical to the post forming conditions.

The heating procedure consisted into two sequences. The first one consisted in a first heating of mold up to 500 °C, only to produce enough expansion to place the part inside the mold in the end of forming state. Indeed, the thermal expansion coefficient of the mold is much higher than the mold. Then a cooling down to ambient temperature was performed after what the part was heated up to 900°C in 3h, and then hold during 2h. After this heating procedure, the bell opened, and the shuttle moved until final position where non-contact measurement operated.

The figure B.1a represents a picture of the mold before the experiments. The green squares locate the spot thermocouples that were placed flush with the mold surface to be able to measure the part contacting. Indeed, the change on pressure at thermocouple interface create discontinuity in measurement. The figure B.1b shows part at the end of the experiment. The green squares represent the two welded thermocouples. The red squares represents black paint zones used as reference for the infrared camera measurement.

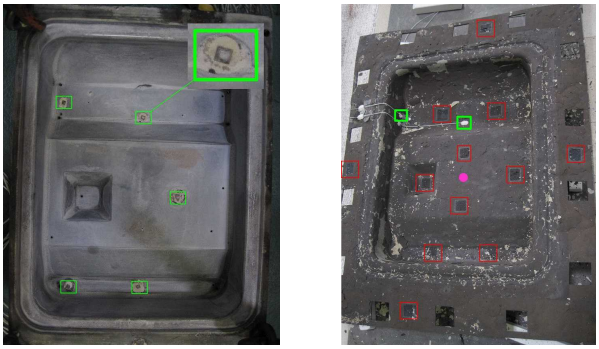

(a) **(b)**

Figure B.1 – Pictures of (a) the mold before the experiment, (b) the part after the experiment

B.1.0.1 Contact measurements

The Figure B.2 shows the graph of temperature evolution of the different thermocouples. The thermocouples TC1 to TC6 corresponds to spots, TC7 and TC8 are welded thermocouples, and the three others are control thermocouples inside the bells.

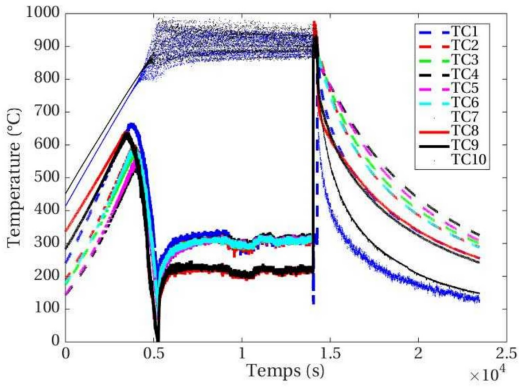

Figure B.2 – Evolution of the temperature at the themocouples points

The graphs presents some issues. Firstly, the spots thermocouples deviate when the setpoint is over 800 °C. When the cooling starts, the problem disappears. This was probably due to an electrical disturbance. Except this problem, the different thermocouples give a continuous response. The figure B.3a, B.3b, B.3c and B.3d, B.3e, B.3f respectively show the evolution of spots and welded thermocouples temperatures at different time scales.

❒ Spot thermocouples

There are clear changes in the slopes of spots curves that seem not to correspond to upper face heat transfers. During the first 15 seconds in the Figure B.3c, the variations seem to follow the natural cooling that is supposed to diffuse through part thickness. After 20 seconds, there are some discontinuities in the slopes. This might be a consequence of an evolution of the contact conditions with the mold and the spot thermocouples. The slopes hierarchy between spots changes in between the 50 and 500 seconds. This may also be a consequence of an evolution of the contact conditions.

❒ Welded thermocouples

There is a large difference between the temperature variations of both thermocouples. In addition, the THC 1 has a noisy signal since the 10 first seconds. The welding might have not resist to the thermal stresses, and the cement paste played the role of insulator. This confirms that a particular attention need to be paid on thermocouple preparation.

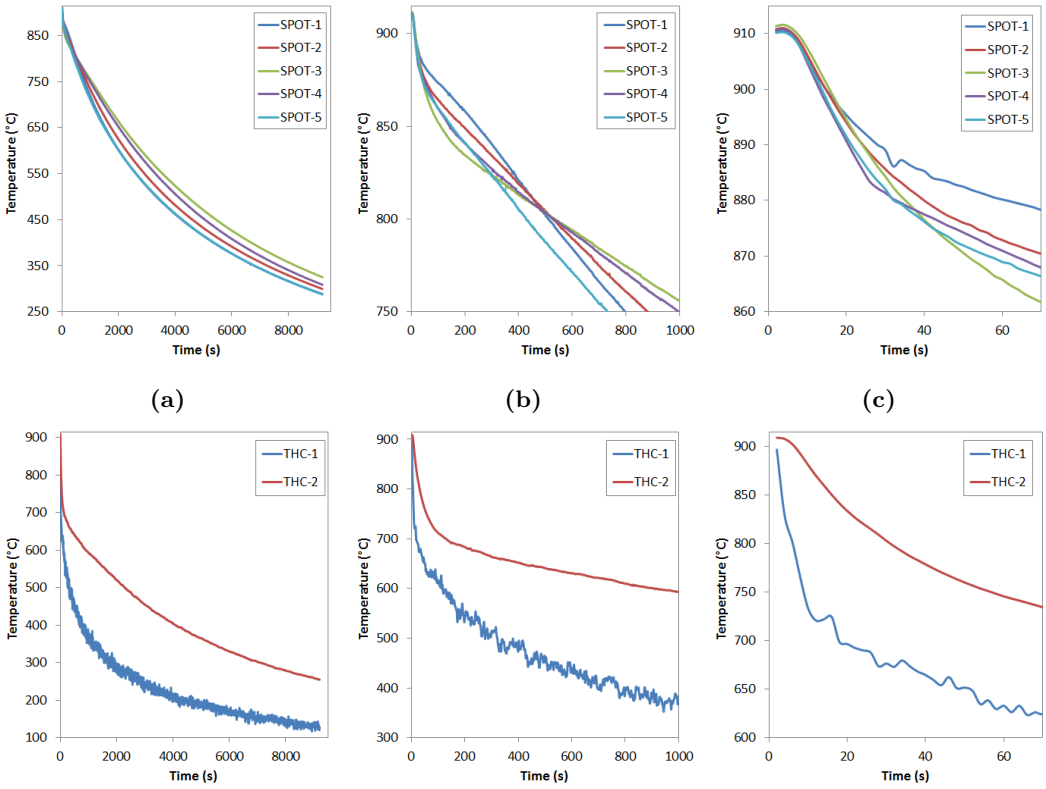

Figure B.3 – Development experiment: temperature vs. time evolution of Spot/Welded thermocouples (a)/(d) whole test, (b)/(e) 0-1000 sec and (c)/(f) 0-70 sec

B.1.0.2 Non contact measurements

❒ Pyroreflectometry

During the process, a problem was observed with the pyro-reflectometry measurement: no reflectivity was measured. By checking afterwards, the surface of the sheet was not at the same altitude as before the experiment when the lasers were set. As the reflectivity measurement is based on the coincidence of incident and reflected radiation, this measurement was not possible. The pyroreflectometer, functioned as two pyrometers monochromatic and a bichromatic pyrometer for this test. The Figure B.4a represents three curves: the two radiance temperatures at 1330 and 1550 nm, and the color temperature which is obtained by using the treatment of both monochromatic signals [225]. When the emissivity is constant over wavelength such as for grey bodies, the color temperature is equal to the true temperature. Both radiance temperature are superposed from 0s to 900s, which means that grey body hypothesis is valid and the color temperature corresponds to true temperature.

The emissivity of the part was required to evaluate true temperatures from camera data. The Equation (B.1) enabled to compute spectral emissivity at the wavelength of the camera

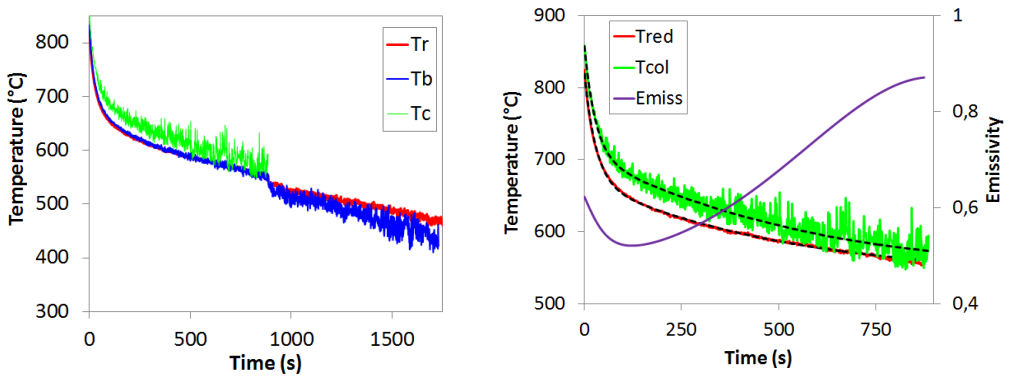

(a) (b)

Figure B.4 – Development experiment: pyroreflectomer data (a) temperature vs. time curves for the red, blue and color associated data, (b) fit of Color temperature evolution

λ, where C_2 (=13488 $\mu m.K$), T and T_L are respectively the second plank's constant, the true and the radiance temperatures. This equation was used to compute the emissivity of the part at the pyrometer laser position by using the color temperature and one of the monochromatic radiance temperatures. The Figure B.4b represents the raw and the fitted curves used for emissivity computation and the emissivity variation during the experiment. The curve was plotted up to 800 s, time until what the color temperature can be considered as true temperature.

$$\epsilon(\lambda = 1.55\mu m) = \frac{e^{C_2/\lambda T} - 1}{e^{C_2/\lambda T_R} - 1} \tag{B.1}$$

❒ Camera

The Figure B.5 represents three images of radiance temperature obtained with the camera at 45s, 500s and 1500s. There is a clear apparition of oxidation at the surface that promote detachment of small chips of oxide layer that cool more rapidly (as observed in the Figure B.1b). The black painting squares seems less emissive than the Ti-6Al-4V itself. Moreover, the painting seemed to enhance the production of chip layer detachment so that they were not used anymore in the next experiments.

The Figure B.5b shows the curves of radiant temperatures from several zones represented on the camera picture. The temperature A and B correspond to surface integrated data while C and D are local data. There are several discontinuities that correspond to oxide chips creation and detachment such as observed with the pyro-reflectometry. The discontinuity of the A zone, which focus on the pyro-reflectometer laser's position happens at the same time. The zones A and B cool down more rapidly than C and D, which is logical because their radiative flux from hot surfaces is lower. Both point and square zone cooled down more rapidly when it is placed far from the vertical surfaces for the same reasons which is particularly highlighted in the Figure B.5d where the corners are more luminous.

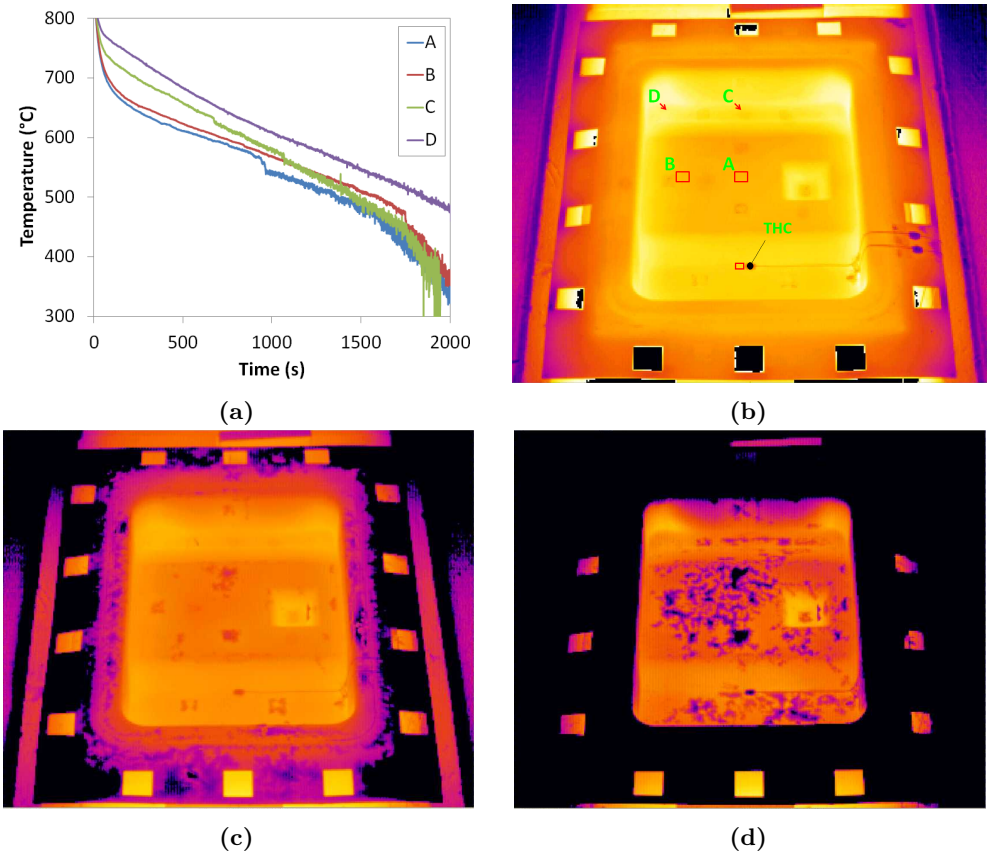

Figure B.5 – Development experiment: camera (a) temperature vs time, thermographies at times (a) 45 sec (with extraction zones of the Figure B.5a's points), (b) 500 sec and (c) 1500 sec

B.1.0.3 Comparisons

The Figure B.6a compares the THC and the camera data extracted closed to the THC as illustrated in the Figure B.5b. The camera data correspond to the radiance temperature. They started from 800 °C because the calibration was performed between 500 and 800°C. The THC and camera temperatures coincide fairly well during the first 1000 seconds. The deviation of the camera data corresponds to the chipping of an oxide layer near from the thermocouple where the camera data was extracted as seen on the Figure B.5d. Normally the camera data should have been inferior to the thermocouple because of the emissivity which is inferior to 1. This indicates that emissivity may have reached a value closed to one at this location during the fifty first second of cooling.

The Figure B.6b compares the radiance temperatures of the pyrometer and the camera (square A). The pyrometer gives the same shape than the camera up to 500°C, but with a lower temperature about 20 °C. This can be due to the spatial integration used to extract the camera data. Indeed, a surface of integration of 10x20mm^2 was used around the central position of the laser. The pyrometer value is probably inferior because the central position corresponds to the highest radiative heat flux (maximum viewing factor).

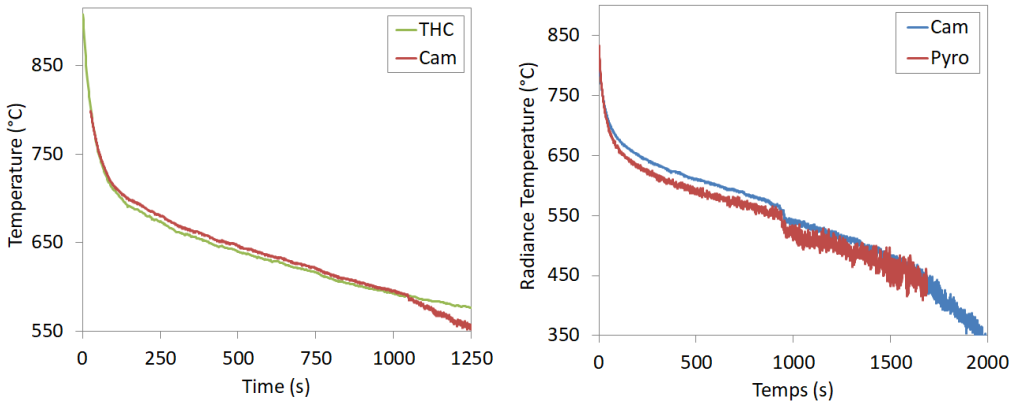

Figure B.6 – Development experiment: comparisons of measurement means (a) thermocouple vs. camera (corrected using Equation (B.1)), (b) camera vs. pyroreflectometer

B.1.0.4 Conclusions

The first objective of this test was to implement a typical cooling experimentation to ensure a good representativeness of the process. The furnace was able to heat up to the SPF temperature. In addition, the spot thermocouples confirmed that the part was in contact with the mold at the starting of the furnace opening. Moreover, the initial contact conditions of post SPF process were reproduced at the starting of the cooling experiment.

A second objective was to implement and evaluate the agreement between the different means of measurement: thermocouple, pyroreflectometer and camera. The agreement between thermocouple and camera was demonstrated, as well as for the camera and the pyroreflectometer. This part allowed to have a good confidence in the measurement by IR camera, especially in the oxidized state. At the beginning, the values was underestimated but the emissivity value provided by the pyroreflectometer allows a correction a posteriori. A question remains concerning the difference of emissivity obtained by the pyoreflectometer (ϵ=0.6-0.8) and the comparison of camera and thermocouple data ($\epsilon \approx 1$).

The pyroreflectometer did not work optimally because the reflectivity measurement was not possible because of the variation of height of the sheet. However, it allowed us to evaluate the "grey" condition of our material, and to justify the use of the color temperature as true temperature.

B.2 Weak radiation method (WRM)

B.2.1 Context

This method is used to compute approximated radiative heat flux between various parts with heterogeneous temperatures. Indeed, the view factors VF based radiative heat flux computation method (cavity radiation BC) is not available for coupled temperature displacement simulation in ABAQUS® . The principle of the method is to compute a first thermal analysis to obtain temperature information to transfer to the coupled simulation just as made for weak thermomechanical coupling.

The full computation method imply to compute VF matrix for every surfaces. The total heat flux at an element surface is computed as the sum for each visible element surfaces contribution such as defined Equation (B.2) where P refers to the parts of the environment,

el to the elements of parts and A to the surface quantity. P_i^v corresponds to the "visible" elements. They correspond to the elements that have no obstacles in between their surfaces. T, ϵ and σ are respectively the temperature, the emissivity and the Stefan-Boltzmann constant.

$$\phi_{rad}^{el} = \sum_{P_i \in P_N} \sum_{el_i \in P_i^v} \left(\frac{\sigma(T_{el_i}^4 - T_{el}^4)}{\frac{1-\epsilon_{el}}{A_{el}\epsilon_{el}} + \frac{1}{A_{el}F_{el/el_i}} + \frac{1-\epsilon_{el_i}}{A_{el_i}\epsilon_{el_i}}} \right) \tag{B.2}$$

B.2.2 Method

The weak formulation method is based on an homogeneous part temperature approximation. Indeed, if a specific surface has an homogeneous temperature evolution with associate emissivity, the computation of the radiative heat flux at an element ϕ_{rad}^{el} can be approximated to $\widehat{\phi_{rad}^{el}}$ with the Equation (B.3) where i and j refer respectively to parts and their surfaces at homogeneous temperatures. $F_{tot}^{el}(j)$ (defined Equation (B.4)) is the sum of VF F_{el/el_i^j} between the concerned element el and the elements el_i^j belonging to constant temperature surface S_j.

$$\phi_{rad}^{el} = \widehat{\phi_{rad}^{el}} = \sum_i \sum_j \frac{\sigma(T_j^4 - T_{el}^4)}{\frac{1-\epsilon_{el}}{\epsilon_{el}} + \frac{1}{F_{tot}^{el}(j)} + \frac{1-\epsilon_i}{\epsilon_i}} \tag{B.3}$$

$$F_{tot}^{el}(j) = \sum_{el_i^j \in S_j} F_{el/el_i^j} \tag{B.4}$$

The Figure B.9 represents an example of such method where the Figure B.9a highlights

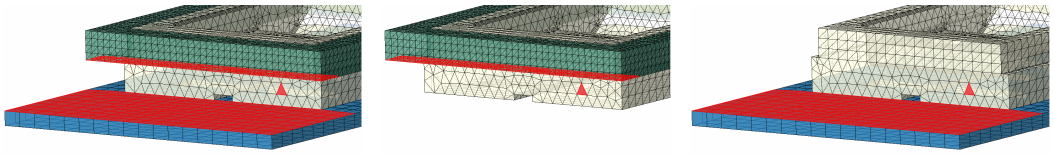

(a) **(b)** **(c)**

Figure B.7 – Example of radiative flux decomposition for prototype testing environment (a) whole model, (b) frame and (c) shuttle contributions.

the element and surfaces that are at stake for radiation flux at surface of red element of the mold. The Figure B.9b and B.9c represents two configurations for VF computation. The equation (B.5) defines the radiation surface heat flux at surface of element of the mold where f_i and s_i refer to frame and shuttle highlighted surfaces.

$$\widehat{\phi_{rad}^{el}} = \frac{\sigma(T_{f_i}^4 - T_{el}^4)}{\frac{1-\epsilon_{el}}{\epsilon_{el}} + \frac{1}{F_{tot}^{el}(f_i)} + \frac{1-\epsilon_{f_i}}{\epsilon_{f_i}}} + \frac{\sigma(T_{s_i}^4 - T_{el}^4)}{\frac{1-\epsilon_{el}}{\epsilon_{el}} + \frac{1}{F_{tot}^{el}(f_i)} + \frac{1-\epsilon_{f_i}}{\epsilon_{f_i}}} + \frac{\sigma(T_{amb}^4 - T_{el}^4)}{\frac{1-\epsilon_{el}}{\epsilon_{el}} + \frac{1}{1-F_{tot}^{el}(f_i)-F_{tot}^{el}(s_i)}} \tag{B.5}$$

This method implies to perform a previous simulation to obtain a first approximation of temperature evolution. This simulation is computed with the hypothesis of surface radiation in coupled thermomechanical model or with full radiation heat transfer analysis. The first solution takes account of thermal contact evolutions while the second focuses on real radiation heat flux. In our case the second solution (heat transfer analysis) was chosen with an intermediate value for thermal conductance value.

B.2.3 Example

B.2.3.1 Model

A simplified version of the air inlet forward bulkheads was used to validate the method. Hard radiative HT condition were used to produce large temperature variations. The part was considered at 800°C with the upward surface exchanging at 20°C with pure radiative HT. For comparison issues, pure heat transfer analyses were performed with perfect cavity radiation BC and the WRM.

There are three steps to perform before to implement the WRM. The first one consists in computing a pure heat transfer analysis to get the right temperature field and its evolution. Then, the geometry is split by selecting surfaces with the most homogeneous temperature variations. Finally, the VF of the different combinations of surfaces that are facing between each others including the ambient environment.

The Figure B.8a shows the temperature field at the end of 100 seconds for the cavity radiation reference model. Three distinct temperature ranges are highlighted and used to define three surfaces for weak formulation such as presented Figure B.8b. In addition to this surface decomposition, a single homogeneous temperature over the whole surface was considered.

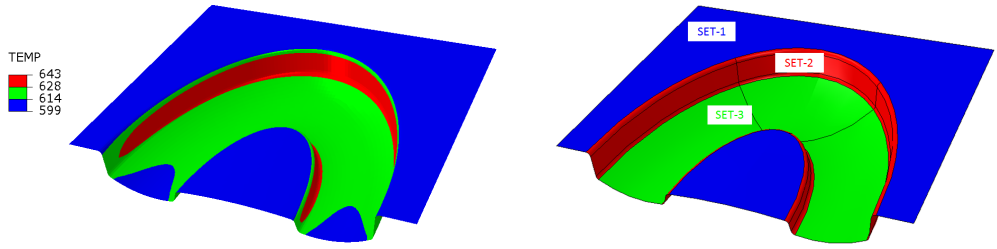

(a) **(b)**

Figure B.8 – Averaged temperatures evolution for (a) ϵ=0.8 and (b) ϵ=0.8

The Figure B.9 shows different VF configurations that was computed and used to compute the radiative heat flux. Indeed, the SET-1 elements exchange radiative flux with SET2 and ambient environment, SET-2 elements exchanges with SET-1, itself, SET-3 and ambient environment whereas SET-3 elements exchange with SET-2, itself and ambient environment. Each associated total VF is a combination of the ones presented in the Figure B.9 such as defined Equations (B.6), (B.7) and (B.8) where j represents the different sets of homogeneous temperature surfaces.

$$q_{[i-j]} = \frac{\sigma(T_j^4 - T_i^4)}{\frac{2(1-\epsilon)}{\epsilon} + \frac{1}{F_{tot}^{el}(i-j)}} \tag{B.6}$$

$$q_i^* = \frac{\sigma(T_{amb}^4 - T_i^4)}{\frac{(1-\epsilon)}{\epsilon} + \frac{1}{1-F_{tot}^{el\ 0}}} \tag{B.7}$$

$$q_i = \sum_{j \in P_N} (q_{[i-j]}) + q_i^* \tag{B.8}$$

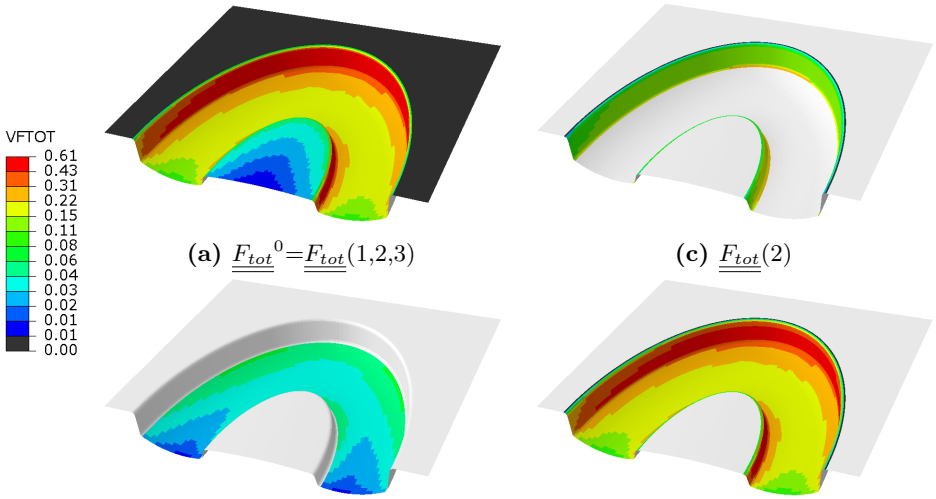

(a) $\underline{\underline{F_{tot}}}^{0}=\underline{\underline{F_{tot}}}(1,2,3)$ **(c)** $\underline{\underline{F_{tot}}}(2)$

(b) $\underline{\underline{F_{tot}}}(3)$ **(d)** $\underline{\underline{F_{tot}}}(2,3)$

Figure B.9 – Viewing factors field distribution for different surface configurations (a) full surfaces (b) SET-2 self, (c) SET-3 self (d) SET-2, SET-3 surfaces

B.2.3.2 Results

The Figure B.10a, B.10b and B.10c show the temperature field after 100 seconds respectively for the cavity radiation BC, the three sets-based and the single set-based WRM with a 0.8 emissivity value.

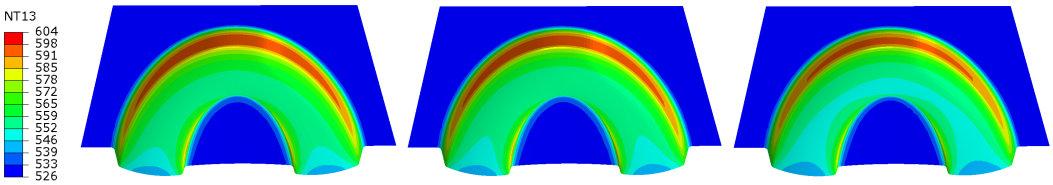

(a) **(b)** **(c)**

Figure B.10 – Temperature field for (a) full Cavity BC (b) three sets-based and (c) single surface-based weak formulation

The Figure B.11 shows a comparisons by set of the temperature difference with error bars (± the standard deviation) with full cavity radiation BC for 0.8 emissivity.

The differences are clearly better for the three sets-based method. The average value for the SET-3 elements is higher in both cases. A focus on temperature field of the SET-3 is made in the Figure B.12. The higher temperature differences for the single surface-based formulation is slightly revealed.

The same simulations with 0.5 emissivity were computed in order to evaluate the influence of such parameter in the formulation. The Figure B.9 compares the gaps with full cavity radiation BC for both weak formulation configurations.

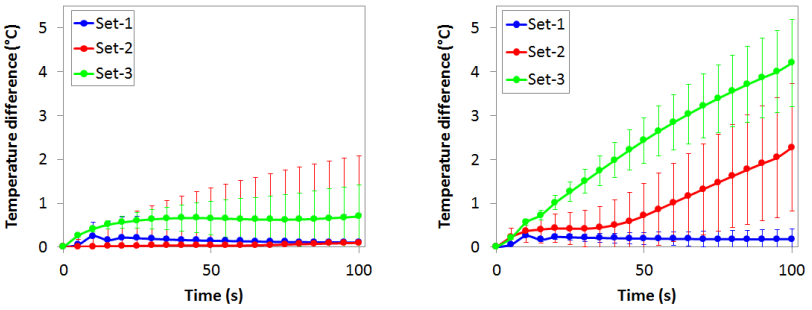

(a) **(b)**

Figure B.11 – Temperature differences for ϵ=0.8 between full cavity BC and (a) three sets-based and (b) single surface-based formulation

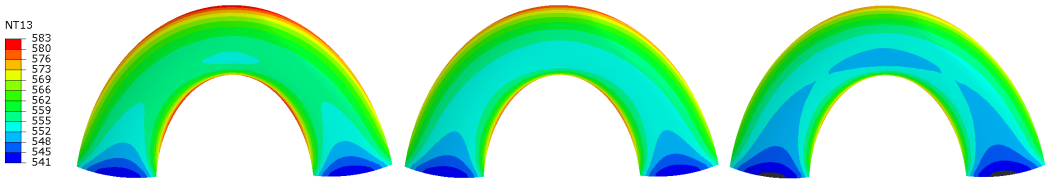

(a) **(b)** **(c)**

Figure B.12 – Temperature field of SET-3 elements for (a) full cavity BC (b) three sets-based and (c) single surface-based weak formulation

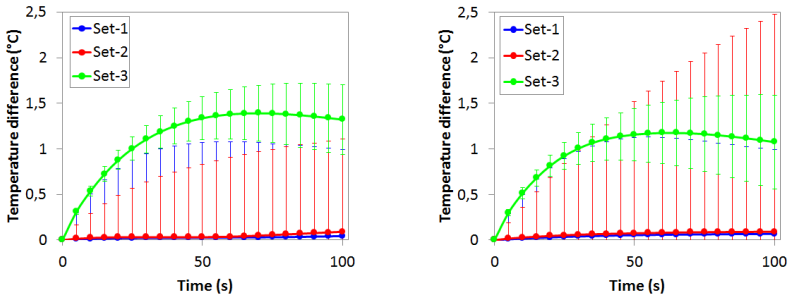

(a) **(b)**

Figure B.13 – Temperature differences for ϵ=0.5 between full cavity BC and (a) three sets-based and (b) single surface-based formulation

B.2.4 Conclusion

The weak formulation method gives very good approximation of view factor based radiative BC proposed in pure heat transfer analysis. This method is very precise and the results are acceptable even with a coarse decomposition of homogeneous temperature surfaces. The gap difference is inferior to 5°C after 100 seconds of pure radiative cooling from 800°C. The effect of emissivity value on the temperature error is rather limited, especially for low emissivity.

Appendix

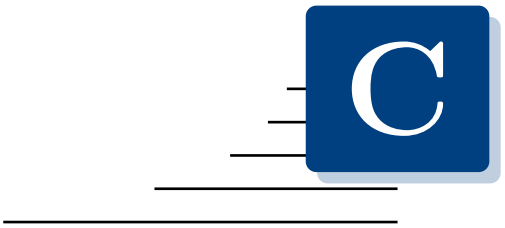

CFD analyses

C.1 Context

This appendix has the objective to present how the CFD simulations have been build, and to evaluate their capability to get the right convection coefficient information. Indeed, there is a large number of existing FE codes, which proposes many different possibilities to build CFD models. The codes that was used is ABAQUS® . It proposes incompressible fluid dynamic analysis with thermal convective problems analysis.

The appendix answers some of the next questions:

- What are the hypothesis made in the models ? What are these theories based on ? Is this method adapted to our problem ?
- How does the model has to be build (geometries, boundary conditions, etc.)?
- How to validate the model ? which level of confidence to give into the results ?

C.2 Bibliographic review

A large part of the developed theories and equations in this appendix were taken from two major books in the field of heat transfers and fluid mechanics: "Fundamentals of Heat and Mass Transfer" written by Incropera et al. [38] and "fluid Mechanics" from Franck M. White [226].

C.2.1 CFD Equations

The equations that govern fluid dynamic is a set of conservation laws which are called the Navier-Stockes equations (NSE). A conservation law mathematically defines the continuity of physical property over time variations. It is defined Equation (C.1) where ϕ is the physical property on which conservation is applied. It states that the volume variation of ϕ in a volume V plus what get in or out of the volume of a surface $\partial\phi$ is equal to production or dissipation term through the volume integration of S.

$$\frac{d}{dt}\int_V \phi dV + \int_{\partial V} \phi \overrightarrow{u}.\overrightarrow{n} dA = \int_V S dV \tag{C.1}$$

The local conservation law which derives from Equation (C.1) by using the Green-Ostrogradski theorem is defined Equation (C.2) where $\frac{\mathrm{D}}{\mathrm{D}t}$ is the material derivative.

$$\frac{\mathrm{D}\phi}{\mathrm{D}t} = \frac{\partial\phi}{\partial t} + \nabla.(\phi\overrightarrow{u}) = S \tag{C.2}$$

With NSE, the conservation law is applied on the density ρ, the quantity of motion ρu_i in the three axis x_i directions and the total energy ρh where h is the specific enthalpy. The first Equation (C.3) defines the mass conservation and is also called the continuity equation. The second equation is the conservation of momentum or Newton's second law of motion defined Equation (C.4) for the x_i coordinate where p is the pressure, μ the dynamic viscosity and g the gravity.

$$\frac{\mathrm{D}\rho}{\mathrm{D}t} = 0 \tag{C.3}$$

$$\frac{\mathrm{D}\rho u_i}{\mathrm{D}t} = -\nabla p + \nabla.(\mu\nabla(u_i)) + \rho g \tag{C.4}$$

The conservation of energy equation can be formulated through different ways. Equation (C.5) is the specific enthalpy form where λ is the heat conduction coefficient, S_h corresponds to the sources and dissipation terms. The contribution of heat exchanges into the buyoancy driven flows is the basis of natural convection problems.

$$\frac{\mathrm{D}\rho h}{\mathrm{D}t} = -\nabla.(p\overrightarrow{u}) + \nabla.(\lambda\nabla(T)) + S_h \tag{C.5}$$

This set of equations were introduced in this forms by Naviers and Stokes to describe the behavior of newtonian fluids. The solution of these equations has not been yet demonstrated, and FEM is a way to approximate the solution. These equations can be adapted regarding to the problems that are modeled, and the hypothesis that can be made. Indeed, CFD problems can be divided in several main categories: compressible and incompressible flow ; laminar or turbulent flows; natural or forced convection; transient or steady state regimes. These different categories and the hypothesis that they involve regarding CFD equations are introduced hereafter.

C.2.2 Compressibility/incompressibility

Newtonian fluids are various but they can be divided into two main categories, liquids and gases. Liquids are considered incompressible while gases can be both accounting environment conditions. The compressibility of a flow concerns the sensitivity of its density to pressure. In the conservation forms of NSE, the compressibility of a fluid have a influence on density term which can be considered constant and get out of divergence and gradient operators. Theoretically, every fluid is compressible. However, the hypotheses of incompressible flow is generally verified using Mach number. The Mach number is equal to the ratio of the fluid velocity and the speed of sound. It traduces the ratio of forces corresponding to motion and compressibility of the fluid. When it is inferior to 0.3, the flow is considered incompressible. The Mach number can be defined by Equation (C.6) for perfect gaz where γ, R_s and T are respectively the compressibility coefficient $\lambda = c_p/c_v$=1.4 for air, the specific constant of gas and the temperature.

$$Ma = \frac{V}{\sqrt{\gamma R_s T}} \tag{C.6}$$

Moreover, a fluid can be considered compressible when the fluid density variations with temperature are negligible compared to the reference temperature density ($\Delta\rho \ll \rho_0$). In this case, the density variations are defined depending only on temperature. This approximation is defined Equation (C.7) and generally called the Boussinesq approximation.

$$\Delta\rho = -\rho_0\beta(T - T_0) \tag{C.7}$$

The Boussinesq approximation enables to simplify the equations (C.3), (C.4) and (C.5) into (C.8), (C.9) and (C.10). In the Equation (C.10), the enthalpy is replaced by the temperature thanks to the relation between both ($dh = c_p dT$).

$$\nabla.\overrightarrow{u} = 0 \tag{C.8}$$

$$\frac{\mathrm{D}u_i}{\mathrm{D}t} = -\frac{1}{\rho_0}\nabla p + \frac{\mu}{\rho_0}\nabla^2\overrightarrow{u} + g \tag{C.9}$$

$$\rho c_p \frac{\mathrm{D}T}{\mathrm{D}t} = \nabla.(\lambda\nabla(T)) + S_h \tag{C.10}$$

In our case, the fluid incompressibility is questionable. Indeed, the velocity of the fluid in natural convection are low, so that $Mc \ll 0.3$. However, the temperature into the boundary layer can vary from 900 °C to 20 °C for which the density of air vary respectively from 0.3 kg.m^{-3} to 1.2 kg.m^{-3}.

The density variation from a mathematical point of view acts on the buoyancy forces that are generated through Archimedes' principle. Thus, the incompressibility approximation can wrongly estimate these forces and associated motions of particles. Martineau et al. [227] performed comparative analysis of a square cavity test case with both compressible and incompressible flows analysis for large temperature difference. They tested constant and varying properties (dynamic viscosity and thermal conduction) for incompressible flows. They showed that they were non negligible differences for velocity fields, but they obtained relatively closed results concerning HT.

When using incompressible flow analysis, the fluid density properties have to be considered constant. In most of the problems, the median temperature between surface and air is used. Indeed, normally the difference of temperatures is supposed to be small, and the behavior is taken linear in between. However, when the temperature difference is large, the choice of the temperature for density is not trivial. A sensitivity analysis is presented on the choice of the reference temperature for the horizontal plate natural convection case in the Section C.4.3.2.

C.2.3 Turbulence modeling

The appearance of turbulences in fluid dynamic corresponds to an unstable phenomena that happens under high velocity conditions. One way to describe turbulence velocity field is to split the velocity component into two contributions as defined Equation (C.11) where u, U and $u^{'}$ are respectively the velocity, the mean velocity and the turbulent velocity components. This method used to describe the velocity is called the Reynolds decomposition [37]. The figure C.1a represents the typical point velocity measurement in turbulent flow [37] where Reynolds decomposition is highlighted. The specificity of turbulent velocity fluctuations is that they have always a three-dimensional spatial character. Moreover, visualizations of turbulent flows reveal rotational flow structures, so-called turbulent eddies, with a wide range of length scales [37].

$$u(t) = U(t) + u^{'}(t) \tag{C.11}$$

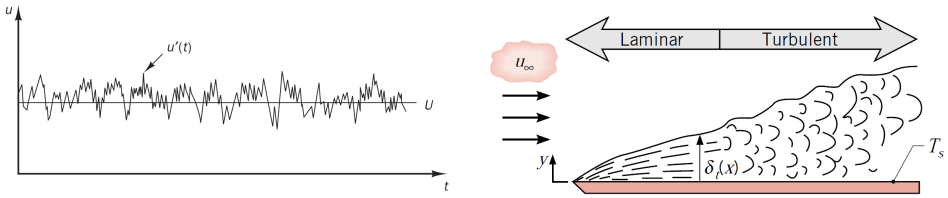

(a) **(b)**

Figure C.1 – (a) Reynolds decompisition of velocity in turbulent flow [37] (b) representation of laminar to turbulent transition flow [38]

There are a very large number of method to model turbulences. Indeed, there are very complex methods that take account of every turbulent length scales velocity such as direct numerical simulation method. Such computations are highly costly in terms on computing resources, so that it is not used for industrial applications [228]. Then, there are large eddy simulation methods that focus only on large scale turbulent motion. Large eddy simulations are mainly used to model far from wall turbulence regimes at high Reynolds number and are not adapted for our problematic [229]. Both previously described models are qualified of direct because no simplifications using reynolds decompositions are made. Then the other models are build using Reynolds decomposition and are called Reynolds averaged Navier Stokes (RANS) models. RANS models are fairly simple models (easy to implement ; simple boundaries and initial conditions) that are widely used in industry, especially the k-ε based models. RANS turbulence models have limited valid fields of application, but for simple geometry and specific case conditions it is a very efficient method to evaluate turbulent flow in a first approach [228]. They are different grades of complexity depending on the number of supplementary equations that describe turbulences.

C.2.3.1 RANS equations

The NSE are time averaged using the Reynolds decomposition defined in the Equations (C.12) and (C.13) where Θ and $T^{'}$ are respectively the average and turbulent components of the temperature. The time averaged turbulent terms equal to zero such as defined in the Equation (C.14) where $\overline{x}$ means the time averaging of x quantity.

$$\overrightarrow{u} = \overrightarrow{U} + \overrightarrow{u}^{'} = \left[U_x + u_x^{'}; U_y + u_y^{'}; U_z + u_z^{'}\right]_{(\overrightarrow{x},\overrightarrow{y},\overrightarrow{z})} \tag{C.12}$$

$$T = \Theta + T^{'} \tag{C.13}$$

$$\overline{u_x'} = \overline{u_y'} = \overline{u_z'} = \overline{T_z'} = 0 \tag{C.14}$$

By this way, the new equations can be defined Equations (C.15), (C.16) and (C.17) respectively the continuity, the momentum and energy RANS equations.

$$\nabla . \overrightarrow{U} = 0 \tag{C.15}$$

$$\frac{\mathrm{D}U_i}{\mathrm{D}t} = -\frac{1}{\rho}\nabla P + \frac{\mu}{\rho}\nabla^2 \overrightarrow{U} + g + \frac{1}{\rho}\left(\frac{\partial(-\rho\overline{u_i' u_x'})}{\partial u_x} + \frac{\partial(-\rho\overline{u_i' u_y'})}{\partial u_y} + \frac{\partial(-\rho\overline{u_i' u_z'})}{\partial u_z}\right) \tag{C.16}$$

$$\rho c_p \frac{\mathrm{D}\Theta}{\mathrm{D}t} = \nabla . (\lambda \nabla(\Theta)) + S_h + \rho c_p \left(\frac{\partial(-\overline{T' u_x'})}{\partial x} + \frac{\partial(-\overline{T' u_y'})}{\partial y} + \frac{\partial(-\overline{T' u_z'})}{\partial z}\right) \tag{C.17}$$

The right hand terms of Equation (C.16) are called the Reynolds stresses τ_{ij} as defined Equation (C.18). The computation of τ_{ij} components resides in the choice of the turbulent model.

$$\tau_{ij} = -\rho\overline{u_i' u_j'} \tag{C.18}$$

Boussinesq proposed that Reynolds stresses might be proportional to mean rates of deformation such as defined Equation (C.19) where k $(= \frac{1}{2}\left(\overline{u'^2}_x + \overline{u'^2}_y + \overline{u'^2}_z\right))$ is the turbulent kinetic energy per unit mass and μ_t the turbulent eddy viscosity.

$$\tau_{ij} = -\mu_t \left(\frac{\partial(U_i)}{\partial x_j} + \frac{\partial(U_j)}{\partial x_i}\right) - \frac{2}{3}\rho k \delta_{ij} \tag{C.19}$$

C.2.3.2 RANS Turbulence models

There are three main categories of RANS-based turbulence models. there are distinguished by their way to compute Reynolds stresses. Either, they computes Reynolds stresses thanks to Equation (C.19) where turbulent Eddy viscosity μ_t can be considered linear or non-linear nor they are computed using differential transport equations with Reynolds Stress Transport Models (RSM) models. Each method presents advantages and weaknesses. ABAQUS® 6.14 software proposed several RANS based turbulence models, the Spalart-Allmaras (SA) [230] which is a single equation model, two k-ε (RNG and realizable) and the SST k-ω models that are two equations based models. Only these models are discussed below.

The SA model was developed initially for aerospace problems with high Reynolds number. The renormalization group (RNG) k-ε RANS model is an evolution of classical RANS one-equation models that smooth out many of the important features of turbulence [231]. The RNG k-ε introduces a dissipation term that is well adapted in our case (open free convection). Then, the k-ε-realizable model's equations are developed from fundamental physical principles and dimensional analysis; the equation for k is derived using first principles, and the equation for ε is postulated using physical insight [229]. These modifications guarantee the physical consistency in the predicted Reynolds stresses, thus improving the accuracy of the predictions [232]. However, it has been developed for high Reynolds number. The k-ω model is based on standard k-ε, but it uses a specific energy dissipation rate $\omega \approx \varepsilon/k$. It is efficient near the wall in the viscous sublayer contrary to k-ε version. Menter [233] defined k-ω SST version, which is an hybrid formulation that blends the standard k-ω model near to the wall with a transformed version of the standard k-ε model (into k-ω form) far from the wall.

The k-ω SST is the more adapted turbulent model because of its possibility to be employed near from the wall boundaries with classical k-ω formulation, and into the bulk with blending functions that enable to switch to the k-ε formulation. Leschziner [234] concluded that k-ε

model can lead to excessive levels of turbulence in stagnation/impingement regions giving rise to excessive heat transfer in reattachment regions. On the contrary, SST k-ω model uses limiter function for turbulent shear stress that prevents excessive shear stress levels in boundary layers [229].

C.2.3.3 SST k-ω equation

The equations of this subsection are defined with the index notation. The Menter's equations are defined as the blending decomposition of the initial Wilcox model [235] and its modified version k-ϵ version where k and ω equations are respectively defined Equations (C.20) and (C.21) and Equations (C.22) and (C.23) where β^*, $\sigma_{k,1}$, λ_1, β_1 and $\sigma_{\omega,1}$ are the Wilcox model coefficient standard k, and β^*, $\sigma_{k,2}$, λ_2, β_2 and $\sigma_{\omega,2}$ the modified standard k-ε model parameters.

$$\frac{\mathrm{D}(\rho k)}{\mathrm{D}t} = \tau_{ij}\frac{\partial U_i}{\partial x_j} - \beta^*\rho\omega k + \frac{\partial}{\partial x_j}\left[(\mu + \sigma_{k,1}\mu_t)\frac{\partial k}{\partial x_j}\right] \tag{C.20}$$

$$\frac{\mathrm{D}(\rho\omega)}{\mathrm{D}t} = \frac{\lambda_1}{\nu_t}\tau_{ij}\frac{\partial U_i}{\partial x_j} - \beta_1\rho\omega^2 + \frac{\partial}{\partial x_j}\left[(\mu + \sigma_{\omega,1}\mu_t)\frac{\partial \omega}{\partial x_j}\right] \tag{C.21}$$

$$\frac{\mathrm{D}(\rho k)}{\mathrm{D}t} = \tau_{ij}\frac{\partial U_i}{\partial x_j} - \beta^*\rho\omega k + \frac{\partial}{\partial x_j}\left[(\mu + \sigma_{k,2}\mu_t)\frac{\partial k}{\partial x_j}\right] \tag{C.22}$$

$$\frac{\mathrm{D}(\rho\omega)}{\mathrm{D}t} = \frac{\lambda_2}{\nu_t}\tau_{ij}\frac{\partial U_i}{\partial x_j} - \beta_2\rho\omega^2 + \frac{\partial}{\partial x_j}\left[(\mu + \sigma_{\omega,2}\mu_t)\frac{\partial \omega}{\partial x_j}\right] + 2\rho\sigma_{\omega,2}\frac{1}{\omega}\frac{\partial k}{\partial x_j}\frac{\partial \omega}{\partial x_j} \tag{C.23}$$

The blending function Equation (C.24) is based on a tangent hyperbolic function F_1 (see Equations (C.25) and (C.26)) that enables to smooth the transition from k-ω to k-ϵ. This function is applied to each subscripted coefficients $\lambda_{1/2}$, $\beta_{1/2}$, $\sigma_{k,1/2}$, $\sigma_{w,1/2}$ to obtained a single set of coefficients for k and ω such as defined Equation (C.27) and (C.28)

$$\phi = F_1\phi_1 + (1 - F_1)\phi_2 \tag{C.24}$$

$$F_1 = tanh(arg_1^4) \tag{C.25}$$

$$arg_1 = \min\left(\max\left(\frac{\sqrt{k}}{\beta^*\omega y}, \frac{500v}{y^2\omega}\right), \frac{4\rho k\sigma_{\omega,2}}{CD_{k\omega}y^2}\right) \tag{C.26}$$

$$\frac{\mathrm{D}(\rho k)}{\mathrm{D}t} = \tau_{ij}\frac{\partial U_i}{\partial x_j} - \beta^*\rho\omega k + \frac{\partial}{\partial x_j}\left[(\mu + \sigma_k\mu_t)\frac{\partial k}{\partial x_j}\right] \tag{C.27}$$

$$\frac{\mathrm{D}(\rho\omega)}{\mathrm{D}t} = \frac{\lambda}{\nu_t}\tau_{ij}\frac{\partial U_i}{\partial x_j} - \beta\rho\omega^2 + \frac{\partial}{\partial x_j}\left[(\mu + \sigma_\omega\mu_t)\frac{\partial \omega}{\partial x_j}\right] + 2\rho(1 - F_1)\sigma_{\omega,2}\frac{1}{\omega}\frac{\partial k}{\partial x_j}\frac{\partial \omega}{\partial x_j} \tag{C.28}$$

The different k-ϵ based turbulence models are based on Boussinesq assumption defined above Equation (C.7). The differences reside in the definitions of turbulent eddy viscosity. For SST k-ω, it is defined by condition Equation (C.29) where a_1 is a constant, $S = \sqrt{2S_{ij}S_{ij}}$ (with $S_{ij} = \frac{\partial U_i}{\partial x_j} + \frac{\partial U_j}{\partial x_i}$), and F_2 is a tangent hyperbolic function. arg_2 is defined Equation (C.31) where y is the turbulent wall distance defined in the next sections.

$$\nu_t = \frac{\mu_t}{\rho} = \frac{a_1 k}{\max(a_1\omega, SF_2)} \tag{C.29}$$

$$F_2 = tanh(arg_2^2) \tag{C.30}$$

$$arg_2 = \max\left(\frac{2\sqrt{k}}{\beta^* \omega y}, \frac{500v}{y^2\omega}\right) \tag{C.31}$$

C.2.4 Mesh Grid

The mesh grid definition is conditioned firstly by the type of flow and the results that need to be extracted from the simulation. Mesh grid has to be fine in the high velocity gradient zones, which are generally located in boundary layers at no-slip surfaces. Thus, It is important to introduce the concept of boundary layer theory before to talk about mesh grid issues.

C.2.4.0.1 Boundary layer

The boundary layer (BL) is the layer which is formed at a surface where the fluid is flowing. It is represented Figure C.2 from velocity and temperature point of view. δ represents the BL thickness beyond what the shear stress τ and the thermal conductivity respectively for the velocity and the thermal BL has no longer influence on the velocity ($u \to u_\infty$) and the temperature ($T \to T_\infty$).

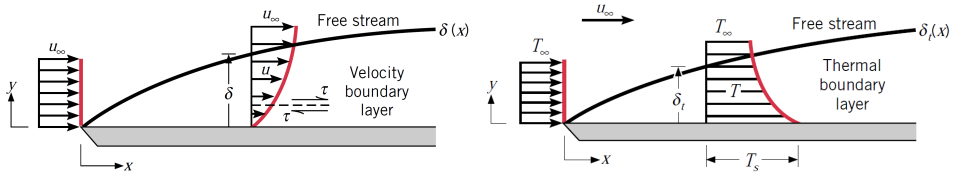

(a) **(b)**

Figure C.2 – (a) Velocity boundary layer (b) Thermal boundary layer [38]

From this boundary layer concept, it is possible to defined interface properties. The Equation (C.39) defines the local friction coefficient which can be determined with the definition of shear stress at the interface τ_s Equation (C.33).

$$C_f = \frac{\tau_s}{\rho V^2/2} \tag{C.32}$$

$$\tau_s = \mu \left.\frac{\partial u}{\partial y}\right|_{y=0} \tag{C.33}$$

Concerning thermal issue, the convection coefficient h can be obtained by combining Equation (C.34) with the heat conduction at the interface defined Equation (C.35). The local Nusselt coefficient is computed as defined Equation (C.36) where $T^*=(T - T_s)/(T_\infty - T_s)$ and $y^*=y/L_c$ are respectively the normalized temperature and perpendicular coordinate.

$$h = \frac{q_s}{T_s - T_\infty} \tag{C.34}$$

$$q_s = -k_f \left.\frac{\partial T}{\partial y}\right|_{y=0} \tag{C.35}$$

$$N_u = \frac{hL}{k_f} = \left.\frac{\partial T^*}{\partial y^*}\right|_{y^*=0} \tag{C.36}$$

C.2.4.0.2 Law of the wall

The turbulent BL can be divided into several layers represented Figure C.3a. Three distinct regions are depicted, the viscouslayer, the buffer layer and the turbulent region. The graph Figure C.3b represents the evolution of dimensionless velocity U^+ as a function of the dimensionless wall distance y^+ which is defined Equation (C.37). Von Karman highlighted first the behavior of fluids in turbulent regime [236] which is firstly linear in the viscous sub layer and then follows a transition (the buffer layer) to a logarithmic evolution. The different curves represent this behavior evolution for different Reynolds number, which means that this behavior is inherent to the fluid properties and not to the flow.

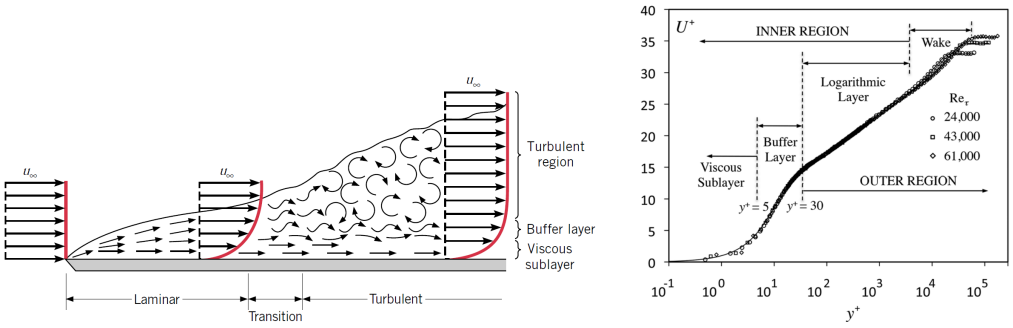

(a) **(b)**

Figure C.3 – (a)Velocity boundary layer development on a flat plate [38], (b) Mean velocity profile of turbulent flow over flat plate at different Reynolds number. The different turbulent sublayers are depicted on the graph [39]

$$y^+ = \frac{y^* U_{fric}}{\nu} \tag{C.37}$$

The law of the wall is defined Equation (C.38) where κ and B are respectively the von Karman's constant (≈ 0.41) and a constant (≈ 5.1). These values can evolve as a function of surface roughness [228].

$$u^+ = \begin{cases} y^+ & - \text{ Viscous sublayer} \\ \frac{1}{\kappa} ln(y^+) + B & - \text{ Log. layer} \end{cases} \tag{C.38}$$

C.2.4.0.3 Wall functions

By using this law of the wall, it is possible to evaluate the fluid velocity with elements whose centers lie in the fully turbulent layer (inertial or log layer) for which such functions are designed. Practically, ABAQUS® uses a hybrid wall functions that enable to work in the different layers independently of the near-wall resolution. The same approach is used to defined law of walls for momentum and energy implementation near the wall [229]. For better evaluation of velocity and temperature profile, most of the CFD FE codes advice to have the first point for computation at $y^+ \approx 11$ which is located at the cross point of the linear and logarithmic functions [237].

C.2.4.0.4 Mesh grid spacing

The mesh grid in CFD modeling is essential. Indeed, the different layers that are formed during turbulent flow require fine mesh near the wall to be described numerically. The

computation of ideal first mesh grid spacing Δs associated to a specific y^+ value was proposed by White [226]. He used the definition of shear stress (Equation (C.33)) and friction coefficient (Equation (C.39)) to evaluate the friction coefficient as a function of Reynolds number (see Equation (C.39)) in the case of laminar and turbulent velocity profiles on flat-plate boundary layer. By this way, it is possible to obtain Δs (see Equation (C.42)) by combining Equations (C.37), (C.40) and (C.41).

$$C_f = \frac{2}{Re_L} \left. \frac{\partial u^*}{\partial y^*} \right|_{y^*=0} = \begin{cases} 0.664/R_{e_x}^{1/2} & \text{if laminar} \\ 0.027/R_{e_x}^{1/7} & \text{if turbulent} \end{cases} \tag{C.39}$$

$$\tau_{wall} = \frac{C_f \rho U_\infty^2}{2} \tag{C.40}$$

$$U_{fric} = \sqrt{\frac{\tau_{wall}}{\rho}} \tag{C.41}$$

$$\Delta s = \frac{y^+ \nu}{U_{fric}} \tag{C.42}$$

C.3 Strategy - Objectives

One difficulty to compare our model to existing experimental case is that most of the aerothermal field of applications where CFD is used are out scale. Indeed, the external buoyant enhanced natural cooling applications are rather nonexistent for our range of temperature differences. It exists some relevant cases that are available to evaluate CFD models. For natural convection, flat plates are common geometries which are widely used experimentally. In our context, the complexity of the geometries and the surrounding environment get similar to external plate natural convection, especially horizontal plate problems.

Kitamura et al. study experimentally the turbulent transition of natural convective flows adjacent to the upward-facing, heated rectangular plates [23]. Their experiments consisted into the visualizations of the flow fields over the plates, and the measurements of average Nusselt numbers. They visualized the velocity magnitude thanks to the density of smoke brought from the four plate edges. The Figure C.4 represents the flow patterns visualization over rectangular plates. The brightness contrast gradient testifies of the shape of velocity field and also the appearance of turbulences.

Firstly, the model was confronted to experimental results from the work of Kitamura et al. [23] especially regarding the average Nusselt correlations and the turbulences appearance. This step enabled to evaluate how the CFD model behaves in the Kitamura's paper experimental conditions. However, their tested temperature range was much lower than the SPF process one. Therefore, the model has been extended to the temperature differences and characteristic length corresponding to the SPF process. Finally, a sensitivity study of the model was performed regarding to two model parameters. Firstly, the mesh grid was analyzed to evaluate its influence, and then set the most adapted one for the process simulations. Secondly, the reference temperature used for fluid density was analyzed. The density of air varies widely with temperature: 1.2 $kg.m^{-3}$ at ambient temperature up to 0.3 $kg.m^{-3}$ at 900 °C. Our CFD analyses are build on incompressible NSE hypothesis which imposes to consider a constant density. That is why it is important to analyze the effect of the density on the obtained fluid flow and heat transfers.

Once a relevant modeling method has been implemented, CFD modeling simulations of different cooling sequences were performed on laboratory tests and on industrial parts. The objective was to extract convection profiles in order to evaluate an appropriate definition

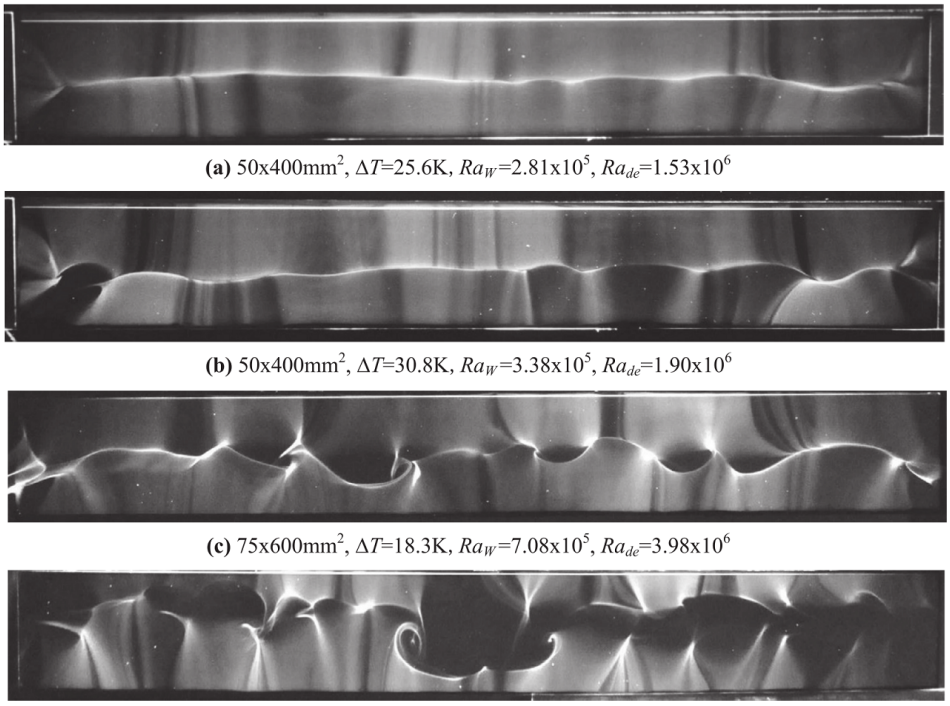

(a) 50x400mm^2, ΔT=25.6K, Ra_W=2.81x10^5, Ra_{de}=1.53x10^6

(b) 50x400mm^2, ΔT=30.8K, Ra_W=3.38x10^5, Ra_{de}=1.90x10^6

(c) 75x600mm^2, ΔT=18.3K, Ra_W=7.08x10^5, Ra_{de}=3.98x10^6

(d) 100x800mm^2, ΔT=21.8K, Ra_W=1.97x10^6, Ra_{de}=1.17x10^7

Figure C.4 – Visualized flow fields over upward-facing rectangular plates [23]

of convection coefficient for thermomechanical simulation as a function of geometry, and temperature. These profiles were used to fit thermal boundary conditions parameters onto experimental data obtained with laboratory cooling tests.

C.4 Horizontal plate model

C.4.1 Model

C.4.1.1 Geometries

The fluid domain is an important parameter that can influence the solution if it is poorly defined. For external natural convection, there is no concrete limiting dimensions. Thus it is important that dimensions are large enough to remove the influence of boundaries. Autodesk® CFD FE code gives some guidelines to design fluid domain dimensions for external natural convection regimes [40]. The Figures C.5a and C.5b respectively gives fluid domain design instructions for table-mounted and air-mounted geometries.

Our model is an horizontal grounded plate following free convection on its upper face. The definition of the fluid geometry is presented Figure C.6. The dimensions are (10x10x6.5)xW where W is the plate width. Dimensions were enlarged compared to guidelines to prevent from the potential troubles that the large temperature differences can induce.

C.4.1.2 Material properties

The material properties can be chosen constant for incompressible fluid analysis. However it is possible to input variable temperature data except for density. Martineau et al. [227] got better results with variable properties instead constant for natural convection with large

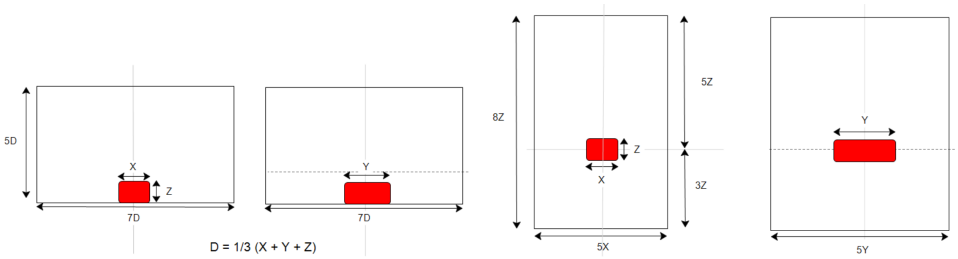

(a) **(b)**

Figure C.5 – Fluid domain design guidelines for external natural convection CFD problems [40]

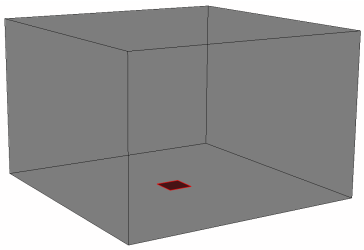

Figure C.6 – Horizontal ground-mounted plate model - fluid domain

temperature differences. There are different properties to input for CFD simulations: the dynamic viscosity μ, the thermal conductivity λ, the linear or volumetric thermal expansion α or β and the constant pressure heat capacity c_p.

Concerning the dynamic viscosity, a Sutherland law [238] were used such as defined Equation (C.43) where μ_{ref}, T_{ref} and S are respectively the reference viscosity, the reference temperature and the Sutherland temperature. For air, these constants are defined table C.1 from CFD-online website [239].

$$\mu = \mu_{ref} \left(\frac{T}{T_{ref}} \right)^{3/2} \frac{T_{ref} + S}{T + S} \tag{C.43}$$

The thermal conductivity varies significantly from ambient temperature up to 900 °C, it is multiplied by three. Sutherland also proposes that thermal conductivity follows the same dependency on temperature [238] with the same kind of equation such as defined Equation (C.44). This law was used to fit data from Engineering Toolbox web site [240]. The Sutherland's law coefficients for thermal conductivity λ_{ref} and S_λ are given table C.1.

$$\mu = \lambda_{ref} \left(\frac{T}{T_{ref}} \right)^{3/2} \frac{T_{ref} + S_\lambda}{T + S_\lambda} \tag{C.44}$$

Concerning the thermal expansion, the ideal gas hypothesis was taken. Indeed, for incompressible fluid assumption, the volumetric thermal expansion β can be derived from the ideal gas law such as defined Equation (C.45)

$$\beta = \frac{1}{V} \left(\frac{\partial V}{\partial T} \right)_P = \frac{1}{T} \tag{C.45}$$

Finally, a second order polynomial expression of the specific heat capacity was build from Engineering Toolbox web site [241]. The coefficients $a^0_{c_p}$, $a^1_{c_p}$ and $a^2_{c_p}$ of the law are presented table C.1

μ_{ref} ($kg.m^{-1}.s^{-1}$)	T_{ref} (K)	S (K)	λ_{ref} ($kg.m^{-1}.s^{-1}$)	S_λ (K)	$a^0_{c_p}$ ($J.kg^{-1}.K^{-1}$)	$a^1_{c_p}$ ($J.kg^{-1}.K^{-2}$)	$a^2_{c_p}$ ($J.kg^{-1}.K^{-3}$)
1.716E-5	273.15	110.4	2.366E-2	232.85	1.38E-4	5.52E-2	968.4

Table C.1 – Material model parameters for air

C.4.1.3 Boundary conditions

The definition of the model were adapted from the ABAQUS® exemple "Conjugate heat transfer analysis of a component-mounted electronic circuit board" [242] inspired from the work of Eveloy and Ro [243]. The ground and the plate respectively Figure C.7a and Figure C.7b where defined as no-slip (u_x=u_y=u_z=0) BC. The temperature of the ground was fixed at the ambient temperature (20 °C). The top of the air box (see Figure C.7c) where associated to the outlet surface with a null pressure. No BC were input to the lateral surfaces of the box (see Figure C.7d) so that a zero Neumann condition were fixed for HT, pressure and velocity. These type of boundary conditions requires that the distance between the plate and the lateral and top surfaces are far enough.

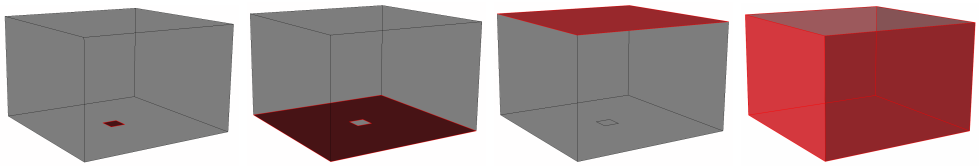

(a) **(b)** **(c)** **(d)**

Figure C.7 – Model geometry with specific surfaces highlighted in red: (a) plate, (b) ground, (c) top and (d) lateral surfaces

C.4.1.4 Initial conditions

The initial conditions that are required for natural convection are:

- Velocity: $\overrightarrow{u} = \overrightarrow{0}$
- Temperature: ambient temperature
- Pressure: zero pressure
- Turbulence: k_{ini}, ε_{ini}, ω_{ini}

For incompressible fluid analysis, the initial pressure has no influence, only the pressure variations count. The computation of turbulent initial data k_{ini}, ε_{ini} and ω_{ini} was made referring to ABAQUS® recommendations [229]. k_{ini} is computed with Equation (C.46) where U_∞ and I are respectively the free stream velocity and the turbulent intensity.

$$k_{ini} = \frac{3}{2}\left(U_\infty I\right)^2 \tag{C.46}$$

For natural convection, it is more difficult to estimate U_∞ contrary to forced convection. One way is to consider the Richardson number (R_i) defined Equation (C.47) as the ratio of buoyancy term and shear flow term. When $R_i \ll 1$, the flow is supposed to tends to natural

convection guided flow whereas on the contrary, $R_i \gg 1$, it tends to forced convection guided flow. The stable portion of the plume generated by the convection flow can be considered as a transition from natural to forced convection flow with R_i=1. By this way, it is possible to estimate a value of U_∞ with Equation (C.48).

$$R_i = \frac{\frac{g}{\rho}\frac{\partial \rho}{\partial z}}{\left(\frac{\partial u}{\partial z}\right)^2} = \frac{G_r}{R_e^2} \tag{C.47}$$

$$U_\infty^2 = g L_c \beta \Delta T \tag{C.48}$$

The turbulent intensity I is a percentage of turbulent flow. Some empirical relation exists for specific applications. The equation (C.49) defines I as a function of Reynolds numbers [228] which is also computed thanks to previous assumptions concerning Richardson number. This equation is originally used for hydraulic pipe system. However, it enables to get a first approximation of this percentage.

$$I = 0.17(R_e)^{-1/8} \tag{C.49}$$

Initial value of ε is computed thanks to Equation (C.50) where C_μ and l are a coefficient of the model and the turbulent characteristic length. l is defined with Equation (C.51) where C_l is a coefficient that depends on the flow type [228] (the value were fixed at C_l=0.07).

$$\varepsilon_{ini} = C_\mu^{3/4} \frac{k_{ini}^{3/2}}{l} \tag{C.50}$$

$$l = C_l L_c \tag{C.51}$$

Concerning initial ω, it is computed thanks to Equation (C.52) where β^* is a turbulent model coefficient.

$$\omega_{ini} = \frac{k_{ini}^{1/2}}{{\beta^*}^{1/4} l} \tag{C.52}$$

C.4.1.5 Mesh

The CFD models were meshed with regular grid (FC3D8 ABAQUS® elements). The conditions for meshing is defined Section C.4 for which first grid to surface spacing has to be carefully computed. The mesh where rectilinear grid with refinement at no-slip surfaces such as presented Figure C.8 where the bottom bold line represent the plate surface.

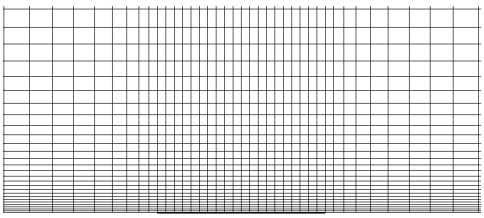

Figure C.8 – Example of mesh grid with a rectilinear refinement near the wall

C.4.1.6 Solving Method

ABAQUS® CFD uses the projection method to solve incompressible NSE. The basic concept for projection methods is the legitimate segregation of pressure and velocity fields for efficient

solution. In practice, the projection is used to remove the part of the velocity field that is not divergence-free. The projection is achieved by splitting the velocity field into div-free and curl-free components using a Helmholtz decomposition. The projection operators are constructed so that they satisfy prescribed boundary conditions and are norm-reducing, resulting in a robust solution algorithm for incompressible flows [229].

For small density variations, the Boussinesq approximation provides the coupling between momentum and energy equations. In turbulent flows, the energy transport includes a turbulent heat flux based on the turbulent eddy viscosity and turbulent Prandtl number. ABAQUS® CFD provides a temperature-based energy equation.

In our case, two different approaches are possible, especially when temperature of surfaces vary. Firstly, it is possible to couple the CFD model with standard HT simulation with varying surface temperatures. This method requires full time computing of physical phenomena and thus it is very costly in computing time. The second way that was chosen is to consider constant temperatures of surfaces in order to get stable HT associated to a specific temperatures configuration. This method enables to limit time computing. One weakness is that it requires to interpolate HT in between computed temperatures. Moreover, ABAQUS® CFD does not enable to impose heterogeneous surface temperatures so that it requires to divide surfaces into constant temperature partitions.

In analyses where the objective is to reach a steady-state solution, ABAQUS® CFD proposes the fully implicit (backward-Euler) method. This method is unconditionally stable, allowing to specify large Courant-Friedrichs-Lewy (CFL) values to significantly increase the time increment size. By default, ABAQUS® CFD uses an automatic time incrementation algorithm that continually adjusts the time increment size to satisfy the stability condition for advection.

C.4.2 Experimental confrontation

In the next section, the model is compared with experimental data from the work of Kitamura et al. [23] on horizontal plate natural convection. They investigated the effect of Rayleigh number on turbulence appearance and HT. They used different plate widths and aspect ratios (AR - the ratio of Length and width) to generate many different Rayleigh numbers and flow conditions.

Both the turbulence transitions and the Nusselt numbers are investigated for squared plates of different sizes and temperatures in order to compare our model to their experimental results. Some visualized flow fields of the reference experimental cases are presented in the Figure C.9. These figures were used to evaluate the agreement of the model, especially the appearance of turbulent flows. The associated average Nusselt number for many plate widths and temperatures are summarized in the plot Figure C.10.

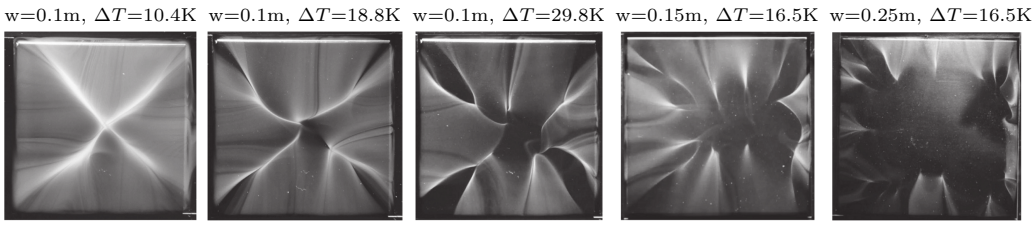

Figure C.9 – Visualized flow fields over upward-facing squared plates [23]

The model for the different geometries is based on the previous descriptions of Section C.4.1. The mesh grid is presented C.11. Most of the simulation results are presented in the near-wall plane (see Figure C.12a). The space between the plate and the near-wall plane is fixed at

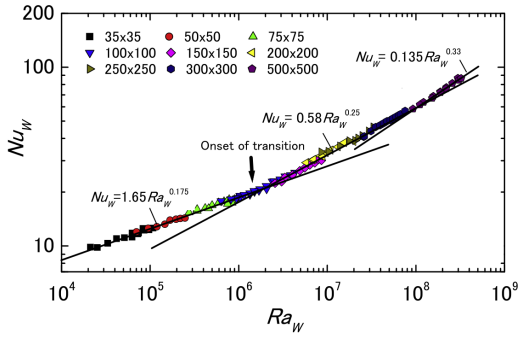

Figure C.10 – Average Nusselt numbers and their correlations from squared plate [23]

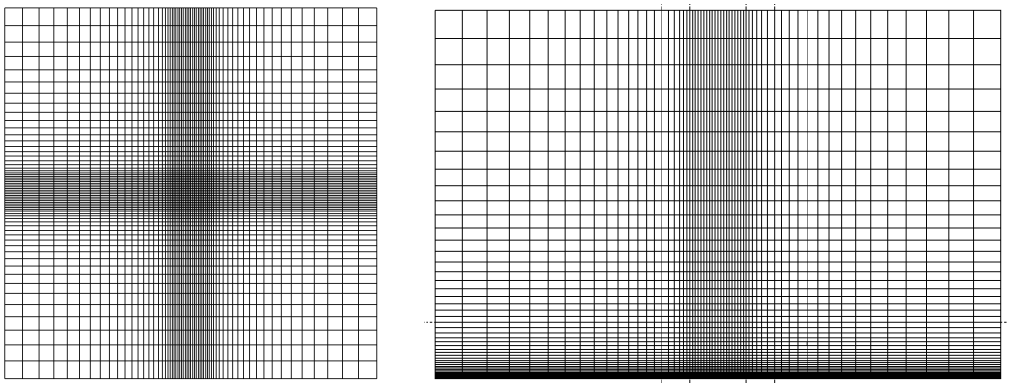

(a) **(b)**

Figure C.11 – Mesh grid of plate model in (a) plate plane and (b) z-axis direction

δ=W/30 in order to catch the effect of HT on velocity, turbulence and temperature field near the plane. Then, stream lines were extracted along a specific path (in red) defined Figure C.12b. This path follows the edges of plate and the diagonals.

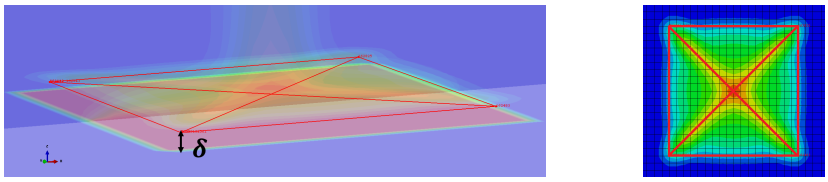

(a) **(b)**

Figure C.12 – (a) Representation of the near wall plane and the stream lines path upward to the plate in red in 3D view, (a) parallel view of plate

C.4.2.1 Small temperature variations

Fives different case were chosen for the impact of the temperature difference on the flow. The Table C.2 references the cases parameters. Stream lines and velocity vectors are represented Figure C.13 for the extrema and mid temperature differences. It is clear that no turbulence happens for these cases (and logically for intermediate cases). Indeed, the velocity vectors and stream lines are perfectly symmetrical. Converning convection coefficient h, the space distribution seems equivalent in the shape with a slight increase when ΔT increases. One

Case	1	2	3	4	5
Width (m)	0.1				
ΔT (°C)	10.6	14.9	18.8	24.5	29.8
R_{aw}	1.03E6	1.4E6	1.76E6	2.04E6	2.33E6

Table C.2 – Description of parameters of testing cases for small temperature variations

remark is that the cross shape that forms the minimum values for HT seems to get narrowed when increasing ΔT.

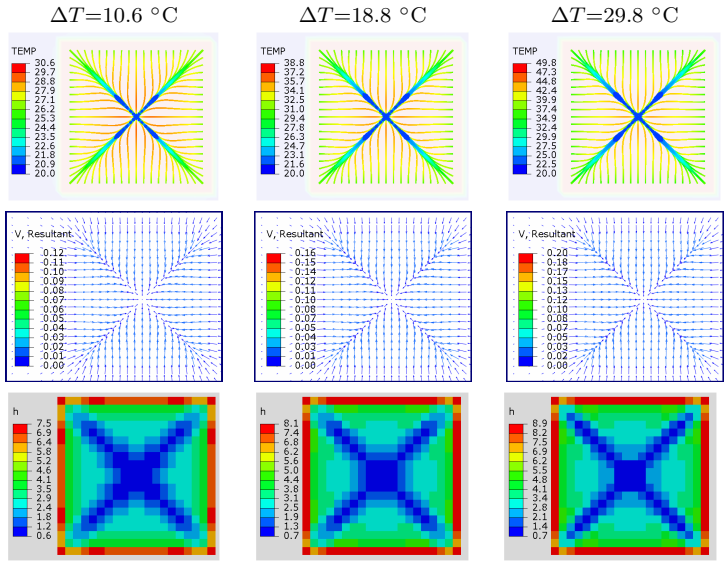

Figure C.13 – Stream lines, velocity vectors (m.s^{-1}) and convection coefficient field (W.m^{-2}.K^{-1}) for the cases 1, 3 and 5

Concerning Nusselt correlations, Figure C.14 represents the average Nusselt number evolution with Rayleigh number. The dashed lines corresponds to Kitamura's correlation with experimental values. There is an important gap between numerical values and correlations. However, the variations seem to correspond.

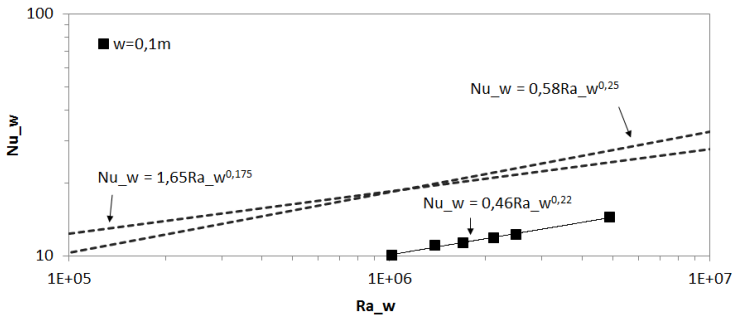

Figure C.14 – log-log curve of Nusselt number evolution with Rayleigh number for small temperature variations

C.4.2.2 Width variations

Fives different case were chosen for the impact of plate width on the flow. The Table C.2 references the cases parameters. The tested cases still correspond to Kitamura's experiments.

Case	2	6	7	8	9
Width (m)	0.1	0.15	0.25	0.5	1
ΔT (°C)	15				
R_{aw}	1.4E6	4.88E6	2.26E7	1.81E7	1.44E9

Table C.3 – Description of parameters of testing cases for width variations

The same kind of results than the previous section are presented in the Figure C.15. The turbulence clearly appear from w=0.25m. Indeed, regarding the stream lines, the center-lines which are totally perpendicular in laminar cases, begin to deviate from Case 7. For Case 8 and 9 the stream lines are even more disturbed. The same conclusion can be drawn for velocity vectors. Concerning convection coefficient field, there is a strong difference for laminar and turbulent field which is largely discontinuous. This phenomena is due to turbulences that influence the velocity gradient which is directly related to the temperature gradient at the plate surface. Indeed, when the mesh is not fine enough to catch gradient sign inversion from a node to an adjacent node, it can create this discontinuities. However, the average value is not impacted.

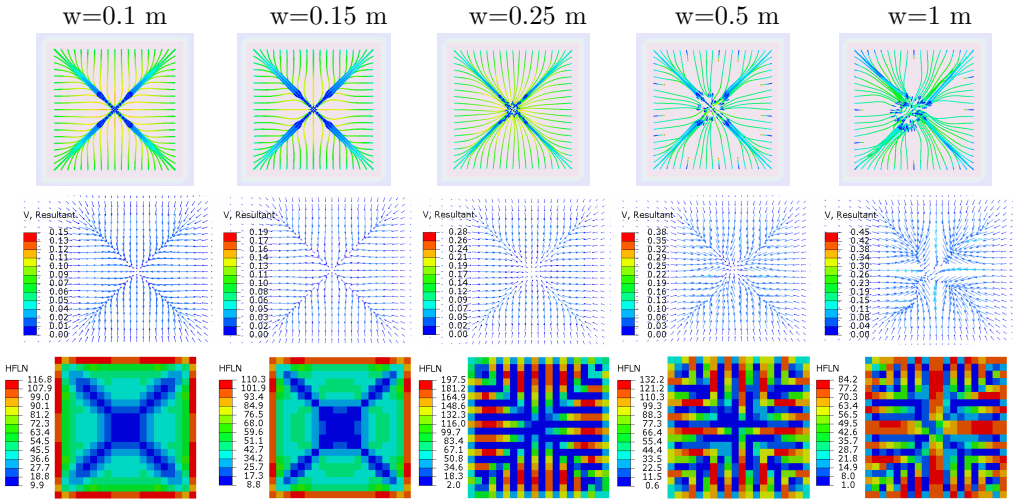

Figure C.15 – Stream lines, velocity vectors (m.s^{-1}) and convection coefficient field (W.m^{-2}.K^{-1}) at ΔT=15 °C and for several plate width

The Figure C.16 shows that turbulences appearance promotes an significant increase and the numerical values get closer to Kitamura's correlations. However, The variation is not equivalent to the turbulent correlation (0.19<0.33).

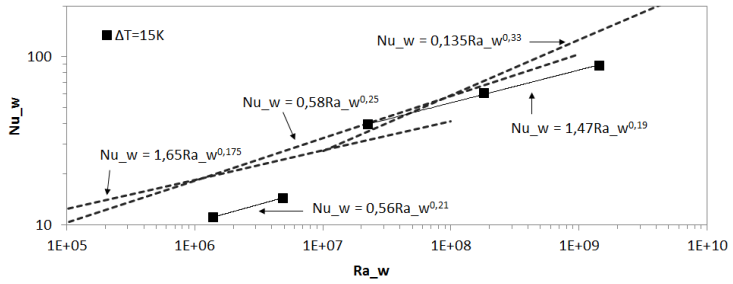

Figure C.16 – log-log curve of Nusselt number evolution with Rayleigh number for width variations

C.4.2.3 Large temperature difference

SPF process involves high temperature differences up to 850 °C such as for the laboratory testing experiments. In this section, two surface temperatures, the SPF temperature (870 °C)„ and an intermediate temperatures (450 °C), were investigated for two different width of 100 mm and 1000 mm. By this way, the model was tested for the whole range of working temperature and Rayleigh number variations. The objective of testing the effect of increasing

Case	$2'$	$6'$	$7'$	$8'$	$9'$	$2''$	$6''$	$7''$	$8''$	$9''$
ΔT (°C)	430					850				
Width (m)	0.1	0.15	0.25	0.5	1	0.1	0.15	0.25	0.5	1
$R_{ax}(\rho(T_f))$(x10^6)	3,7	13	58	470	3700	1,6	5,6	26	2100	1600
$R_{ax}(\rho(T_\infty))$(x10^6)	11	38	170	1400	11000	9.9	33	150	1200	9900

Table C.4 – Description of parameters of testing cases for large temperature variations

largely the temperature for both W=0.1 m and W=1 m is important to evaluate how the model behaves on high temperature for which no correlation law exists. The Figure C.17 summarizes the previous results for width variation at ΔT=15 °C, but also the equivalent cases (defined in the Table C.4) for ΔT=430 °C and ΔT=850 °C. Except for the two laminar cases 2 and 6, the increase in temperature seems not to be preponderant on the space distribution of convection coefficient for the width w≤0.5 m. However, the distribution of convection coefficient seems more impacted for the large plates such as if the fluid flow would be more turbulent. In addition, the increase of temperature difference produces a rise of the heat transfer. It is probably a consequence of the increase of turbulence intensity.

The Figure C.18a shows the evolution of Nusselt number with Rayleigh number for the three different ΔT. There is like a translation of Rayleigh numbers which is more important for ΔT=430 °C than ΔT=850 °C. This is partly due to a strong variation of the density which is not taken into account into the analysis. Thus, a modified Rayleigh number $R_{a_w}^*$ which is computed with the density at free stream temperature T_∞ (instead of the film temperature T_f=(T_∞+T_{plate})/2) was used to plot new evolution of Nusselt number Figure C.18b. The evolution of the three curves seems not to obey to classical power law models for the high Rayleigh with such high temperature differences.

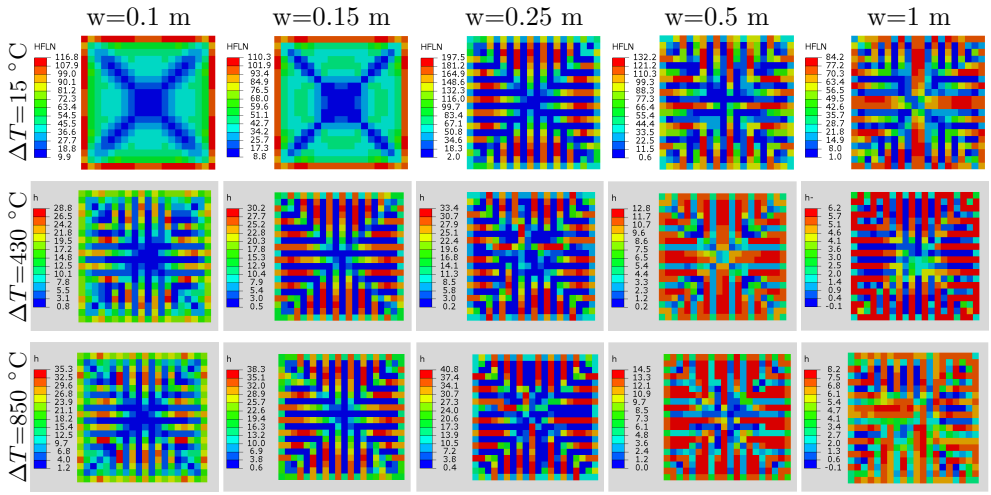

Figure C.17 – Convection coefficient field ($W.m^{-2}.K^{-1}$) for ΔT=15 °C, ΔT=430 °C and ΔT=850 °C

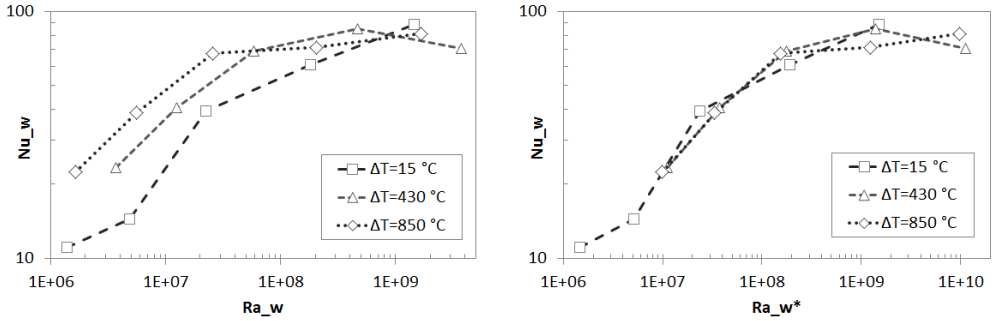

(a) **(b)**

Figure C.18 – log-log curve of Nusselt number evolution at difference temperature of 15, 430 and 850 °C as a function of (a) R_{aw} and (b) R_{aw}^{*}=$R_{aw}(\rho(T_{\infty}))$

C.4.2.4 Discussion

One objective of this section was to analyze the behavior of the model for the Kitamura's work configurations on two aspects: the appearance of turbulences and the Nusselt number correlations. The tested configurations was plate widths between 0.1-1 m with difference temperatures between 10.6-29.8 °C.

Concerning the Nusselts number correlations, the model shows a good agreement concerning the slopes (referring to exponent of power law correlation model) with a significant gap of Nusselt values for low plate width with small temperature differences (law Rayleigh). However, the Turbulence appearance for these low Rayleigh number configurations (which are supposed to be at the transition regime) does not produce any turbulence. On the contrary, when increasing the width and consequently the Rayleigh number turbulences happen and the Nusselts number slightly increase to reach Kitamura's order of magnitude. However, the slopes do not correspond. The Nusselts number correlations of numerical and experimental Kitamura's work are confronted in the Figure C.19. The CFD model seems to underestimate the laminar flows while the turbulent flows leads to similar values than Kitamura's correlation laws. On the contrary the slopes of the numerical correlation laws are in better agreement for the laminar flow than the turbulent one.

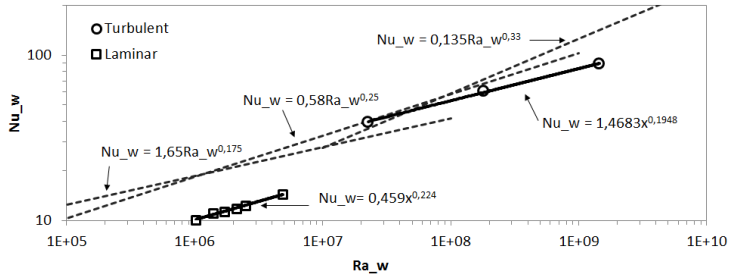

Figure C.19 – log-log curve of Nusselt number evolution with Rayleigh number

The second objective of this section was to analyze the behavior of the model when increasing the plate temperature up to SPF process temperatures. The classical Nusselt versus Rayleigh correlation power law model does not work with the simulation results for ΔT=430 °C than ΔT=850 °C. This is partly due to the classical Rayleigh number estimation that is not adapted for such property variations at these temperature differences. However, by using a modified Rayleigh number taking account of a constant density at air temperature (such as for our incompressible analysis) the different curves combine better. Concerning turbulences at high temperatures they seem to be enhanced with totally unsymmetrical distribution of convection coefficients.

C.4.3 Model sensitivity

In the next section, different parameters of the model were tested in order to analyze the sensitivity of the model to its definition. the mesh grid sensitivity and the reference temperature for density are two important issues in CFD modeling as mentioned in the Section C.2. Indeed, the mesh sensitivity is a parameter that plays an important role in turbulent layer computation. Concerning the sensitivity on the reference temperature for density, it was highlighted that for large temperature differences the density varies significantly so that it is interesting to evaluate the impact of choosing a constant density for incompressible fluid analysis.
In addition, the turbulence model k-ε was compared to k-ω. However, k-ε-based simulations were not producing any turbulences regardless to mesh refinement. That is why no sensitivity to turbulence model is presented.

C.4.3.1 Mesh grid

The mesh sensitivity was tested for two plate temperatures of T_{s1}=870 °C and T_{s2}=35°C with a fluid temperature T_∞=20 °C. Indeed, the sensitivity on mesh grid is supposed to be depending on turbulence intensity. Therefore, in addition to plate temperatures, two different sizes of plate (w=0.1 m and w=1 m) were tested in order to evaluate the mesh sensitivity for several Rayleigh numbers associated to different turbulence regimes.

The mesh variations are represented in the Figure C.20a. The whole mesh definition stays constant except the vertical mesh refinement in the described area. The meshing parameter that evolves is the first mesh grid size which then varies linearly until the upper green line. The mesh refinement is measured using the first normalized mesh sizes y^* such as defined in Equation (C.53) where δ_s is the first mesh size to surface. Height values of y^* were tested with y^*=$10^{-\gamma}$ and γ=[1:0.25:2.75]. Three different meshes y_1^* (=$10^{-1.5}$), y_2^* (=10^{-2}) and y_3^* (=$10^{-2.5}$) are respectively presented in the Figure C.20b, C.20c and C.20d which focuses on the red rectangular zone of the Figure C.20a.

$$y^* = \frac{\delta_s}{\mathrm{w}} \tag{C.53}$$

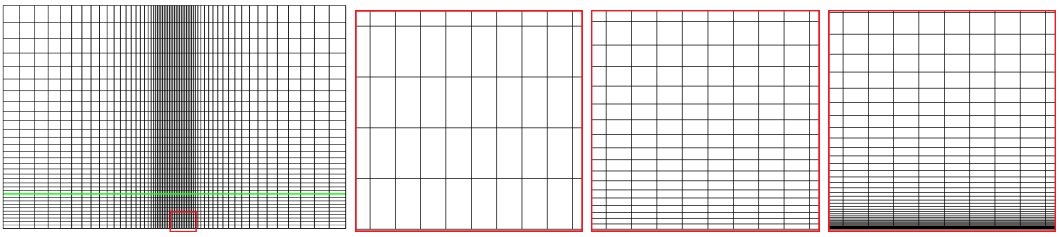

Figure C.20 – Mesh grid at (a) plate surface, (b) O$\overrightarrow{z}$ axis and near-wall resolution for (c) y_1^*, (d) y_2^* and (e) y_3^*

The Figure C.21 shows the evolution of convection coefficient field for the four cases as a function of mesh refinement y_1^*, y_2^* and y_3^*. Firstly, increasing the mesh grid refinement near the wall produces the appearance of turbulences. Indeed, the four different configurations are almost fully laminar for the law mesh refinement definition whereas when increasing mesh refinement, only the configuration with ΔT=15 °C and w=0.1 m stays laminar. This confirms that a minimum first mesh size is required to model turbulent flow. Then, for both configurations with w=0.1 m, the convection coefficients globally increase when reducing y^* value. On the contrary, for w=1 m, the convection coefficient fields have different distributions.

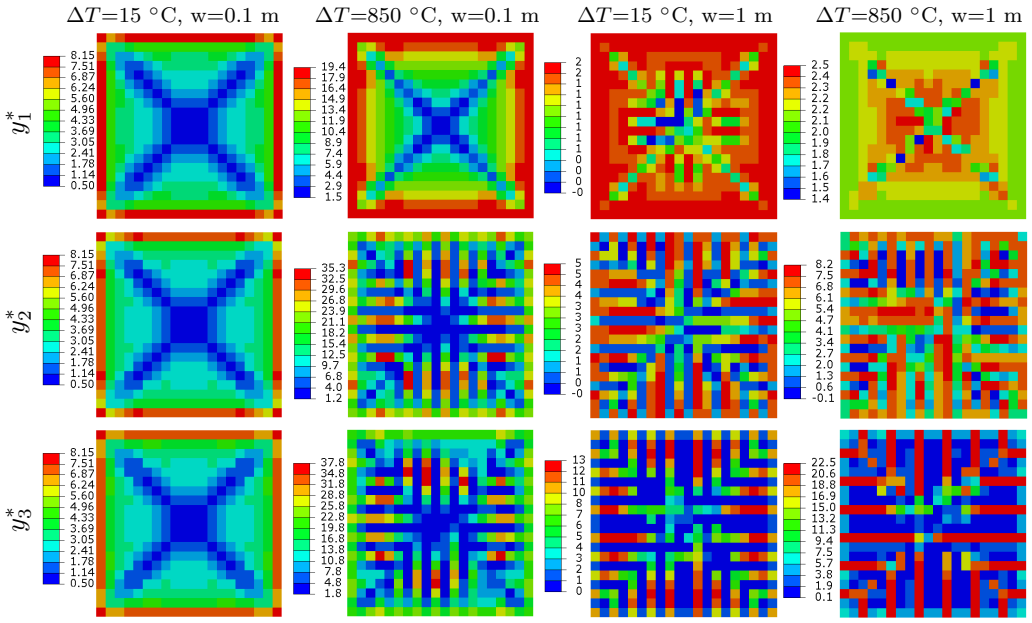

Figure C.21 – Convection coefficient field (W.m^{-2}.K^{-1}) for the y^* tested values

This is confirmed with average Nusselt number variations presented in the Figure C.22. Globally the HT seems not to converge to the same result when reducing the first node to compute temperature gradient in the normal axis for high turbulences regime. This can be due to the wall functions that are used for velocity and temperatures that may not be adapted for too fine mesh configurations in turbulent regime.

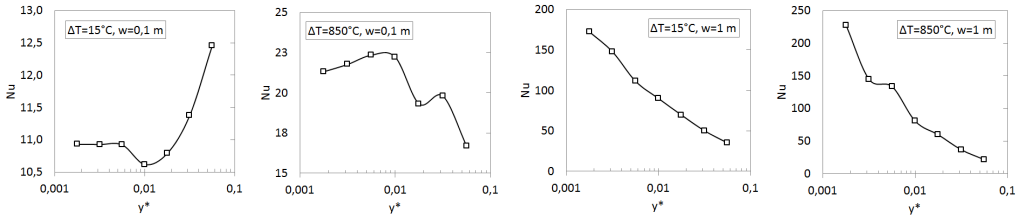

Figure C.22 – Average nusselt number sensitivity to near-wall mesh grid refinement

C.4.3.2 Reference temperature

described in the Section C, for incompressible fluid simulations, the density is considered constant. However, in our case, with large temperature gradient, the density varies significantly. Most of the air around the surface has a temperature which is the limit temperature. However the bouyancy forces generated through HT at the origin of convection are not influenced by the density variations into the model. The boussinesq hypothesis can have an impact from two different ways. It may result in wrong velocity distribution and finally convection coefficient distribution, but also modify the intensity of HT.

In order to evaluate the impact of the fixed density parameter on the HT intensity, several values of density corresponding to temperatures inside the boundary layer were tested. Five different densities were used at temperature between T_∞=20 °C and T_s=870 °C such as defined in the Figure C.23. Two levels of turbulences equivalent to two width (w=100 mm and w=1000 mm) were tested. The model was meshed with a first mesh size with y^+=11. The Table C.5 summurized the parameters for the fives tested cases.

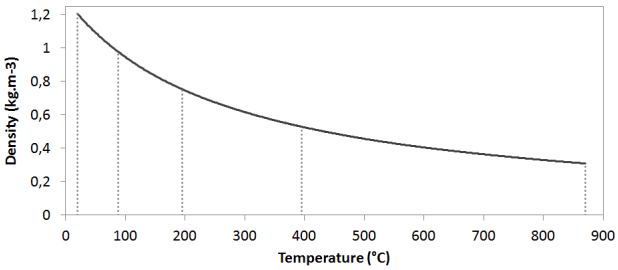

Figure C.23 – Variation of air density with temperature with corresponding selected temperature for the sensitivity analysis

T_ρ (°C)	20	88	195	395	870
ρ (kg.m^{-3})	1.20	0.98	0.75	0.53	0.3
	ρ_1		ρ_2		ρ_3

Table C.5 – Reference temperature and associated tested densities

The Figure C.24 presents the stream lines and convection coefficients for the six cases. It presents significant differences for the 0.1 m width. Indeed, the regime passes from turbulent at ρ_1 to laminar when increasing the reference temperature (decreasing density). Logically, the Average Nusselt evolution (see Figure C.25) increases when regime becomes turbulent. Concerning the 1 m width, turbulences occur at each densities. Nevertheless, the turbulences seems to get harder when increasing the density. .

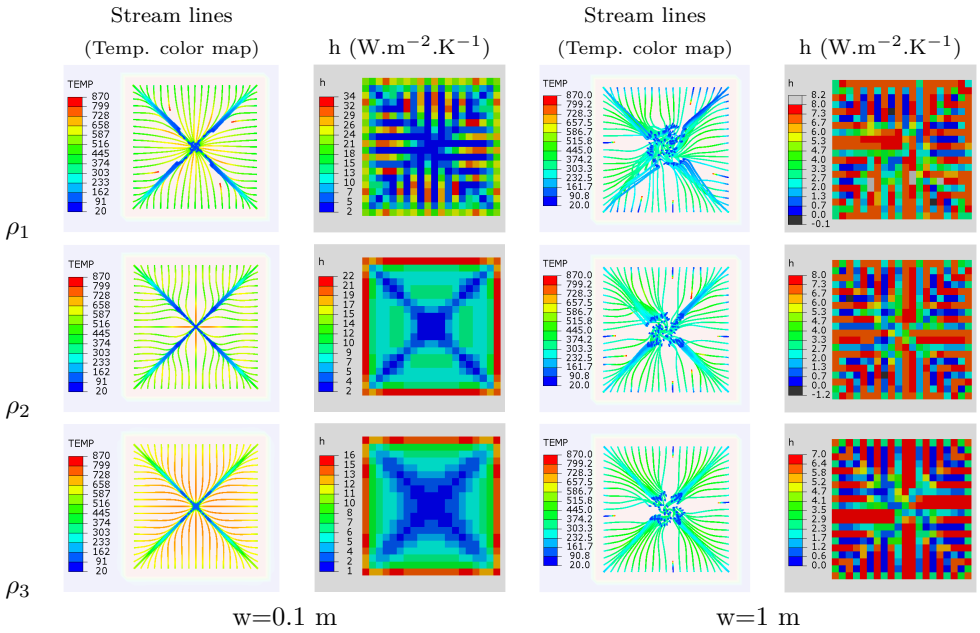

Figure C.24 – Temperature, norm of velocity, stream lines and convection coefficient fields in the near-wall parallel plane for the two width configurations at ρ_1, ρ_2 and ρ_3

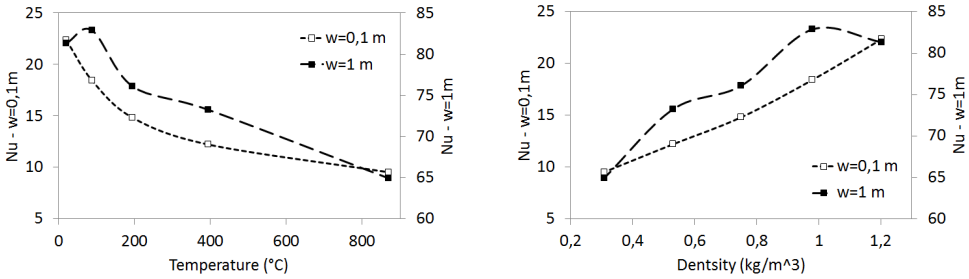

(a) **(b)**

Figure C.25 – Average Nusselt number variation as a function of (a) temperature and (b) corresponding density

C.4.3.3 Discussion

Before all the comparison of k-ω SST with k-ε was performed with a clear incapability to model turbulences for k-ε model which was not included in this sensitivity study. The model sensitivity was tested regarding to two parameters for k-ω SST model: the mesh grid, and the reference density. Both parameters were tested for different width and temperature difference to analyze the sensitivity of the model in the Kitamura's configurations and also closed to the process conditions

Concerning mesh sensitivity, the results showed that there is a strong sensitivity, and that there is a minimum refinement to obtain the appearance of turbulences. Concerning HT, the average Nusselts number seems to converge for low width whereas no convergence were found for large plates. Indeed, the average Nusselt number tended to increase as the mesh grid is refined. Additional simulations have to be performed to evaluate if this phenomenon is inherent to the FEM code, or if it can be stabilized by improving mesh grid or refinement.

Concerning the reference density, the model exhibited an important sensitivity for low Rayleigh regime (w=0.1m) where the turbulent flow passes to laminar when increasing reference temperature for density. For high Rayleigh, the impact is weaker. In terms of heat transfers, when the regime is turbulent (for large plate), the Nusselt number passes from 82.5 to 65 for an air dentity respectively taken at 20°C and 870°C which corresponds to to a decrease of 21%. For smaller plates, it passes from 22.5 to 9.5 which corresponds to 58% decrease. This influence is significant for small plate dimensions. In the process conditions, the parts are much larger than the one meter width plate that reveals a fairly low sensitivity to the density parameter.
This sensitivity is important to take account because in reality the density varies largely and the real HT induced by convection flow is impacted by this change of properties. Some studies on the effect of incompressibility hypothesis over large temperature differences natural convection on heated square cavity [227]. The authors used a dimensionless temperature parameter ε as defined Equation (C.54) to evaluate the temperature differences.

$$\epsilon = \frac{T_s - T_\infty}{2 * (T_s + T_\infty)} \tag{C.54}$$

For an equivalent ε=0.6 (identical to largest temperature differences in SPF cooling step), they showed that the effect of compressibility in numerical solution (with Direct numerical solution) is not negligible. However the difference in the solutions of Ttemperature, velocity and HT under specific profile is less than 15%. For our objectives of using of CFD simulation, such errors are acceptable.

C.4.4 Conclusion

A horizontal plate model was used to investigate the capability and the validity of a k-ω-based turbulent model to reproduced high temperature convection flows during SPF part cooling. The experimental comparison with Kitamura's work on horizontal plate natural convection has demonstrated that low Rayleygh regimes were not totally adapted. Indeed, turbulent regimes were not detected, and average Nusselt values were underestimated even if their slopes were acceptable. Therefore, the convection coefficient of laminar region obtained from CFD analysis in the SPF context needs to be carefully adjusted.

Concerning high Rayleigh turbulent regimes, the model behaves better. At low difference temperatures, the turbulences were reproduced and the HT were fairly good, even though underestimated for highest Rayleigh values. In this case, convection coefficients may be slightly increased.

Concerning the large temperature difference analysis, the result are difficult to discuss because the horizontal plate were not yet investigated experimentally. However, the various tested cases involving different Rayleigh numbers seem to vary according to a common law that is not a classical power law model. This can comes from the incompressible flow hypothesis that do not consider the effect of density variations with the temperature that might affect the fluid flow and the heat transfer. Indeed, the analysis of the selected density value reveals a significant influence on the flow and heat transfers for the small scale plates. On the contrary the large plates seems weakly affected by this parameter which is satisfactory for the simulations in the SPF process configurations. A high temperature model with compressible flow would help to evaluate the validity of our model.

Finally, a last analysis has been made on the influence of mesh refinement of the solution. One one hand, the results of the low size plates seemed to converge to a asymptotic average HT value. On the other hand, the average HT for large size plates increases as the mesh is refined. The hybrid wall-function approach used in the k-ω turbulence model is supposed to be independent of the near-wall resolution since the cell-center adjacent to the wall can be

located anywhere within the inner layer [244] which is the case for almost every tested mesh. This effect might come from the parallel-to-plate mesh size which was constant for each case. The height to width ratio of the near-wall cells might be at the origin of this phenomenon.

To conclude, the developed model gave fairly good results compared to Kitamura's experimental results, especially for high Rayleigh regimes which correspond to our process conditions. The effect of large temperature differences and the density variation, which are SPF process issues that have not been investigated in the literature, seems to be considered in this model. The computed HT are certainly not quantitative but the CFD based HT distribution and its evolution with temperature have been used as an estimation.

C.5 Natural convection outside the press: industrial geometry

C.5.1 Model

The geometry simplifications for the CFD analysis are shown in the Figure C.26. As for the Part-Frame experiment, the differences in massiveness of parts and their associated thermal responses made necessary to take account of the heterogeneous temperatures of surfaces. An a-priori simulation was used to evaluate the temperature heterogeneity of the parts during the experiment using literature hypothesis (horizontal plates based correlations) for the convection coefficients.

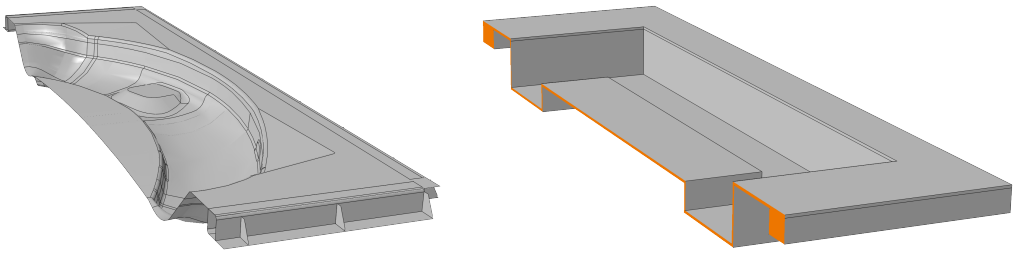

(a) **(b)**

Figure C.26 – Picture of (a) mold and extraction frame and (b) top mold for SPF forming

The Figure C.27a shows the temperature field obtained with the a-priori simulation after 250, 750 and 2000 seconds. The temperature field cartography does not significantly evolve during the ambient cooling step.

The Figure C.27b is a graph comparing mean temperature evolution of the associated surface (in red and blue). Five sets of temperatures at different times (represented by the grey lines with markers) are defined from this graph. These sets have been used in the CFD analysis to evaluate the effect of this heterogeneity during the global temperature decrease.

The geometry of the air box used for the CFD analysis is presented in the Figure C.28a. The global mesh is presented in the Figure C.28b and a zoom in the Figure C.28c. The finite element procedure and the BC are implemented in accordance with the model implemented for the horizontal plate presented in the appendix C.4.

C.5.2 Results

The Figures C.29 shows the evolution of the norm of the velocity vectors field for the five times. The plume intensity (velocity and size) reduces while the temperature of the assembly is reduced.

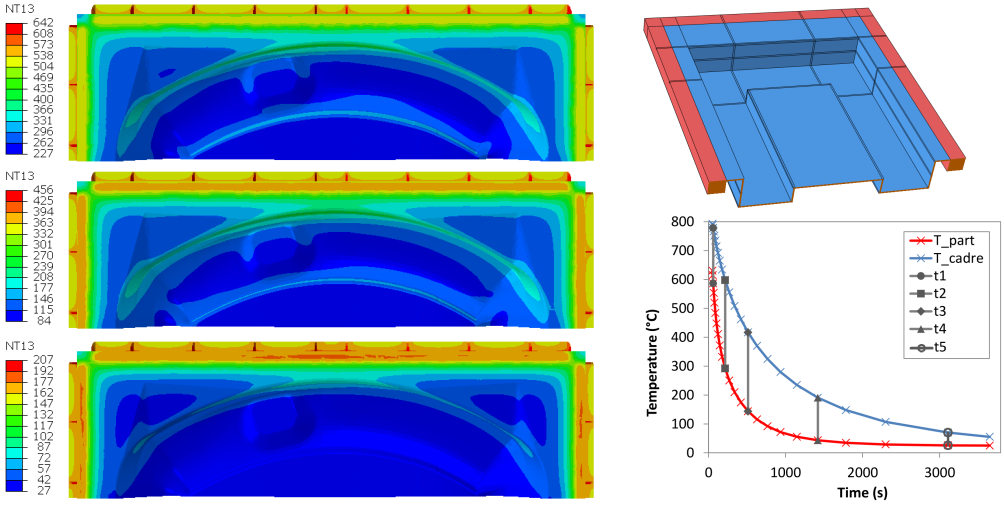

(a) **(b)**

Figure C.27 – A-priori thermal simulation results (a) temperature field at t=[250;750;2000] sec outside the press, (b) surface BC simplifications for CFD analysis and (c) homogeneous temperature variation and the five times sets

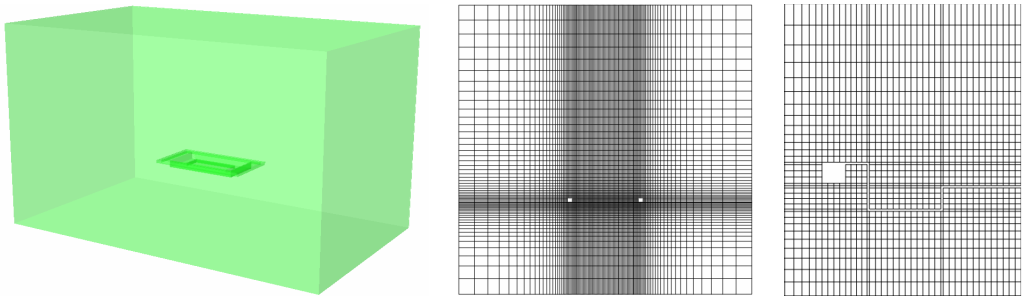

(a) **(b)** **(c)**

Figure C.28 – CFD analysis of the industrial geometry: (a) fluid environment geometry, half of a mesh representation on a cut-plane (b) scale 1, (c) zoom on the assembly

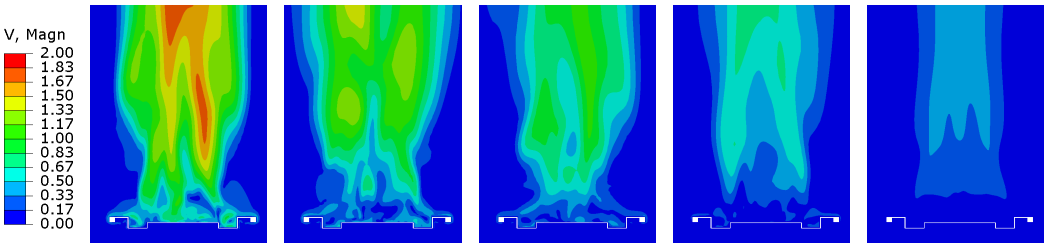

(a) t_1 **(b)** t_2 **(c)** t_3 **(d)** t_4 **(e)** t_5

Figure C.29 – Norm of the velocity vectors field for each temperature sets

The Figures C.30a and C.30b respectively represents the velocity vectors plot and the temperature field closed to the assembly surface for the five temperature sets once the steady state is reached. Both fields are not symmetrical because of turbulences. The bottom surface of part shows a clear conductive-based flow especially in the confined zones below the dome region of the part. The velocities are low and the temperatures high contrary to the top

surface where the flow is turbulent. The maximum value of the temperature scale is the averaged fluid temperature computed thanks to the Equation (C.55) where T_{fr}, T_p and T_∞ are respectively the frame, part, and ambient air temperatures at each temperature set. It is interesting to notice that the air around the frame region has its temperature increased such that to be superior to the frame temperature which generate negative convection coefficient.

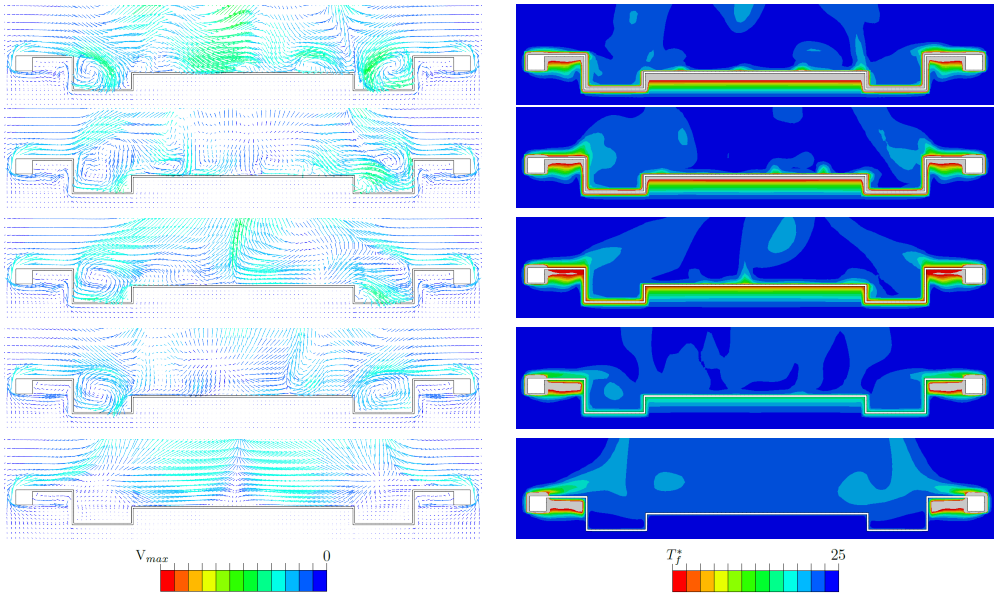

(a) **(b)**

Figure C.30 – Evolution for the five temperature sets t_1 to t_5 (from top to bottom) of (a) the velocity vectors with V_{max} the maximum velocity for each sets and (b) the temperature field with T_f^* defined in the Equation (C.55)

$$T_f^* = \frac{\frac{T_{fr}+T_p}{2} + T_\infty}{2} \tag{C.55}$$

The Figure C.31 shows the instantaneous convection coefficient computed from CFD analysis for the steady state of t_3 set simulation. The turbulences generate disturbance of the symmetrical behavior of the fluid flow, especially for the top surface which confirms what is highlighted in the Figure C.30.

For the computation of exploitable HTC values, about twenty increments over around ten seconds after reaching steady state were averaged in order to get representative value.

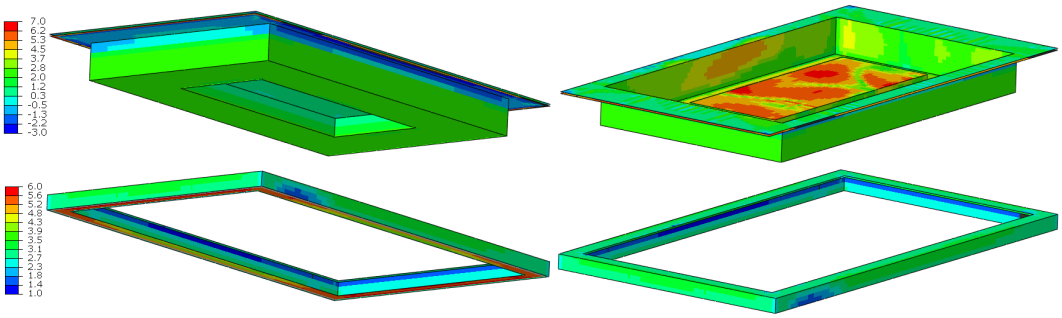

Figure C.31 – convection coefficient of the top and bottom surface of part and frame ($W.m^{-2}.K^{-1}$) at time t_3

C.5.3 Convection modeling

The results of CFD analyses of the five sets of temperatures enabled to split the surfaces of the geometry according to their associated HTC variations as represented in the Figure C.32. The colors of the horizontal surfaces of the part are turquoise and blue respectively for the top and bottom sides. The vertical surfaces of of the part are orange and green respectively for the top and bottom sides. Finally the frame surfaces are in red colors.

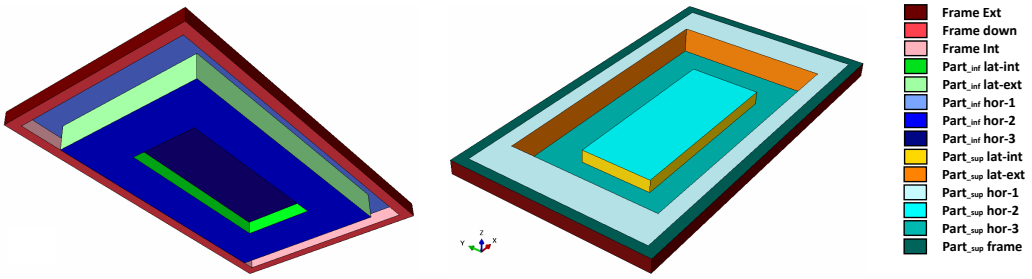

(a) **(b)**

Figure C.32 – Surface definitions of homogeneous convection behaviors

A NCC model has been defined for each surfaces using constant, linear or bi-linear functions of space for each sets of temperatures. A linear interpolation is made in between each set of temperatures for the model parameters. The evolution in space and time of the NCC distribution is rather complex to represent. An example of the comparison between simulation and model based coefficient is given at the time t_0 for the top and bottom surface of part is given in the Figure C.33.

In order to represent the temperature variation of the NCC models, the surface averaged evolutions of HTC is plotted in the Figure C.34 as a function of surfaces given in the Figure C.32. A distinction is made between surfaces perpendicular to x and y axis. Indeed, the effect of rectangular shape of the assembly promotes different fluid flows on both sides of the assembly. However, the models used to described HTC distribution for each surface are not considered homogeneous such as illustrated in the Figure C.33.

C.5.4 Discussion

The results obtained from CFD analyses seems to be in agreement with the physical phenomena. Indeed, the global decrease of the NCC corresponds to well known behavior of

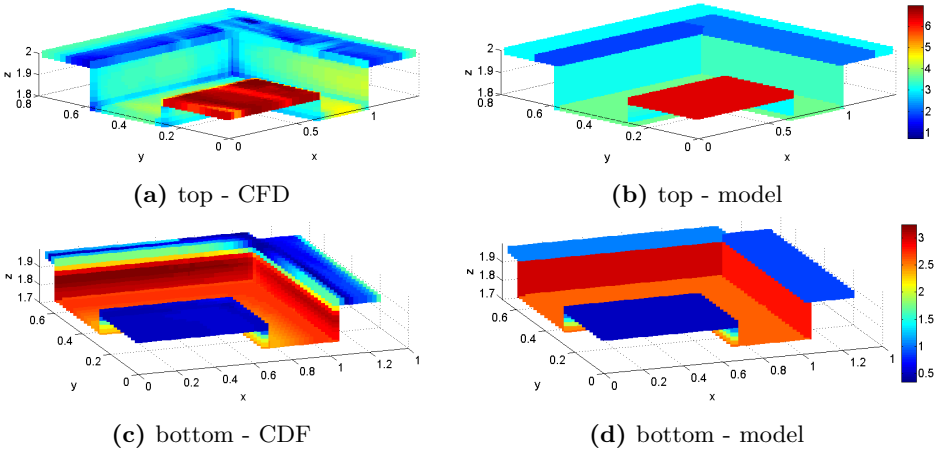

(a) top - CFD **(b)** top - model

(c) bottom - CDF **(d)** bottom - model

Figure C.33 – Comparison of convection coefficient ($W.m^{-2}.K^{-1}$) for CFD based and model for top and bottom surfaces of part at time t0

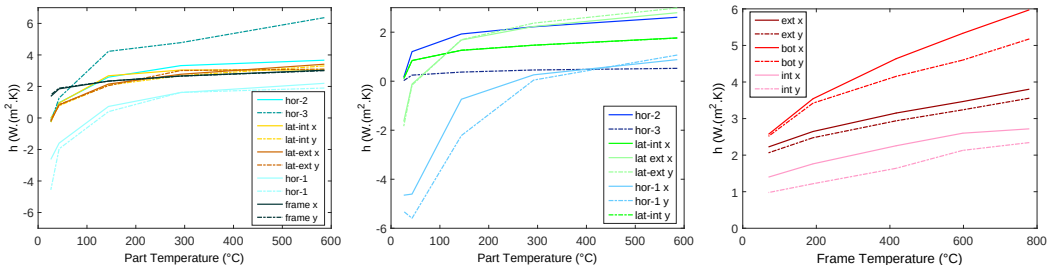

(a) part - top **(b)** part - bottom **(c)** frame

Figure C.34 – Time evolution of space-averaged NCC for split surfaces (Figure C.32)

fluid mechanics. In addition the effect of the geometry, especially the effect of warmer frame surfaces, highlights specific heat transfers that could have not been evaluated without these analyses.

However, significant HT discontinuities are obtained for the top surface between the central dome and the rest as shown in the Figure C.33a. It is probably a consequence of the implemented turbulence model. Indeed, it has been shown in the Section C.4.2 that the model tends to underestimate the laminar flow regions. Observing the Figure C.30, the dome seems much more subjected to turbulent flow than exterior or deep zones.

Therefore, the NCC models have to be be adjusted according to the regime to which it is subjected. However, it not obvious to estimate the level to which the NCC has to be adjusted.

Appendix

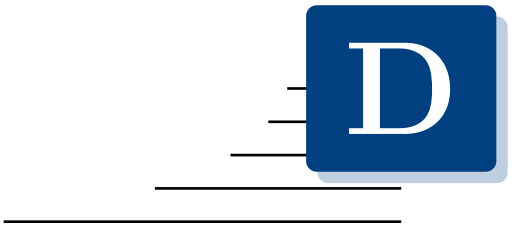

Simulation of the process

D.1 Thermo-physical properties

Three different material are used in the model, the Ti-6Al-4V titanium alloys (part), the 32Cr-Mo refractory alloy (Mold) and the Inconel 718 alloy (Frame). Each of them have thermal and physical properties that depends on the temperature. The Table D.1 gives the thermal conductivity, the heat capacity and the coefficient of thermal expansion for the Ti-64, the Inconel 718 and the 32Cr-Mo alloys.

Temp. (°C)	μ (W.m^{-1}.K^{-1})	C$_p$ (J.kg^{-1}.K^{-1})	α (10^{-6})
Ti-64			
20	6.6	530	8.67
870	18	920	13.63
Inc-718			
20	9.5	427.1	12.12
870	21.4	573.2	16.55
32Cr-Mo			
20	11.8	472.8	11.5
100			14.2
150			15.1
250			16.1
900	24.1	605.7	17.4

Table D.1 – thermo-physical properties of Ti-64, Inc-718 and 32Cr-Mo alloys

The Figure D.2 gives a comparison of the temperature dependence of the Young modulus for each material.

Temp. (°C)	Ti-64 (GPa)	Inc-718 (GPa)	32Cr-Mo (GPa)
20	106.7	200.7	153.5
100	104.2	196	151.9
200	101.2	190.1	149.9
300	97.8	184.3	147.9
400	93.4	178.4	145.9
500	87.4	172.5	143.9
600	79.2	166.7	142.5
700	68.2	159.5	139.3
800	53.9	149.1	133.6
870	41.4	139.1	123.2

Table D.2 – Temperature depedence of the Young Modulus for Ti-64, Inc-718 and 32Cr-Mo alloys

D.2 Weak radiation method: upward surface of the part

The Figure D.1 shows the simplification made for the viewing factors estimation. Indeed, the radiative HT are not symmetric inside the press because of the open cavity. In order to simplify the computation, the door through which the exterior environment radiation HT pass is modeled instead of the press' walls with an emissivity of 1.

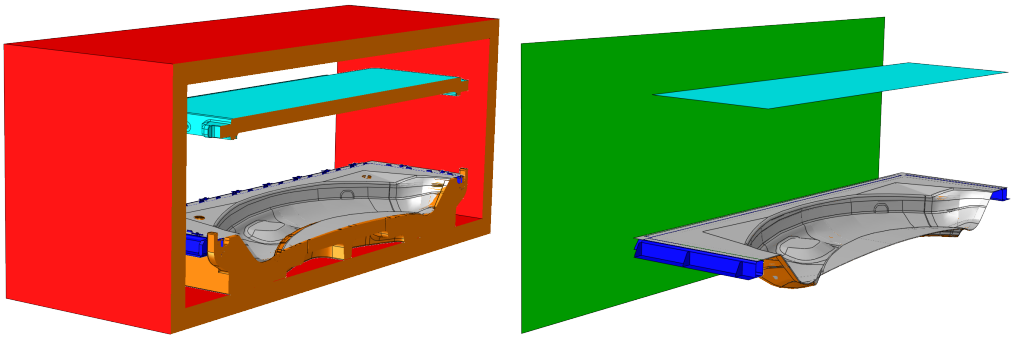

(a) **(b)**

Figure D.1 – Weak radiation coupling simplifications: (a) real geometries and (b) WRM-based simplified version

The Figures D.2a, D.2b and D.2c gives the three geometrical configurations that were used to compute the radiative flux received by the upward surface inside the press. However, the viewing factors have been computed considering the symmetry F_{tot}^{sym} or not F_{tot}. By this way, it is possible to consider the raditive HT promoted by the rest of the press without being included into the simulation.

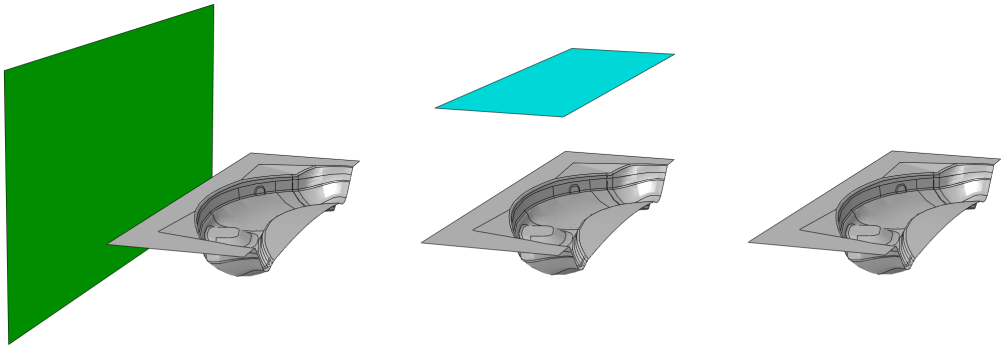

(a) $\Sigma_{Pa/E}$ **(b)** $\Sigma_{Pa/U}$ **(c)** $\Sigma_{Pa/Pa}$

Figure D.2 – Weak radiation coupling: viewing factors interface configurations

The Equations (D.1) and (D.2) give the radiative HT received from the upper die and the part itself considering the symmetry where $T_{\partial\Omega_U}$, $T_{\partial\Omega_{Pa}{}^+}$ are the averaged temperatures of the respective surfaces obtained from experimental data and a-priori computation. The Equation (D.2) gives the radiative HT through the open press' door with a slight difference due to the used emissivity of 1 and the temperature $T_{\partial\Omega_E}$ taken as the shopfloor temperature.

$$\widehat{\phi^M_{rad}}(\Sigma_{Pa/U}) = \sigma(T^4_{\partial\Omega_U} - T^4)\left[2\frac{1-\epsilon}{\epsilon} + \frac{1}{F^{M\,sym}_{tot}(\Sigma_{Pa/U})}\right]^{-1} \tag{D.1}$$

$$\widehat{\phi^M_{rad}}(\Sigma_{Pa/Pa}) = \sigma(T^4_{\partial\Omega_{Pa}} - T^4)\left[\frac{1-\epsilon}{\epsilon} + \frac{1}{F^{M\,sym}_{tot}(\Sigma_{Pa/Pa})}\right]^{-1} \tag{D.2}$$

$$\widehat{\phi^M_{rad}}(\Sigma_{Pa/E}) = \sigma(T^4_{\partial\Omega_E} - T^4)\left[\frac{1-\epsilon}{\epsilon} + \frac{1}{F^{M}_{tot}(\Sigma_{Pa/E})}\right]^{-1} \tag{D.3}$$

The Equation (D.4) enables to compute the symmetric viewing factor of the press $F_{tot}(\Sigma_{Pa/Pr})$ using a combination of the $F^{sym}_{tot}(\Sigma_{Pa/M})$, $F_{tot}(\Sigma_{Pa/E})$ and $F_{tot}(\Sigma_{Pa/Pa})$. Then, $\widehat{\phi_{rad}}(\Sigma_{Pa/Pr})$ is computed with the Equation (D.5) where the temperature of the press $T_{\partial\Omega_{Pr}}$ is taken equal to the upper die one.

$$F_{tot}(\Sigma_{Pa/Pr}) = 1 - F^{M\,sym}_{tot}(\Sigma_{Pa/M}) - \left[F^{M}_{tot}(\Sigma_{Pa/E}) - F^{M}_{tot}(\Sigma_{Pa/Pa})\right] \tag{D.4}$$

$$\widehat{\phi^M_{rad}}(\Sigma_{Pa/Pr}) = \sigma(T^4_{\partial\Omega_{Pr}} - T^4)\left[2\frac{1-\epsilon}{\epsilon} + \frac{1}{F^{M}_{tot}(\Sigma_{Pa/Pr})}\right]^{-1} \tag{D.5}$$

Finally, the radiative HT received by the upward surface is computed using the sum of each contribution as defined in the Equation (D.6).

$$\phi^{M\in\partial\Omega_{Pa}{}^+}_{rad} = \widehat{\phi^M_{rad}}(\Sigma_{Pa/Pr}) + \widehat{\phi^M_{rad}}(\Sigma_{Pa/U}) + \widehat{\phi^M_{rad}}(\Sigma_{Pa/Pa}) + \widehat{\phi^M_{rad}}(\Sigma_{Pa/E}) \tag{D.6}$$

D.3 Finite Element Method

The traditional FEM is used in our study relies on the application of Galerkine methods. These enable to transform a continuous problem of differential equations into a discrete problem. The fundamental principle of dynamics can be reduced for example to the virtual powers theorem by multiplying the Equation (D.7) by an infinitesimal velocity field $\overrightarrow{\delta v}$. The weak (also called variational) formulation of the integral form of the fundamental principle of

dynamics is obtained by integrating this equation onto a volume ω as defined in the Equation (D.8).

$$\overrightarrow{div}\left(\underline{\underline{\sigma}}\right) + \rho\overrightarrow{g} = \overrightarrow{0} \tag{D.7}$$

$$\int_{\Omega} \overrightarrow{div}\left(\underline{\underline{\tilde{\sigma}}}\right).\overrightarrow{\delta v}dV + \int_{\Omega} \overrightarrow{g}.\overrightarrow{\delta v}dV = \overrightarrow{0} \tag{D.8}$$

When using the divergence properties, the symmetry of σ tensor and applying the Ostrogradski-Gauss theorem, the Equation (D.9) can be obtained where $\underline{\underline{\tilde{\varepsilon}}}\left(\overrightarrow{\delta v}\right)$ is the strain rate tensor associated to the infinitesimal velocity field $\overrightarrow{\delta v}$.

$$\int_{\Omega} \underline{\underline{\tilde{\sigma}}} : \underline{\underline{\tilde{\varepsilon}}}\left(\overrightarrow{\delta v}\right) dV + \int_{\Omega} \overrightarrow{g}.\overrightarrow{\delta v}dV + \int_{\partial\Omega} \underline{\underline{\tilde{\sigma}}}.\overrightarrow{\delta v}dS = \overrightarrow{0} \tag{D.9}$$

Using the same method, the integral form of the variational form of the heat equation can be obtained as defined in the Equation (D.10) where δT and ϕ_{bc} are respectively an infinitesimal temperature field and the surface flux at boundaries $\partial\Omega$ of the domain Ω such like radiation, convection or conduction BC.

$$\int_{\Omega} \rho c \frac{\partial T}{\partial t}\delta T dV + \int_{\Omega} \lambda \overrightarrow{grad}(T).\overrightarrow{grad}(\delta T)dV = \int_{\partial\Omega} \phi_{bc} dS \tag{D.10}$$

The Lax-Milgram theorem demonstrates the existence and uniqueness of a function v solution of the problem in the case where $\underline{\underline{\tilde{\sigma}}}$ is symmetric.

D.3.1 Discretization

With the weak formulation, it is possible to discretize the mathematical model equations to obtain the numerical model equations. The Galerkin method, one of the many possible FEM formulations, can be used for discretization.

The discretization implies looking for an approximated solution to Equations (D.9) and (D.10) in a finite-dimensional subspace of exact solutions (Hilbert space $\mathscr{H}$) H so that $T \simeq T_{\mathscr{H}}$. This implies that the approximate solution is expressed as a linear combination of a set of basis functions φ^i that belong to the subspace such as defined in the Equations (D.11) and (D.12).

$$\overrightarrow{v} = \sum_i v^i \varphi^i(x) \ , \ \overrightarrow{\delta v} = \sum_j \delta v^j \phi^j(x) \tag{D.11}$$

$$T = \sum_i T^i \varphi^i(x) \ , \ \overrightarrow{\delta T} = \sum_j \delta T^j \phi^j(x) \tag{D.12}$$

The test functions are defined in a superior or equal dimension order Hilbert subspace. The basis functions are generally polynomials. ABAQUS® proposes first and second order polynomial functions. For Galerkine method, the Hilbert subspace is identical for both basis and test functions. The weak formulation for thermal equation gives the Equation (D.13).

$$\rho c \frac{\partial T_i}{\partial t} \sum_i \int_{\Omega} \varphi_i \varphi_j dV + \sum_i T_i \int_{\Omega} \lambda \overrightarrow{grad}(\varphi_i).\overrightarrow{grad}(\varphi_i)dV = -\sum_i \int_{\partial\Omega} \phi^i_{bc} dS \tag{D.13}$$

By this way, the integral terms being independent of the temperature field, it is possible to define a system of equations with the matrix form as defined in Equation (D.14) where $[C_p]$, $[K_\lambda]$ and $\{F\}$ are respectively the heat capacity matrix, the thermal conductivity matrix and the nodal heat flux vector.

$$[C_p]\{\dot{T}\}(t) + [K_\lambda]\{T\}(t) = \{F\}(t) \tag{D.14}$$

Using the backward Euler integration, it is possible to obtain $\{\dot{T}\}$ vector as defined in the Equation (D.15) and then obtain a matrix form of a linear equations system as defined in the Equation (D.16). The same method is applied for Mechanical equations.

$$\{\dot{T}\}(t) = \frac{\{T\}(t) - \{T\}(t - \Delta t)}{\Delta t} \tag{D.15}$$

$$[K_T]\{\Delta T\}(t) = \{F_T\}(t) \tag{D.16}$$

D.3.2 Implicit solver

In ABAQUS® Standard the temperatures are integrated using a backward-difference scheme, and the nonlinear coupled system is solved using Newton's method. ABAQUS® Standard offers an exact as well as an approximate implementation of Newton's method for fully coupled temperature-displacement analysis. An exact implementation of Newton's method involves a nonsymmetric Jacobian matrix as illustrated in the following matrix representation of the coupled equations:

$$\begin{bmatrix} K_{uu} & K_{uT} \\ K_{Tu} & K_{TT} \end{bmatrix} \begin{Bmatrix} \Delta u \\ \Delta T \end{Bmatrix} = \begin{Bmatrix} F_u \\ F_T \end{Bmatrix} \tag{D.17}$$

where and are the respective corrections to the incremental displacement and temperature, are submatrices of the fully coupled Jacobian matrix, and are the mechanical and thermal residual vectors, respectively. Solving this system of equations requires the use of the unsymmetric matrix storage and solution scheme. Furthermore, the mechanical and thermal equations must be solved simultaneously.

The Newton's method enables to solve partial differential equation system. It consists in solving the zero of a system by considering linear approximation. The matrix form of heat equation can be considered for example such as defined in Equation (D.18).

$$f : [\Delta u] \rightarrow [K]_{(t+\Delta t)}\{\Delta u\} - \{F\}_{(t+\Delta t)} \tag{D.18}$$

Supposing a small variation of displacement Δu such that f variation can be computed with linear approximation, the displacement increment that provide a zero can be estimated thanks to Equation (D.19). Even if the linear hypothesis is not true, this method enables to get closer than the zero value.
The Equation (D.20) defines the k+1^{th} approximation of the zero displacement vector computed from kth value using the first order linear hypothesis. A good approximation of the zero value of f can be easily obtained by repeating several times the computation such as represented in the Figure D.3.

$$f(\{\Delta u\}) \simeq 0 = f(\{\Delta u\}_0) + f^{'}(\{\Delta u\}_0)(\{\Delta u\} - \{\Delta u\}_0) \tag{D.19}$$

$$\{\Delta u\}_{k+1} = \{\Delta u\}_k - \frac{f(\{\Delta u\}_k)}{f'(\{\Delta u\}_k)} \tag{D.20}$$

The incremental displacement (and temperature) vector is obtained iteratively until the residual error is inferior to a critical value. The convergence rate is function of the (non-)linearity of the problem. Indeed, when the thermomechanical problem has strong non-linearities, it generates large variation of $f^{'}$ for which the Newton's method can not converge. In such cases, the time increment is automatically controlled to adapt theses evolutions of convergence rate during a simulation.

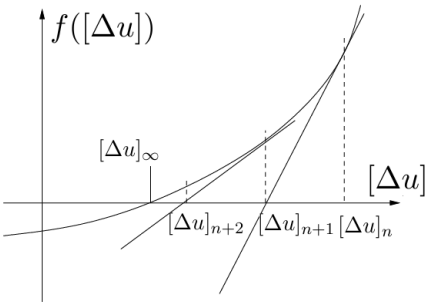

Figure D.3 – Geometric explanation of Newton's method

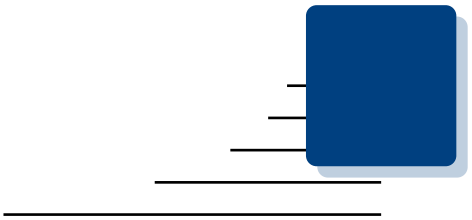

Bibliography

[1] Jean-Jacques Blandin and Michel Suery. Superplasticité. *Ref : TIP552WEB - Mise en forme des métaux et fonderie*, 7 1996.

[2] Alain Porte. Air Intake structure for aircraft engine, US patent appl.: US 06/328/258 B1, 2001-12-11. Aerospatial Matra (ex: Airbus Commercial Aircraft).

[3] H. J. Frost and M. F. Ashby. *Deformation-mechanism maps : the plasticity and creep of metals and ceramics*. Pergamon Press, 1982.

[4] Gerd Lütjering and James C. Williams. Fundamental Aspects. In *Titanium*, pages 15–52. Springer Berlin Heidelberg, Berlin, Heidelberg, 2007.

[5] Bijish Babu. Physically Based Model for Plasticity and Creep of Ti6Al4V. *Licenciate thesis*, 2008.

[6] David Woodford. *Strain rate sensitivity as a measure of ductility*, volume 62. American Society for Metals, 01 1969.

[7] E. Alabort, P. Kontis, D. Barba, K. Dragnevski, and R. C. Reed. On the mechanisms of superplasticity in Ti-6Al-4V. *Acta Materialia*, 105:449–463, feb 2016.

[8] Héloise Vigié, Thalita de Paula, Martin Surand, and Bernard Viguier. Low Temperature Strain Rate Sensitivity of Titanium Alloys. *Solid State Phenomena*, 258:570–573, dec 2016.

[9] Guang Chen, Chengzu Ren, Xuda Qin, and Jun Li. Temperature dependent work hardening in Ti–6Al–4V alloy over large temperature and strain rate ranges: Experiments and constitutive modeling. *Materials & Design*, 83:598–610, 2015.

[10] S.L. Semiatin, V. Seetharaman, and I. Weiss. Hot workability of titanium and titanium aluminide alloys - an overview. *Materials Science and Engineering: A*, 243(1-2):1–24, March 1998.

[11] E. Alabort, D. Putman, and R.C. Reed. Superplasticity in Ti–6Al–4V: Characterisation, modelling and applications. *Acta Materialia*, 95:428–442, 2015.

[12] Gerd Lütjering and James C. Williams. *Titanium*, chapter Alpha + Beta Alloys, pages 203–258. Springer Berlin Heidelberg, 2007.

[13] P Homporová, C Poletti, M Stockinger, and F Warchomicka. Dynamic phase evolution in titanium alloy Ti-6Al-4V. *12th World Conference on Titanium, Beijing, China; Zhou, L*, pages 19–42, 2011.

[14] S. L. Semiatin, S. L. Knisley, P. N. Fagin, D. R. Barker, and F. Zhang. Microstructure evolution during alpha-beta heat treatment of Ti-6Al-4V. *Metallurgical and Materials Transactions A*, 34(10):2377–2386, 2003.

[15] R. Julien, V. Velay, V. Vidal, Y. Dahan, R. Forestier, and F. Rézaï-Aria. Characterization and modeling of forged Ti-6Al-4V Titanium alloy with microstructural considerations during quenching process. *International Journal of Mechanical Sciences*, 142-143:456–467, jul 2018.

[16] A. Longuet, Y. Robert, E. Aeby-Gautier, B. Appolaire, J. F. Mariage, C. Colin, and G. Cailletaud. A multiphase mechanical model for Ti-6Al-4V: Application to the modeling of laser assisted processing. *Computational Materials Science*, 46(3):761–766, 2009.

[17] R. A. Barrett, P. E. O'Donoghue, and S. B. Leen. An improved unified viscoplastic constitutive model for strain-rate sensitivity in high temperature fatigue. *International Journal of Fatigue*, 48:192–204, 2013.

[18] V. Velay, H. Matsumoto, V. Vidal, and A. Chiba. Behavior modeling and microstructural evolutions of Ti–6Al–4V alloy under hot forming conditions. *International Journal of Mechanical Sciences*, 108-109:1–13, apr 2016.

[19] Simone Matteï. Rayonnement thermique des matériaux opaques. *Ref : TIP201WEB - Physique énergétique*, 1 2005.

[20] Nenad Milošević and Ivana Aleksić. Thermophysical properties of solid phase Ti-6Al-4V alloy over a wide temperature range. *International Journal of Materials Research*, 103(6):707–714, jun 2012.

[21] Adam Pagan, Bartomeu Massuti-ballester, and Georg Herdrich. Total and Spectral Emissivities of Demising Aerospace Materials. *Frontier of Applied Plasma Technology*, 9(1):1–6, 2016.

[22] Milton Van Dyke. *An Album of a Fluid Motion*. The Parabolic Press, 1982.

[23] K. Kitamura, A. Mitsuishi, T. Suzuki, and F. Kimura. Fluid flow and heat transfer of natural convection adjacent to upward-facing, rectangular plates of arbitrary aspect ratios. *International Journal of Heat and Mass Transfer*, 89:320–332, 2015.

[24] R. J. Goldstein, E. M. Sparrow, and D. C. Jones. Natural convection mass transfer adjacent to horizontal plates. *International Journal of Heat and Mass Transfer*, 16(5):1025–1035, 1973.

[25] H. Skok, S. Ramadhyani, and R. J. Schoenhals. Natural convection in a side-facing open cavity. *International Journal of Heat and Fluid Flow*, 12(1):36–45, 1991.

[26] E. Bilgen and H. Oztop. Natural convection heat transfer in partially open inclined square cavities. *International Journal of Heat and Mass Transfer*, 48(8):1470–1479, 2005.

[27] V. C. Mariani and L. S. Coelho. Natural convection heat transfer in partially open enclosures containing an internal local heat source. *Brazilian Journal of Chemical Engineering*, 24(3):375–388, 2007.

[28] D. Angirasa, J. G M Eggels, and F. T M Nieuwstadt. Numerical simulation of transient natural convection from an isothermal cavity open on a side. *Numerical Heat Transfer; Part A: Applications*, 28(6):755–768, 1995.

[29] J. F. Hinojosa, C. A. Estrada, R. E. Cabanillas, and G. Alvarez. Numerical Study of Transient and Steady-State Natural Convection and Surface Thermal Radiation in a Horizontal Square Open Cavity. *Numerical Heat Transfer, Part A: Applications*, 48(2):179–196, 2005.

[30] G Geers. Multiple impinging jet arrays: an experimental study on flow and heat transfer. 2004.

[31] Tadhg S. O'Donovan and Darina B. Murray. Jet impingement heat transfer - Part I: Mean and root-mean-square heat transfer and velocity distributions. *International Journal of Heat and Mass Transfer*, 50(17-18):3291–3301, 2007.

[32] L. F G Geers, M. J. Tummers, T. J. Bueninck, and K. Hanjalić. Heat transfer correlation for hexagonal and in-line arrays of impinging jets. *International Journal of Heat and Mass Transfer*, 51(21-22):5389–5399, 2008.

[33] Thermal contact resistance. *Thermopedia*, pages 479–490, 2011.

[34] Ruifeng Dou, Tianran Ge, Xunliang Liu, and Zhi Wen. Effects of contact pressure, interface temperature, and surface roughness on thermal contact conductance between stainless steel surfaces under atmosphere condition. *International Journal of Heat and Mass Transfer*, 94:156–163, 2016.

[35] J. M.P. Martins, D. M. Neto, J. L. Alves, M. C. Oliveira, and L. F. Menezes. Numerical modeling of the thermal contact in metal forming processes. *International Journal of Advanced Manufacturing Technology*, 87(5-8):1797–1811, 2016.

[36] Brian Thomas and Michel Bellet. Modeling of Stress, Distortion, and Hot Tearing. *ASM Handbook, Volume 15: Casting*, 15:449–461, 12 2008.

[37] W. Versteeg, H. K and Malalasekera. *An Introduction to Computational Fluid Dynamics*. Pearson edition, 2007.

[38] Frank P. Incropera, David P. DeWitt, Theodore L. Bergman, and Adrienne S. Lavine. *Fundamentals of Heat and Mass Transfer*, pages 560–597. Sixth edit edition, 2007.

[39] Marc Perlin, David R. Dowling, and Steven L. Ceccio. Freeman Scholar Review: Passive and Active Skin-Friction Drag Reduction in Turbulent Boundary Layers. *Journal of Fluids Engineering*, 138(9):091104, 2016.

[40] External Passive Cooling | CFD 2019 | Autodesk Knowledge Network.

[41] Anthony Barnes. Superplastic forming 40 years and still growing. *Journal of Materials Engineering and Performance*, 16:440–454, 07 2007.

[42] David Serra. Superplastic forming applications on aero engines. A review of ITP manufacturing processes. *6th EUROSPF Conference*, 09 2008.

[43] Zhi Zeng, Yan Zhang, Yi Zhou, and Quan Jin. Superplastic forming of aluminum alloy car body panels. *Materials Science Forum*, 475-479:3025–3028, 01 2005.

[44] Tomoyuki Kudo, Akira Goto, and Kazuya Saito. High strain rate blow formability of newly developed al-mg-high-mn alloy. *Materials Science Forum*, 735:271–277, 12 2012.

[45] Donato Sorgente, G. Palumbo, Leonardo Daniele Scintilla, Riccardo Brivio, Gabriele Carozzi, and Luigi Tricarico. Superplastic forming of a complex shape automotive component with optimized heated tools. *Materials Science Forum*, 838-839:494–499, 01 2016.

[46] Denis Garriga-Majo, Robin Paterson, Richard Curtis, Rajab Said, Richard Wood, and Javier Bonet. Optimisation of the superplastic forming of a dental implant for bone augmentation using finite element simulations. *Dental materials : official publication of the Academy of Dental Materials*, 20:409–18, 07 2004.

[47] Ruslan Z. Valiev, Dmitri A. Salimonenko, Nikolai K. Tsenev, Patrick B. Berbon, and Terence G. Langdon. Observations of high strain rate superplasticity in commercial aluminium alloys with ultrafine grain sizes. *Scripta Materialia*, 37(12):1945 – 1950, 1997.

[48] Patrick B. Berbon, Nikolai K. Tsenev, Ruslan Z. Valiev, Minoru Furukawa, Zenji Horita, Minoru Nemoto, and Terence G. Langdon. Superplasticity in alloys processed by equal-channel angular pressing. *Interceram*, 42, 1998.

[49] A.V Sergueeva, V.V Stolyarov, R.Z Valiev, and A.K Mukherjee. Enhanced superplasticity in a Ti-6Al-4V alloy processed by severe plastic deformation. *Scripta Materialia*, 43(9):819 – 824, 2000.

[50] Young Gun Ko, Woo Gyeom Kim, Chong Soo Lee, and Dong Hyuk Shin. Microstructural influence on low-temperature superplasticity of ultrafine-grained Ti–6Al–4V alloy. *Materials Science and Engineering: A*, 410-411:156 – 159, 2005.

[51] Hiroaki Matsumoto, Kazuki Yoshida, San-Hak Lee, Yoshiki Ono, and Akihiko Chiba. Ti–6Al–4V alloy with an ultrafine-grained microstructure exhibiting low-temperature–high-strain-rate superplasticity. *Materials Letters*, 98:209 – 212, 2013.

[52] J. St. Doltsinis, J. Luginsland, and S. Nölting. Some developments in the numerical simulation of metal forming processes. *Engineering Computations*, 4(4):266–280, apr 1987.

[53] X. D. Ding, H. M. Zbib, C. H. Hamilton, and A. E. Bayoumi. On the optimization of superplastic blow-forming processes. *Journal of Materials Engineering and Performance*, 4(4):474–485, aug 1995.

[54] Yibin Xiang and Shichun Wu. Numerical simulation of cavity damage evolution in superplastic bulging process. *Journal of Materials Processing Technology*, 116(2-3):224–230, oct 2001.

[55] Li Chuan Chung and Jung-Ho Cheng. The analysis of instability and strain concentration during superplastic deformation. *Materials Science and Engineering: A*, 308(1-2):153–160, jun 2001.

[56] Li Chuan Chung and Jung-Ho Cheng. Fracture criterion and forming pressure design for superplastic bulging. *Materials Science and Engineering: A*, 333(1-2):146–154, aug 2002.

[57] L. Carrino, G. Giuliano, and G. Napolitano. A posteriori optimisation of the forming pressure in superplastic forming processes by the finite element method. *Finite Elements in Analysis and Design*, 39(11):1083–1093, 2003.

[58] Mohammad A. Nazzal, Marwan K. Khraisheh, and Basil M. Darras. Finite Element Modeling and Optimization of Superplastic Forming Using Variable Strain Rate Approach. *Journal of Materials Engineering and Performance*, 13(6):691–699, dec 2004.

[59] Camille Robert. *Contribution to the numerical simulation of sheet metal forming proceses - application to incremental sheet forming and superplastic forming.* PhD thesis, Arts et Métiers ParisTech, 2009.

[60] M. Rollin, L. Penazzi, V. Velay, A. Dupuy, and S. Gallet. A new numerical strategy for SPF pressure profile computing based on statistical strain rate controlling. *International Journal of Mechanical Sciences*, 141(April):479–490, 2018.

[61] G Bernhart, F Nazaret, A Martinier, C Gao, T Cutard, and P Lours. Design of SPF dies based on advanced material behaviour models. *Materials Science Forum*, 448:123–130, 2004.

[62] V. Velay, T. Cutard, and N. Guegan. Thermal behaviour modelling of superplastic forming tools. *Materialwissenschaft und Werkstofftechnik*, 43(9):799–804, 2012.

[63] Appasaheb Adappa Keste, Shravan Haribhau Gawande, and Chandrani Sarkar. Design optimization of precision casting for residual stress reduction. *Journal of Computational Design and Engineering*, 3(2):140–150, 2016.

[64] J.D. Pollard, S. Rahimi, A. Watford, M. Jackson, and B.P. Wynne. The Determination of Residual Stress in Extruded Ti-6Al-4V by Contour Method and Finite Element Analysis. In *Proceedings of the 13th World Conference on Titanium*, pages 305–310. may 2016.

[65] F Pascon, G Bles, C Bouffioux, S Casotto, S Bruschi, and A M Habraken. Prediction of distortion during cooling of steel rolled rings using thermal-mechanical-metallurgical finite element model. *GRIPS' Sparkling World of Steel*, 01 2004.

[66] Robert Pietzsch, Miroslaw Brzoza, Yalçin Kaymak, Eckehard Specht, and Albrecht Bertram. Simulation of the Distortion of Long Steel Profiles During Cooling. *Journal of Applied Mechanics*, 74(3):427, 2007.

[67] Xiaodong Wang, Fei Li, Quan Yang, and Anrui He. FEM analysis for residual stress prediction in hot rolled steel strip during the run-out table cooling. *Applied Mathematical Modelling*, 37(1-2):586–609, 2013.

[68] K. C. Ganesh, M. Vasudevan, K. R. Balasubramanian, N. Chandrasekhar, S. Mahadevan, P. Vasantharaja, and T. Jayakumar. Modeling, prediction and validation of thermal cycles, residual stresses and distortion in type 316 LN stainless steel WELD joint made by TIG welding process. *Procedia Engineering*, 86:767–774, 2014.

[69] Yannick Robert, Jean-François Mariage, Georges Cailletaud, and Elisabeth Aeby-Gautier. Modélisation numérique du procédé de soudage par laser YAG impulsionnel d'un alliage de titane (TA6V). In *Materiaux 2006*, Dijon, France, 2006.

[70] Yannick Robert. *Simulation numérique du soudage du TA6V par laser YAG impulsionnel : caractérisation expérimentale et modélisation des aspects thermomécanique associées à ce procédés.* PhD thesis, Mines de Paris ParisTech, 2007.

[71] Abdul Arif, Abhishek, and K. N. Pandey. Thermo-mechanical Modeling for Residual Stresses of Friction Stir Welding of Dissimilar Alloys. *International Journal of Engineering Science and Technology*, 5(06):1195–1204, 2013.

[72] Marcel Bachmann, Jan Carstensen, Luciano Bergmann, Jorge F. dos Santos, Chuan Song Wu, and Michael Rethmeier. Numerical simulation of thermally induced residual stresses in friction stir welding of aluminum alloy 2024-T3 at different welding speeds. *International Journal of Advanced Manufacturing Technology*, 91(1-4):1443–1452, 2017.

[73] X. K. Zhu and Y. J. Chao. Numerical simulation of transient temperature and residual stresses in friction stir welding of 304L stainless steel. *Journal of Materials Processing Technology*, 146(2):263–272, 2004.

[74] Hariharasudhan Palaniswamy, Pamela Mondalek, Maciek Wronski, and Subir Roy. Efficient simulation of press hardening process through integrated structural and CFD analyses. In *AIP Conference*, volume 966, pages 966–970, 2014.

[75] G. J. Chen, Y. Zhang, W. Shen, L. J. Qin, N. Deng, and X. C. Yao. Numerical Simulation on Cooling System of Hot Stamping Mold In B-Pillar. In *Advanced High Strength Steel and Press Hardening*, pages 353–358. WORLD SCIENTIFIC, may 2016.

[76] A Shapiro. Finite element modeling of hot stamping. *Steel Research International*, 80(9):658–664, 2009.

[77] A. J. Wagoner Johnson, C. W. Bull, K. S. Kumar, and C. L. Briant. The influence of microstructure and strain rate on the compressive deformation behavior of Ti-6Al-4V. *Metallurgical and Materials Transactions A*, 34(2):295–306, feb 2003.

[78] P. S. Follansbee and G. T. Gray. An analysis of the low temperature, low and high strain-rate deformation of Ti6Al4V. *Metallurgical Transactions A*, 20(5):863–874, may 1989.

[79] C Pélissié, L Guétaz, X Baillin, F Moret, D Guichard, and J.M. De Monicault. Deformation modes of ti-6al-4v at cryogenic temperatures. *Revue de Metallurgie. Cahiers D'Informations Techniques*, 93:1510–1519, 12 1996.

[80] S. Di Iorio, L. Briottet, E. F. Rauch, and D. Guichard. Damage mechanisms and rupture criterion of PM Ti-6Al-4V at 20K. *Materials Science Forum*, pages 287–290, 2005.

[81] M. Zhang, J. Zhang, and D.L. McDowell. Microstructure-based crystal plasticity modeling of cyclic deformation of Ti-6Al-4V. *International Journal of Plasticity*, 23(8):1328–1348, aug 2007.

[82] E Orowan. Problems of plastic gliding. *Proceedings of the Physical Society*, 52(1):8–22, jan 1940.

[83] U. F. Kocks, Ali S. Argon, and M. F. Ashby. *Thermodynamics and kinetics of slip*. Pergamon Press, 1975.

[84] H. Mecking and U. F. Kocks. Kinetics of flow and strain-hardening. *Acta Metallurgica*, 29(11):1865–1875, 1981.

[85] F R N Nabarro. Fifty-year study of the Peierls-Nabarro stress. *Materials Science and Engineering*, pages 234–236, 1997.

[86] A. K. Mukherjee, J. E. Bird, and J. E. Dorn. Experimental Correlations for High-Temperature Creep. *Transactions of the American Society for Metals*, 62:155–179, 1969.

[87] M.F Ashby. A first report on deformation-mechanism maps. *Acta Metallurgica*, 20(7):887–897, jul 1972.

[88] S.L. Robinson and O.D. Sherby. Mechanical behavior of polycrystalline tungsten at elevated temperature. *Acta Metallurgica*, 17(2):109–125, feb 1969.

[89] J Harper and J.E Dorn. Viscous creep of aluminum near its melting temperature. *Acta Metallurgica*, 5(11):654–665, nov 1957.

[90] G.B. Viswanathan, S. Karthikeyan, R.W. Hayes, and M.J. Mills. Creep behaviour of Ti-6Al-2Sn-4Zr-2Mo: II. Mechanisms of deformation. *Acta Materialia*, 50(20):4965–4980, dec 2002.

[91] Badea, Lavina, Surand, Martin, Ruau, Jacques, Viguier, and Bernard. Creep behavior of Ti-6Al-4V from 450°C TO 600°C. *International peer-reviewed journal*, 76, 01 2014.

[92] F. R. N. Nabarro. Creep at very low rates. *Metallurgical and Materials Transactions A*, 33(2):213–218, feb 2002.

[93] Conyers Herring. Diffusional Viscosity of a Polycrystalline Solid. *Journal of Applied Physics*, 21(5):437–445, may 1950.

[94] Terence G. Langdon. An Analysis of Flow Mechanisms in High Temperature Creep and Superplasticity. *Material Transactions*, 46(9):1951–1956, 2005.

[95] T.G. Langdon. A unified approach to grain boundary sliding in creep and superplasticity. *Acta Metallurgica et Materialia*, 42(7):2437–2443, jul 1994.

[96] J.E. Bird, A.K. Mukherjee, J.E. Dorn, D.G. Brandon, and A. Rosen. Quantitative Relation between Properties and Microstructure. *Israel Universities Press*, pages 255—-342, 1969.

[97] A. K. Ghosh and C. H. Hamilton. Mechanical behavior and hardening characteristics of a superplastic Ti-6AI-4V alloy. *Metallurgical Transactions A*, 10(6):699–706, jun 1979.

[98] Hiroaki Matsumoto, Takuro Nishihara, Vincent Velay, and Vanessa Vidal. Superplastic Property of the Ti-6Al-4V Alloy with Ultrafine-Grained Heterogeneous Microstructure. *Advanced Engineering Materials*, 20(1):1700317, jan 2018.

[99] D. Lee and W.A. Backofen. Superplasticity in some titanium and zirconium alloys. *Trans. Met. Soc. AIME*, 239:1034–1040, 1967.

[100] Taku Sakai, Andrey Belyakov, Rustam Kaibyshev, Hiromi Miura, and John J. Jonas. Dynamic and post-dynamic recrystallization under hot, cold and severe plastic deformation conditions. *Progress in Materials Science*, 60:130–207, mar 2014.

[101] T. Furuhara, B. Poorganji, H. Abe, and T. Maki. Dynamic recovery and recrystallization in titanium alloys by hot deformation. *JOM*, 59(1):64–67, jan 2007.

[102] F. H. Norton. *The creep of steel at high temperatures.* McGraw-Hill book company, 1929.

[103] R.S. Rosen, S.P. Paddon, and M.E. Kassner. The Variation of the Yield Stress of Ti Alloys with Strain Rate at High Temperatures. *Journal of Materials Engineering and Performance*, 8(3):361–367, jun 1999.

[104] A. Majorell, S. Srivatsa, and R. C. Picu. Mechanical behavior of Ti-6Al-4V at high and moderate temperatures-Part I: Experimental results. *Materials Science and Engineering A*, 326(2):297–305, 2002.

[105] Hans Conrad. Effect of interstitial solutes on the strength and ductility of titanium. *Progress in Materials Science*, 26(2-4):123–403, jan 1981.

[106] Jiao Luo, Miaoquan Li, Weixin Yu, and Hong Li. The variation of strain rate sensitivity exponent and strain hardening exponent in isothermal compression of Ti-6Al-4V alloy. *Materials and Design*, 31(2):741–748, 2010.

[107] J. Luo and M.Q. Li. Strain rate sensitivity and strain hardening exponent during the isothermal compression of Ti60 alloy. *Materials Science and Engineering: A*, 538:156–163, mar 2012.

[108] Yang Nan, Yongquan Ning, Houquan Liang, Hongzhen Guo, Zekun Yao, and M.W. Fu. Work-hardening effect and strain-rate sensitivity behavior during hot deformation of Ti–5Al–5Mo–5V–1Cr–1Fe alloy. *Materials & Design*, 82:84–90, 2015.

[109] Y. Estrin and H. Mecking. A unified phenomenological description of work hardening and creep based on one-parameter models. *Acta Metallurgica*, 32(1):57–70, 1984.

[110] E. O. Hall. *Yield Point Phenomena in Metals and Alloys*. Springer US, Boston, MA, 1970.

[111] Y. Bergström and H. Hallén. An improved dislocation model for the stress-strain behavior of polycrystalline α-Fe. *Materials Science and Engineering*, 55(1):49–61, aug 1982.

[112] H. Mecking and U.F. Kocks. *Strength of Metals and Alloys*, chapter A Mechanism for Static and Dynamic Recovery, pages 345–350. Elsevier, 1979.

[113] P. G. Shewmon. *Transformation in Metals*. Mc Graw-Hill book Company, 1969.

[114] A.K. Ghosh and R. Raj. Grain size distribution effects in superplasticity. *Acta Metallurgica*, 29(4):607–616, apr 1981.

[115] M Zhou and F P E Dunne. Mechanisms-based constitutive equations for the superplastic behaviour of a titanium alloy. *The Journal of Strain Analysis for Engineering Design*, 31(3):187–196, may 1996.

[116] F.P.E. Dunne. Inhomogeneity of microstructure in superplasticity and its effect on ductility. *International Journal of Plasticity*, 14(4-5):413–433, jan 1998.

[117] M.Kh. Rabinovich and V.G. Trifonov. Dynamic grain growth during superplastic deformation. *Acta Materialia*, 44(5):2073–2078, may 1996.

[118] F. Li, D.H. Bae, and A.K. Ghosh. Grain elongation and anisotropic grain growth during superplastic deformation in an Al-Mg-Mn-CU alloy. *Acta Materialia*, 45(9):3887–3895, sep 1997.

[119] R. Panicker, A.H. Chokshi, R.K. Mishra, R. Verma, and P.E. Krajewski. Microstructural evolution and grain boundary sliding in a superplastic magnesium AZ31 alloy. *Acta Materialia*, 57(13):3683–3693, aug 2009.

[120] T. G. Langdon. Fracture processes in superplastic flow. *Metal Science*, 16(4):175–183, apr 1982.

[121] Atul H. Chokshi and Terence G. Langdon. A model for diffusional cavity growth in superplasticity. *Acta Metallurgica*, 35(5):1089–1101, may 1987.

[122] A H. Chokshit and Amiya Mukherjee. An analysis of cavity nucleation in superplasticity. *Acta Metallurgica*, 37:3007–3017, 11 1989.

[123] G. Gurewitz, N. Ridley, and A.K. Mukherjee. Elevated temperature cavitation in creep and superplasticity of Ti–6Al–4V alloy. In *Proceedings of ICF International Symposium on Fracture Mechanics*. Science Press, 1984.

[124] T. Ahmed and H.J. Rack. Phase transformations during cooling in α+β titanium alloys. *Materials Science and Engineering: A*, 243(1):206–211, 1998.

[125] R. Castro and L. Seraphin. Contribution à l'étude métallographique et structurale de l'alliage de titane TA6V. *mémoires scientifiques revue de métallurgie*, 1966.

[126] C.M. Sellars and W.J. McTegart. On the mechanism of hot deformation. *Acta Metallurgica*, 14(9):1136–1138, sep 1966.

[127] F. Povolo. On the analysis of stress relaxation data. *Journal of Nuclear Materials*, 96(1-2):178–186, 1981.

[128] T. W. Kim and F. P.E. Dünne. Determination of superplastic constitutive equations and strain rate sensitivities for aerospace alloys. *Proceedings of the Institution of Mechanical Engineers, Part G: Journal of Aerospace Engineering*, 211(6):367–380, 1997.

[129] Ji Hyun Sung, Ji Hoon Kim, and R. H. Wagoner. A plastic constitutive equation incorporating strain, strain-rate, and temperature. *International Journal of Plasticity*, 26(12):1746–1771, 2010.

[130] J.H. Hollomon. Tensile deformation. *Trans. AIME*, 162:268–290, 1945.

[131] E. Voce. Title of the Article. *Journal of the Institute of Metals*, 74:537–562, 1948.

[132] D. Nouailhas. Unified modelling of cyclic viscoplasticity: Application to austenitic stainless steels. *International Journal of Plasticity*, 5(5):501–520, 1989.

[133] H.W. Swift. Plastic instability under plane stress. *Journal of the Mechanics and Physics of Solids*, 1(1):1–18, oct 1952.

[134] A. Hensel and T. Spittel. Kraft-und hitsbedarf bildsamer Formgebungsverfahren. *VEB Deutscher Verlag filr Grundstoffindustrie*, 1978.

[135] J.L. Chaboche. Constitutive equations for cyclic plasticty and cyclic viscoplasticity. *International Journal of Plasticity*, 5:247–302, 1989.

[136] Jean Marc Pipard, Tudor Balan, Farid Abed-Meraim, and Xavier Lemoine. Elasto-visco-plastic modeling of mild steels for sheet forming applications over a large range of strain rates. *International Journal of Solids and Structures*, 50(16-17):2691–2700, 2013.

[137] G.R. Jonhson and W.H. Cook. A constitutive model and data for metals subjected to large strains, high strain rates and high temperatures. In *Proceedings of the 7th International Symposium on Ballistics*, 1983.

[138] Woei-Shyan Lee and Chi-Feng Lin. High-temperature deformation behaviour of Ti6Al4V alloy evaluated by high strain-rate compression tests. *Journal of Materials Processing Technology*, 75(1-3):127–136, mar 1998.

[139] G Germain, Y Ayed, T Braham-Bouchnak, and A Morel. Identification de lois de comportement représentatives des conditions d'usinage pour des alliages de titane à différentes teneurs alpha/beta. In *21ème Congres Français de Mécanique*, Bordeaux, 2013.

[140] Yancheng Zhang, J.C. Outeiro, and Tarek Mabrouki. On the Selection of Johnson-cook Constitutive Model Parameters for Ti-6Al-4V Using Three Types of Numerical Models of Orthogonal Cutting. *Procedia CIRP*, 31:112–117, jan 2015.

[141] Mahmoud Harzallah, Thomas Pottier, Johanna Senatore, Michel Mousseigne, Guénaël Germain, and Yann Landon. Numerical and experimental investigations of Ti-6Al-4V chip generation and thermo-mechanical couplings in orthogonal cutting. *International Journal of Mechanical Sciences*, 134:189–202, dec 2017.

[142] Hubert W. Meyer and David S. Kleponis. Modeling the high strain rate behavior of titanium undergoing ballistic impact and penetration. *International Journal of Impact Engineering*, 26(1-10):509–521, dec 2001.

[143] Seyed Vahid Sajadifar and Guney Guven Yapici. High Temperature Flow Response Modeling of Ultra-Fine Grained Titanium. *Metals - Open Access Metallurgy Journal*, 2015:1315–1327, 07 2015.

[144] Zhi-jun TAO, Xiao-guang FAN, He YANG, Jun MA, and Heng LI. A modified Johnson–Cook model for NC warm bending of large diameter thin-walled Ti–6Al–4V tube in wide ranges of strain rates and temperatures. *Transactions of Nonferrous Metals Society of China*, 28(2):298–308, feb 2018.

[145] J. L. Chaboche. A review of some plasticity and viscoplasticity constitutive theories. *International Journal of Plasticity*, 24(10):1642–1693, 2008.

[146] J. Lin and Jianbo Yang. GA-based multiple objective optimisation for determining viscoplastic constitutive equations for superplastic alloys. *International Journal of Plasticity*, 15(11):1181–1196, January 1999.

[147] A. Miller. An Inelastic Constitutive Model for Monotonic, Cyclic, and Creep Deformation: Part I—Equations Development and Analytical Procedures. *Journal of Engineering Materials and Technology*, 98(2):97, apr 1976.

[148] Lallit Anand. Constitutive equations for hot-working of metals. *International Journal of Plasticity*, 1(3):213–231, 1985.

[149] P Delobelle. Sur les lois de comportement viscoplastique à variables internes. *Rev. Phys. Appl.*, 23:1–61, 1988.

[150] S. Msolli, Olivier Dalverny, Joël Alexis, and Moussa Karama. Effects of the Unified Viscoplastic Formulation and Temperature Terms on the Thermomechanical Behavior of Soldering Materials. *Key Engineering Materials*, 498:219–226, 2012.

[151] P. S. Follansbee and U. F. Kocks. A constitutive description of the deformation of copper based on the use of the mechanical treshold stress as an internal state variable. *Acta Metall*, 36(1):81–93, 1988.

[152] Nemat-Nasser & al. Dynamic response of conventional and hot isostatically pressed Ti–6Al–4V alloys: experiments and modeling. *Mechanics of Materials*, 33(8):425–439, August 2001.

[153] R.C. Picu and A. Majorell. Mechanical behavior of Ti–6Al–4V at high and moderate temperatures—Part II: constitutive modeling. *Materials Science and Engineering: A*, 326(2):306–316, mar 2002.

[154] Jiao Luo, Miaoquan Li, Xiaoli Li, and Yanpei Shi. Constitutive model for high temperature deformation of titanium alloys using internal state variables. *Mechanics of Materials*, 42(2):157–165, February 2010.

[155] Bijish Babu and Lars-Erik Lindgren. Dislocation density based model for plastic deformation and globularization of Ti-6Al-4V. *International Journal of Plasticity*, 50:94–108, nov 2013.

[156] Sabine Denis, Pierre Archambault, Elisabeth Aeby-Gautier, André Simon, and Gérard Beck. Prediction of Residual Stress and Distortion of Ferrous and Non-Ferrous Metals: Current Status and Future Developments. *Journal of Materials Engineering and Performance*, 11:92–102, 02 2002.

[157] S. A. Meguid and L. E. Malvern. An experimental investigation into load relaxation in aluminium (HE30TB) and mild steel (EN1A). *International Journal of Mechanical Sciences*, 24(5):299–312, 1982.

[158] J. L. Chaboche and G. Rousselier. On the Plastic and Viscoplastic Constitutive Equations—Part II: Application of Internal Variable Concepts to the 316 Stainless Steel. *Journal of Pressure Vessel Technology*, 105(2):159, 1983.

[159] M.K. Khraisheh, H.M. Zbib, C.H. Hamilton, and A.E. Bayoumi. Constitutive modeling of superplastic deformation. Part I: Theory and experiments. *International Journal of Plasticity*, 13(1-2):143–164, 1997.

[160] M Surand. *Etude du comportement viscoplastique en traction et en fluage de l'alliage TA6V de 20 a 600 °C*. PhD thesis.

[161] P Germain and P Suquet. Continuum Thermodynamics. *Journal of Applied Mechannics*, 50, 1983.

[162] David L. McDowell. A nonlinear kinematic hardening theory for cyclic thermoplasticity and thermoviscoplasticity. *International Journal of Plasticity*, 8(6):695–728, 1992.

[163] Max Planck. *The theory of heat radiation*. Philadelphia, P. Blakiston's Son & Co.

[164] Adrian Bejan and Allan D. Kraus. *Heat transfer handbook*. J. Wiley, 2003.

[165] D. Rittel and Z. G. Wang. Thermo-mechanical aspects of adiabatic shear failure of AM50 and Ti6Al4V alloys. *Mechanics of Materials*, 40(8):629–635, 2008.

[166] L. González-Fernández, E. Risueño, R. B. Pérez-Sáez, and M. J. Tello. Infrared normal spectral emissivity of Ti-6Al-4V alloy in the 500-1150 K temperature range. *Journal of Alloys and Compounds*, 541:144–149, 2012.

[167] Petter Hagqvist, Fredrik Sikström, and Anna Karin Christiansson. Emissivity estimation for high temperature radiation pyrometry on Ti-6Al-4V. *Measurement: Journal of the International Measurement Confederation*, 46(2):871–880, 2013.

[168] Daniel Soler, Patxi Aristimuño, Ainhara Garay, and Pedro J. Arrazola. Uncertainty of temperature measurements in dry orthogonal cutting of titanium alloys. *Infrared Physics and Technology*, 71:208–216, 2015.

[169] Longfei Li, Kun Yu, Kaihua Zhang, and Yufang Liu. Study of Ti-6Al-4V alloy spectral emissivity characteristics during thermal oxidation process. *International Journal of Heat and Mass Transfer*, 101:699–706, 2016.

[170] J. C. Heigel, E. Whitenton, B. Lane, M. A. Donmez, V. Madhavan, and W. Moscoso-Kingsley. Infrared measurement of the temperature at the tool–chip interface while machining Ti–6Al–4V. *Journal of Materials Processing Technology*, 243:123–130, 2017.

[171] J. M.P. Martins, J. L. Alves, D. M. Neto, M. C. Oliveira, and L. F. Menezes. Numerical analysis of different heating systems for warm sheet metal forming. *International Journal of Advanced Manufacturing Technology*, 83(5-8):897–909, 2016.

[172] R Muvunzi and S Matope. Review. (July):75–84, 2017.

[173] Zhiqiang Zhang, Peng Gao, Chaoyang Liu, and Xiangji Li. Experimental and simulation study for heat transfer coefficient in hot stamping of high-strength boron steel. *Metallurgical and Materials Transactions B*, 46, 09 2015.

[174] E. Hachem, G. Jannoun, J. Veysset, M. Henri, R. Pierrot, I. Poitrault, E. Massoni, and T. Coupez. Modeling of heat transfer and turbulent flows inside industrial furnaces. *Simulation Modelling Practice and Theory*, 30:35–53, 2013.

[175] Jimmy Nils Erik Kluge, T. S. Lundström, L. G. Westerberg, and T. Nyman. Modelling heat transfer inside an autoclave: Effect of radiation. *Journal of Reinforced Plastics and Composites*, 35(14):1126–1142, 2016.

[176] Carlo Cintolesi, Håkan Nilsson, Andrea Petronio, and Vincenzo Armenio. Numerical simulation of conjugate heat transfer and surface radiative heat transfer using the p1 thermal radiation model: Parametric study in benchmark cases. *International Journal of Heat and Mass Transfer*, 107:956–971, 04 2017.

[177] John Howell, R. Siegel, and M. Pinar Mengüç. *Thermal Radiation Heat Transfer*. 09 2010.

[178] *Abaqus Theory Manual, Version 6.12*, chapter 2.11.4 Cavity Radiation. Simulia, 2012.

[179] J. R. Lloyd and W. R. Moran. Natural Convection Adjacent to Horizontal Surface of Various Planforms. *Journal of Heat Transfer*, 96(4):443, 1974.

[180] Tetsu Fujii and Hideaki Imura. Natural-convection heat transfer from a plate with arbitrary inclination. *International Journal of Heat and Mass Transfer*, 15(4):755–767, 1972.

[181] Ayla Dogan, S. Baysal, and Senol Baskaya. Numerical analysis of natural convection heat transfer from partially open cavities heated at one wall. *Isi Bilimi Ve Teknigi Dergisi/ Journal of Thermal Science and Technology*, 29(1):79–90, 2009.

[182] A. M. Clausing, L. D. Lister, and J. M. Waldvogel. Combined convection from isothermal cubical cavities with a variety of side-facing apertures. *International Journal of Heat and Mass Transfer*, 32(8):1561–1566, 1989.

[183] E. Bilgen and A. Muftuoglu. Natural convection in an open square cavity with slots. *International Communications in Heat and Mass Transfer*, 35(8):896–900, 2008.

[184] F. Penot. Transfert de chaleur par convection naturelle dans une cavité rectangulaire isotherme ouverte sur une face. *Revue de Physique Appliquée*, 15(2):207–212, 1980.

[185] A. M. Clausing. An analysis of convective losses from cavity solar central receivers. *Solar Energy*, 27(4):295–300, 1981.

[186] a. M. Clausing. Convective Losses From Cavity Solar Receivers—Comparisons Between Analytical Predictions and Experimental Results. *Journal of Solar Energy Engineering*, 105(1):29, 1983.

[187] Patrick Le Quere, Joseph A.C. Humphrey, and Frederick S. Sherman. Numerical calculation of thermally driven two-dimensional unsteady laminar flow in cavities of rectangular cross section. *Numerical Heat Transfer*, 4(3):249–283, 1981.

[188] José Octavio Juárez, Jesús Fernando Hinojosa, Jesús Perfecto Xamán, and Manuel Pérez Tello. Numerical study of natural convection in an open cavity considering temperature-dependent fluid properties. *International Journal of Thermal Sciences*, 50(11):2184–2197, 2011.

[189] Éliton Fontana, Adriano Da Silva, and Viviana Cocco Mariani. Natural convection in a partially open square cavity with internal heat source: An analysis of the opening mass flow. *International Journal of Heat and Mass Transfer*, 54(7-8):1369–1386, 2011.

[190] Éliton Fontana, Claudia A. Capeletto, Adriano Da Silva, and Viviana C. Mariani. Three-dimensional analysis of natural convection in a partially-open cavity with internal heat source. *International Journal of Heat and Mass Transfer*, 61(1):525–542, 2013.

[191] Ge Song, Tor Bjørge, Jens Holen, and Bjørn F. Magnussen. Simulation of fluid flow and gaseous radiation heat transfer in a natural gas-fired furnace. *International Journal of Numerical Methods for Heat and Fluid Flow*, 7(2-3):169–180, 1997.

[192] Angela O. Nieckele, Monica F. Naccache, and Marcos S. P. Gomes. Numerical Modeling of an Industrial Aluminum Melting Furnace. *Journal of Energy Resources Technology*, 126(1):72, 2004.

[193] Noam Lior. The cooling process in gas quenching. *Journal of Materials Processing Technology*, 155:1881–1888, 11 2004.

[194] Olivier Macchion, Said Zahrai, and J. Bouwman. Heat transfer from typical loads within gas quenching furnace. *Journal of Materials Processing Technology*, 172:356–362, 03 2006.

[195] B. Wang, G.and Xiao, L. Zhang, K. Rong, and Q. Wang. Heat transfer coefficient study for air quenching by expenriment and cfd modeling. volume 2, pages 271 – 276, 2008.

[196] Bowang Xiao, Qigui Wang, Gang Wang, Richard D. Sisson, and Yiming Rong. Robust methodology for determination of heat transfer coefficient distribution in convection. *Applied Thermal Engineering*, 30(17):2815 – 2821, 2010.

[197] Yassine Bouissa, Davood Shahriari, Henri Champliaud, and Mohammad Jahazi. Prediction of heat transfer coefficient during quenching of large size forged blocks using modeling and experimental validation. *Case Studies in Thermal Engineering*, 13:100379, 12 2019.

[198] N. Zuckerman and N. Lior. Jet impingement heat transfer: Physics, correlations, and numerical modeling. *Advances in Heat Transfer*, 39(C):565–631, 2006.

[199] A.K. Mohanty and A.A. Tawfek. Heat transfer due to a round jet impinging normal to a flat surface. *International Journal of Heat and Mass Transfer*, 36(6):1639–1647, jan 1993.

[200] A. A. Tawfek. Heat transfer and pressure distributions of an impinging jet on a flat surface. *Heat and Mass Transfer*, 32(1-2):49–54, nov 1996.

[201] Manish Kumar Tiwari, Achintya Mukhopadhyay, and Dipankar Sanyal. Numerical simulation of optimal multiple-input, multiple-output control of jet impingement cooling of a glass plate. *Numerical Heat Transfer; Part A: Applications*, 46(4):401–424, 2004.

[202] Abubakar El-Jummah, Reyad Husain, Gordon Andrews, and John Staggs. Conjugate heat transfer computational fluid dynamic predictions of impingement heat transfer: The influence of hole pitch to diameter ratio x/d at constant impingement gap z. *Journal of Turbomachinery*, 136:121002, 12 2014.

[203] Makatar Wae-Hayee, Perapong Tekasakul, and Chayut Nuntadusit. Influence of nozzle arrangement on flow and heat transfer characteristics of arrays of circular impinging jets. *Songklanakarin Journal of Science and Technology*, 35(2):203–212, 2013.

[204] M. Michael Yovanovich. Four decades of research on thermal contact, gap, and joint resistance in microelectronics. *IEEE Transactions on Components and Packaging Technologies*, 28(2):182–206, 2005.

[205] M. G. Cooper, B. B. Mikic, and M. M. Yovanovich. Thermal contact conductance. *International Journal of Heat and Mass Transfer*, 12(3):279–300, 1969.

[206] B. B. Mikić. Thermal contact conductance; theoretical considerations. *International Journal of Heat and Mass Transfer*, 17(2):205–214, 1974.

[207] Dong Huan Liu and Xin Chun Shang. The physical-mechanism based high-temperature thermal contact conductance model with experimental verification. *Chinese Physics Letters*, 30(3):5–8, 2013.

[208] Hui Zhao, Abraham J. Salazar, and Dusan P. Sekulic. Analysis of fin-tube joints in a compact heat exchanger. *Heat Transfer Engineering*, 30(12):931–940, 2009.

[209] C. V. Madhusudana and L. S. Fletcher. Contact heat transfer - The last decade. *AIAA Journal*, 24(3):510–523, 1986.

[210] A Shapiro. LS-DYNA Features for Hot Forming. *FEA Information Engineering Journal*, 1(4):127–134, 2014.

[211] Fernando H. Milanez, Michael M. Yovanovich, and Marcia B.H. Mantelli. Thermal Contact Conductance at Low Contact Pressures. *Journal of Thermophysics and Heat Transfer*, 18(1):37–44, 2004.

[212] *Abaqus Analysis User's Guide, Version 6.12*, chapter 23.2.4 Rate-dependent plasticity: creep and swelling. ANSYS, Inc., 2012.

[213] *Abaqus Analysis User Subroutines Reference Manual, Version 6.12*, chapter 1.1.1 Rate-dependent plasticity: creep and swelling. Simulia, 2012.

[214] *Abaqus Analysis User's Guide, Version 6.12*, chapter 29.6.2 Choosing a shell element. Simulia, 2012.

[215] *Abaqus Analysis User's Guide, Version 6.12*, chapter 37.1.2 Contact pressure-overclosure relationships. Simulia, 2012.

[216] *Abaqus Analysis User's Guide, Version 6.12*, chapter 38.1.2 Contact constraint enforcement methods in Abaqus/Standard. Simulia, 2012.

[217] R. F. Muraca and J. S. Whittick. *Inonel Alloy 718 (2nd Edition)*. Western Applied research & development, Inc., 04 1972.

[218] *Abaqus Analysis User's Guide, Version 6.12*, chapter 36.3.6 Adjusting contact controls in Abaqus/Standard. Simulia, 2012.

[219] Quentin Sirvin, Vincent Velay, Rebecca Bonnaire, and L. Penazzi. Mechanical behaviour modelling and finite element simulation of simple part of Ti-6Al-4V sheet under hot/warm stamping conditions. *Journal of Manufacturing Processes*, 38:472–482, 02 2019.

[220] M. C. South, G. B. Wetherill, and M. T. Tham. Hitch-hiker's guide to genetic algorithms. *Journal of Applied Statistics*, 20(1):153–175, 1993.

[221] O.T. Bruhns and D.K. Anding. On the simultaneous estimation of model parameters used in constitutive laws for inelastic material behaviour. *International Journal of Plasticity*, 15(12):1311 – 1340, 1999.

[222] T. Harth, S. Schwan, J. Lehn, and F.G. Kollmann. Identification of material parameters for inelastic constitutive models: statistical analysis and design of experiments. *International Journal of Plasticity*, 20(8):1403 – 1440, 2004.

[223] Necmi Dusunceli, Ozgen U. Colak, and Coskun Filiz. Determination of material parameters of a viscoplastic model by genetic algorithm. *Materials & Design*, 31(3):1250 – 1255, 2010.

[224] Mitsuo Gen and Runwei Cheng. *Genetic Algorithms and Engineering Optimization*. Wiley Series in Engineering Design and Automation. John Wiley & Sons, Inc., Hoboken, NJ, USA, dec 1999.

[225] D. Hernandez and E. Milcent. Pyro-réflectomètre bicolore à fibres optiques pour mesures "in situ". *Journal de Physique III*, 5(7):999–1011, jul 1995.

[226] Frank M. White. *Fluid mechanics*. McGraw Hill, 2011.

[227] Richard C. Martineau, Ray A. Berry, Aurélia Esteve, Kurt D. Hamman, Dana A. Knoll, Ryosuke Park, and William Taitano. Comparative Analysis of Natural Convection Flows Simulated by Both the Conservation and Incompressible Forms of the Navier-Stokes Equations in a Differentially - Heated Square Cavity. (January):1–58, 2009.

[228] W. Versteeg, H. K and Malalasekera. *An Introduction to Computational Fluid Dynamics - a completer*. 2007.

[229] *Abaqus Analysis User's Guide, Version 6.12*, chapter 33.2.2 Initial conditions in Abaqus/CFD. Simulia, 2012.

[230] P. Spalart and S. Allmaras. A one-equation turbulence model for aerodynamic flows. *30th Aerospace Sciences Meeting and Exhibit*, (April 2015), 1992.

[231] V. Yakhot, S. A. Orszag, S. Thangam, T. B. Gatski, and C. G. Speziale. Development of turbulence models for shear flows by a double expansion technique. *Physics of Fluids A*, 4(7):1510–1520, 1992.

[232] Tsan-Hsing Shih, William W Liou, Aamir Shabbir, Zhigang Yang, and Jiang Zhu. A new k-ε Eddy Viscosity Model for High Reynolds Number Turbulent Flows. *Compurers Fluids*, 24(3):227–238, 1995.

[233] F. R. Menter. Two-equation eddy-viscosity turbulence models for engineering applications. *AIAA Journal*, 32(8):1598–1605, 1994.

[234] M. A. Leschziner. The Computation of Turbulent Engineering Flows with Turbulence-Transport Closures. In *Advanced Turbulent Flow Computations*, pages 209–277. Springer Vienna, 2000.

[235] Reassessment of the scale-determining equation for advanced turbulence models. *AIAA Journal*, 26(11):1299–1310, 1988.

[236] TH Von Karman. Mechanical similitude and turbulence. *National Advisory Committee for Aeronautics; Washington, DC, United States*, mar 1931.

[237] *ANSYS FLUENT 12.0/12.1 Documentation*, chapter 12.3.1 Near-Wall Mesh Guidelines. Simulia, 2009.

[238] William Sutherland. Lii. the viscosity of gases and molecular force. *The London, Edinburgh, and Dublin Philosophical Magazine and Journal of Science*, 36(223):507–531, 1893.

[239] William Sutherland. Lii. the viscosity of gases and molecular force, 1893.

[240] Thermal Conductivity of air. Engineering ToolBox - www.engineeringtoolbox.com.

[241] Specific Heat at Constant Pressure and Varying Temperature of air. Engineering ToolBox - www.engineeringtoolbox.com.

[242] *Abaqus Example Problems Manual, Version 6.12*, chapter 6.1.1 Conjugate heat transfer analysis of a component-mounted electronic circuit board. Simulia, 2012.

[243] Valérie Eveloy and Peter Rodgers. Prediction of electronic component-board transient conjugate heat transfer. *IEEE Transactions on Components and Packaging Technologies*, 28(4):817–829, 2005.

[244] *Abaqus Analysis User's Guide, Version 6.12*, chapter 6.6.2 Incompressible fluid dynamic analysis - SST k–omega turbulence model. Simulia, 2012.

Résumé

Etude et optimisation des conditions de refroidissement de pièces en alliage de titane obtenues par le procédé de formage superplastique

Les nouveaux programmes de l'industrie aéronautique font appel pour de nombreuses applications à des pièces en alliage de titane. C'est notamment le cas pour des pièces d'entrée d'air et carénages du mât réacteur. Certaines de ces pièces sont obtenues par mise en forme à chaud, notamment par le procédé de formage superplastique (SPF). L'analyse des différentes opérations de fabrication a mis en évidence des variabilités de conditions opératoires lors du défournement. Une des voies d'amélioration concerne une meilleure maîtrise des conditions de refroidissement et de manipulation des pièces après mise en forme à chaud. Cette thèse a pour but de développer un modèle éléments finis pour modéliser l'étape de défournement de tôles en alliage de titane Ti-6Al-4V formées avec le procédé SPF. Cette étape de refroidissement, combinée au chargement mécanique subi lors de l'extraction, génère des distorsions des pièces en fin de processus de fabrication. Une première étape a consisté à caractériser le comportement du matériau dans les conditions du procédé de façon à identifier un modèle de comportement qui est ensuite implémenté dans un code élément finis. Une deuxième étape a visé à reproduire, mesurer et caractériser les échanges thermiques en présence lors des différentes phases du défournement pour définir les conditions limites thermiques du modèle. Pour finir un modèle global du procédé de formage, défournement et détourage a été développé et appliqué à une pièce industrielle. Ce modèle a permis de mettre en évidence l'importance du chargement thermomécanique subi par la pièce au cours du défournement.

Mots-clés : Formage superplastique - SPF, Refroidissement, Echanges thermiques, Comportement mécanique, Alliage de titane, Simulation numérique

---

Abstract

Study and optimization of cooling conditions of titanium alloy parts manufactured by superplastic forming process

The new programs of aeronautical industry use titanium alloy parts for many applications. This is particularly the case for panels, air inlets and fairings parts of pylons. Some of these parts are obtained by hot forming, in particular by the superplastic forming process (SPF). The analysis of the different manufacturing operations has highlighted variability in the operating conditions during the unmolding process. One way of improvement is to a better control of the conditions of cooling and handling of the parts after the forming stage. The purpose of this thesis is to implement a finite element model to reproduce the pot-forming steps of sheet metal in Ti-6Al-4V titanium alloy formed with the SPF process. The cooling step combined with the mechanical loading encountered during the extraction generates distortions of the parts at the end of the manufacturing process. A first step consisted in characterizing the material behavior under the process conditions so as to identify a rheological law implemented in a finite element code. A second step aimed to reproduce, measure and characterize the heat transfers present during the different phases of unloading to define the thermal boundary conditions of the model. Finally, a global model of the forming, unmolding and trimming steps was developed and applied to an industrial part. This model has enabled to highlight the importance of the thermomechanical loading undergone by the part during the cooling and part removing operations.

Keywords: Superplastic Forming - SPF, Cooling, Heat transfers, Mechanical behavior, Titanium alloy, Numerical simulation